226p

(NASA-CR-135804) SPACE PROGRAMS SUMMARY NO. 37-12, VOLUME 2 FOR THE PERIOD 1 SEPTEMBER - 1 NOVEMBER 1961 (Jet Propulsion Lab.) 226 p

N73-74163

Unclas
00/99 19333

Space Programs Summary No. 37-12, Volume II

for the period September 1, 1961 to November 1, 1961

CLASSIFICATION CHANGE
TO = UNCLASSIFIED
By authority of [redacted] E.O. 11652
Changed by [redacted] Date 5-25-73

GT. F
W/ 9-1-67

jpl
JET PROPULSION LABORATORY
CALIFORNIA INSTITUTE OF TECHNOLOGY
PASADENA, CALIFORNIA

December 1, 1961

This document contains information affecting the national defense of the United States, within the meaning of the Espionage Laws, Title 18 U.S.C., Sections 793 and 794, the transmission or revelation of which in any manner to an unauthorized person is prohibited by law.

CONFIDENTIAL

CONFIDENTIAL

NATIONAL AERONAUTICS AND SPACE ADMINISTRATION
CONTRACT NO. NASw-6

Space Programs Summary No. 37-12, Volume II [U]

for the period September 1, 1961 to November 1, 1961

Copy No. JA 71

JET PROPULSION LABORATORY
CALIFORNIA INSTITUTE OF TECHNOLOGY
PASADENA, CALIFORNIA

December 1, 1961

CONFIDENTIAL

CONFIDENTIAL

Preface

The *Space Programs Summary* is a two-volume bimonthly publication of the Jet Propulsion Laboratory. Research and development activities conducted by JPL having specific application to space programs under the sponsorship of the National Aeronautics and Space Administration are reported in this publication. Unclassified and classified activities will be documented in Volumes I and II, respectively.

The projects reported herein were undertaken in partial fulfillment of National Aeronautics and Space Administration Contract NASw-6.

W. H. Pickering, *Director*
Jet Propulsion Laboratory

This document contains information affecting the national defense of the United States, within the meaning of the Espionage Laws, Title 18, U.S.C., Sections 793 and 794, the transmission or revelation of which in any manner to an unauthorized person is prohibited by law.

Space Programs Summary No. 37-12
Volume II

Copyright© 1962
Jet Propulsion Laboratory
California Institute of Technology

CONFIDENTIAL

Contents

PART ONE: RÉSUMÉ 1

I. Lunar Program 1

II. Planetary–Interplanetary Program 1

III. Deep Space Instrumentation Facility 1

PART TWO: LUNAR PROGRAM 2

I. *Ranger* 2

A. Systems 3
B. Guidance and Control 17
C. Engineering Mechanics 22
D. Propulsion 24
E. Lunar Capsule 25

II. *Surveyor* 50

A. System Design Summary 51
B. Scientific Instrument Payload 56
C. System Analysis 57
D. Flight Control 75
E. Electronics 88
F. Electrical Power Supply 116
G. Thermal Control 118
H. Engineering Mechanics 124
I. Propulsion 133
J. Spacecraft Vehicle and Mechanisms 139
K. Reliability and System Test 150
L. Missions Operations 162

PART THREE: PLANETARY–INTERPLANETARY PROGRAM 168

I. Program Status 168

A. Objectives 168
B. Missions 168
C. Program Activities 169

II. *Mariner* A 170

A. Guidance and Control 170
B. Engineering Mechanics 179

III. *Mariner* B 189

A. Guidance and Control 189
B. Engineering Mechanics 192

IV. *Voyager* 199

Contents (Cont'd)

PART FOUR: ADVANCED DEVELOPMENT 200

I. Lunar 200
A. Friction and Lubrication in a Space Environment 200
B. Development of Stable White Surfaces 200
C. Thermal Control Device Evaluation 201
D. Determining Relative Humidity in Sterilizing Gas Mixtures Containing Ethylene Oxide 202

II. Planetary–Interplanetary 205
A. Space Sciences 206
B. Secondary Power 207
C. Engineering Mechanics 212
D. Propulsion 213

References 221

Editor's Note:

Additional documentation of the Lunar and Planetary–Interplanetary Programs and material on the DSIF can be found in Volume I of this summary.

PART ONE
RÉSUMÉ

I. Lunar Program

12085

During this reporting period the major *Ranger* effort was involved with two unsuccessful efforts to launch *Ranger* RA-2 at AMR. Just prior to the third launch attempt, all effort to make the October 20 to 26 firing period was cancelled as a precautionary measure, based upon information concerning the inflight failure of an *Agena* the preceding night. This exercise at the Cape, of necessity, made certain demands upon the *Ranger* RA-3 and -4 manpower; however, these operations are still progressing on schedule.

II. Planetary – Interplanetary Program

A slippage in the schedule of the *Atlas–Centaur* vehicle, announced during September 1961, resulted in the cancellation of the *Mariner* A project and a reprogramming of the *Mariner* B project. To provide a mission to Venus in 1962, the *Mariner* R project was initiated, with a reduced weight spacecraft based on *Mariner* A and *Ranger* technology for use with the *Atlas–Agena* B vehicle. This new *Mariner* B design, to be used with the *Centaur* vehicle, is intended to be launched at all Mars and Venus opportunities in the period 1964 to 1967.

III. Deep Space Instrumentation Facility

System tests are presently being made on the newly installed Cassegrain feed system at Goldstone. To improve the performance of the phase-lock receiving system at Goldstone, a redesign of the unit is underway. A site has been selected at Goldstone for the large antenna of the Advanced Antenna System and supporting studies on feed and structural designs are being made.

PART TWO
LUNAR PROGRAM

I. *Ranger*

Ranger spacecraft RA-2, *Agena* 6002, and *Atlas* 117D were mated for flight on October 18, 1961. When the spacecraft power was turned on for on-pad checks, a malfunction in the telemetry encoder appeared, resulting in the loss of two binary data channels. The spacecraft was returned to the hangar where the defective module was replaced and the spacecraft was remated in time for the first scheduled launch attempt on the night of October 19. The countdown progressed smoothly until $T-45$ minutes, when an electrical malfunction was discovered in the *Atlas* and the count was terminated. The trouble was later traced to a faulty cable splice.

The flight was rescheduled for October 22 and then postponed to October 23 when it was decided to return the spacecraft to the hangar for replacement of some components in an effort to reduce the magnetic field at the magnetometer. During this period, components of the Lyman-alpha experiment were also exchanged to remove a source of intermittent noise.

The second countdown again proceeded smoothly to about $T-40$ minutes, when another cancellation was required because of a leak in the *Atlas* vernier engine hydraulic system.

The scheduling of the next launch attempt was complicated by time requirements for the *Atlas* vernier repair and by interference with other projects on the range. It was finally possible to schedule for October 25; preparations for the countdown had started when word was received from Lockheed that the *Agena* could not be cleared for launch, due to the inflight failure of a *Discoverer* on the previous day. Telemetry data showed abnormal drops in hydraulic system pressure, resulting finally in loss of engine gimbal control.

Pending further investigation of the *Agena* hydraulic problem, the flight of *Ranger* RA-2 was postponed until November 18, on which date it was launched into a low Earth orbit. An *Agena* guidance malfunction prevented achievement of the desired elliptical trajectory.

For *Rangers* RA-3, -4, and -5, the primary effort has been to bring the scheduled PTM operations to a successful conclusion. Efforts are continuing for a better understanding of certain specified spacecraft characteristics and for maintenance of RA-3 and -4 operations on schedule. Basic testing of RA-3 spacecraft has been completed and preparations are now being made for the final system test prior to shipment to AMR. This basic testing included system tests, temperature–vacuum tests in the space simulation chamber, and match-mate test with the flight shroud and adapter. In addition, measurement of weight, center-of-gravity, and moments-of-inertia have been completed. The initial dummy runs were very satisfactory and the last two were cancelled.

Ranger RA-4 operations consisting of assembly, subsystem test, and calibration have also been progressing satisfactorily, although there are several areas where flight hardware delivery is behind schedule.

A. Systems

1. Spacecraft Flight Performance

The following is a summary of the inflight performance of the *Ranger* RA-1 spacecraft. Part *a* is devoted to a flight summary which describes certain aspects of the trajectory, the flight sequence, and spacecraft telemetry which are of particular importance in determining how the various systems of the spacecraft actually performed during the lifetime of the mission. Part *b* summarizes the performance of each of the major spacecraft systems and certain subsystems as well as the engineering experiments.

a. Flight summary. *Ranger* RA-1 was launched from AMR Cape Canaveral on August 23, 1961 at 10.26 seconds after 5:04 AM, EST. The GMT of liftoff was 235:10:04:10.26 Z (All subsequent references to time will be in GMT.) The ascent phase and injection into parking orbit were normal. The spacecraft shroud was ejected as programmed. The spacecraft transponder was kept in two-way lock with the launch checkout telemetry trailer (LCTT) for 7½ minutes after liftoff except for an unexplained momentary dropout.

The *Agena* restart sequence began at the proper time but the fuel valve failed to operate and ignition did not occur. The result of this was the expulsion of sufficient oxidizer gas to add a velocity increment of approximately 70 meters/sec. The subsequent electrical and mechanical separation of spacecraft from the *Agena* appears to have been normal. The spacecraft was injected at 10:27.23 Z into a satellite orbit with a period of 91.15 minutes and apogee and perigee of 313.3 and 105.6 statute miles, respectively. By August 28 (4.6 days later), the last day on which the spacecraft signal was tracked, the orbit had decayed to a period of 89.19 minutes with apogee and perigee of 202.9 and 96.2 statute miles, respectively.

The spacecraft controller is programmed to issue a sequence of ten discrete commands to different units in the spacecraft within 6 hours after injection. A list of these commands and the programmed times is given in Table 1.

The spacecraft can also accept commands (roll override, hinge override, and antenna transfer) from the ground as a backup for Controller Commands 5 and 8 or to correct certain nonstandard conditions.

Controller Command 2 was programmed at the time indicated as the result of an incident which occurred during the countdown on August 3. When this command was sent from the blockhouse, it apparently caused the controller to issue all the other programmed commands. Subsequently, this step was eliminated from the countdown procedure and the time of the programmed command delayed in order to minimize the effect in case of a similar occurrence during flight.

Table 1. *Ranger* command sequence

Number	Command	Time from liftoff, min
1	Increase transmitter power	30.3
2	Turn-on scientific instruments high-voltage	78.7
3	Extend particle analyzer boom and solar panels	33.6
4	Start Sun acquisition	58.7
5	Start Earth acquisition	90.3
6	Change data encoder rate gyro scale	115.3
7	Open semiconductor detector aperture	203.7
8	Switch transponder transmitter to high-gain antenna	247.0
9	Reduce modulation on beacon transmitter	363.7
10	Turn-on friction-lubrication experiment	367.0

Telemetry records indicate that all programmed events took place. The nature of the orbit was such that it is impossible to determine the exact time of any of the programmed commands. Command 1 occurred before the Mobile Tracking Station (DSIF 1) in South Africa acquired the spacecraft signal. At the time of Command 3 the signal was too noisy. All the other commands occurred during periods when the spacecraft was not in view of any tracking station. In each case, however, subsequent telemetry indicated that each commanded function did occur within the proper time interval.

Probably the most serious effect of the satellite trajectory was the fact that the spacecraft was in the Earth's shadow about 45% of the time during each orbital revolution. Each time the spacecraft returned to the sunlight, the attitude control system, if operating normally, would commence its acquisition procedure with a consequent heavy drain on the supply of nitrogen gas used for activation. This gas supply was exhausted within 19 hours after injection, sometime after the 5th orbit (the last orbit tracked on August 23) and before the 13th orbit (the first orbit tracked on August 24.)

A number of apparently related conditions appeared with the first data obtained on August 24, lasted throughout all passes tracked on that day (up to the 21st orbit) and did not show up again after that. (1) The attitude control (A/C) power converter was overloaded, indicated by the converter monitor voltage reading of zero. (2) Spikes appeared on the analog trace of all the attitude control measurements. (3) Except for the spikes, all the attitude control measurements (rates, positions, and light

detector) had null values (due to the absence of dc power). (4) The 400-cps tone on Channel 1 exhibited a considerable degree of what can best be described as amplitude modulation. The modulation was variable, especially in amplitude, with at least two identifiable frequency components present at times. (5) The data encoder commutator was stepped faster than normal by the controller generally increasing its speed to a maximum error of about 4% on the 15th and 16th orbits, then decreasing back to normal by the 20th orbit. This apparently was done without skipping any segments. The Lyman-alpha telescope scanning times were also affected and it is quite likely the scientific data automation system (DAS) was similarly affected, but this has not yet been established.

The frequency of the spikes, occurring every 0.41 to 0.42 second, corresponds to drops in amplitude of the 400-cps signal. It is believed that both phenomena resulted from the A/C converter overload interrogation process. The cause of some of the other things which were happening is still not known. It would seem logical to assume that the excessive current requirements in the A/C system which caused the converter to go into overload are the result of loss of nitrogen gas but this cannot be proved. Nor does it explain why the overload condition subsequently disappeared.

The ground-to-spacecraft command link was successfully tested on August 25. The ground transmitter at Goldstone Az-El site (DSIF 3) switched the transponder transmitter from the high- to the low-gain omnidirectional antenna during the 30th orbit. During the following orbit the same station switched the 3-watt transmitter to the high-gain antenna and back again. Then the LCTT transmitter switched it back to the high-gain antenna where it remained for the rest of the flight. The reason for leaving it on the high-gain antenna was that the received signal level at the DSIF stations was usually higher in this mode, even when locked on a side lobe, than it was when the transponder was transmitting over the low-gain antenna with its −10-db coupler.

On August 26 the hinge and roll override commands were transmitted by DSIF 2 at Goldstone but there was no way to determine their effect on the spacecraft since the spacecraft was not stabilized due to the loss of A/C gas, and hence the rate gyros were usually saturated.

The first indication of the main battery failing was on the 61st orbit on August 27, approximately 91 hours after liftoff. The last good telemetry was recorded 40 minutes later at 05:49 Z. After that the ¼-watt transmitter, which has its own battery power supply, continued to operate, usually with no modulation, until after the 83rd orbit, the last pass tracked on August 28. During this period sporadic modulation appeared on the beacon signal when the solar panels were supplying enough current to activate the data encoding system. The transponder signal was occasionally picked up at these times. The last signal received from the spacecraft was a momentary one from the transponder at 23:53.36 Z on August 28 during the 89th orbit. Apparently the beacon battery was dead by then.

The orbit of *Ranger* RA-1 created serious problems in recovering and reducing telemetry data. Of a total of 36 spacecraft engineering measurements, all of which are sampled by commutation, 23 are sampled by the data encoder only once every 1000 seconds. All of the power system and temperature measurements are included in this group. Proper reduction of these telemetered measurements for evaluation requires that the ground decommutator be synchronized with the spacecraft commutators. This is done by using the 400-cps tone on IRIG Channel 1 and synchronization tones for each of the three commutator speeds. Since the sync tone for the slowest rate measurements (Rate 3) is sampled only once every 1000 seconds, and because the station passes were always less than 10 minutes or 600 seconds, the ground decommutators were seldom synchronized with the spacecraft Rate 3 commutator decks. As a result these samples usually had to be decommutated by hand.

During the 92-hour lifetime of the main battery (through 61 orbital revolutions) portions of 39 orbits were tracked by the DSIF stations and the LCTT. The total tracking coverage was approximately 500 minutes including all the periods when the spacecraft signal was lost or below receiver threshold in the middle of a pass. A reasonable estimate of the total amount of useful telemetry obtained would be 300 to 400 minutes. Table 2 shows a breakdown of this coverage by days:

b. Subsystem performance.

General system performance. The overall performance of the *Ranger* RA-1 spacecraft was successful considering the nature of the orbit flown. In most cases where an element of the spacecraft did not perform as it was designed to do, it was because it was not designed to operate in a near-Earth environment. No malfunctions were detected that would warrant making any design or hardware changes in *Ranger* RA-2.

Space sciences subsystems. The value of most of the scientific experiments was seriously reduced because of proximity to the Earth and lack of attitude stabilization. The data automation system (DAS) exhibited occasional minor malfunctions such as premature program reset,

Table 2. *Ranger* tracking coverage

Date	Tracking time, min	Stations
8/23	41	DSIF 1, 2, 3
8/24	109	DSIF 1, 2, 3, 5, LCTT
8/25	145	DSIF 1, 2, 3, 4, 5, LCTT
8/26	151	DSIF 1, 2, 3, 4, 5, LCTT
8/27	53[a]	DSIF 2, 3, 4, LCTT
	Total 499	

[a] Before battery failure.

data register reset, and extra counts in the frame-count register. The scientific instruments, in general, performed as expected considering their operating environment. The magnetometer was saturated by the Earth's field throughout the mission.

Telecommunications subsystems. All available information indicates that all elements of the spacecraft communications system performed within their design tolerances. This includes the transponder, data encoder, command system, and ¼-watt transmitter. The high-gain antenna drive indicated a higher power output than specified when the transponder was switched on to the high-gain antenna.

Guidance and control subsystems. The spacecraft controller apparently issued all programmed commands in the proper sequence but the exact times cannot be verified. It also provided a 1-pps signal to the data encoder for commutator stepping with a high degree of accuracy except on the second day of flight when the stepping rate increased. The same is true of the 1 pulse per 1000 seconds provided to the Lyman-alpha telescope. The accuracy of the 1-pps signal to other scientific instruments has not been thoroughly checked.

The performance of the attitude control system was difficult to evaluate because of the limited amount of telemetry obtained before gas depletion. Sun acquisition, as indicated by solar panel current measurements, was only observed on one pass. On other occasions it appeared that the Earth sensor had locked on the Sun. No valid conclusions can be drawn concerning limit cycle performance, antenna pointing accuracy or gas consumption rate. Measurements of the rate gyros showed that they were usually saturated due to spacecraft tumbling after the nitrogen gas was gone.

Because the spacecraft was seldom oriented toward the Sun, the solar panels provided only intermittent power, resulting in an almost continuous drain on the launch back-up battery. This main battery's lifetime of about 92 hours is considered normal in view of the system power demands. The few correlated measurements of panel current and temperature available indicate normal performance under the circumstances prevailing.

The power conversion and distribution system apparently functioned normally. The overload in the attitude control dc-to-dc converter on August 24 was probably caused by excessive power demands in that system resulting from gas depletion and marginal overload design conditions. Some of the other symptoms previously described, which occurred simultaneously, may have been caused by noise generated by the A/C converter's interrogation of its load.

The operating lifetime of the ¼-watt transmitter battery was less than 5.6 days, compared to a design value of 10 days. Whether this was due to a discrete failure, or the battery life was reduced by its unexpected environment, is not known.

Not enough data was obtained to make any definite evaluation of the advanced development solar cell experiment.

Engineering mechanics subsystems. Shock, vibration, and acceleration levels during boost phase of the mission were generally as expected. Spacecraft separation, both electrical and mechanical, was apparently normal. The erection of the SCREPA boom and solar panels was apparently normal.

Temperature measurements of elements within the main hexagonal frame of the spacecraft showed good agreement with values calculated for the actual orbit. The temperature of such external elements as the solar panels, Earth sensor, and magnetometer showed considerably more variation than the hex temperatures but this is to be expected considering the orbit.

The friction-lubrication experiment was designed to measure coefficients of friction in the near-total vacuum of space. Although the value of the data obtained was greatly reduced due to the low-altitude orbit, the experiment apparently performed normally under the circumstances. Its self-contained battery power supply operated longer than it was designed to do.

2. Trajectory Analysis

Ranger RA-3 and -4 standard trajectories have been updated to reflect the changes in mission philosophy since the generation of the standard trajectories reported in Reference 1. The most significant changes have been the consideration of additional launch dates and the extension of range launch azimuths. In addition, the impact

locations have been changed to increase the performance of the seismometer experiment.

From the experience gained during the launching of the *Ranger* RA-1 it has become evident that increased launch periods and launch windows for *Ranger* RA-3 and -4 missions would be of interest. This requires that all affected mission constraints be re-evaluated. A study is now being conducted to determine the extent of these changes.

All months from January to May 1962 are being considered to cover the possibility of slippage in the *Ranger* RA-3 or -4 launch dates. June and subsequent months are precluded because of conflict with the scheduled *Mariner* R mission launch preparation. A launch period of 6 days encompasses all possible launch days in each lunar month under consideration. Further increase of the launch period in any lunar month would result in serious degradation of the mission objectives. A launch azimuth range of 90 to 114 degrees is being considered to extend the launch window during each launch day.

Some of the characteristics of the *Ranger* RA-3 and -4 updated standard trajectories are presented in Table 3 for all of the launch dates under consideration.

Previously the *Ranger* RA-3 and -4 standard trajectories were designed so that the probe would descend vertically onto the lunar surface. This would give the most desirable pictures from the television experiment. These trajectories impacted approximately 42 degrees from the Earth's projection on the Moon's surface giving an acceptable Earth–Moon–probe angle for the seismometer experiment at impact. For Earth–Moon–probe angles greater than 45 degrees the seismometer antenna patterns indicate the transmission of useful seismometer data is doubtful because librations of the Moon will cause the Earth–Moon–probe angle to vary after lunar impact. A typical result is shown in Figure 1. Clearly the Earth–Moon–probe angle is undesirable for large portions of the lunar month after impact.

The impact locations can be biased from the vertical impact locations to minimize the Earth–Moon–probe angle after lunar impact. These biased trajectories result in an unretarded velocity vector at lunar impact which is canted to the local vertical. This degrades the pictures from the television experiment.

Tradeoffs between the seismometer and television experiments were considered and a bias angle of 14 degrees (Fig 2) was selected as a compromise. This bias angle gives an unretarded velocity vector at impact which is canted 10 degrees from the local vertical. A bias angle

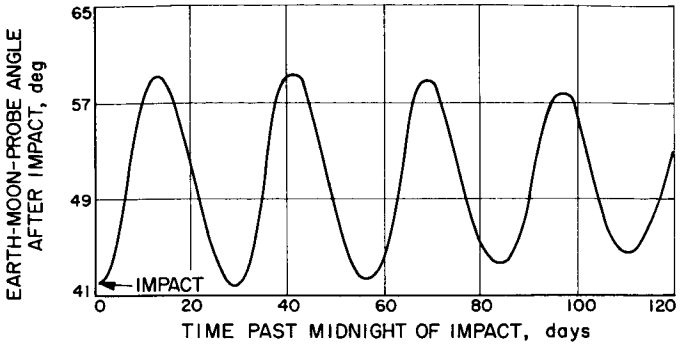

Figure 1. Effects of lunar libration on the Earth–Moon–probe angle after impact

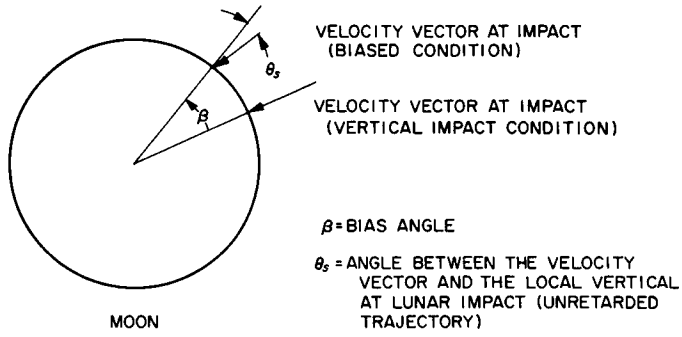

Figure 2. Lunar impact parameters

of 14 degrees is used in the updated *Ranger* RA-3 and -4 trajectories.

3. Test and Operations

a. Ranger *RA-1.* The assembly and test schedule for *Ranger* RA-1 spacecraft is shown in Table 4. Additional data on *Ranger* RA-1 testing and space simulation can be found in *SPS 37-8* through *-11.* The remaining tests performed on RA-1 spacecraft will be reviewed in this summary; the flight test will not be included.

Magnetometer tests. The spacecraft was taken to the Malibu low-field magnetic site (Fig 3) to measure its magnetic flux and to determine the flux components of the spacecraft in its operational modes. During the Malibu tests, on RA-1, it was found that the spacecraft battery was not within its designed specification; however, there was not sufficient time to change the design, but a redesign was accomplished for the RA-2 spacecraft. A modification to the scientific transformer–rectifier (T–R unit), determined to be necessary during the Malibu test on the PTM, was evaluated and found to be adequate. The RA-1 flight spacecraft permanent magnetic flux density as seen by the magnetometer was determined to be

Table 3. *Ranger* RA-3 and -4 trajectories

Mission	Launch conditions			Injection conditions			Impact conditions		
	Date	Azimuth, deg	GMT	Geocentric latitude, deg	Geocentric longitude, deg	GMT	Selenocentric latitude, deg	Selenocentric longitude, deg	Unretarded velocity, meters/sec
RA-3	1-22	90	14.59	−10.5	21.6	15.11	−2.3	329.3	2684.9
		114	17.56	−11.5	339.5	17.93	−3.0	328.6	2692.2
	1-23	90	15.83	−6.4	14.0	16.32	−3.4	327.5	2684.9
		114	18.67	−7.4	333.8	19.01	−4.0	326.9	2692.2
	1-24	90	17.07	−2.1	355.4	17.52	−4.7	326.1	2684.8
		114	19.77	−3.1	328.3	20.08	−5.3	325.5	2692.2
	1-25	90	18.32	2.1	359.3	18.73	−5.8	325.0	2684.8
		114	20.88	1.0	323.0	21.16	−6.5	324.4	2692.2
	1-26	90	19.58	6.1	352.3	19.96	−6.7	324.2	2684.7
		114	22.00	4.9	317.9	22.25	−7.4	323.6	2692.2
	1-27	90	20.84	9.6	345.8	21.19	−7.2	323.9	2684.7
		114	23.12	8.3	313.4	23.35	−8.0	323.3	2692.1
RA-3 alt	2-21	90	16.10	0.6	1.8	16.52	−5.6	326.0	2684.9
		114	18.71	−0.4	324.8	19.00	−6.2	325.3	2692.1
	2-22	90	17.34	4.6	354.8	17.73	−6.5	325.1	2684.9
		114	19.81	3.5	319.7	20.07	−7.2	324.5	2692.0
	2-23	90	18.58	8.3	348.2	18.94	−7.1	324.6	2684.9
		114	20.91	7.1	315.1	21.15	−7.8	324.1	2692.0
	2-24	90	19.81	11.4	342.4	20.14	−7.2	324.4	2684.9
		114	22.00	10.0	311.2	22.22	−8.1	323.8	2691.9
	2-25	90	20.99	13.7	337.8	21.30	−7.0	324.4	2685.0
		114	23.06	12.1	308.3	23.26	−8.1	323.9	2691.6
	2-26	90	22.05	14.9	335.3	22.35	−6.5	324.6	2685.3
		114	24.05	13.2	306.8	24.24	−7.6	324.2	2691.2
RA-3 alt	3-23	90	17.74	11.0	343.2	18.07	−7.4	324.3	2670.2
		114	19.96	9.6	311.7	20.18	−8.2	323.7	2676.9
	3-24	90	18.92	13.5	338.3	19.23	−7.2	324.3	2670.2
		114	21.01	11.9	308.5	21.22	−8.2	323.8	2676.6
	3-25	90	20.00	15.0	335.2	20.30	−6.7	324.3	2670.4
		114	22.01	13.3	306.6	22.20	−7.9	323.9	2676.2
	3-26	90	20.92	15.3	334.6	21.21	−6.0	324.5	2670.6
		114	22.90	13.4	306.3	23.09	−7.2	324.2	2675.6
	3-27	90	21.64	14.2	336.8	21.95	−5.1	324.8	2670.9
		114	23.67	12.4	307.9	23.87	−6.3	324.6	2675.1
	3-28	90	22.18	11.9	341.5	22.51	−4.0	325.3	2671.0
		114	24.33	10.0	311.1	24.54	−5.2	325.2	2674.5
RA-4	4-21	90	18.05	15.3	334.5	18.35	−7.1	323.3	2648.4
		114	20.06	13.7	306.0	20.25	−8.2	322.8	2654.1
RA-4 alt	4-22	90	19.01	15.8	333.4	19.30	−6.7	323.7	2648.6
		114	20.97	14.1	305.4	21.16	−8.0	323.3	2653.6
	4-23	90	19.76	15.0	335.0	20.06	−5.7	323.9	2648.9
		114	21.76	13.2	306.6	21.96	−7.0	323.7	2653.0
	4-24	90	20.33	13.0	339.3	20.64	−4.7	324.2	2649.1
		114	22.42	11.2	309.5	22.63	−5.9	324.1	2652.5
	4-25	90	20.74	9.9	345.3	21.09	−3.4	324.7	2649.2
		114	22.98	8.1	313.7	23.21	−4.6	324.6	2652.2
	4-26	90	21.06	5.8	352.7	21.44	−2.0	325.3	2649.4
		114	23.45	4.1	319.0	23.71	−3.0	325.3	2651.9
	5-21	90	18.50	14.0	337.2	18.81	−4.9	322.7	2625.3
		114	20.56	12.3	307.9	20.76	−6.2	322.6	2628.6
	5-22	90	18.94	11.1	343.1	19.27	−3.8	323.3	2625.4
		114	21.13	9.4	312.0	21.36	−5.0	323.3	2628.2
	5-23	90	19.26	7.2	350.3	19.63	−2.4	324.0	2625.5
		114	21.61	5.5	317.2	21.86	−3.5	324.0	2627.9
	5-24	90	19.52	2.7	358.2	19.93	−1.5	324.8	2625.6
		114	22.02	1.0	323.0	22.30	−2.6	324.9	2627.8
	5-25	90	19.75	−2.2	6.6	20.20	0.2	325.6	2625.6
		114	22.40	−3.9	329.3	22.72	−0.8	325.7	2627.7
	5-26	90	19.96	−7.1	15.3	20.45	1.5	326.6	2625.6
		114	22.77	−8.8	335.8	23.12	0.5	326.8	2627.8

Table 4. *Ranger* RA-1 assembly and test schedule

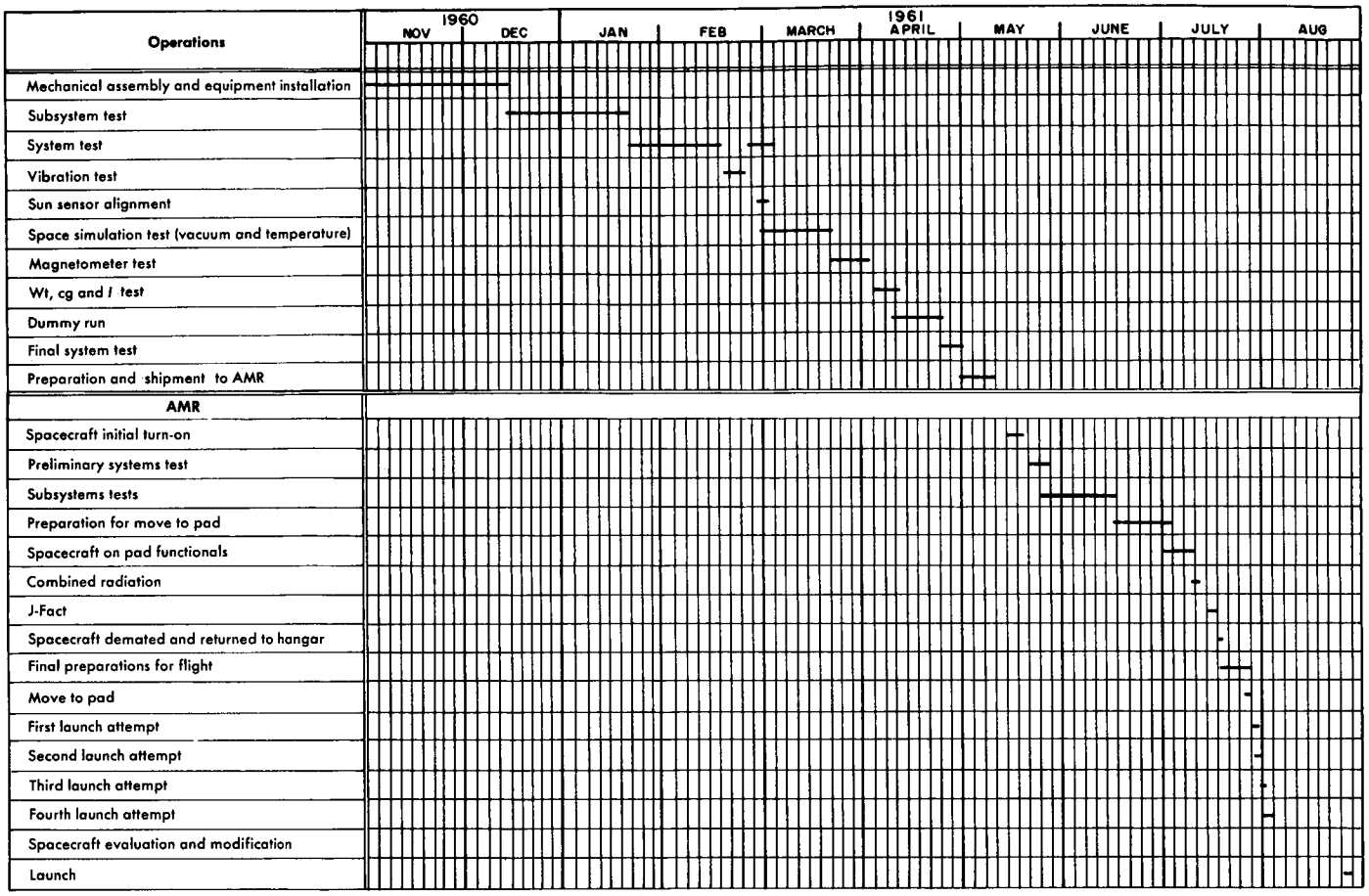

approximately 4 gamma, which was higher than desirable, but adequate to achieve a meaningful measurement in an interplanetary field.

To assure that the permanent magnetic flux density of the spacecraft had not changed due to components being changed, magnetic calibrations of the spacecraft were performed at AMR. The spacecraft was mounted on a specially prepared turntable. A station magnetometer was mounted at a fixed distance from the spacecraft. The spacecraft was then rotated about the roll axis and the short-term variations of the fixed station magnetometer were attributed to the permanent magnetic flux density component normal to the roll axis and the induced field, which had been low during the Malibu tests. The spacecraft was then removed from the calibration fixture, the observed change in the reading of the station magnetometer being recorded as the permanent field of the spacecraft along the roll axis. It was necessary that this be accomplished in a short period of time to avoid local variations in the Earth's field. To validate subsequent data from the spacecraft, another station magnetometer monitored the Earth's field and its control information was used to correct the spacecraft data for local variations. These measurements were in good agreement with the data obtained at the Malibu site.

Weight, center-of-gravity, and moment-of-inertia. The spacecraft was set up in a near-flight configuration for the weight, center-of-gravity, and moment-of-inertia tests. The major deviation from flight configuration was the lack of launch and back-up batteries. The center-of-gravity was determined in the *XZ* and *YZ* planes. The moments-of-inertia were determined about the *X-X*, *Y-Y* and *Z-Z* axes with those of the *X-X* and *Y-Y* taken about arbitrary but known distances from spacecraft Station 500. The spacecraft weight was determined by using an electronic weighing kit employing a load cell with a readout in micro-in./in.; the readout was then converted to pounds.

Dummy runs. The primary objectives of this series of tests was to check out the final countdown procedure, to acquaint the operators and evaluation personnel with the

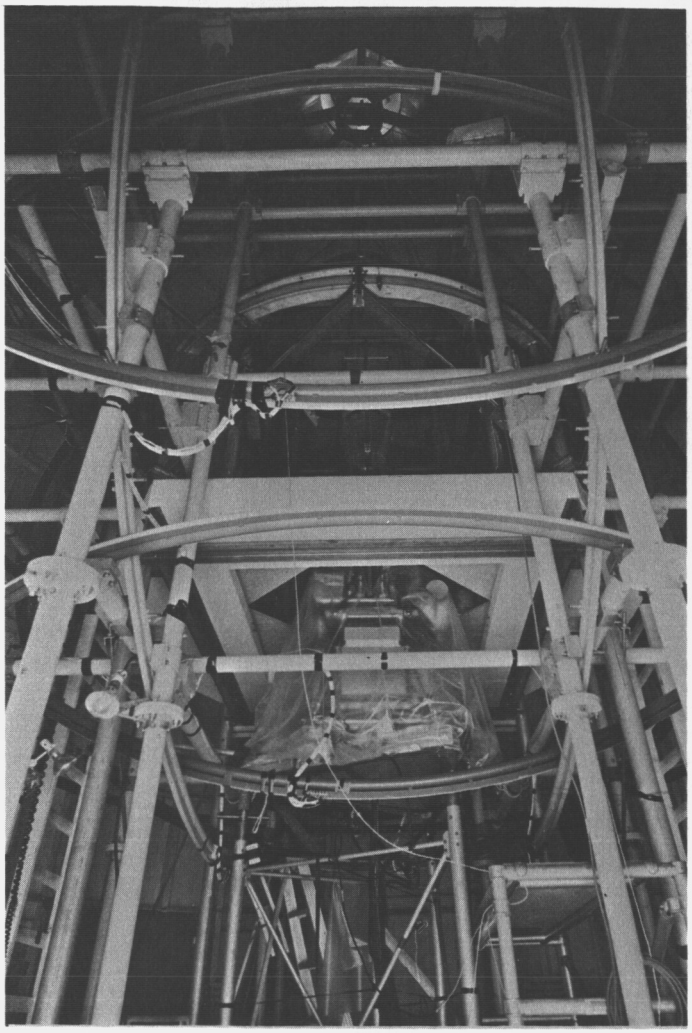

Figure 3. Magnetometer test setup

spacecraft in its launch configuration and to verify the compatibility among the blockhouse, spacecraft, hangar, and launch checkout trailers.

The blockhouse equipment was designed to provide essential controls: e.g., applications of spacecraft power, and a minimum of functional monitoring. The main spacecraft evaluation took place in the hangar or spacecraft checkout facility (SCF) which received information either via hard lines interconnecting with the spacecraft or through an RF telemetry link. The launch checkout station consisted of an RF trailer containing both a transmitter and associated receiver for purposes of evaluating the spacecraft communication system. The launch checkout telemetry trailer supported the RF trailer and spacecraft in providing real-time and tape memory storage of data. All of the equipment was brought together to support RA-1 dummy runs in a launch configuration.

Three dummy runs were performed during which operating procedures were developed by extensive revision of existing rough drafts. The final procedure used in the actual AMR countdown was a result of the dummy run procedure revisions.

The launch direction team became acquainted with the spacecraft and its modes of operation, and performed as a well-disciplined organization during and prior to the final countdown.

Final system test. Evaluation of the spacecraft prior to shipment to AMR required that a complete system test be performed. Only minor deficiencies were detected during this test, and the spacecraft was shipped to AMR on April 6, 1961.

Prelaunch test and operations. Upon the arrival of the RA-1 spacecraft at AMR, a comprehensive survey was made of the spacecraft to determine the nature and extent of any damage which may have occurred to the spacecraft during shipment to AMR. No damage was found. After assembly, the spacecraft was placed on the system test fixture and connected to the ground support equipment (GSE).

Grounding, wiring integrity, and power turn-on checks (*SPS 37-8*) were then performed before undertaking the preliminary system test. The preliminary system test was performed to obtain a quick-look evaluation of how well the spacecraft was performing functionally. The results of the preliminary test allowed proper proportioning of the scheduled time for subsystem checkouts.

Subsystem checkouts provided for rechecking of telemetry and validating calibrations of the scientific experiments. These checkouts also enabled verification of the spacecraft's permanent magnetic field, mapped at the Malibu magnetometer site.

After completing all subsystem testing, the spacecraft launch and backup battery and the ¼-watt transmitter batteries were installed. The spacecraft was then readied for a complete system test prior to performing the first on-launch-pad spacecraft checkout. After this system test and corrections of the deficiencies detected, the final mechanical work (e.g., installation of the live firing squibs) was performed. The spacecraft was finally installed on the flight *Agena* adapter and the aerodynamic shroud installed. The spacecraft was then purged with dry nitrogen and then moved to Launch Complex 12 where it was mated with the *Agena* on top of the *Atlas* booster vehicle.

Approximately 1 week was then allowed for performing spacecraft functional tests. These tests were used to

study the spacecraft in its new environment and to establish the actual AMR countdown procedure for RA-1. Upon completion of the spacecraft functional tests, a combined RF interference test was performed. No RF interference was noted. A joint flight acceptance test (J-Fact) was then performed. The purpose of this test was to demonstrate to AMR that all participating agencies (GD/A, LMSC, and NASA/JPL) would work together without interference. The J-Fact was completed and the spacecraft was returned to Hangar AE for its final functional and mechanical checkouts. Finally, in the Hangar AE, after installation of flight batteries and flight solar panels, a final systems test was performed and a careful mechanical inspection *(final spacecraft button-up)* was performed. The spacecraft was then certified as being in a flight-ready state, after which it once again was installed on the flight adapter, the aerodynamic shroud installed, the spacecraft purged with dry nitrogen and returned to the launch complex, 2 days prior to launch. An on-pad electrical checkout was again made.

The first launch attempt was made on July 29, 1961 but was scrubbed at 0502 EST due to electrical power outages at AMR. The second launch attempt was made on July 30, but had to be cancelled due to a leak in the spacecraft attitude control gas system. The spacecraft was again returned to Hangar AE when the defective gas pressurization was replaced with a new bottle and associated regulator. The spacecraft was returned to the launch complex and time was picked up on Countdown 3 at 1900 EST on July 31. The third launch attempt was cancelled when the *Atlas* booster vehicle experienced difficulty with a Lox tanking valve. On August 1 time was picked up on Countdown 4 which again had to be scrubbed because of multiple spacecraft controller commands, when Command 2 was issued. The spacecraft was returned to Hangar AE and extensive troubleshooting undertaken which resulted in system field modifications to prevent a recurrence of this failure. On Agust 23, 1961 at 0504 EST RA-1 was launched from AMR.

b. **Ranger *RA-2.***

Prelaunch operations. The period of operations starts with the arrival of the spacecraft at AMR and finishes with the first scheduled launch period. The spacecraft arrived at Hangar AE, AMR, on the morning of August 25, 1961. The RA-2 flight spacecraft was moved to the system test fixture and updated to the final flight configuration. After system grounding checks were performed, power was applied to the spacecraft (September 31), and a satisfactory power survey was performed.

On September 6, 1961 the first system test of RA-2 at AMR was performed. The following discrepancies were noted: (1) Attitude control subsystem; when Command 4 (Sun acquisition) was activated, a negative roll valve light came on at the GSE, indicating that a valve was blowing-by gas. This function should have been initiated by Command 5. The GSE electronics were checked out in the laboratory, and the spacecraft attitude control modules were replaced. (2) Scientific subsystem; the Lyman-alpha telescope would not start scanning upon coded initiation from the timer-controller. The three 1000th second pulses from the timer-controller were too narrow for proper initiation of the Lyman-alpha telescope scan; hence controller Set 5 was replaced with Set 9.

Telemetry and scientific subsystem calibrations were started on September 7. Telemetry calibrations of the scientific subsystem continued through September 15.

System Test 2 of RA-2 at AMR was performed on September 18; during this test the following discrepancies were noted: (1) GSE in the communications and data automation system (DAS) observed noise which caused phase errors leading to out-of-sync conditions. It was determined that the noise transients on the 60-cps primary line voltage supply had affected all hangar checkout areas at AMR. (2) Scientific subsystems noted one procedural difficulty in the excitation of the cadmium sulfide detector, as well as a failure in the operation of the friction experiment. The failure in the friction experiment was due to a faulty output amplifier, a nonflight item, and was replaced. The SCRE–DAS calibrations were again checked after the test was completed using a spare 90-degree unit.

Telemetry calibrations of rate-gyro and nitrogen pressure transducer were completed on September 19. Mechanical preparations for match-mating the spacecraft to the *Agena* adapter continued from September 20 through September 28. The only discrepancy noted during these preparations was the damaged high-gain antenna (No. 9). It was received with a damaged ground plane, and returned to JPL for repair. Match-mate operations were completed on September 29.

In-hangar functional checkout was accomplished on September 30. The following discrepancies were noted: (1) DAS readout of the triple coincidence telescope was out of tolerance. The faulty readings were traced to a malfunctioning transducer. It was to be repaired and replaced after the October 9 J-Fact. (2) A magnetometer temperature translator was out of band due to miswiring. An adapter for 25A1P1 was fabricated for use during the J-Fact, but will be repaired and replaced prior to October 14. (3) DAS readout of the boom SCRE was out

of tolerance due to batteries running down. The batteries were replaced, and a recheck was normal.

Nitrogen purging of the spacecraft–shroud assembly began October 1, and continued until operations were started to move the spacecraft shroud assembly to Complex 12 for mating to the Agena vehicle prior to the J-Fact.

Match-mating of the spacecraft with the *Agena* was completed October 2 and a dummy run was conducted from Hangar AE, the blockhouse (Complex 12) and the spacecraft umbilical tower. The following deviations were noted: (1) RF and telemetry trailer power failed due to a 225-ampere fuse blowing at $T-225$ minutes. A delay of 20 minutes ensued, and telemetry calibrations were invalidated. (2) Case II temperatures monitored during the test were 4 to 5°F lower than those associated with the RA-1 spacecraft. (3) Scientific subsystems reported deterioration of the SCRE batteries. (4) Minor procedural changes were effected to improve the operations prior to the J-Fact.

Dummy Run 2 of RA-2 spacecraft was performed on October 4. No operational problems were noted during this test.

On October 9 the joint flight acceptance test (J-Fact) was performed. The following discrepancies were noted:

(1) Case IV temperature transducer out of tolerance.

(2) Opening of the controller-commutator during the test.

(3) Channel 4 noise spikes seen in all areas on RF signal.

(4) Repetition of scientific subsystem problems seen in Dummy Run 2.

Final mechanical preparations were undertaken between October 9 and 14. Magnetometer mapping of the spacecraft took place after final mechanical cleanup on the morning of October 14.

Final system test of RA-2 spacecraft was conducted on October 14.

All subsystems reported normal operation during the test, except for the Lyman-alpha temperature transducer, which was out-of-tolerance, and a faulty frequency response was detected on the SCRE. These units were replaced on October 17.

On October 17, 1961, the spacecraft was mated with the LMSC adapter, and the shroud installed.

Match-mate operations between the *Ranger* spacecraft and the *Agena* vehicle began on October 18. These were completed and JPL began its precountdown. After about 45 minutes running time it was noted, at the RF trailer and central recorder in the hangar, that no binary channels were present. Failure of these channels caused interruption of the test. The failure, while thought to be discrete, caused the spacecraft to be demated from the *Agena*, and brought back to Hangar AE for investigation of the failure.

The *Ranger* precountdown was again started on October 19. It was completed without difficulty with all subsystems and evaluation reporting in the *green*.

It was decided after the first launch attempt was scrubbed that rescheduling would be a matter of a 48-hour delay, to demate the spacecraft, return it to the hangar, and install the spare units of the scientific experiments still in doubt.

Launch operations. The JPL–AMR countdown began when range time was picked up at 2100 hours on October 19, 1961. The first firing period of 8 days began on October 20. After the first launch attempt a rescheduling meeting was held. Due to the schedule firing of a *Titan* at AMR on the second day of the *Ranger* RA-2 firing period, the shot was rescheduled to October 22, a 48-hour hold.

On October 22 the operations proceeded normally until $T-226$, when Command 2 was activated.

At $T-110$ a 10-minute hold was called by JPL, prior to *Agena* critical tanking operations, to enable a further evaluation of Channel 4 irregularities. At $T-102$ the hold was released with Lyman-alpha data on Channel 4 evaluation completed and a decision made to fly, even though the irregular performance data could not be adequately explained without compromising the primary mission objective.

After the gantry had been moved back, and the built-in 70-minute hold was completed, range time was again picked up at $T-60$ with the spacecraft subsystems and performance evaluation reports still *go* (green report).

At $T-40$, a series of holds began. First, a 15-minute hold was called to rerun the GE guidance loop tests. Another extension of 10 minutes, then still another of 15 minutes were called for the same reason, until at 0245 EST an extended hold of 1 hour, 15 minutes was called to move the gantry back around the bird to gain access to the GE guidance electronics. No 28-volt power

was getting through the guidance system. At 0310 EST the first launch attempt was scrubbed.

Prior to the second launch attempt, the RA-2 scientific experiments still in doubt as a result of Channel 4 evaluation (Lyman-alpha) and magnetic mapping of the friction package (Spare 5) were to be rechecked and the spares installed if calibration checks proved them to be better components.

The AMR Countdown 2 for RA-2 was picked up at 2100 on October 23. Operations proceeded with normal indication in all systems until $T-60$, when the 70-minute built-in hold was called. At this time the test conductor reported that a leak had developed in the vernier engine hydraulic subsystem but did not expect to exceed the built-in hold time to resume the count. However, during investigation of this problem, it was found that a booster regulator in the sustainer engine had also malfunctioned.

With all other systems *go* (green report) at the end of the 70-minute hold, at 0131 EST the test conductor called an additional 15-minute hold. At 0145 EST, it was decided to replace the booster regulator and transducer in the sustainer engine, and an additional 50-minute hold was called. This was accomplished with an additional 15-minute hold being called for clean-up operations.

Time was picked up shortly before 0300 EST, at $T-60$ in the countdown. At $T-47$, an hydraulic leak developed again in the vernier engine system. Investigation showed that the entire engine would have to be replaced. Hence, at 0310, the launch was scrubbed.

On October 24, prior to the start of JPL and range (recycled) portions of the *Ranger* RA-2 countdown, it was announced that the test had been scrubbed due to *Agena* hydraulic subsystem (guidance) difficulties. The problem was picked up in a recent *Agena-Discoverer* flight, and incipient trouble seen in other tests pointed to a design fault.

LMSC reported that the *Agena* validation could be run concurrently with the system modification of vehicle 6002, making it possible to reschedule the *Ranger* RA-2 launch for the first day of the second firing period.

c. **Ranger *RA-3*.** Scheduled testing has been completed on the PTM; however, the bus is now being used for some special unscheduled tests. These have consisted of a dynamic model analysis (determination of vibrational modes), command receipt tests, and DSIF receiver threshold checks. It is planned that the PTM will be kept as an RA-3 design entity, at least until after the first flight of the design. In the interim, it is being kept available for any pertinent special tests.

One such test will be to check operational compatibility between the spacecraft and the altimeter. This test ideally should have been accomplished during the subsystem and system test operations, but due to unavailability of a test altimeter, this was impossible. It was therefore deemed advisable to perform such a test at the earliest possible time, even at the expense of adding a couple of days to the overall test schedule. This appeared justified since Wiley would be at work on the flight altimeters shortly after delivery of the first test unit, and if system incompatibilities or shortcomings did exist it was essential to know of these and take corrective measures as soon as possible. Fortunately the tests worked out well, obviating the necessity for any significant circuit changes.

Following the last reporting period, the PTM was subjected to low and high composite vibrational tests, dummy run testing, a sterilization gas test, and a live squib test.

The configuration used for the vibrational testing consisted of the basic bus with all operating electronics fitted with dynamic mockups of the solar panels, lunar survival capsule, and radio altimeter. The spacecraft was shaken in each of three planes (normal to the x, y and z axes of the spacecraft) in accordance with JPL specifications. The attitude control gas system was pressurized (1000 psi), the gamma-ray boom was pressurized (125 psi) and the mid-course motor fuel tank was filled with 14.6 pounds of water. Post-shake verification tests were run after each plane of vibration exposure. No failures were noted during the low-frequency vibration tests that could be directly laid to vibrational environment. A shorted capacitor in the three phase-inverter was traced to a design fault. The voltage rating had been selected too low to withstand normal transient spikes.

The same configuration as that used for low frequency checks was employed for the high frequency testing and verification testing was likewise performed. Again, no failures were noted that were directly traceable to environmental testing. However, a somewhat specatacular event did occur due to high frequency shaking normal to the z axis (centerline or roll axis of the spacecraft). As previously mentioned, the gamma-ray boom, a pneumatic telescoping extension device, was pressurized to 125 psi for these tests to ensure that no leaks would occur during vibration. The collet used to retain the boom in the retracted position is locked by a pyrotechnically

operated pin puller (live pyrotechnics were not employed in this test). The collet used on the PTM was made of aluminum, whereas the flight design utilizes stainless steel. The aluminum collet was used on the PTM due to early delivery requirements on the PTM. The three axes of low-frequency vibration and the x and y axes of high-frequency vibration had peened the soft aluminum collet with the pin of the retaining pin puller sufficiently to allow the collet to disengage, thereby allowing the boom to extend. This is not felt to be a design problem in that the flight collets are of stainless steel and therefore not subject to the peening effect. It is interesting to note that this incident represented the first time the boom was extended (other than on models or in artist's conceptions) on a spacecraft and in a 1-g field. A post-incident photograph can be seen in Figure 4.

The PTM was next subjected to dummy run testing. The configuration used was similar to that used for *Rangers* RA-1 and -2. The spacecraft was mounted on the LMSD *Agena*-adapter-forward equipment section and was connected to the blockhouse-hangar complex through the umbilical cable. Precountdown and countdown procedures were executed a total of three times each. Early operations were poor, in that sufficient time was not available to check out the launch complex equipment prior to the beginning of dummy run testing and many errors in cabling and console wiring were noted. These were reworked as they were discovered. The read-write-verify (RWV) equipment was used to issue commands to the spacecraft. This is the equipment that will be used at the Goldstone DSIF site to modulate the transmitter for commands during the actual mission. Early in the testing, it was noted that issued commands were not being received in the spacecraft with the desired repeatability; i.e., every fourth or fifth command would either be garbled or not received at all. The RWV GSE was checked for accuracy and some modifications were made. This did not, however, completely cure the problem. Eventually, the trouble was traced to the spacecraft command subsystem. Evidently, the command registers were being upset whenever power to the spacecraft was turned off, so that when power was turned on again, the issuance of a clear command (a normal procedure used prior to the issuance of any commands) could not efficiently clear all the registers. Therefore, when a command was issued, the registers were somewhat biased, depending on how badly they had been upset at last power turn-off. Two circuit modifications were enacted and subsequent testing has shown that the problem has been resolved. For some strange reason, the flight spacecraft have not been bothered nearly as badly by this problem as has the PTM; however, the modifications are applicable to the flight spacecraft and will assure an even higher reliability of correct commands being transmitted during flight. The Space Flight Operations Plan is also being revised to include the issuance of the clear command prior to the issuance of any group of commands in flight (e.g., mid-course maneuver and terminal maneuver stored commands, real time commands, etc.) in case spacecraft noise, solar flares, etc. upset the registers. This should also lend more reliability to the issuance of commands. The balance of the dummy run testing was conducted without incident.

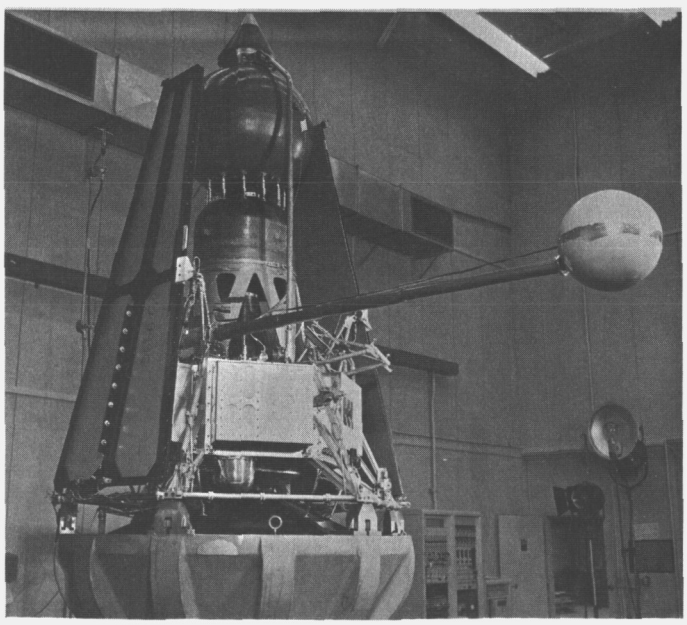

Figure 4. Gamma-ray boom extended

Following dummy run testing, a quick test was made with the LMSD shroud coupler. A test at LMSD had shown that ethylene oxide gas (used for terminal surface sterilization) affected the harp material used on the coupler by increasing its transmissibility by a factor of 50%. The retest of the output of the spacecraft's omni-antenna through the LMSD shroud coupler showed no degradation in performance.

An opportunity was then afforded to test the PTM with the first operable prototype of the radio altimeter, furnished by Aeronutronic. The test was conducted in two parts: first, allowing the radio altimeter to run free-radiating to determine if any RF interference were noted on the spacecraft due to the altimeter or if spacecraft RF could trigger the altimeter's fusing signal (capsule sequence initiation) prematurely; and second, to inject simulated received signals into the altimeter to allow

calibration of the altimeter lunar reflectivity telemetry. The first test revealed no RF interference problems on either the spacecraft or the altimeter. The second test enabled the development of a technique for calibrating the telemetry, although the PTM system was not actually calibrated. This type of calibration must be tailored for each spacecraft and time did not allow a complete calibration of the PTM. However, information was received from the altimeter on the correct channel and the commutation system did operate as designed.

The PTM was then set up for the live squib test (pyrotechnic and extension system). This test included the mounting of accelerometers to measure shock levels; AMR RF interference simulation, with checks at each squib location as to received energy levels; and the actual operation of all squib operated extensions and events.

For this test the spacecraft was mounted on the LMSD *Agena* mockup. Live squibs were installed, including a lashup for *Agena*-spacecraft separation squibs (pin pullers and separation plug spin-offs). The Aeronutronic (ADF) capsule and radio altimeter extension pyrotechnics were also included (capsule separation bolt-cutters, squib-switches, etc.). Prior to the actual squib test, the LMSD shroud was installed and the spacecraft was subjected to terminal surface sterilization gassing for 10 hours. Subsequent visual inspection (and later electronic tests) revealed no damage to the bus equipment, ADF capsule, or prototype altimeter due to the gassing. The spacecraft was then removed to the safe area, the umbilical was installed, and recorders were attached to the accelerometers. With the LMSD shroud removed, the PTM was then radiated with simulated powers of *Atlas*, *Agena*, and AMR tracking RF sources (nine in all). A thermistor was installed at each squib location and direct energy levels were measured with spacecraft power on. Subsequent analysis showed that no location received more energy than -40 db of that considered to be sufficient to ignite a squib. The RF opaque LMSD shroud is considered to be capable of at least an additional 10 db of isolation, giving a total of -50 db margin. An interesting incident happened during this test. At one point, the RF interference personnel called for transfer of the spacecraft's radiation output from the omni-antenna (0 db) to the high-gain antenna (18.5 db) with a simultaneous request to transfer the transponder to high power (full 3 watts). The transponder was not designed to operate at full power while the spacecraft was mounted on the booster. However, the blockhouse personnel transferred the antennas and applied full-power to the transponder. To accomplish the latter, CC&S command A-1 must be issued. This means that the CC&S relay hold (a safe relay clamping voltage), must be removed since command A-1 is not normally issued until 22 minutes after launch. This rendered the spacecraft pyrotechnic system vulnerable to inadvertent actuation due to transients, etc. This condition existed for approximately 1 minute without incident. (Note: The relay hold feature is but one of several safing devices utilized in the RA-3, -4, and -5 design; however, the integrating inertia switches, etc. were disabled or by-passed to simplify this test.) The next portion of the test involved firing the squibs. This was done by transferring to internal power and disconnecting the umbilical (thus testing the live squibs against any incurred transients) and allowing the spacecraft to time its way to the first squib event, solar panel extension. This event occurs 30 minutes after launch. The umbilical was then reconnected and the CC&S GSE was connected by direct access to allow stimulation of each squib event without having to time through a 66-hour mission. The next event was mid-course motor turn-on and turn-off (Conax valve operation), followed by gamma-ray boom extension, deployment of the omni and radio altimeter antennas, vidicon lens cover opening, capsule–spacecraft separation bolt-cutter actuation and capsule squib switch initiation. The latter started the ADF capsule sequence by actuating the spin-motor initiator, the retro-motor initiator and the payload-motor separation squibs (bolt-cutters). The test was considered successful with all squibs blown, excepting some of the bolt cutters on the capsule. This was subsequently traced to a discontinuity in the separation plane contacts (caused by the presence of foreign material) and, in one case, a broken wire. These devices were eventually fired successfully.

In order to extend the gamma-ray boom in a 1-g field, a trough was constructed that allowed the spectrometer sphere to ride out on nylon slides. The clamp that retains the omni-antenna, which normally separates violently from the spacecraft in a direction normal to the roll axis, was tethered by a cord and attached weight. The test showed that the clamp will separate cleanly from the spacecraft. The simulated LMSD separation squibs were fired at the time of normal injection without effect on the spacecraft.

Flight spacecraft. Most of the design problems were detected in the PTM and subsequent modifications were enacted. However, some problems have been noted that are unique to the flight spacecraft and bear mentioning here. Component failure rates are much higher on the flight spacecraft than those recorded on the PTM. This is an exact reversal of the experience noted on the *Ranger* RA-1 and -2 program. The only difference between the RA-3 PTM and the flight spacecraft is heat sterilization.

Although no failures are directly traceable to heat damage, it is felt that heat sterilization does shorten the expected life of electronic components and circumstantial evidence seems to bear this out. In any case, the failure rate on the flight spacecraft is not alarmingly high.

A design fault has been noted on the gamma-ray spectrometer. The unit was originally designed to be hermetically sealed. However, vacuum chamber tests have shown that the seal is not perfect and a slow leak results in arcing and permanent damage after about 15 to 18 hours in vacuum. The design is being changed to vent the unit to atmosphere, so that it will not be turned on, in the mission, until 4 hours after launch. This will allow internal surface sterilization, previously accomplished by using the sterilant gas as the pressurant.

An extensive investigation is underway to determine if reflections from the spacecraft can enter and affect proper operation of the Earth and Sun sensors. Light baffles are being added to the Earth sensor hood and reflection tests are being run on the Sun sensors. Some aging effects have been noted on the Sun sensors, particularly after heat sterilization. However, it has not yet been proven that this effect impairs the operation.

Initial power turn-on and subsystem testing. Initial power turn-on and subsystem testing took place during the period from July 24 through September 21, 1961. Most of the problems discovered during the period were those which remained unresolved from the PTM testing. The problems included a transient resulting from exciting the Earth sensor with a step function light input and the starting of the antenna hinge motor. The power converters showed a marked instability during switching transients. One wiring error was found in the spacecraft cabling.

Because of delivery problems many of the equipments tested during this phase were nonflight items. As a result, some of the testing had to be repeated when flight items were delivered.

System testing. System testing was conducted during the period from August 22 through September 18. During this period three systems tests were conducted. Many of the problems discovered in the first two systems tests were resolved by procedural change, recalibrations, and equipment adjustments. System test Number 3 was postponed for approximately a week to allow additional time for the vidicon and gamma-ray subsystems to resolve existing problems. System test Number 3 showed several additional procedure, operator, and GSE problems that were defined resolved following the actual test. Prior to environmental testing calibrations on several transducers were checked to insure a valid environmental test.

Environmental testing. The basic RA-3 spacecraft engineering equipment, without the lunar capsule, omni-antenna, and the radio altimeter, was subjected to a series of environmental temperature tests during the period from September 23 to October 9. This test series was conducted to calibrate spacecraft temperature transducers, temperature-sensitive communications measurements to verify theoretical temperature control calculations and to evaluate the flight system interface problems in real time during a normal flight sequence.

Specifications indicated that the vacuum pressure should have been less than 10^{-5} mm Hg. The lowest pressure that could have been obtained with existing equipment was 2.5×10^{-4} mm Hg.

During the temperature calibration period several discrete equipment failures were noted. None of the failures could be directly attributed to the near-space environment.

The mission verification portion of the test proved satisfactory with the exception that operation and discrete equipment failures with the vidicon and gamma-ray equipment were noted. None of the failures detected were directly attributed to the near-space environment. The malfunction noted with the gamma-ray equipment was later resolved by repeating that portion of the test using the spacecraft PTM and the flight modules of gamma-ray equipment.

Weight, center-of-gravity, and mass moments-of-inertia. During the period from October 16 through 19, 1961, the basic bus weight as well as the center-of-gravity and moments-of-inertia for both launch and mid-course maneuver configurations of the spacecraft were determined. Due to the present state of the lunar capsule assembly it was decided to establish the basic bus parameters at this time and integrate the ADF unit parameters as these became available.

Dummy run testing. During the period from October 16 through 19, a precountdown test and two dummy run tests were conducted. The results of the second dummy run test showed that the procedure and equipment problems were well defined; therefore, further dummy runs at JPL were cancelled.

Pressure vessel calibration and leak checks. The weekend of October 21 and 22 was devoted to pressure vessel telemetry loop calibrations. A multiple-point calibration was performed on the mid-course motor fuel (300 psi)

and helium (3000 psi) tanks and the attitude control nitrogen (3000 psi) system. A quantitative leak-check of the attitude control, cold-gas system indicated that the system was leaking at approximately 25 to 30 times the 100 cc/hour maximum allowable rate according to the specification. This problem is presently under investigation.

Live pyrotechnic firing test. A pyrotechnic firing test was conducted on October 23 to verify the ability of the spacecraft to fire live pyrotechnics. Review of test data showed that procedural errors invalidated portions of the telemetered event indications. Sensitivity of other telemetry channels to the event pulses was noted and will be investigated prior to shipment of the spacecraft to AMR.

Match-mate. A series of tests with the RA-3 flight adapter and shroud were conducted. These tests showed that several shields in the adapter wiring harnesses were loose and one plug on the spacecraft separation connector was incorrect. Prior to the mechanical match-mate, a leg spring constant determination was conducted. Mechanical match-mate of the spacecraft to the LMSC adapter was conducted according to flight operational procedures. During the RF coupler retro fitting to the omni-antenna, an interference was noted between the Earth sensor cable and LMSC shroud. This problem is being investigated. Techniques for the coupler retro fitting were developed and will be incorporated in future testing. RF loop checks were performed to establish radiating characteristics preparatory to the AMR on-pad checkout.

Following the match-mate testing approximately 1 week was allowed for mechanical and electrical preparations for the final systems test at JPL. During this period, the spacecraft electronic support cases received final temperature control painting, cable securing, and system calibrations. A period was allowed for testing with the Deep Space Instrumentation Facility (DSIF) receiving equipment and alignment of the various optical sensors. The final system testing at JPL is scheduled for November 6, 1961.

At this time, there are several delivery problems concerning flight acceptance equipment which are still unresolved. These areas include the radio altimeter, antenna hinge servo potentiometer, gyros, and gamma-ray boom detector. Present schedules indicated that these problems will be solved prior to the final systems test at AMR. The spacecraft testing schedule is being maintained.

d.* Ranger *RA-4. Mechanical assembly and alignment of *Ranger* RA-4 was started on August 21, 1961 and completed to the extent that initial power turn-on testing was started on September 26. The problems associated with the mechanical assembly were as follows: (1) Sterilization of the bus assembly resulted in warping the structure so that Plane A (Station 500) was out of flat by 0.115 inch (allowable tolerance is 0.005 inch). This, however, can be compensated for by suitable shimming. (2) A wire in the ring harness was found to be parted near a splice. This damage occurred sometime during the sterilization process.

By October 31 initial power turn-on, system grounding checks, and a large portion of calibrations were completed. It is expected that by November 6 RA-4 will be on schedule except for gyro, communications calibrations, and vidicon subsystem checkout. During these calibrations and testing the following difficulties were encountered:

(1) The transponder was returned to the cognizant engineer because of AGC difficulties.

(2) The antenna drive unit had a faulty potentiometer, and is believed to be a sterilization problem.

(3) The attitude control pressure regulator had an O-ring failure.

(4) The autopilot electronics unit failed.

e.* Ranger *follow-on. Preliminary planning for test operations on the *Ranger* follow-on TV experiment incorporating the RCA supplied TV subsystem indicates that most of the three sets of system test equipment presently being used on RA-3 and -4 will be suitable also for these operations. The anticipated schedule for the follow-on testing would require only three sets of system test equipment just as are now being used on the existing *Ranger* programs. It is anticipated that a fourth set would be advisable to act as a spare in the event of failure. This appears justified by the fact that the GSE will have had a great deal of time on it by the time the last of the *Ranger* follow-on spacecraft has undergone test operations.

The existing basic system test equipment will be augmented by RCA furnished equipment of two basic categories, each of these in different quantity.

(1) Flight operation type information recovery equipment.

(2) TV subsystem analysis type equipment.

The first of the two types will be furnished to the Goldstone tracking station and in addition two sets will be utilized during system test operations at JPL and one (additional) at AMR. These will all be equipment of the type to analyze and present a TV picture from the

transmitted signal from the spacecraft. All installations will be essentially the same except for a photo printer. JPL will possess only one to cover two test operations.

The second of the two types will be equipment to connect by hard line to the TV subsystem in the spacecraft by means of a direct access connector. This will allow some penetration into the working circuitry to simulate, monitor, and analyze the operation of the TV subsystem. Two of these types of equipment will be utilized at JPL for subsystem and system test operations, and a third set will be utilized during similar operations at AMR.

All this equipment will be built into standard JPL type system test racks. A complete TV subsystem test position will thus consist of approximately eight racks and will bet set up in an area quite similar to the one used for RA-3 and -4 testing except that the side occupied by the scientific GSE on RA-3 and -4 will be replaced by the RCA TV test equipment.

The basic testing and sequence of tests will be quite similar to the RA-3 and -4 test operations. It is possible that the first flight type spacecraft will have to be checked out at JPL using the PTM TV subsystem. This may be necessary due to unavailability of the first flight TV until AMR test operations start. Though not desirable, this probably could be accomplished by allowing sufficient time during the AMR scheduling to correct for any very minor types of interface problems. It is anticipated that the remainder of the flight TV units will be available at JPL for a major portion of the test operations.

Design. The basic RA-3 type bus has been stripped (design-wise) of the ADF capsule and radio altimeter, the vidicon experiment, and the gamma-ray experiment (including the extendable boom). The RA-3 type omni-antenna has been replaced with a RA-1 type omni-antenna. The omni-antenna deployment boom has also been removed. The RA-3 type high-gain antenna has been replaced with a *Mariner* R type, which incorporates circular polarization. Three new science experiments have been tentatively chosen and will be mounted on the bus so as to have a clear view of the lunar surface during terminal maneuver. At present, the experiments are (1) dosimeter, (2) ion chamber, and (3) radiation counters. These experiments will provide their own data conditioning and will be telemetered through the bus communication system.

The following bus subsystems require (virtually) no changes to accommodate the new mission: attitude control, central computer and sequencer, power (with the exception of the science power module), command and mid-course propulsion. The data encoder will require slight modification as will the squib firing assembly. Redesigns will be required on the ring harness, the squib harness, and some of the case harnesses.

It is planned that an S-band communications ranging experiment will be included. This will require a high-gain antenna capable of L-band with circular polarization and S-band capability. It has been indicated that the antenna can be provided without introducing any untenable transients in the spacecraft design. In order to maintain a constant cg and moment of inertia design, it may be necessary to carry ballast to compensate for the ranging experiment to be added on later flights.

The RCA vidicon tower–spacecraft interface is being kept as clean as possible. The RCA passenger is fairly self contained. Operating at full power only during the last 10 minutes of the mission, it contains its own transmitters, power sources, sequencer, and telemetry as well as six high resolution vidicon cameras. It will be necessary to add a directional coupler on the bus to allow the RCA transmitters to feed the high-gain antenna on the bus. During cislunar cruise, RCA telemetry will be fed through the bus communication system. A real-time ground originated command will be used to turn on the experiment during terminal maneuver. The missions will be operated quite like those of the RA-3 program, with mid-course trajectory correction and terminal positioning. The later *Ranger* missions will not orient the spacecraft's roll axis with the velocity vector in terminal maneuver, but rather will orient the camera cluster axis with the velocity vector. The camera axis is 30 degrees out from the $-Z$ axis of the spacecraft in the roll-yaw plane and in the Y direction, i.e., directly opposite the high-gain antenna.

B. Guidance and Control

1. Autopilot Analysis

The *Ranger* RA-3, -4, and -5 spacecraft have the capability of trajectory correction by firing a small rocket motor. The function of the autopilot is to maintain a stable vehicle attitude and proper heading during this mid-course maneuver. Two measures of performance of the autopilot are: (1) angular error of the vehicle's added velocity vector from the desired direction, and (2) stability.

The autopilot block diagram is shown in Figure 5. The basic function of the autopilot, stabilizing the vehicle attitude, is accomplished by using angular rate and position signals from gyros to control four jet vane actuators which position jet vanes in the exhaust stream of the rocket motor. The controlling torques result from forces on the jet vanes.

The disturbing torques arise from the motor thrust vector not passing through the center of mass of the vehicle. Stabilizing the vehicle implies pointing the total thrust vector through the vehicle center of mass. If this is done, the thrust vector will not be pointed in the desired direction in space, and the error will be exactly the amount by which the center of mass missed the unmodified thrust vector. To correct this situation, a path guidance loop is added, which has the effect of rotating the entire vehicle backward through the angle of the center of mass misalignment. The vehicle then maintains a stable attitude with its thrust vector in the proper direction.

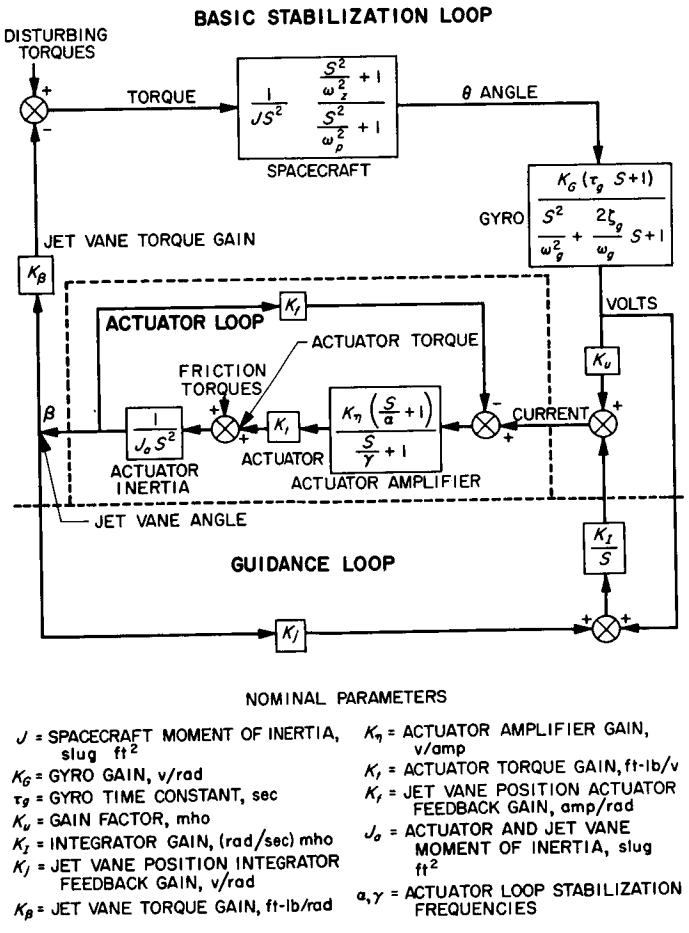

Figure 5. Autopilot block diagram

The path guidance loop consists of combining the vehicle position signal with the jet vane position signal, and integrating the two to drive the jet vane actuator. Since the steady-state operation requires the vehicle angle to have the opposite sign of the jet vane angle, the input to the integrator should go to zero when the vehicle position reaches its proper value.

The investigation described illustrates the effect on autopilot stability and error due to the following: (1) tolerance buildups, (2) vehicle structural resonances, and (3) nonlinearities in components.

Effects of individual component tolerance variations as well as worst case combinations were investigated. The detail of the jet vane actuator as a position feedback servo is shown in Figure 5. If the actuator loop is approximated by a second order transfer characteristic

$$\frac{\text{jet vane angle}}{\text{input signal}} = \frac{K_a}{\frac{S^2}{\omega_a^2} + \frac{2L_a}{\omega_a} S + 1}$$

a root locus analysis of the autopilot system may be made. Because the natural frequencies of the autopilot system fall into a low frequency and a relatively higher frequency grouping, we may break the root loci into two groups, one showing low frequency as in Figure 6, and the other showing higher frequency behavior as in Figure 7. Note that, from Figure 6, instability is indicated for too low, or decreasing, loop gain. Figure 7 indicates instability for increasing loop gain. The system must therefore have some loop gain between the upper and lower limits for stability. The gain margins for nominal case parameter values are: high = 4.5, low = 1/6. Gain margins were measured for individual component tolerances as well as worst case combinations and are shown in Table 5.

Vehicle structural resonances include primary structural vibration modes as well as flexible appendages such as the magnetometer boom and solar panels. The effect of a resonance on the autopilot depends on its frequency as well as the size and mass of the vibrating member. Since the solar panels would have the greatest effect on both counts, they were chosen as the primary target for this part of the study. The single axis transfer function angle/torque for a spacecraft with an undamped flexible appendage about the same axis is

$$\frac{1}{JS^2} \frac{\frac{S^2}{\omega_z^2} + 1}{\frac{S^2}{\omega_p^2} + 1}$$

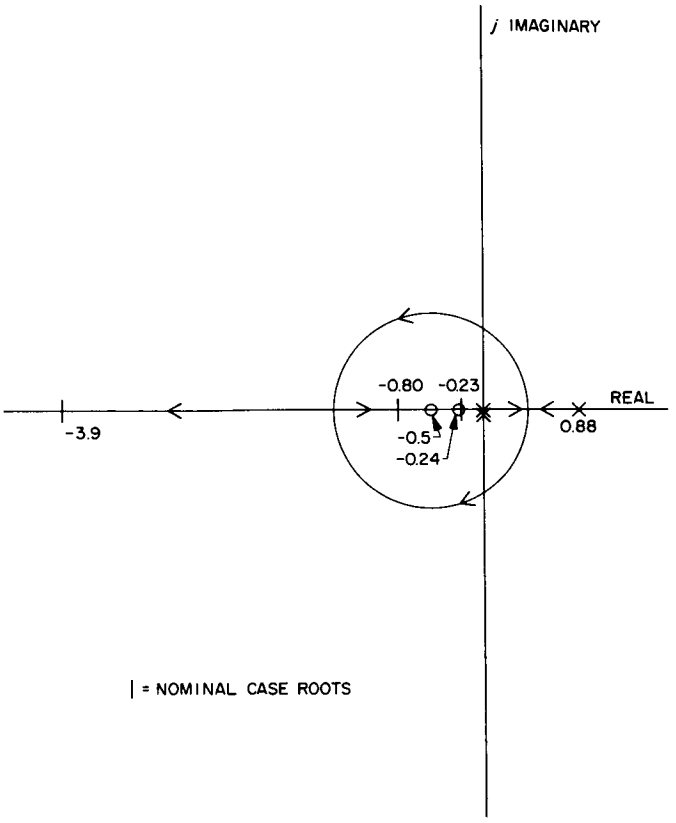

Figure 6. Low-frequency root loci

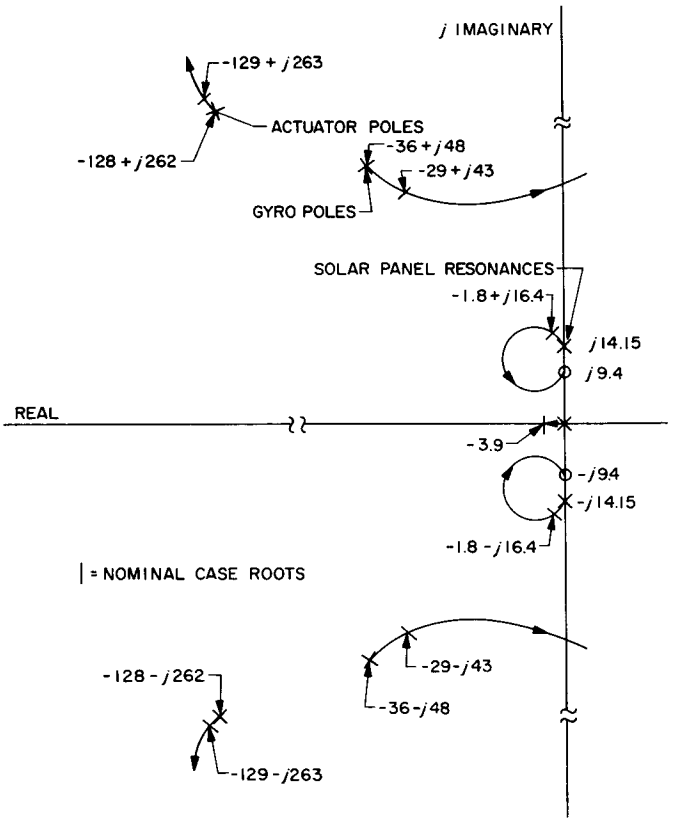

Figure 7. High-frequency root loci

Here J is the moment of inertia of a completely rigid structure, $\omega_z/2\pi$ is the cantilevered natural frequency of the flexible appendage, and $\omega_p/2\pi$ is a higher frequency which depends on size and mass of the member. In the case of two identical solar panels there will still be only one pair of poles and one pair of zeros. ω_z would be the same as for a single panel, while ω_p would be greater.

There are four distinct nonlinearities in the autopilot. Two of these, the actuator amplifier saturation and the jet vane position limits, were not considered effective since studies showed that their limits were not approached. The variation of jet vane torque with position has the effect of a simple gain variation, so it was treated as part of the gain margin problem. The fourth nonlinearity, the friction in the jet vane actuator, was investigated extensively. The effect of the friction is to stabilize the actuator loop at extremely high gains; however, it also introduces a lag in jet vane position which can have deleterious effects on the total autopilot performance. This was studied analytically with the describing function method. The block diagram for this approach is shown in Figure 8. The friction is represented by the equation

$$F = -F_0 \sin \dot{\beta}$$

where F_0 is the magnitude of the friction and $\dot{\beta}$ is the jet vane angular velocity. The describing function for the friction is a particularly simple one:

$$N = \frac{F}{\dot{\beta}} = -\frac{F_0 \sin \dot{\beta}}{\dot{\beta}}$$

A plot of

$$\frac{1}{N} = -\frac{|\dot{\beta}|}{F_0}$$

extends from the origin along the entire negative real axis and appears on Figure 9. Figure 9 is a Nyquist

Table 5. Gain margins for RA-3, -4, and -5

Characteristics	Rigid body, no friction		Solar panel resonances included, no friction	Friction in and solar panels in
Nominal parameter values	High	8.25	3.44	4.53
	Low	1/6.55	1/6.35	1/5.9
Worst case tolerance comb	High	4.6	1.97	3.1
	Low	1/7.25	1/6.96	1/5.05

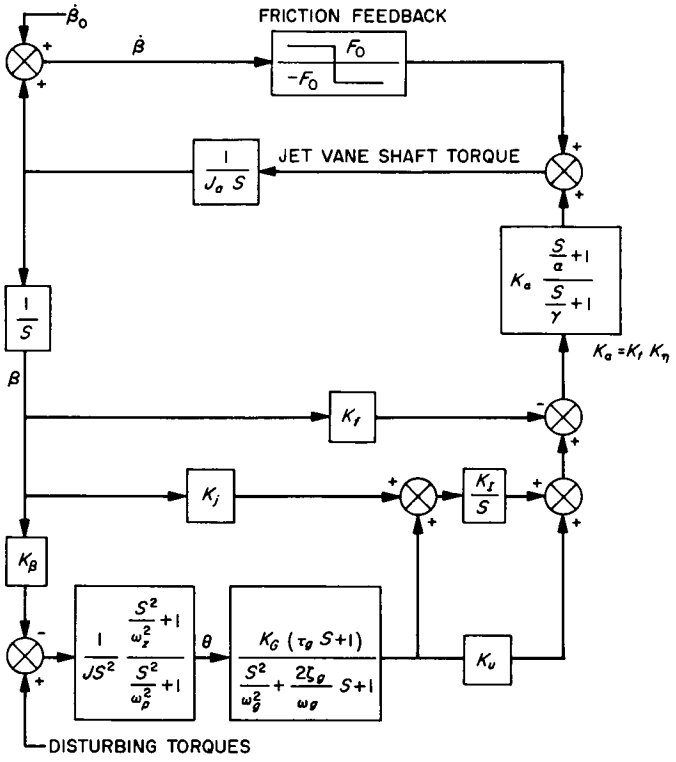

Figure 8. Analytical function method

diagram of linearized autopilot spacecraft system transfer characteristic

$$G(s) = \frac{\text{jet vane angular velocity}}{\text{actuation shaft torque}}$$

versus the nonlinear element $1/N$. The intersection at $\omega \approx 2$ rad/sec indicates a limit cycle at that angular frequency.

The results of the analytical portion of the investigation predicted:

(1) The autopilot would remain stable for any combination of tolerance buildups.

(2) The effect of the solar panel resonance would be to reduce at both ends the region of loop gain for which the system remained stable. Thus the gain margins would be approximately halved.

(3) Friction in the actuator should produce a stable limit cycle period of 3.1 seconds for a rigid structure, and 2.5 seconds if solar panel resonance effects are included.

The analog computer studies confirmed these results. Measurements had good numerical correlation with analytical data.

2. Control Gyro Module

Fabrication of control gyro modules has been delayed due to a number of difficulties. Paramount of these difficulties is a design weakness uncovered in the Minneapolis-Honeywell DGG 49-E12 gyro. This weakness has resulted in a series of five gyro failures due to insulation breakdown in the signal generator, torquer Dualsyn windings. Four of the five failures occurred after thermal sterilization and the fifth occurred during temperature testing. Minneapolis-Honeywell has since reported that the double Formvar insulated wire, used in the Dualsyn winding, was a marginal choice for high temperature application and that high quality Formvar wire has been increasingly more difficult to procure. These reasons coupled with a high in-house rejection rate of Formvar Dualsyns has resulted in an across the board change to Nyleze insulated wire. All *Ranger* gyros are being returned to Minneapolis-Honeywell for rework to the Nyleze insulated Dualsyns. Five gyros with this change have now been received, of which three have been assembled into the first *Ranger* RA-3 gyro module. An expedited rework schedule at Minneapolis-Honeywell will provide six gyros in November and the balance of five gyros in December.

A second difficulty, although it has not produced any discrete gyro failures, has resulted in the rejection of several gyros from system usage. These particular gyros cause an approximate 10-cycle oscillation in the attitude control system. An intense investigation by JPL and Minneapolis-Honeywell has been undertaken to pinpoint the reason for the gyro oscillation. This investigation has

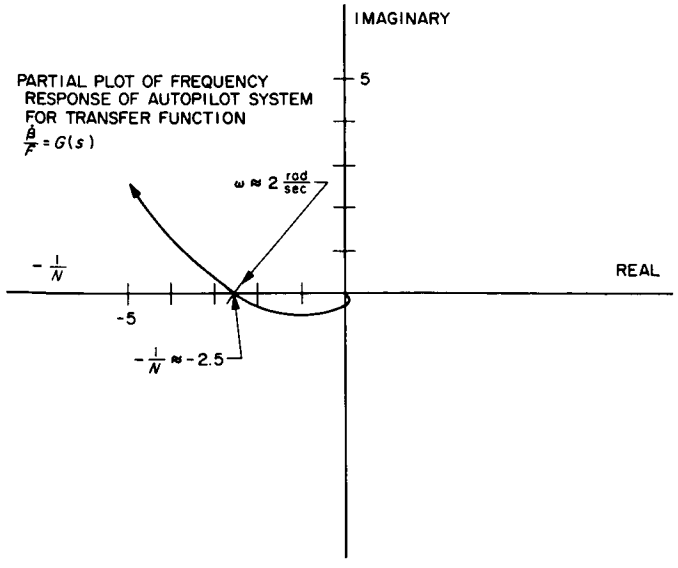

Figure 9. Lunarized autopilot transfer characteristic

uncovered a number of minor differences in E-12 gyros from the *Ranger* RA-1 and -2, E-5 gyros, but the exact reason why some gyros oscillate has not been determined.

Areas under investigation are gimbal damping, jewel and pivot clearance, signal generator sensitivity change with temperature, Dualsyn electrical null shift with dc current levels, and the effect of lateral forces present in the Dualsyn. Each of these areas has added to the refinement of the mathematical model of the gyro for computer studies. An understanding of interaction of these effects is expected to produce an answer to the oscillation problem. Since areas of control, other than closer control of jewel and pivot clearance, have not been determined for the reworked gyros, Minneapolis-Honeywell has been requested to conduct additional tests on completed units as a means of screening out gyros with a tendency to oscillate. Most important of these tests is the monitoring of the dc rebalance current using a special set of high-gain capture loop electronics furnished by JPL. A maximum noise limit has been specified for this test as a performance criterion.

3. Velocity Shutoff Subsystem

The magnitude of the velocity increment to be added to the spacecraft during the corrective mid-course maneuver of *Rangers* RA-3, -4, and -5 will be measured by an accelerometer and integrator combination. Since a digital computer is carried in the CC&S unit and the size of the corrective velocity increment is transmitted digitally from Earth, a digital accelerometer is required. This system is under development at JPL and will be used in combination with the CC&S digital computer for mid-course motor shutoff.

This digital accelerometer system consists of a force balance accelerometer with a pulse torqued rebalance loop to provide capture current to the proof mass. In this mode of operation the pulsing rate is directly proportional to the applied acceleration and each pulse produced represents a constant value of velocity increase (or decrease, depending on the direction of the applied acceleration). In the *Ranger* system application this value, or scale-factor, will be 0.1 ft/sec of velocity increase.

Accurate performance testing and flight acceptance of this unit has now progressed through a total of seven digital accelerometer modules.

Upon receipt from the vendor, the unit is given a complete visual inspection using a 10-power stereo microscope. This pinpoints any cold solder joints, nicked wires or printed wires and assists in showing up any possible cracked components. The next phase is the functional electronic test of the electronic package using a simulated accelerometer to provide input signals. A complete record is made of all internal and external voltages, currents, and waveforms that are necessary to prove satisfactory operation of the circuit. Next the actual accelerometer is connected to the digital circuit and the phasing, gain, and quadrature of the 200-kc position signal is checked. When these tests are completed and the data obtained has been reviewed, the unit is then transferred to the Leitz optical dividing head for highly accurate testing of the accelerometer and the entire loop.

Due to the fact that this is a unidirectional digital system it is not possible to obtain the desired performance data on the accelerometer transducer itself in the digital mode. Therefore, all tests such as null offset, torquer scale-factor and alignment of the sensitive axis must be obtained with an analog loop closed around the accelerometer. This loop is closed by means of an external amplifier which is connected to the accelerometer independent of the digital loop. This amplifier contains its own 200-kc oscillator ac preamplifier, demodulator, and dc torquer driver amplifier. The torquer input current is monitored by means of a precision series resistor and a Tinsley vernier potentiometer.

After the required analog data is obtained, the digital loop is closed and accurate testing of the various digital parameters is started. Because of the low acceleration input (0.07 g in *Ranger*), it is necessary to set the dividing head and also establish the true zero g input point with extreme accuracy. The analog loop method establishes the sensitive axis position to ± 2 arc seconds. The Leitz dividing head has an internal calibration of ± 2 arc seconds also. By these means it is possible to establish the acceleration input level to about $\pm 0.02\%$ of the maximum applied (0.07 g).

Because the permanent magnet torquer used in the accelerometer is temperature sensitive, a thermistor compensation network is provided to adjust the torqueing pulse current as a function of the magnet temperature. Accurate testing of the digital calibration must then be accomplished to be sure the compensation network is correct. A sealed cover is placed over the complete module, accelerometer, and alignment fixture and hot or cold air is forced through the enclosure. Thermocouple sensors within the box permit control of the air temperature within ± 0.5°C. Temperature testing proceeds to cover the range of 0 to 70°C. Standard test points are at 0, 15, 35, 55, and 70°C. To ensure that the true g input is still 0.07 g, the actual position of the sensitive axis must be established as each temperature is reached and thermal stability is obtained. This is done by closing the analog

loop and taking a complete set of data at each temperature. The digital loop is then closed and a 1000-second measuring period is used to establish the digital calibration. This long period is necessary because of the low pulse rate of 22.4 pps at 0.07-*g* input level.

Flight acceptance testing of the module consists of performing the following tests:

(1) Complex wave vibration.

(2) Static acceleration (centrifuge).

(3) Vacuum-temperature.

(4) Mid-course motor vibration.

Tests 1 and 2 are performed nonoperating, and Tests 3 and 4 are done with power applied and monitoring equipment attached. This simulates the actual flight conditions because during the boost phase of high vibration and acceleration the module power is turned off.

Upon satisfactory completion of the preceding tests, the module is temperature sterilized for 24 hours at 125°C. A complete retest of the digital and analog parameters is then accomplished and any required trimming of the null offset or digital calibration is done. The module is then allowed to operate continuously in the digital mode at 22.5 pps for a varying period of time depending on system delivery schedules. The longest period so far is 527 hours. Each day a set of digital readings is taken and recorded to determine if any drift trends are present in the operating system.

Final accurate testing is performed just prior to shipment of the spacecraft to AMR, and consists of digital and analog readings at room temperature only. Testing at AMR is of lower accuracy and is used to detect deterioration, gross changes, or failures before flight.

C. Engineering Mechanics

1. Hardware Design and Fabrication

a. Electrical coating of the antenna cone. A high rejection rate has been encountered in the bonded gold and silver electrical coating for the fiberglass RA-3 omni-antenna cone. The difficulty has been in obtaining a sufficiently sensitized surface by chemical means so that adherent copper, silver, and gold electroplates result.

A recently initiated backup technique consists of adhesive bonding 0.001-inch silver foil to the fiberglass surface, high temperature soldering (antimonial tin) a doubler to the longitudinal seam to maintain electrical continuity during the RA-3 aerodynamic heating phase, followed by gold electroplating.

Other processes being evaluated for possible immediate or future use are:

(1) Gold plating of electrically conductive (70% Ag) epoxy soldered (Ecobond 56) fiberglass.

(2) Electroless precious metal deposition onto fiberglass.

(3) Flame spraying precious metals onto fiberglass treated with special adhesives.

(4) Elevated temperature firing of precious metal organic compounds.

b. High-gain antenna pivot arm insulator. In order to provide thermal and electrical insulation between the high-gain antenna and the spacecraft frame, an epoxy-fiberglass joint was used. An epoxy adhesive was used to bond the tube into the main aluminum tube of the pivot arm. In addition, thin wall aluminum sleeves were bonded into the epoxy fiberglass tube to provide a ductile surface for riveting.

c. Capsule separation sensor. In order to provide a secondary capsule separation input for *Ranger* RA-3, a separation sensor was mounted on the mid-course propulsion propellant tank. An analysis of the attachment problem indicated that adhesive bonding would be preferable and that the adhesive system should have the following attributes:

(1) High shear and peel strength.

(2) Good vibration resistance.

(3) Heat resistance (125°C for 24 hours).

(4) Hard vacuum stability.

(5) If possible, nonnutrient and sporicidal.

The propellant tank was annealed 6Al-4V titanium, while the separation sensor body was 6061-T6 aluminum. Three adhesive systems were considered: (1) a filled epoxy (Armstrong A-g), (2) a silicone rubber (Products Research Corp. PR-1930), and (3) a polyurethane (Products Research Corp. PR-1927).

Because of its high peel strength, high temperature stability (300°F continuous service), shock resistance, and sporicidal characteristics, the polyurethane was selected.

The need for a heat resistant ($<300°F$), high peel strength adhesive which can be applied with contact pressure and cured at ambient temperature was apparent in this application. The material selected met all the requirements but were formulated as a potting compound. Silicone adhesives are heat stable but have poor shear and peel strength. Epoxy adhesives, modified for flexibility, lose much of their heat stability. A polyurethane or possibly a polyurethane modified epoxy could be developed for high temperature ($>300°F$) adhesive joints, requiring flexibility.

d. Omni-antenna cable. Two problem areas were noted in the fabrication and assembly of the coaxial cable into the omni-antenna boom. These were identified as follows:

(1) Because of vibrational loads, the cable must be supported at least intermittently inside the boom.

(2) The cable must be supported axially to minimize the load on the connector pin attachment points.

To damp the vibrational loads, it was decided to use semi-resilient spacers attached to the cable. These spacers were dimensioned to have a nominal interference fit with the boom of 0.010 inch. They must also be stable at 125°C, resilient enough to pass through a necked-down portion of the boom (ID 0.93 to 0.80 inch), and as light weight as possible. The material selected was Emerson and Cumming's Eccosil 4640, a silicone rubber syntactic foam (i.e., the silicone rubber is filled with 150-micron hollow glass spheres). The density is therefore reduced to 40 lb/ft^3. Samples of the Eccosil 4640 were cast and evaluated. Except for a rather low tear resistance, the material was acceptable.

Before a mold could be designed and fabricated, a cable assembly had to be made for the PTM. Two alternate materials for the spacers were proposed:

(1) A medium sponge neoprene (AMS-3198).

(2) A medium sponge silicone rubber (AMS-3195).

Because of availability, the former was selected and bonded to the cable with a neoprene adhesive. A prototype assembly was made and exposed to 125°C for 24 hours with no deleterious effects noted. The cable together with the two squib leads was assembled into the boom without undue difficulty.

To provide axial support, a collar attached to the connector, was bonded to the cable. Because the cable shielding had to be grounded carefully into the connector prior to application of the adhesive, a special bonding technique had to be used. An annular clearance of only 0.010 to 0.015 inch between the cable and the connector sleeve required that a 0.063-inch hole be drilled into the sleeve to permit introduction of the adhesive.

e. Attitude control tubing joints. Studies are currently being made to determine the adequacy of welded tubing joints for the attitude control system. This design is being studied as a replacement for the mechanical flare-type fittings currently in use on the *Ranger*. Although the all-welded system should be more reliable, it does pose some problems.

One of the problems being studied is the determination of internal tube cleanliness after welding. Any deposits formed inside the tube on welding, which could subsequently loosen and enter the gas stream, would be detrimental to control jet operation. Studies so far on this problem have proved that it is possible to weld tubing, keeping the interior clean.

Additional tests are being run to determine the probability of making leak-free joints. This poses a problem, as it may not be possible to adequately inspect all joints after installation. During preliminary tests using a specially designed joint, it appears that 100% reliability can be obtained.

2. Sterilization

Heat sterilization is apparently the most effective method of sterilizing spacecraft components. Eventually entire spacecraft will be heat sterilized in one operation. Twenty-four hours at 125°C will insure that no viable organisms exist; but in a large, complex spacecraft will 24 or even 48 hours insure that all parts have been exposed to 125°C for 24 hours?

As a preliminary step in answering this question a program was initiated. Two spheres of Stycast 2850 6T (a typical filled epoxy potting compound) were cast which had thermocouples located at the center at half the radius, and at the outer surface.

The spheres were placed in a forced convection oven, at ambient temperature with the oven set to control at 125°C. Figure 10 shows the resulting curve for the 1½-inch sphere while Figure 11 shows a similar curve for the 1¾-inch sphere. It is apparent that the thermal lag under the conditions of this test is not significant, essential equilibrium being obtained at all specimen locations in 15 to 25 minutes after the oven had stabilized. Further evaluation is required to determine thermal diffusivity of complex assemblies.

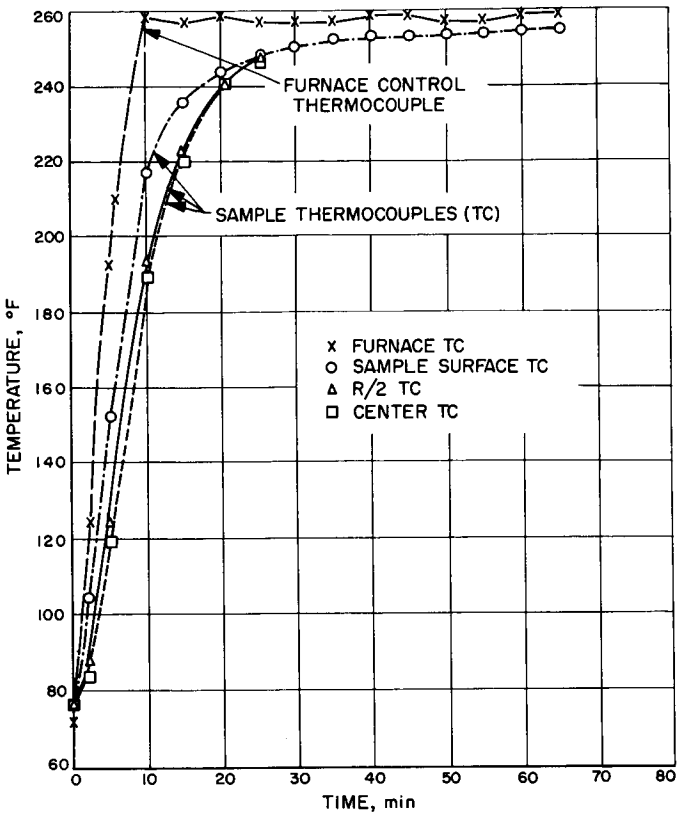

Figure 10. Thermal diffusion into 1½-inch sphere of Stycast

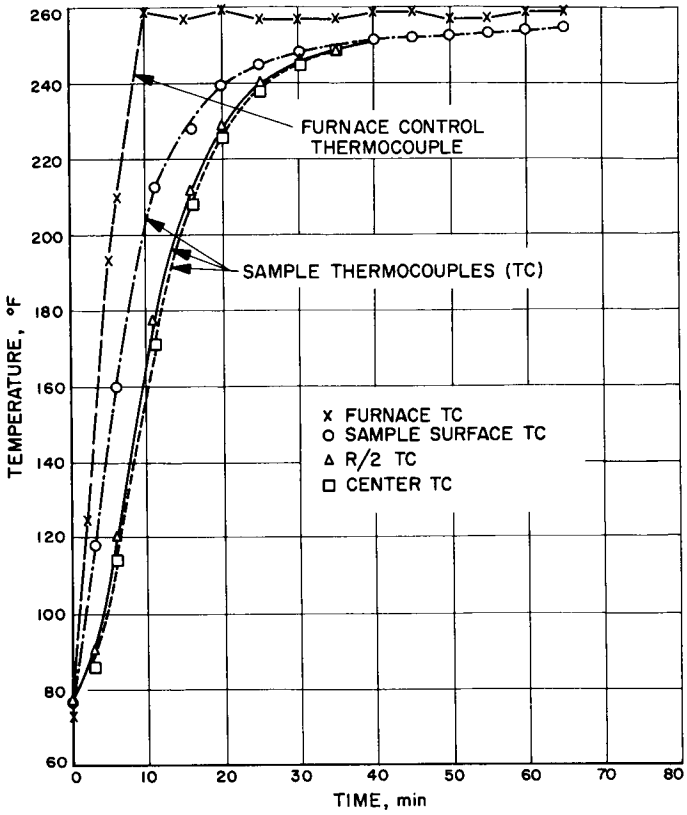

Figure 11. Thermal diffusion into 1¾-inch sphere of Stycast

D. Propulsion

A mid-course propulsion maneuver will be required of *Ranger* spacecraft RA-3, RA-4, and RA-5 in order to accomplish lunar impact. This maneuver will be accomplished through the use of a small, monopropellant-hydrazine-fueled propulsion unit of 50 pounds vacuum thrust and capable of delivering a variable total impulse in conjunction with an integrating accelerometer system. Functionally the rocket is of the pressure-fed constant-thrust type. Injection pressure is obtained from compressed helium which passes through a pressure regulator and forces the propellant from a bladdered tank, to the rocket engine. The rocket engine contains a quantity of catalyst to accelerate the decomposition of anhydrous hydrazine. Engine ignition is accomplished through the injection of a small quantity of a hypergolic oxidizer, nitrogen tetroxide.

All valving functions for the propulsion unit are accomplished with explosively actuated valves. A more detailed description of the propulsion system and a chronological history of its development are contained in *SPS 37-3* through *-11*.

Development efforts on the *Ranger* propulsion unit have been essentially completed. During this report period the assembly and flight acceptance testing of the RA-4 and RA-4 spare propulsion units were completed and the RA-4 unit was installed in the spacecraft. In accord with current Laboratory decisions, the partially assembled units intended for *Ranger* RA-5 and the RA-5 spare were excluded from the *Ranger* program and turned over to the *Mariner* propulsion project engineer for use in the *Mariner* R program.

The mid-course propulsion system design presently being used on *Ranger* spacecraft RA-3, -4, and -5 will also be used on the RA-6, -7, -8, and -9 spacecraft. Procurement has been initiated for the propulsion systems required for spacecraft as well as that required to replace RA-5 and RA-5 spare.

E. Lunar Capsule

1. Introduction and Summary

Under a Jet Propulsion Laboratory subcontract calling for the development of a lunar capsule, Aeronutronic Division of Ford Motor Company is supplying a lunar seismographic capsule and ancillary equipments for *Ranger* flights RA-3, -4, and -5. As the *Ranger* spacecraft approaches the Moon, the capsule is to be separated from the spacecraft and braked to allow a survivable landing which emplaces a sensitive seismometer on the lunar surface. Data from the seismometer is to be relayed back to Earth receiving stations for an extensive period of time after each landing.

Included in the subsystem are the following components: an altimeter for sensing the proper instant of separation; a spin-rocket motor to provide stabilization during the retro-rocket braking; a retro-rocket; a crushable impact limiter to absorb residual energies; and the survival package. The survival package is a sphere which is fluid-floated inside the hollow, spherical impact and to allow erection by Moon gravity to the local vertical after the assembly comes to rest.

Conventional chemical batteries are used to supply the required power. Near-constant temperature for the survival sphere equipments is provided by the use of a cryogenic insulation and a small quantity of water which cools by evaporation to the vacuum surroundings during the lunar days. The water also offers a safety feature for night operation by virtue of its latent heat of freezing.

The entire subsystem is characterized by simplicity. The separation, braking, and landing are an open loop process; passive devices are employed wherever feasible; and the number of independent and necessary events in the functional sequence is held to a minimum.

As was indicated in *SPS 37-11*, two final design proof tests of complete landing spheres were planned, one an airplane drop, the other a testing machine impact. These tests were delayed several weeks by unfavorable development test results. Furthermore, it was necessary to introduce two more design proof test impacts of partially completed landing spheres to provide the necessary assurance that the revised parts were qualified.

Considering the major elements external to the landing sphere, it can be reported that the altimeter has progressed as planned. Wiley Electronics has delivered two satisfactory design proof tested flight prototype altimeters and the flight unit fabrication is proceeding on schedule.

The retro-rocket program is proceeding satisfactorily considering the critical schedule requirements. The previously encountered failures were diagnosed, and the corrections were confirmed by test firings. The motor has now operated at least once under all conditions of environment to be tested. Two motors have ignited successfully in the Arnold Engineering Development Center (AEDC) altitude chamber, and one of these was a complete firing. It produced an impulse about 1½% greater than expected. Two more confirmation rounds are ready for spun, static firings at Bacchus. Twelve motors for qualification at AEDC are now being loaded, and the flight motors will follow in time for delivery, about 6 weeks before the scheduled flight date.

In summary, completion of the lunar capsule development is later than desirable. Certain critical design proof tests and qualification tests are yet to be conducted. However, flight hardware components for all assemblies are being constructed or delivered on a schedule consistent with the starting of landing-sphere final assembly work early in November. That starting date allows a small margin between scheduled completion time and the required delivery times for flight. Assuming successful test results in a number of design proof and qualification areas, it seems likely that the capsule subsystem can be completed and will be suitable for launching on schedule.

2. Testing and Systems Considerations

a. General.

Weight control. The latest revision to the capsule weight status is presented in Table 6. Weight changes show a redistribution of potting materials and wiring. As reported previously, final weight trimming by adjustments of the impact limiter weight will be employed to achieve a particular retro-velocity increment. This weight trimming will not be accomplished until completion of the retro-motor qualification tests. Note that the expected gross weight exceeds the 325-pound allocation. This overage results primarily from the increase in weight of the retro-motor. The weight of the retro-motor heat shield, however, is still uncertain because several designs are being evaluated.

Specifications. A general review of all the functional and environmental specifications is in process to insure their consistency with each other and with recent minor design changes. Several specifications for the lunar capsule have been revised during the reporting period. Environmental specification for Condition IV (Impact), was modified so that the acceptance test subjects the capsule to a larger temperature variation than previously required. The performance of the electronic equipment will

consequently be recorded over the increased lower and upper extremes to provide a larger calibration range. The lunar capsule sterilization functional specification has been expanded to incorporate recent data and new procedures in both the assembly and testing programs. A safety feature has been added to the power and sequencing assembly functional specification for a 5-*g* arming switch which redundantly deactivates the external power supply until after launch. Also, on the basis of spin-motor performance and lower clamp separation tests, the timing distribution has been revised.

Sterilization. Near completion is a list of bonding and potting agents to be used in the capsule equipment. Each resin is identified with a means for guaranteeing sterilization whether it be by dry-heat temperature soak, liquid sterilizing additives, or by virtue that the material is inherently sporicidal. Where interface connections are to be made during assembly, detailed procedures have been established incorporating the use of ethylene oxide gas and liquid surface sterilants. Recognizing that these sterilants present a personnel hazard, safety practices and procedures are being made an integral part of the sterilizing procedure.

System description. To permit ready visualization of the functioning of the capsule elements, it is convenient to recapitulate the functional events from pre-launch through those that occur after landing.

Table 6. Lunar capsule weight summary

Components	Expected Weight (lb)	Previous Weight[a] (lb)
Retro-rocket payload		
Survival sphere		
Electronics, antenna, batteries, wiring	24.3	23.1
Structure, insulation, devices	12.7	14.4
Water	3.7	3.6
Seismometer	7.8	7.8
Flotation fluid and outer shell	8.2	7.5
Survival sphere total	56.7	56.4
Impact limiter cover and rocket-motor/sphere interconnection	37.1	39.3
Vibration damper	1.3	1.2
Control timer, batteries, wiring	1.4	1.4
Total retro-rocket payload	96.5	98.3
Motors		
Retro-rocket motor and igniter	213.3	208.5
Spin-motor, igniter and attachment	2.3	2.2
Total separate weight	312.1	309.0
Bus mounted equipment		
Altimeter and antenna	6.6	6.5
Altimeter support and deployment	2.0	2.0
Motor support structure and separation	3.6	3.6
Bus interface J-box and connectors	0.8	1.0
Retro-rocket heat shield	3.0	3.0
Total lunar capsule	328.1	325.1

[a]Weight as reported in *SPS 37-11*.

Prior to launch and after acceptance testing, the system is assembled in a sterile manner, balanced, given a final check, and then installed on the *Ranger* bus. Since bus guidance and control is the source of direction for the retro-velocity decrement, particular care is taken to insure the following:

(1) Alignment of the separable capsule assembly itself to minimize capsule contributions to any separation errors.

(2) Weight, center-of-gravity, and moment-of-inertia are within the tolerance demanded by the bus control system.

(3) Dynamic balance of the capsule assembly to tolerances which minimize the velocity errors that could arise when the capsule subsequently is spin-stabilized and decelerated for landing.

A 1-*g* mercury position switch permits the turning on and off of the survival sphere battery during the long interval between landing sphere closure and final assembly to the bus (approximately 4 to 5 weeks). An analysis of the thermal behavior from final assembly to landing shows that since the insulation is ineffective prior to its evacuation on the Moon, the steady-state temperature increase will not exceed about 10°F due to the 1 watt of internal power dissipation.

To accomplish both a safety-arming function and to ensure that the capsule transmitter is on for tracking purposes during terminal maneuver, two acceleration switches are employed which close during boost at 5 ± 0.5 *g* acceleration. One is utilized in the power and sequencing assembly (P&SA) to keep the external power supply isolated from the squib circuitry. The other is located within the survival sphere to bypass the previously mentioned mercury switch, thus providing positive assurance that thereafter the transmitter will always be supplied power regardless of the acceleration field experienced by the sphere. These two acceleration switches are associated with integrating circuits that require a velocity increment of about 140 ft/sec before activating closure in a 5-*g* field.

During transit, the retro-motor is protected by a thermal radiation shield which keeps the temperature of the motor, and thus the burning distance, within limits. The design objective for the shield is an effective drop of the propellant temperature of not more than 11.5°F during the 66-hour transit. To adjust the retro-motor initiation time to permit nominal burnout at a specific altitude (approximately 1000 feet), the temperature of the motor under this shield is measured with a thermistor. With

an effective temperature drop anywhere between 4 and 19°F during the transit cooling period, and with an initial temperature (under the shield) anywhere from 57.3 to 87.3°F, the ignition timer circuitry controls the motor ignition time so that burnout occurs at the required altitude with no pre-launch adjustment.

The completion of the spacecraft terminal maneuver aligns the capsule-assembly roll-axis parallel to the trajectory. Upon command from the spacecraft, both bus omnidirectional antenna (on top of the landing sphere) and the capsule altimeter are deployed. The altimeter is released by either of a redundant pair of explosively actuated bolt cutters and erects to a position so that the RF beam axis is parallel to the roll axis. This erection is such that it imposes a small net roll impulse in order not to upset the spacecraft attitude. Once in position, the altimeter is held in place by redundant latches.

At 60 seconds prior to bus impact on the Moon, the spacecraft turns on the altimeter, using spacecraft power to actuate a thermal switch in the altimeter. The altimeter has a warm-up time of 15 seconds. It fuzes when the spacecraft reaches an altitude of approximately 70,000 feet. At this altitude, the altimeter closes a relay which connects bus power to accomplish (1) lower clamp (primary) separation of the capsule from the support structure by firing four redundant bolt cutters and (2) initiation of the power and sequencing assembly in the capsule itself by firing two parallel squib switches.

The power and sequencing assembly (P&SA), in addition to providing power for all subsequent functional events prior to landing, contains three electrical timers, all three of which are initiated at the fuzing event. The first of these (spin-motor timer) provides a delay of 130 $\pm$20 milliseconds to insure release of the separation clamp prior to spin-motor initiation. The spin-motor initiation delay is always greater than 15 milliseconds and the maximum clamp opening time does not exceed 125 milliseconds. Hence, at the extreme, spin-motor ignition always occurs after clamp opening. Physical separation of the capsule from the support structure is accomplished by the axial component of impulse delivered from canted spin-motor nozzles (approximately 20 lb-sec). This impulse produces a velocity increment of approximately 2 ft/sec. The torque component of the impulse produces a minimum spin of 300 rpm. The spin-motor burning time does not exceed 1.3 seconds.

The second P&SA timer accomplishes the firing of the retro-motor. The nominal delay of this circuit is 2 seconds, but in flight the delay is automatically varied over the increment 1.7 to 2.3 seconds, depending on the measured temperature of the retro-motor. The retro-motor burns for approximately 10 seconds with the nominal burn-out altitude occurring at 1000 feet.

The third P&SA timer fires two bolt cutters on the separation clamp between the landing sphere and the retro-motor. This event occurs 13.0 $\pm$0.5 seconds after P&SA initiation.

The survival sphere is completely enclosed by the impact limiter and no circuits pass through the fluid space. Hence, to activate the sphere functions, an integrating inertia switch (20 *g* for 1 second) is closed by acceleration from the retro-motor thrust. This switch immediately closes the power circuit once more, causes pre-impact uncaging to occur, and initiates an internal sequence timer for the following post-impact events.

(1) A 15-minute delay after initiation accomplishes post-impact caging.

(2) A 16-minute delay after initiation accomplishes sphere venting by firing the two penetrator squibs. The penetrators pierce the shells and the impact limiter which releases to Moon vacuum the survival sphere flotation fluid. This release also vents the seismometer caging fluid, opens the vent line for the boil-off valve, and exposes the insulation to lunar vacuum.

(3) A 30-minute delay after initiation turns on the seismometer centering motor and turns off power to the sequence timer itself.

After the seismometer is uncaged and centered, any motion of its pendulum provides the signal that modulates the transmitter. The carrier center frequency and the subcarrier center frequency are slightly temperature sensitive. Therefore, in addition to the primary seismic data, the thermal performance of the survival sphere in the lunar environment is read out at the receiving sites of the Deep Space Instrumentation Facility (DSIF) at Goldstone Lake, California.

b. Design proof tests. For each major assembly of the capsule subsystem, a final demonstration is conducted to assure that flight-design equipment satisfies the functional specifications, after that equipment has been subjected to the conditions of the environmental specification.

Subsequently produced but identical units can then be subjected to less rigorous functional or environmental requirements as acceptance tests. By favorable comparison of the functional performance of an acceptance-tested unit with that of the design-proof-tested unit, a

nondestructive means is obtained to provide assurance of satisfactory in-flight performance.

During this reporting period, a large portion of the design proof test program has been completed. Not yet tested are one of the two complete landing spheres and many of the tests of major assemblies that require an extensive and destructive qualification test series; i.e., spin- and retro-motors. Also remaining to be tested are components for which changes were found necessary by design proof test failures and for which a retest in the final configuration is required. Finally, the design proof test of either design for the retro-rocket thermal radiation shield has yet to be accomplished because attempts at design proof tests have indicated unexpected thermal gradients in the retro-motor. The present status of each of these tests is as follows:

Lower clamp. The purpose of this test (successfully completed on August 15) was to establish that both the impulse and time of separation were within specification. The principle of the ballistic pendulum was used to measure impulse resulting from the clamp separation, and high-speed cameras and an oscilloscope were used for recording data.

Spin-motor. The purpose of this test is to qualify the spin-motor assembly for flight. Twelve randomly selected units from the total lot will be fired after being subjected to environmental conditioning.

Payload separation. The purpose of this test (successfully completed on September 9) was to verify separation of the payload from the retro-motor and to obtain information on separation velocity (Fig 12). A dummy landing sphere and retro-motor were assembled on the Gisholt dynamic balance machine using flight hardware which included the upper clamp assembly and vibration dampers. The landing sphere was supported to simulate the zero-*g* condition of flight. The bolt cutters were fired through slip-rings on the spin table. High-speed cameras were used to record data. Three separation tests were conducted, using a single unit of the redundant bolt cutters. The separation velocity was found to be approximately 0.5 ft/sec.

Major structural test of capsule assembly. This test was successfully completed on August 11 and was reported in *SPS 37-11.*

Landing sphere. Two complete landing spheres have been constructed for design proof test (DPT-3 and DPT-4). The test plan calls for one of these to be air-dropped onto a concrete surface, passed through a thermal-vacuum test, and then be disassembled for examination. The second sphere was to be subjected to design proof spin acceleration, vibration, and machine impact before entering the thermal-vacuum test.

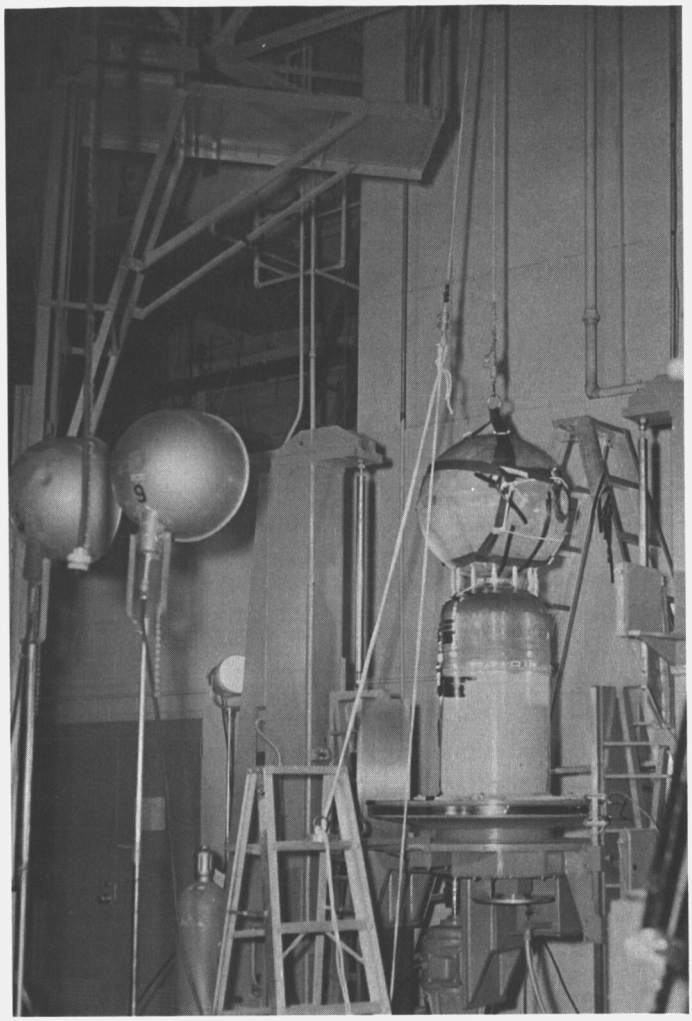

Figure 12. Payload separation design proof test

Both the air-drop and the machine impact were selected to be severe enough to furnish impact conditions which were in excess of 95% of all possible lunar impact conditions. Because only 5% of a complete impact population will impact flatter than an angle of 58 degrees from vertical, and less than 5% will experience a resultant velocity of more than 220 ft/sec, the aircraft altitude and airspeed were selected so as to furnish an impact velocity of 220 ft/sec at an angle of 58 degrees from vertical. This drop test was conducted at Edwards Air Force Base on October 12, 1961. Only at-site observations are available, but everything appeared to have operated (or to be operating) satisfactorily except that one of the two redundant penetrators did not emerge from the impact limiter.

The machine impact test was performed at the highest normal velocity component that could be reasonably expected with a simple normal impact. For this condition, only 5% of the complete population experiences a normal component that exceeds 155 ft/sec; hence, that value was chosen for the machine test. The post-impact thermal-vacuum test consists of a 3-day exposure in a 225°F environment followed by a 3-day exposure to surroundings at liquid nitrogen temperature, both of these tests in a hard vacuum. During this test cycle, it is expected that the sphere payload will rise to the water boil-off temperature, remain there until the end of the hot-cycle, and then during the cold-cycle drop nearly linearly to allow extrapolation to the 14-day behavior during the lunar night. By measuring the water consumed during boil-off, it is expected that the heat-flow-rate during the hot-cycle can be confirmed, and an approximation of the cold-cycle performance can be obtained from the internal and external temperature measurements. Then, following the thermal-vacuum test, the spheres will be competely disassembled with a predetermined step-by-step procedure, and tests will be conducted on parts as they become accessible. The intent of these tests is to accurately measure the subsystem post-impact performances and to put these subsystem elements into the life cycle test.

Recently, one of the complete landing spheres (DPT-4) accidentally shorted during assembly, seriously damaging the sealed-in battery set. A replacement sphere (DPT-5) is currently being constructed, and DPT-4 has been modified to provide a better thermal test since it can no longer be used as a complete test unit. The replacement unit (DPT-5) will be machine-impact tested according to the test plan, but it will not be ready before early November.

Bolt cutters. The purpose of this test is to qualify the flight lot of bolt cutters. These cutters have been environmentally conditioned and are now being fired for qualification. Each of 44 cutters will be required to cut a bolt identical to those used in flight. Firing current and action time will be recorded for each firing.

Retro igniter squib. The purpose of this test was to qualify the flight lot of S11A2 squibs to a reliability of at least 0.995 at the 95% confidence level that at least one of two will fire. Forty-four squibs were fired after environmental conditioning at simulated flight environment with no failures. The data system consisted of a photo tube to measure light output and an oscilloscope to record firing current, action time, and output. A second test will be conducted after aging the squibs until the latest feasible date before launch time.

Capsule battery. This test program is intended to demonstrate that the Electric Storage Battery Model 184 battery would satisfy the electrical, environmental, and sterility requirements of the survival sphere.

Supposedly sterile batteries Numbers 14, 15, and 16 were scheduled to complete the design proof tests. All eventually developed electrolyte leakage during shipping or storage despite the fact that earlier non-sterile batteries had performed well after impact. In addition, results obtained from the microbiologic study of battery module Number 13B, which had been purposely contaminated by the vendor, showed that the Bisonite resin used for encapsulation was not sporicidal and, therefore, the battery construction was unsuitable for flight use.

Spore growth, however, could be cultured only in the resin used in the battery case. The entire interior of the battery was shown to be sterile. These battery-module results were contradictory to earlier sterility tests which had shown the case resin used (Bisonite with formalin) to be sporicidal. However, the conclusion drawn from the Number 13B tests is that batteries Numbers 14, 15, and 16 were not proved to be sterile. Battery design proof tests were suspended pending the arrival of three more batteries with a change in case resin to assure sterilization. A design and manufacturing process change was instituted which is expected to eliminate electrolyte leakage.

The first new battery was received on October 2 and was installed in the test sphere. This sphere was impacted on October 13. However, at this writing it had not been opened to examine the contents for survival. The second battery was received on October 6 and is being employed in fabricating DPT-5, the second complete design proof test sphere. The third battery was received on October 10 and is being used for separate electrical and environmental tests. The battery will not be considered to be proven until all three tests are complete. However, the batteries are now sterile, and none has given any indication of leakage. Because the leakage could be directly traced to a design and process flaw that has been corrected, the batteries no longer appear to be a critical item.

Switch assembly. The tests of capsule mercury switches and 20-*g* acceleration switch have been combined since they are now potted into single assembly. The mercury switches permit the capsule to be turned on and off during ground handling. The 20-*g* inertia switch starts the post-landing sequence of events when it is actuated during the retro-thrust portion of the lunar flight. The individual components have been qualified, but it is necessary to retest them in the new flight assembly.

Caging pin motor. The purpose of this test (successfully completed on October 4) was to qualify the explosive pin motors used to actuate the pre-impact uncage and the post-impact uncage device to a system reliability of 0.995 at the 95% confidence level. Since three pin motors are used in parallel for each function, this required the successful firing of 20 units after environmental conditioning with no failures allowed. The motors demonstrated their ability to push approximately a 15-pound force when actuated. An oscilloscope was used to record firing current and action time.

Squib switch. The purpose of this test was to qualify the M7 squib switch for flight use. The units were subjected to the specified environmental extremes, and some units failed to function properly when fired. A new lot of M7 switches is now on hand for testing and two other lots of different types of switches are on order: a set of modified M7 switches with a higher no-fire current, and a different type of switch from the Atlas Powder Company. Testing will continue as these new units arrive. It is expected, however, that the new lot of regular M7 switches can be made to survive the humidity-temperature test by encapsulating them in a thin shell of epoxy resin.

Altimeter support structure. This test was first conducted on August 23. The test was unsuccessful in that the torque impulse imparted to the bus during antenna deployment was in excess of the 0.15 ft-lb-sec specified, because of a combined design and process error.

The purpose of this test was to static load, vibrate, shock, and operate the deployment and latching mechanism of the altimeter support structure, checking wiring circuitry and altimeter alignment before and after the test. A dummy altimeter was installed on the support structure, and this assembly was vibrated and shocked as a part of the design proof test. The deployment test to check the impulse imparted to the bus was conducted under simulated space conditions of vacuum and cold. High-speed cameras and strain-gages were used to record data. A telescope and mirror grid system was used to check alignment. The alignment remained within 0.1 degree throughout the test. However, since the impulse was in excess of 0.15 ft-lb-sec, the design was proven not to be acceptable.

The support structure was redesigned in the deployment, latching, and wire-routing areas. The parts of the test which were repeated were those for which there was question concerning the design adequacy. Thus, the new assembly was subjected to the complete vibration sequence and then tested for deployment impulse. The design proof vibration was conducted without incident. The deployment and latching mechanism operated satisfactorily after proper adjustment, and a measured value of 0.14 ft-lb-sec of impulse was obtained. The acceptance test of each flight altimeter support structure will include deployment tests to adjust the torque impulse.

Thermal radiation shield. The test program for the thermal radiation shield includes two major areas, structural and vacuum-thermal. The structural testing consists of vibration and shock at proof test levels. The vacuum-thermal test consists of simulating the outer space environment on the lunar capsule assembly and monitoring temperature of the retro-motor to determine the heat loss, to measure thermal gradients within the propellant, and to determine the best location for the timer-control-thermistor. An inert retro-motor is instrumented at 31 points with thermistors which indicate temperature changes as small as 0.1°F. The test is conducted in a vacuum condition of 3×10^{-5} mm Hg, and a liquid nitrogen-cooled wall at −190°C simulates dark space. Quartz lamps are used to simulate solar flux, and a heated base plate simulates the bus structure. The test is conducted for a minimum period of 10 hours, or until stabilization occurs.

An initial test on a multilayer, aluminized Mylar blanket configuration was completed on October 8 (Fig 13). The test was conducted for 6 hours; at that time it was evident that the motor dome had developed a cold spot and the test was stopped. The temperature was found to be as desired in all other areas, however. An extra collar, high enough to cover the lower part of the impact limiter, was added to the top of the blanket, and the test was repeated; little improvement was noted.

These tests made it clear that the shaded part of the impact limiter was conducting heat away from the rocket-motor through the vibration dampers and the separation collar, at a more rapid rate than had been anticipated. Balsa wood is a good insulator; hence, most of the conduction occurred edgewise through the impact limiter cover, which is made of layers of fiberglass laminate and rubber.

It will be necessary to change the design to keep the lower half of the impact limiter warmer. Hence, the tests to date have proven to be of a developmental nature, rather than the expected design proof demonstration.

Thermal control valve. The purpose of the test was to subject the valves to simulated flight environment at the design proof levels of vibration, sterilization, and 3000-*g* shock. This series of tests was successfully completed on September 7, 1961.

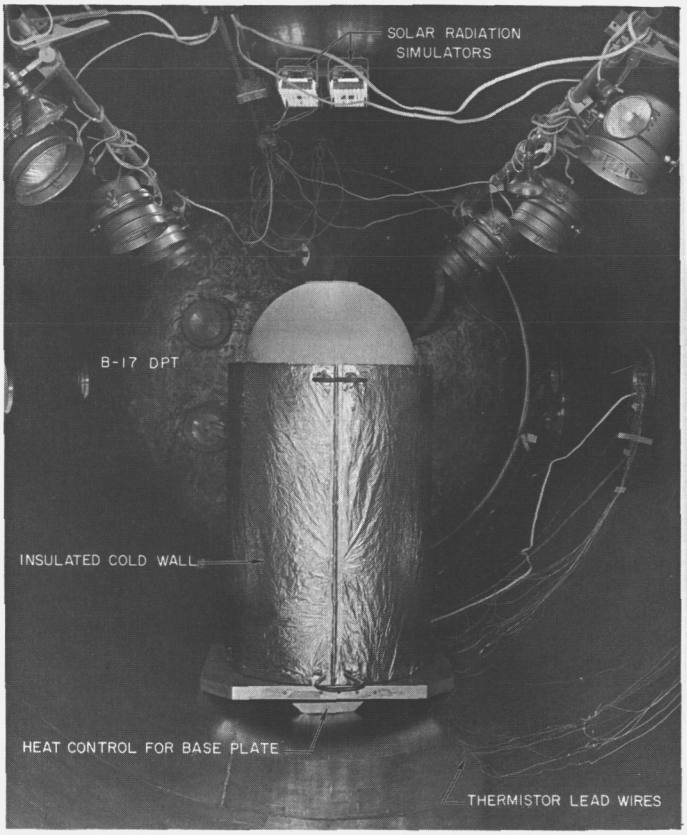

Figure 13. Thermal radiation design proof test shield

Bulkhead seal. This test first appeared to be successful but was later rejected as a result of microscopic inspection which showed minute cracks in the glass seal. It is not certain that the cracks would be harmful, since the test proved the functional capability of the part and it was not certain that the cracks had occurred during test.

A second proof test of the seismometer bulkhead seals at 1000-psi pressure and 3000-*g* shock was conducted on October 9. Crack-free units were selected for test and all were found to be crack free on post-test microscopic examination.

Power and sequencing assembly. This was a design proof test of the battery and timer assembly that is mounted between the retro-rocket and the survival sphere. One assembly was subjected to vibration, shock, and acceleration. It then operated satisfactorily, but electrolyte leaked from the battery. Hence, from an assembly viewpoint, the test was unsuccessful. The decision was made to redesign the assembly for the following reasons, only one of which resulted from this test:

(1) To add a spin motor delay circuit which was shown to be required by the B-1 design proof test.

(2) To add an in-flight-arming circuit for increased safety.

(3) To change the design of the battery pack to prevent electrolyte leakage, using Yardney PM-01 cells.

(4) To change the wiring terminals to improve the safety and ease of connecting wires to the assembly.

The design proof testing of two assemblies with the new design features is scheduled for 26 October. No difficulty in passing the test is anticipated because the Yardney cells have been separately tested and the added circuitry is similar to that which passed.

Venting squib. The purpose of this test is to qualify the flight lot of venting squibs. All simulated flight environmental conditioning has been completed, and the units are ready to be fired. The data to be recorded will be pressure output, firing current, and action time.

External wiring. Design proof tests of the external wiring were conducted in conjunction with the structural tests. All test conditions were satisfied, but on engineering review, the workmanship was judged unacceptable and, thus potentially unreliable. Tests of the wiring are to be repeated, now that acceptable workmanship has been obtained.

Radar altimeter. In addition to the previously delineated tests, a major design proof test for the radar altimeter has been accomplished. This test was accomplished primarily by the subcontractor (Wiley Electronics).

Throughout the design proof tests from August 15 to 31, 1961 and subsequent tests at Aeronutronic, no failure occurred of a nature which would require any design change. The unit did not perform satisfactorily in the simulated deep space environment as a result of the inadequacy of the test chamber. Arcing and corona discharge occurred at the maximum altitude attainable in the test chamber (approximately 175,000 feet). In later tests in the Aeronutronic high-vacuum chamber at altitudes above 250,000 feet, the unit performed normally. Since the altimeter will never be operated in actual use except at sea level and in the hard-vacuum environment in the vicinity of the Moon, the altimeter's failure at 175,000 feet was not significant.

Two units for design proof test have been constructed. Design proof unit Number 1 has been successfully completed and unit Number 2 is nearly complete. All tests performed at the subcontractor's facility have been successfully accomplished; there remains only the vibrational test of a complete altimeter assembly on its support

structure and the high-vacuum operating test, both of which are to be performed at Aeronutronic.

c. Acceptance tests. Implementation of the formal acceptance test program for all major subassemblies has proceeded during this reporting period. Test plans have been written in close coordination with Aeronutronic quality control engineers and, as hardware becomes available for either flight use or design proof testing, it is subjected to these acceptance tests. A summary of the acceptance test status, plus a brief outline of each test, follows:

Retro-motor support structure and lower clamp. This test will consist of subjecting the support structure and lower clamp assembly, including all wiring and electrical contacts, to flight level static loading and vibration. An electrical checkout will be performed both before and after the test. A thorough mechanical inspection will then be performed, and the parts will be placed in bond to await flight installation.

Altimeter support structure. This test will subject the altimeter support structure, with a previously flight-accepted altimeter, and all wiring to flight levels of vibration. The structure alone will be static loaded. The assembly will be aligned so that the altimeter axis is parallel to the bus centerline within 0.1 degree. The deployment and latching mechanism will be tested for proper operation, and the impulse imparted to the bus will be measured. After final electrical checks and mechanical inspection, the altimeter and support structure assembly will be placed in bond to await flight.

Spin motor. This test will consist of a cold flow of the manifold-nozzle assembly on the spin-motor test fixture at ambient conditions. The following measurements will be made for each assembly: spin-motor gas generator chamber pressure (1000 $\pm$50 psi), spin-motor torque (greater than 70 ft/lb), and out-of-plane torque (less than 2 in./lb). This test is for the flight units selected from the qualification lot. Following this nondestructive test, the qualification units will be hot-tested.

Inertia switch. This switch senses retro thrust (20 *g*) and initiates the timing sequence within the sphere. Fifteen switches from Inertia Switch Co. have been acceptance tested and found suitable for flight use. The test verified the acceleration calibration, the built-in time delay, and the electrical performance. The switches were placed in bond for fabrication of flight assemblies.

Radiation shield. The details of this test must await the time when the flight design is selected. This unexpected delay results from the design proof tests now being conducted.

Thermal control valve. This test measures the cracking pressure, holding pressure, and leakage rate for each thermal control valve used in design proof and flight payloads. Several valves have been accepted to date and put in bond. Testing is continuing as required.

Bulkhead terminal seal. This hydraulic pressure test employs water at 450 psi for each seal prior to its use in either a design proof test or a flight landing sphere.

Vibration dampers. This test consists of wearing in the dampers until a friction level of 22 $\pm$2 pounds is achieved. The spring must then demonstrate a rate of 400 lb/in.

Electronic acceptance tests for sphere assemblies. Acceptance test plans were prepared and used in acceptance testing the electronic assemblies, which were fabricated into the DPT-3 and -4 design proof test spheres. The acceptance tests consisted of electrical and nondestructive environmental tests to show that the assemblies performed as required. The list of acceptance test plans is as follows: (1) switch assembly, (2) RF assembly, (3) seismometer amplifier and VCO, (4) sequence timer, (5) antenna, and (6) coaxial cable.

Ground adapter acceptance test. An acceptance test plan was prepared and followed in testing the two ground adapter units. The tests consisted of measuring electrical performance over a specified range of temperatures. Verification was obtained that the units met or exceeded the design requirements.

d. Systems test.

Goldstone tests. An over-all system test was performed at the Goldstone DSIF during the period of September 25 to 30, 1961. This test determined the capability of the data handling link and was under the direction of JPL. Aeronutronic supplied the necessary flight-type hardware and a *quiet box* for the test. JPL supplied the simulated lunar quakes on magnetic tape and the associated isolation amplification equipment.

Prior to shipment of the equipment to Goldstone, a closed-loop test, exclusive of the RF link, was performed at JPL on September 23 to verify equipment operation. Some difficulty was experienced with a nonlinear waveform presentation, which was found to be an isolation amplifier clipping.

The attenuation of the Aeronutronic quiet box so far exceeded expectations that it was possible to connect the DSIF receiver directly to the output of the box, and even then it was possible to reduce the signal amplitude

below the threshold of the Goldstone receiver. Thus, it was not necessary to place the capsule transmitter and seismic amplifier with its heavy temperature control chamber on the boresighting tower, which greatly simplified the test.

At Goldstone, trial runs were made at various seismic amplifier input levels before connection to the 960-mc phase-lock receiver to obtain records for comparative purposes. Each run required approximately 1 hour and contained several types of simulated lunar disturbances from the microseismic level to quaking conditions. After completion of these preliminary closed-loop tests, the entire RF system was employed. The receiver was operated at threshold level, and one run was made with high-level seismic inputs. As expected, the receiver lost lock occasionally. All other tests were run with the receiver 3 db above threshold. These latter test runs demonstrated the capability of the lunar seismic amplifier system from microseismic noise level up to hard clipping. The seismic preamplifier noise level was approximately equal in peak-to-peak amplitude to the RF link noise at design threshold.

All the data outputs from the test runs made were recorded on magnetic tape for reduction at JPL. Quick-look records were also made to verify the taped data.

The tests were run with a 7-cps low-pass filter in the seismic simulation, tape playback output. Some concern was expressed as to the validity of this simulation because the actual seismometer can transduce signals up to 20 cps. To resolve this question, the entire closed-loop system test was rerun on October 5 with a 20-cps filter. Since the seismometer flight amplifier and the associated ground adapter both employ 5-cps low-pass filters, there should be no noticeable difference in the performance.

Photographs of the Aeronutronic portions of the test equipment are shown in Figures 14 and 15.

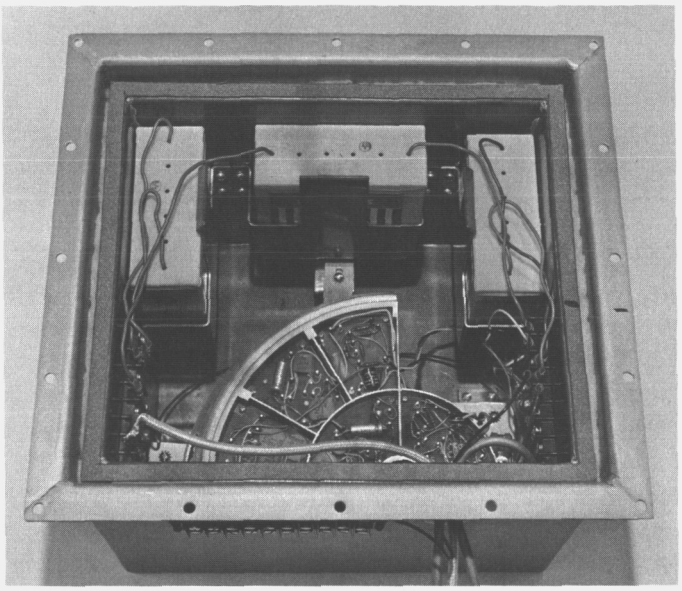

Figure 14. Seismometer amplifier in thermal box

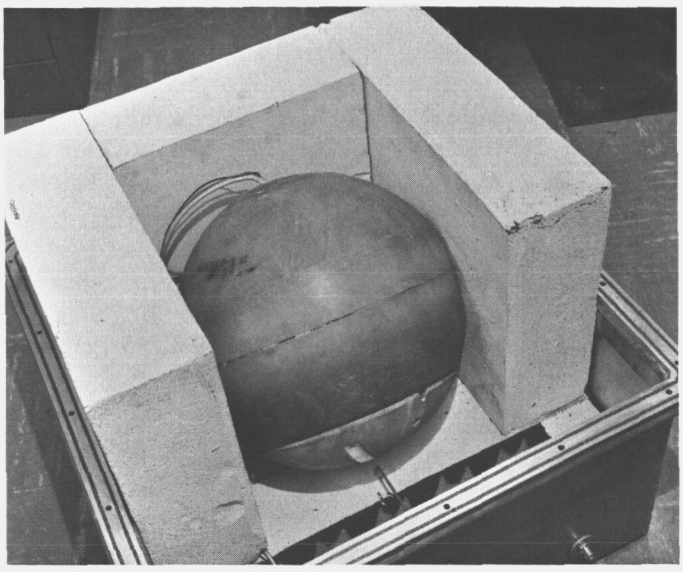

Figure 15. Radiation mockup in quiet box

Systems tests. During the first 2 weeks of October, several systems tests were conducted at JPL. Aeronutronic personnel installed prototypes of the altimeter, support structures, dummy motor, and power and sequencing assembly on the *Ranger* PTM bus. Four primary tests were conducted:

Altimeter RF compatibility. The Wiley Number 1 prototype altimeter was turned on for periods of about 3 minutes to determine if there was any interference between it and other spacecraft equipment. This was the first time a flight prototype altimeter had operated with the complete spacecraft. The altimeter video and AGC voltages were monitored to determine if there was any PTM interference with the altimeter. The altimeter was also operated with its target simulator and RF shroud to provide a normal altitude fuzing signal. The test conclusions were that the altimeter operation was normal in the presence of the bus and that the altimeter did not interfere with any of the other equipment. The exercise also provided a valuable rehearsal of checkout procedures to be used before the actual launching.

Sterilization test. The capsule equipment was left on the spacecraft under the shroud and exposed to the pre-launch sterilization gassing procedure. Live ordnance

squibs and instrumentation wiring were installed for this test.

RF radiation bath. After sterilization, the entire spacecraft was exposed to strong radio-frequency radiation to ascertain if there was any effect on the ordnance items.

Systems test with live squibs. An abbreviated flight sequence was run with the spacecraft to actually fire all live ordnance items. The Ford-provided equipment included fifteen ordnance squibs. Instrumentation was provided to record the firing currents and timing sequence of all squibs.

The results of these tests were quite favorable. There was no indication of any interaction problems from this test series. The ethylene oxide appeared to have damaged some of the contacts that cross the capsule separation joint, despite earlier component tests that indicated no effect from ethylene oxide. Not all squibs fired, probably as a result of the contact deterioration. Had this been an actual flight, no failure would have resulted because of the redundancy employed.

Hercules vibration tests. Hercules Powder Company conducted vibration tests on two live retro-motors installed in a complete capsule (Fig 16) composed otherwise of parts from the dynamic mockup. The shake program was performed according to the same design proof test specifications as were used to prove the structure itself. Particular interest centered on the low-frequency (5 to 40 cps) lateral vibrations as a comparison of the dynamic characteristics of a live motor with those of the inert motor in the regions of greatest amplifiation. The test results indicated slightly lower over-all amplitude gains (3 to 4½) than were experienced in vibration tests of the dynamic mockup at Aeronutronic using an inert motor (4½ to 5½). Gains in the motor region were correspondingly reduced.

The first resonant modes of the capsule assembly with a live motor and with an inert motor were found to be the same in the region of 12 to 13 cps. There were no significant peaks found between 13 and 30 cps on the live motor assembly. It resonated somewhat between 30 and 36 cps, but gains were low for this mode (1½ to 2). Thus, it can be concluded that the live motor has somewhat more damping than the inert motor even in the first mode, has similar stiffness characteristics, and damps out the second mode almost completely. The motors were X-rayed and fired after this test. No damage from vibration could be detected; thus these tests are considered successful.

Lockheed vibration tests. A major structural compatibility test was scheduled for the period of September

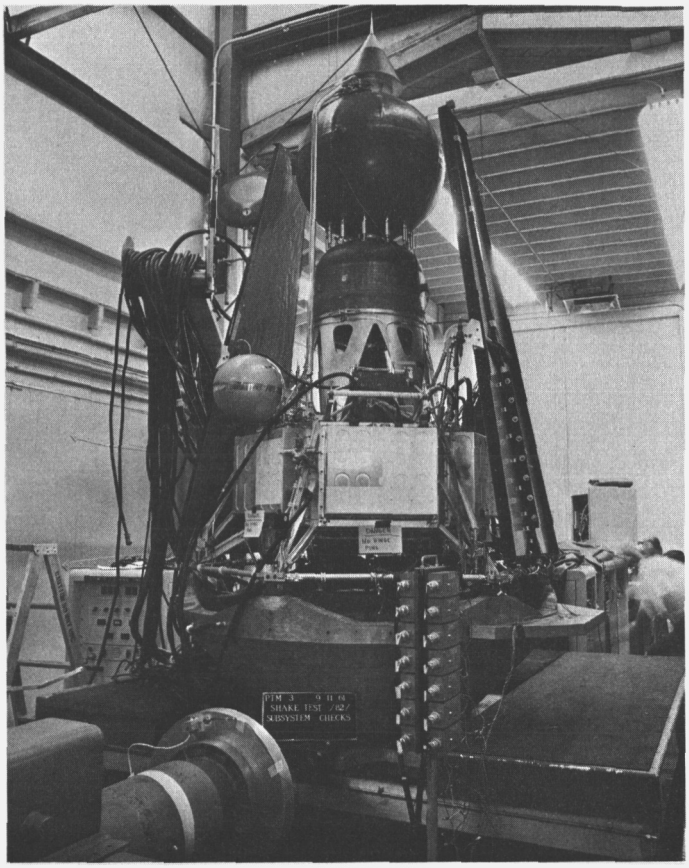

Figure 16. Lunar capsule assembly and spacecraft

25 to 29, at the Lockheed Space and Missile Company, in Sunnyvale. This test was supported by both JPL and Aeronutronic because the bus and the capsule were to be tested in conjunction with the *Agena* B adapter and the spacecraft shroud. The test was delayed by structural difficulties with the *Agena* B adapter and the shroud. Further postponements were then required by instrumentation delays. The tests finally were conducted on October 5 and 6.

The test assembly, which consisted of the Lockheed *Agena* B adapter, JPL RA-3 bus, and the capsule dynamic mockup, was enclosed in the Lockheed shroud. The test was to be performed at 1.0-*g* (zero-to-peak) input at the bottom of the bus. Lockheed placed several limiting sensors on the system consisting of accelerometers and displacement measuring devices. If these instruments sensed motions in excess of certain predetermined levels (2 *g* on shroud, 6 *g* on the impact limiter equator, etc.), the sensors automatically reduced the input levels.

After an exploratory run at ¼-*g* input, the Y plane shake was run at a nominal 1-*g* input. During this sweep, apparently the shroud accelerometer actually limited the

input level to ¾ *g*, and, consequently, the impact limiter never experienced accelerations greater than 2.5 *g* through the first resonant mode of the capsule (12 to 13 cps). The observed acceleration level on the motor was about the same at the second resonant frequency (24 to 26 cps). These values are read from rough data on a VTVM during the shake test. The tape data has not yet been reduced. The shake in the *X* and Z planes was similar. The output levels never exceeded 3 *g* at the impact limiter. However, considering the limitations on the input, there appeared to be no indication of any problem of dynamic interaction between the *Agena* B adapter, the bus, and the capsule.

Gisholt balance machine. Gisholt representatives were called on August 28 to assist in placing the spin balance machine into operating order and to re-establish its capabilities and operating characteristics. Some difficulty had previously been encountered in determining the accuracy achieved in a given operation.

Upon completion of adjustment, the performance in relation to capsule requirements was evaluated. The accuracy of balance at 300 rpm was proven to be within 1 in.-oz. The variance allowance for the capsule is 36 in.-oz of unbalance; thus, it is clear that the machine performs considerably beyond current needs. At low balance speeds (150 and 180 rpm), however, the machine did not indicate dynamic unbalance reliably at all. Testing will continue during the next report period and will include a practice operation of the final, field balancing operation planned for AMR.

3. Major Assembly Status

a. General. For each of the major subsystems, effort has continued in planning for and implementing fabrication, assembly, and acceptance testing of flight equipment. These efforts have culminated in a well coordinated plan to support the scheduled RA-3 launch date. Most subsystem hardware has been fabricated or is on order to support this schedule.

The assembly process for the landing sphere (which includes the survival sphere), is described in the capsule assembly flow chart (Fig 17). Each box of this flow chart has a detailed step-by-step procedure associated with it. These detailed procedures will be used by the technicians in making the assembly and by the inspectors for certification. In addition, all assemblies are made under the direction of the product qualification department of the project rather than by the engineers responsible for the developments.

The sterile assembly glove box, in which flight assemblies will be completed, is on hand, and the training program for its use is underway. The design proof assembly, DPT-5, which was recently added to the test program, will be assembled therein as part of this training program.

b. Retro-rocket. At the writing of the last *SPS*, three motors of old construction were on hand at Bacchus. These motors were to be used to diagnose the failure of motors DR-11 and DR-12. Production was started on eight motors containing design changes, believed at that time to be adequate to correct the intermittent failures previously encountered.

During this reporting period, all eleven of these motors were fired. Table 7 is a list of all test firings to date, and brief descriptions of the last eleven test firings are given.

Table 7. 1961 Retro-motor static firings

Number	Date	Results
PR-2	6 April	Nozzle graphite insert failed at 4.5 seconds
PR-1	10 April	Successful
PR-3	15 April	Case failed due to stand restraint
DR-1	22 April	Failed at ignition (high pressure)
DR-7	2 May	Failed at ignition (high pressure)
DR-2	12 May	Successful
DR-3	18 May	Successful
DR-4	26 May	Failed 50 milliseconds after ignition (high pressure)
DR-5	9 June	Successful
DR-6	17 June	Pressure measurement adapter failed at 0.15 second
DR-8	22 June	Case failed at 0.2 second
DR-9	3 July	Failed at 0.2 second because of faulty test stand setup
DR-10	7 July	Successful
DR-11	14 July	Burnthrough aft dome at 7.9 seconds, accompanied by high pressure
DR-18	15 July	Successful
DR-12	17 July	Failure similar to DR-11 at 5.5 seconds
DR-15	28 July	Full duration. Nozzle exit cone lost 0.3 second prior to burnout. No unusual pressure rise
DR-13	20 August	0.8 second hang-fire; otherwise normal
DR-14	23 August	Intentional fail (0.28 second) separated bond
DR-16	24 August	Intentional fail (6.3 seconds) similar to DR-11
DR-19	31 August	Success: exit cone failed at burnout
DR-20	3 September	Spin fire: hang fire (0.8 second) and insulator fail at 8.8 seconds
DR-26	20 September	Success
DR-17	23 September	Success
DR-23	25 September	Success (vibrate and spin fire)
DR-22	26 September	Vibrate and spin fire. Failed 1.8 seconds; faulty nozzle seal
DR-24	29 September	AEDC test failed 4.2 seconds same as DR-22
DR-25	6 October	AEDC full-duration success

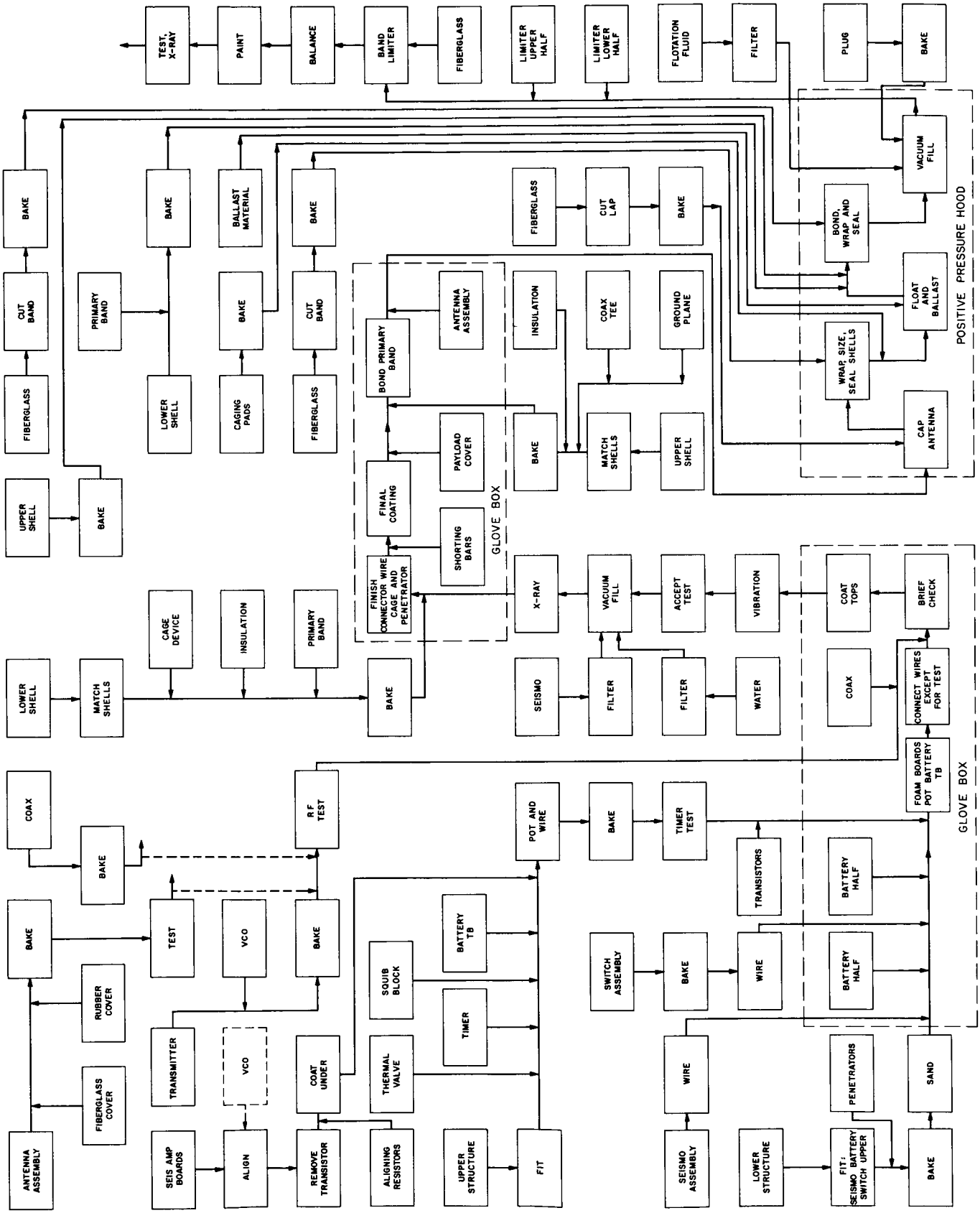

Figure 17. Capsule assembly flow chart

DR-13. One of the postulated failure modes for DR-11 and DR-12 was bond separation due to stress concentrations at the junction of propellant and case in the aft end. DR-13 was modified by including a 5/16-inch radius fillet in the grain at the aft dome interface. This modification was made to simulate the stress relief incorporated in the grain redesign then in production. The unit was hydrostatically pressurized to 400 psi to determine the extent of case growth and was extensively instrumented for firing.

After a hang-fire of 0.88 second, the firing proceeded for full duration with no indication of failure. At that time, the hang-fire was attributed to water soaking and leeching of the grain surface during the hydrostatic test. Corrective drying measures were instituted.

DR-14. Case bond separation in the aft dome was considered to be the most probable cause of failure of DR-11 and DR-12. To verify this, a fixture was designed to apply hydrostatic pressure to the motor chamber at a rate comparable to the ignition pressure rise, so that dynamic loadings could be simulated. The motor was pressurized to 470 psi at a rate 10% in excess of normal ignition pressure rise rate, and the unit was examined by X-ray. Examination disclosed a bond separation extending almost entirely around the aft dome and back nearly to the tangent line of the case. Calculations were made and it was estimated that 400 $in.^2$ of new burning area were exposed by the separation. This additional surface would add about 400 psia to the chamber pressure which would definitely cause the case to fail. It was decided to fire the unit in a battleship stand to see if the failure behaved similarly to DR-11 and DR-12.

Failure occurred at 0.3 second. After a normal ignition transient, the pressure started to rise and continued to 800 psia when the case failed. The test strongly confirmed that, as postulated, bond separation was the cause of the type of trouble experienced on DR-11 and DR-12.

DR-16. Inspection of this unit after a hydrotest to 400 psia disclosed a bond separation over 30 to 40% of the periphery of the aft dome. The separation extended up to 2 inches forward at some point. An estimated 30 $in.^2$ of additional burning area were present. The motor was fired in the battleship stand. The motor ignited normally, then the pressure curve rose to about 100 psia excess pressure after 0.4 second of burning, then regressed to normal and slightly below and failed at 6.7 seconds due to a burn-through in the aft dome. In all respects, the failure was a repeat of DR-11 and DR-12.

This completed the diagnostic firings. The results gave high confidence that the design and process changes employed on the eight motors in production were correct.

DR-19. This was the first unit containing the design changes (discussed in detail in *SPS 37-11*). DR-19 was subjected to a high-rate hydrostatic load test approximating the ignition environment. Inspection revealed no damage. The motor was fired and was successful in all respects except that the nozzle exit cone failed just before burnout. The motor chamber was ignited at a simulated pressure altitude of 75,000 feet. The pressure curve for the modified grain design was as predicted by analysis.

DR-20. This motor was fired in a special fixture which spun it at 300 rpm. Two malfunctions occurred on the test but neither was associated with the grain-case problem observed previously.

First, there was a hang-fire of about 0.8-second duration. The hang-fire was similar to that in DR-13 which had been attributed to water soaking. Since DR-20 had not been subjected to hydrotest, it could not have been the cause of the hang-fire. Careful examination of the high-speed film of the firing disclosed that partially burned igniter pellets were ejected from the motor at ignition and that debris, apparently from break-up of the igniter basket, was also ejected. It was concluded that the rubber-nylon igniter basket was marginal and was breaking up prematurely on some firings. A fiberglass basket was designed and prepared for all subsequent tests.

Second, a burn-through in the aft dome occurred at 8.82 seconds of burning (0.3 second before nominal burnout). The burn-through was not accompanied by excess chamber pressure as had been the problem with previous case failures. Since this was the first unit fired while spinning, the possibility of increased liner erosion due to spinning had to be considered; however, it was not apparent why the erosion rate should have increased perceptibly at this low-spin rate. Three conflicting considerations had to be evaluated:

(1) The liner was thinner by 3% than the acceptable minimum in the area of failure. The liner had been accepted on waiver.

(2) The igniter basket break-up could have allowed $BKNO_3$ pellets to collect in the propellant slots, thus exposing the liner to a more severe environment.

(3) The unit was spinning and, even though an erosion rate increase was not calculable, the data from this test required that it be considered a possibility.

At this point, six motors were on hand. The problems observed on DR-11 and DR-12 were apparently solved but three new questionable areas had been uncovered: (1) the nozzle was structurally marginal under the aluminum attachment ring, (2) the igniter basket was marginal and apparently was breaking up on some firings, and (3) the insulator was subject to question because of the one failure. The schedule was such that a conservative approach was mandatory. Therefore the following steps were taken:

(1) The igniter basket was changed to fiberglass and extra precautions were taken to mount it securely to the shaft. The basket configuration and construction selected is very similar to the design used in the *Minuteman* igniter. Igniter chamber firings were made to verify the basket integrity, and the new igniter was included on all subsequent motors.

(2) The nozzle was structurally augmented to assure its integrity, and production of this design was expedited by the subcontractor so that the modified version could appear on all subsequent firings.

(3) The insulator situation was somewhat more difficult to resolve because of lead times involved. It was apparent that further information was needed to determine if the failure was spin correlated, a result of the igniter basket break-up, or simply the result of inadequate insulation. In order to obtain the needed information, it was decided to fire two additional spinning motors. The two additional motors were DR-22 and DR-23.

DR-26. DR-26 was fired statically without spin with the modified nozzle and igniter and with insulation in the critical area 3% greater than that of DR-20. The unit was successful in all respects and served as verification for both the igniter and nozzle changes.

DR-17. This unit was fired identically to DR-26 above, except that it included vibration dampers and had the electrical contact board assemblies bonded on the motor case.

DR-17 history included temperature cycling from 40 to 80°F, the temperature at which it was fired. In addition, it had also been subjected to a high-rate hydrostatic test, simulating ignition loads. The motor chamber was evacuated for ignition to simulate 100,000 feet altitude. The firing was successful in all respects.

DR-23. DR-23 was subjected to vibration tests of design proof levels and suffered no damage. The motor was spin-fired, and the test was completely successful. The insulation in the critical area was 8% thicker than that of DR-20. It was concluded that it would be conservative to establish a minimum acceptable thickness for the insulator at 20% greater than the liner in this successful firing, a value 28% thicker than DR-20. This decision allowed motor cases with liners already constructed to be used for acceptance testing and flight. This firing, together with DR-20 indicated no performance variation due to spinning.

DR-22. This unit was subjected to design proof vibration and spin fired. The motor failed at 1.8 seconds due to gas leakage around the nozzle attachment ring. Hercules' diagnosis concluded that faulty installation of the nozzle damaged the O-ring used to seal the attachment. Ignition was satisfactory at an evacuated chamber pressure simulating 140,000 feet.

DR-24. This motor was fired at AEDC in the altitude cell. DR-24 and DR-25 were intended to demonstrate adequacy of the nozzle exit cone, in addition to furnishing further verification of ignition capability at high altitude. During the test set-up at AEDC, a technician accidentally broke the igniter shaft and the nozzle had to be disassembled to replace the igniter. The motor failed at 4.2 seconds because of loss of the nozzle. Ignition was satisfactory and burning was normal up to 2.8 seconds, when the chamber pressure record indicated gas leakage had started. The chamber pressure dropped an estimated 100 psi prior to complete release of the nozzle. Due to the very low cell pressure (115,000 feet equivalent), the propellant burning stopped instantaneously. The unit was allowed to cool before the cell pressure was brought back to sea level, and thus the remains of the motor were preserved. Inspection of the parts showed clearly that gas leakage at the nozzle-case attach point had again been the cause of failure.

In light of data from DR-22, Hercules had been reviewing the nozzle installation procedure and had concluded the cause of failure was damage to the O-ring pressure seal on assembly. Installation procedure was changed and provisions made to protect the O-ring, but because of the short time interval between the two tests, these procedures were not in use when the nozzle was re-installed on DR-24.

DR-25. DR-25 was fired in the AEDC altitude facility at a simulated pressure altitude of about 110,000 feet. The firing was full duration and preliminary data indicates all components performed satisfactorily. A close examination of the nozzle exit cone will be made at Bacchus, and if any indication of near failure exists, additional insulation will be included in all flight and flight acceptance nozzles. Since this is now the only

achievable test of the exit cone at full-flow prior to acceptance tests, a conservative approach must also be taken in this regard.

Preliminary information on performance indicates the specific impulse based on actual propellant loaded weight is slightly higher than had been expected by approximately 1.5%.

The present configuration of the retro-motor has performed successfully under all environmental tests planned for the development program except vacuum soak of the propellant. Two additional firings are scheduled at Bacchus about October 18, 1961. These tests will be used to (1) demonstrate vacuum soak capability, (2) check the flight wiring and ignition system, and (3) obtain further data on spin firings.

Flight acceptance tests are scheduled to start October 15, 1961, and should be completed in the next reporting period. Loading is proceeding well and flight units will be ready for delivery October 15, 1961, subject to the flight acceptance test results.

c. Spin motor. The last two development firings of the spin motor are to be conducted during the week of October 9. These firings are intended to confirm the suitability of minor design changes in the manifold-to-case and the manifold-to-tube joints.

A total of 19 qualification test and flight units are planned. Except for 4 manifolds and 12 nozzle tubes, all detail parts for these units are on hand. Subassemblies of metal and graphite parts are complete for 15 units; final assembly of the nozzles and manifolds and casting of the propellant will commence following the two firings noted. A total of 12 qualification rounds will be fired. Prefiring conditioning of these rounds will be used to demonstrate compliance with the system environmental specifications.

All firings will be made on a special test fixture which will measure the total spin torque impulse and the equivalent unbalanced moment about the retro-system center of gravity. An experimental test fixture was completed some time ago and a large number of cold flow runs (using dry nitrogen) were made. These interim tests were conducted to isolate problems involved in accurate and simultaneous measurement of the relatively large spin torque and the comparatively minute out-of-plane torques. Areas investigated included the effects of forcing frequencies of the nozzles, resonance modes of the fixture, optimum location and attachment of load sensors, frequency response of the instrumentation, calibration techniques, and test procedure. This information was used in the design of the hot firing fixture, which is now being built.

During these preliminary tests, a major improvement in the method of limiting torque vector misalignment was established. It was determined that the individual nozzles could be reworked after assembly on the basis of cold flow tests, and thus it is possible to limit the out-of-plane torque to a value well within the system requirements. The requirement is 0.006 radian. However, on cold flow adjustment, the spurious torque vector was reduced to about 0.003 radian for three nozzle sets. It is planned to use this trimming method for all flight and acceptance units.

d. External structures. Most of the development of the non-landing-sphere structures is complete. Some development work continued on the altimeter support and erection system, in that the alternative design was completed and tested. It was found that the original design model exceeded the allowable torque-impulse limit on erection. The alternative design incorporates a longer time constant system (10 seconds) but reduces the impulse to the specified value. This design also includes a change in the manner of passing the external wiring across the hinge-joint. In addition, some improvements were made to the latch by adding a positive acting spring latch to supplement the magnetic latch.

Retro-motor thermal shield. Work has been proceeding on two different designs for the retro-motor thermal shield. One unit of each type has been fabricated for use in the system thermal tests. It is intended that a decision as to which design to use for flight will be based on the results of this test.

The first of these arrangements consists of cylindrical aluminized Mylar shields supported on the ends by rigid rings which are spaced by light aluminum tubes. The assembly is split on a diameter, forming two independent *clam-shells*, each of which is hinged to the retro-motor support structure near the bus. In the shielding positions, the halves of the lower ring are clamped together by bolts, and the upper ring is held closed and in position just below the equator of the impact limiter by four cables that attach under the clamp ring on the upper flange of the impact limiter. When the omnidirectional antenna is deployed, the upper support cables are released, which opens the latches on the upper ring. On electrical signal, switched by the altimeter antenna reaching the fully deployed position, bolt cutters release the lower ring, allowing springs at the hinge points to rotate the clamshells about 45 degrees to the open position. A slip rod prevents rebound after the open position is reached.

The thermal shielding consists of six layers of aluminized Mylar. The five inner layers are 0.001 inch thick and aluminized on both sides; the outer layer is 0.003 inch thick and aluminized on the inside only. Calculations indicated that this shielding would maintain the retro-motor temperature within a 12°F band for 66 hours while radiating to dark space, and that the stabilization temperature in direct solar radiation is satisfactory. Tests conducted at Aeronutronic showed that there was no observable change after extended baking at temperatures higher than the 400°F boost transient.

The test unit is fabricated and is presently available for test. The second shield configuration was developed in part by the National Research Co. (NRC), in accordance with technical requirements established by Ford. It consists of 40 layers of single, aluminized, crinkled Mylar film 0.00025 inch thick, with an outer layer of 0.002-inch-thick Mylar aluminized on the inside only. Separate blankets are used over the retro-motor and the motor support structure.

The retro-motor portion is assembled to a light aluminum ring at the upper end, which attaches to the impact limiter dampers and extends down to the lower Marman clamp. This portion, which weighs about 1 pound, remains with the retro-motor during spin-up and firing. A similar piece is permanently attached to the retro-motor support structure, and a smaller section to the clamp, to allow retro-motor separation.

Empirical data obtained by NRC from other applications of similar blankets indicates thermal insulation characteristics 20 to 30% better than the calculated values for the rigid shield. Additional advantages include simplicity of installation and reliability inherent in a non-operating component. Matters yet to be evaluated include the additional retro-motor weight and the possible need for provision of openings in the lower shield for escape of the spin-rocket exhaust.

e. Landing sphere. Evolution of the landing sphere to the final, flight configuration was accomplished during the past reporting period. This evolution has involved an intensive developmental test program on hardware produced from a combined program of: (1) prototype and developmental fabrication of subsystem hardware, and (2) operational development of a pilot-line assembly process to accomplish fabrication of flight-type landing spheres, whether for development or design proof test. This approach was deemed the most effective way to develop a reproducible procedure for accomplishing the uniquely integrated assembly of a sealed survival sphere and to provide as much practice of the procedures as possible. The required development series was enlarged considerably as a result of unfavorable test results on early models. The developmental process thus has taken considerably longer than had been scheduled earlier.

The major developmental tests accomplished during this period consisted of tests on the following landing sphere or survival sphere vehicles:

An insulation test vehicle (ITV-4) was fabricated of 18 layers of 0.020-inch Dacron felt with interleaved aluminum foil assembled into a test sphere. The hemispherical insulation muffs incorporated glass paper strips laid over the butt-joint gaps of the felt petals. Nylon recentering ties were installed at the top and bottom of the sphere. The insulation included cutouts for penetrators, antenna coax, and caging foot, with penetrator blast shields simulated by rubber patches. Equilibrium heat loss at 32°F was measured to be 2.32 watts in the LN_2 chamber.

A second test vehicle (ITV-5) incorporated insulation similar to that of the first, except the glass paper was installed as full layers rather than as strips. All cutouts were omitted. A flight-type Microdot coax was laid through the insulation muff. Equilibrium heat rate at 32°F was measured to be 2.57 watts with an uncertain error due to instrumentation difficulties. Subsequent to this test, the coax was removed, the instrumentation repaired, and the heat rate measured at 2.46 watts at 32°F in the LN_2 chamber.

Upon disassembly, it was found that the instrumentation wires were improperly installed. The vehicle has been reassembled and is being subjected to further testing. Preliminary results indicate a heat rate on the order of 1.6 watts, which would be tolerable.

As a result of these tests, design proof insulation assemblies are being constructed of 30 layers of 0.013-inch Dacron felt with full interleaved layers of 0.0048-inch glass paper and 0.00045-inch aluminum foil. On the basis of experimental results obtained to date on samples of this insulation, it is believed that the cold-environment heat-rate for these models will fall in the range of 1 to 1.5 watts provided that the construction is accomplished with great care.

The primary functional objective of the ordnance test vehicle (OTV-1) was to test, under representative conditions and in a flight assembly, the operation of the penetrators and caging devices. This assembly consisted of a flight-design inner sphere structure with penetrators, water valve, blast shields, caging device assembly, a test Dacron felt insulation, dummy antenna, and prototype

shells. Special g-switches to arm on spin-up and a special timer were placed in the potting material, which filled most of the unused cavities within the structure. A flight-type impact limiter was used.

The impact test consisted of a short spin at 300 rpm to initiate pre-impact uncaging, a 3-minute hold, and a straight 90-degree nonspinning impact at 168.4 ft/sec on the antenna end of the assembly (the reverse of the direction expected in flight).

The penetrators failed to fire following impact, and the assembly was removed for X-ray and then for disassembly. The following summary records the results of this inspection and the actions taken.

Both the prototype insulation shell and prototype flotation fluid shell failed in impact. Analysis had shown them inadequate for this test condition; hence, the results were expected. All subsequently constructed vehicles had and will have thicker shells. Failure of the insulation shell resulted in damage to electronic components in the squib block, thus preventing successful operation of the post-impact cager and the penetrator.

Battery power was intermittent because of a poor solder joint. This assembly was not inspected by the design proof and flight article procedures.

The penetrators and post-impact cager fired when the circuits were energized after disassembly. One penetrator shield failed to retract because of failure of the rubber retractor. The retractor was redesigned to provide for a more positive attachment to the shield.

Pre-impact uncaging was normal. The test provided valuable information for redesign of the shells and penetrator shield system. Test objectives related to penetrator-insulation compatibility were not accomplished because it was necessary to remove the upper insulation shell to fire the penetrators.

A second ordnance test vehicle (OTV-2) assembly will include the flight-type sphere structure, timer, squib block, caging foot, flotation fluid, flotation fluid shell, and impact limiter. Test prototype items in the assembly included the batteries, antenna coax, antenna, ground plane, and insulation shell. Dummy items included penetrators (inactive), seismometer, and dummy insulation consisting of ten layers of 0.040-inch Dacron felt with interleaved foil. The primary purpose of the test was to study the functional performance of the caging systems under simulated pre-flight and flight environments. Secondary objectives were to further test the integrity of the sphere structure, insulation shell, flotation fluid shell, and impact limiter under conditions of spinning impact at 45-degree inclination.

X-ray examinations of the assembly were made prior to and after impact. The caging device successfully withstood all pre-impact environments and functioned properly during that part of the test sequence. However, major failures of auxiliary systems occurred which compromised the results of the post-impact caging test. Further, a failure occurred in the caging device itself which prevented post-impact caging. The test failures and corrective action are summarized as follows:

The antenna cover cracked, permitting Freon to seep into the balsa antenna. The ground plane broke loose from the insulation shell, thus allowing the Freon from the antenna to wet the insulation. The flight antenna will have a rubber cover and the ground plane-insulation shell joint has been redesigned to provide more strength. Both of these design improvements are included in DPT-3.

Chemical action in the water tank caused generation of gas which forced water out the thermal valve cavity seal. Flight and design proof models have a protective coating inside all tank areas to prevent corrosion. Fill water will be of a specified pH factor and electrical conductivity and will have ¼% sodium dichromate added to inhibit corrosion. The valve cavity has been redesigned to provide more positive sealing.

An isolation resistor in the pre-impact uncaging circuit became flooded with Freon. The resistor burned but failed to open the circuit, thus causing a continuous drain on the battery during the cycle. The voltage applied to the recaging circuit, fired a 1-ampere parallel fuse but was not great enough to fire the recage motors. The pre-impact uncaging operated normally. Subsequent assemblies incorporate a redesigned resistor housing to provide positive sealing against the Freon.

The antenna coax was improperly installed and failed on impact. Design proof models have a redesigned coax installation which incorporates commercially available cable.

Except as noted, all components satisfactorily passed the test. Post-impact erection with the non-flight type insulation was determined to be within 7 degrees.

Transmitter. The 960-mc telemetry transmitter is the link between the lunar capsule and the Earth-based receiving sites. In combination with the antenna, it provides an effective radiated power of at least 50 milliwatts in the direction of the Earth.

A developmental transmitter was subjected to a simulated landing impact in ETV-1. After the test, two capacitors were found to be fractured, although this type of capacitor had never failed in numerous high-impact component qualifications tests and a number of identical capacitors in the same compartment were in good condition. After replacement of one of the capacitors, the transmitter operated within specification. The other capacitor is so restrained by its mounting that its fracture did not affect operation. It is believed that one of the capacitors was slightly damaged during an assembly soldering operation, and failure of the other may be attributable to a slight misalignment of the cavity feed. The shock resulted in a negligible transmitter frequency shift.

Two flight-type transmitters have been assembled for test in DPT-3 and DPT-5 (the latter unit originally intended for DPT-4). Both transmitters include a new addition to the design: a booster circuit to provide additional bias to the second multiplier. The subcarrier oscillator signal is properly isolated to prevent wave-form distortion and is rectified to produce an added 10 volts of bias. This allows a more favorable impedance match to be used in the second multiplier, improving the power output and efficiency of the transmitter.

Antenna. The position of the capsule on the Moon may be as much as 45 degrees off the Earth–Moon line. The antenna axis is pointed nominally up from the lunar center of mass by the erection of the capsule. A broad-beam antenna is, therefore, necessary to provide as much gain as possible while maintaining a circularly symmetrical beam.

The flight capsule antenna (*SPS 37-11*), in its latest version, provides a gain of about 2 db (rather than the 0 db previously reported) 45 degrees off the beam axis, and has a nominal impedance of 50 ohms.

A thin rubber covering has been added to the antenna assembly. In some impact tests, it appeared that flotation fluid had been absorbed by the balsa antenna dome. While this action does not affect the electrical performance of the antenna, the ability to erect properly is handicapped if too much fluid is absorbed. The rubber cover is elastic enough to remain continuous even though the epoxy-fiberglass shell on the dome may crack and will prevent absorption of the fluid. No degradation in electrical performance has been measured.

Antenna coax. A major effort was exerted to verify whether 50-ohm Microdot miniature coaxial cable would serve as a suitable replacement for the extruded transmitting cable previously considered. This effort was brought about by the lack of reproducibility which was obtained with extruded copper/etched cables. Thermal tests showed that the Microdot cable has a conductivity of 0.0049 Btu-in./hr-°F. Also, the RF insertion loss on all cables tested has been equal to or less than 0.05 db/in. With an effective cable length of 5 inches, this cable meets the thermal requirements without significantly degrading the RF output. Impact tests of this cable showed no significant deformation or change in electrical characteristics. Experience has revealed that, by virtue of its simplicity, assembly of this conductor is much easier to control. Temperature soaking after fabrication is used to provide a permanent helical shape. This latter procedure conveniently satisfies the sterilization requirement also.

Thermal valve. Final testing of the thermal control valve for the boil-off liquid has also been completed. This is a pressure-modulating, spring-loaded valve with an orifice which opens at approximately 70°F to permit evaporative cooling of the capsule. At this temperature, the heat-flow rate is 5.2 Btu/hr (1.53 watts), which allows the capsule temperature to decay about 2°F/hr. When the temperature drops to 50°F, the valve closes, and with subsequent heating it again cycles through the hysteresis loop. Compatibility of valve operation, liquid evaporation, and seismometer response were tested at Mt. Wilson. During the portion of the cycle when the valve was open, disturbance was noted on an average of only once every 8 minutes. The pulse lasts for a fraction of a second, is one-sided with an average peak amplitude of 3 times the normal peak-to-peak background level, and appears to be critically damped since there is no evidence of ringing.

Seismometer amplifier. A low-noise, extremely stable amplifier is required to raise the fractional microvolt output of the seismometer to a useful level. The design for a satisfactory amplifier was prepared some months ago, but particularly sensitive areas of the circuit have been undergoing exhaustive tests to determine the best possible components and circuit configurations.

A developmental seismometer amplifier was subjected to simulated landing impact in ETV-1. Examination of the electronics after the test revealed that two diodes were fractured. An examination of subassembly photos taken during sphere build-up shows what probably is a chip in one of the diodes prior to assembly. The other diode was probably chipped on disassembly. Photos of the unit during disassembly clearly show the chip late in the disassembly process, while pictures taken earlier do not. Lighting has an influence on visibility of the chip in the photograph. Because this was a developmental

assembly, current assembly standards and rigid inspection practices were not fully developed. After the diodes were replaced, the seismometer amplifier operated as before impact. This developmental model has been undergoing life test since September 1 with continuous recording of noise output.

Three seismometer amplifiers have been constructed in accordance with established quality control procedures for design proof tests in DPT-3, -4, and -5. The last one was also employed in the DSIF tests at Goldstone.

The transfer function of the flight design seismic amplifier is

$$H(s) = (Ma + b)\left(\frac{1}{1 + 0.0159S}\right)^3$$

$$a = \frac{795S}{(1 + 3.18S)(1 + 0.0045S)}\, xe_{in}$$

$$\left.\begin{matrix} m = 600 \\ b = 0 \end{matrix}\right\} \text{ when } 0 < |a| < 0.0002633$$

$$\left.\begin{matrix} m = 145 \\ b = 0.1198 \end{matrix}\right\} \text{ when } 0.0002633 < |a| < 0.002633$$

$$\left.\begin{matrix} m = 0 \\ b = 0.5 \end{matrix}\right\} \text{ when } 0.00263 < |a| < \infty$$

The transfer function of the seismometers is, according to information from CIT

$$H(S) = \frac{0.213S^3}{S^2 + 2S + 2\pi}$$

and the units are v/cm.

The transfer function of the VCO is

$$f = 560 + 30v$$

where v is the input voltage.

Timing. The post-landing events of recaging and venting the sphere are controlled by an electronic sequence timer. The internal timing sequence and system have been described in previous reports. An additional function, a shorting timer, has been added to shunt the tip-over switches during launch to guard against the latter opening during flight.

Developmental sequence timers have survived undamaged and, in operating condition, simulated landing impacts in SLL-1, SLL-2, OTV-1, OTV-2, and ETV-1. Three timers have been assembled in accordance with established quality control procedures for DPT-3, -4, and -5. No difficulties or changes are expected in this assembly, and fabrication of subassemblies (flip-flops, gates, and clocks) for flight units is complete.

The starting timer, shown schematically in Figure 18, begins timing upon closure of a 5-g switch during launch. If, at the end of the timing interval (nominally 1.5 seconds), the g-switch is still closed, the silicon-controlled rectifier will be triggered, firing the squib switches, which then shunt the tip-over switches. If the g-switch should open before the timer completes its timing operation, the circuit will reset itself in less than 400 milliseconds. The starting timer is not fooled by high-level shock of less than 1-second duration or by high-amplitude vibration down to 0.5 cps. When the squib switches fire, the circuit disconnects itself from the power supply and, hence, will not reduce capsule battery life even if the g-switch were to be permanently closed by landing impact.

A design proof model of the new circuit, in which a 5-g switch by-passes the mercury switches, is being constructed to be included in DPT-5, but the unit is not required to survive the landing impact and will be given a separate design proof test before installation.

f. Capsule battery. Serious problems developed with the main capsule battery during this reporting period. The battery is a secondary, silver-zinc, high-capacity unit built especially to Aeronutronic electrical, dimensional and environmental requirements by the Missile Battery Division of the Electric Storage Battery Company. The original purchase order called for the delivery of nine batteries. Six were for development purposes and three were to be sterile and suitable for design proof testing.

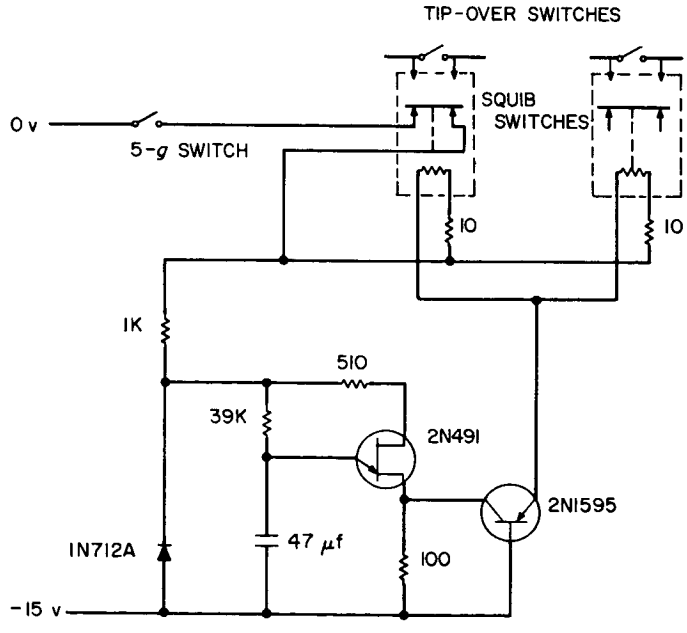

Figure 18. Lunar capsule starting timer

The first six batteries gave excellent electrical performance but the later units were only a partial success under environmental conditions.

Serious trouble was recognized when two situations arose. First, the sterile design proof battery Number 1 was delivered leaking electrolyte. Subsequently, the next two design proof batteries also developed leaks under shelf storage conditions. Second, a test battery module supplied by the vendor was found not to be sterile. The test module had purposely been contaminated with spores during manufacture to see if the materials within the batteries were sporicidal. The sterility test showed that the Bisonite resin used for encapsulation of the cells was not sporicidal.

These developments prompted a thorough review of the capsule battery. Technical consultation was obtained from the Aeronutronic and Electric Storage Battery Research Laboratories. The following design and production problems were recognized:

(1) The Bisonite resin used for fabricating bipolar frames and for final encapsulation was not sporicidal and a substitute had to be found.

(2) The silver sheet supporting the battery plates did not bond well to the bipolar frame. Electrolyte leakage around the end of a sheet would cause a cell short.

(3) Electrolyte could leak out through the stranded leads, although they had been soldered solid. The leads were placed within ⅛ inch of each other during encapsulation, and would often develop leakage resistance.

(4) The zinc battery plates would swell during charging and cut the separators against the sharp bipolar frames.

The vendor was asked to deliver three more design proof batteries incorporating design changes to overcome the existing problems. The vendor agreed and cooperated in establishing an accelerated program for the vendor's development, producing and testing of the batteries. The agreed-upon changes in the new batteries were:

(1) The design for fabricating bipolar frames and for encapsulation was changed from Bisonite to the proven sporicidal resin carbination, Epon 815 with TETA.

(2) The silver support sheets were to be sealed to the bipolar frames by improved surface treatment and the use of the sporicidal adhesive Plastilock 604.

(3) Solid wires were used for the leads from the battery cells. A terminal board was placed in the encapsulation to keep all wires sealed and separated.

(4) The plate separators were strengthened by the addition of nylon spacers. The edges of the bipolar frames were rounded. Slightly less zinc powder was used in the negative plates.

(5) Increased attention was given to quality control procedures.

After these changes were instituted, three new design proof batteries were delivered on October 2, 6, and 10. The first battery, Number 18, was installed within the BTV battery test sphere. The BTV was impacted on the Hyge machine on October 13, but no test results are available. The second battery, Number 19, is to be installed in the complete design proof survival sphere, DPT-5. The third battery, Number 20, was started on repeating the separate electrical and environmental tests made with the developmental batteries. The measurements made on these three batteries have shown satisfactory values. Apparently much of the recent battery trouble was due to the shift in their manufacture from a model shop to a pilot line. The batteries made in the model shop survived impact tests and operated satisfactorily thereafter.

Consideration was given to a method of improving battery reliability by decreased cycling before flight. It was originally planned that the flight discharge would be the third discharge. This much cycling gives maximum energy storage but might increase the probability of failure during lunar operation. Therefore, it has been decided to make the flight discharge the second discharge.

When some single battery sections were failing, thought was given to the isolation of the paralleled battery sections by diodes to improve reliability. It was, therefore, decided to include the diode configuration of Figure 19 in the BTV test sphere. The test would permit a later decision as to use of diodes in the actual flight capsules. The use of the diodes would allow a capsule to function with a shorted battery cell, although, for a shorter period of time. The penalty is potential unreliability of the diodes. If the diodes survive impact, an attempt will be made to analyze quantitatively the trade-off in this regard.

g. Voltage controlled oscillator. After the ETV-1 impact, the Dorsett Model 0-8 was found to be defective. Disassembly and subsequent inspection revealed that a resistor had been broken by impact because of insufficient potting compound in the VCO housing. Dorsett had been employing a silicone rubber for encapsulation by a

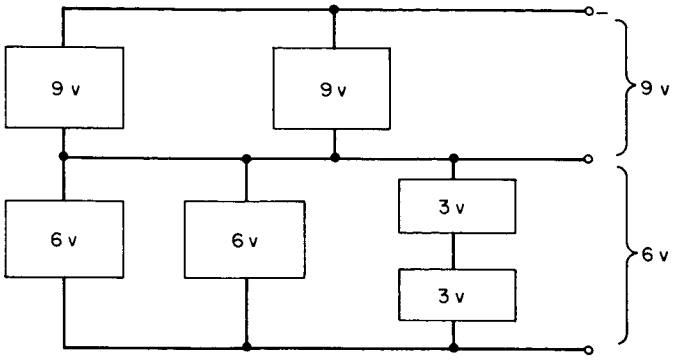

BATTERY CONFIGURATION PLANNED FOR FLIGHT

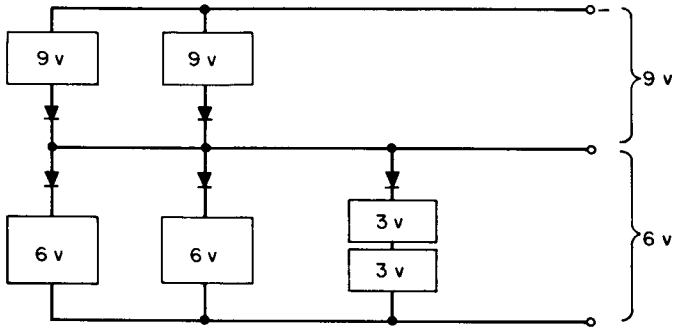

BATTERY CONFIGURATION WITH DIODES UNDER CONSIDERATION

Figure 19. Battery configurations

pressure-gun technique, but this material is too soft for high-level impacts. Consequently, a stiffer material, Hysol 15-058, and vacuum impregnation are now employed. Dorsett VCO's were reordered under the new requirements. Six of the new VCO's have been received, and four of them have been baked at 125°C for 24 hours and placed in the BTV for qualification testing.

To increase the likelihood of success in this area, a back-up VCO development was initiated as soon as the ETV-1 failure was noted. Quotations were solicited from ten VCO suppliers for compatible electrical and physical units. Only one supplier, Vector Manufacturing Company, replied favorably. Five of the Vector VCO's have been received and four will also be tested along with the Dorsett units in BTV. The outcome of this test will be used to determine which VCO should be tested in DPT-5 and which should be used for flight.

h. External electronics and ground adapter.

Altimeter. A fuze-type radar altimeter is provided to measure slant range from bus to lunar surface and to signal bus-capsule separation at a range of approximately 70,000 feet. The exact fuzing range depends upon the final measured values of retro-rocket performance to be obtained at a later date. In addition, the altimeter is to provide a telemetering signal proportional to the received echo strength. When obtained, this data will have significant scientific value in attempting to describe the lunar surface and also will improve engineering knowledge for future lunar landing missions.

The subcontract for the flight altimeters was let to Wiley Electronics Company. Work on the altimeter subcontract during the reporting period concentrated on fabrication and design proof testing of two flight prototypes. The work successfully completed represents the passing of a number of critical milestones in the altimeter program. The milestones of primary interest are the successful completion of design proof tests and subsequent delivery of prototype Number 1 to Aeronutronic on schedule, and the completion by Wiley of their portion of the design proof tests of prototype Number 2 and its delivery to Aeronutronic, also on schedule.

The altimeter prototype Number 1, which was completed August 15, was made as nearly as possible like the flight unit and weighed 6 pounds, 11 ounces. The 3 ounces of overweight accumulated from an overweight dust cover and several heavy flanges in the waveguide assembly which had not been machined as they will be for flight. Also, in several areas, the foam potting of the electronic assemblies was denser than desired. Because the changes required to reduce the unit's weight to 6 pounds, 8 ounces would not affect the electrical or mechanical performance of the altimeter, this unit represents a good prototype of the flight units.

As a result of additional tests performed on the first unit, which were not part of the design proof test as such, the gain of the signal conditioning circuit was found to be lower than desired and a change was made to increase its gain for the second prototype and all flight units. In the performance of the functional tests of the first prototype and subsequent tests, the unit has been turned on and operated successfully approximately 250 times. During none of the tests except when arcing and corona were present in the medium-high altitude test, did false fuzing occur. Throughout the performance tests, the unit sensitivity was approximately 15 to 20 db better than required to operate with the maximum anticipated path attenuation and the minimum expected transmitter peak-power output.

The fuzing accuracy was recorded with an input signal level 7.5 db less than the minimum anticipated signal return and measured with instrumentation that has an inherent accuracy of approximately ±75 feet. The meas-

ured variation in fuzing range throughout these tests was ±150 feet maximum.

The tests described were performed with the unit operating from auxiliary power. The altimeter was fitted with a battery pack, but since no prototype battery was available, the battery performance will be tested separately under the various environmental conditions. The battery, which is being supplied by Electric Storage Battery Company under a contract with Aeronutronic, will be evaluated and tested separately for all the environmental requirements to which it will be subjected as part of the altimeter package. Two prototype batteries have been received by Aeronutronic and are presently undergoing these tests.

The second prototype altimeter unit which has been delivered to Aeronutronic, is now undergoing the final high-vacuum tests, low-frequency vibration tests, and boresight tests and should be made available to JPL by October 17. This unit weighed 6 pounds, 8.5 ounces with a dust cover which is 1 ounce overweight. A new gold-plated dust cover has been shipped from Wiley to Aeronutronic and should be available for replacing the unplated cover before delivery of the unit to JPL.

The second prototype was built to the flight configuration except for minor differences in the flight unit which are presently being requested by Aeronutronic. These exceptions are:

(1) The inclusion of a means of supporting the altimeter weight along a line through the center of gravity of the unit during the mechanical alignment of the unit on the bus.

(2) A 20-degree rotation of the tabs making up the boresight pad attach points on the periphery of the antenna.

(3) A change in the size of the battery case to accommodate the ESB battery which is smaller than originally anticipated.

During the temperature operational run of the second prototype unit, a failure occurred in the unit, and it was found that a tolerance build-up of resistances in a bleeder which determines the AGC delay voltage had caused the delay voltage to be nearly zero. At this bias point, the AGC amplifier was unduly sensitive to temperature variations. Two resistors were added to the AGC circuit to set the delay voltage to the same level as in prototype Number 1, which would assure maintenance of this voltage in the flight units. In a retest of the unit under the specified temperature conditions (32 and 140°F), satisfactory performance was demonstrated.

During the 24-hour sterilization of the unit at 125°C, one of the matched pairs of input mixer crystals failed. For flight units, these crystals will be baked for 24 hours prior to receiving acceptance. The crystals that were in prototype Number 2 had not been baked because the contract for the prototype units did not require this procedure to be performed on all components. A matched pair of crystals were baked and used to replace the ones that failed. No change in performance since baking of the replacement crystals has been found in any test.

The electrical performance of the second prototype, Number 2, was the same as the first in that it had comparable margin of receiver sensitivity, and the measured ranging accuracy was the same.

The antenna patterns recorded from both altimeters were better than anticipated from early analysis. The combination of the narrow antenna beam (virtually free of side lobes) and its tight signal AGC loop with a large dynamic range, essentially insures the system against fuzing from a normal return in an off-normal approach. The first side lobe of the antenna beam merges with the primary lobe and is only noticeable as a slight bulge in the primary beam at approximately 5.5 degrees, and the first side lobe gain is down 16 db from the primary gain. The remainder of the side lobes are down 30 db or more from the primary lobe. The dynamic range of the signal AGC of both units was found by test to be at least 60 db, starting at the minimum anticipated return signal, and was capable of suppressing noise and unwanted signals occurring with the desired signal return.

Much attention during this reporting period was given to assuring that a sterile battery pack would be available to power the altimeter in the flight units. The contract with ESB for a single unit battery has a promised delivery which, if not met, could jeopardize the program. Therefore, a parellel effort is being conducted with Yardney Electric Corporation and Wiley Electronics to develop a back-up battery pack. Yardney agreed to develop a process which could be used to supply small battery cells which are internally sterile. Wiley was informed of the agreement, given the appropriate specification, and agreed contractually to supply battery pack kits for the altimeter which will contain sets of six internally sterile Yardney HR-1 type cells and a case to fit the pack when assembled with cryogenic insulation. Yardney will also supply a case to hold the ESB battery when wrapped with cryogenic insulation. The sterile battery pack for the flight units will be assembled by Aeronutronic with

either the ESB battery or the Yardney cells, whichever is proven best by test.

Two altimeter test sets are being made by Wiley for use in the program. The first set is due for delivery November 1. The second set is to be delivered to Aeronutronic along with the delivery of the last flight unit in early January 1962. This second unit is the breadboard test set. This test set is presently on loan to Aeronutronic and is being used to support tests at Aeronutronic and JPL. After delivery, it will afford a back-up test unit for the operations of AMR.

As a result of the excellent performance of the altimeter through the design proof tests, the present status of build-up of the flight units, and the present indications of strict adherence to good quality control methods, it is considered that the flight altimeters will meet the requirements for which they were designed.

Power and sequencing assembly. A redesign of the power and sequencing assembly (P&SA) has been accomplished since the previous report. A prototype model has been constructed and is presently at JPL for system tests. The redesign was undertaken to provide additional safety by (1) introducing an internal arming function to prevent P&SA operation prior to launch, and (2) using solderless connections to the external wiring harness in installation on the head of the retro-motor.

Arming. The power and sequencing assembly is to be inoperative for reasons of safety until it has experienced a positive axial acceleration of 5.00 ±0.25 g for 1.5 ±0.5 seconds. This condition will exist twice under normal launch conditions.

Starting (fuzing). Operation of the P&SA is to begin upon occurrence of the altimeter fuzing signal, when the internal power supply is to be connected to the timing and switching circuits. Power for starting is supplied from the bus 22-volt (safe) supply, switched by the altimeter fuzing relay.

Spin-motor ignition. To allow adequate time for lower Marman clamp pullaway, spin-motor ignition is to be initiated 130 ±20 milliseconds after fuzing.

Retro-motor ignition. The time of retro-motor ignition (t_F) after fuzing is expressible by the linear function

$$t_F = 2 + K(T_g - T_m)$$

T_g is the actual retro-motor temperature as measured by a sensor, whose actual location does not influence the P&SA design. T_m is the mean predicted motor temperature at firing time corresponding to a 2-second delay. The correction coefficient K is the change in firing time/deg of departure from mean temperature. Tolerance is ±50 milliseconds. The ignition load is 2.0 amperes. At present $T_m = 16°C$ and $K = 0.023$ sec/°C, but final establishment of these parameters can be made after final retro-motor tests.

Retro-motor/sphere separation. The bolt cutters which separate the retro-motor from the survival sphere are to be fired no earlier than time of retro-motor burn-out and no later than 1 second after burn-out. Again, establishment of separation time depends upon final retro-motor tests. The current required for this event is 4.0 amperes.

Figure 20 shows a functional block diagram of the new P&SA, and Figure 21 is the schematic. Some of the functions, component descriptions, development history, and present problems follow.

Battery. The P&SA battery has been a source of unsatisfactory performance. Two parallel efforts to provide batteries are in progress. A purchase order has been placed with Electric Storage Battery Company for sealed sterile battery packs. Prototypes are expected by November 15 and flight units in pairs on December 15, February 1 and April 1. The long development time is due more to the tight geometric constraints imposed rather than to sterilization or sealing problems. The alternative battery pack consists of 24 Yardney PM-01 cells, in a series-parallel arrangement. A purchase order has been placed with Yardney for special test cells and sterile PM-01 cells. The cells will be assembled at Aeronutronic into battery packs physically and electrically interchangeable with the ESB batteries. Six special test cells, contaminated with

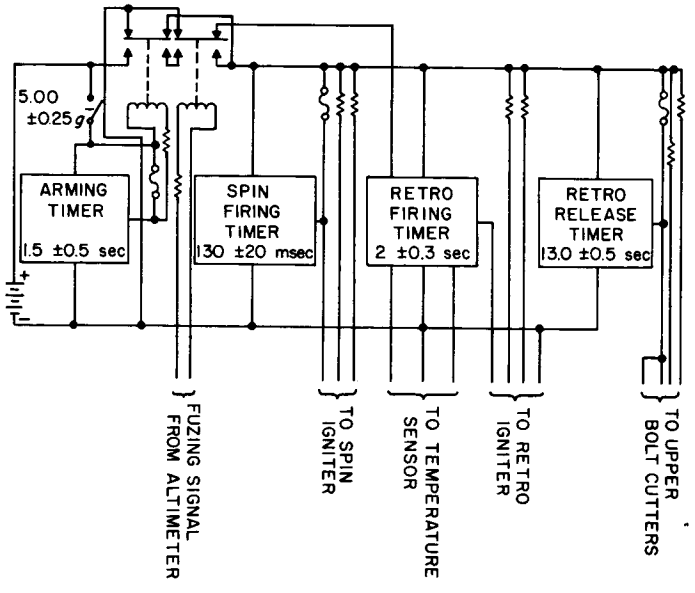

Figure 20. P&SA block diagram

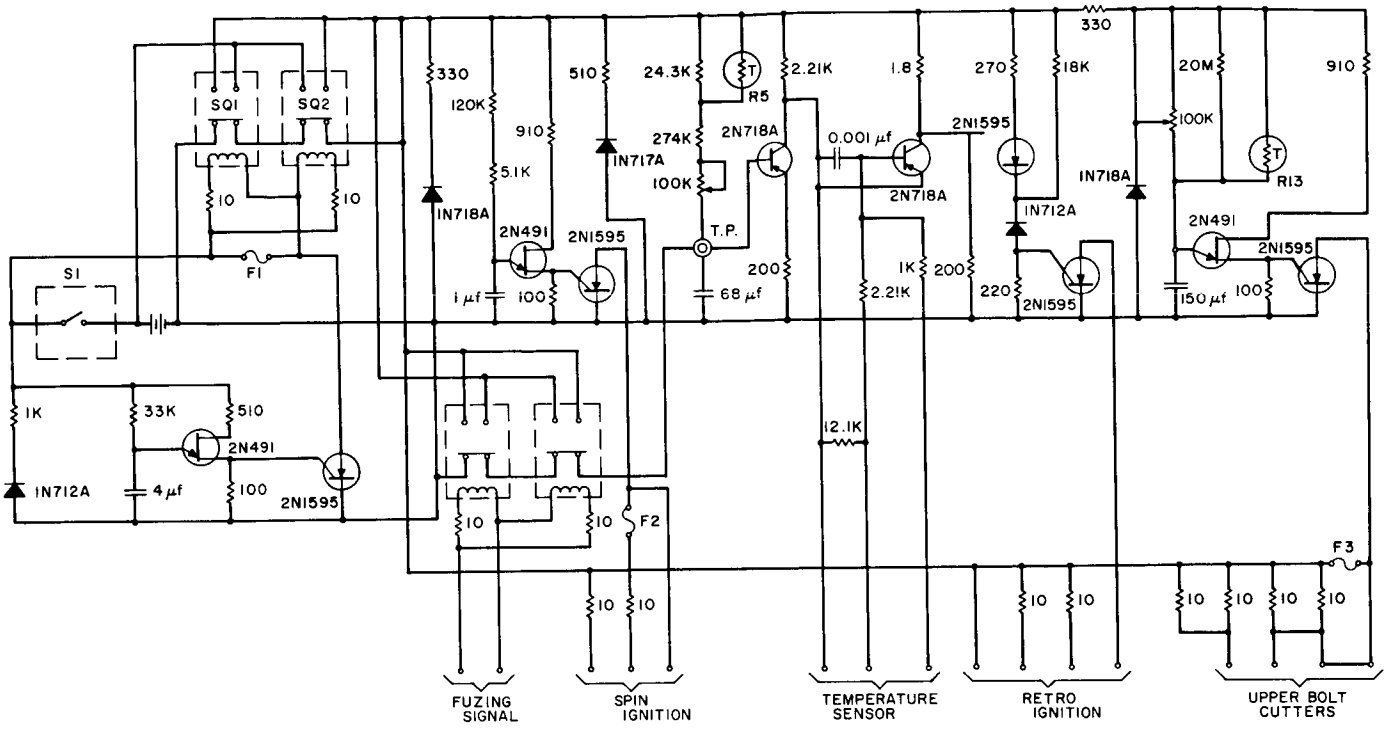

Figure 21. P&SA schematic

spores before sterile fabrication, have been received for culture tests.

Difficulty has been encountered in attempting to seal the Yardney cells. When sealing of filling holes has actually been accomplished, leaks have occurred because of cracking cases or around the terminals. Four efforts to encapsulate batteries completely have failed because of electrolyte leakage during the encapsulation cure. It is believed that neither standard nor sterile silver-zinc cells can be sealed and encapsulated to fit the space available in the P&SA and still be reliable. As a result, a battery case has been designed and fabricated which can be hermetically sealed and which will allow cells to breathe within. It will be necessary to coat the terminals with epoxy or rubber before sealing in the case to avoid shorts from electrolyte leakage.

Squib switches. Figure 20 shows only two squib switches, but each of these actually represents two in parallel, as shown by Figure 21. To date, the best (actually the only) squib switch suitable for the application has been the National Northern M-7. However, especially after temperature-humidity cycling, its reliability has been found questionable (100% success in all sphere tests thus far tested notwithstanding). The difficulty is believed to be entry of moisture into the squib-switch. As a result a group of 50 squib switches encased in fiberglass/epoxy jackets will be subjected to qualification tests.

g-switch and arming timer. A Sandia integrating and latching g-switch had been considered for arming the P&SA. However, its size and sensitivity to axial alignment rendered it undesirable. The simple 5-g switch (Inertia Switch Co. 6UC114D) in conjunction with electronic integration and squib-switch latching is therefore much more effective.

When the g-switch is closed, a capacitor in the arming timer begins to charge. If the capacitor voltage reaches a fixed threshold, it causes a unijunction transistor to conduct, producing a pulse to trigger a silicon-controlled rectifier. When the SCR conducts, firing either of two squib-switches, the P&SA is armed. If the g-switch should open before capacitor voltage reaches threshold, the timer resets within 300 milliseconds. The circuit is immune to high amplitude shocks up to 1 second in duration.

Spin firing timer. A simple timer, operating on the same principle as the arming timer, will provide delay for ignition of the spin-motor.

Retro firing timer. The circuit design of the retro firing timer remains unchanged. When the timer is started, a capacitor is allowed to charge. When the capacitor volt-

age reaches a threshold value (dependent upon retro temperature), a Schmidt trigger circuit switches and triggers the retro igniter SCR. The mean temperature (corresponding to 2 seconds delay) calibration is variable from 11 to 21°C by a potentiometer. The slope of the temperature-time correction curve is variable from 0.018 to 0.028 sec/°C, by a change of resistor.

Retro release timer. Because of packaging difficulty, the purchased retro release timer has been abandoned. The components for this function occupy approximately half the space the purchased timer did. It is functionally identical to the arming and spin firing timers. This timer has a potentiometer externally accessible for calibration.

Packaging. The addition of two timers, a g-switch, and two squib switches has caused considerable crowding of components in the P&SA. The first effort, retaining a commercial timer, resulted in a rather complicated layout and insufficient room for acceptable component spacing. The second effort replaced this timer with three circuit boards which will fit in layers filling the P&SA space not occupied by the battery pack. The adapter to the retro-motor is retained in its present form. The same over-all cylindrical envelope is maintained. External connections will be made by crimp-on lugs attaching to stud terminals disposed about the periphery of the package on top.

Ground adapter. Two end-product ground adapter units have been completed and tested. One unit (Number 1) participated in DSIF tests at Goldstone. It has been found desirable, to avoid adjustments in the early days of use, to pre-age the ground adapter battery. Even after such pre-aging, more than the specified 1000 hours of life remain. Because of late delivery of printed circuit boards, construction of ground adapter Number 3 is late, and delivery probably will not be accomplished before October 27.

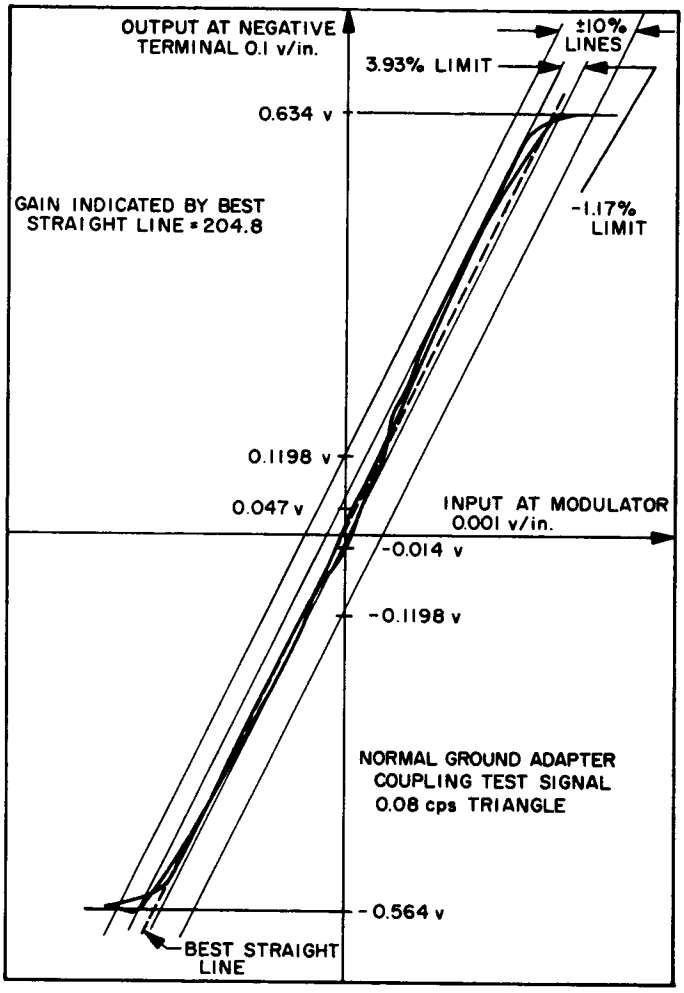

Figure 22. Over-all system linearity

A test of linearity, operating the DPT-5 seismometer amplifier and the prototype ground adapter in tandem, showed performance well within the specified ±10% limits, as illustrated in Figure 22. Nearly identical results were achieved using other combinations of seismometer amplifiers (DPT-3, 4) and the prototype ground adapter.

II. *Surveyor*

The scientific instruments to be carried on the first two flights (Spacecraft SC-1, SC-2, and SC-3) have been selected and incorporated into the spacecraft design. Spacecraft configuration improvements include reassignment of certain electronic equipment within the thermally controlled compartments A and B and addition of a third compartment (C) containing scientific instrument electronic auxiliaries that are operative only during the lunar day. The high-resolution telescope has been combined with a separate television camera. Dynamic clearance between the *Centaur* shroud and the spacecraft is adequate with a 4-ft shroud extension.

The spacecraft weight is currently estimated to exceed the 2500-lb maximum by about 1%. Several possibilities for weight reduction are under study.

The daily launch window duration has been analyzed for every permissible launch day within the seven launch months currently planned. Alternative techniques for achieving the desired landing locations on the Moon and design requirements for spacecraft acquisition and tracking during transit have been evaluated. In flight control development, attention has been focused on the vernier phase control system to optimize the range-velocity trajectory, ensure adequacy of stability margins, and refine attitude and lateral velocity dispersion data at vernier engine cutoff.

Many electronic component breadboard models have been constructed and tested, such as the electronic commutator for the television system and the solid-state portion of the transmitter. The GEC 1349 vidicon has been selected for the television system. As a result of radiation pattern tests of the omnidirectional antenna on a spacecraft model, a conical reflector has been added behind the antenna to reduce interference. All components for the altitude marking radar are receiving unit tests. The Electric Storage Battery Company has been selected to develop the spacecraft batteries, and an improved charge regulator has been incorporated in the power management design.

A study of limiting loads and spacecraft stability as a function of vertical and lateral landing velocities has been completed. For the drop tests of spacecraft model T-1, a test setup for simulation of lunar gravity has been developed.

The first test firing of a heavy-wall main retro-engine was successfully made. A high-altitude facility for tests of the vernier propulsion system has been completed and checked out.

The equipment for spacecraft weight, balance, and thrust alignment measurement has been designed. The antenna/solar panel positioner and mechanisms for instrument deployment are undergoing design refinement and laboratory testing. Vacuum tests with a full-scale model of the subsurface sampler are being made to verify design characteristics.

An analysis of the timing of launch functions from spacecraft installation on the *Centaur* to launch has resulted in construction of a preliminary launch countdown chart.

A. System Design Summary

1. System Description

The group of scientific instruments (designated List II) to be carried on the first two flights (SC-1, SC-2, SC-3) has been selected and incorporated into the spacecraft system design. A functional block diagram for the complete spacecraft is shown in Figure 23. The individual blocks denote equipment modules. Those modules that make up the spacecraft basic bus are shown distinct from those associated with the scientific payload.

The basic bus configuration is shown in Figure 24. Figure 25 shows the complete spacecraft configuration consisting of the basic bus and scientific payload; the instrument-deployed, post-loading configuration is shown. The installed configuration on the *Centaur* is shown in Figure 26.

a. General arrangement. The equipment arrangement has been slightly altered over that shown in the preceding bimonthly report. A third compartment, designated Compartment C and containing scientific instrument electronic auxiliaries that are operative only during the lunar day, has been added.

The assignment of electronic equipment modules between the active thermally controlled compartments A and B has been optimized, from consideration of the following factors: thermal dissipation, lateral center of gravity constraints, and wiring harness weight and complexity. The locations of equipment in Compartments A, B, and C are detailed in Figure 23. Basic bus equipment is contained largely in Compartment A and in a portion of Compartment B.

b. Scientific payload. The scientific payload list including end instruments and associated electronics and mechanisms is detailed in Table 8, Item 3.0. The physical

Table 8. Weight breakdown

Item	Maximum allowable weight, lb	Current weight, lb
1.0 Basic bus	553	557.5
1.1 Flight control	45.5	46.4
Sensor group		
Secondary solar sensor		
Attitude control system		
1.2 Electronics	90.9	93.9
Data link (antennas, transmitters, receivers and transmitters, RF transmission, diplexer)		
Control command decoder		
Central signal processor		
Altitude marking radar		
Doppler velocity sensor and altimeter		
Power control system		
TV camera No. 4 (downward-looking)		
Engineering data processing		
Mechanisms auxiliaries		
1.3 Electrical power	38.5	38.5
Solar panel		
Batteries	(30)	
1.4 Mechanisms	18.0	30.0
Antenna/solar panel positioner		
Omni directional antenna extension gear		
1.5 Spacecraft vehicle	154.7	161.6
Spaceframe		
Landing gear		
Compartments A, B, and C		
Electrical wiring		
Pneumatic lines		
Retro-rocket release mechanism		
Centaur separation sensor		
Engineering sensors		
Installation bracketing		
1.6 Spacecraft propulsion (dry)	205.4	207.1
Main retro-rocket inerts		
Vernier propulsion system inerts		
Vernier propulsion system propellant ullage		
Vernier propulsion system helium		

Item	Maximum allowable weight, lb	Current weight, lb
2.0 Usable propellant (total)	1602	1605
2.1 Main retro-rocket propellant		1445
2.2 Vernier rocket propellant		160
3.0 Scientific payload (total)	345	361.3
3.1 Television		61.7
Camera/mirror assemblies Nos. 1, 2, 3		(43.2)
Decoder and processor		(1.3)
High-resolution telescope/camera assembly		(14.9)
Camera No. 4 scientific experiment auxiliaries		(2.3)
3.2 Subsurface sampler		42.9
3.3 Surface sampler		16.0
3.4 Spacecraft anchoring		10.5
3.5 Sampler processor		18.9
3.6 X-ray spectrometer		28.9
3.7 X-ray diffractometer		21.1
3.8 Gas chromatograph		13.4
3.9 Surface geophysical system		39.9
Density and acoustic sensor		
Density background counter		
Thermal diffusivity instrument		
Magnetic susceptibility instrument		
Acoustic sensor		
Acoustic source		
Soil mechanics experiment		
Resistivity instrument		
Radiation pyrometer		
3.10 Subsurface geophysical probe		5.7
3.11 Tape recorder		10.6
3.12 Radiation detector		4.8
3.13. Scientific instrument mechanisms auxiliaries		2.7
3.14 Scientific instrument thermal auxiliaries		5.2
3.15 Scientific payload batteries		62.0
3.16 Electrical wiring		17.0

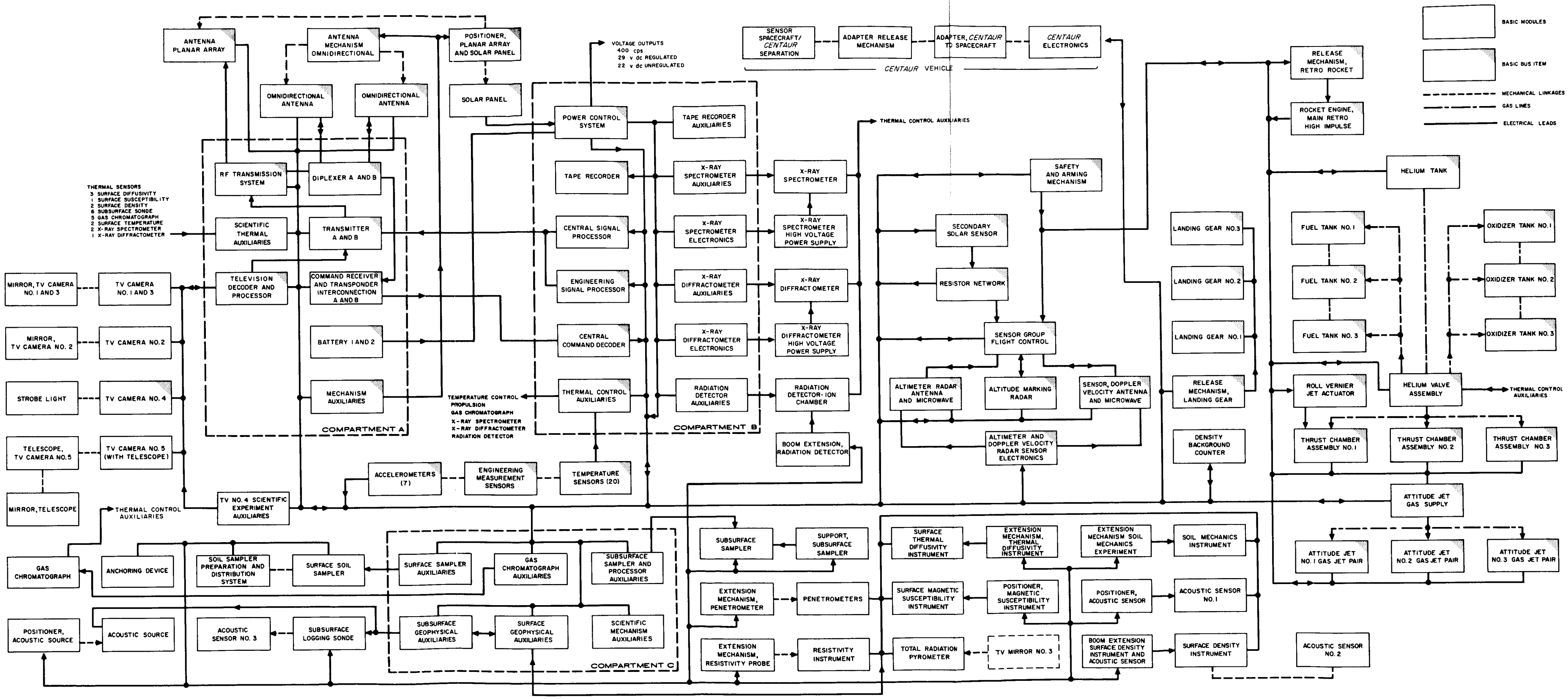

Figure 23. Spacecraft SC-1, SC-2, and SC-3 functional block diagram

locations are shown in Figures 23 and 24. The high-resolution telescope has been combined with a separate television camera and removed from its former position above Compartment B, thus allowing unobstructed thermal radiation.

c. Centaur installation. The interconnect structure has been increased in length over that shown in the preceding bimonthly report to accommodate the *Centaur* hydrogen vent lines. This change has allowed elimination of the folded feed on the marker radar. Dynamic clearance between the *Centaur* shroud and the spacecraft is adequate with the 4-ft shroud extension.

2. Weight and Balance

a. Weight. Current weight estimates and comparisons with the maximum allowable weights are given in Tables 8 and 9. A gross summary in terms of basic bus, usable fuel, and scientific payload is given in Table 1 and a detailed weight breakdown in Table 9. Each of the items in the weight breakdown corresponds to the equipment modules described in the functional block diagram of Figure 23. The total separated weight is currently estimated to be 2543.8 lb, which corresponds to a 27.5 lb (or about 1%) excess over the maximum allowable weight of 2500.0 lb. This weight increment is primarily in the basic bus (24.5 lb), and has grown slightly over that previously reported. This increase has largely occurred in the antenna/solar panel positioner and is based on realistic estimates of the present detailed design.

Weight saving design studies to date indicate the following possible weight reductions for the basic bus: (1) use of beryllium for antenna/solar panel positioner structure—5 lb; (2) use of ablatalite in place of the present main retro nozzle insulation material—10 to 15 lb. In addition, continued refinement of the loads and more detailed stress analyses may allow further reductions.

Table 9. Spacecraft weight summary

Item	Maximum allowable weight, lb	Current weight, lb
Total separated weight (includes maximum allowed scientific payload weight of 345 lb)	2500.0	2543.8
Basic bus	553.0	577.5
Usable fuel	1602.0	1605.0
Scientific payload	345.0	361.3

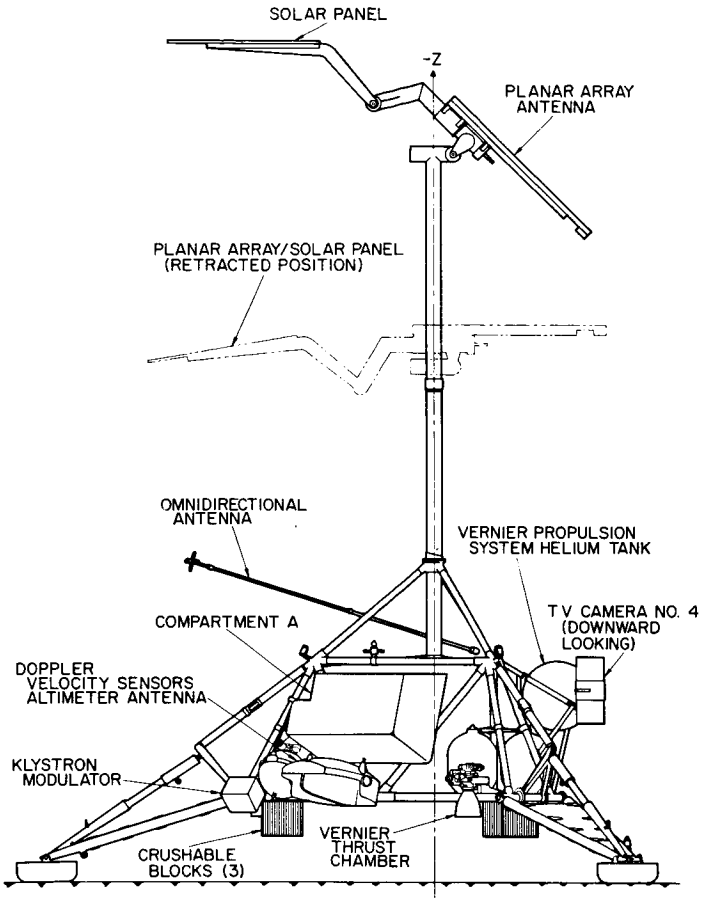

Figure 24. Spacecraft basic bus

In the scientific payload, the weight increment is 16.3 lb above the target value of 345 lb. The bulk of this increase is due to the inclusion of the tape recorder (10.6 lb), which was added after the desired instrument list was specified. The remaining weight increment (5.7 lb) is due to the addition of another television camera in conjunction with the high-resolution telescope. Studies are currently under way on the heavy items, such as the subsurface sampler and deployment mechanisms, to assess weight saving possibilities.

b. Balance. The center of gravity locations corresponding to the present spacecraft configuration are shown in Figure 27. The maximum allowable vertical center of gravity location of Z = 17.5 in. is determined by touchdown stability requirements and corresponds to a stable landing on a 15 deg slope at a lateral velocity of less than 7.5 ft/sec or on a 30 deg slope at a lateral velocity of less than 2.0 ft/sec. These data correspond to a high coefficient of friction ($\mu = 1$) between the landing gear foot pads and the lunar surface. For 20% lower coefficient of friction, landing stability would be significantly improved.

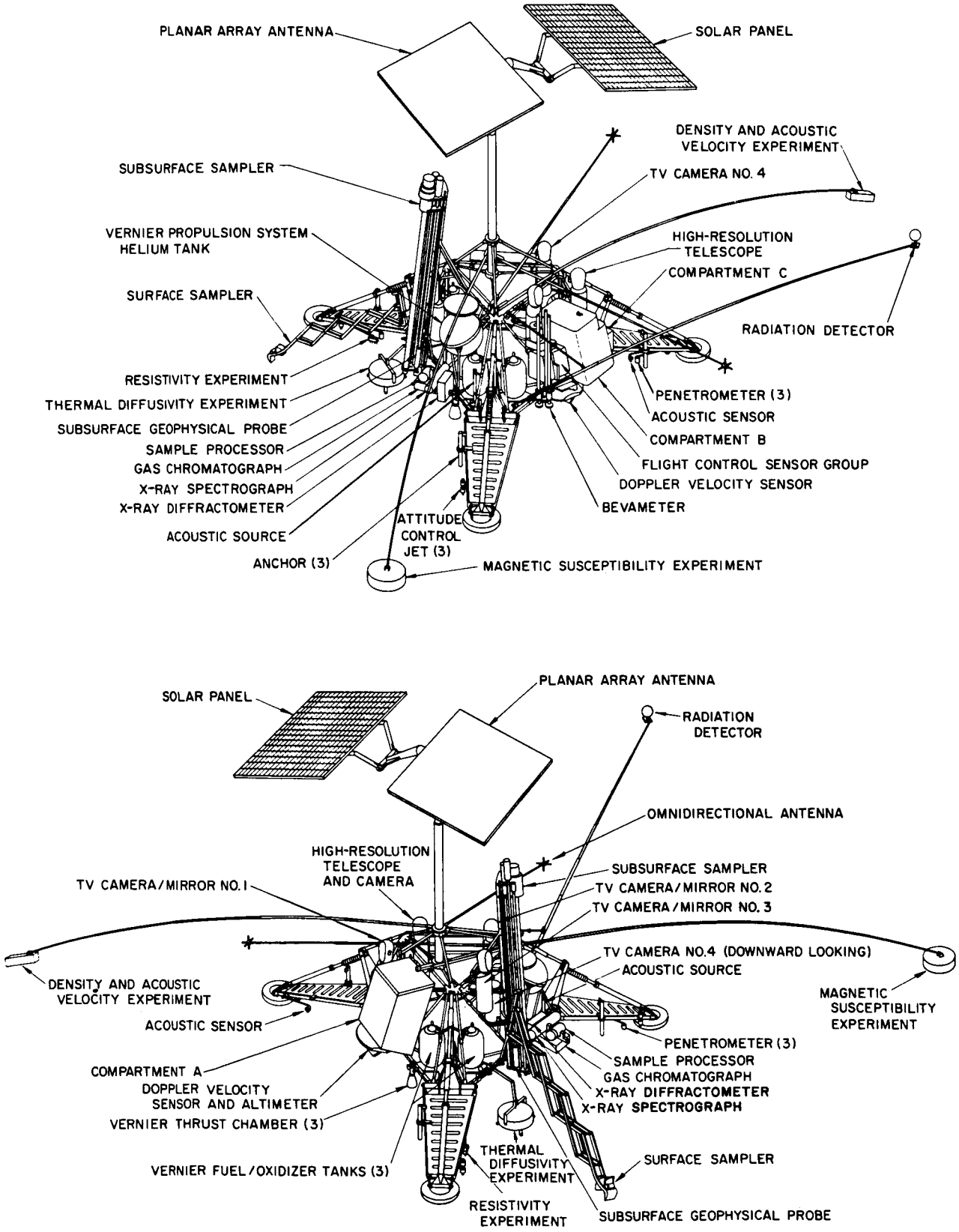

Figure 25. Two views of spacecraft with instruments deployed after landing

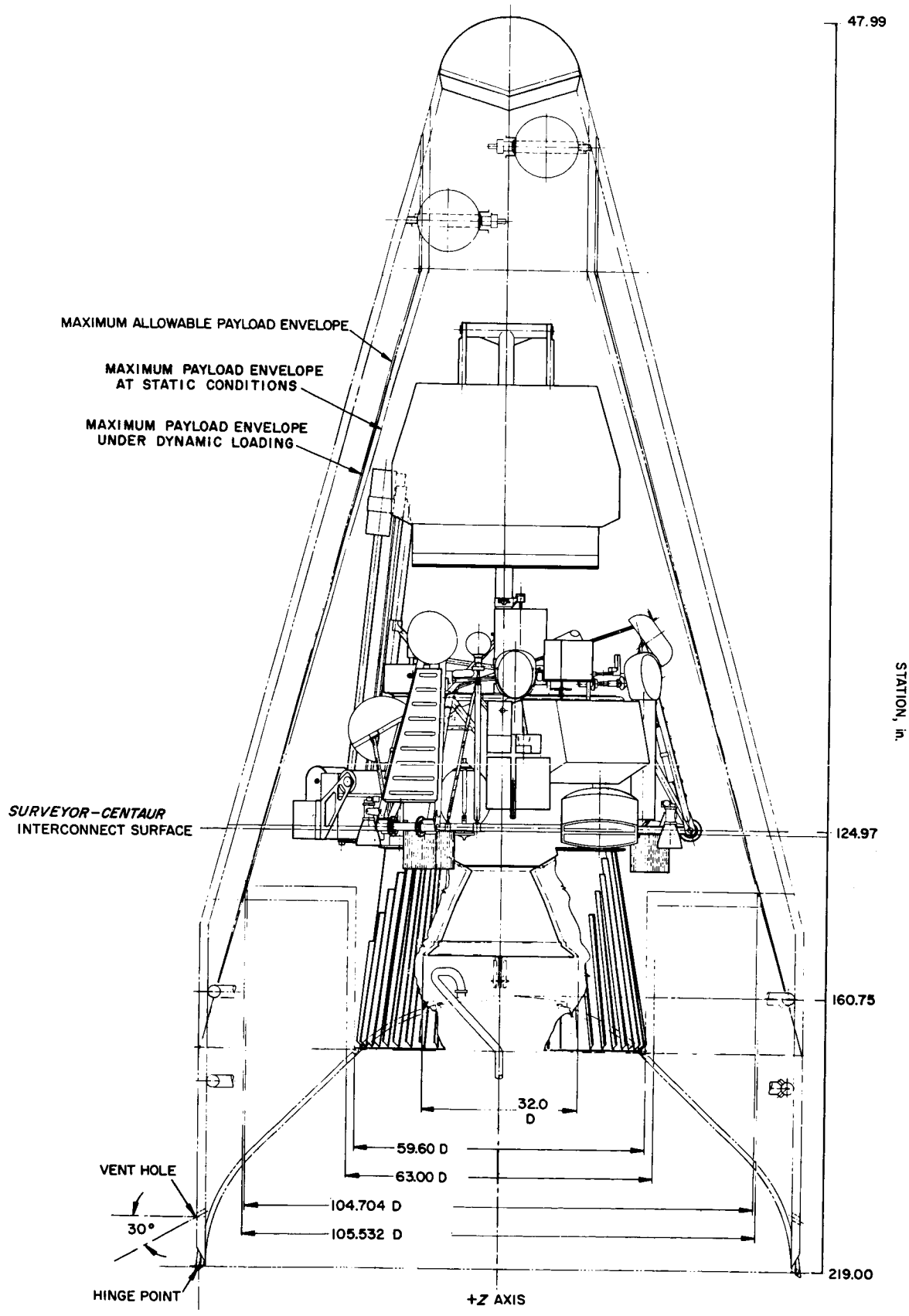

Figure 26. Spacecraft as installed on Centaur

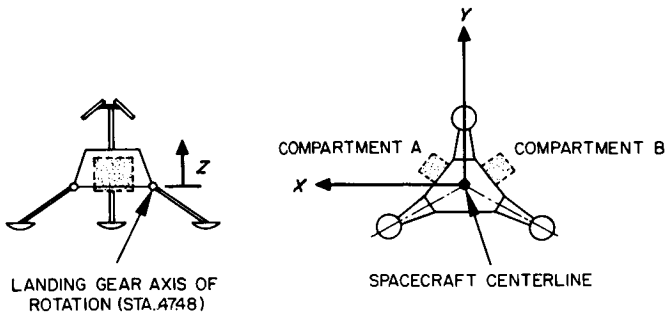

COORDINATE SYSTEM

CONFIGURATION	CENTER OF GRAVITY LOCATION, in.					
	MAX ALLOWABLE		CURRENT			
	WEIGHT	Z	WEIGHT	Z	X	Y
ON *CENTAUR* (STOWED)	2500	10.35	2543.8	11.81	−0.11	−0.20
SEPARATED	2500	9.92	2543.8	11.38	−0.11	−0.21
RETRO-ROCKET JETTISONED	841	14.77	884.8	16.23	−0.39	−0.77
TOUCHDOWN	741	16.00	784.8	17.46	−0.44	−0.86

Figure 27. Spacecraft balance summary

The lateral center of gravity shown in Figure 27 corresponds to the main retro-engine thrust line being on the spacecraft centerline. For balance purposes, the main retro thrust line will be offset $x = -0.39$, $y = -0.77$ from the spacecraft centerline to make the thrust vector pass through the spacecraft center of gravity.

B. Scientific Instrument Payload

1. Introduction

The status of integration of the JPL-specified scientific instruments into the *Surveyor* spacecraft is described in this section. The televison system (discussed in Sec E) and the surface and subsurface sampling and processing system (discussed in Sec J) are also parts of the instrument payload.

2. Scientific Payload for Spacecraft SC-1 through SC-3 — List II

Agreement has been reached with JPL on the list of instruments (List II) to be carried on *Surveyor* spacecraft SC-1, SC-2, and SC-3. This list of instruments and their weights are shown in Table 8 in Sec. A. The selected List II instruments and their associated electronics and mechanisms do not exceed the 345 lb allocated for scientific payload in spacecraft having 2500 lb separated weight.

3. Instrument Integration Status

Design reviews have been held with Midway Laboratories, Philips Electronics Inc., Lamont Geophysical Observatory, Texaco Experiment, Inc., Marshall Laboratories, and Beckman Instruments, Inc. as a part of the JPL prototype instrument procurement. A number of changes have resulted from these reviews, some of which are described below.

a. X-ray diffractometer. The X-ray diffractometer experiment has required a data transmission bandwidth of 10 kc, which has necessitated the use of the high-power (10 watts radiated power) transmitter during the soil analysis period. As a result, the X-ray diffractometer experiment required approximately 2000 watt-hr of electrical energy. A study of the data rate requirements and scaling methods has resulted in an agreement to preprocess the data in the instrument to reduce the required bandwidth sufficiently to permit transmission by the low-power transmitter. Since the experiment analysis time would not be increased, use of the low-power transmitter would significantly reduce the total power required to transmit the X-ray diffractometer data. The effect of this change on the spacecraft data processing system is now being studied. A photograph of the breadboard diffractometer is shown in Figure 28.

b. Physical parameters package. The physical parameters package includes three radiometers for making temperature measurements — one for surface temperature, one for surface thermal diffusivity, and one for subsurface temperature. It was originally intended to use one radiometer for all three applications. This concept placed a limitation on the radiometer size, since the subsurface radiometer must be small enough to fit within the drill hole. Radiometer development problems have prompted the decision not to impose this size limitation on the surface instruments. Off-the-shelf radiometers will be considered for these applications. Hughes Aircraft Company is studying the effect of larger radiometers on the spacecraft configuration.

The soil mechanics experiment consists of two vertically loaded flat circular plates of different sizes for measuring bearing strength of the lunar surface and a spudded annular ring, loaded vertically and in torsion, for measuring the surface shear strength. Agreement has been reached on the spacecraft/instrument mechanical interface by which General Motors will provide all mechanical functions required by the instrument. This responsibility includes lowering of the bearing plates and the shear ring to the lunar surface and their manipulation for measuring the surface characteristics. Mounting to the spacecraft will be accomplished by hardware supplied as part of

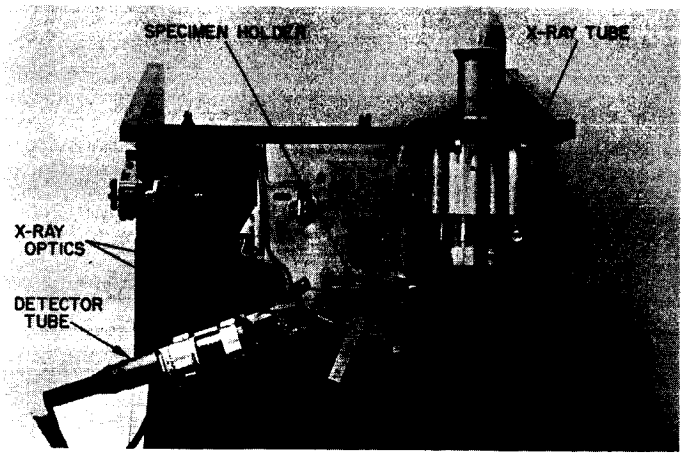

Figure 28. Breadboard diffractometer

the instrument. Hughes Aircraft Company will provide electrical power and data processing as required by the instrument. The complete experiment including manipulation gear and data processing equipment is not to exceed 11 lb.

c. Plasma probe. Data processing for the plasma probe has been a problem due to the wide dynamic range of the output and to its bipolar nature. In order to obtain reasonable accuracy (10%) at the low end of the range, high accuracy (0.1% of full scale) is necessary at the top of the scale. This capability requires digital data transmission. The *Surveyor* analog-to-digital converter is designed to handle only positive voltages. It was originally intended to shift the voltage level of the plasma probe output to accommodate its bipolar output nature. However, it is not possible to use voltage level shifting schemes due to the low permissible voltage drift (1 mv).

Two schemes for handling the data are being considered: (1) modifications of the present analog-to-digital converter to handle bipolar signals or (2) construction of a dc inverting amplifier. In the latter scheme, both instrument output and inverter output would be sampled for each data cycle and the output which is positive would be used. A tentative decision has been made to use the inverting amplifier approach.

C. System Analysis

1. Guidance and Trajectory

a. Launch window analysis. An analysis has been made of the daily launch window duration for every permissible launch day within the seven launch months presently planned. A launch azimuth restriction of 90 to 114 deg east is assumed. The analysis considers Goldstone visibility, as well as the approach speed constraints at impact as reported in the preceding bimonthly summary.

The method used is empirical and graphical. From the lunar ephemeris program, a plot of the Goldstone elevation angle versus time is obtained for a particular impact date in question, shown as the truncated sinusoid in Figure 29. Along the right-hand side, a suitable scale for the unbraked impact speed is marked off. The unbraked impact speed must be confined between the limits 2700 and 2615 meters/sec, shown as horizontal lines AD and BC, respectively. The upper limit is set by the vernier fuel provision for the terminal descent phase, while the lower limit is imposed by the three-sigma flight path angle dispersion at main retro burnout for a 1-deg thrust attitude error. Dotted lines EF and GH, at 2680 and 2642 meters/sec, respectively, are shown also to indicate the more conservative limits within which the transit trajectories should be confined whenever possible.

From operational considerations, a pre-impact Goldstone visibility duration of 60 min and a post-impact visibility duration of 180 min are considered to be minimum requirements. Defining visibility as that condition where the elevation angle exceeds 5 deg, the straight lines *AB* and *DC* are drawn as shown. The area within the box *ABCD* is then the largest permissible impact speed and arrival time region, while *EGHF* represents a more conservative and desirable domain.

For the actual impact date of April 28, 1964, the partial derivative of V_{impact} with respect to T_f, the time of flight for a particular launch azimuth, can be evaluated from the trajectory program and has been found to be essentially constant for reasonable changes in flight time. For the sake of illustration, it is assumed that points *J* and *K* are obtained corresponding to launch azimuths of 90 and 114 deg, respectively. The vis viva energy, C_3, at injection, is held constant throughout the launch window. It is also assumed that these points are outside the permissible region as shown.

First, two parallel lines are drawn through *J* and *K* with a slope equal to $\partial V_{impact}/\partial T_f$. Now C_3 must be changed in a direction to slide the line *JK* into some new position such that at least a portion of it falls within the region of interest. One possibility is the new position *LM* which intersects the line *DC* at *F*, giving a maximum V_{impact} of 2680 meters/sec. Hence the permissible launch duration is defined by the interval *LF*, which in this case turns out to be 92 min with a launch azimuth range of 90 to 107 deg (obtained by linear interpolation). If C_3 is further increased until the new position *NP* is assumed, the entire 90 to 114 deg launch azimuth window falls

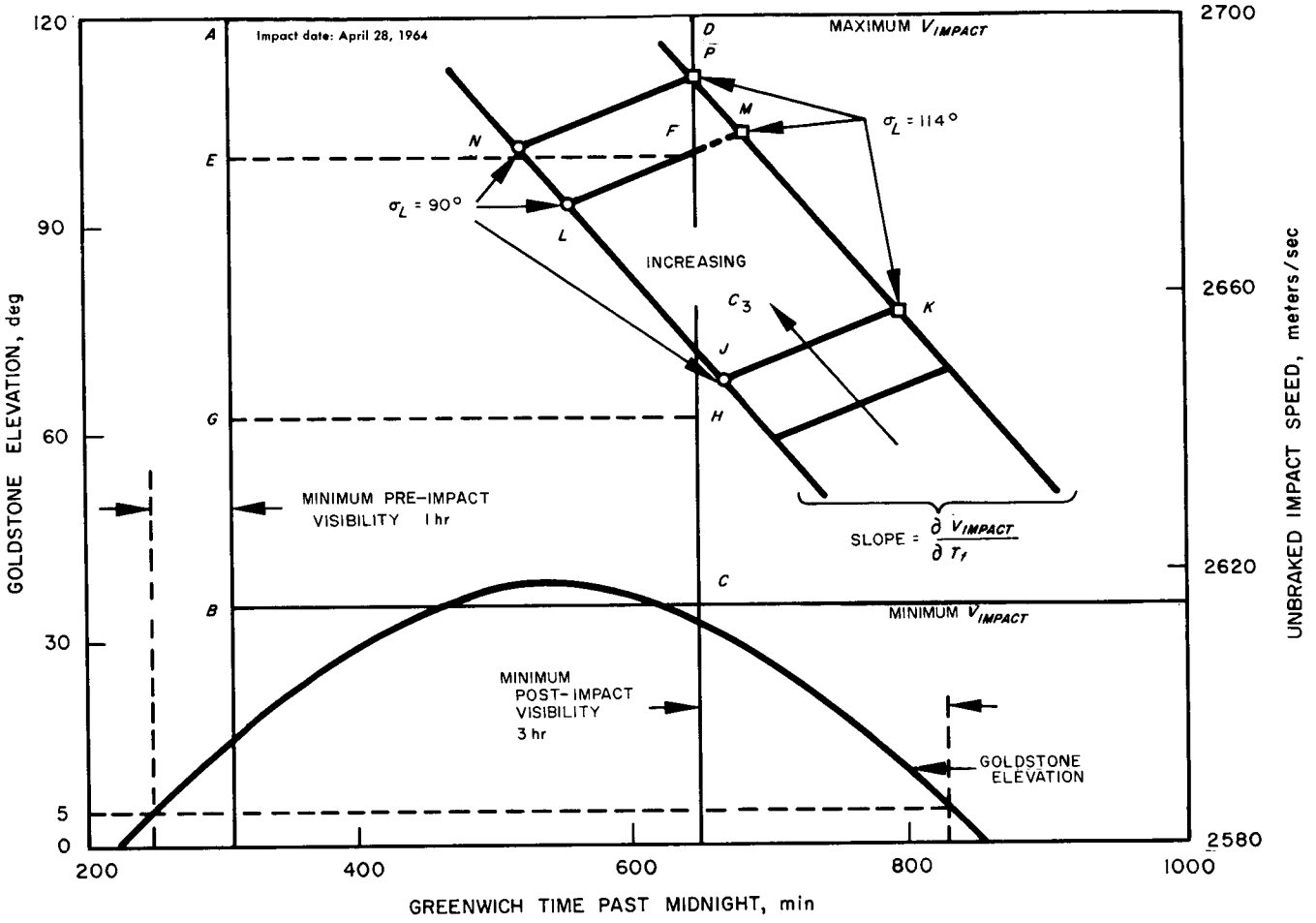

Figure 29. Launch window analysis

within the permissible region, giving a total launch time of 125 min, but with a higher impact speed range of 2681 to 2691 meters/sec.

For this particular impact date, either value of C_3 or some value in between will be satisfactory. However, in consideration of the relative importance of terminal descent operation versus post-landing operation, the first mode, *LM*, which gives the lower impact speed range at the sacrifice of some launch duration or post-impact visibility duration would probably be chosen. A similar analysis may be applied to cases where the launch window tends to fall to the left of the line *AB* and 60 min of pre-impact Goldstone visibility is required for the terminal descent operation.

Table 10 summarizes the results of the graphical launch window analysis of all the launch dates during the allotted launch months. It is seen that the majority of the cases present no problem. Where an "x" appears in a column marked either pre-impact or post-impact visibility problem, it is implied that the launch window is dangerously narrow (but still equal to or longer than 50 min) when the conservative impact speed limits of 2642 to 2680 meters/sec are imposed. If the same speed limits cause the launch window to shrink below 50 min, a double x is used to designate this condition. For those problematical impact dates, another set of impact speeds is used (corresponding to a different value of C_3) in order to extend the launch window. It may be seen that if the broader limits of 2615 and 2700 meters/sec are used, no problem with the launch windows should exist. However, with the narrower limits, there are approximately nine days out of 56 during which it is inadvisable to launch, and seven more days during which launch conditions are marginal.

The remedies for these launch window restrictions are: (1) Where post-impact visibility (or high impact speed) is a problem, it may be relieved by the addition of vernier fuel. Each pound increase results in roughly 2.5 meters/sec increase in maximum unbraked impact speed capability. Thus, about 8 to 10 lb increase in fuel would solve this problem if present altitude-velocity sensor limitations could be relaxed.

(2) Where pre-impact visibility (or low-impact speed) is a problem, it can be remedied only by decreasing the total thrust attitude error during the main retro phase. Fairly crucial is gyro drift during the time prior to ignition but after the final attitude maneuver. For a drift rate no greater than 1 deg/hr, error analysis has shown that the three-sigma thrust attitude error is 0.91 deg. In that case, the lower limit of 2615 meters/sec can be used with confidence. The limit 2642 meters/sec is for a 1.5 deg error.

The analysis did not include the effect of the minimum boost plus coast arc requirement imposed by the *Atlas/Centaur* vehicle. This is expected to cut the launch window slightly at the high azimuth end, during those days of minimum lunar declination. The IBM trajectory program has now been modified to include the most recent estimate of the boost plus coast arc requirement. Further launch window analysis will be made as up-to-date modifications and restrictions are generated.

b. Mid-course fuel requirement for landing site relocation. There are apparently two simple alternatives in the design of transit trajectories for landing at a desired location on the surface of the Moon:

(1) If the coordinates of the desired landing location are known well in advance of the actual launch date, the proper injection conditions can be determined such that the nominal trajectory does in fact impact the Moon at the proper point. These injection conditions can be inserted in the *Centaur* guidance computer prior to launch in the form of stored constants.

(2) The nominal trajectory may be designed without regard to impact coordinates but merely in accordance with some arbitrary constraint such as vertical approach. The landing offset is then taken out by the midcourse correction at the same time as the injection errors.

Relative tradeoffs between the two approaches are being determined. Alternative 1 imposes no penalty on *Centaur* capability since it requires no change in the vis viva energy at injection. The constants which will have to be inserted in the guidance computer are those which approximate the right ascension and declination of the pseudo-asymptote of the outgoing Earth conic. These numbers will be dependent on the particular landing site selected. Thus, because of the lead time involved in changing the stored constants for the computer, selection of the landing site for a particular launch must be made at least a month or so in advance.

Alternative 2 has the advantage of eliminating the need for changing the *Centaur* constants. On the other hand, it does require for a fixed required confidence level a certain provision of vernier fuel in addition to what is presently considered to be the required amount for midcourse correction of injection errors alone. The following analysis gives an approximate answer with regard to the additional fuel requirement.

The geometry of Figure 30 and the planar representation of the miss geometry of Figure 31 is considered. The origin of Figure 31 corresponds to the vertical approach impact coordinates of the particular day in question. If any offset in landing coordinates is to be made, it may be

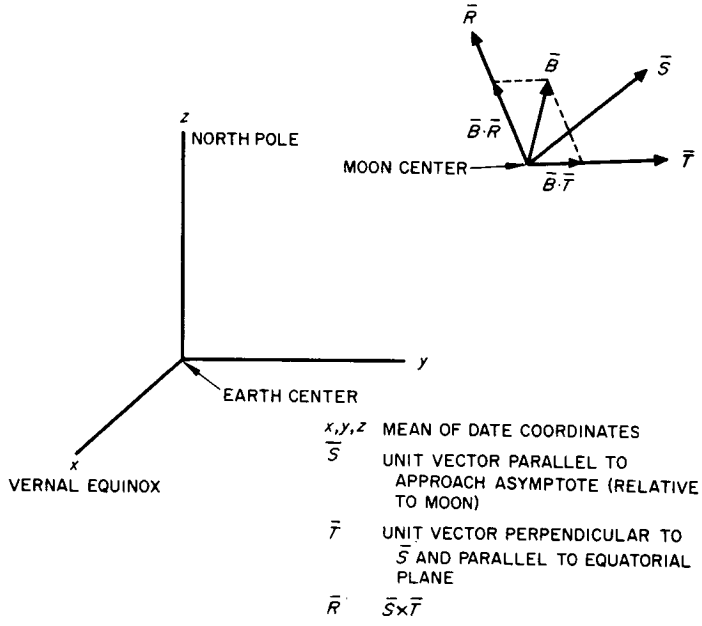

Figure 30. Coordinate systems

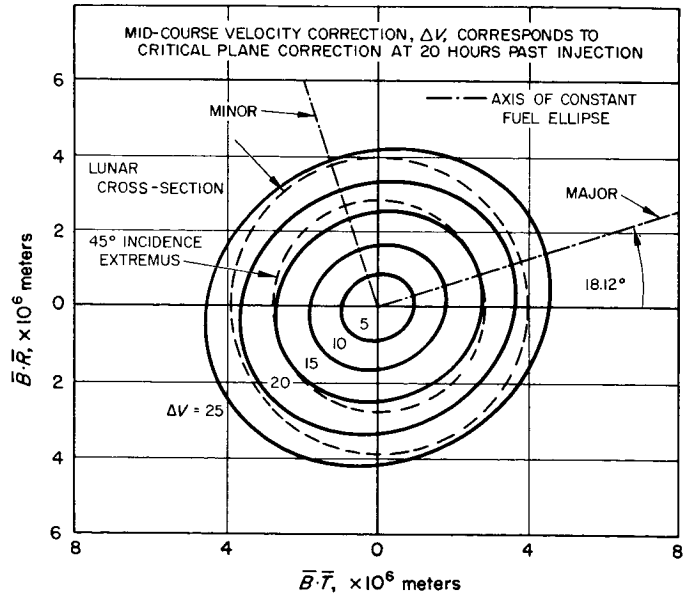

Figure 31. Miss geometry for April 24, 1964
67.1-hr trajectory

Table 10. Results of graphical launch window analysis

Impact date	Visibility problem			Chosen unbraked impact speed range within permissible launch window, m/s	Permissible launch window, min	Permissible launch azimuth range, deg	Visibility from Goldstone, min	
	Pre-impact	No problem	Post-impact				Pre-impact for launch at start of permissible window	Post-impact for launch at end of permissible window
8- 2-63			X	2600 2620 2640 2660 2680 2700	50	90-103.3	310	180
8- 2-63					95	90-114	260	185
8- 3-63		X			100	90-112.0	260	180
8- 3-63					115	90-114	185	240
8- 4-63		X			122	90-114	185	240
8- 5-63		X			135	90-114	185	240
8- 6-63		X			130	90-114	210	240
8- 7-63		X			202	90-114	152	305
8- 8-63		X			155	90-114	90	400
8- 9-63		X			158	90-114	80	440
10-30-63		X		2600 2620 2640 2660 2680 2700	175	90-114	90	395
10-31-63		X			175	92-114	60	460
10-31-63					193	90-114	60	442
11- 1-63		X			100	101-114	60	575
11- 1-63					195	90-114	60	470
11- 2-63	X				50	106.5-114	60	660
11- 2-63					197	90-114	60	510
11- 3-63	XX				50	107.8-114	60	685
11- 3-63					180	92.2-114	60	555
11- 4-63	XX				50	107.5-114	60	710
11- 4-63					170	92-114	60	590
11- 5-63	XX				50	107-114	60	715
11- 5-63					170	90-114	60	595
11- 6-63	X				60	104.5-114	60	700
11- 6-63					160	90-114	60	600
4-24-64		X		2600 2620 2640 2660 2680 2700	170	90-114	280	240
4-25-64		X			155	90-114	270	240
4-26-64		X			165	90-114	280	210
4-27-64		X			132	90-114	295	180
4-28-64		X			92	90-107	305	180
4-28-64					125	90-114	270	180
4-29-64		X			68	90-105	310	180
4-29-64					125	90-114	250	180
4-30-64			X		50	90-99.5	310	180
4-30-64					120	90-112.5	240	180
5- 1-64			XX		40	90-98.5	310	180
5- 1-64					105	90-109.5	245	180
8-19-64			XX	2600 2620 2640 2660 2680 2700	30	90-99	315	180
8-19-64					78	90-114	265	180
8-20-64			XX		40	90-100	300	180
8-20-64					80	90-114	260	180
8-21-64		X			85	90-112	290	180
8-21-64					92	90-114	280	180
8-22-64		X			100	90-114	315	180
8-23-64		X			112	90-114	240	230
8-24-64		X			125	90-114	250	245
8-25-64		X			135	90-114	175	310
8-26-64		X			142	90-114	165	370

Table 10. Results of graphical launch window analysis (continued)

Impact date	Visibility problem			Chosen unbraked impact speed range within permissible launch window, m/s	Permissible launch window, min	Permissible launch azimuth range, deg	Visibility from Goldstone, min	
	Pre-impact	No problem	Post-impact				Pre-impact for launch at start of permissible window	Post-impact for launch at end of permissible window
				2600 2620 2640 2660 2680 2700				
2-14-65		X			255	90-114	60	515
2-15-65		X			250	90-114	95	455
2-16-65		X			240	90-114	105	425
2-17-65		X			225	90-114	150	375
2-18-65		X			200	90-114	145	355
2-19-65		X			175	90-114	155	340
2-20-65		X			160	90-114	180	295
2-21-65		X			130	90-114	195	275
				2600 2620 2640 2660 2680 2700				
5-13-65		X			150	90-114	210	280
5-14-65		X			140	90-114	265	240
5-15-65		X			120	90-114	275	210
5-16-65		X			105	90-114	250	195
5-17-65		X			90	90-114	255	180
5-18-65			X		55	90-106	250	205
5-18-65					78	90-114	250	180
5-19-65			XX		45	90-109.5	270	180
5-19-65					60	90-114	245	180
5-20-65			X		50	90-109	280	180
5-20-65					68	90-114	260	180
				2600 2620 2640 2660 2680 2700				
8- 9-65			XX		45	90-107	285	180
8- 9-65					65	90-114	265	180
8-10-65			XX		40	90-105	300	180
8-10-65					63	90-114	275	180
8-11-65			X		50	90-110	300	180
8-11-65					60	90-114	290	180
8-12-65		X			60	90-114	315	180
8-13-65		X			70	90-114	295	210
8-14-65		X			80	90-114	280	245
8-15-65		X			95	90-114	260	280
8-16-65		X			130	90-114	270	280

regarded as an intentional creation of a miss (B·T, B·R). The fuel required at midcourse may be obtained as follows.

Let

$$\left\| K \right\| = \begin{vmatrix} \frac{\partial \overline{B}\cdot\overline{T}}{\partial \dot{x}} & \frac{\partial \overline{B}\cdot\overline{T}}{\partial \dot{y}} & \frac{\partial \overline{B}\cdot\overline{T}}{\partial \dot{z}} \\ \frac{\partial \overline{B}\cdot\overline{R}}{\partial \dot{x}} & \frac{\partial \overline{B}\cdot\overline{R}}{\partial \dot{y}} & \frac{\partial \overline{B}\cdot\overline{R}}{\partial \dot{z}} \end{vmatrix}$$

evaluated at time of midcourse correction

$$\equiv \begin{vmatrix} k_{11} & k_{12} & k_{13} \\ k_{21} & k_{22} & k_{23} \end{vmatrix} \qquad (1)$$

C is defined as

$$\left\| C \right\| = \begin{vmatrix} k_{11} & k_{12} & k_{13} \\ k_{21} & k_{22} & k_{23} \\ k_{31}' & k_{32}' & k_{33}' \end{vmatrix} \qquad (2)$$

where

$$\begin{aligned} k_{31}' &= k_{12}\,k_{23} - k_{13}\,k_{22} \\ k_{32}' &= k_{13}\,k_{21} - k_{11}\,k_{23} \\ k_{33}' &= k_{11}\,k_{22} - k_{12}\,k_{21} \end{aligned} \qquad (3)$$

Then, for "critical plane" correction (that condition which yields a minimum velocity requirement) of a given $\overline{B}\cdot\overline{T}$ and $\overline{B}\cdot\overline{R}$,

$$\begin{bmatrix} \Delta\dot{x} \\ \Delta\dot{y} \\ \Delta\dot{z} \end{bmatrix} = \left\| C \right\|^{-1} \begin{bmatrix} \overline{B}\cdot\overline{T} \\ \overline{B}\cdot\overline{R} \\ O \end{bmatrix} \quad (4)$$

The velocity required may then be calculated

$$\Delta V = \sqrt{(\Delta\dot{x})^2 + (\Delta\dot{y})^2 + (\Delta\dot{z})^2} \quad (5)$$

In Figure 31, contours of constant ΔV requirement are shown as the family of concentric ellipses centered about the origin. The contours for grazing and 45 deg incidence are shown as dotted circles. It is clear from the figure that to obtain a displacement as far out from the nominal vertical impact point as the 45 deg capability allows, a midcourse velocity increment of about 16 meters/sec is required. In terms of fuel requirement, this increment amounts to 13 lb. In actual practice, the fuel penalty will be somewhat less. The reason is that the midcourse correction of injection errors and landing relocation can be made simultaneously rather than in sequential fashion. The magnitude of the ΔV vector needed to remove a given offset is always less than or at most equal to the sum of the magnitudes of two successive maneuvers (which are not in general in the same direction) to remove the same offset. Further analysis will be carried out to determine the maximum ΔV required to achieve a given landing offset from any point within or on an actual three-sigma dispersion ellipse.

Capability will exist in the Data and Operations Control Facility orbit determination and midcourse correction program for emergency landing site selection. However, the confidence level on mission success would be sacrificed if this capability were used for a prior site selection since total fuel capacity would be based on a standard trajectory with expected injection dispersions. It can be concluded at this time that the fuel penalty will in fact be appreciable and that Alternative 1, if it does not impose any undue operational difficulties, should be adopted as the standard method for selecting specific landing locations.

2. DSIF/Spacecraft Acquisition and Tracking Considerations

a. Summary. A study has been in progress to determine the spacecraft design requirements and spacecraft/DSIF interface requirements necessary to provide (1) the required tracking and communication link between the Deep Space Instrumentation Facility and the spacecraft and (2) a high probability of acquisition of the spacecraft by the DSIF even in the event of certain nonstandard situations. This study has necessarily encompassed three areas: the level of tracking and communications necessary to meet the orbit determination and mission transit operations requirements, the tracking requirements imposed by the various trajectory considerations, and equipment design restraints necessary to meet the requirements of Items 1 and 2.

The current status of these studies is given below. In summary, it can be stated that: (1) as long as tracking and two-way communication is established within approximately ½ hr after injection, the required system performance can be met; (2) for those "worst" cases where injection takes place near the Johannesburg Deep Space Station, tracking or communication will not be possible from this station with its current angular rate and maximum doppler shift limitations. However, tracking and communication will be established at the next DSS (Woomera) within the required ½ hr after injection.

b. Requirements for early DSIF acquisition and tracking. The acquisition of the spacecraft by the DSIF net and the establishment of two-way communications as soon as possible after injection is desired for two reasons: (1) to get early doppler and angle tracking data for orbit determination, and (2) to get the spacecraft into its normal cruise attitude (i.e., roll axis pointing at Sun) for thermal control and battery charging considerations.

Ideally, the spacecraft is tracked in doppler and angle from the DSIF net from injection, or as soon thereafter as possible, until just prior to the midcourse correction, which takes place nominally 20 hr after injection. In order to meet the landing location accuracy requirements (67 km, 3σ), orbit determination prior to midcourse must contribute an uncertainty at the Moon of no more than 30 km (3σ). Detailed data on the distribution of tracking data points throughout this 20 hr interval and total number of "good" data points required is not currently available. However, preliminary studies by JPL and STL indicate that:

(1) Continuous tracking for the first 8 hr after injection with data points every 10 sec will meet the orbit determination requirements.

(2) Loss of tracking data for the first half hour after injection will increase the orbit determination uncertainty no more than 10%.

From this data it may tentatively be concluded that if the establishment of tracking is delayed up to approximately ½ hr after injection, adequate orbit determination will still be possible. This subject needs more detailed study to verify the above statements when such additional items as loss of data points due to TWX transmission, actual data rates to be used in relaying the information from the DSIF stations to the Data Operations Center (DOC), throwing out "bad" data in the computer program, etc., are considered.

On separation from the *Centaur*, the spacecraft automatically goes into a "rate stabilize" mode. In this mode, the spacecraft angular rates imposed during separation are slowed down and stopped by the cold gas attitude control system. The vehicle is then held in whatever attitude it happens to stop until it is acquired by the DSIF and commanded into the Sun acquisition mode. Thus, if the vehicle acquisition is delayed, the spacecraft will stay in some random attitude relative to the Sun throughout this delay period instead of the normal coast attitude (i.e., vehicle roll axis pointing toward the Sun). This results in improper vehicle thermal control since the thermal control design is predicated on the fixed and known vehicle/Sun attitude. It has been determined that this "wrong" orientation of the vehicle relative to the Sun can be tolerated without effect on the vehicle performance for up to, but not to exceed, 1 hr after injection.

In summary, it appears that the acquisition of the spacecraft by the first DSIF can be delayed up to ½ hr after injection without degrading the orbit determination capabilities and without adverse effects on the spacecraft itself.

c. DSS limitations. The Deep Space Instrumentation Facility network is employed and its design is optimized for use with space probes at large distances from the Earth. It is not intended for tracking of near-Earth satellites. Thus first-pass tracking of interplanetary or lunar probes shortly after injection while the vehicle is still close to the Earth is limited by the following DSS characteristics: (1) angular line-of-sight limits, (2) angular tracking rate characteristics, (3) frequency tuning limits, and (4) time required for acquisition.

The tracking antenna at the Johannesburg DSS is an 85-ft paraboloid on a polar mount (one axis of the mount parallel to the polar axis of the Earth). The antenna can be driven about the polar axis, in hour angle[a], from +90 deg (western horizon) to −90 deg (eastern horizon). It can also be driven about an axis perpendicular to the polar axis (declination) from the northern horizon to the polar axis in the south which is above the horizontal by an angle equal to the latitude of the station (25° 53′, south). Thus, the angular coverage from this station is as indicated in Figure 32.

These DSS antennas are capable of angular tracking rates in either axis up to but not exceeding 0.7 deg/sec. Thus tracking of low altitude passes (just after injection) are severely limited by this consideration. In addition, the DSS transmitter and receiver frequency tuning range is limited to ±70 kc about a preselected center frequency. Thus, the maximum range of doppler shifts that can be accommodated in one pass is limited. As with the angular rate limitation, this consideration also affects only the low altitude passes.

The latter limitation (maximum doppler shifts) is made even worse by the uncertainty in the spacecraft transmitter and receiver frequencies. That is, in order to guarantee acquisition, the DSS frequencies must be variable over a range large enough to encompass the maximum doppler shifts plus the uncertainty in the spacecraft transmitter and receiver frequencies. The specifications on these frequencies is currently ±45 kc for the transmitter and ±42 kc for the receiver. To reduce these uncertainties, the frequencies will be measured just prior to launch and transmitted to the DOC for use by the DSS.

In addition to the above limitations, a finite time is required for acquisition of the spacecraft by the DSS. This time may vary from approximately 1 min if spacecraft angular position and frequency are accurately known to as long as 15 min if angle and frequency search are required. This acquisition time is also a limitation for the low altitude passes in which the visibility time from the DSS is very short.

d. Trajectory considerations. The tracking limitations due to the DSS/spacecraft geometry during the first pass following injection are a function of injection location. Figure 33 shows the locus of all possible injection points as a function of lunar declination. The numbered injection points correspond to particular computer runs. Also shown in the figure are the injection points which were selected for consideration below. The following paragraphs discuss the angle, angular rates, and doppler and time limitations inherent in these trajectories as determined in the 7090 computer program for the *Surveyor* standard trajectories.

DSS/spacecraft angle limitations. The location of the possible injection points for the years 1963 through 1965 are shown in Figure 33 as well as the location of the Johannesburg DSS antenna and the coverage from Johannesburg for vehicle altitudes of 100 and 400 miles. The trajectory of the spacecraft after injection is such that for the first half hour, it will travel essentially along a curve similar to the curves bounding the injection points at $\sigma_L = 90$ and 114 deg. Therefore, it can be seen from Figure 33 that it is possible for the spacecraft to pass by the Johannesburg DSS without ever coming into the zone of coverage when the altitude is not much greater than 100 miles at the time of passage. This will be the case for

[a]Hour angle referred to here is station-centered hour angle, distinct from geocentric hour angle which is equal to the former only at astronomical distances, i.e., distances which are large compared to the radius of the Earth.

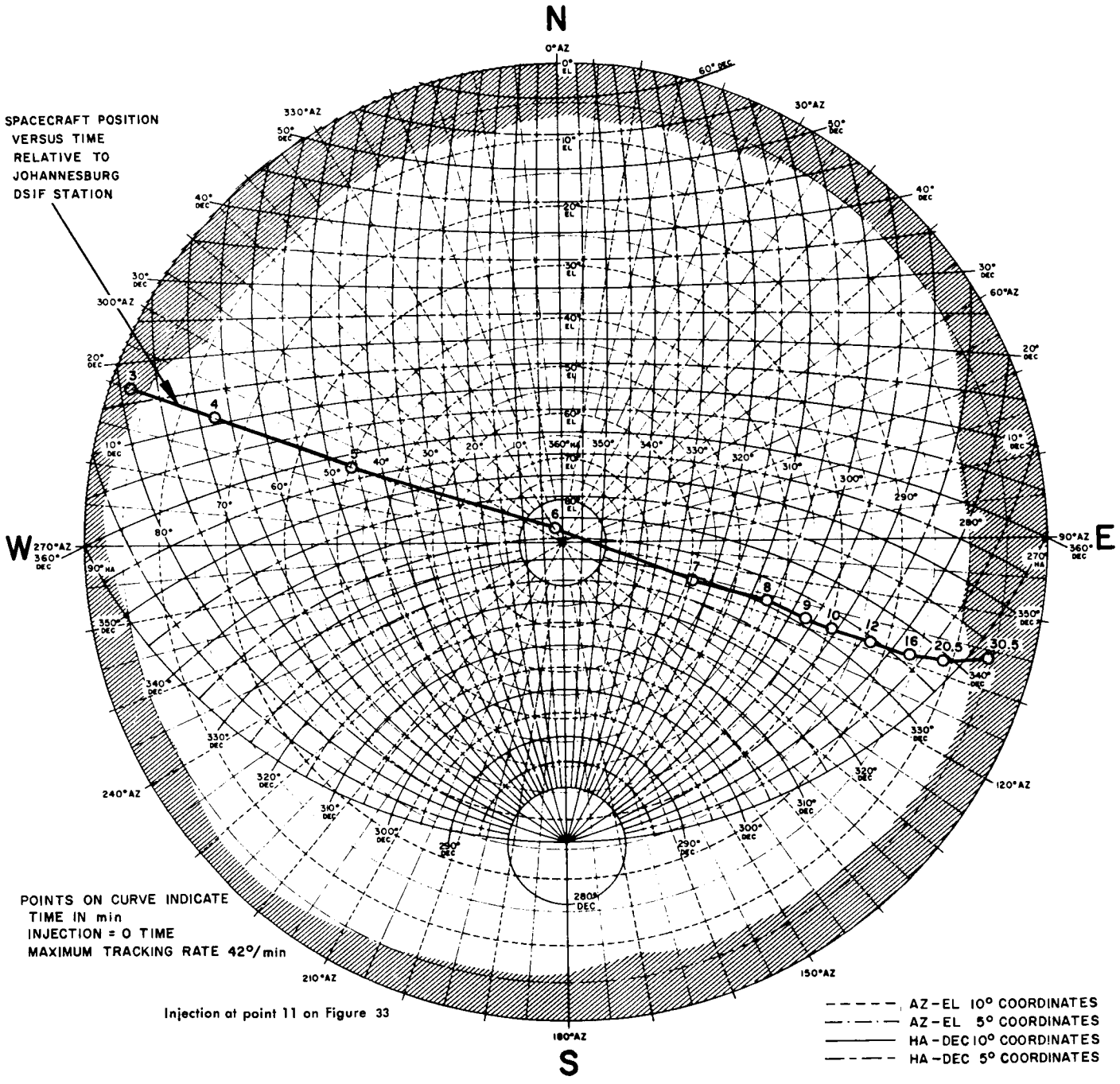

Figure 32. Johannesburg Deep Space Station coverage

injection at 100 miles altitude near the DSS with values of launch azimuth (σ_L) near 90 deg and near 114 deg.

DSS/spacecraft angle rate limitations. Two typical cases for line-of-sight angles and angular rates (injection at points 2 and 11, Fig 33) are plotted in Figures 34 and 35. The track of the spacecraft is also shown in Figure 32 for Case 11.

Figure 34 shows that the spacecraft is visible from the Johannesburg DSS for about 24 min and that the hour angle changes most rapidly at about 5.5 min after injection. The largest value of hour angle rate is slightly more than 0.7 deg/sec, which is the maximum angular tracking rate of the DSS antenna. This is the case, therefore,

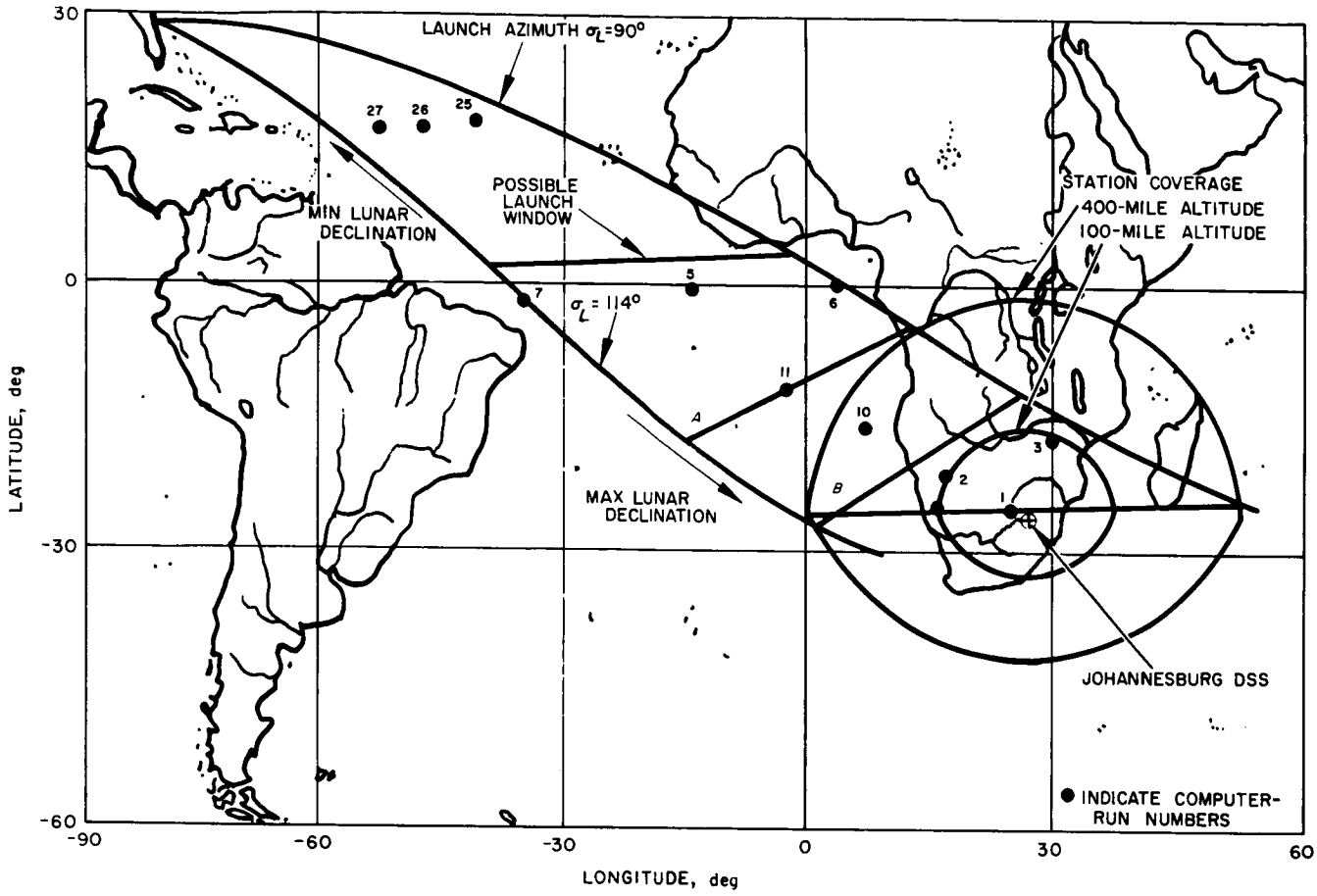

Figure 33. Map of injection points

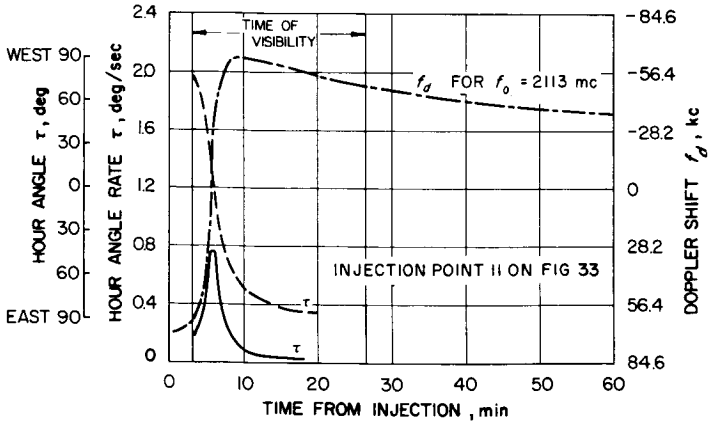

Figure 34. Tracking characteristics at Johannesburg DSS

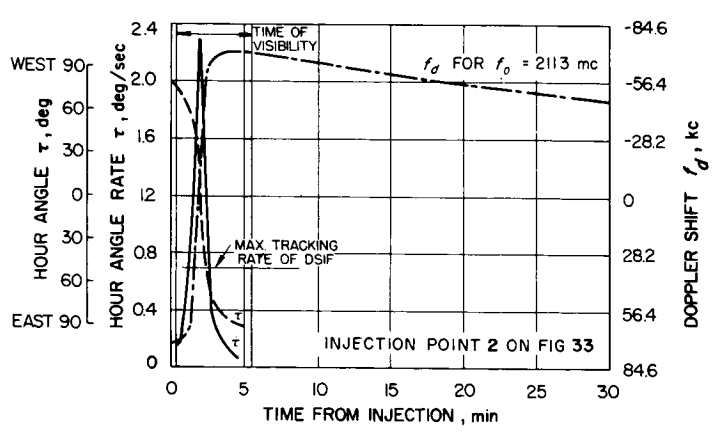

Figure 35. Tracking characteristics at Johannesburg DSS

where the DSS is on the borderline of being able to track in angle throughout the visible period.

For injection points farther down-range (nearer South Africa), the angular rates encountered are greater, as can be seen from Case 2 (Fig 35). The hour angle rate for Case 2 exceeds the antenna tracking capability from about 1 min to about 3 min after injection. The hour angle rate exceeds the antenna driving rate by such a large amount, in fact, that it would take approximately 1 min for the antenna to catch up after the hour angle

rate drops to below 0.7 deg/sec. This means that for Case 2 the antenna would be able to track for about ½ min immediately after the spacecraft appears above the western horizon (if it could acquire in that time) and then again for about 2 min before it disappears over the eastern horizon. In this case, if the antenna were set to about −50 deg hour angle (40 deg above the eastern horizon) and no attempt was made to track until the spacecraft reached this angle, then it should be able to track for about 3 min before the spacecraft disappears below the horizon.

The acquisition time may be the limiting factor here. The time required for acquisition is about 1 min if angle and frequency are well known. If only rough angle and frequency information are available, this step may take up to 15 min, in which case acquisition would not be possible at all for these late injection cases.

DSIF/spacecraft doppler shift limitations. Tuning range of the DSS transmitter and receiver places another constraint on spacecraft design and on tracking capability. The DSS tuning range of both the transmitter and receiver is ±70 kc from the nominal, where the nominal frequency is determined by crystal selection. The station requires about 8 hr advance notice to change crystals. This tuning range in conjunction with the spacecraft transmitter and receiver frequency uncertainties result in a doppler coverage of up to approximately ±50 kc (one way).

Figures 34 and 35 also show the doppler shifts seen by the DSS for Cases 11 and 2. It can be seen from the figures that the total doppler shift exceeds the 50 kc limit. To accommodate these large frequency changes, it will be necessary to bias the DSS transmitter and receiver center frequencies to a value such that tracking will be possible during all of the last part of the pass. This will result in an inability to track for about the first few minutes of these low altitude passes.

The rate of change of doppler frequency places demands on the dynamic response of the spacecraft transponder phase lock loop. The rate of change of frequency is greatest at the time of nearest approach, which is the same time the angular rates are maximum. It appears that the rate of change of frequency will always be less than 1 kc/sec^2 when the angular rates are less than 0.7 deg/sec. Thus, a dynamic response of the spacecraft transponder phase lock loop of at least 1 kc/sec^2 is adequate.

Time until first acquisition. Computer studies indicate that, for injection points as far as possible up-range from Line *A* (Fig 33), the spacecraft will be visible at the Johannesburg DSS within 15 min after injection. If injection takes place down-range from Line A and is not acquired by the Johannesburg DSS, it will be visible at the Woomera DSS within 20 min after injection. Thus, in any event, the maximum time from injection to first DSIF acquisition will be less than 30 min. (assuming a 10 min acquisition time).

e. Conclusions.

(1) Mission performance will be satisfactory if tracking is established within ½ hr after injection.

(2) For injection points down-range of Line *B* (Fig 33), the Johannesburg DSS will probably not be able to track at all due to coverage and/or angular rate limitations.

(3) For injection points between Line A and Line B, the DSS will probably not be able to track until after the spacecraft passes overhead. Tracking from overhead to the eastern horizon is possible if acquisition can be accomplished in the limited time available (from 3 to 20 min).

(4) For injection points up-range from Line A, the DSS should be able to track from nearly first visibility over the western horizon until it can be acquired by the next DSS.

(5) For injection points up-range from Line A, tracking will be established at Johannesburg within ½ hr from injection.

(6) For injection points down-range from Line A, where tracking from Johannesburg is not possible, tracking will be established at Woomera within ½ hr from injection.

3. Design Mission Sequence for List II Payload

A mission sequence has been prepared which includes all currently known system, operational, and DSIF constraints. The design mission sequence is presented to illustrate the experiments that may be completed, within the constraints listed below, on the first lunar day, the first lunar night, and the second lunar day for a particular worst-case trajectory (a late launch on the last day of the launch window).

The principal constraint which limits activity during the first lunar day is the energy available for scientific payload operation. This energy is 3871 watt-hr, based on 150 hr of daylight. It will increase as the launch day occurs earlier in the window. Thus a progressively greater proportion of the scientific experiment requirements can be fulfilled during the first lunar day.

a. Mission Constraints. The design mission sequence presented in Table 11 is based on the following constraints:

(1) The scientific payload will be the List II complement of instruments and auxiliaries, which consists of the following:

(a) Surface geophysical experiments
(b) Subsurface geophysical probe
(c) Subsurface sampler
(d) Surface sampler
(e) Gas chromatograph
(f) X-ray spectrometer
(g) X-ray diffractometer
(h) Radiation detector
(i) Television
(j) Tape recorder
(k) Auxiliaries (mechanism, thermal, battery)

(2) The total energy consumed during the first lunar day by the scientific payload will be 3871 watt-hr, based on a 150 hr period of daylight. The energy consumed by the scientific payload during the lunar night will be 4128 watt-hr.

(3) A standard trajectory is selected which represents the worst case in terms of time from touchdown to the first day/night terminator:

(a) Launch date: August 6, 1963
(b) Launch azimuth: 114 deg
(c) Total flight time: 63.9 hr
(d) Time from touchdown to dusk: 6.8 days (based on 0 deg horizon)

(4) Utilization of the DSIF will conform to the following guidelines:

(a) Injection to 48 hr following lunar nightfall: 24 hr/day DSIF coverage.
(b) Remainder of first lunar night: daily tracking missions alternating between Woomera and Johannesburg stations.
(c) Just before lunar dawn to 24 hr after sunrise: 24 hr/day coverage.
(d) Remainder of second day: Goldstone tracking missions on second, fourth, sixth, and eighth days; Woomera and Johannesburg each two tracking missions.
(e) Second lunar night: Woomera and Johannesburg each three tracking missions.
(f) Third lunar day: Goldstone two tracking missions.
(g) Repeat (e) and (f) for remainder of mission.

Table 11. *Surveyor* design mission sequence

DSIF time[a], hr	Visibility G	W	J	Significant event	Time, hr	min	Data transmitted[b]
				Prelaunch readiness tests, transmitter on (low power)			Engineering data
−65				LAUNCH-INJECTION — Preprogrammed after *Centaur* burnout: gear extend, omnidirectional antennas extend, nitrogen solenoid valve open.	−63	52	Engineering data Mechanisms Flight control Vehicle Electrical power Data link
					−63	32	
				Separation — Rate-stabilized mode, automatic.			
				DSIF acquisition — Position solar panel, Sun/star acquisition and verification, begin first coast phase.			
−60				ENGINEERING DATA TRANSMISSIONS[b] (periodic)			
−55							
				Radiation detector sampling[c]	−52	30	Engineering data Flight control Vehicle Data link Electrical power Radiation detector
−50				ENGINEERING DATA TRANSMISSIONS (periodic)	−51	30	
−45				MIDCOURSE CORRECTION — Transfer to inertial mode; roll, pitch attitude maneuver; incremental velocity correction, roll, pitch attitude maneuver, Sun/star acquisition and verification, begin second coast phase.	−45	30	Engineering data Flight control Vehicle Data link Electrical power Propulsion
					−45	15	
				ENGINEERING DATA TRANSMISSIONS (periodic)			

Table 11. *Surveyor* design mission sequence (continued)

DSIF time[a], hr	Visibility G	Visibility W	Visibility J	Significant event	Time, hr	Time, min	Data transmitted[b]
							Engineering data Flight control Vehicle Data link Electrical power
−40				ENGINEERING DATA TRANSMISSIONS (periodic)			
−35							
−30							
−25							
−20							
−15							
−10							
−5							
0				TERMINAL DESCENT	−00	32	Engineering data, TV
					−00	00	
				TERMINAL DESCENT			
−0.5				START TERMINAL DESCENT PHASE Position and lock planar array and solar panel Transfer to inertial mode Execute roll, pitch, roll attitude maneuver.	−00	32	Engineering data Mechanisms Flight control

Table 11. *Surveyor* design mission sequence (continued)

DSIF time[a], hr	Visibility G W J	Significant event	Time, hr	Time, min	Data transmitted
		TV on, camera No. 4	—00	20	
		Switch to planar array			Data link
		Start TV scan	—00	18	TV data
—0.25					
		Retro delay magnitude, thrust phase control power on, radars to warm	—00	08	Engineering data Flight control Vehicle Propulsion Electrical power TV (intermittent)
		Marking radar on	—00	05	
		Marking radar enable command	—00	04+	
		Retro ignition	—00	03+	
		Retro burnout	—00	02+	
		Vernier descent			
0		TOUCHDOWN	—00	00	
		FIRST LUNAR DAY			
0		TOUCHDOWN — Initial deployment, preliminary TV surveys, instrument deployment	00	00	Engineering data[1], TV data
		Surface geophysical experiments	+02	20	Engineering, TV, surface geophysical data[2]
5		Radiation detector sampling, stowed position	+04	20	Radiation detector[3]
		Deploy radiation detector, begin sampling, extended position	+06	20	
10					
15					
20		First complete TV survey (corrected program)	+20	32	TV data
		Surface sampler, pulverizer operation, TV, begin surface soil analysis (gas chromatograph)	+21	47	Engineering, TV, gas chromatograph[4]
		X-ray spectrometer: background count, standard sample analysis	+21	57	X-ray spectrometer
			+22	57	
		X-ray spectrometer: surface soil analysis	+23	50	X-ray spectrometer
			+24	50	

Table 11. *Surveyor* design mission sequence (continued)

DSIF time[a], hr	Visibility G	W	J	Significant event	Time, hr	min	Data transmitted
25				X-ray spectrometer: standard sample analysis	+25	35	X-ray spectrometer
					+26	05	
				X-ray diffractometer: standard sample and background count	+26	27	X-ray diffractometer
					+27	27	
				X-ray diffractometer: begin surface soil analysis	+28	11	X-ray diffractometer
					+29	11	
				Completion of surface soil analysis, gas chromatograph	+29	51	
30				X-ray diffractometer: complete surface soil analysis	+29	55	X-ray diffractometer
					+30	55	
35							
40							
45				Subsurface sampler, pulverizer, TV operation; begin soil analysis first subsurface level (gas chromatograph)	+45	35	Engineering, TV, gas chromatograph
					+46	05	
				X-ray spectrometer: standard sample analysis	+46	35	X-ray spectrometer
				X-ray spectrometer: first subsurface level soil analysis	+46	49	X-ray spectrometer
					+47	49	
				X-ray spectrometer: standard sample analysis	+48	17	X-ray spectrometer
					+48	47	
				X-ray diffractometer: begin first sub-level analysis	+49	01	X-ray diffractometer
					+50	01	
50				X-ray diffractometer: complete first subsurface level analysis, complete gas chromatograph analysis	+50	29	X-ray diffractometer
					+51	29	
				Special TV survey: high resolution, photometric, colorimetric, polarimetric.			TV data
55					+55	39	
60							
65							

[a] DSIF time: G = Goldstone, W = Woomera, J = Johannesburg

Table 11. *Surveyor* design mission sequence (continued)

DSIF time[a], hr	Visibility G W J	Significant event	Time, hr min	Data transmitted
70		Second complete TV survey	+69 30 +70 45	TV data
75				
115				
120		Third complete TV survey	+119 00 +120 15	TV data
160		Scientific temperature sampling rate increased to 1 per 30 sec.	+162 00	
165		D/N TERMINATOR	+165 00	Engineering data, scientific temperature
		Scientific temperature sampling rate decreased to 1 per hour	+168 00	
170				
		SPECIAL REQUIREMENTS – FIRST LUNAR NIGHT		
SPECIAL SCIENTIFIC DATA REQUIREMENTS DURING FIRST LUNAR NIGHT		Surface resistivity measurement Surface thermal diffusivity measurement (2½ hr)		Periodic engineering data, periodic scientific temperature data and radiation detector data will be tape-recorded to maximum of 18 hr/day during DSIF down periods.

Table 11. *Surveyor* design mission sequence (continued)

DSIF time[d], hr	Visibility G	W	J	Significant event	Time, hr	min	Data transmitted
SURVEYOR DESIGN MISSION SEQUENCE, SECOND LUNAR DAY[d]							
−5				Scientific temperature sampling rate increased to 1 per 30 sec.	−03	00	
0				N/D TERMINATOR (TD + 21.1 days)	00	00	Engineering data, scientific temperature
				Scientific temperature sampling rate decreased to 1 per hour	+03	00	
5							
20				Fourth complete TV survey	+21	00	TV data
					+22	15	
25							
				Subsurface sampler, pulverizer operation, TV, begin soil analysis, second subsurface level (gas chromatograph)	+38	00	Engineering, TV, gas chromatograph
					+38	30	
				X-ray spectrometer: standard sample analysis	+39	00	X-ray spectrometer
40				X-ray spectrometer: second subsurface level soil analysis	+39	10	X-ray spectrometer
					+40	10	
				X-ray spectrometer: standard sample analysis	+40	30	X-ray spectrometer
					+41	00	
				X-ray diffractometer: begin second subsurface level soil analysis	+41	10	X-ray diffractometer
					+42	10	
				X-ray diffractometer: complete second subsurface level soil analysis; complete gas chromatograph analysis	+42	30	X-ray diffractometer
45					+43	30	

Table 11. *Surveyor* design mission sequence (continued)

DSIF time[d], hr	Visibility G W J	Significant event	Time, hr min	Data transmitted
65				
70	W	Fifth complete TV survey	+68 30 +69 45	TV data
		Gas chromatograph: standard sample analysis		Engineering, gas chromatograph
75			+74 45	
85		Subsurface sampler, pulverizer, TV operation, begin soil analysis, third subsurface level (gas chromatograph)	+87 00	Engineering, TV, gas chromatograph
		X-ray spectrometer: standard sample analysis	+87 30 +88 00	X-ray spectrometer
		X-ray spectrometer: third subsurface level soil analysis	+88 15 +89 15	X-ray spectrometer
90		X-ray spectrometer: standard sample analysis	+89 47 +90 17	X-ray spectrometer
		X-ray diffractometer: begin third subsurface level soil analysis	+90 33 +91 33	X-ray diffractometer
		X-ray diffractometer: complete third subsurface level soil analysis, complete gas chromatograph analysis	+92 05 +93 05	X-ray diffractometer
95				
120	W	Sixth complete TV survey	+119 00 +120 15	TV data
125				
135		Subsurface sampler, pulverizer, TV operation, begin soil analysis, fourth subsurface level (gas chromatograph)	+136 30	Engineering, TV, gas chromatograph
		X-ray spectrometer: standard sample analysis	+137 00 +137 30	X-ray spectrometer
		X-ray spectrometer: fourth subsurface level soil analysis	+138 04 +139 04	X-ray spectrometer

Table 11. *Surveyor* design mission sequence (continued)

DSIF time[d], hr	Visibility G W J	Significant event	Time, hr	Time, min	Data transmitted
140		X-ray spectrometer: standard sample analysis	+140	17	
			+140	47	X-ray spectrometer
		X-ray diffractometer: begin fourth subsurface level soil analysis	+141	24	
			+142	24	X-ray diffractometer
		Complete gas chromatograph analysis	+143	04	
			+143	37	X-ray diffractometer
145		X-ray diffractometer: complete fourth subsurface level soil analysis	+144	37	
160		Seventh complete TV survey	+160	30	TV data
			+161	45	
165					
185		Subsurface sampler, pulverizer, TV operation, begin soil analysis, fifth subsurface level (gas chromatograph)	+185	30	Engineering, TV, gas chromatograph
		X-ray spectrometer: standard sample analysis	+186	00	
			+186	30	X-ray spectrometer
		X-ray spectrometer: fifth subsurface level soil analysis	+187	15	
			+188	15	X-ray spectrometer
190		X-ray spectrometer: standard sample analysis	+189	45	
			+190	15	X-ray spectrometer
		X-ray diffractometer: begin fifth subsurface level soil analysis	+191	00	
			+192	00	X-ray diffractometer
		Complete gas chromatograph analysis	+192	40	
		X-ray diffractometer: complete fifth subsurface level soil analysis	+193	30	
			+194	30	X-ray diffractometer
195		COMPLETION OF COMPOSITION ANALYSIS			

[a]Time referenced to touchdown.

[b]Various engineering data will be transmitted periodically during transit coast phases.

[c]May be recorded.

[d]Time referenced to the night/day terminator.

NOTES:

(1) Engineering data refers to engineering commutator data. Although not periodically shown, engineering data will normally be sampled each hour and during special operations.

(2) After completion of the surface geophysical measurements, surface temperature will be measured hourly for 1 month, with increased sampling rates at the terminators.

(3) Radiation detector data will be required continuously for the life-time of the spacecraft as permitted by DSIF availability and TV transmissions.

(4) Gas chromatograph will require a total operating period of 5 hr for each composition analysis.

(5) High power transmitter operation is required during TV surveys (vidicon readout), X-ray diffractometer and X-ray spectrometer operation, tape recorder readout, and high bandwidth surface and subsurface geophysical experiments. (It appears probable at this time that the required telemetering bandwidth for the X-ray diffractometer experiment will be reduced to allow data transmission in the low-power transmtter mode. This will result in a significant saving of energy which can be utilized for analysis of additional subsurface levels during the first day).

D. Flight Control

1. Introduction

The flight control subsystem consists of those elements of the spacecraft that provide velocity control and attitude control during the transit phase of the *Surveyor* mission. Functionally, the lunar radar and propulsion elements are part of this subsystem, although they are discussed in other sections of this report. Elements of the flight control subsystem treated in this section include optical sensors, inertial instruments, attitude controls, and flight control electronics.

2. System Design

a. Summary. Principal attention has been focused on the vernier phase control system during this report period. The main points of the investigation have been to establish the optimum range-velocity trajectory; to ensure that adequate stability margins exist; and to determine with greater precision the dispersions in attitude and lateral velocity at vernier engine cutoff. To aid this study, an analog computer simulation covering the entire vernier phase is being used. Work has also been started in programming a digital computer to obtain more exact results. It is planned to expand the digital simulation to a six-degree-of-freedom model at a later date.

b. Vernier phase control. Besides ensuring a soft, upright landing, the vernier phase control system must be designed to utilize vernier engine fuel in the most efficient way, requiring that the maximum possible thrust range be used for velocity control. Since the vernier engines are also used for pitch and yaw attitude control, the maximum and minimum thrust channel command must be limited in order to provide moment control at all times. For example, if the thrust command were to saturate the three engines, the pitch and yaw attitude channels would have to develop larger than normal moment commands to achieve control, resulting in effectively lowering the gain of the attitude control loops. When the thrust command limit exceeds the engine thrust capability, the attitude loops exhibit a stable limit cycle. The amplitude and frequency of this limit cycle oscillation are dependent on a number of system parameters. The amplitude is closely related to the amount by which the thrust command exceeds the engine capability.

An analog computer model in two degrees of freedom has been used to investigate this limit cycle behavior (Fig 36). The model is somewhat simplified but provides insight into the pitch/yaw coupled behavior when the thrust command produces engine saturation. Preliminary results indicate that for a thrust command limit 10 lb greater than a single engine thrust capability, the limit cycle amplitude will be less than 10 deg peak-to-peak at a frequency of less than 1 rad/sec.

Although a small amplitude limit cycle does not constitute a serious problem in trajectory control, it is undesirable from the standpoint of television. Therefore serious consideration must be given the tradeoff between vernier engine fuel consumption and the attitude control behavior desired for television coverage.

Two possible design modifications are being considered to alleviate this problem. One consists of changes in the inner rate loop during doppler attitude control: for example, using the gyros in the rate mode to eliminate the conditionally stable behavior of the loop as now designed. The other consists of using the vernier engine chamber pressure transducers to control the level at which the thrust command limiter operates. Neither approach has yet been examined in detail. For the present, the principal effort will be to establish the accuracy with which the thrust level can be held by the thrust channel limiter and then determine the fuel penalty resulting when the electronic limit level is set low enough to prevent any limit cycle oscillation.

As described in previous reports, the range-velocity trajectory implemented in the variable thrust phase of vernier control will be a series of three straight-line segments. The points of intersection of these segments lie on a reference parabola corresponding to a near-maximum thrust descent trajectory. Figure 15 illustrates the relation of this parabola to the trajectories corresponding to an electronic limit thrust level and ultimate engine capability.

In descending to the control law trajectory the spacecraft will intersect the third segment and in general overshoot before recovering to the actual control law. The higher the point of intersection, the greater the overshoot and the longer the recovery time. The reason for the overshoot is that the electronic limit on thrust corresponds to a dR/dV capability which cannot satisfy the straight line control law in the upper range of each segment. If the initial point of intersection were to coincide with the upper end of the third control law segment, the spacecraft would follow a trajectory very nearly that of the reference parabola, recovering to the control law only shortly before entering the second segment. By the same token, the trajectory in the first and

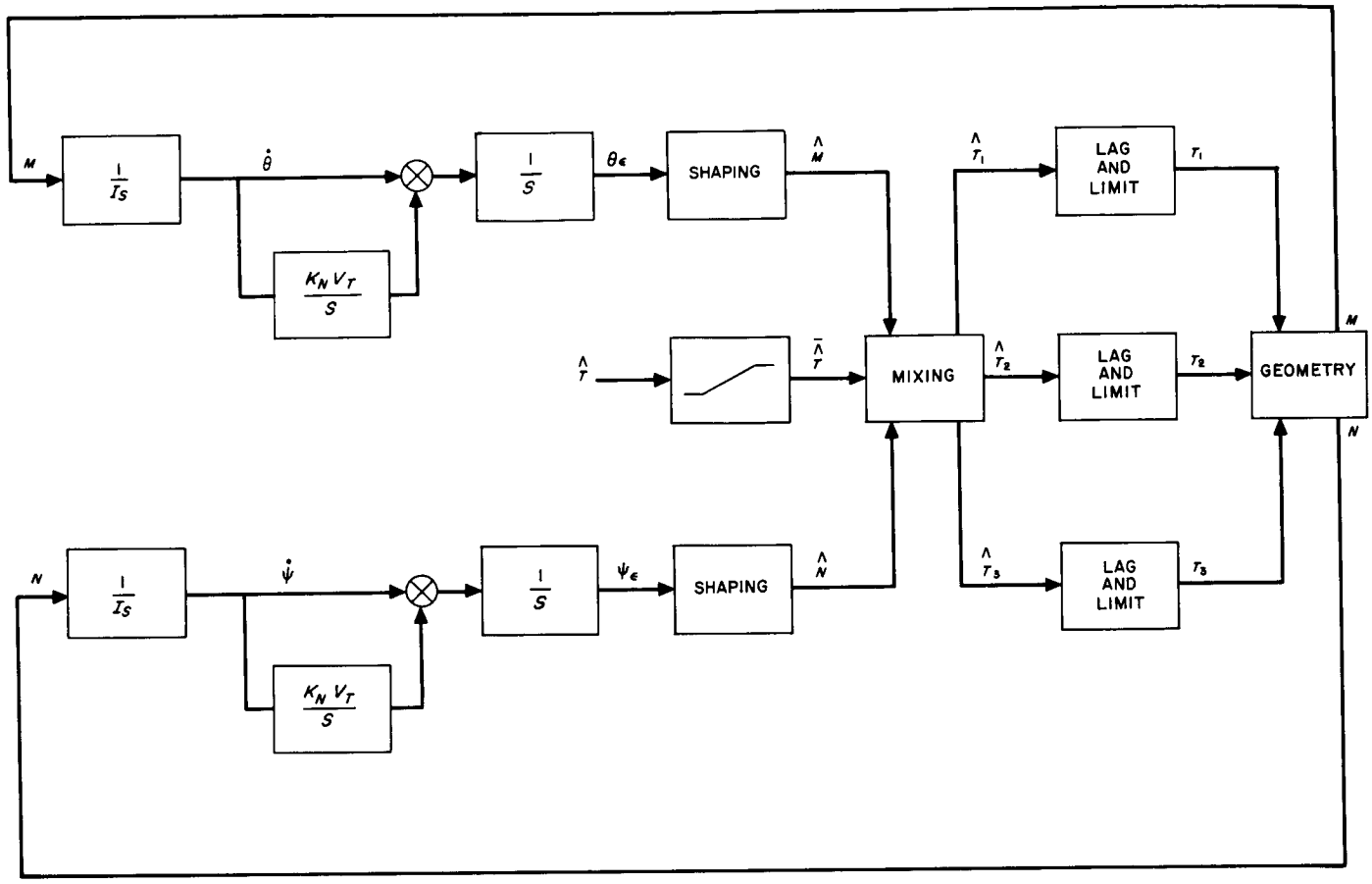

Figure 36. Computer model with two degrees of freedom

second segments will more nearly follow the reference parabola than the straight line sections. Because the effective maximum thrust, as defined by the electronic limit, exceeds the thrust corresponding to the reference parabola, the trajectory recovers to the control law near the lower end of each segment. The electronic limit trajectory shown in Figure 37 corresponds to a slightly lower thrust level than the engine capability trajectory. This is required if the pitch-yaw limit cycle oscillation is to be avoided.

3. Subsystem Test

a. Single-axis air bearing table. Most of the fabrication of the basic single-axis test table has now been completed, as shown in Figure 38. The air bearing itself consists of a segment of a 10 in. diameter sphere. The mating bearing pad is 5 in. across and contains 17 orifices, each 0.013 in. in diameter. The bearing journal is so constructed that the table is supported by a teflon ring when the air pressure is removed, thus preventing damage to the bearing surfaces.

The bearing has been designed to support a load of 900 lb. with an operating pressure of 100 psi. Gas consumption has been minimized such that the table can be operated for a full day on a single bottle of nitrogen. The platform consists of a 2-in. plate of aluminum alloy 5 ft in length. Weight of the table alone is 448 lb. The moment of inertia is calculated to be over 50 slug-ft^2.

Shown in the photograph are two 200-in.^{3} accumulators for gas jet nitrogen supply. These tanks have been volumetrically matched to avoid table unbalances which would result if a different amount of gas were to be used from each tank. The remainder of the table equipment will be mounted around its periphery for accessibility and to increase the moment of inertia. It is planned that the entire top will remain clear for installation of flight control components to be tested.

Attempts have been made to determine the magnitude of spurious torques about the table roll axis. Preliminary results indicate drifts of less than 10 deg/hr might be expected, but accurate measurements have not

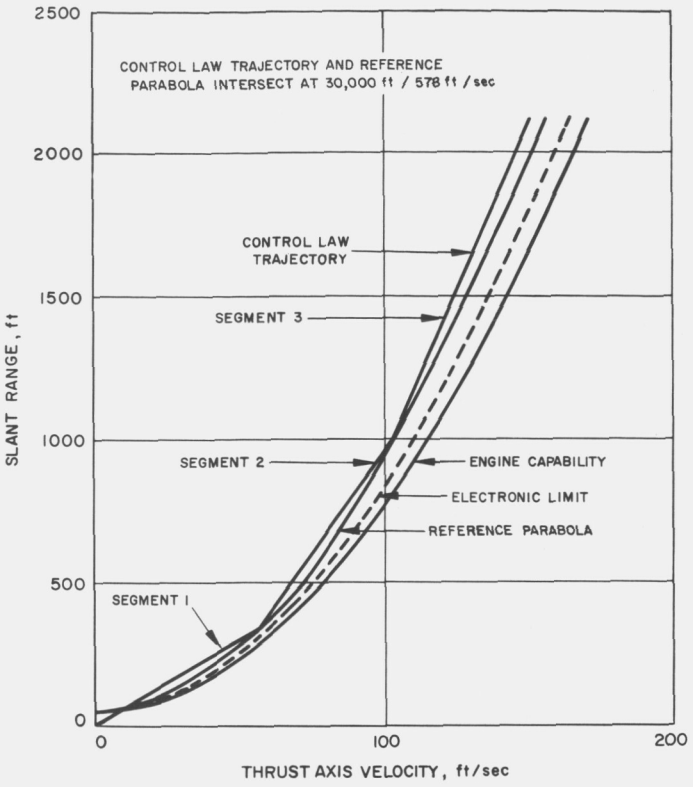

Figure 37. Spacecraft descent trajectory

yet been achieved in the present location due to uncontrollable air currents. It is planned to move the table into a new laboratory in which the environment will be controlled to minimize disturbances due to air currents and building vibrations. The table tends to align itself with the Earth's magnetic field, due to steel in the accumulators, indicating that a compensating field coil will be needed.

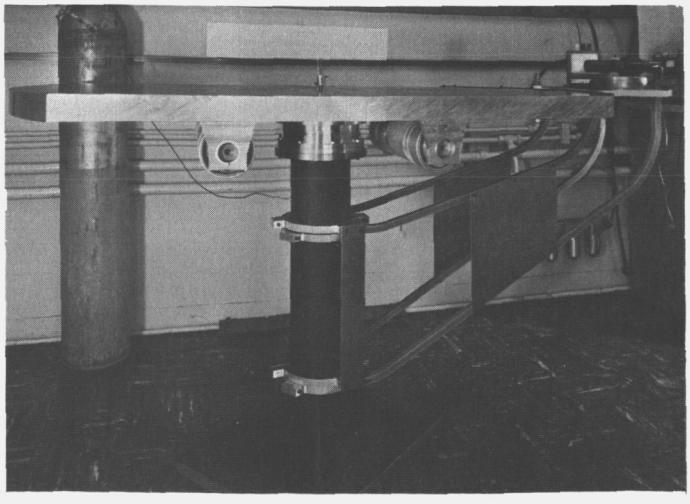

Figure 38. Single-axis air bearing table

b. T-2 test program. During this report period, considerable effort has been devoted to detailed analysis of the requirements of the control system and general configuration of the T-2 test vehicle. The purpose of the T-2 program is to exercise the vernier retro phase control system and evaluate the system performance by simulating as nearly as possible the last few hundred feet of the landing trajectory. To perform this test, a special lightened version (180 lb maximum) of the *Surveyor* spacecraft will be dropped from a tethered balloon and restrained from hitting the ground by a snubbing line. Details of this configuration are given in Section K. The following is a brief discussion of the items being considered in the anaylsis of the control system.

The nominal thrust characteristics of the vernier engines are shown in Figure 39 . In sea level operation, not only are the thrust levels reduced compared to vacuum conditions but the rate of thrust change per milliampere of differential current is also reduced. The rate at sea level is about 70% of the rate in vacuum conditions. This gain reduction must be considered when adjusting the electronics gain for any desired loop gain.

Preliminary T-2 test plans call for igniting the vernier engines and stabilizing the vehicle in attitude before release from the supporting balloon. Thus, all drops will be made with at least a minimum programmed thrust of 60 lb. The actual trajectory depends on the weight, thrust, and drag of the vehicle. Figure 40 shows descent trajectories of a 180 lb vehicle with 60 lb thrust for various values of the drag coefficient area product, C_DS. The zero-drag case is included for comparison. The T-2

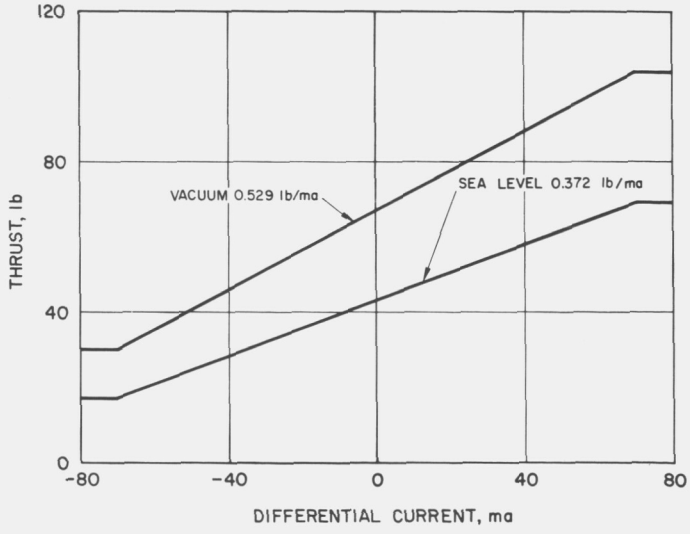

Figure 39. Nominal vernier engine thrust vs differential control valve current

vehicle minimum programmed thrust trajectory is expected to be within the curves for C_DS values of 10 and 20 ft^2, based on preliminary estimates of vehicle drag coefficient.

Terminal velocity (when drag equals weight) for these trajectories, as well as time from balloon release, are also shown in Figure 40. The expected trajectory should have a terminal velocity between 70 and 98 ft/sec, and the time to fall 300 ft would be between 6 and 6.5 sec. Thus it appears that drop tests in inertial modes should be kept to within 5 to 6 sec and 200 to 300 ft, since a longer drop would not result in any substantial velocity increase. Higher velocities result in larger aerodynamic moments, which could require moment control far in excess of that required by the spacecraft in lunar landing.

After release from the balloon and a period of minimum programmed thrust descent to gain velocity, the maximum programmed thrust descent can be initiated.

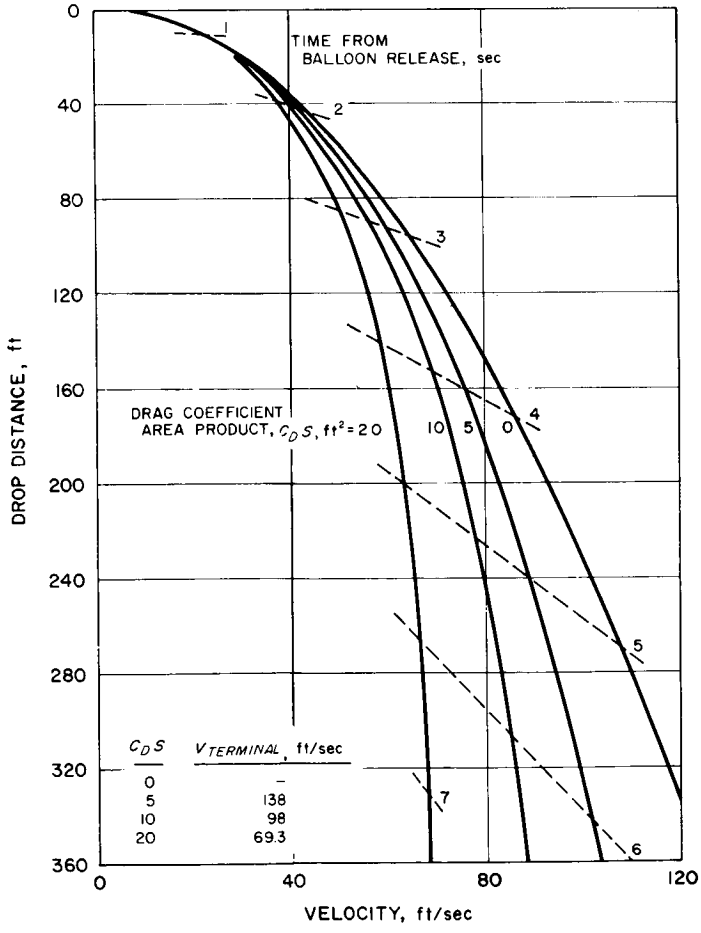

Figure 40. T-2 trajectories with minimum programmed thrust

T-2 trajectories starting with an initial velocity and maximum programmed thrust of 190 lb are shown in Figure 41. The curves are computed as incremental altitude and time to reach zero velocity as a function of initial velocity and C_DS. However, once an initial velocity and C_DS are chosen, the curve represents the trajectory to zero velocity. For example, the total trajectory, composed of a minimum programmed thrust phase to attain 50 ft/sec and then instantaneous initiation of maximum programmed thrust for the remainder of the descent to zero velocity, would take about 17 to 19 sec and 309 to 388 ft of altitude for a T-2 vehicle with C_DS of 20 and 10 ft^2, respectively. The altitude given does not include snubber stretch or safety factor. Also included in Figure 41 is the locus of terminal velocities with minimum programmed thrust T, which indicates the maximum initial velocity possible.

The spacecraft loop gain, for a velocity loop gain K_v of 250 lb/ft/sec is approximately 5100. If this K_v were maintained in the T-2 vehicle, the loop gain would be about 15,700 because of the change in engine characteristics and mass. Although this large loop gain does

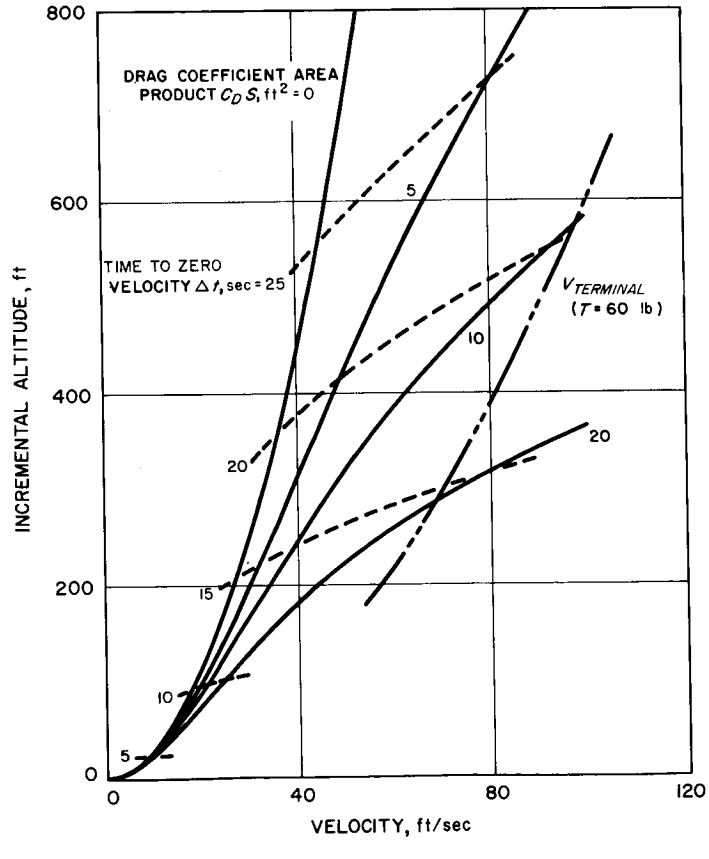

Figure 41. T-2 trajectories with maximum programmed thrust and initial velocity

not cause instability, it does reduce the stability margin of the velocity loop. It may be desirable therefore to reduce K_r to approximately 81 lb/ft/sec to maintain the same loop gain for the T-2 vehicle as for the spacecraft.

A new constant deceleration descent and the attendant straight-line approximation of this reference trajectory (V vs R parabola) must be established for the T-2 vehicle because of its lower maximum deceleration capability. If the T-2 vehicle thrust is programmed such that at every instant the sum of thrust and drag is constant and greater than the weight, a constant deceleration descent is maintained. With a 180 lb T-2 vehicle and 190 lb of maximum programmed thrust, the maximum deceleration is about 1.8 ft/sec^2 as compared to 6.0 ft/sec^2 for the spacecraft based on an 800 lb vehicle and 280 lb maximum programmed thrust.

The slopes of straight-line segments dV/dR of the T-2 reference parabola would, in general, be less than those for the spacecraft because of the lower deceleration, as shown in Figure 42. The line segments of the T-2 reference parabola are based on the same ranges as for the spacecraft since range is the switching criterion used in the spacecraft.

To achieve similar real-time behavior of the attitude control system in T-2 in relation to the spacecraft, adjustments will have to be made to maintain the same inner rate loop gain used in the spacecraft. This can be achieved in part by arranging the T-2 configuration as nearly as possible for the same angular acceleration to moment commands as in the spacecraft. This requires that the vernier engine moment arms be reduced to compensate for the lower moments of inertia of the T-2 vehicle. It is unlikely, however, that complete compensation can be achieved in a practical configuration with the severe weight limitations imposed on the vehicle due to operating in the Earth's gravity field. Consequently, it is expected that an adjustment in the gain of the moment command channel will be required.

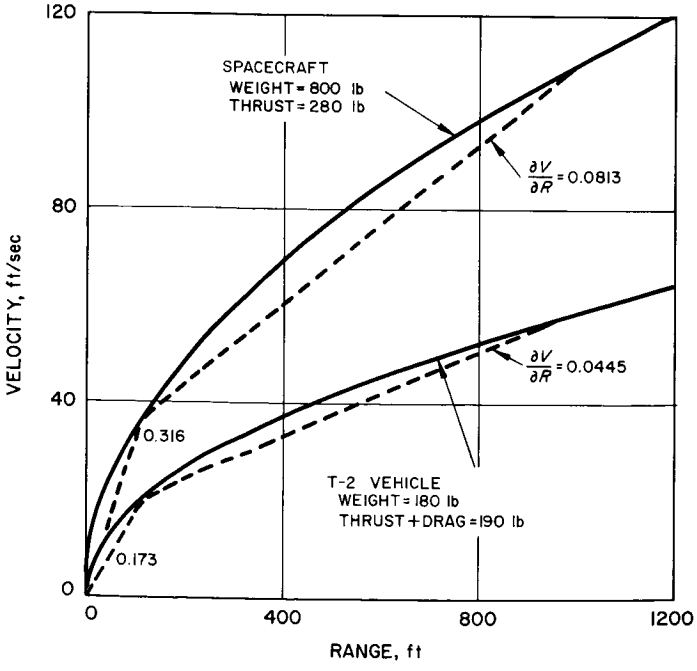

Figure 42. Range vs velocity profiles

4. Sensor Group Integration

The general arrangement of the sensor group instruments on a central truss-type support has undergone minor changes since the last report. The Moon sensor was moved to the center of the support structure when space became available as a result of redesign to reduce weight. Figure 43 shows a layout of the present sensor group assembly.

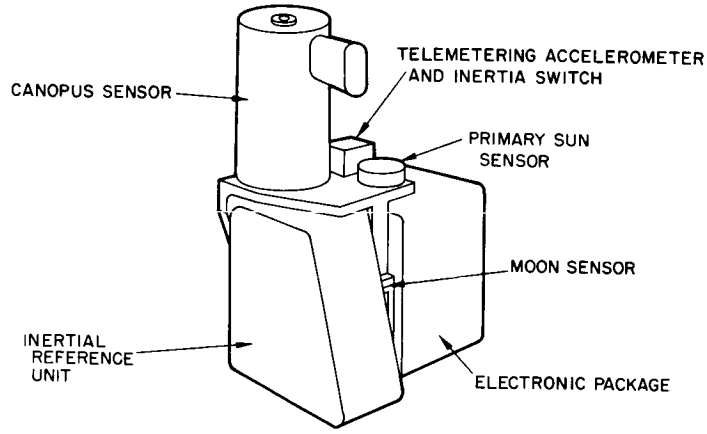

Figure 43. Sensor group assembly

A detailed drawing of the support structure has been completed and the first static acceleration and vibration test model will be machined from a forged billet of 75S-T6 aluminum. The structure will be tested to assure minimal distortions with loading to simulate retro-rocket thrust effects and also to assume adequate structural integrity under vibration with appropriate unit masses attached.

Electrical interconnections within the flight control group will be with a branched harness and a single cable between the inertial reference unit and the elec-

tronics package. The cable from the inertial reference unit to the electronics package is kept separate since it affects the package thermal design significantly. Thermal gradients are not large between the remaining units, and a common harness appears appropriate. The details of the wiring harness design are still under study. However, it appears that a weight reduction will result if a junction terminal strip is placed near the position of the telemetering accelerometer.

5. Optical Sensors

a. Canopus sensor. The Canopus sensor design concept was outlined in the previous bimonthly report. The star sensor electronics have been modified somewhat to use the capabilities of the instrument more fully. Figure 44 shows the revised star sensor block diagram. A threshold mode switch has been eliminated and the function is now performed by logic circuits within the flight control electronics unit.

An amplitude-sensitive star channel has been added which can provide additional verification of roll position through the construction of a strip star map from telemetered data. A plot of the estimated output characteristic is shown in Figure 45.

The breadboard model of the Canopus sensor is expected to be demonstrated in the near future. Completion of the breadboard was delayed to allow fabrication of mechanical parts similar to those to be used in the design verification models. The electronic portions of the breadboard model have been completed and tested extensively at room temperature and at high and low temperature extremes. The AGC loop has been closed. The forward portion of the loop was found to have a gain variation of ± 0.5 db when exposed to ambient temperatures of $-40°$ C to $85°$ C under the worst conditions of supply voltage variation.

A series of crude environmental tests were performed on the photomultiplier tubes to obtain initial assurance that the tubes would survive sterilization, vibration, and shock exposure. The tests summarized in Table 12 were preliminary and monitored only dark current and change in tube gain with an unfocused standard light input.

A star-Sun simulator is being designed to provide Sun and Canopus characteristic radiation for calibration and checking of the Canopus sensor. The device will use a single tungsten filament lamp as a source, with filters added to approximate the spectral distribution of the objects.

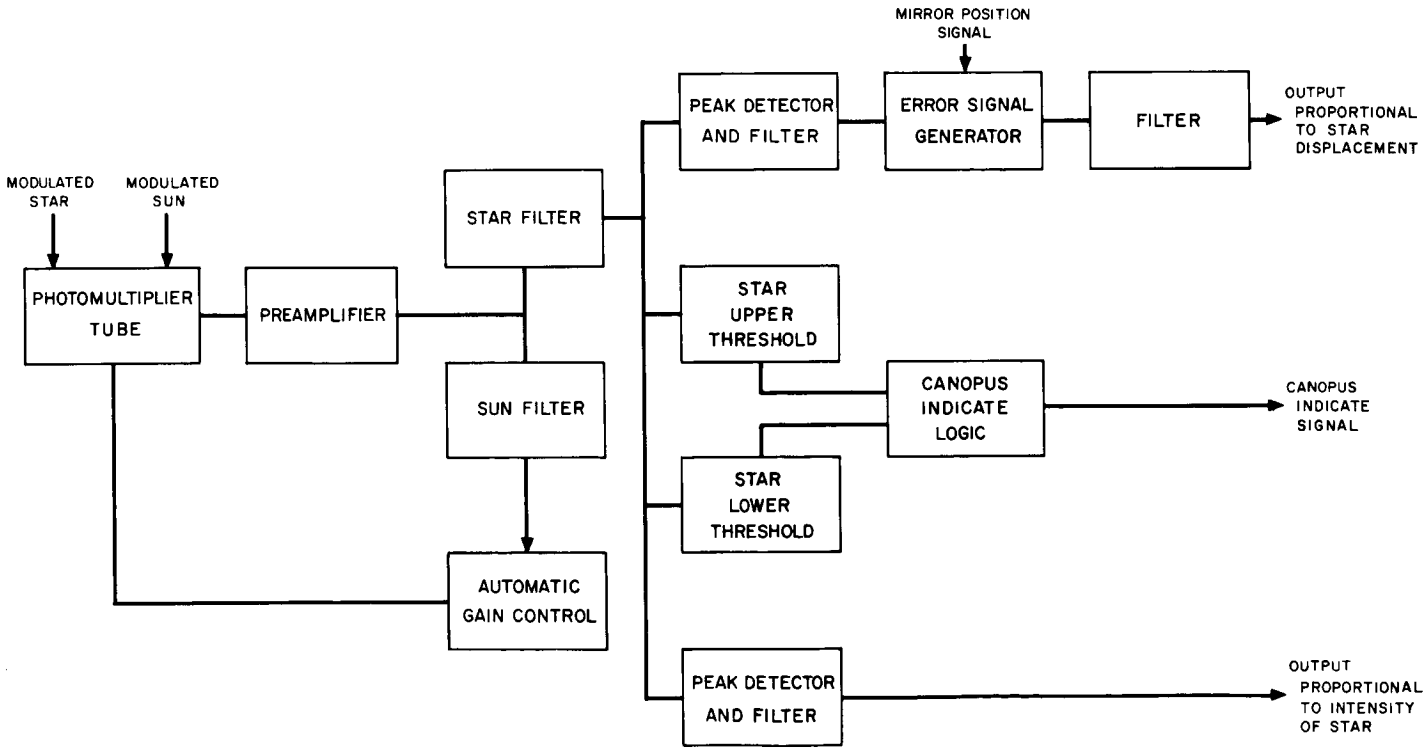

Figure 44. Revised star sensor electronics

Table 12. Photomultiplier tube environmental tests

Environment		Photomultiplier tube number									
		1	2	3	4	5	6	7	8	9	10
125° C temperature soak	15 hr	—	X	X	—	—	X	X	—	Used for potting test (no environmental tests run)	X
	48 hr	—	—	X	—	—	—	X	—		X
Vibration 15 g, 18 to 1500 cps		X	X	X	X	X	X	X	X		—
100 g shock	Tube horizontal	—	X	—	X	—	—	—	—		—
	Tube vertical	—	X	—	X	—	—	—	—		—
200 g shock	Tube horizontal	X	X	X	X	X	X	X	X		X
	Tube vertical	X	X	X	X	X	X	X	X		X
300 g shock	Tube horizontal	X	—	—	X	—	—	—	—		—
	Tube vertical	f	—	—	f	—	—	—	—		—
Other			*								

— Not subject to this particular environment
f Failure
X No visible degradation of performance
* Failed when dropped on floor

A tabulation of measurements on the relative spectral distribution and intensity of the Sun, Canopus, Capella, Procyon and Sirius has been received from Lick Observatory. Data accuracy to 0.01 magnitude is claimed. Accuracy greater than 0.1 magnitude does not seem to be required for calibration of the Canopus sensor.

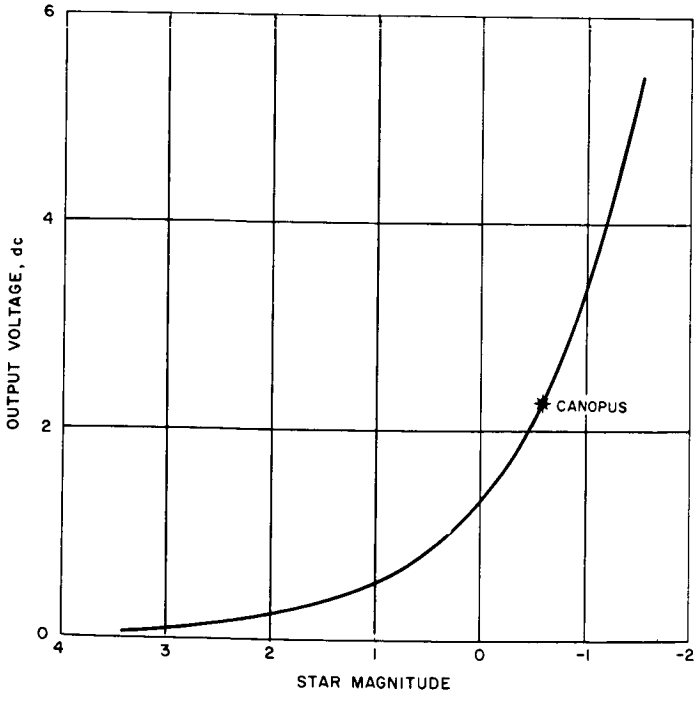

Figure 45. Output characteristics of Canopus sensor amplitude channel

The simulator and a star sensor will be subjected to a series of tests at a mountain location using the observatory data and actual measurements to calibrate the simulator and to verify calculated sensor performance. Sunlight will be used during a daytime test to establish the nominal operating point of the Canopus sensor. The artificial Sun intensity will be adjusted to produce the same operating point. At night, starlight will be allowed to enter the star channel and the resulting signal will be compared with the artificial star signal.

Allowance in these measurements for different stars is made by a calibrated amplifier or attenuator in the electronics, since the photomultiplier is a very linear device. Allowance for the atmosphere can be made by putting a filter of atmospheric transmission value in front of the tracker for comparison with real sources and removing the filter for simulating signals as in space.

A basic study of the ambiguity problem has been completed with the following results. Single stars other than Canopus will be rejected by the sensor logic circuits. Star groups will not cause an interference problem, although the Vega complex may approach to within 0.1 magnitude of the anticipated sensor lower threshold

setting. Sky background interference does not appear significant. The most pessimistic estimate of the brightest portions of the Milky Way indicates an effect equivalent to that of a star at least two magnitudes less intense than Canopus. The planets Mars and Jupiter each pose a possible interference problem about once a year over the time span 1963 to 1967. The threshold setting of the Canopus-indicate signal could logically be set to 0.4 magnitude relative to Canopus. An overlap of 0.1 magnitude is possible with Mars and Jupiter unless the accuracy of the data on the planet intensities is improved over the present 0.2 magnitude uncertainty. The selection of the actual threshold setting and final definition of the ambiguity problem solution will not be completed until after extensive field tests of the Canopus sensor.

b. Primary Sun sensor. Detail drawings of the primary Sun sensor have been completed and a model is being fabricated. This model incorporates all the anticipated features of a final design except for the method of cell mounting. The correct selection of mounting technique is considered essential since physical motion of a cell is perhaps the most probable source of sensor null shifts during severe environmental exposure. Vibration, shock, and temperature tests are being conducted on the four cell-mounting techniques shown in Figure 46 to provide experimental data to justify selection of an appropriate technique.

Method A involves encapsulating the whole cell in a silicone rubber compound (G.E. RTV-60) and using a silicone rubber quad ring to center the cell accurately. Method B uses silicone rubber quad rings to support the cell at the ends where the glass structure is the strongest. A silicone rubber washer and retaining ring are used to keep the cell in place. Method C uses a beryllium copper locator for support at one end, with

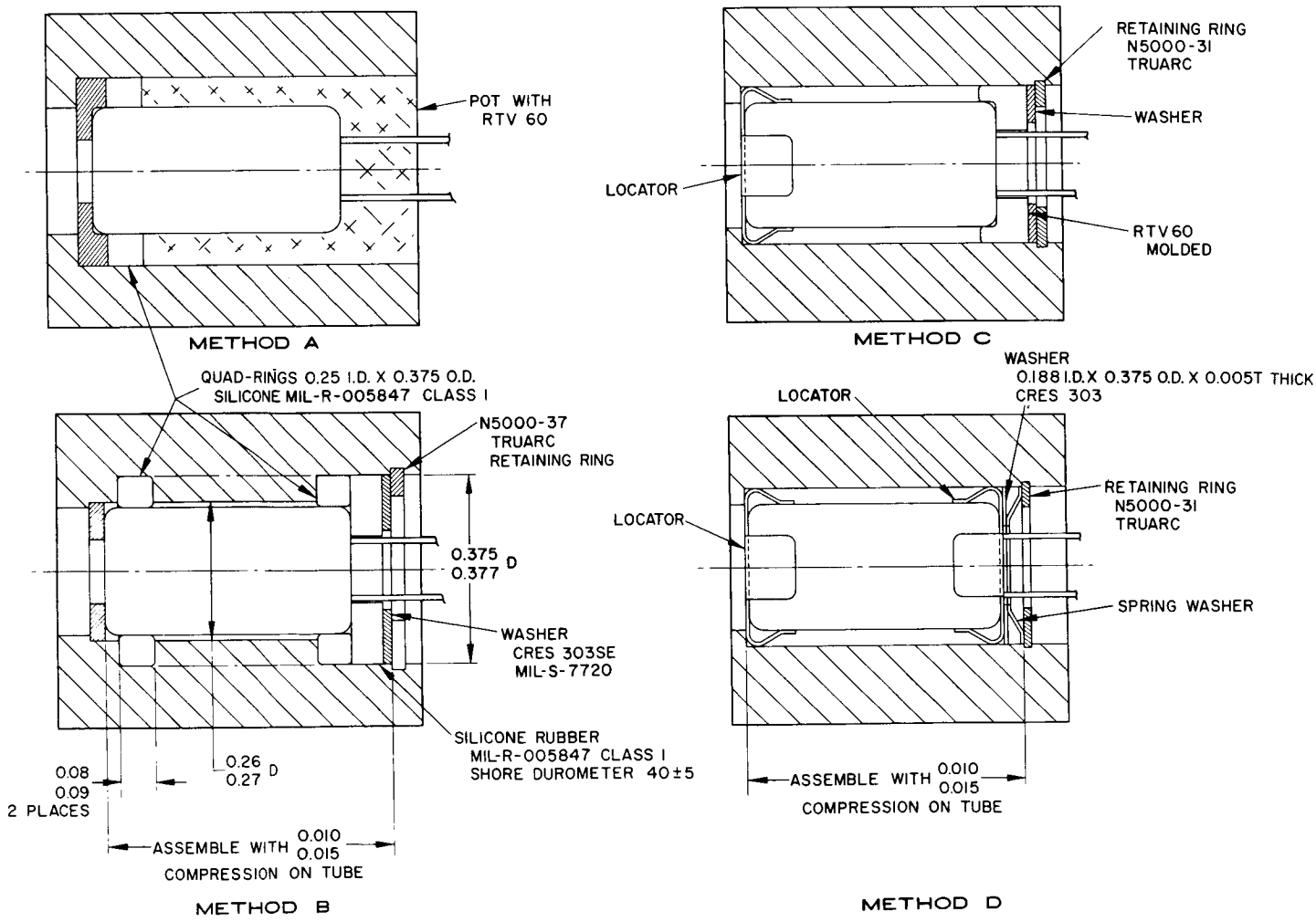

Figure 46. Experimental photocell mounting techniques

a silicone rubber washer and retaining ring at the other end of the cell. The beryllium copper locator is in the form of a cap with spring fingers which fit around the cell. An aperture in the locator permits illumination of the sensitive surface of the cell. Method D uses a beryllium copper locator at each end of the cell, with a spring washer and retaining ring to hold the cell in place.

Additional tests being conducted on the Clairex cells include determination of power dissipation ratings at elevated temperatures, cell resistance as a function of temperature, and sensitivity changes resulting from prolonged exposure to high and low temperatures.

c. Secondary Sun sensor. A model of the secondary sensor has been built (Fig 47) and will be tested on completion of the Sun sensor test facility. The model incorporates a fifth cell in addition to the four cells which each cover a quadrant of the hemisphere. The fifth cell has been added as a solution to a possible reflection problem during lunar surface operation. The cell would have a limited field of view of about ± 5 deg and would therefore be relatively unaffected by lunar surface or spacecraft reflections. An unambiguous sun direction indication would then be possible by using this cell in conjunction with the other four cells. The exact configuration will be decided after further study of the reflection problem.

d. Moon detector. A preliminary breadboard model of the Moon detector used to provide additional verification of Canopus position has been built and tested in the laboratory (Fig 48). A similar flight unit would be 3 by 4 by 0.8 in. and would weigh approximately 0.2 lb.

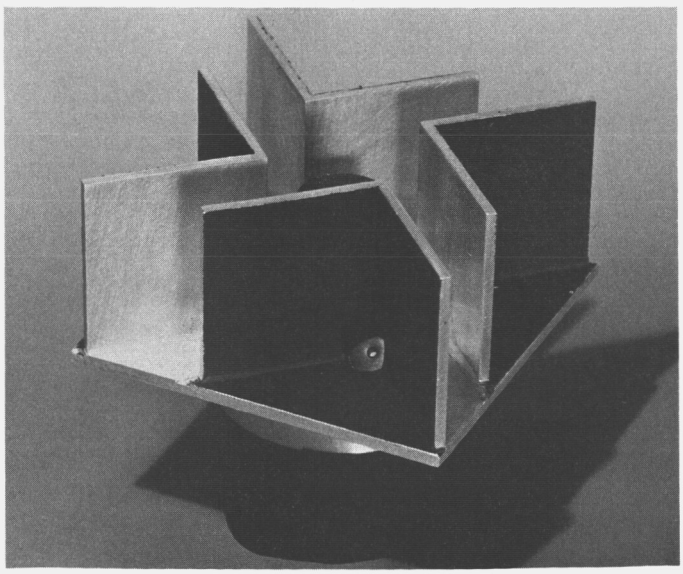

Figure 47. Model of secondary Sun sensor

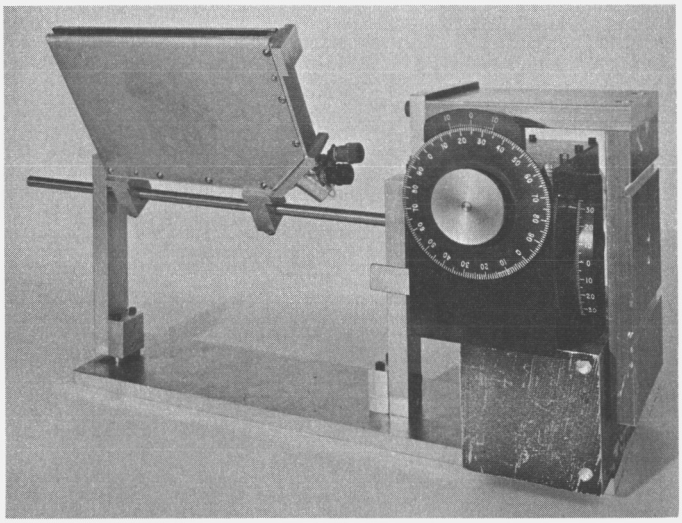

Figure 48. Preliminary Moon detector on test position

The tests were conducted using an artificial Moon in a darkroom test setup. Some rough comparisons between the artificial and actual Moon have been made and further tests using the actual Moon as a target are planned. Curves of the detector response are shown in Figure 49.

6. *Inertial Reference Unit*

The inertial reference unit consists of a set of three strapped-down, single-axis gyros and a forced-balanced linear accelerometer, supported in a thermally controlled mount and installed as a unit in the flight control sensor group.

a. Instruments. Two accelerometers have been purchased for Hughes evaluation, one from Donner Scientific Div., the other from Palomar Scientific Corp. The Palomar unit was received on October 3, 1961 and is now undergoing evaluation testing.

b. Unit design. The temperature response time of the "T" mounting structure has been one of the most important aspects of thermal design under study. Original plans for a common block mounted heater have been abandoned in favor of individual 10-watt operational heaters on each of the gyros. This direct application of heat will reduce the temperature limit cycle amplitude: i.e., decrease the magnitude of variations about the nominal operating temperature of 180° F. Another change has been the addition of 50-watt warmup heaters to each gyro. These heaters will decrease the time required for inertial reference unit warmup to operating temperature, which will speed up laboratory testing as well as launch operations.

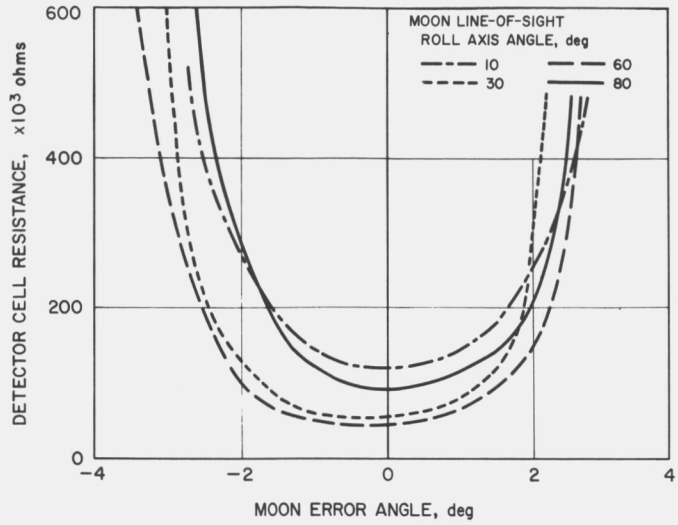

Figure 49. Moon detector response

A problem which had previously been unsolved was that of providing a thermal environment for gyro testing that would make results comparable to performance obtained in system operation. A test fixture which will satisfy these requirements has been designed and is undergoing final evaluation (Fig 50).

The outer block is aluminum, precisely machined to obtain perpendicularity and parallelism of all surfaces. A vacuum bottle is inserted into a resilient material which protects it against breakage. The inner member mounts to the outer block and can be rotated for exact input axis alignment. The gyro is supported on the inner member, which is mechanically and thermally identical to one-third of the inertial reference unit "T" mounting structure. Essentially all the heat flow is by conduction through the "T" section cylindrical cross section and finally rejection into room ambient by free convection. Radial losses are very low. Since this test block will be used by gyro manufacturers and at Hughes for all gyro acceptance testing, compatible and truly representative data and results will be achieved.

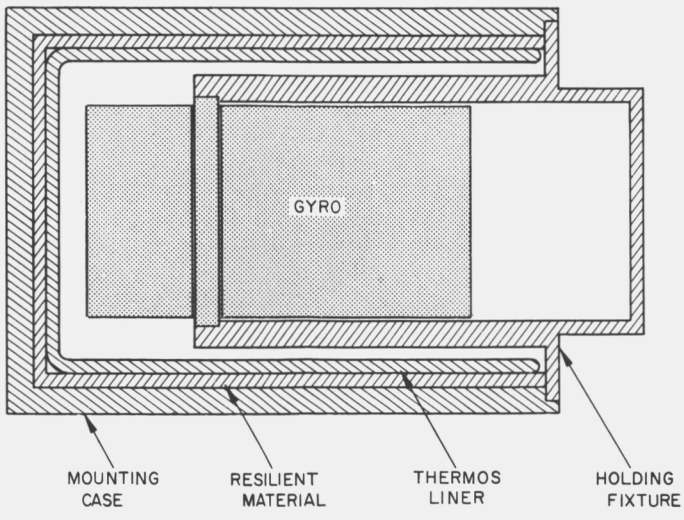

Figure 50. Gyro test fixture

The IBM 7090 computer has been utilized in several aspects of the thermal design. One important phase that is still under study is design of the heat conduction path and space radiator which form the final link in the thermal control system. Temperature distribution and gradients throughout this portion of the system must be carefully controlled for optimum performance. The exact radiator/conduction path contact areas and locations will be determined as well as optimum radiator thickness required for proper response to a variable solar load.

c. Mechanical design. The first engineering model of the inertial reference unit is shown in Figure 51. The "T" mounting section houses three dummy gyros which are thermally similar to the actual gyros in case size, material, and heater and sensor arrangements. The twin conduction paths mount to opposite sides of the "T" structure at the "thermal center" and terminate on the

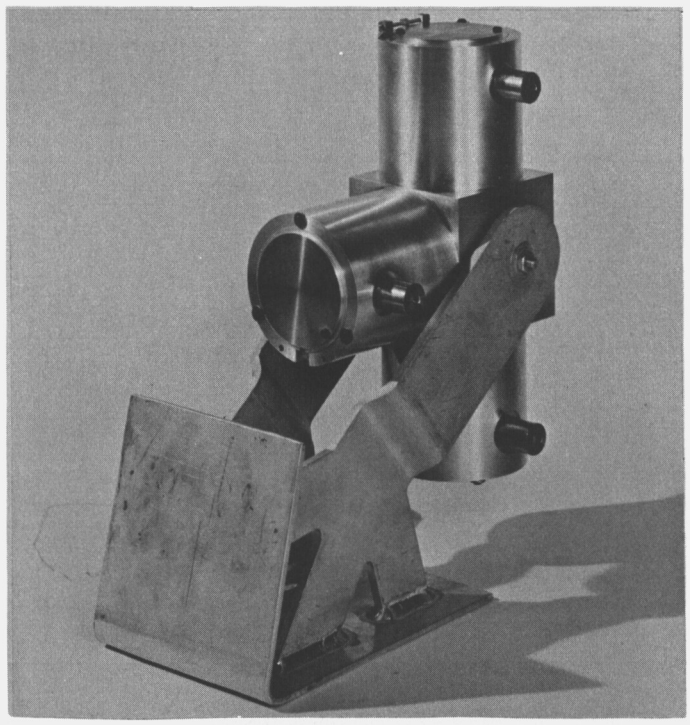

Figure 51. Model of inertial reference unit

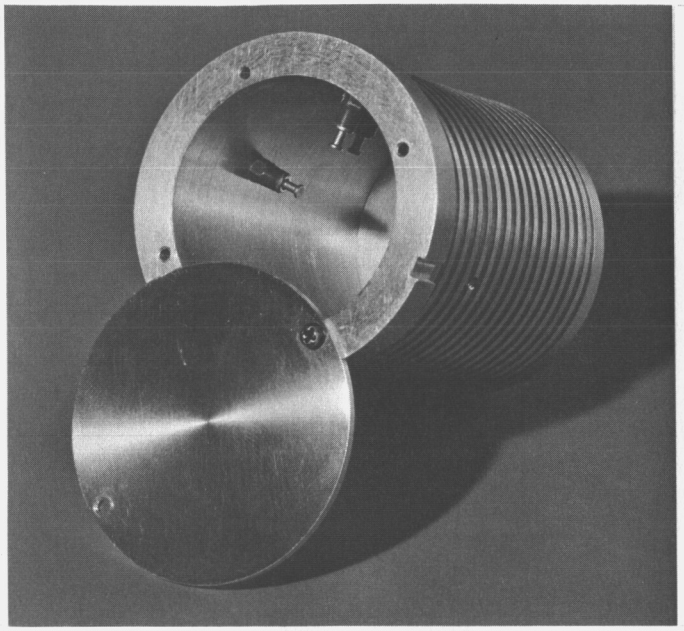

Figure 52. Dummy gyro

angular space radiator. The sloped portion of the radiator takes advantage of the horizontally projected area that is loaded by solar energy during the majority of the flight and serves to reduce the average heater power required for maintenance of gyro temperature. The three spacers on the "T" are the mechanical interface of the inertial reference unit and form the reference plane for all axis adjustments and tolerance measurements. These spacers, besides taking the mechanical loads, are designed for minimum heat loss, the expected value being approximately ½ watt each. The inertial reference unit mounted on these spacers was subjected to 100-g impact loads in all orthogonal planes and showed no perceptible damage.

Figure 52 shows a dummy gyro in greater detail. The helical grooves will house temperature sensor wire and heater wire in separate grooves in the same manner as the actual instruments. Figure 53 shows the holding fixture and all the electronic components (less power transistor) which make up the total temperature control unit of the inertial reference unit. All components will be interconnected using the welding technique and finally encapsulated to form a thermally and mechanically sound unit.

7. Attitude Controls

a. Gas jet subsystem. Procurement specifications and work statements for both the gas tank and the squib-operated valves have been released. A Bourns Inc. Model 304 or equivalent pressure transducer is being purchased.

Engineering model drawings for the pressure control unit have been released for fabrication. Some subassembly units are undergoing test. Testing of the prototype solenoid valve shows that the solenoid force at minimum voltage is at least twice the calculated force applied on the valve.

Evaluation of pressure seals required between the gas tank and the controls is under way. The gas charging valve design is also being evaluated, using proposed materials, threads and seals.

Engineering models of the jet valve pairs are being evaluated. A vacuum thrust measurement assembly is being fabricated to evaluate the nozzle design parameters in a bell jar.

b. Vernier roll actuator. The design of the roll actuator is still being studied in order to minimize the weight and power requirements. The second breadboard model constructed produced the required 5.5 lb force over a stroke of 0.4 in. Hysteresis caused by friction between the plunger and the case was excessive, however, and improved bearings are being considered to increase the actuator efficiency. A model of the vernier engine with simulated restraining forces and an actual actuator is being constructed to aid in an analog computer roll control system study.

8. Control Circuitry

During the report period most of the control circuitry has been undergoing detailed evaluation and optimization in breadboard tests. A few changes have been incorporated in the basic circuit configuration, involving the jet valve switching amplifier, the primary Sun sensor excitation, and the logic circuits.

Difficulties were encountered in using undemodulated ac error signals to trigger the jet valve switching amplifiers. Therefore, phase-sensitive detectors have been added to generate dc error signals as suggested in the last report.

A schematic of a typical jet valve circuit is shown in Figure 54. The resistor network on the input mixes the pitch, yaw, and roll signals to produce signals in "jet coordinates." The resistor-capacitor network produces the lag feedback around the on-off amplifier. The fixed amplitude of feedback voltage is taken directly from the jet valve coil. A zener diode circuit is used in order to get a standard amplitude of feedback signal

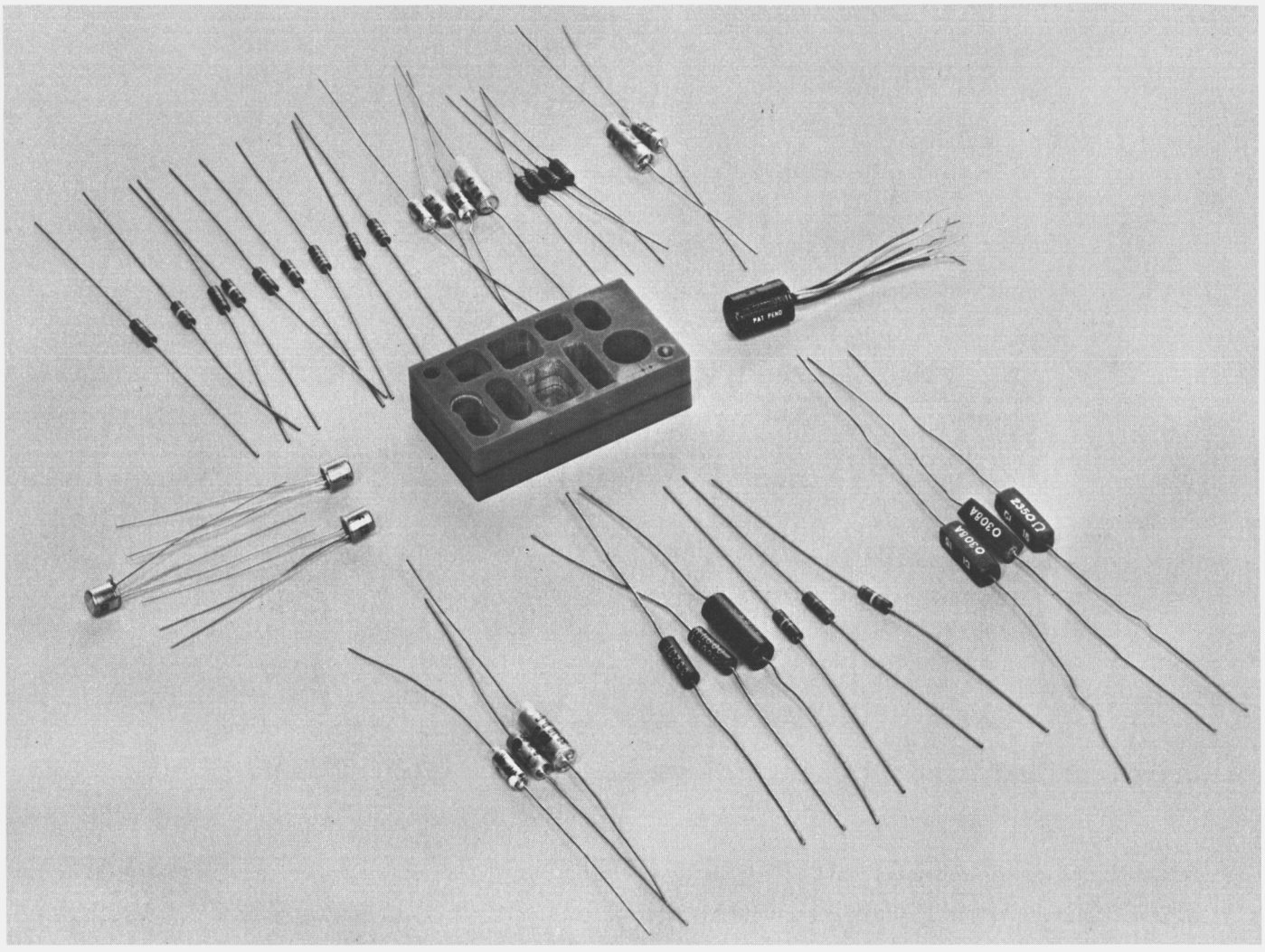

Figure 53. Temperature control unit of inertial reference unit

in the presence of large tolerances on the +22 volt supply. The diode across the coil removes large induced voltages at the collector of the transistor switch when the coil is turned off quickly. Figure 55 shows a breadboard on-off jet valve circuit. There are two amplifiers on this board and two jet valves are shown with the circuit.

The previous report showed the primary Sun sensors energized with transformers whose primary windings were in series. Because of the large variation in sensor resistance, this circuit suffers from interaction between sensors and does not provide a constant excitation to the sensors. The circuit of Figure 56 has been chosen because it avoids all interactions. Each sensor will have a circuit of this type. The transformer will be the standard one used in all of the flight control circuits. The fixed resistors will be chosen equal to the nominal sensor cell resistance. The load will be chosen so that it matches the source resistance when coupled with this particular transformer.

The logic circuits have been modified to permit the use of parts with larger tolerances and to avoid the use of the −29 volt supply. This change was effected by changing the forms of the logical expressions while the fundamental statements remained unchanged.

The breadboard logic circuits are shown in Figure 57. The chassis contains the logic circuits while the box of switches and lights represents an input source and an output indicator. Figure 58 shows the breadboard switching circuits.

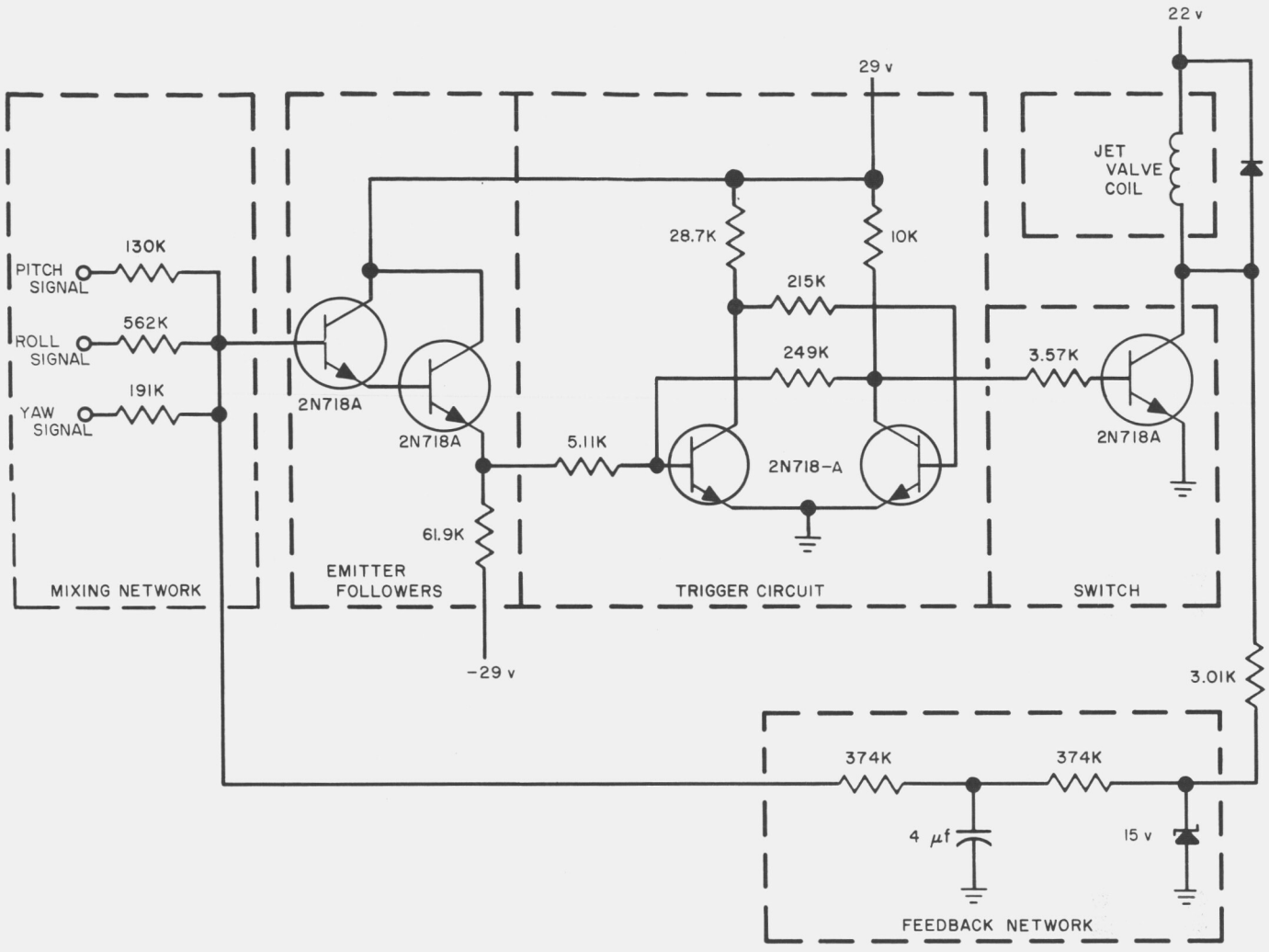

Figure 54. Typical jet valve control circuit

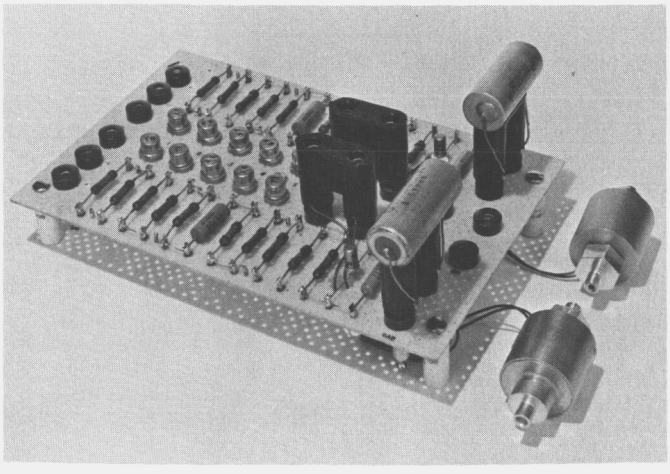

Figure 55. Jet valve control circuit breadboard

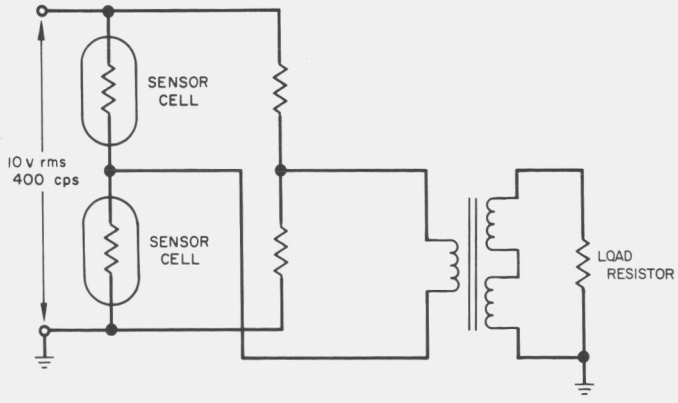

Figure 56. Revised primary Sun sensor excitation circuit

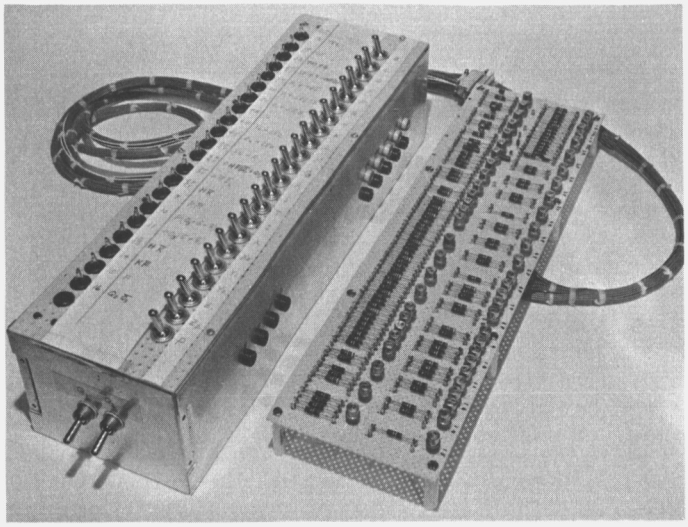

Figure 57. Flight control automatic logic circuitry breadboard

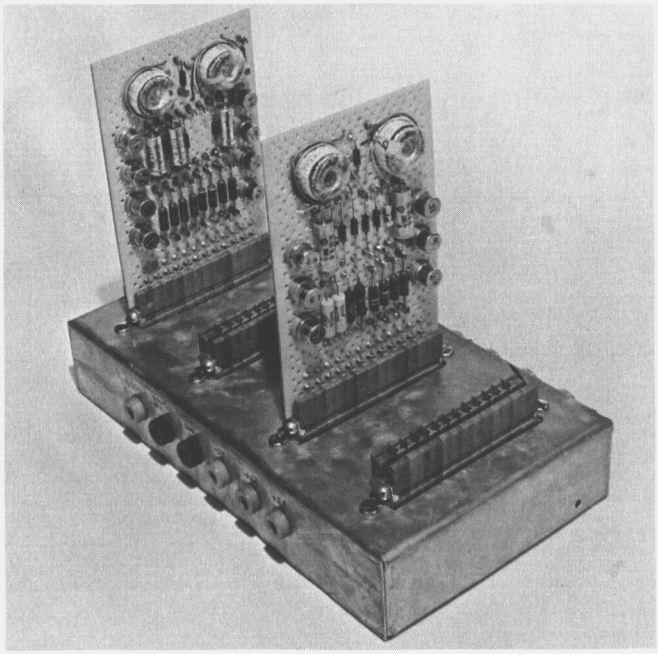

Figure 58. Flight control switching circuitry breadboard

E. Electronics

1. Introduction

This section covers the various systems involved in telecommunication (including the demodulator circuits for the Deep Space Station), the television system, and the radar systems. The spacecraft power management and the flight control electronics are discussed in Sections F and D, respectively.

2. Planar Array (High-Gain Antenna)

The primary function of the planar array antenna is to increase the effective radiated power for the wideband television channel. It is a slotted-waveguide type planar array. Circular polarization is accomplished by utilizing crossed slots and simple slots in a manner that produces two orthogonal linearly polarized planar arrays in the given aperture. The two interlaced arrays are fed in time quadrature. Higher-order beams characteristic of this slot are eliminated by reduced slot spacings attained through the use of wave-slowing corrugations in the system waveguide.

The linear array fabricated in X-band waveguide has yielded much useful information. Pairs of separated slots did prove to be reflectionless as suggested in the last report; hence, the array was inherently well matched. Patterns taken on this array indicated that some phase error was present but not enough seriously to degrade the gain. Most of this error was caused by the last group of slots and can easily be nullified by a slight change in slot spacing at the end of the array. The axial ratio was less than 1.6 db over the entire main lobe. This figure was obtained with a ground plane simulating the entire planar array.

A measurement fixture for taking 2295-mc slot conductance data in full size waveguide has been received and put in operation. Data shows a phase shift in the wave passing a heavily coupled separated slot pair in the waveguide. Methods of measuring this phase shift are being considered so that the slot spacing can be corrected.

Gain computations have resulted in a set of planar array slot placement parameters yielding an aperture of 92%. The computed pattern for this set of conditions shows that all spurious lobes are suppressed by at least 18 db.

A waveguide fixture with a removable top plate is being fabricated. This fixture will allow easy fabrication and testing of various linear array designs before fabrication of the breadboard planar array.

New test fixtures for the feed line of the planar array are being designed and fabricated in full-size waveguide for testing at the design frequency of 2295 mc. Information obtained on a test fixture scaled to a higher S-band

frequency (*SPS 37-11*, Vol II) is being used in the design of these fixtures. Two fixtures are being built one for the transition from coaxial line to the feed line and one for taking slot conductance data on the nonresonant slots that feed the individual linear array sections of the planar array.

A full-size, nonoperating mechanical prototype of the planar array is being fabricated to determine the feasibility of construction by the ultrasonic welding technique. This specimen will be environmentally tested to prove out the method at an early date. It is scheduled to be delivered the latter part of October.

3. Omnidirectional Antennas

The omnidirectional antenna system consists of two low-gain (2 db) circularly polarized turnstile antennas. These antennas are positioned in such a way as to minimize interference and shadowing effects due to the spacecraft and to provide complete spherical coverage.

A quarter-scale model of the spacecraft with quarter-scale antennas was used in a series of radiation pattern studies conducted during the last 2 months. The patterns indicate that severe interference problems occur due to the presence of the metal spacecraft. In an attempt to minimize these interference effects, a small conical reflector was placed immediately behind the antenna, between the spacecraft and the turnstile antennas. These conical reflectors shield the antennas from most of the irregular surfaces of the metal spacecraft and allow more accurate control of the antenna radiation coverage.

A set of patterns has been taken using one antenna. The experimental setup used for these measurements is shown in Figure 59. Figure 60 shows the omnidirectional antenna used; Figures 61a, b, and c are views of the quarter-scale model. Figure 62 shows the set of patterns obtained with the setup of Figure 59.

Another series of patterns has been taken using two antennas with conical reflectors oriented opposite each other on the spacecraft. These patterns indicate that complete coverage about the spacecraft can be obtained with very few interference and shadowing effects in the angles of interest of each antenna. The opposite orientation of the two antennas results in the least difficult coverage problem; however, the optimum orientation for uninterrupted telemetry in the event of a vehicle stabilization failure requires that one of the antennas be approximately 45 deg off the diametrically opposite axis of the other. The problem of optimum orientation has not as yet been completely solved.

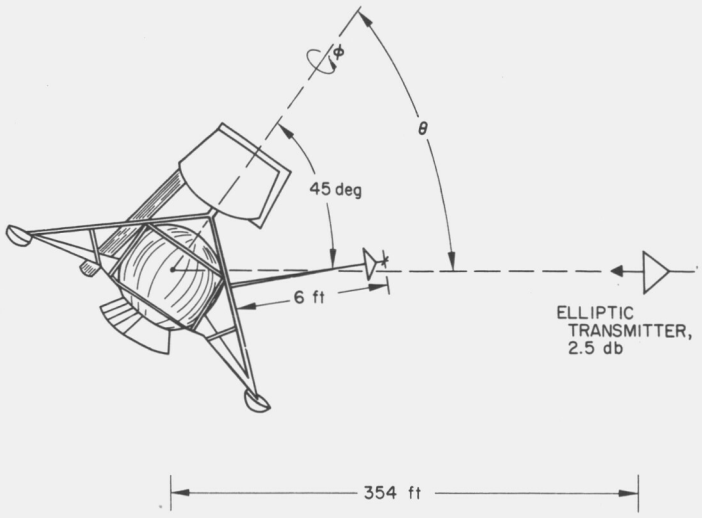

Figure 59. Arrangement for omnidirectional antenna test

The experiments discussed above indicate that the spacecraft interference effects are minimized by using a conical reflector behind the antenna and imply that the physical configuration of the spacecraft can be changed from the flight to flight with little effect on antenna patterns. Design of the full-scale antenna is being changed to include a conical reflector. This change necessitates a design study to optimize the angle and size of the

Figure 60. Omnidirectional antenna

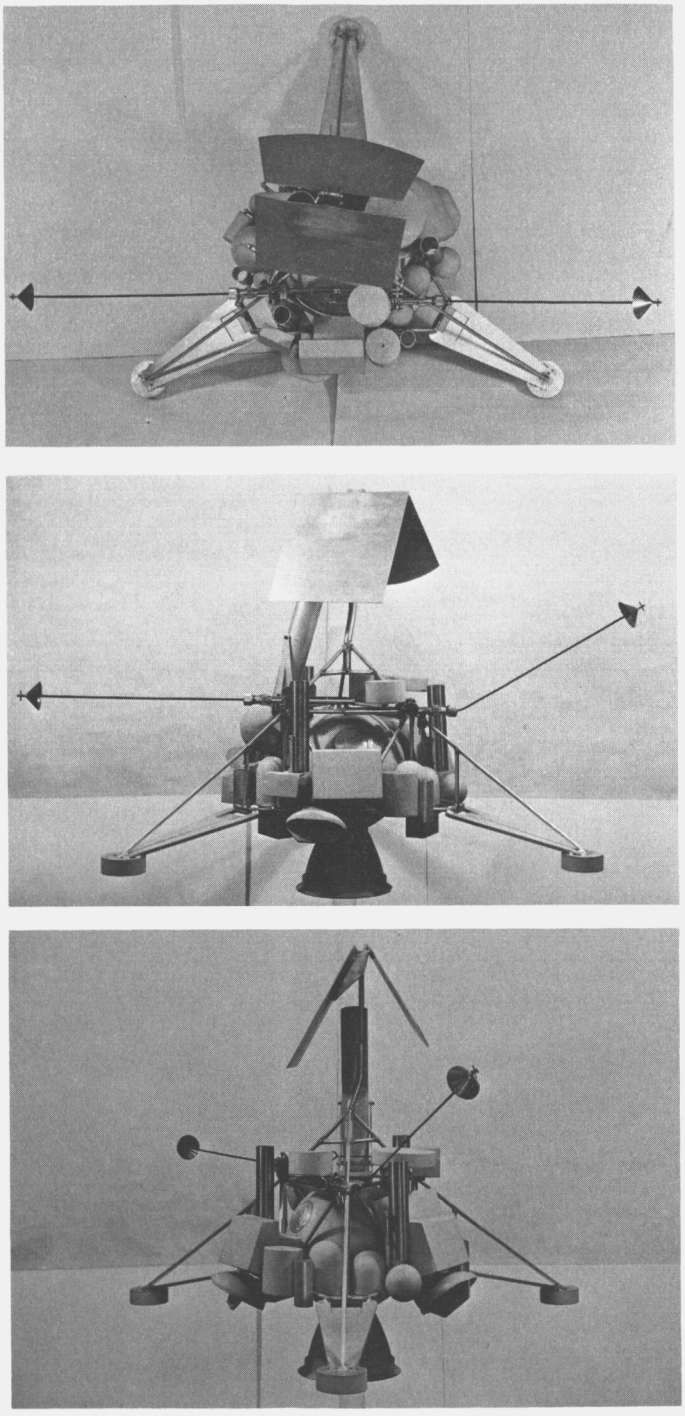

Figure 61. Quarter-scale spacecraft model for omnidirectional antenna

reflector cone. This study is now under way and several variations of the present design are being considered to obtain increased coverage in the reverse hemisphere of each antenna unit. Such improvements will assure telemetry despite unscheduled vehicle attitudes.

A full-scale model of the spacecraft is being constructed and preparations are being made to conduct omnidirectional coverage studies on this model.

4. DSIF Demodulator

a. General. The demodulator for the Deep Space Instrumentation Facility (DSIF) serves as a frequency-modulation and phase-modulation detector for received signals. The DSIF demodulator has four modes of operation: (1) Wide band: In the wide-band mode of operation, television and telemetering data in an intermediate frequency (IF) bandwidth of 3.3 mc are detected. (2) Narrow band: The narrow-band mode of operation is used for the detection of telemetering information within a 40-kc IF bandwidth. (3) Emergency mode: The emergency mode of operation provides detection of information with a 4.4-kc IF bandwidth. (4) Phase-lock mode: The phase-lock mode is used for detecting phase-modulated signals within a 3.3 mc bandwidth. All detected signals are supplied to the Command and Data Handling Console (CDC) where they are processed.

Circuit development on the DSIF demodulator has been completed. System tests are in progress and the circuit design prior to final packaging is being completed. The electrical characteristics of the demodulator are shown in Table 13.

b. Functional description. A block diagram of the DSIF demodulator is shown in Figure 63 and a schematic diagram in Figure 64. A 60-mc signal with a 3.3-mc bandwidth is supplied from the DSIF receiver to the input of the first IF amplifier. The first IF amplifier has a gain of 40 db and a bandwidth of 8 mc. The second stage in the amplifier can be gain-controlled over a 20-db range with no degradation of the passband response. Up to 40 db of gain control range may be obtained with slight degradation.

The first IF output signal is applied to the mixer where it beats with the first oscillator (LO) signal and generates the second IF signal at a frequency of 39 mc. The first LO is crystal-controlled and operates at a frequency of 99.000 mc. The second IF amplifier has a power gain of 35 db and a bandwidth of 4 mc. The second IF output signal is applied both to the limiter and to the automatic gain control (AGC) detector.

The AGC detector monitors the IF level at the second IF output and supplies a dc voltage which is filtered, amplified, and fed back to the first IF amplifier to maintain the second IF output signal at a constant amplitude.

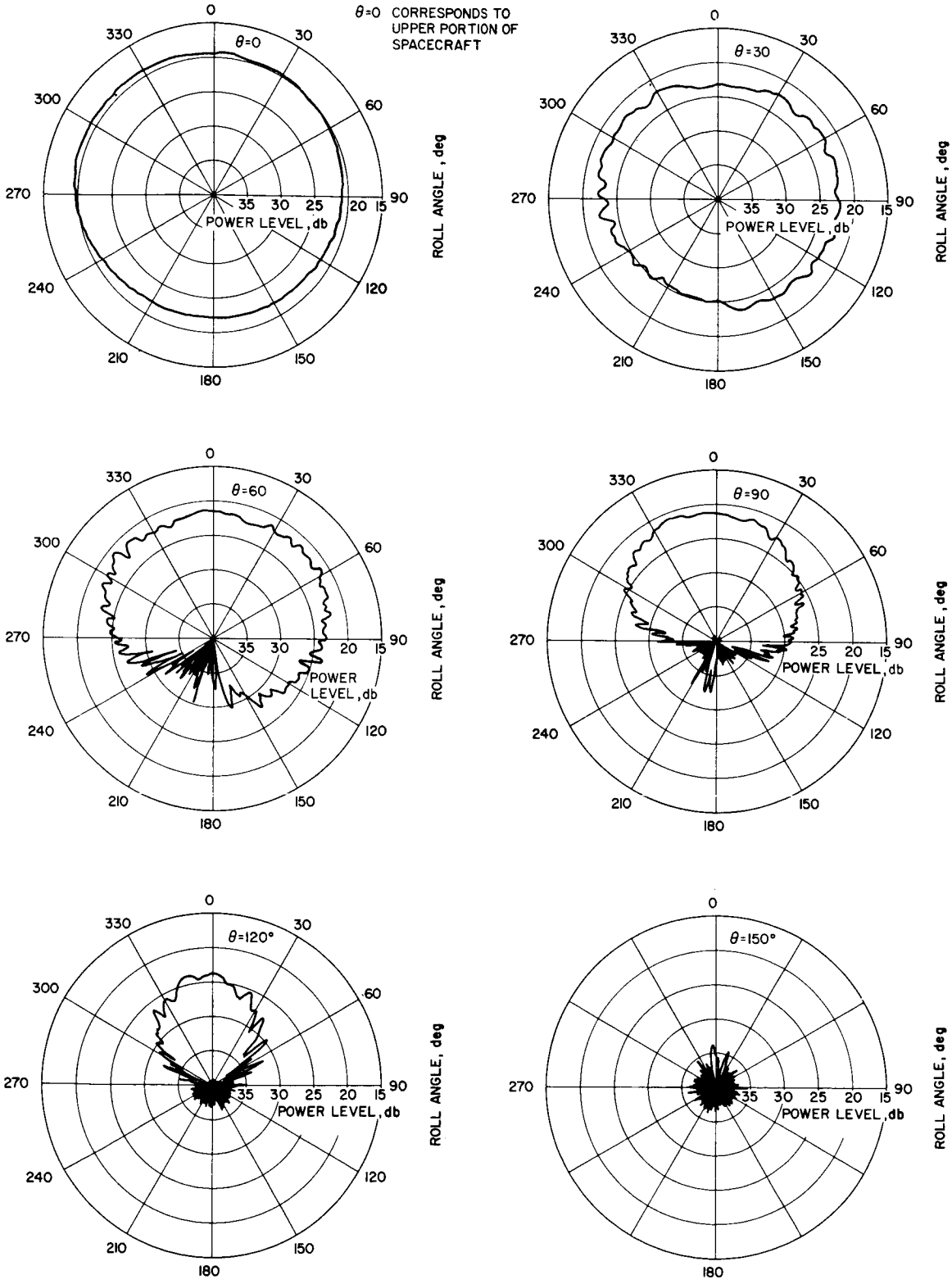

September 7, 1961

θ = angle between spacecraft roll axis and line of sight to transmitter, deg

Frequency = 8460 mc

Figure 62. Antenna patterns with one turnstile

Table 13. DSIF demodulator electrical characteristics

Electrical power	120 v ± 12 v 60 cps
Signal input range	−35 to −60 dbm
AGC dynamic range	40 db
AGC output voltage	
Automatic	0.5 to 4 v
Manual	−4 to 8 v
AGC output impedance	10 k
Input impedance (60 mc)	50 ± 5 ohms
Video 3 db bandwidth	
Wideband	1.0 cps to 220 kc
Narrow band	200 cps to 10 kc
Emergency	0.1 cps to 2 kc
Phase lock	1 to 250 kc
Video output voltage	5 v peak-to-peak
Video output impedance	<1 k
Video phase distortion	<0.1 rad
Over-all frequency stability	
Long term	± 10 ppm
Short term	2 cps/sec
First IF frequency	60 mc
First IF bandwidth	8 mc
First LO stability	
Long term	± 5 ppm
Short term	1 cps/sec
Second IF frequency	39 mc
Second IF bandwidth	4 mc
Second LO stability	
Long term	± 5 ppm
Short term	1 cps/sec
Third IF frequency	4.5 mc
Third IF bandwidth	40 kc
Third LO stability	
Long term	± 5 ppm
Short term	1 cps/sec
Fourth IF frequency	455 kc
Fourth IF bandwidth	4.4 kc
Wide-band frequency discriminator	
Peak-to-peak frequency separation	5 mc
Linearity	1%
Narrow-band frequency discriminator	
Peak-to-peak frequency separation	150 kc
Linearity	5%
Emergency frequency discriminator	
Peak-to-peak frequency separation	30 kc
Linearity	2%
Phase-lock loop bandwidth	200 cps
VCXO stability	
Long term	± 5 ppm
Short term	1 cps/sec

The amplitude is maintained constant for a 40-db variation of the input signal. Provisions also are made whereby the DSIF receiver 60 mc IF amplifier strip can be gain-controlled by the DSIF demodulator. Gain control can be either automatic or manual.

The limiter removes high-frequency amplitude noise and modulation to which the AGC loop can not respond. The output signal from the limiter is supplied to the wide-band frequency discriminator, second mixer, and the 39-mc phase-detector amplifier.

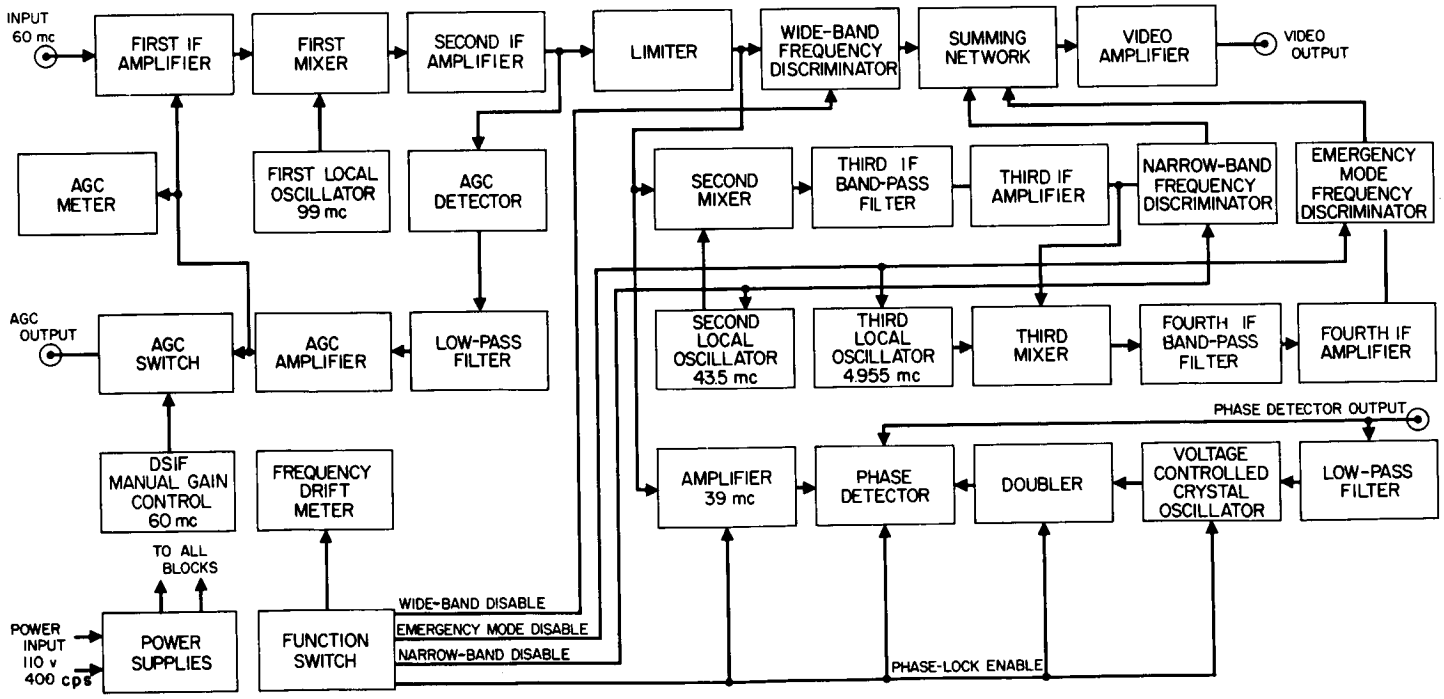

Figure 63. DSIF demodulator block diagram

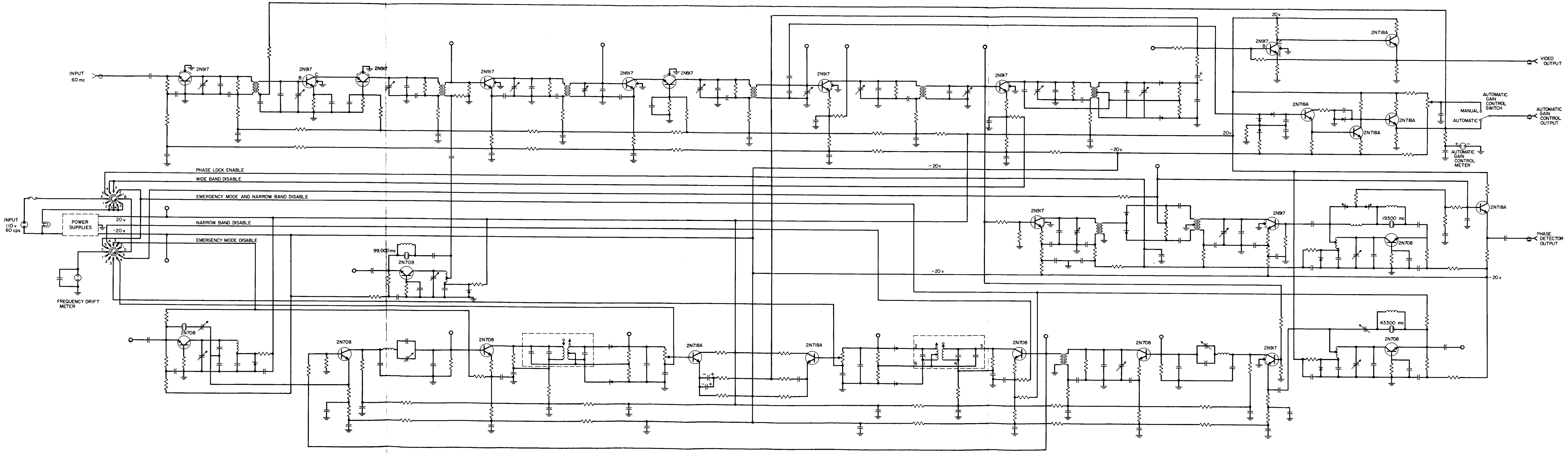

Figure 64. DSIF demodulator schematic diagram

In the wide-band mode of operation, the wide-band frequency discriminator is turned on by the function switch and either the television signal or the group of telemetering subcarrier signals are detected. The detected video signal passes through the summing network to the video amplifier and thence to the output connector. From this point the signal goes to the CDC.

In the narrow-band mode of operation, the function switch turns on the narrow-band frequency discriminator and second LO. The limiter output signal applied to the second mixer combines with the second LO signal to generate the third IF signal. The third IF signal, at a frequency of 4.5 mc, is passed through a narrow-bandpass filter with a 3-db bandwidth of 40 kc, amplified, and coupled to the narrow-band discriminator. The narrow-band discriminator output is fed through the summing network and video amplifier to the output connector. The narrow-band frequency discriminator response characteristic has 150 kc peak-to-peak frequency separation.

In the emergency mode of operation, the function switch turns on the third LO and the emergency mode discriminator. The third IF signal is mixed with the third LO signal to generate the fourth IF signal at a frequency of 455 kc. The fourth IF signal is filtered by a narrow-bandpass filter with a 3-db bandwidth of 4.4 kc, amplified, and fed to the emergency-mode discriminator. The video signal from the discriminator passes through the summing network and video amplifier to the output connector.

In the phase-lock mode of operation, the phase-lock circuitry is turned on by the function switch. The limiter output signal is amplified and fed to the phase detector. The phase detector output signal is supplied both to a low-pass filter and to an output connector which goes to the CDC. The low-pass filter determines the closed-loop parameters for the phase-locked loop. The dc voltage from the filter controls the voltage controlled crystal oscillator (VCXO) such that the doubler output frequency is maintained in phase quadrature with the second IF centerline frequency.

The frequency-drift meter monitors the dc outputs of the narrow-band discriminator, emergency mode discriminator, and phase detector. Any voltage other than a null indication represents an offset in the operating point on the discriminator S curve.

Commercial power supplies provide the required voltages and currents to operate the DSIF demodulator circuits.

5. Signal Processing

a. Engineering signal processing. The engineering data pertains to the spacecraft itself rather than to the scientific experiments. The signal processing provides four modes (Figure 65) for transmitting engineering data. A 1-to-5 counter and a 1-to-20 counter are used to provide a 100-word frame for Modes 1, 2, and 4 and to provide a 50-word frame for Mode 3. The bit rates used are 550, 1100, and 4400 bits/sec.

Mode 1. Mode 1 employs a 100-word frame and is to be used primarily at the midcourse correction. The available bandwidth at midcourse correction allows a bit rate of 1100 bits/sec. However, if desired, the data may be transmitted at the full lunar distance by lowering the bit rate to 550 bits/sec. In either case, the information is frequency-modulated on a subcarrier oscillator which in turn phase-modulates the carrier. This mode telemeters the signals associated with the Sun and star trackers, the precession and error signals from the gyros, vernier engine pressures and gas pressures in the propulsion system, the magnitude bits used to confirm magnitude command, and signals from the transponder interconnections. Mode 1 uses the high-power transmitter and a low-gain antenna.

Mode 2. Mode 2 employs a 100-word frame and is to be used primarily during the first part of the terminal descent, on a time sharing basis with TV when the high-gain antenna is available. The availability of the high-gain antenna allows a rate of 4400 bits/sec, or 4 frames per second, to be transmitted. Mode 2 telemeters signals associated with the altitude-marking radar, the altimeter and doppler radar, the gyro precession and error signals, fuel and engine pressures, and main-bus voltages and currents.

Mode 3. Mode 3 employs a 50-word frame and is to be used primarily during the final part of the terminal descent. This mode, an abbreviated version of Mode 2, is able to transmit a bit rate of 550 bits/sec when a high-power transmitter and low-gain antenna are used. Data telemetered at the rate of 1 frame per second includes on/off signals relating to retro-ignition and burnout, altitude marks from the altitude-marking radar, analog outputs from the doppler and altimeter radar, and vernier engine pressures.

Mode 4. Mode 4 is designed primarily for use on the lunar surface but also includes signals which allow its use to facilitate initial acquisition by the DSIF. Mode 4 uses a 100-word frame and requires the low-power transmitter and high-gain antenna when transmitting from the lunar surface and the low-power transmitter and

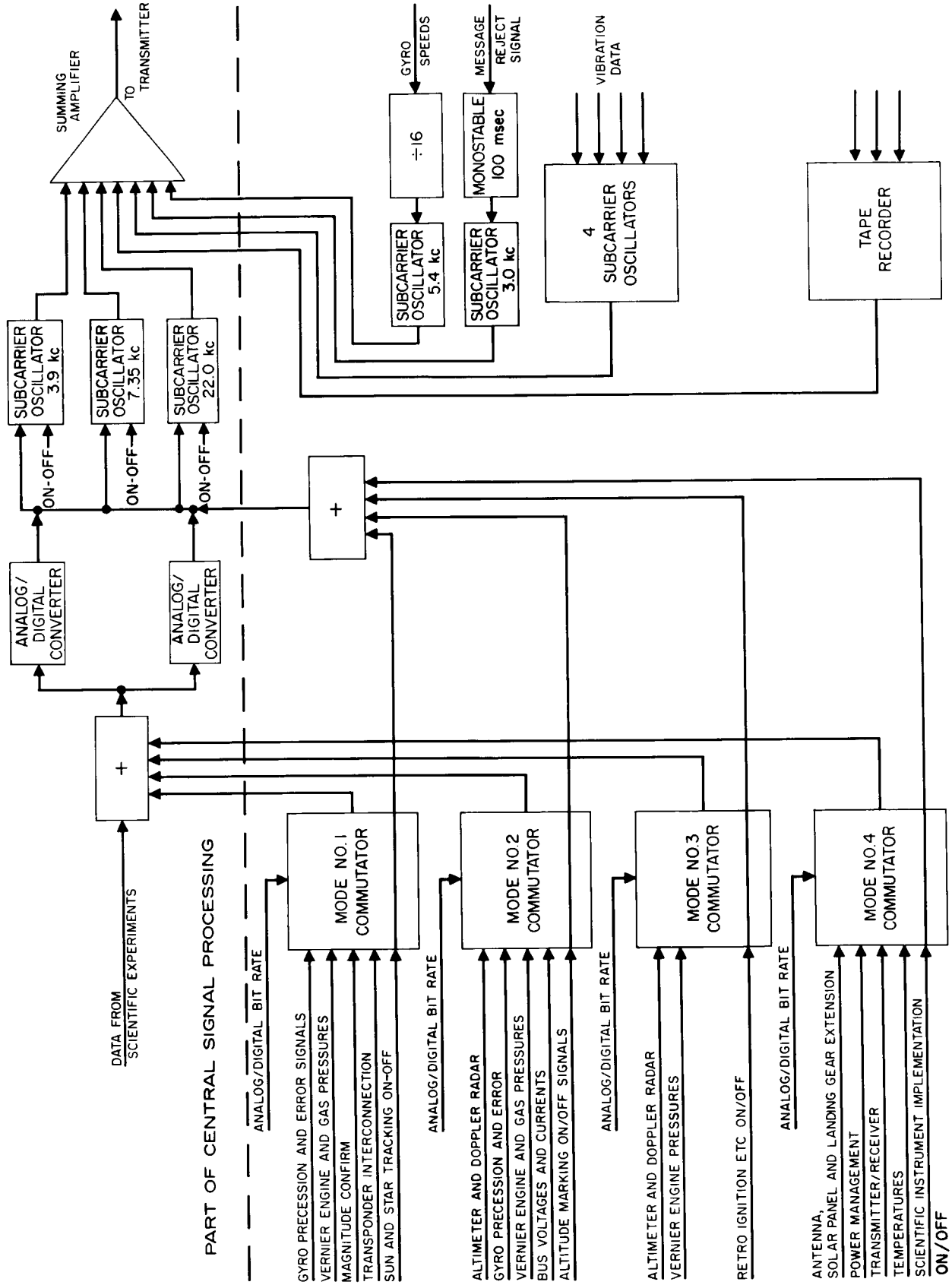

Figure 65. Engineering data transmission

low-gain antenna during initial acquisition by the DSIF. The rate used is 550 bits/sec. Information telemetered includes data regarding elevation or extension of the solar panel, scientific instruments, antennas, and landing gear, power management parameters; transmitter and receiver parameters; and temperature sensors.

Noncommutated engineering data. In addition to the commutated date telemetered in the four modes, certain other engineering data are transmitted on separate subcarrier oscillators. These data include the message-reject signal, which is sent in the form of a 3.0-kc subcarrier keyed on for 100 msec; the scaled-down pitch, yaw, and roll gyro speeds; and vibration data obtained during boost and landing.

b. Bandwidth requirement for scientific data. Subcarrier deviation previously had been adjusted so that there was no possibility of overmodulation (deviation of the transmitted carrier farther than the half-bandwidth of the receiver IF amplifier). As a result of increased subcarrier requirements and reduced decibel margins, it has become necessary to abandon this ultraconservative design criterion and adjust deviations and bandwidths such that the carrier deviation exceeds the IF passband a small part of the time.

By means of a computer, the percentage of time that overmodulation may be expected with a particular set of subcarrier frequencies and deviations has been calculated using the expression for instantaneous frequency deviation. This expression was solved for ten points during each cycle of the highest frequency subcarrier and the resultant deviation was compared to an overmodulation threshold representing one-half the IF bandwidth; the fraction of computations in which this threshold would be exceeded indicates the overmodulation. The process was repeated with several sets of random subcarrier phases to obtain an average. With this method the present low-power transmitter subcarrier structure over-modulates 0.1% of the time when a 40-kc IF bandwidth is used, which appears to be an acceptable value.

Further, the effect on overmodulation of narrowing the IF bandwidth in the low-power transmitter case was examined by using several thresholds with a rather pessimistic set of phases. The results, shown in Figure 66, indicate that an order of magnitude increase in overmodulation results from narrowing the receiver bandwidth by 25% and that gaining 3 db by narrowing the receiver to 20 kc would result in some 8% overmodulation.

c. Summary of decibel margins. Table 14 summarizes the status of the telecommunications decibel margins. The minimum margin shown is based on assuming an arithmetic addition of all the most unfavorable tolerances.

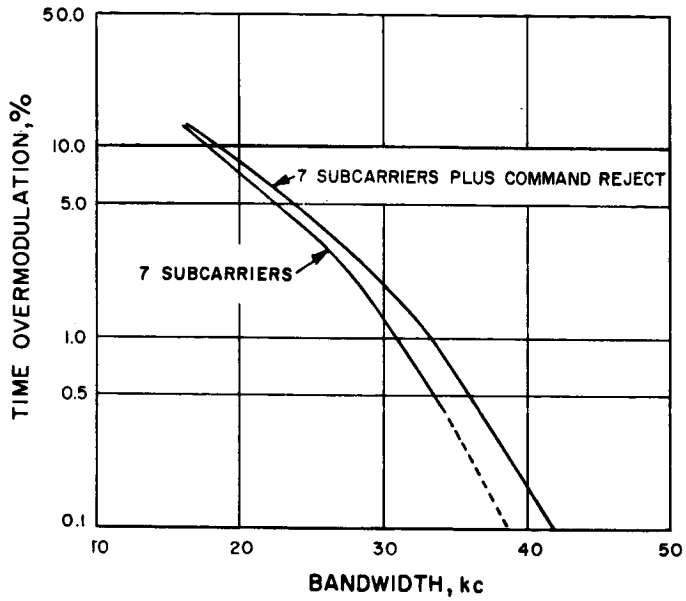

Figure 66. Bandwidth overmodulation

A positive number indicates the signal strength is above the worst case condition by the number of decibels given; a minus sign indicates insufficient signal to provide operation under worst case tolerances.

At present, all margins are positive except the TV emergency mode and the low-data-rate scientific-data mode. These modes now show negative margins of 0.8 and 0.75 db respectively as a result of reduction in DSIF receiving gains. If these negative margins persist, adjustment of system parameters to restore acceptable margins will be necessary. Resolution of the scientific-data-mode problem is not particularly pressing, since the full 40-ks bandwidth is not required for Spacecraft SC-1 and SC-2 (Missions P-42 and P-43) payloads. Parameters of the emergency TV will be adjusted from time-to-time to maintain the decibel margin near zero for this mode.

d. Spacecraft temperature measurements. A total of 57 temperature points must be monitored in the spacecraft. Of these, 27 are engineering data measurement points and 30 are associated with the scientific instruments. Among the 30 measurement points in the scientific payload, approximately 16 are basic to the particular experiment involved; i.e., without them the basic data from the experiment would be either meaningless or severely degraded.

A study has been made to determine the best way of accomplishing the temperature sensing. The main topics covered by the study, and significant conclusions, are as follows:

Table 14. Summary of decibel minimum margins

Mode	Minimum margin, db
Earth to Surveyor	
Transit phase (carrier only)	+17.0
Transit phase (carrier-modulated)	
Carrier	+3.0
Subcarrier	+4.1
Lunar phase command mode	+5.2
Surveyor to earth	
Transponder mode	+1.9
Transit phase recorded data playback	
Carrier	+42.9
Subcarriers (each of seven)	+7.9
Midcourse correction	
Carrier	+16.6
Subcarrier	+9.7
Engineering data	
Carrier	+9.0
Subcarrier	+2.8
Television	
Primary mode	+0.5
Emergency mode	−0.8
Scientific data	
High data rate (3 mc bandwidth)	+0.5
Low data rate (40 kc bandwidth)	−0.75

(1) Types of sensor: Thermocouples, thermistors, and linear resistive sensors were considered. Linear resistive sensors, such as platinum, will be used wherever possible, primarly because they combine high sensitivity (volts per degree) with high stability and repeatability.

(2) Sensor parameters: The choice of sensor parameters, such as resistance, physical dimensions, and excitation voltage were shown to be a matter of tradeoff among different sources of error. For instance, increasing the excitation voltage increases the sensitivity of a sensor in volts per degree. This in itself improves the accuracy because the fixed effects and other errors in the processing circuitry become smaller in comparison to the signal. However the increased power resulting from the higher excitation will cause an error due to self-heating; the magnitude of this error depends on the thermal paths leading from the point being sensed.

(3) Compensation for lead resistance: The error caused by changes in resistance of the leads can be reduced by use of heavy-gage, low-resistance leads or by increasing the resistance of the sensor. Where the leads are very long or a sensor of very low resistance must be used, and when very accurate temperature measurements must be made, one of several techniques of compensating for the variations in lead resistance can be used. Since the temperature sensing circuits are essentially bridges that are operated in an unbalanced condition, this compensation is not perfect at all temperatures. Graphs for determining the residual error due to this cause have been developed.

(4) Commutation: Commutation lowers the average power required by the sensors, reducing self-heating and therefore improving accuracy. In addition, there is a saving in processing equipment. In the case of temperature measurements that are basic to the particular experiment involved, the reduced reliability that would result from commutation may become significant (one failure may throw out other measurements being commutated).

(5) AC vs dc excitation: DC excitation will be used, mainly because the inputs to the analog-to-digital commutator and digital converter are dc.

(6) Thermal insulation: Both to reduce heat loss from compartments during the lunar night and to prevent heat conduction along the sensor leads from affecting measurements, it is proposed to insert short sections of thermal insulation in the leads. These sections might consist of wire such as Advance which, while a good conductor, has low thermal conductivity; the additional lead resistance must be accounted for in the sensor calibration.

(7) Thermal electromotive force: The larger voltages obtainable from resistive sensors in comparison with those obtainable from thermocouples, greatly reduce the problem of thermal electromotive force.

As a result of the above information, it has been decided that all temperature measurement sensors will be of the resistance-thermometer type except for differential thermocouples required for certain experiments.

e. Central signal processor.

Summing amplifiers. The output signals from the various subcarrier oscillators are added together by the use of nine operational-type summing amplifiers in the central signal processor. Six summing amplifiers are used for the frequency modulation (FM) mode and three for the phase-modulation mode.

The summing amplifiers associated with the FM mode are shown in block diagram in Figure 67, and in schematic detail in Figure 68. This method of summing maintains the required gain in each channel for all on-off combinations of the subcarrier oscillators. Each summing amplifier uses two high-gain silicon planar transistors. The amplifiers have various bandwidths that lie within the 1 cps to 300 kc video band.

Analog-to-digital converter. A breadboard of one analog-to-digital converter was built and tested and is now ready for integration with the rest of the signal

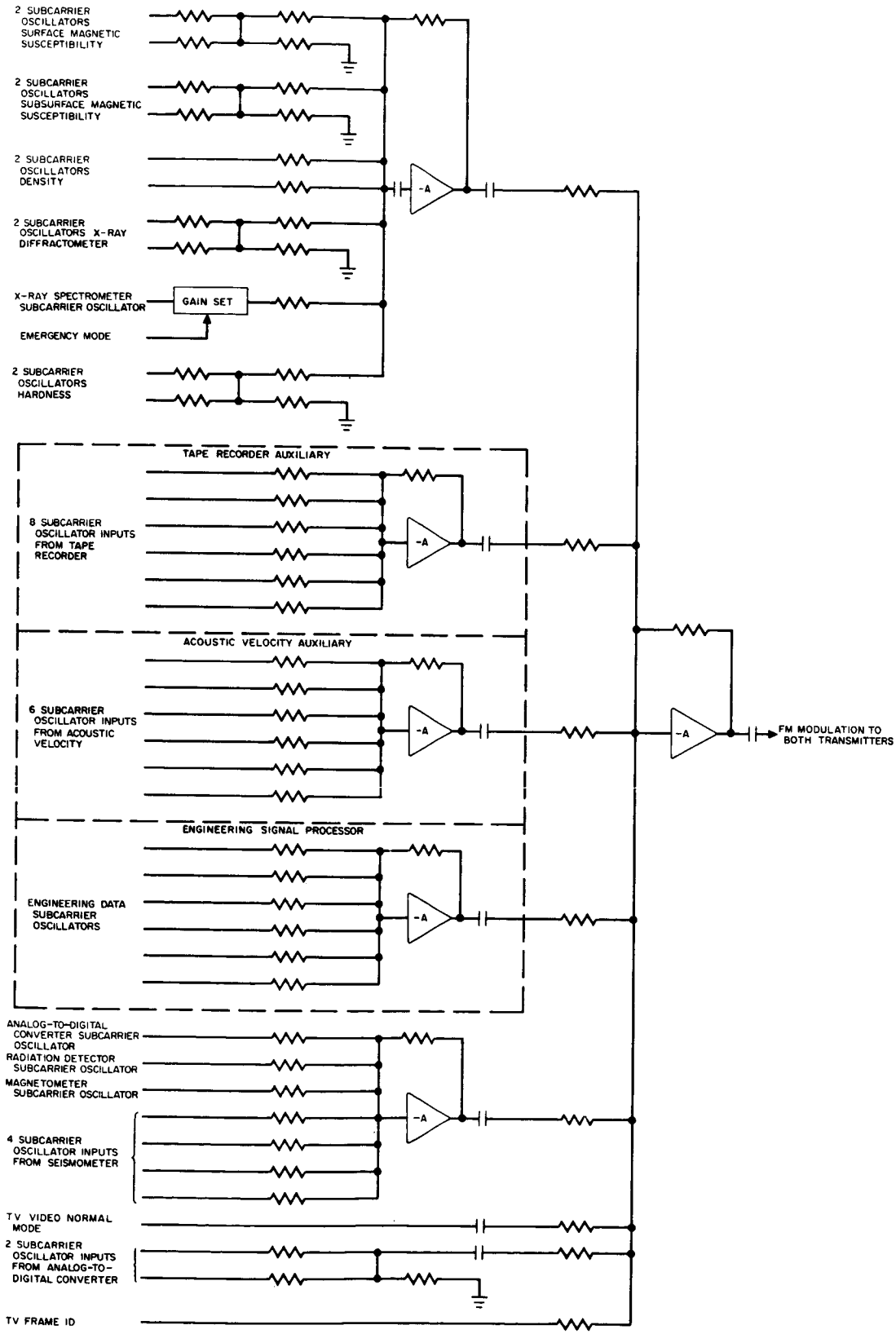

Figure 67. Central signal processor summing, FM mode

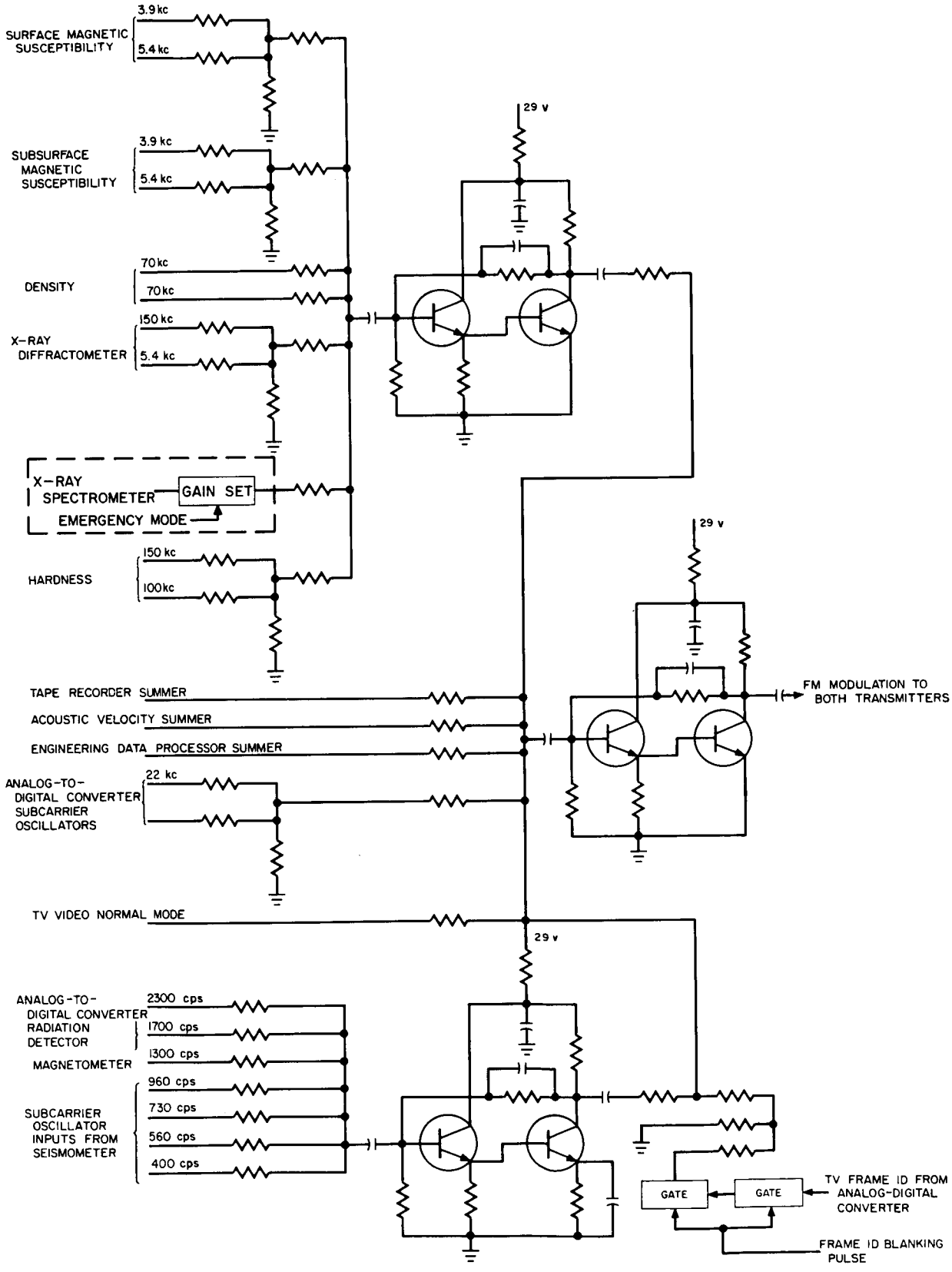

Figure 68. Central signal processor summing circuits, FM mode

processing system. It is complete with an electrical conversion unit power supply and all necessary logic to allow it to operate. The basic circuitry of the converter is shown in Figure 69.

The null error amplifier serves as a preamplifier for the comparator. It is a wide-band dc amplifier, chopper-stabilized against drift and clamped to prevent saturation. It provides a gain of 10 and is accurate at null to within 0.05%.

The A100 amplifier is a high gain dc amplifier with an output clamped to provide the proper logic levels. It has a differential input stage to reduce drift, bias error, and limit noise. Its gain is approximately 50,000, thus giving an over-all gain from add point to output of 500,000.

Inputs are compared to a −5 volt reference to arrive at a digital representation of the analog input voltage. The reference is derived from a zener diode, stable to within 0.05%, and is seen through a low impedance amplifier to prevent errors due to loading. Adjustments are made to compensate for initial errors in the zener voltage, amplifier error, and error in the binary voltage weighter switches. The function of the binary voltage weighter is to provide proportional parts of the reference for comparison with input voltage. The circuitry consists of electronic switches controlled by flip-flop logic and a precision resistance network connected to the add point of the comparator.

Electronic commutator. A breadboard of the commutator for the TV subsystem was built and checked out.

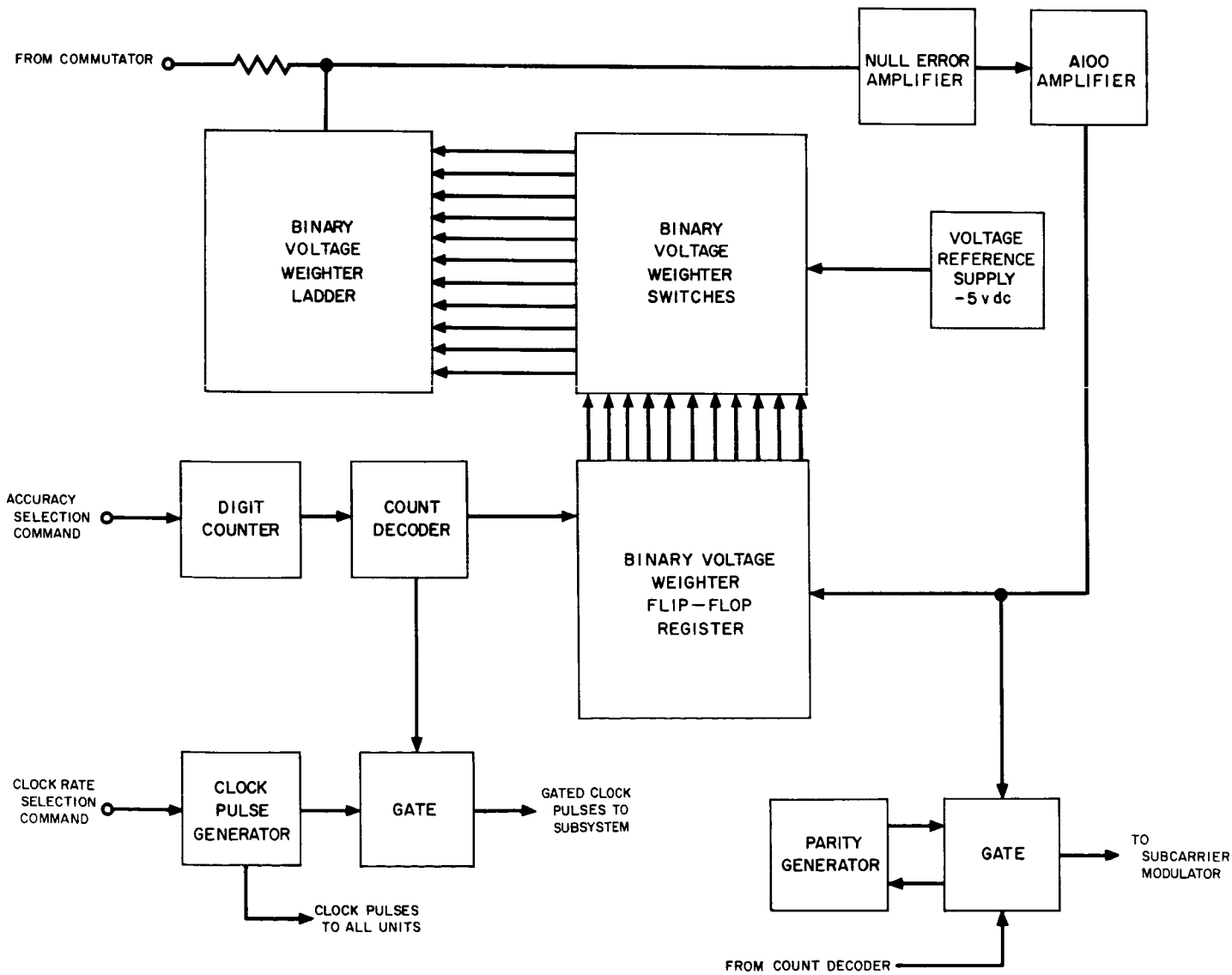

Figure 69. Analog-to-digital converter

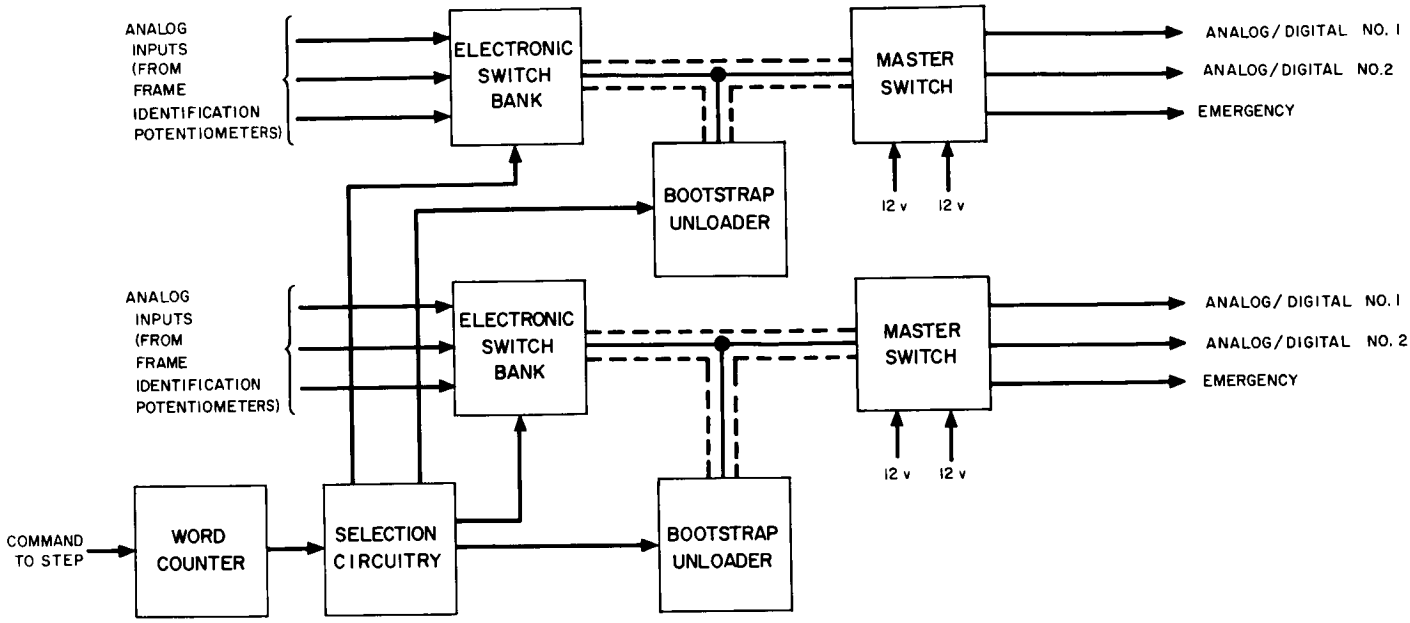

Figure 70. Electronic commutator for TV subsystem

This commutator monitors the frame identification signals from the TV cameras during the picture-taking sequence. A typical commutator with 16 channels also has been built and is connected alternately to ground and 5 volts to simulate typical inputs. This breadboard commutator will be used for system integration of the signal processing breadboards and will serve to test and evaluate the commutation system. Figure 70 is a partial block diagram of the commutation system.

The commutators are made up of electronic switches which consist of a single transistor in the inverted connection and control logic. The offsets of the electronic switches are matched against the offset of the master switch to provide less than 0.01% bias error through the commutator.

The impedance seen looking into an electronic switch is nulled out by a negative resistance provided by the bootstrap unloader circuit. The base drive current required by the electronic switches is also provided by the bootstrap unloader.

The master switch serves to match out the offset of the electronic switches, as mentioned above, and also provides isolation between the redundant analog-to-digital converters. In addition, a switch is provided to bypass these converters in the emergency mode.

6. Command Decoding

a. Circuit development. The preliminary design of the command decoding organization and logic has been completed, and configurations for all the command decoder circuits have been chosen. Development and preliminary design have been completed and preliminary circuit schematics have been released for product design. A final circuit design review was held, and recommendations of the review panel will be incorporated in final designs scheduled for completion on November 1.

b. Command decoder breadboard. A breadboard of one central decoder and two subsystem decoders has been constructed and checked out. This breadboard is being integrated into the larger telecommunications breadboard . A word generator which can generate any ordinary or fill-in command has been used to test the command decoder breadboard. This equipment contains a 48 flip-flop shift register and toggle switches to select any address and command.

c. Subsystem decoders. Five subsystem decoders (including two for flight control) are required for the basic bus subsystems. The use of additional decoders to provide redundant command outputs for each of the basic bus commands was considered. This provision will not be included since the number of additional components is high (almost 1000 parts are required in the four additional decoders required) and the reliability of the nonredundant decoders is considerably higher than that of some of the nonredundant subsystems which comprise the basic bus.

A tentative grouping of scientific experiments requires the use of 14 subsystem decoders for the scientific sub-

system groups. Several of these groups require two subsystem decoders, since the number of commands required exceeds 32. Thus, a total of 19 subsystem decoders tentatively are required by the spacecraft.

Many of the subsystem loads driven by the subsystem decoders require less current than the 5.0 ma capability of each decoder output (as shown in the last *Space Programs Summary*). In order to conserve spacecraft power and maximize subsystem decoder reliability, it is desirable to decrease the current supplied to these loads by increasing the decoder matrix resistors associated with these outputs; as information becomes available, these changes will be incorporated, provided there is no effect on hardware delivery.

7. Transmitter

The first breadboard model of the solid-state portion of the spacecraft transmitter has been operated. This model included integration of the main parts of the exciter, the transistor power amplifier, and the varactor multiplier circuits. Output power of 100 milliwatts at a frequency of 2295 mc was achieved.

As a result of information gained from other programs, increased emphasis has been placed on establishment of proper mechanical design for microwave stripline circuits. A comparison of relative advantages of stripline and point-to-point wiring techniques also is being pursued.

a. Exciter. The transmitter exciter circuit has been changed slightly as shown in Figure 71. The phase modulator has been placed between the receiver voltage controlled oscillator input and the summing point, since phase modulation is used only in the transponder mode.

A breadboard model of the voltage controlled oscillator has been frequency locked to the frequency discriminator and satisfactorily modulated. The X5 transistor multiplier has been built and used to drive the transistor power amplifier. Preliminary circuits of the phase modulator and the voltage controlled crystal oscillator have been designed, and these circuits will be included in a second breadboard model of the exciter.

b. Transistor power amplifier. A three-stage transistor power amplifier was built for the first transmitter breadboard model to raise the power from 5 to 700 milliwatts. A second breadboard has been built to evaluate different high frequency power transistors and circuit configurations. Power efficiency and reliability are the primary design consideration in the development of the power amplifiers.

c. Transmitter multiplier chain (lumped parameter). The first transmitter breadboard model contained two lumped-parameter varactor frequency doublers. They

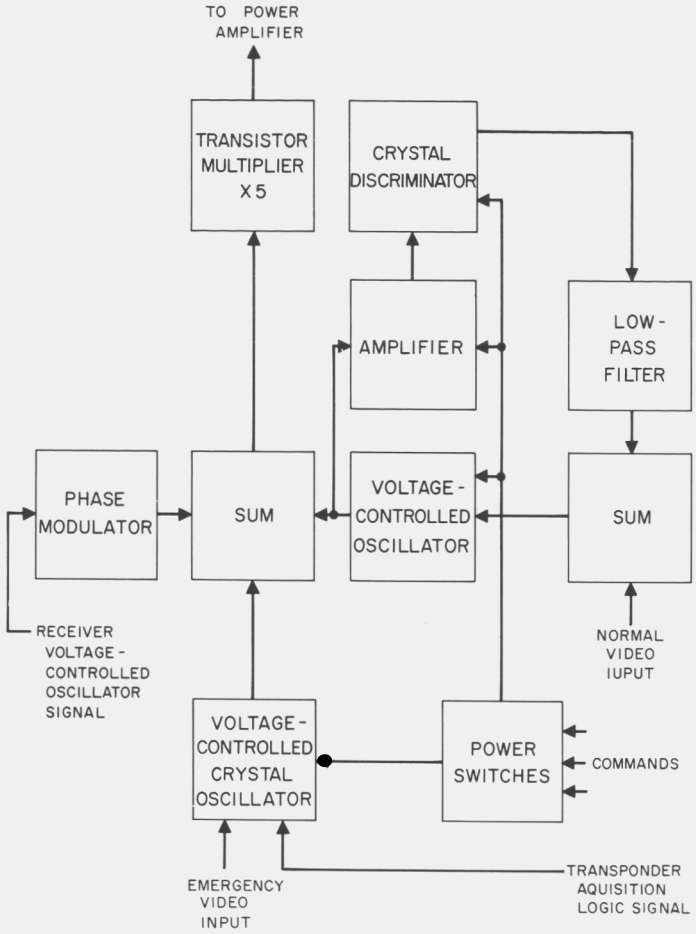

Figure 71. Exciter circuit

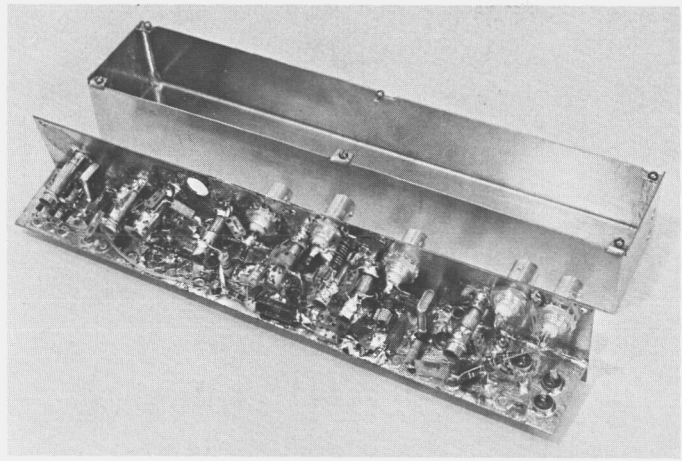

Figure 71A. Transmitter exciter breadboard

delivered 400 milliwatts power at a frequency of 382.5 mc when driven with 700 milliwatts of power at a frequency of 95.62 mc. To reduce the complexity of the design, a single varactor quadrupler has been built for the second breadboard. It has not been evaluated as yet.

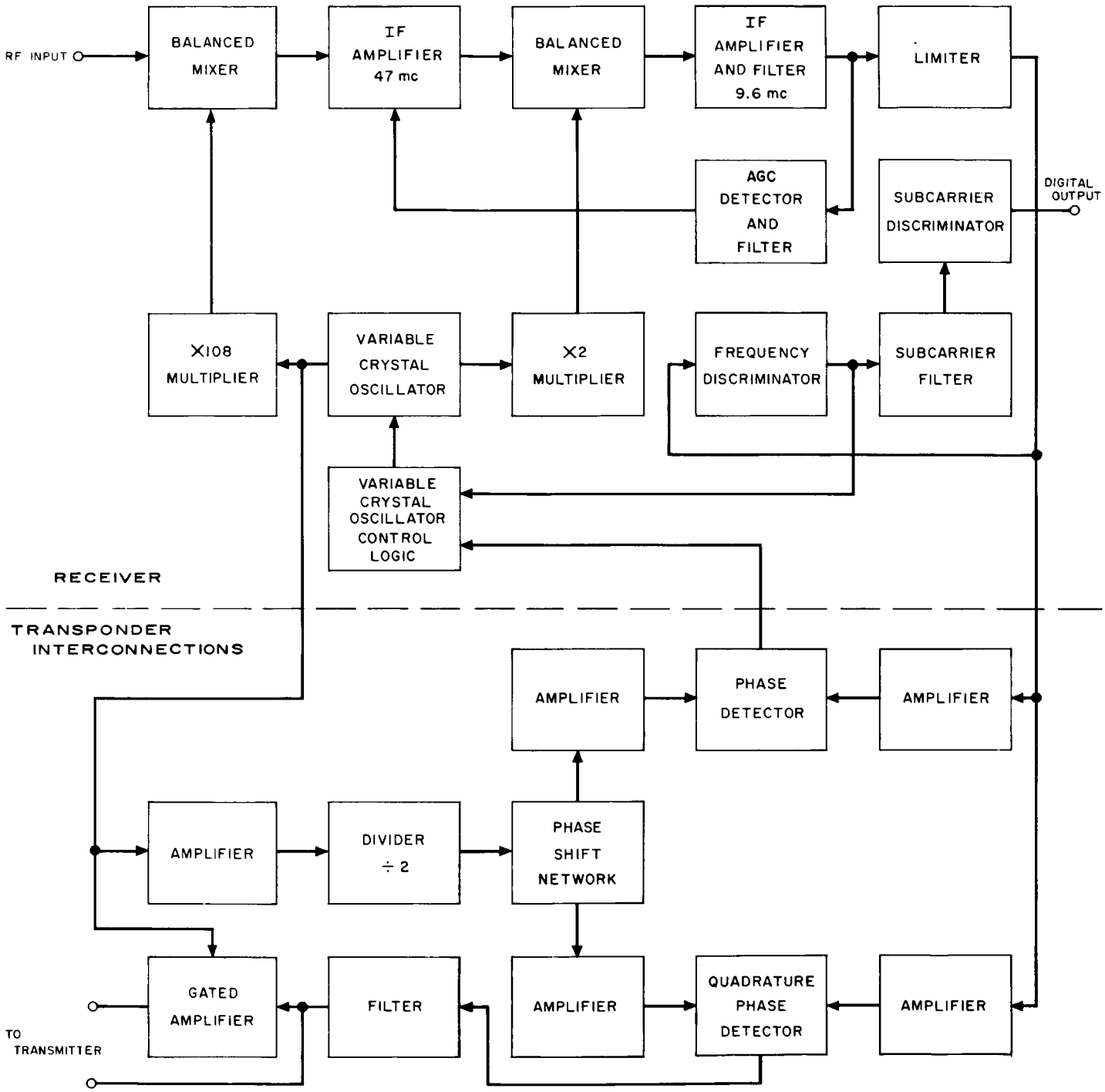

Figure 72. Command receiver-transponder interconnections block diagram

d. Distributed-constant circuits. A second breadboard version of the X3, X2 stages of the multiplier chain shown in the previous report has been subjected to vibration tests. Phase deviation measurements were made by comparing two identical models, one under vibration and one (the reference model) at rest. Both multiplier circuits were driven by the same oscillator, and the relative phase of the power from each circuit was measured at the output of a balanced modulator. The circuit under test was subjected to the specified sinusoidal vibration levels for the retro stage environment. Measurable phase deviations were found to occur at several discrete vibration

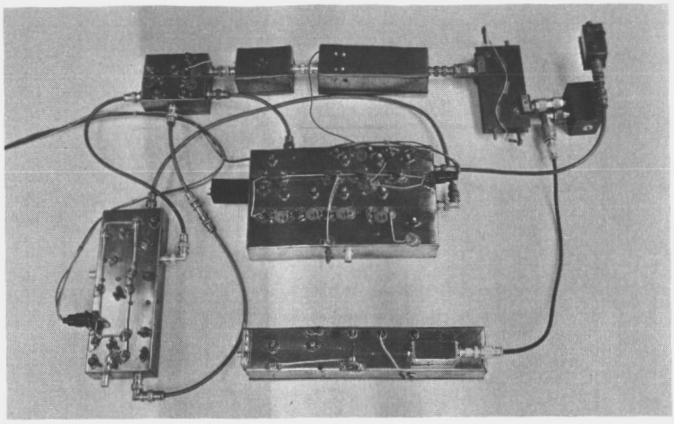

Figure 72A. Command receiver-transponder interconnections breadboard

frequencies from 0 to 2600 cps. In the bands for which a deviation limitation has been imposed, the unit satisfied requirements with a safety factor of 10.

TRANSPO ON-OFF

Four development models have been fabricated and tested; the conversion loss for the X3, X2 combination has been between 5 and 5.2 db. The driving circuitry and the multiplier stages were assembled and mated satisfactorily from the impedance viewpoint; however, considerable output power appeared in extraneous lines located 96 and 192 mc from the output frequency. Extra filtering will be incorporated in the redesigned lower stages for greater suppression. No discernible power was present at the receiver frequency.

e. Traveling-wave tube. A breadboard version of the traveling wave tube has produced 10.8 watts of power at 2295 mc with about 15 milliwatts drive. This result has been obtained with a tube incorporating the metal-ceramic construction and other mechanical design features planned for the flight models. A beam efficiency of 17% was achieved. Based on this beam efficiency, it is calculated that an efficiency well in excess of the desired 20% will be achieved in the "depressed-collector" mode. Furthermore, an efficiency of 26% already has been observed in the traveling wave tube being developed for Project Syncom; the tube tested for Surveyor uses the same basic structure, and it is expected that both tubes will exhibit about the same efficiency under depressed-collector conditions.

8. Command Receiver and Transponder Interconnections

The command receiver is a double conversion FM receiver. It must operate continuously throughout the life of the spacecraft. Reliability and power efficiency are the important factors in the design of the receiver, since available power is severely limited. The receiver also is able to operate in a phase-locked mode by energizing the transponder interconnection circuit. The reason for not operating as a phase-tracking receiver at all times is that the phase-locked mode requires significantly more power than the frequency tracking mode.

The receiver and transponder interconnections are shown in Figure 72. Basically, there is little change from the circuitry described in the June Bimonthly Progress Report; the local oscillator multiplier has changed and will be described in more detail in a following paragraph. There have also been some minor changes in the arrangement of the amplifiers which distribute the receiver oscillator signal; these changes were necessary to reduce signal leakage which had caused interference with transmitter operation.

a. Breadboard receiver system. All the components of the receiver and transponder interconnection system have been breadboarded and are undergoing optimization and evaluation. A schematic diagram is shown in Figure 73. The frequency tracking parts have been connected into a breadboard system, and closed-loop operation has been obtained. However, only qualitative measurements of closed-loop performance have been made to date. These measurements include observing the tracking ability and a cursory look for spurious responses. It is anticipated that spurious responses will be a problem, and detailed measurements will be conducted to determine their effects.

Most of the breadboard transponder circuits also have been operated with the receiver system. Tracking in the phase-locked mode has been obtained. Power switching and the gating of the receiver oscillator signal by the transponder acquisition signal remain to be incorporated into the system breadboard.

b. Local oscillator. Breadboard models of two versions of the local oscillator have been built. The first (Fig 74) has been successfully integrated into the command receiver breadboard system.

The block diagram of the second configuration is shown in Figure 75. The 2N917 transistor is used to develop power at 344.25 mc, and only one varactor multiplier (an X6) is needed. The second system will be simpler to adjust and should have less low frequency sideband because of the greater isolation achieved in transistor multipliers over varactor multipliers and because of the high frequency amplifier. In addition, power limiting is achieved at a higher frequency in the second system, which should increase system reliability. A decrease in efficiency in the second system will require about 75

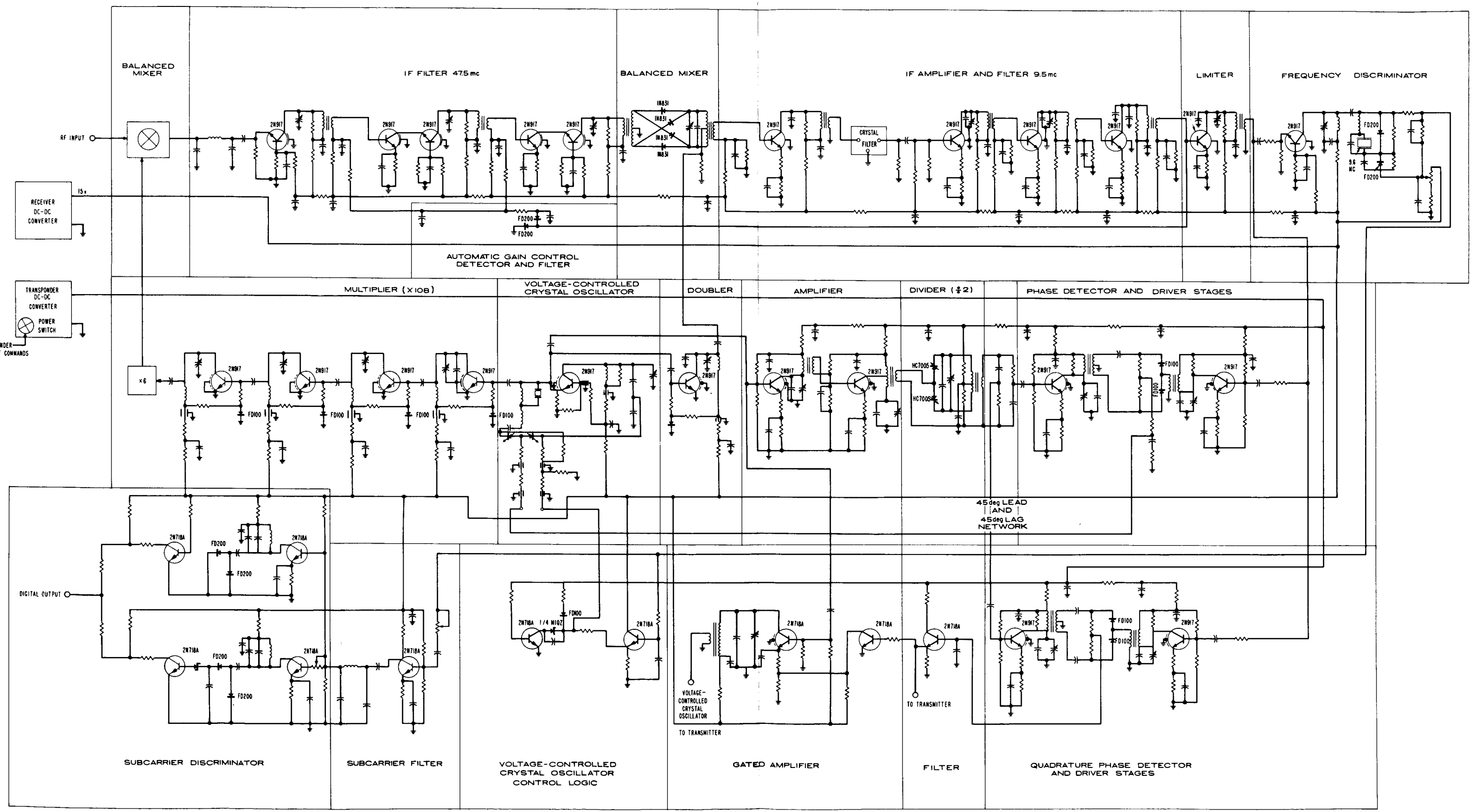

Figure 73. Command receiver-transponder interconnection schematic diagram

milliwatts additional power. A schematic diagram of the lumped parameter portion of the second system is shown in Figure 76. The breadboard circuit is producing 20 milliwatts power at 344.25 mc with an input power of 360 milliwatts. Preliminary distributed constant circuits

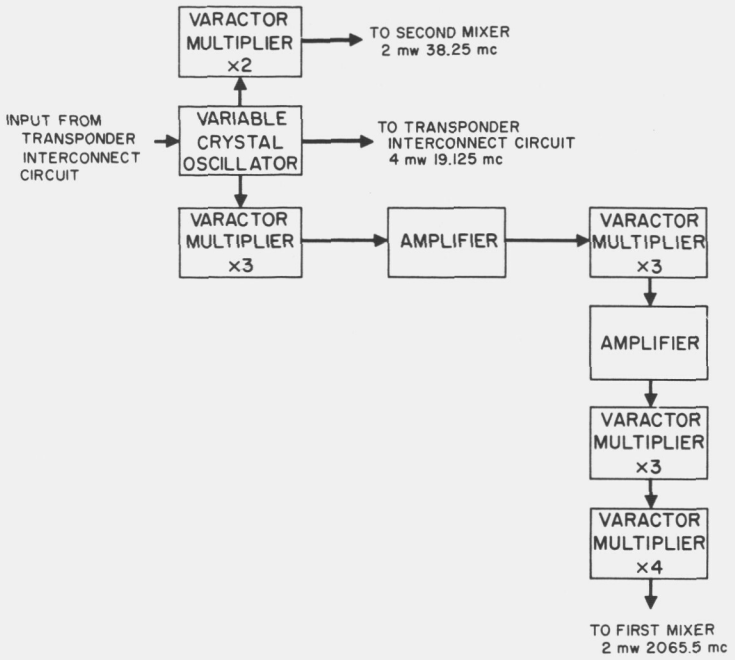

Figure 74. Command receiver local oscillator first breadboard model

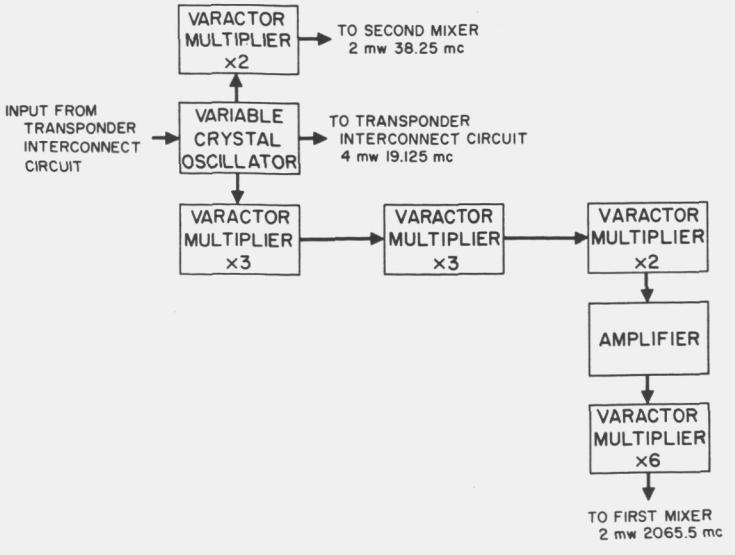

Figure 75. Command receiver local oscillator revised configuration

for the new configuration are now being assembled into a chain.

c. VCXO control logic. The receiver voltage controlled crystal oscillator is controlled by one of two sources: the frequency discriminator in the receiver or the phase detector in the transponder interconnection circuit. The VCXO control logic selects the proper control signal.

As shown in the over-all receiver schematic (Fig 73), the VCXO frequency is controlled by the bias voltage across a pair of HC7005 varactor diodes. During normal operation, the transponder interconnection circuits are turned off and the negative side of the modulation input to the oscillator remains at ground potential. The frequency discriminator output, which varies about a 10-volt

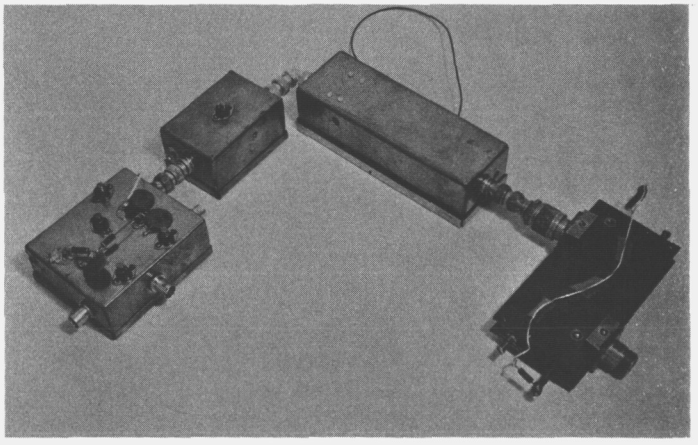

Figure 75A. Command receiver local oscillator breadboard

quiescent level, feeds the positive side of the modulation input through an emitter follower to control the oscillator.

Activation of the transponder circuitry applies power to the 2N718A circuit in the VCXO logic which clamps the positive side of the modulation input to 10 volts, disconnecting the frequency discriminator. Since the phase detector circuit has been energized, it may control the VCXO through the negative side of the modulation input.

9. Television System

a. Vidicon. The choice of the vidicon for the television cameras had been narrowed to two types, as reported in *Space Programs Summary 37-10*: the RCA C74015 and a modified GEC 1343. Both vidicons are electrostatically focused and magnetically deflected. The GEC 1343 is a pure electrostatic tube, but GEC has supplied, at Hughes request, sample tubes which are essentially the

1343 type with the electrostatic deflection electrodes removed so that they may be deflected with a magnetic yoke. The number assigned to the modified tube is GEC 1349.

Both types of vidicons, C74015 and GEC 1349, have been operated with no alignment devices in the breadboard camera system. The C74015 exhibits very poor focus uniformity. Severe raster skewing results from a change in focus voltage. In contrast, the GEC 1349 has excellent focus uniformity and does not exhibit raster skewing. Beam-landing errors have been found to be considerably greater in the C74015 than in the GEC 1349. The GEC 1349 is a fully ruggedized vidicon while the C74015 is of conventional construction. For the above reasons, the GEC 1349 has been selected for *Surveyor*.

b. Video amplifier. Circuit design of a low-noise transistor video amplifier has resulted to date in a circuit which has a sensitivity of 13 millimicroamperes peak-to-peak for an output peak signal to rms noise ratio of 45 db. The schematic diagram of the amplifier is shown in Figure 77.

The input impedance of the amplifier is maintained at 400 kilohms, achieving a good power match from the vidicon target and providing adequate sensitivity. However, this high input impedance, reacting with the input capacitance, results in a roll-off in frequency response above 30 kc. Equalization is employed between the two feedback pair amplifiers to overcome this effect and maintain the amplifier gain constant over the required bandwidth. The second feedback-pair feeds a keyed clamping circuit which clamps the video signal to the black reference level during every horizontal blanking pulse. An emitter follower then drives the sync and blanking adder circuit and another emitter follower couples the signal to the output. The over-all gain of the video amplifier is 308 volts/microampere. The gain is constant to within 3 db from 0.1 cps to 220 kc.

Temperature compensation is employed throughout the video amplifier to eliminate the effects of base-to-emitter potential variations over the operating temperature range. Temperature tests on the breadboard have been made. Over a range of 0° to 70°C, the gain vari-

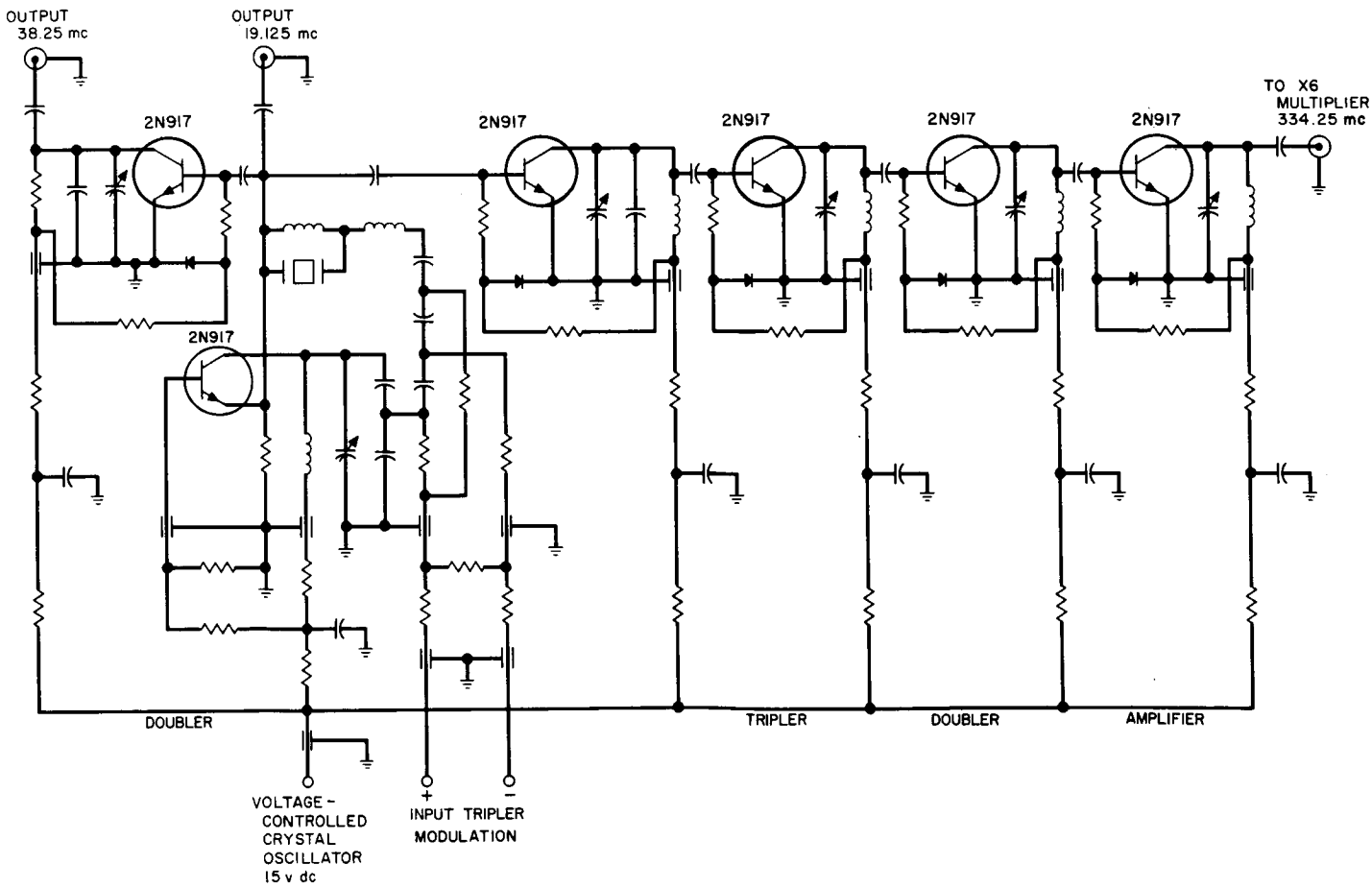

Figure 76. Receiver local oscillator lumped parameter circuit

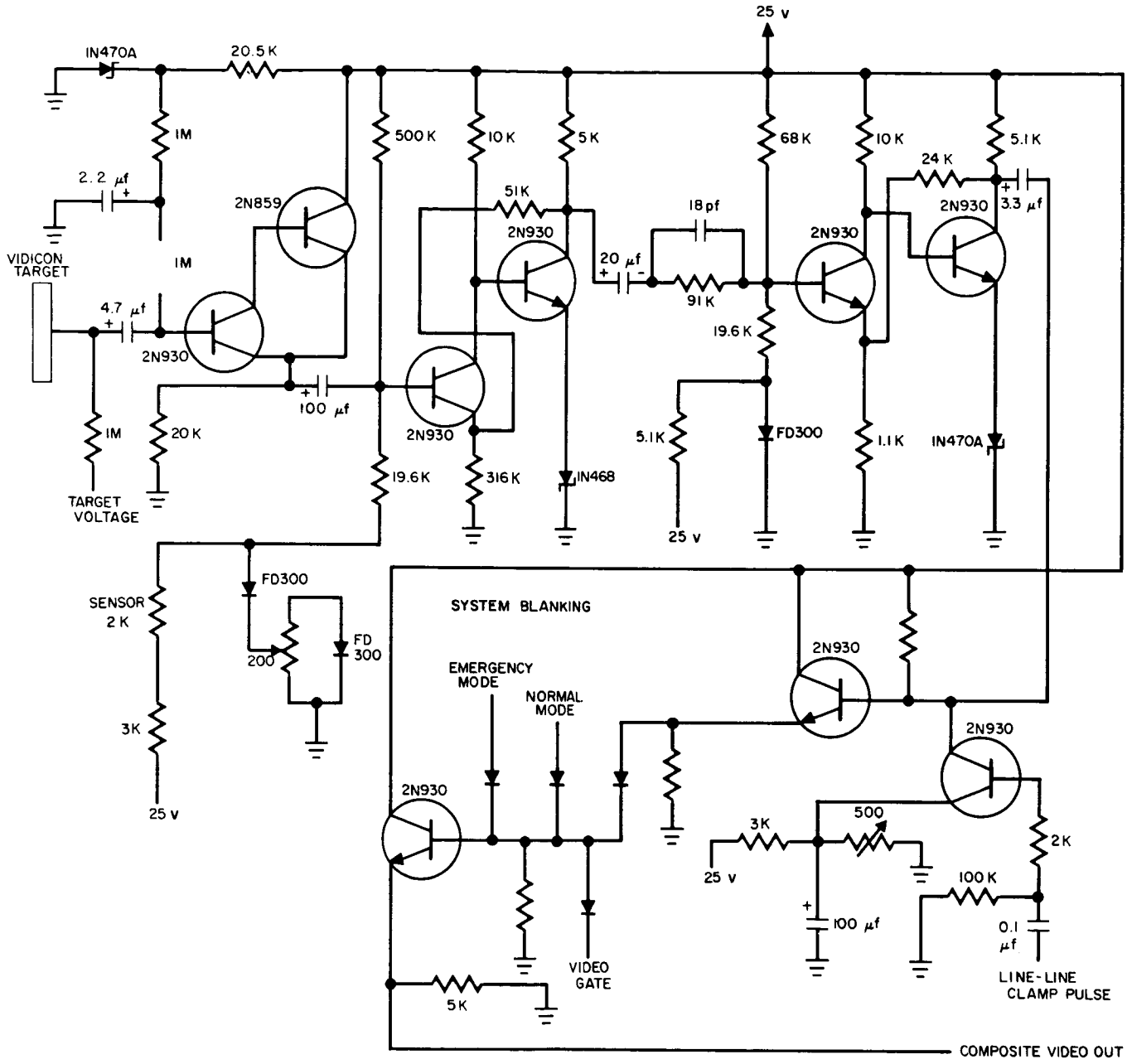

Figure 77. Video amplifier

ation has been measured to be less than 5%. The dynamic range at the output of the amplifier is 5 volts peak-to-peak at either extremity of the temperature range. At other temperatures within this range, the dynamic range is greater than 5 volts peak-to-peak.

c. Video logic. The video logic circuit (Fig 78) provides actuation signals to the shutter, and video gates to the video amplifier circuit and signal processing system, to control the flow of either video or frame identification information to the transmitter. Figure 79 shows the

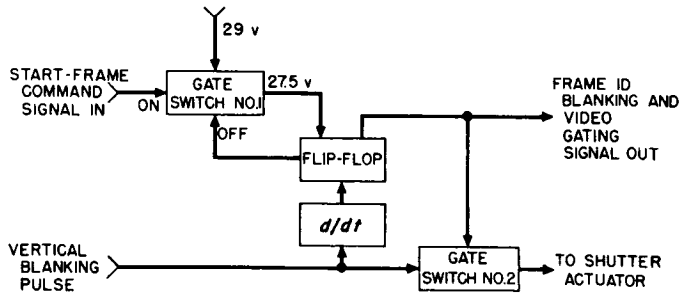

Figure 78. Video logic circuit

signal sequence and Figure 80 is the schematic diagram of the circuit.

The start-frame command turns on a positive feedback gate, allowing the vertical blanking pulse to drive an offset bistable multivibrator. The multivibrator is designed to turn on in the proper state when the positive feedback gate supplies power to it.

The leading edge of the first vertical blanking pulse triggers the bistable multivibrator to the opposite state, supplying the power to the second positive feedback gate. The multivibrator also provides a gate pulse to turn on the video gate and to blank the frame ID code. The output of the second positive feedback gate energizes the shutter trigger circuit.

The trailing edge of the first vertical blanking pulse turns off the second positive feedback gate. The second vertical blanking pulse returns the bistable multivibrator to its original state. The resulting output turns off the first positive feedback gate, which removes all power to the video logic circuit. The video logic circuit is then ready to receive another command signal when it occurs.

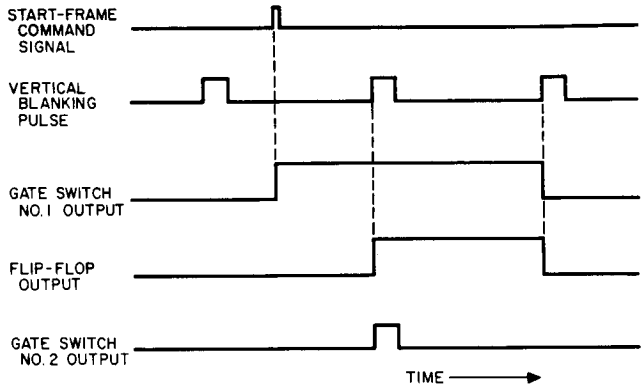

Figure 79. Video logic timing sequence

d. Variable focal-length lens. The detailed specification for the variable focal length lens for the television

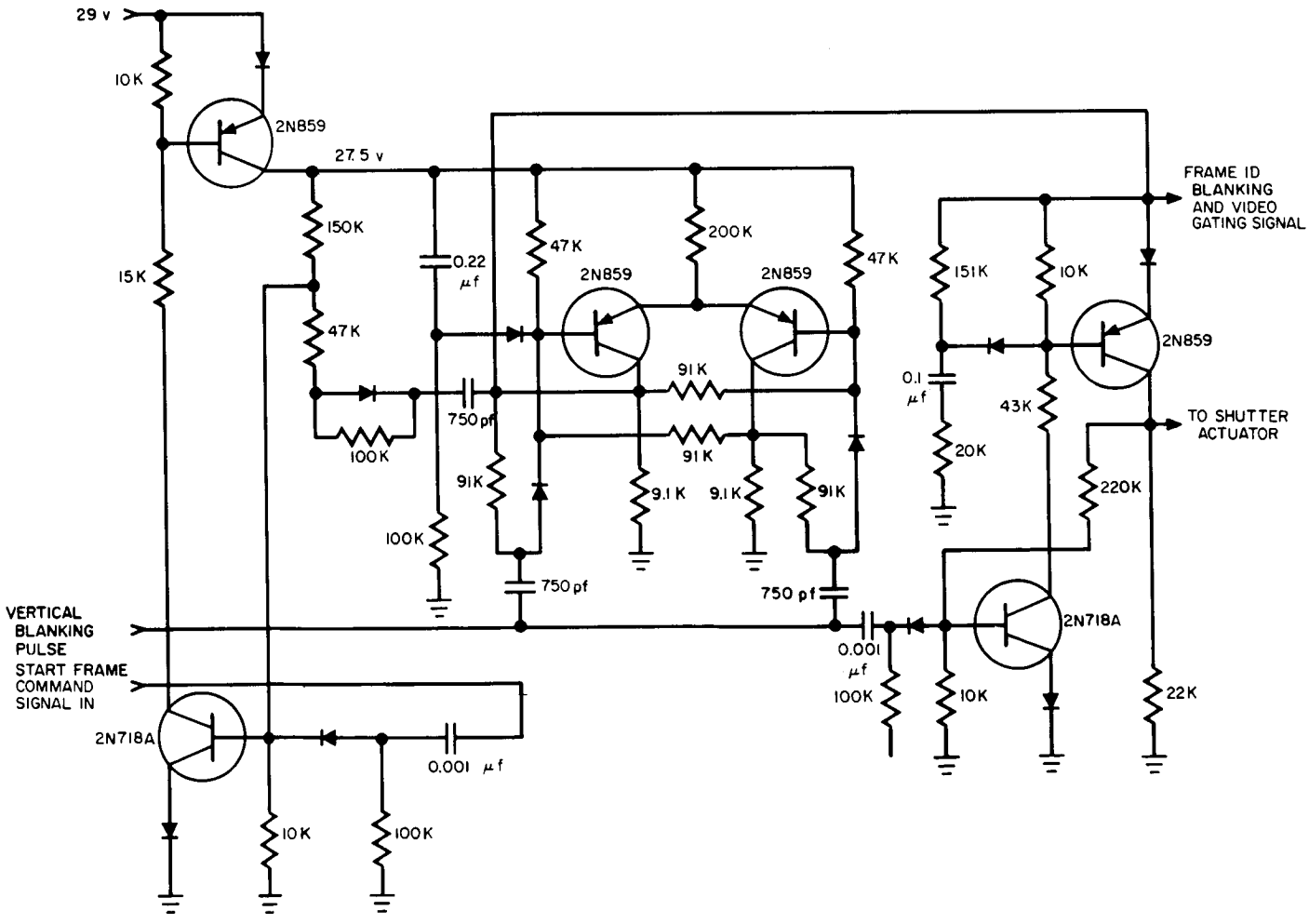

Figure 80. Video logic circuit schematic

cameras has been completed and issued with a request for quotation to several lens manufacturers. The lens assembly consists of a variable focal-length lens with motor-reflex viewer behind the lens for supplying light to the iris-control light sensor. A solenoid-actuated focal plane shutter is used. A removable motor driven filter subassembly attaches to the front of the lens proper. Some of the principal functional requirements of the lens are as follows:

(1) Focal length: continuously variable from 25 to 100 mm.
(2) Focus range: 6 feet to infinity.
(3) Lens aperture: continuous from f/4 to f/22.
(4) Resolution: equal or greater than 70 line pairs per mm over the entire image.

e. Lens mechanisms circuits. The detailed operation of the lens-mechanisms control system was described in the last bimonthly Progress Report. The block diagrams have been implemented and breadboard circuits are in operation. Figure 81 shows the logic for the step servo motor control. Figures 82 and 83 show the circuit diagrams of a typical control circuit.

10. Diplexers

Two identical diplexers are used, one with each receiver. A sample diplexer has been received from Rantec Corporation. Although evaluation is not complete, preliminary tests indicate that its performance is significantly better than required in this system.

11. RF Switches

A mechanical transfer switch is being modified by Transco Products Inc., to eliminate the 15-watt holding power required for their present design. The new switch will resemble the original design except for a latching mechanism which will be substituted for the spring solenoid arrangement. These switches are to be used for all switching of microwaves in the spacecraft, including antenna and traveling wave tube switching.

12. Electronics Packaging

a. Packaging concept. Continuing effort is being placed on the packaging techniques for the Hughes produced electronics. This effort is directed toward minimum weight and volume while maintaining a high degree of reliability, consistent with proved packaging techniques.

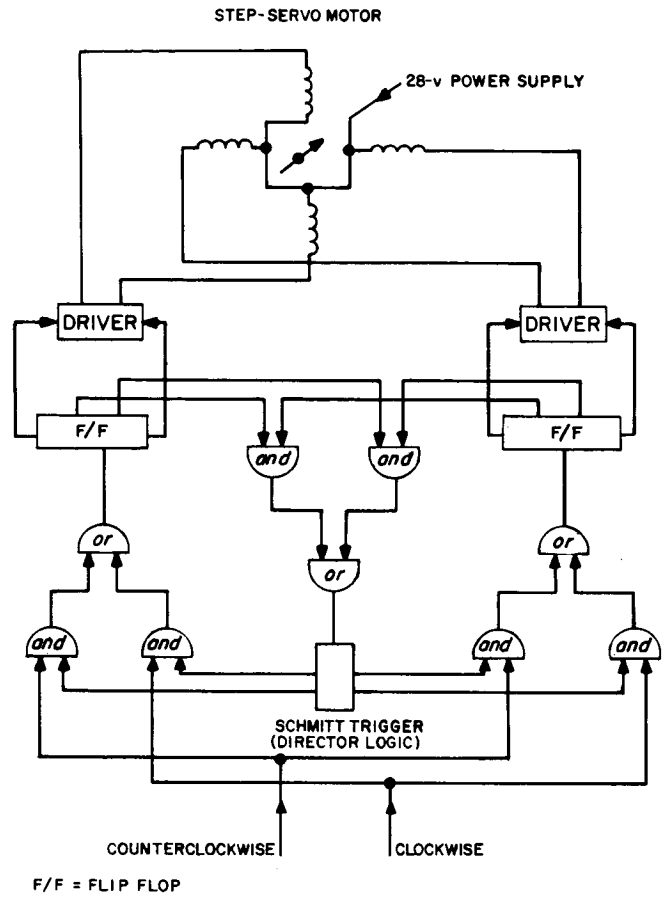

Figure 81. Step servo motor control logic block diagram

During this report period, emphasis has been placed on modular construction for functional circuits such as flip-flops using the parallel etched-circuit board technique. To minimize weight, modules will be "freeze-coated" (dip-coated with encapsulant) rather than solidly encapsulated. A decision has been made not to use the plated-on circuitry technique. It is felt that the plated-on circuitry process is not sufficiently developed at this time. Work will continue on this process for possible later use.

The structural and weight advantages of a sandwich-type chassis were discussed in the last report. One cover member is an aluminum plate; the other cover member is a 0.032 in. printed circuit board. The thermal properties of such a chassis have now been investigated. A 0.010 in. aluminum cover plate is adequate structurally and also adequate thermally for most chassis. Chassis with high and relatively even dissipation will have an aluminum plate of greater than 0.010 in. Chassis with high localized

dissipation will have an aluminum bracket, to which high dissipation components are mounted, permanently attached to the chassis face at the edge of the chassis. Various types of foam sandwich materials are being investigated. Prototype chassis are being fabricated using 2 lb/ft³ polyurethane foam. Rather than foaming "in-place," a 0.1-in. thick sheet of foam is being bonded between the circuit board and the aluminum plate.

b. Vidicon cooling. Testing has continued to establish the requirements for thermoelectric cooling of the TV vidicon tube. It has been demonstrated that the face of a vidicon tube can be maintained at 30°C with less than 1°C temperature difference between the center and the outside of the face when the shutter (at 51°C) is radiating to the face. Tests are being run to establish an optimum system for heating the vidicon face from low temperatures up to 30°C.

13. Radars

a. Altitude-marking radar. All units for the altitude-marking radar breadboard have been designed and fab-

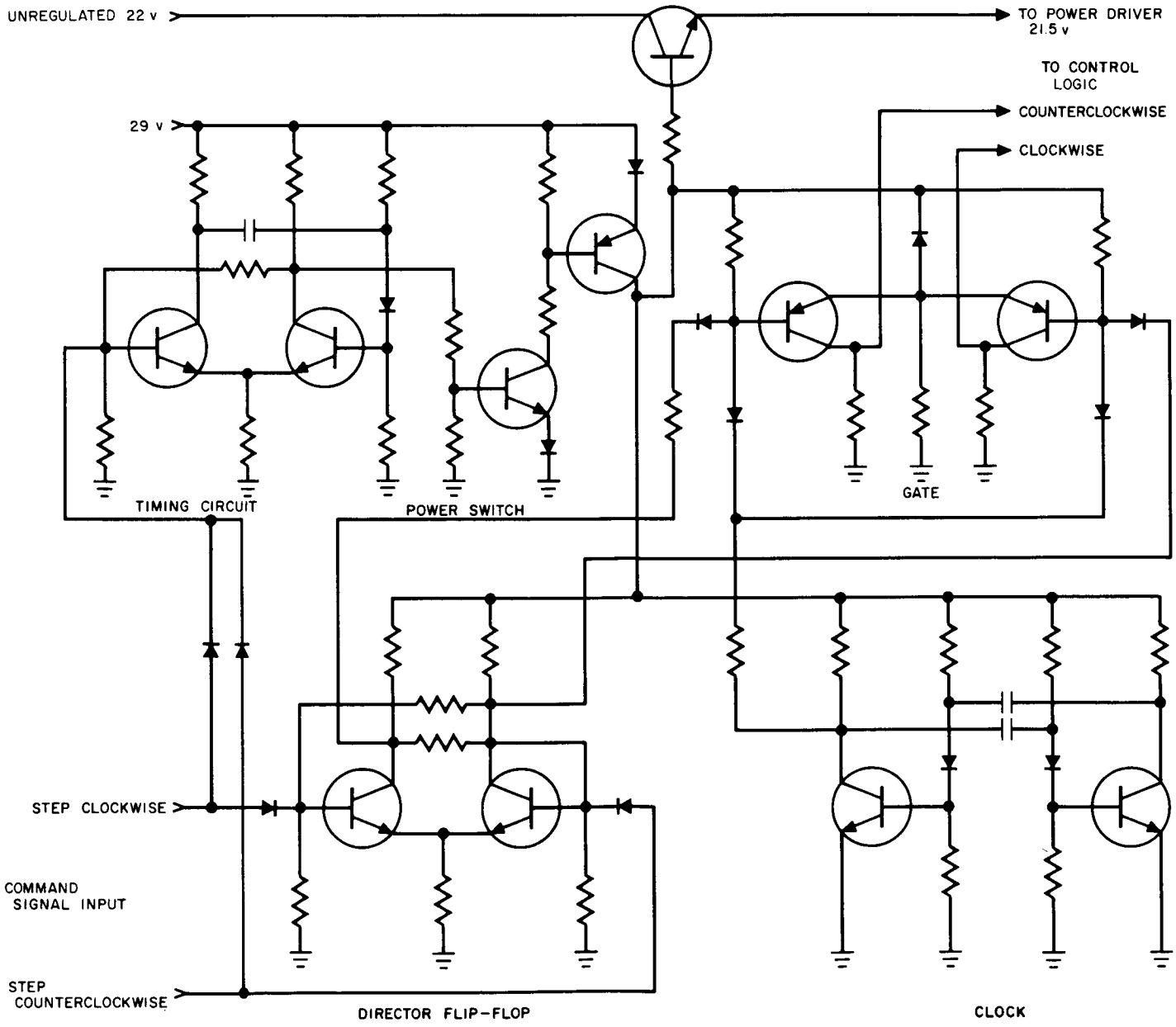

Figure 82. Step servo motor command logic

ricated or purchased and are in unit test. A light-weight fiberglass antenna dish similar to the one to be used for the prototype design has been obtained from Raymond Deicer. Patterns with this dish and the Hughes-designed feed have given gains of 34.3 db with sidelobes of approximately —30 db.

The RF unit, including magnetron, three-port circulator, and transmitter/receiver tube, has been received from Metcom. The entire weight of this package is 16 ounces with a specification of 1 kw peak power and 3 microsecond pulse length at 350 pps. (The prototype will have a peak power of 2 kw in the same package.)

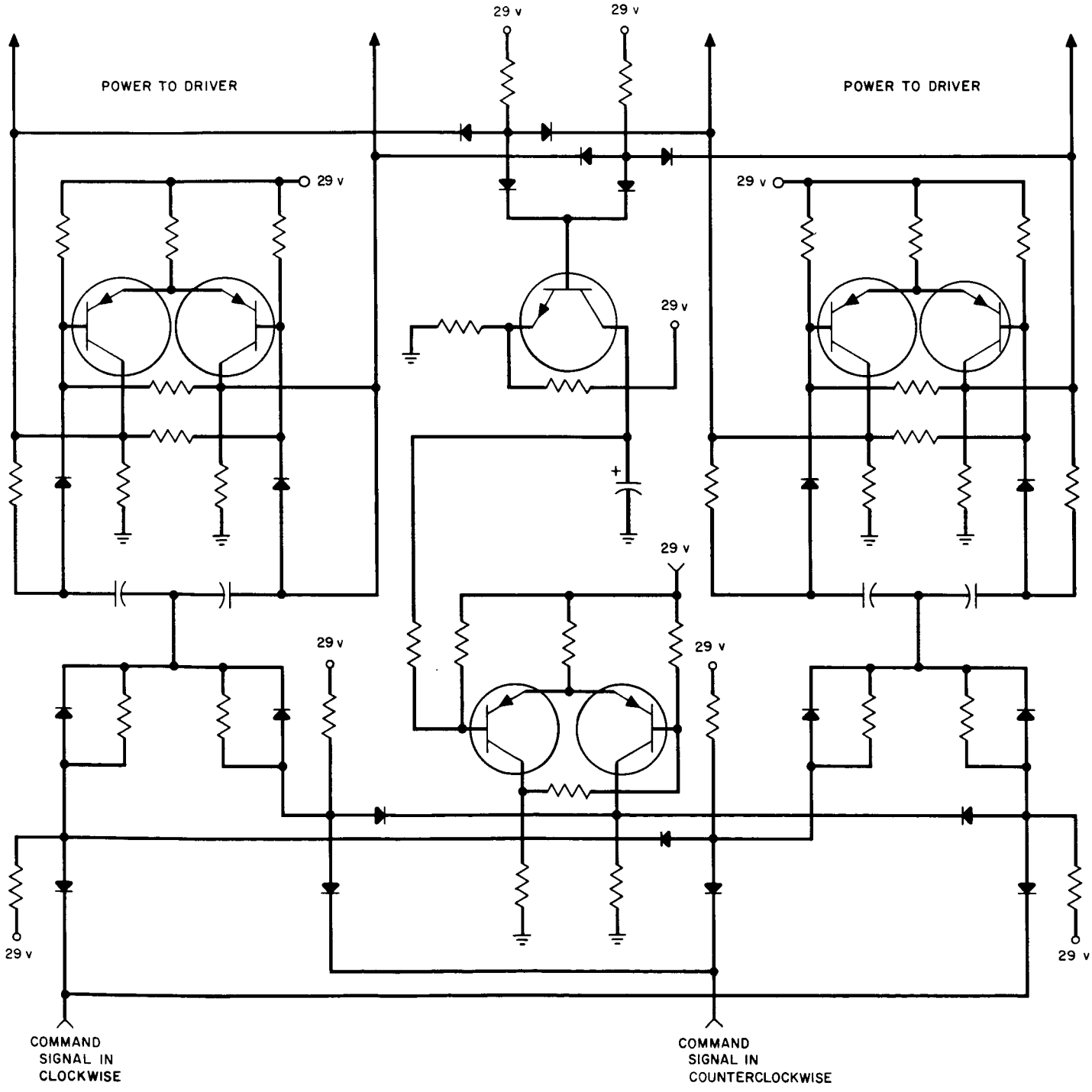

Figure 83. Step servo motor control logic schematic diagram

A block diagram of the altitude-marking radar transmitter/receiver is given in Figure 84. The local oscillator is a solid-state crystal oscillator/multiplier chain and provides a stable frequency local oscillator source.

The use of a frequency-stabilized magnetron with this local oscillator eliminates the requirements for an AFC. Considerable emphasis, however, is placed on the temperature characteristics of the magnetron. Figure 85 shows frequency vs time for several initial conditions of temperature. In these tests, the filament supply was turned on 30 seconds before the 28 volt dc main supply; the unit was soaked at the indicated temperature for 30 minutes before data was recorded. The maximum variation in frequency from turn-on to 10 minutes operation was 3.5 mc for an initial temperature range of 120°F. The final temperature uncertainty is expected to be only a fraction of 120°F.

The IF amplifier has a 30-mc center frequency and a 4-mc bandwidth, and thus will tolerate a frequency variation greater than the measured value. The tests on the magnetron have been made with the solid-state modulator in the same environment; the modulator is not an appreciable factor in the frequency variation of the magnetron.

Receiver noise figure measured with a 2.7 db IF noise-figure and a typical Orthomode mixer is 9.0 db. A plot of noise figure vs local oscillator power is given in Figure 86.

A complete bench model breadboard of the synchronizer (Fig 87) and video processor (Fig 88) has been built and tested. These circuits consist of the repetition rate generator, precision delay circuitry, video gates, integrators, and firing circuits. Two channels in the video processor require the presence of video signals with an intervening delay corresponding to the target closing velocity. This circuit prevents firing on isolated noise transients.

A simulated target was obtained by time-modulating a Rutherford delay generator with a Hewlett-Packard function generator. This output was used to trigger a pulse generator, the output of which was mixed with noise from a GR noise generator to give a simulated

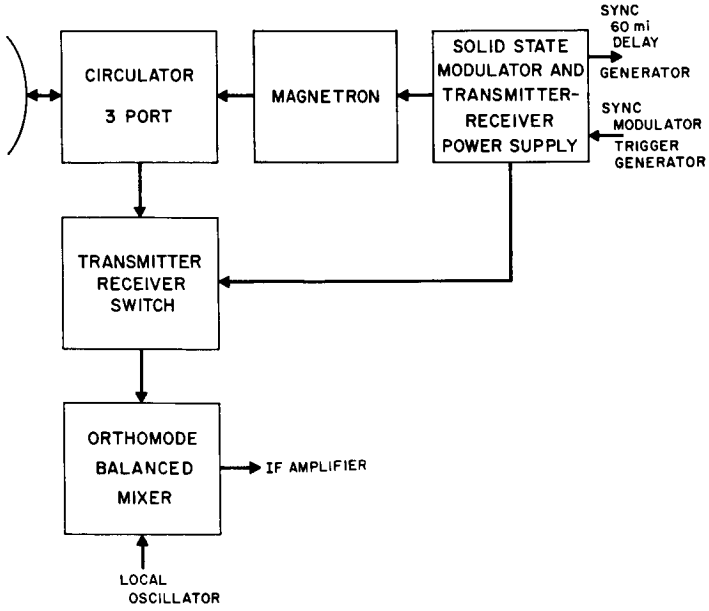

Figure 84. Transmitter-receiver for altitude-marking radar

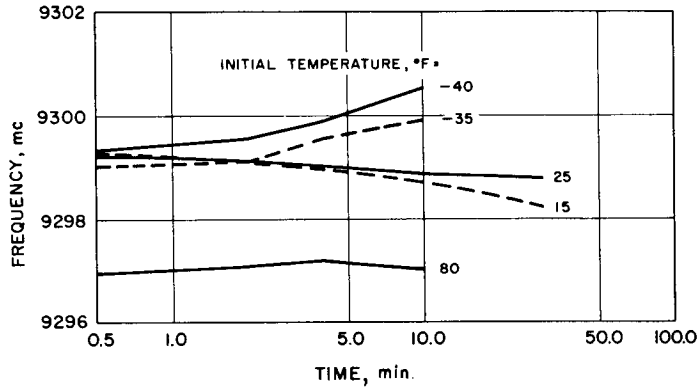

Figure 85. Magnetron frequency vs temperature

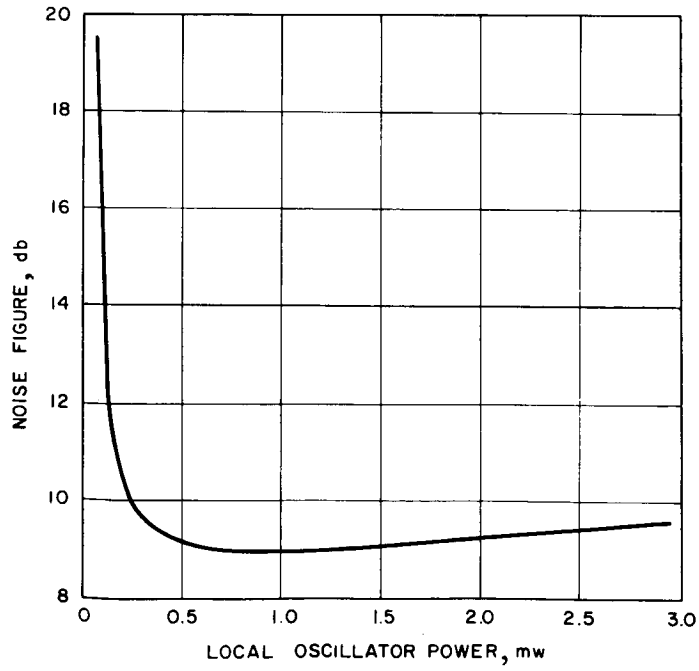

Figure 86. Receiver noise vs local oscillator power

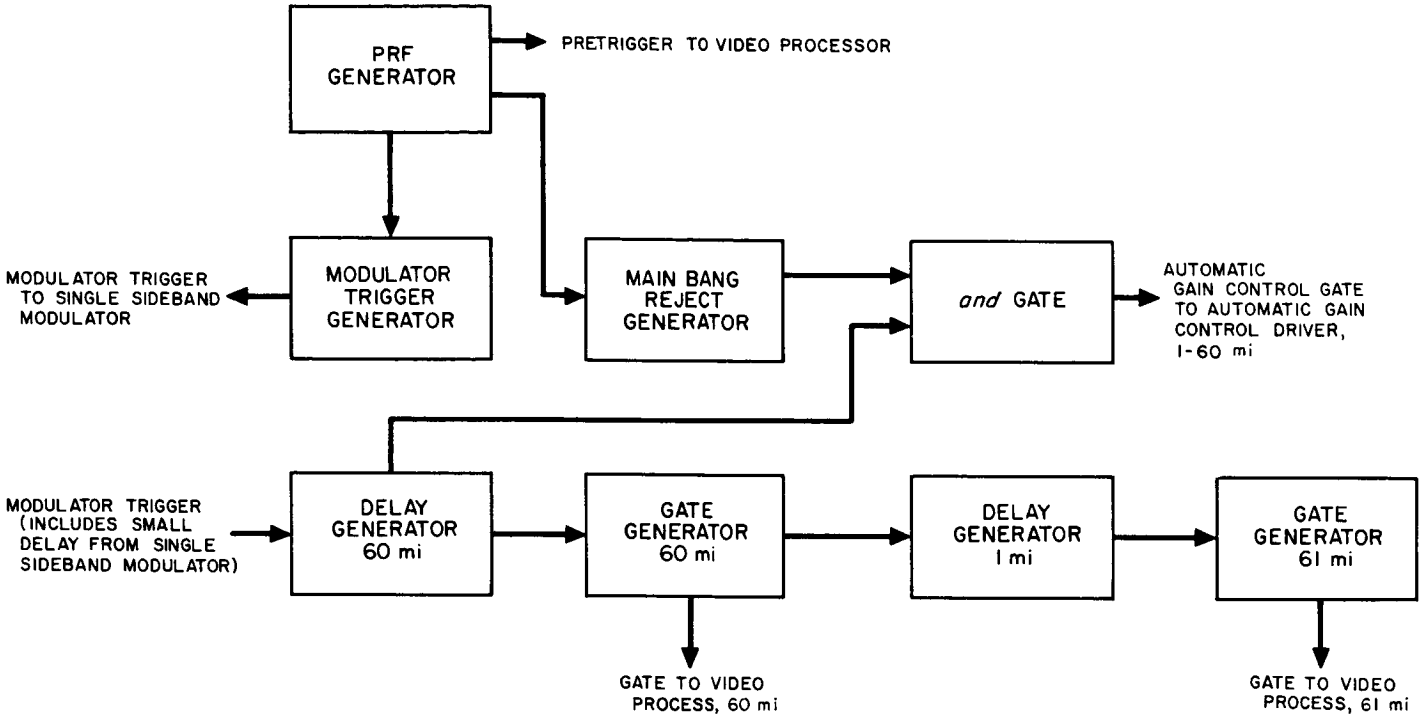

Figure 87. Synchronizer for altitude-marking radar

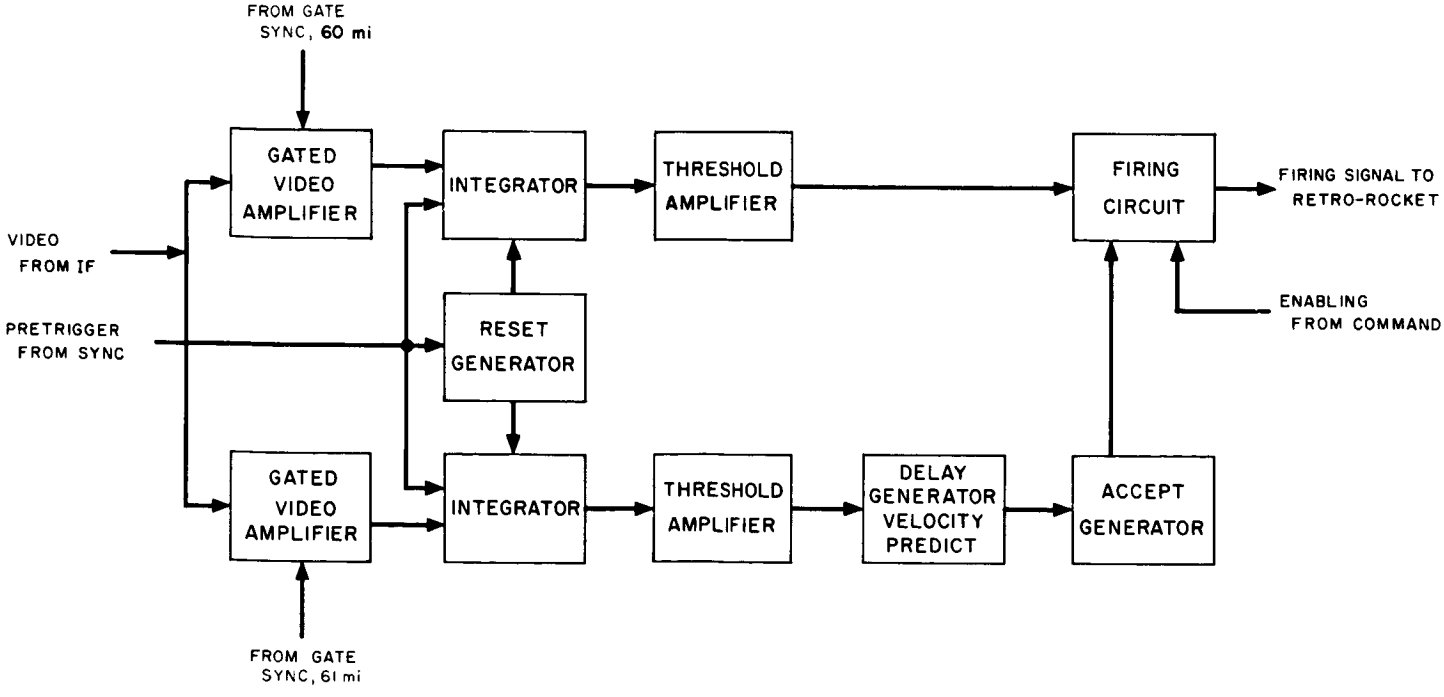

Figure 88. Video processor for altitude-marking radar

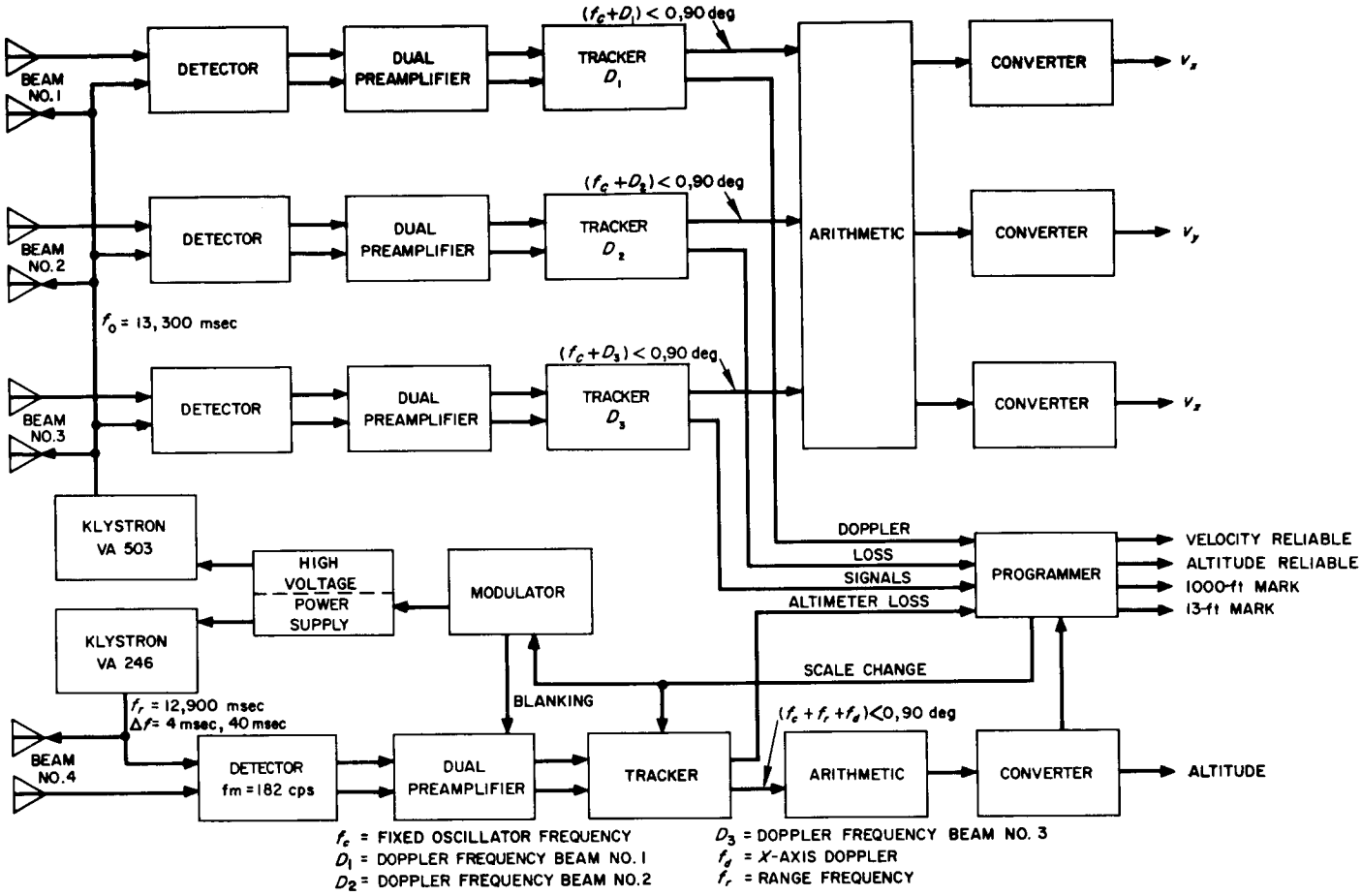

Figure 89. Radar altimeter and doppler velocity sensor

video pulse at 0 db peak signal to rms noise ratio based on the noise power in a 5-mc bandwidth and signal velocity corresponding to 9000 ft/sec.

The unit was operated for a limited time only, so that probability of detection and false alarm rates was not determined. However, it was operated for several periods up to an hour without missing the target when it was moving in the proper direction and without acquiring when the target was moving in the wrong direction and without a false alarm. A roofhouse breadboard unit, to be mounted on the antenna, has been built and similar tests are being performed.

b. Radar altimeter and doppler velocity sensor. The system design of the radar altimeter and the doppler velocity sensor (Fig 89) has been completed by Ryan Electronics. At this time much of the circuitry has been breadboarded and initial performance tests are being conducted. The preamplifiers and altimeter sawtooth generator have been tested, and the latter meets unit specifications over a temperature range of −50 to 50°C.

The high voltage klystron power supply is in test. The frequency tracker breadboard has been completed and the tracking loop closed. Evaluation of portions of the loop, including single-side-band modulator and quadrature generator, is in process.

F. Electrical Power Supply

1. Introduction

The electrical power to operate the *Surveyor* spacecraft is provided by an oriented solar panel and a silver-zinc storage battery system. Recent estimates of lunar surface thermal characteristics have raised the

predicted operating temperature of the solar panel, which in turn has reduced the output voltage and power. In order to provide the same generating capability that was previously possible, the solar panel area has been increased 0.8 ft². Improvements in the solar panel design have made it possible to acquire the additional panel area without exceeding the 8.5 lb weight allocation previously assigned.

Both technical and contractual quotations have been received for development and test of the silver-zinc battery, and the Electric Storage Battery Company has been selected. Corresponding quotations on the solar cell development and test activities have been received and are presently under evaluation.

2. Solar Panel

As part of the design evolution of the flight solar panel, a detailed analysis has been made of second order effects which influence the functional performance of the panel and its output. Table 15 lists the four new design parameters and their predicted effect on panel performance. Recent data has raised the predicted lunar surface temperature from a maximum of 105° to 110° C. In addition, it is felt that the uncertainty in the emissive characteristics of both the solar panel and the lunar surface represents an additional 10° C temperature upper limit tolerance. As a result, the panel design temperature is presently set at 120° C.

Table 15. Effect of design change on solar panel performance

Design change	Resultant voltage loss, volts	Resultant power loss, watts	To provide 44 watts	
			Additional modules/series string required	Additional area required,* ft²
Increased operating temperature, 105° to 120°C	−4.7	−5.8	4	1.47
Increased bus voltage, 28.7 to 29 v	−0.3	−0.5	1	0.37
High temperature performance degradation, 5%	0	−2.2	0	0.31
Seasonal variation and error in solar intensity, 4.9%	0	−2.15	0	0.31
Total	−5.0	−10.65	5	2.46

*Area increase dictated by use of 31 parallel strings of 26 series-connected modules, operating at 120°C.

The second effect which must be considered in the panel design concerns both the accuracy of the solar constant and its seasonal variation. The uncertainty in its absolute value is approximately 2%, and the seasonal change due to the variation in the radial distance of earth to sun represents an additional 3%.

Another source of performance loss is exposure to simultaneous high temperature and ultra high vacuum environment. Tests conducted at Hughes Aircraft Company have shown as much as 10% loss in performance during a 10 day exposure at 250°F and 10^{-4} mm Hg. A total of 5% degradation in panel performance has been assumed for this analysis.

Consideration of these individual performance uncertainties creates a requirement for more generating capacity and more efficient utilization of the solar panel output. Geometric studies of the shroud constraint and the antenna solar panel positioner kinematics and a check of inertial load effects and landing stability requirements have shown that approximately 0.8 ft² can be added without significant penalty. In addition, an optimum charge regulator will be incorporated in the power management system (see 5, below) to take advantage of the energy generated at times other than that corresponding to maximum panel temperature. Figure 90 illustrates how it is possible to obtain an increase of approximately 50% in panel output during transit and approximately 33% during the first day's surface operations. As a result, the average power available to the system is now in excess of 44 watts.

3. Solar Simulator

A contract for a solar simulator to be used in testing solar cell modules has been awarded to Optical Coating Laboratory, Inc. (OCLI), Santa Rosa, California, with delivery due in mid-January 1962. This light source is designed to simulate sunlight in Earth-space, both in intensity and spectral distribution, to an accuracy consistent with the preliminary AIEE photovoltaic solar simulator specification. These requirements are much tighter than those imposed for conventional tungsten light sources used in thermal control studies and have not yet been satisfied by any commercially available light source.

The OCLI design uses two lamps: a tungsten lamp for energy of wavelengths greater than 750 millimicrons and a xenon lamp for energy between 300 and 750 millimicrons. Interference filters partially correct the output of each lamp and a cold mirror-combiner mixes the two beams into a collimated beam 3 in. in diameter, large enough for a five-cell series-connected solar cell module.

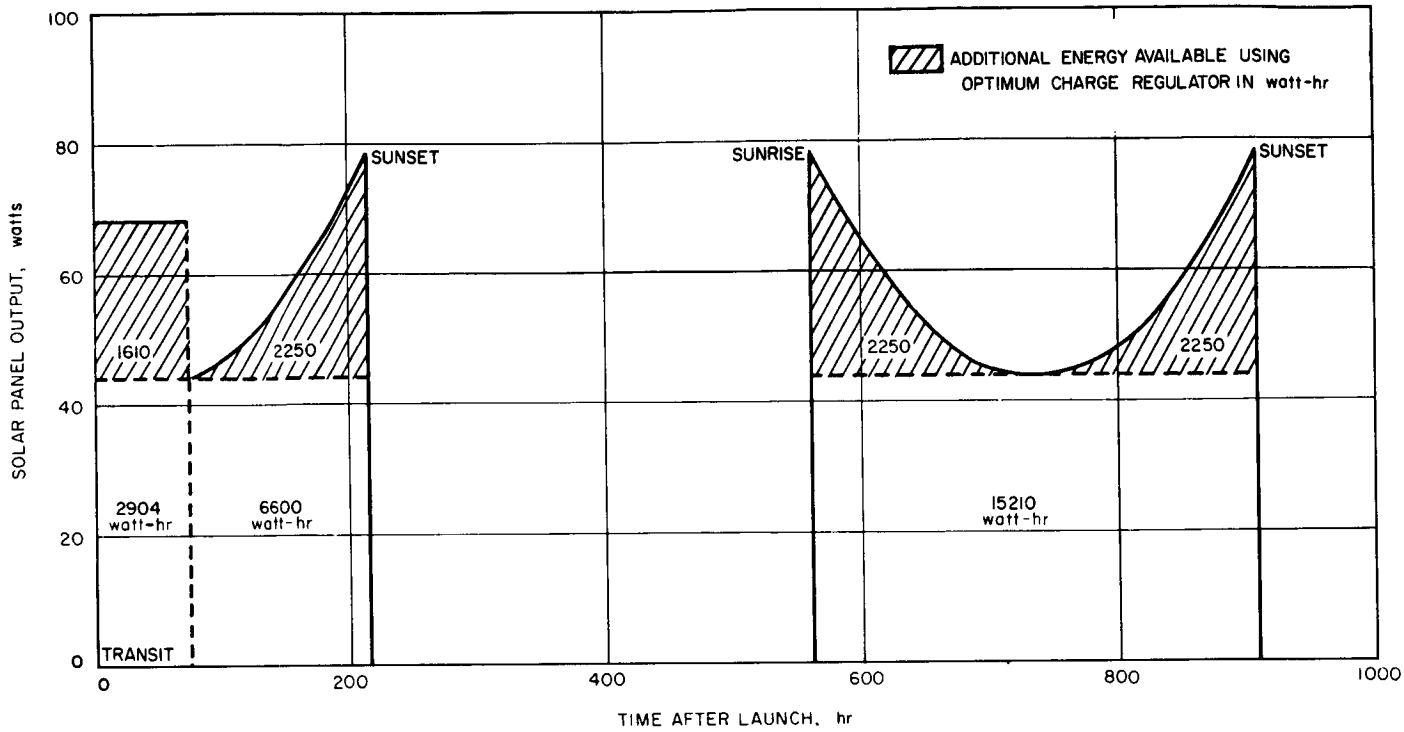

Figure 90. Solar panel power output

4. Battery

The charge-discharge cycle life tests and functional performance testing of three sealed Electric Storage Battery Company cells are continuing. Tests are being conducted on 25 amp-hr cells and have accumulated more than 7 weeks operating time, corresponding to a lunar operational point well into the second lunar night. The tests are being conducted using simulated *Surveyor* operational loads and temperatures and have shown satisfactory performance data. Tests of the Eagle-Picher 20 amp-hr cells have been discontinued because the batteries did not demonstrate the required design capacity.

5. Power Management

Late in the period covered by this report, the decision was made to modify the power management system and incorporate an optimum charging system in order to utilize more fully the power available. This method of power control is described in the last bimonthly progress report. The system being designed has only one optimum charge regulator and one boost regulator instead of two as described previously. Circuit design on this system has begun and breadboards of parts of it have been constructed and tested.

G. Thermal Control

1. Compartment Group

In a continuing effort to optimize both the thermal control and packaging requirements of Compartments A and B, minor changes have been introduced in the compartment arrangements. These design improvements have in general resulted in (1) maximization of component packaging efficiency: i.e., minimum compartment surface area; (2) minimization of the wiring harness nighttime heat loss and weight; (3) optimized distribution of compartment internal power generation, and (4) provision for sufficient top surface area on both Compartments A and B (2.54 ft^2 and 1.9 ft^2, respectively) to dissipate the lunar day loads.

Table 16 lists the new compartment arrangements. In addition to component relocation between the two compartments, the components listed in Table 17 have been removed. These components will be designed to survive the lunar night (−300°F) and therefore will not require nighttime thermal control. Also listed in Table 16 is the compartment lunar day and night average power dissipation. The high-power-transmitter power dissipations are listed separately since they will require the definition of the Compartment A lunar day transient capability.

Table 16. Compartment arrangement

Compartment A				Compartment B			
Component	Volume, in.³	First day average power, watts	Night average power, watts	Component	Volume, in.³	First day average power, watts	Night average power, watts
Transmitters (2), low-power	366	5.0	3.3	Central command decoder	108	0.06	0.06
Receivers (2)	216	1.5	1.5	Central signal processor	168	1.05	1.5
Diplexers (2)	24	Negligible	Negligible	Engineering signal processor	108	0.167	0.167
RF transmission system	29	Negligible	Negligible	Power control system	174	4.68	1.71
Batteries (2)	1800	Negligible	Negligible	Tape recorder	360	0	*
TV decoder and processor	33	0.104	Negligible	Tape recorder auxiliaries	47	*	*
Mechanism (fraction) auxiliaries	59	*	*	X-ray spectrometer electronics	345	Negligible	Negligible
Scientific thermal auxiliaries	160	0.167	0.07	X-ray spectrometer auxiliaries	27	Negligible	Negligible
Subtotal	2687	6.781	4.87	X-ray diffractometer electronics	35	Negligible	Negligible
Transmitter, high-power	—	9.5	—	X-ray diffractometer auxiliaries	18	Negligible	Negligible
Total	2687	16.28	4.87	Thermal control auxiliaries	132	0.167	0.07
				Radiation detector auxiliaries	18	0.17	0.17
				Total	1542	7.1	3.67

*Not yet determined.

Table 17. Equipment removed from Compartments A and B

	Volume, in.³
Gas chromatograph auxiliaries	45
Subsurface sampler and processor auxiliaries	115
Surface sampler auxiliaries	29
Surface geophysical auxiliaries	133
Subsurface sampler and processor auxiliaries	92
Remaining mechanism auxiliaries	164
Altimeter-velocity sensor radar electronics	272
Total	850

Table 18. Estimate of lunar night heat losses

Heat Path	Compartment A, watts	Compartment B, watts
Supports	0.67	0.67
Thermal switches (0.132 watt/switch)	1.19 (9 switches)	0.79 (6 switches)
1 in. super-insulation (0.113 watt/ft²)	1.59	1.21
Wire leads	1.60	1.70
Total	5.05	4.37

Table 18 presents the current estimates of Compartment A and B lunar night heat losses. These estimates result in a lunar night power dissipation deficit of approximately 0.88 watt. Efforts to reduce the deficit include a possible redesign of the structural supports and/or an increase in the thickness of the super-insulation. Both alternatives will no doubt result in a lesser spacecraft weight penalty than that associated with an increase in power dissipation.

The present lunar noon steady state dissipating capability with the antenna/solar panel mast in its non-extended position is estimated to be 13.5 and 9.7 watts for Compartments A and B, respectively. With the mast raised by 43 in. these capabilities increase to 22.0 and 15.2. Compartment B capability has been increased greatly since the last report as a result of the removal of the telescope optics from above the compartment. View factors from the compartment radiating surfaces have been analytically estimated and are currently being verified experimentally using the JPL developed "view factor button."

The view factor button is a convex parabolic mirror, 1 in. in diameter. Used in conjunction with any spacecraft model, the device provides a simple laboratory method for determining radiation view factors. The button (Fig 91), is attached to the spacecraft surface and photographed from a position along the axis of evolution. The photographs are then enlarged and by use of a transparent calibrated grid, the view factor to the surrounding spacecraft structure (reflected by the button) can be determined.

Based on a high-power transmitter power dissipation of 37.5 watts in conjunction with a high power mode

utilization of 38 hr. during the first lunar day, preliminary transient analyses have been completed to determine the maximum transmitter on-time and duty cycle. The results, given in Figure 92, indicate a maximum on-time varying from 1 to 3 hr. between lunar noon and terminator, corresponding to a duty-cycle period of 18 to 75% utilization. As indicated in the figure, the total duty cycle period is greatly reduced when the planar array/solar panel assembly is in the extended position.

2. *Remote Subsystem Group*

Preliminary analyses of the vernier fuel and oxidizer tanks indicate that only fuel tank No. 2 (near leg 2) will require electrical heating during transit. All other tanks receive adequate insolation such that by proper selection of surface coating the temperature can be maintained above 20°F. Fuel tank No. 2 is completely shaded by the solar panel so that an assumption of no heating from the panel results in a typical requirement of 0.4 watt heating in conjunction with an insulating blanket having an effective emittance factor, f_ϵ, of 0.005. This can be met with 1 in. of aluminized mylar super-insulation.

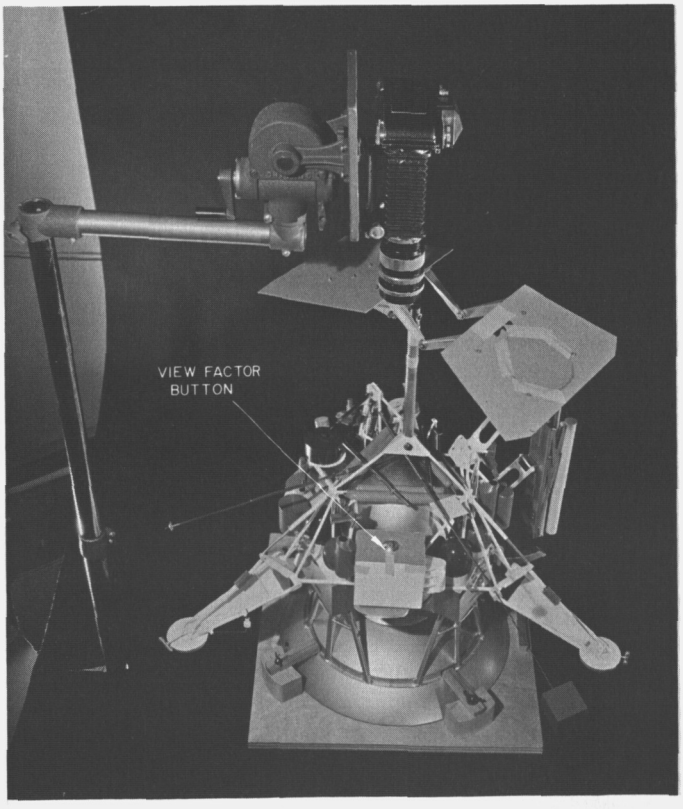

Figure 91. Determination of radiation view factors

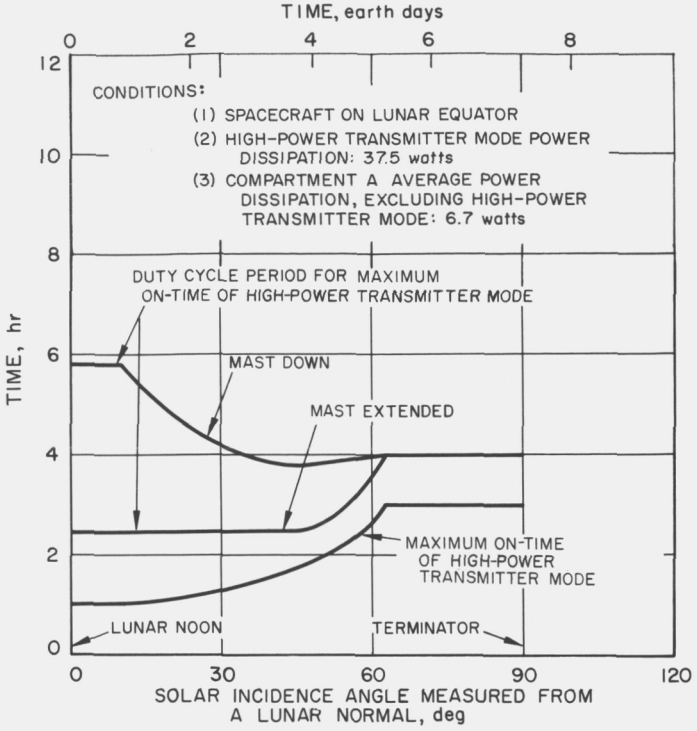

Figure 92. High-power transmitter duty cycle and maximum on-time

Since it has been shown that the doppler antenna dishes will reach —190°F at the end of transit, it is desirable to relocate both the klystron tube package and the signal data converter. Figure 93 shows the temperature history of the klystron box with various surface coatings. The figure assumes a minimum solar absorptance (0.1) and solar illumination of one end of the package. The figure indicates that proper coating selection can

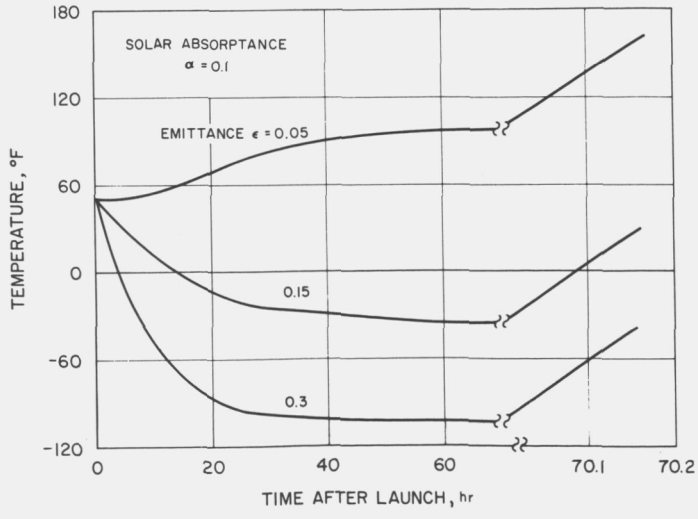

Figure 93. Klystron box temperature during transit

control the temperatures during most of transit and that the heat capacity of the unit will be adequate for transient control during the 5 to 10 min operating time period. The signal data converter has been relocated to receive direct insolation and will exhibit a similar temperature profile.

The effect of the altitude marking radar on retro-rocket engine thermal control has been established. Figure 94 indicates the temperature-time history of the retro nozzle both with and without the altitude marker radar attached, based on a constant propellant temperature of 50° F. With the radar attached the heat loss from the main retro is reduced by approximately 40%. Further design modifications are in progress to increase the marker radar electronics temperature (now at −20° F) to something above 0° F.

3. Scientific Instruments

Technical contacts have been established with all instrument suppliers in an effort to better define the thermal problems associated with each instrument. In order for Hughes Aircraft Company to become more familiar with the suppliers' thermal capability, many meetings have been held at the suppliers' facilities.

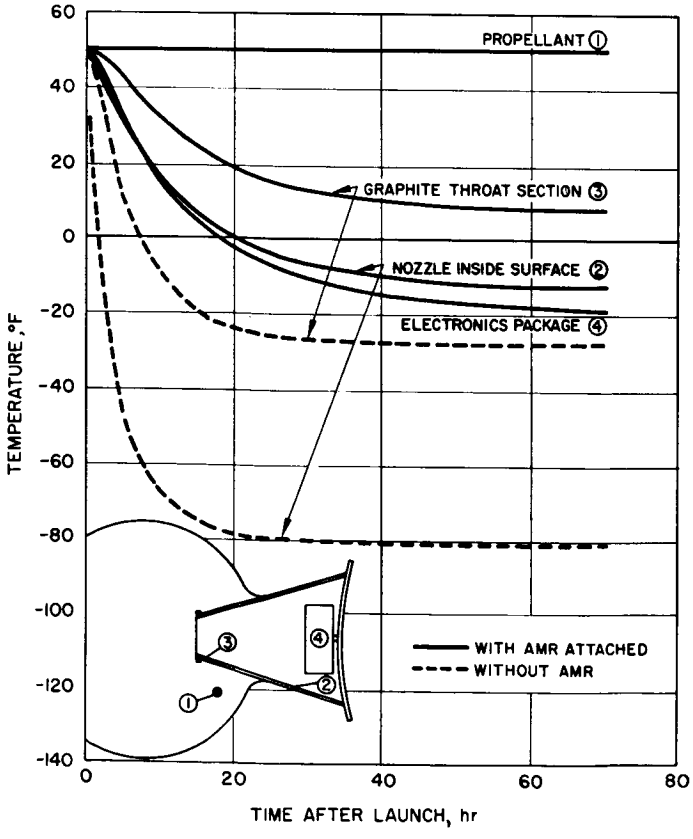

Figure 94. Retro-engine transient temperature during transit

Definition of the seismometer thermal requirements and the implementation of a suitable control technique continues to be one of the more difficult thermal problems. The instrument not only has a tight temperature range (±20°C) but also has been shown to be affected by nonsymmetrical temperature variations in the lunar structure directly beneath the legs. Since lunar temperature variations of 3° to 5° F between adjacent legs can cause measurable error in the instrument, the thermal properties of the lunar subsurface become very important in the design of the seismometer thermal control system.

The present design concept consists of adequate instrument insulation to achieve the ±20°C temperature variation and deployment of an insulating blanket over the lunar surface immediately surrounding the instrument in an attempt to minimize any nonsymmetric subsurface temperature variations. Since the lunar thermal properties determine the insulating blanket or "sombrero" size, JPL has indicated that the system should be optimized based on the two single-body lunar models shown in Table 19.

The analytically designed sombrero will then be checked for performance with a two body mode consisting of a 1-cm. layer of dust above a homogeneous layer of pumice with the following properties:

Thermal conductivity, $K = 6 \times 10^{-2}$ gm-cal/cm—°Csec

Density, $\rho = 1.0$ gm/cm^3

Specific heat, $C = 0.2$ cal/gm —°C

Absorptance, $\alpha = 0.93$

Emittance, $\epsilon = 0.875$

The layer of dust has the properties listed in the first lunar model above.

Surface and subsurface temperature variations of both the dust and rock models are shown in Figures 95 and 96.

Table 19. Single-body lunar models

Property	Homogeneous dust	Homogeneous rock
Thermal conductivity, K, gm-cal/cm − °C − sec	3×10^{-4}	5×10^{-4}
Density, ρ, gm/cm^3	1.8	3.0
Specific heat, C, cal/gm − °C	0.2	0.2
Absorptance, α	0.93	0.93
Emittance, ϵ	0.875	0.875

It is noted that neither model results in the surface temperature limits of 260 and —244°F.

Due to the extremely high power dissipation (35 watt total) during operation and the extreme wiring harness requirement, both the X-ray spectrometer and the X-ray diffractometer high voltage power supplies have been removed from Compartment A. To minimize the amount of high voltage wiring required, a new location adjacent to the soil analysis group has been selected. At the present time the necessity of lunar night thermal protection has not been determined. The survival temperature may be as high as —148°F. Should a heating requirement exist, even assuming a combination of both power supplies into a single unit, a scientific payload penalty of approximately 14.5 lb for 1.79 watts of heating must be accepted. Table 20 shows the various thermal capabilities and requirements of both the individual and combined high voltage power supplies.

Initial analysis of the radiation detector has indicated that if the entire instrument is maintained above —67°F, the resultant power requirement will be approximately 0.4 watt or equivalent to 3.2 lb of battery for the typical 450 hr heating period. Since the associated electronic circuitry dissipates only 0.015 watt, the requirement must be met essentially by heaters. Two alternatives presently exist. Both assume, as the *Surveyor* scientific instruments interface description indicates, that helium can be substituted for the argon gas presently used in the ionization chamber, giving the chamber itself lunar night operational capability and leaving only the few cubic inches of electronics to be thermally protected. An investigation is currently under way to determine if the electronics can be designed to survive the lunar night (—300°F). If protection is required, it can be either in the form of moving the electronics in question to Compartment B or providing point-source heating in order to minimize the thermal control power requirements.

4. Thermal Switch

Testing of the prototype switches during early September indicated that the closed conductance, while close to design requirements, was being limited not by the contact conductance but rather by the conductivity of the solder used to join the foils to the inner contact plug. A design change has been introduced and the new switches will go into thermal-vacuum test by mid-October.

As indicated throughout the development of the switch, the low thermal conductivity-high modulus of elasticity polystyrene switch case is not adaptable to heat sterilization at 125°C. An investigation to determine the thermal penalties involved in the utilization of a heat sterilizable material in place of the polystyrene has been initiated. Preliminary results indicate two candidate materials, both of which are thermally inferior to the polystyrene. The properties and associated thermal penalties of the three materials are listed in Table 21.

Table 20. High-voltage power supply thermal capabilities

Item	Combined HVPS	Diffractometer HVPS		Spectrometer HVPS	
		Specified	Passively attainable	Specified	Passively attainable
Maximum operating temperature[a]	185°F + (Diffractometer operating) 165°F (Spectrometer operating)	230°F	205°F +	140°F	178°F
Minimum operating temperature	[c]	−85°F	[c]	−40°F	[c]
Maximum non-operating temperature	127°F	257°F	125°F	257°F	123°F
Minimum non-operating temperature	−295°F	−130°F	−290°F	−130°F	−295°F
$T\Delta_{MAX}$ during run[a]	58°F (Diffractometer operating) 38°F (Spectrometer operating)	—	80°F	18°F	55°F
Power required to maintain night temperature to −100°C (−148°F)[a]	1.79 watts	—	1.59 watts	—	1.174 watts

[a]Important advantages of combined system.
[b]Plus sign indicates steady state has not been reached.
[c]Not yet determined.

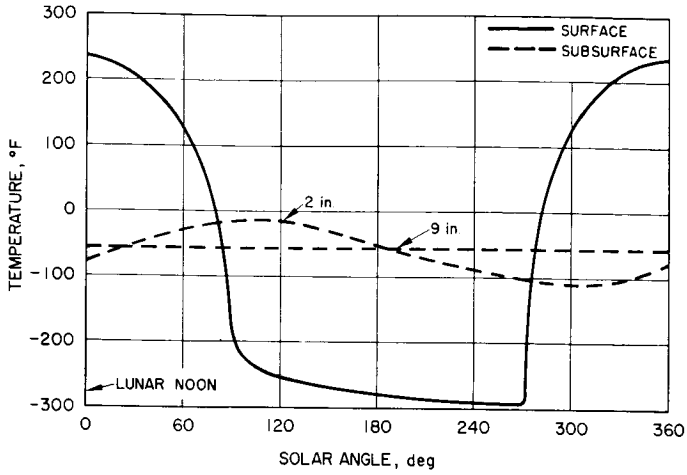

Figure 95. Homogeneous dust lunar model

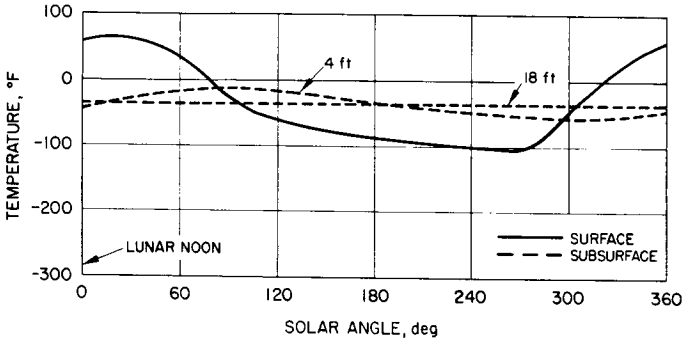

Figure 96. Homogeneous rock lunar model

The elastic modulus of the ablatalite is not presently known, and therefore the additional heating required to offset the lunar night heat loss through the switches cannot be estimated. At the present time, however, there is no excess of natural internal power dissipation, and therefore any penalty must be met by direct heating. The result would be a battery weight increase of approximately 8 lb/watt of heating required.

Table 21. Switch materials

Property	Polystyrene	Fiberglas laminate	Ablatalite
Thermal conductivity, K, Btu/hr ft°F	0.07	0.33	0.07
Elastic modulus, psi	0.5×10^4	6×10^4	*
Tensile strength, psi	$5\text{-}9 \times 10^3$	$2\text{-}3 \times 10^5$	8×10^3
Maximum usable temp, °F	170	260	400
Thickness required, in.	0.010	0.045	0.010*
Resultant additional heating required for Compartments A and B, watts	0	1.0	*

*Not yet known.

A second series of contact seizure tests is in progress. The contacts were allowed to outgas in the open position for 7 days prior to closure. The vacuum facility has a capability of about 10^{-7} mm Hg. The initial tests were conducted at this vacuum level, although they were allowed to outgas for only 2 days. The initial tests indicated no measurable seizure under static contact at pressures of 20 psi.

A preliminary test, consisting of submerging a switch radiator in liquid nitrogen (—320°F), has indicated that no fundamental radial thermal stress problem exists.

5. Super-Insulation

Due to the short development schedule, it has been deemed advisable to limit the testing of so-called semi-infinite blankets of ¼ mil aluminized Mylar super-insulation and to concentrate on verifying the over-all conductance of an insulated system similar to that of Compartment A and B. The effective conductance will then include not only the heat losses through the central undisturbed portions of the insulation but also those losses attributable to edge and corner effects as well as those attributable to wiring harness and support pass-throughs. The test compartment is 13 by 23 by 24.5 in. and has a 1 in. double wall available for insulation. Drawings have been completed and fabrication is in process. Testing is to be initiated in late October.

6. Surface Coatings

A program in conjunction with the Radiation Laboratory at UCLA is presently under way to determine the optimum thermal radiation coatings for the various portions of the spacecraft. The most critical requirements involve low absorptance-high emittance surfaces (good radiators), and therefore attention will be focused on achievements in that area.

The low α-high ϵ coatings currently under investigation, together with their prospective areas of utilization, are as follows:

Thermal switch radiators

(1) Anodized 1199 aluminum
(2) Vycor second surface mirror
(3) Mylar second surface mirror
(4) Tedlar second surface mirror
(5) White paint such a Vita-Var or Pittsburgh DMA 311

General vehicle use

(1) White paint such as Vita-Var or Pittsburgh DMA 311
(2) Mylar second surface mirror
(3) Tedlar
  (a) Second surface mirror
  (b) White pigmented film

Initial results indicate that a 1/16 in. thick sample of Vycor (aluminized back surface) yielded properties of $\alpha = 0.122$, $\epsilon = 0.854$, and the Pittsburgh Paint (DMA 311) was found to yield $\alpha = 0.244$, $\epsilon = 0.910$. The data on the Tedlar and Mylar samples are not yet available.

The glass surfaces are subject to shock fracture. This aspect will be investigated on panels now being assembled. The test panels will be subjected to the critical shock and vibration environments. Tedlar mirror film should be superior to Mylar for infrared emittance by virtue of its large absorption band in the infrared. The plastic mirror films are expected to be vastly superior to glass in resisting shock. The anodized 1199 aluminum sample preparation has indicated some difficulty in anodizing thin foils due to the extreme softness of the aluminum. An order has been placed for thick plate stock of 1199 so that the thermal switch radiator could be made integral with the anodized control surface. The effectiveness of white paints depends to a large extent on the method of application and their "yellowing" characteristics. Vita-Var has been recently recommended; however, verification data have not yet been received.

7. Heating in Vernier Engine Exhaust

A preliminary estimate of the effects of vernier engine exhaust on adjacent *Surveyor* components has been made. The analysis involves approximation of free jet boundaries and calculation of pressures and heat transfer rates at surfaces within these boundaries using free molecular theory. First indications are that a small insulating layer is required on exposed surfaces of the crushable landing pads and the doppler antenna, involving a net weight increase of less than 1 lb. Insulation may also be required on the nozzle of the main retro-engine; calculations in this area have not been completed. Forces appear to be negligible.

Using engine characteristics furnished by Reaction Motors Division, and assuming an isentropic expansion, an exhaust Mach number of 4.9, exhaust temperature of 1178°F, exhaust velocity of 9310 ft/sec, and density of 7.67×10^{-6} slugs/ft^3, computations were made for the nozzle exit plane. The assumption of a Prandtl-Meyer expansion to zero ambient pressure then resulted in a stream turning angle of 94.5 deg from the nozzle axis. The method of Latvala (Ref 1) was next used to estimate the boundary of the free jet; roughly a circular arc of 53 in. radius tangent to the Prandtl-Meyer expansion line at the exit plane. This line encompasses portions of the doppler antenna, the crushable landing pads, and the retro-engine nozzle.

Local pressures were calculated using free-molecular theory (Ref 2) and density gradient estimates (Ref 3) for conditions
sure accommodation coefficient of 0.5 and impingement on a surface normal to the flow velocity, pressures of 0.0161 lb/ft^2 were estimated on the antenna and pads and 1.61 lb/ft^2 on the retro nozzle.

Local heat transfer rates were also estimated using the Schaaf and Chambre free molecular theory. A thermal accommodation coefficient of 1.0 and normal impingement resulted in heat transfer rates of 0.076 Btu/sec ft^2 on the antenna and pads and 7.6 Btu/sec ft^2 on the retro nozzle. An upper temperature limit of approximately 300°F is permissible for the aluminum honeycomb of which the crushable pads are likely to be fabricated. If the emissivity is 0.8, then a peak surface temperature of 270°F is indicated. It is likely, however, that a low emissivity coating is required for transit protection. If the emissivity is 0.1, an insulator 0.02 in. thick is necessary to limit honeycomb temperature to 300°F. (Thermal properties of the insulator are conductivity of 0.15 Btu/hr ft°F, density of 120 lb/ft^3, and specific heat of 0.25 Btu/lb°F, values typical of phenolic materials.) This represents a total weight requirement for the three pads of 0.47 lb. Similar analysis for the doppler antenna indicates an insulation weight of approximately 0.4 lb.

Thermal analysis of the retro-engine nozzle under these heating conditions has also been started. Although it appears likely that an insulation requirement exists, the amount depends on the results of a detailed two-dimensional analysis which has not yet been completed.

H. Engineering Mechanics

1. Touchdown Dynamics

Final values for the landing gear design parameters, optimized on shock absorber load and "package" acceleration considerations, have been established. (Package

acceleration refers to the acceleration of a point displaced 3 ft laterally from the spacecraft center of gravity.) An investigation has shown that shock absorber loads increase with site slope. Parameter optimization was carried out with touchdowns on a 15 deg slope with vertical and lateral velocities of 20 and 5 ft/sec, respectively.

With the gear parameters established, an investigation was made to determine the worst landing conditions from a load and acceleration viewpoint. Variation of package acceleration with touchdown incidence (Fig 97) was determined. The dispersion ellipses relate touchdown incidence angle and lateral velocity. Ellipses A, B, and C each have a maximum lateral velocity of 5 ft/sec and maximum incidence angles of 5, 10, and 7 deg, respectively. Shock absorber load variations are similar to the acceleration variations shown. A design point corresponding to the maximum load and acceleration along Ellipse C has been chosen. This corresponds to a maximum allowable load and acceleration of 8900 lb and 16 g, respectively. A landing velocity boundary, corresponding to these levels is given in Figure 98. It lies well outside the desired landing criteria dispersion ellipse.

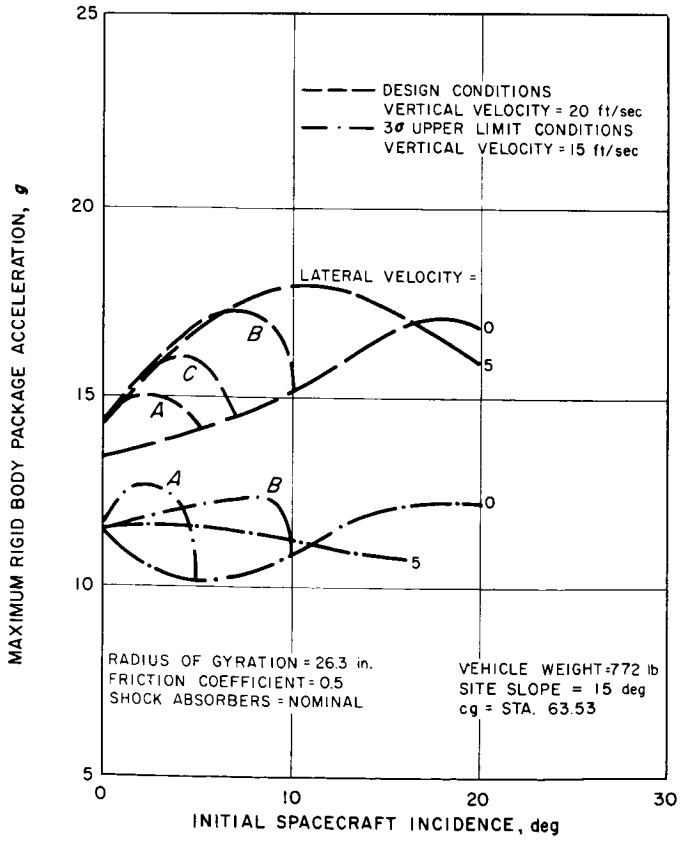

Figure 97. Package acceleration vs touchdown incidence

Figure 97 also shows the comparison between package accelerations levels at the design landing condition and at the 3σ upper limit flight control condition. Shock absorber load variations give corresponding levels of approximately 9000 and 5600 lb.

Spacecraft touchdown stability has been investigated extensively. Stability boundaries — vertical velocity versus lateral velocity — for various site slopes are shown in Figure 98. In the configuration considered, all boundaries lie outside the desired landing criteria dispersion ellipse for site slopes of 15 deg or less. The term Δcg denotes the center of gravity height above spacecraft station 47.48, the plane of the landing gear pivot points. Variation in Δcg between 14 and 20 in. yields less than 1 g change in accelerations and a few hundred pounds change in shock absorber loads. The effect on stability is shown in Figure 99. An increase in Δcg reduces stability. An increase in radius of gyration reduces stability (Fig 99), but also effects a fairly large reduction in load and acceleration levels. The effect of small ($<5\%$) variation in touchdown weight from the nominal 772 lb on loads and accelerations has been shown to be small but beneficial. This is also true of the effect of pitch rate. The effect on stability and loads of variations in friction coefficient has yet to be determined. Earlier work, however, has shown that a decrease in friction coefficient results in improved stability but also increases center of gravity vertical accelerations.

2. *Full-Scale Drop Tests (T-1)*

Preparations are in progress for a series of drop tests of a full-scale model of the spacecraft (T-1) under simulated lunar gravity. Approximate lunar gravity will be simulated by applying to the spacecraft center of gravity, through a cable, a constant upward lift force equal to about five-sixths of the vehicle's earth weight. This "anti-gravity" force will be maintained nearly constant and vertical as the vehicle drops onto the simulated lunar surface, as well as during its subsequent motion on the surface.

Surveys of existing local facilities used in drop-testing aircraft revealed a simple method for maintaining a constant force in the lift cable. A piston and air cylinder is connected to a large precharged reservoir. If the volume of the reservoir is large enough, the piston motion has a negligible effect on the piston pressure. Such an arrangement can be readily designed to accommodate

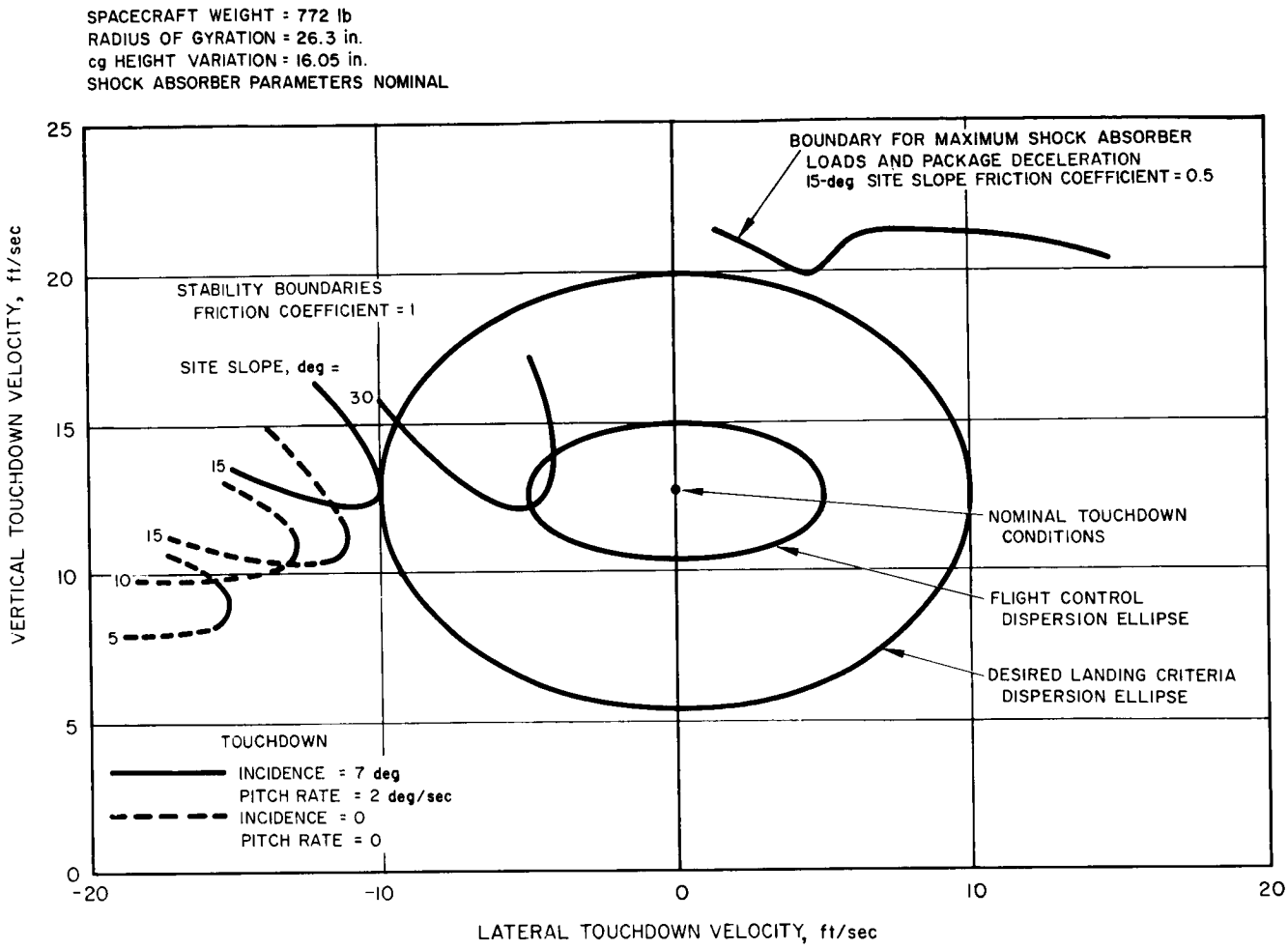

Figure 98. Landing velocity boundaries

as much vertical cable motion as required. However, some of the drop tests planned for T-1 include downhill drops onto highly sloped surfaces; as a result, the spacecraft is expected to move through considerable lateral distances before coming to rest. The fact that the anti-gravity force cable must be kept vertical during this lateral motion imposed an additional design requirement on the constant lift apparatus which existing facilities were unable to accommodate. This difficulty, however, was overcome through the design of a unique rolling pulley mechanism which will cause the constant lift cable to follow the lateral motion of the spacecraft automatically without imposing additional lateral forces of any significance.

A mockup of the Hughes rolling pulley design (Fig 100) has been constructed, subjected to a series of proof tests, and found to operate satisfactorily. It will be incorporated into the final drop test setup. Developmental tests have also been performed on the constant force piston cylinder device and a satisfactory, low mass, low friction design has been obtained (Fig 101).

A schematic of the final drop test setup which will incorporate all the anti-gravity apparatus is shown in Figure 102. A simple scaffold (a) about 50 ft high, will straddle a 30 by 20 ft lunar surface platform (b) and support the track (c) for the anti-gravity force mechanism. The scaffold will also support a bifilar pendulum apparatus (d) which will be used to drop the spacecraft (T-1) with the required initial velocities. The constant vertical lift apparatus consists of constant pressure cylinders (f) and (g) which maintains a constant force in cable (h) and a lightweight pulley trio (j) which will not allow the attach cable (k) to deviate significantly from the vertical during motion of the spacecraft.

The T-1 vehicle is being constructed so that its center of gravity and radius of gyration can be adjusted to permit investigation of the landing stability for reason-

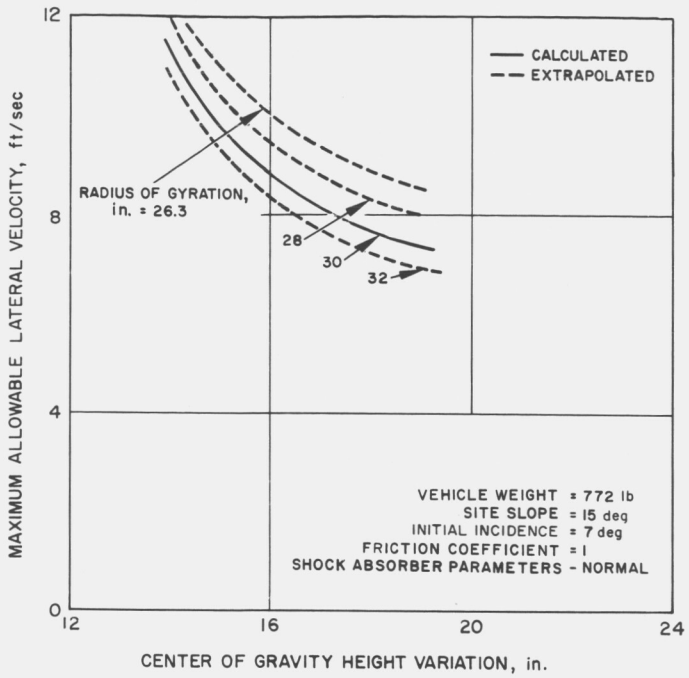

Figure 99. Effect of center of gravity height variation

able excursions in these variables. The drop tests can therefore be performed on a representative configuration to determining the ultimate center of gravity location or radius of gyration of flight-type spacecraft.

3. Shock Absorber Procurement

A letter contract with National Water Lift Company (NWL) of Kalamazoo, Michigan, was initiated on August 9, 1961 for development of the shock absorber. The basic shock absorber design consists of a liquid spring and orifice type damping for which the orifice flow is programmed as a function of stroke by means of a metering pin to alleviate high initial loads. A layout of the shock absorber column is shown in Figure 103. Although the hydraulic preload is sufficient to keep the column fully extended for the post landing condition, a cam detent lock and a squib initiated lock are incorporated for reliability. The basic layout (Fig 103) and preliminary drafts of the reliability program and flight acceptance test specification have been completed and coordinated with NWL. Design evaluation has indicated

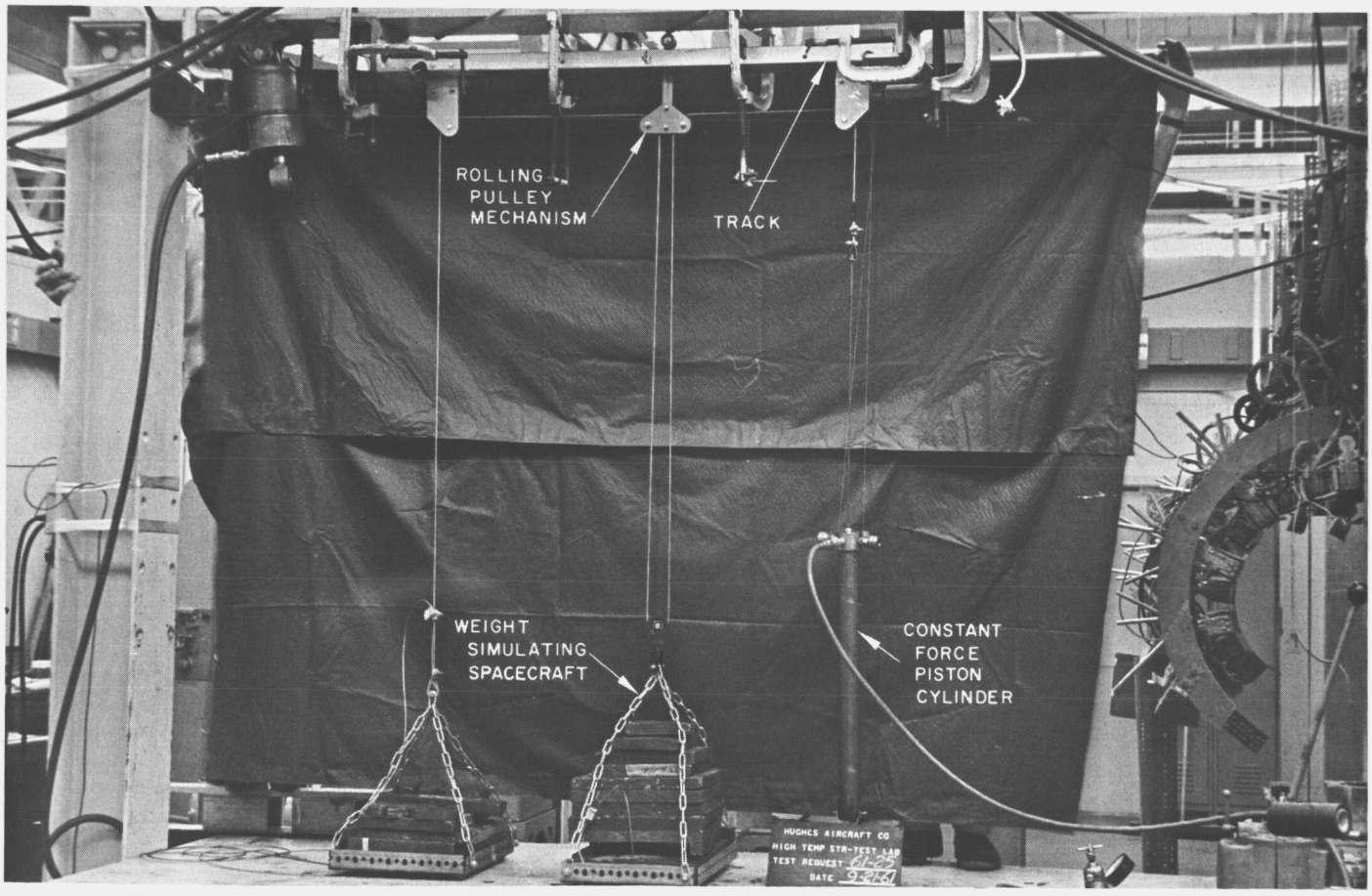

Figure 100. Rolling pulley constant vertical force device

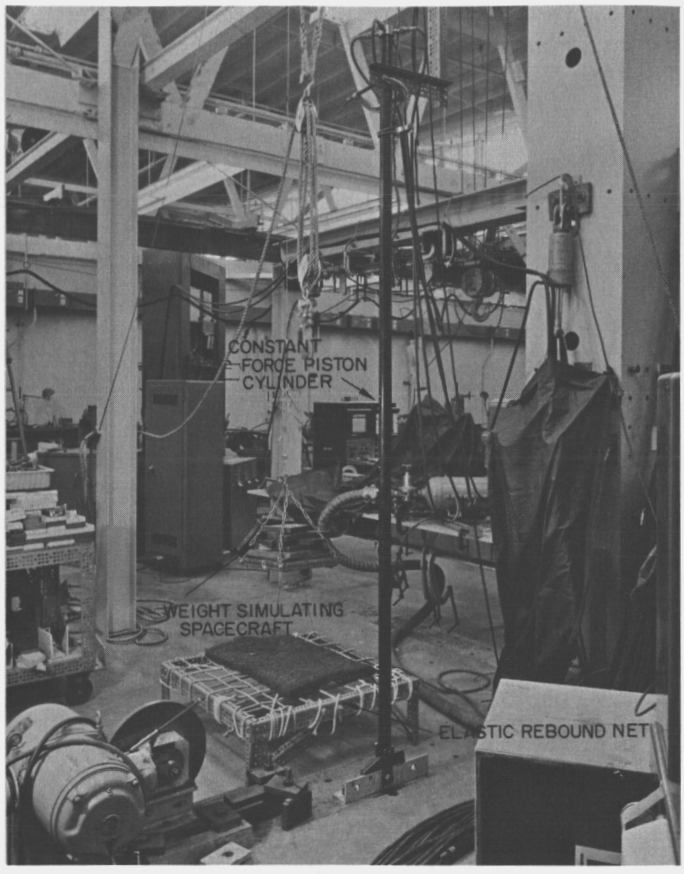

Figure 101. Constant force drop test device

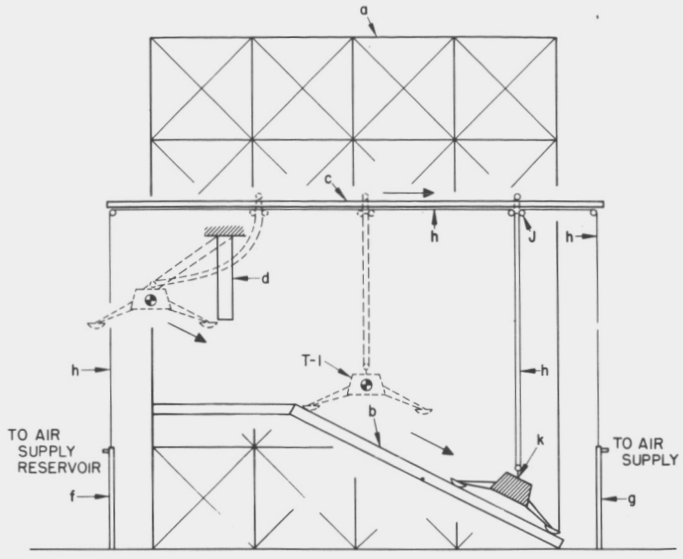

Figure 102. Lunar gravity drop test facility

that a simple spring-bellows temperature compensator is desirable and that the shock absorber will fail as a pressure vessel before any excessive-deflection condition is reached.

Development testing is being carried out on several components. A simulated cam detent lock mechanism has been built for verifying the design of this unit for both holding capability and override properties. A cylinder, piston rod, and gland seal assembly to duplicate the liquid spring is being built. This unit will be pressurized to preload conditions and periodically checked for leakage over an 18-month period to evaluate the storage life effects on the seals. A fully representative cylinder, rod, and gland assembly has been built for the development testing of the liquid spring characteristics and damping orifice design.

4. Separation Dynamics

The analysis of the *Surveyor-Centaur* separation function has been re-examined using present data for the separation clearance envelope and for weight and balance. The addition of an impulse to the *Surveyor* due to

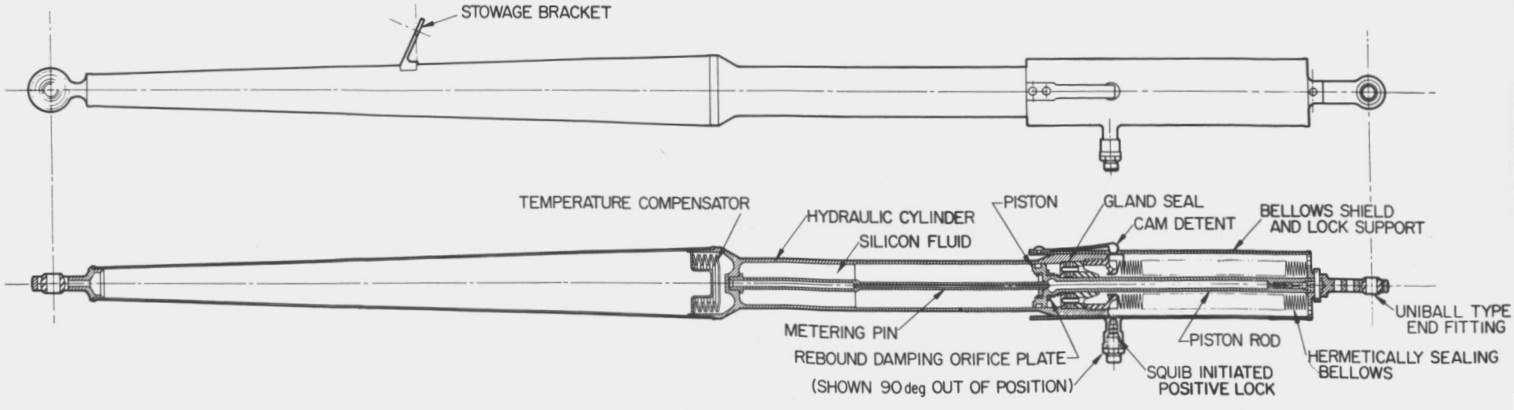

Figure 103. Landing gear shock absorber column

non-uniformity in operation of explosive bolts has also been included for an extreme case. Assuming that the impulse per bolt is 1.33 lb-sec and that one bolt gives the maximum impulse while the remaining two bolts contribute nothing (giving the worst pitching impulse with the lowest separation impulse), the spring parameters presently specified are still satisfactory. The resulting separation velocity is 5.0 ±0.2 in./sec and the final pitch rate is 1.42 deg/sec for this condition. Because GDA has been assigned responsibility for the payload adapter and the separation device, further work on this task will be discontinued except for a limited monitoring function.

The jettisoning of the retro-rocket using the vernier thrust as the separation mechanism has also been investigated. For this analysis, it is assumed that the spacecraft and retro-rocket have a common pitch rate prior to separation; after separation, the retro-rocket continues to pitch but the spacecraft angular velocity is eliminated by the flight control system. Figure 104 defines the maximum allowable retro-thrust as a function of the initial spacecraft/retro pitch rate for various levels of the vernier thrust. It has been decided to program maximum vernier thrust after the tail-off of the retro-thrust, but means of assuring that the retro-thrust is below the maximum allowable value at separation have not yet been selected.

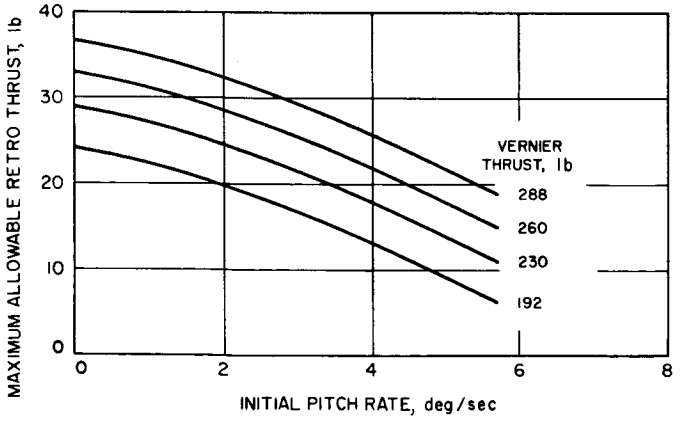

	Spacecraft	Retro-Rocket
Lateral offset of thrust axis, in.	0	0.2
Angular misalignment of thrust axis, deg	0	0.1
Mass, slug	27.4	4.225
Moment of inertia about cg, slug-ft²	—	6.05

Figure 104. Maximum retro-thrust vs pitch rate at separation

5. Structural Design Criteria and Loads

A preliminary version of the Structural Criteria and Loads document has been published and used as a basis for a formal review. Key points of the document were scope; margin of safety; boost, descent, and landing load factors; fatigue criteria; boost phase vibration input; design load conditions; superposition of loads; and temperatures.

The criteria govern primary structure but also provide information for the design of components attached to the spaceframe. No weight, center of gravity, moment of inertia, or elastic deformation restrictions were imposed. The response to sinusoidal vibration input at the separation plane was estimated to be ten times the input level, based on the assumptions that the effective equivalent viscous damping is 5% and that the major resonant frequencies do not coalesce. The response to white Gaussian random input was calculated on the basis of one major resonance for each component – i.e., proportional to the square root of the resonant frequency times the dynamic amplification factor times the power spectral density at that frequency.

The design load factors which resulted from the review and subsequent discussions with JPL personnel are shown in Table 22. The vibration load factors were derived from Tables 23 and 24, which reflect revised

Table 22. Boost flight conditions limit design load factors

n_z = load factor in longitudinal or thrust direction, positive downward
n_t = load factor in any lateral direction

Boost flight condition	Acceleration, g			
	Liftoff, maximum q and Mach 1		Remainder of powered flight	
Loading	n_z	n_t	n_z	n_t
Quasi-static	2.2	±0.4	0-5.8	±0.1
Sinusoidal vibration (zero to peak)	$\pm 25.0\ \beta_i$	$\pm 20.0\ \gamma_i$	$\pm 25.0\ \beta_i$	$\pm 20.0\ \gamma_i$
Random vibration (3σ value)	$\pm 4.8\ \lambda_i$	$\pm 4.8\ \lambda_i$	$\pm 2.1\ \lambda_i$	$\pm 2.1\ \lambda_i$

Component	β_i	γ_i	λ_i*
Retro-rocket	0.20	0.12	0
Compartment A	1.00	0.63	0
Compartment B	1.00	0.63	0
Soil analysis group	0.80	1.0	0
Planar array antenna and solar panel	1.00	0.63	0
Subsurface sampler	1.00	0.63	0
Vernier tanks	0.80	1.00	0
Flight control sensor group	0.80	1.00	0
Surface sampler	0.80	1.00	0
Nitrogen tank	0.80	1.00	0
All other	0.80	1.00	1.00 to 2.00

*For items whose fundamental frequencies are above 100 cps but less than 400 cps, $\lambda_i = 0.1\ \sqrt{\text{fund freq.}}$ Frequency estimates to be supplied later.

Table 23. Mechanical input vibration at *Surveyor/Centaur* separation plane[a]

Input axis	Frequency, cps	Level	Remarks
Longitudinal	5-40	2.5 g O-p VFSW[b]	Throughout powered flight.
	40-1500	2.0 g O-p VFSW	
	100-1500	White Gaussian acceleration, 2.0 g rms	Throughout powered flight except during liftoff, maximum q and/or Mach 1.
	100-1500	White Gaussian acceleration, 4.5 g rms	During liftoff, maximum q and/or Mach 1.
Lateral	1-2.5	2.0 in. O-p VFSW (1.28 g maximum)	Throughout powered flight.
	2.5-40	1.25 g O-p VFSW	
	40-1500	2.0 g O-p VFSW	
	100-1500	White Gaussian acceleration, 2.0 g rms	Throughout powered flight except during liftoff, maximum q and/or Mach 1.
	100-1500	White Gaussian acceleration, 4.5 g rms	During liftoff, maximum q and/or Mach 1.

[a]Applicable to all components and assemblies except that, due to impedance effects, input may be depressed so that retro-rocket will not have response in excess of specified values, provided retro-rocket resonant frequencies are well above *Atlas/Centaur* lower bending frequencies.
[b]Variable frequency sine wave.

Table 24. Assembly vibration (any input axis)[a]

Input axis	Frequency, cps	Level	Remarks
Any	100-1500	White Gaussian acceleration, 2.0 g rms	Throughout powered flight except during liftoff, maximum q and/or Mach 1.
	100-1500	White Gaussian acceleration, 4.5 g rms	During liftoff, maximum q and/or Mach 1.

[a]Though neither source nor transmittal mechanism of high frequency vibrations are completely determined, vibration levels applied at attachment of equipment assemblies may not be less than those shown.

mechanical vibration information as it appears in the final version of JPL Specification 30240. Both axial and quasi-static loads are to be applied simultaneously, but only the maximum or minimum load resulting from the root sum square of the sinusoidal and random vibration in one direction at a time is to be superimposed. In cases where the major resonances are below 100 cps, the random vibration is negligible. The response of major items whose resonances occur outside the retro-rocket resonance band appears too high based on information supplied by GDA.

In order to assure that each spaceframe tube and joint is subjected to its maximum requirement in the absence of information defining the relations between the internal and external loads, arbitrary but characteristic frequencies were assigned to the various items attached to the spaceframe. The vibration load factors are applied first all in one direction and then successively in the opposite direction to form the other design conditions. Hence, the design conditions are like normal modes.

The lunar landing loads, including dynamic overshoot, are less than 30 *g* vertically coupled with small lateral accelerations. The maximum lateral acceleration, due in large part to angular acceleration, is about 30 *g* at the antenna. The simultaneous vertical acceleration in this condition is less than 15 *g*. Only one case has been studied in detail to determine the elastic transient response.

Margins of safety of 0% on yield and 25% on ultimate strength have been used to provide adequate structural reliability based on MIL-HDBK-5 *A* values (corresponding to values guaranteed by manufacturers) and 3σ applied load values. No margins on yield and 10% on ultimate strength are to be associated with 5σ or greater applied load values.

At the review with JPL, the need was cited for investigation of thermal stresses at the time of impact and during lunar operation. Plans for verification of inputs and responses shown in the criteria include S-1 and S-2 vibration tests, landing tests, analog computer studies, *Centaur* research and development flight vibration data acquisition, retro-rocket and vernier firing vibration measurements, and other static tests.

6. Dynamic Load Studies

Analytical studies have been completed in two areas: retro-rocket response to mechanical vibration and spacecraft response to landing shocks, in order to derive improved estimates of the dynamic loads to be imposed on the spacecraft. Analog computer studies for boost and

landing loads are in progress at Computer Engineering associates.

A separate analysis of the retro-rocket has been made in order to determine the effects of the viscoelastic properties of the propellant material on structural loads during the boost phase. The mechanical properties of the propellant were taken from data published by Space Technology Laboratories, Inc. The STL Reference 4 shows the properties of a polyurethane inert solid propellant material and experimental data from a frequency response test of a system composed of the material. The data define the elastic properties and a displacement-proportional damping property of the material. This damping property was converted to equivalent velocity-proportional or viscous damping in order to use existing computer programs.

The analytical model of the retro-rocket is the lumped mass-spring-damper system shown in Figure 105. The model shows an element for the nozzle mass and five elements for the mass of the propellant and its container. Four springs and four viscous dampers represent the elastic and damping properties of the propellant. The elasticity of the container is shown by a spring, and the retro-rocket support structure is shown by a spring and damper.

To determine the retro-rocket response during the boost phase to a vibratory axial input at the spacecraft/*Centaur* separation plane, the model was forced axially at the spring support over the frequency range from 0 to 1300 cps. Maximum axial support loads occurred at 46 cps, the first natural frequency of the system.

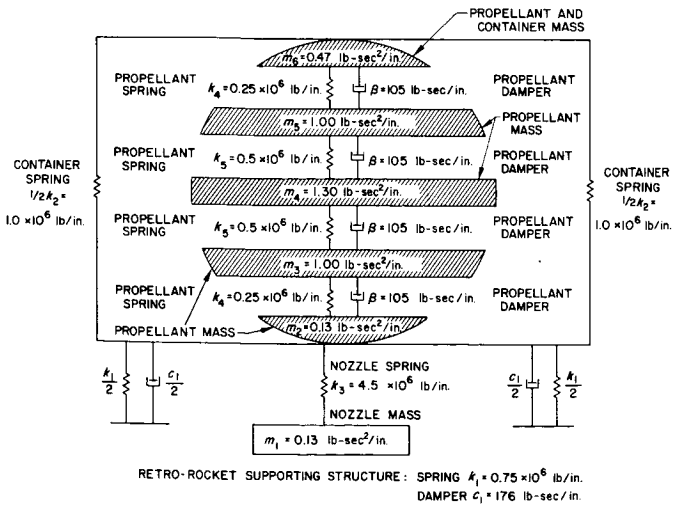

Figure 105. Mathematical model for retro-rocket study

The spring force was 11.5 times the weight of the retro-rocket. Previous analyses for load factors of the spacecraft treated the retro-rocket as a rigid body and assumed an amplification factor of 10.0.

Preliminary studies have been performed to determine the dynamic loads acting on the spacecraft components during landing. The input forces used in these studies were obtained from rigid-body analyses of the motion of the spacecraft after impact. The mathematical model to which these forces were applied is shown in Figure 106. The results of these studies indicate that some of the components will undergo accelerations approximately twice as great as the rigid-body accelerations of the spacecraft. Only one vertical impact has been analyzed so far; other conditions will be analyzed after a suitably complex mathematical model of the spacecraft has been established.

A subcontract has been awarded to Computer Engineering Associates for more detailed analog computer studies of the dynamic response of the *Surveyor* spacecraft to various boost and landing dynamic load environments. The subcontract is divided into two phases. Phase I involves the formulation of an idealized three-dimensional mathematical model of the spacecraft from which bending moments, axial loads, and torques in all the spaceframe members may be measured on the analog computer or deduced therefrom. This model will be limited to 80 degrees of freedom and 120 stiffness elements. If a sufficiently comprehensive model can be devised, it will be simulated on the CEA direct analog computer and subjected to various dynamic loads, constituting Phase II. The information to be gained from this phase will include sinusodial frequency response characteristics (transmissibility curves), random response, and transient touchdown response, of units and structure. In addition, a design for the basic framework will be evolved by an iteration technique, taking into account the behavior of the spaceframe in the critical loading conditions.

The results of the study will be of value in indicating design changes which might result in decreases in structural weight. Work under this contract was begun on September 27, 1961 and is expected to be completed before January 1962.

7. *Lateral Vibration Test (S-1)*

The detailed test plan for the lateral vibration test of S-1 has been established and the spaceframe model

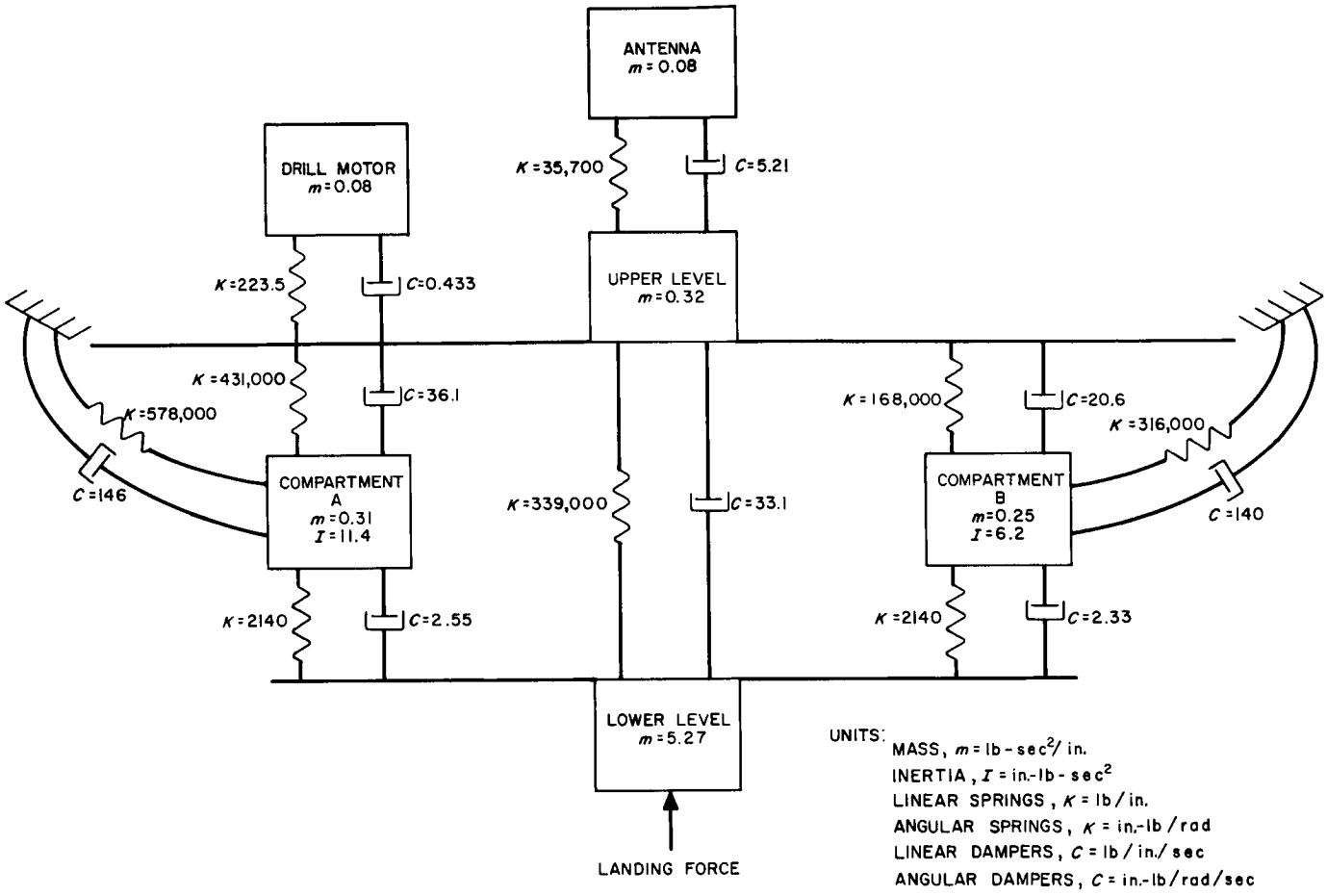

Figure 106. Mathematical model for landing loads

is being instrumented. The test will be a lateral sinusoidal vibration test in the 5 to 200 cps frequency band on the newly acquired slide table driven by the Hughes 25,000 lb 249 Calidyne shaker. Three configurations will be studied: Configuration A — S-1 spaceframe, ballasted units on a rigid fixture; Configuration B — S-1 spaceframe, ballasted units, and Hughes payload interconnect (9 in. shorter than present design); and Configuration C — S-1 spaceframe, ballasted units, and Hughes payload adapter with Y9052a Scotchfoam bonded to the interior. Configuration A will be tested in six lateral directions; B and C, in two lateral directions each.

Fifteen accelerometers are being attached to the large mass units (retro-rocket, Compartments A and B, antenna mast, and drill) in order to obtain lateral translational accelerations and some pitching-against-the-spaceframe angular accelerations. Forty-nine strain gages to be used for static tests also are being attached to the spaceframe as shown in Figure 107. The strain gage data should prove helpful in correlating rigid body accelerations with internal loads and providing joint design data. Four potentiometers are being attached to the antenna to measure its motion in order to clarify the shroud interference problem.

Consolidated Electro-Dynamics recording oscillographs will be used to record the data. The response of two of the accelerometers on the simulated retro-rocket and Compartments A and B will be monitored on oscilloscopes to assure loading does not exceed structural capability. Logarithmic sweeps of 10 min. each will be used to determine resonant frequencies and maximum accelerations. Studies at particular frequencies will be conducted as required. It is planned to complete the tests by November 15, 1961 and data reduction by December 22, 1961.

8. *Spaceframe Stress Analysis*

A matrix analysis of the spaceframe is currently being programmed which will provide the forces, torques, and bending moments in all structural members. The struc-

CONFIDENTIAL

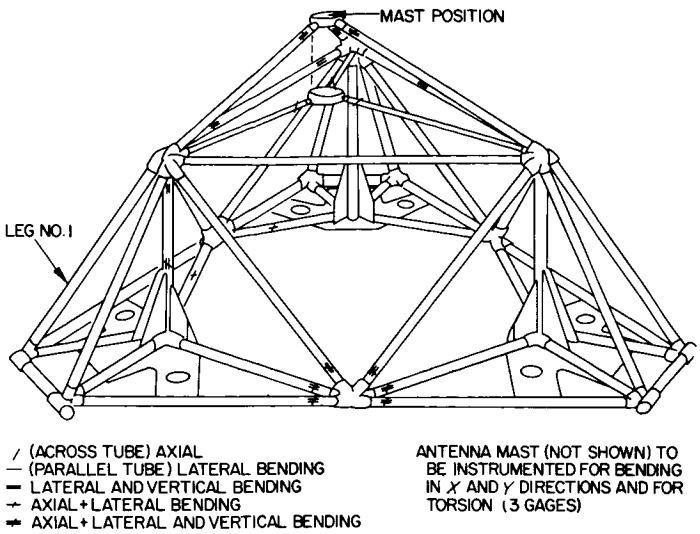

Figure 107. Strain gage locations for lateral vibration test

ture is analyzed as a unit: i.e., all structural members are considered at one time. Loads from the component masses are transmitted to the spaceframe tubes through the attaching brackets. However, the components and their supporting brackets are not considered part of the structure proper.

The spaceframe is first analyzed as a pin-jointed truss in order to obtain a first approximation of the axial loads at the ends of the tubes. This solution is later corrected to obtain the effect of tube bending on axial loads. The spaceframe is then solved as a set of fixed-ended members to obtain bending and twisting moments at the ends of the tubes. Joint deflections are accounted for in this portion of the problem. Springs are used to simulate the support provided by the adapter during boost.

In the analysis, the matrices defining structural behavior are set up by a digital computer program. The load matrices are set up in an independent program so that the tapes containing the inverse of the major matrices may be used repeatedly for many different load cases. Following the actual stress analysis, the effects of changes in tube sizes will be considered.

Thermal loading conditions will be the first to be treated. Such conditions involve temperature distributions which may result from sterilization, retro and vernier engine firing, and solar radiation. The calculation of stresses caused by exposure of the spacecraft to a possible temperature distribution during heat sterilization will be completed by mid-October. The second problem will consider the maximum-load touchdown case, which will be critical for most spaceframe members. Stresses caused by thermal gradients during landing will be computed and superposed on the load case.

9. *Material Properties Tests*

In order to supplement the small amount of data available concerning the effects of the space environment on metals, a limited test program is being planned. Specimens of the primary structural materials (7178-T6 and 7075-T6 aluminum) will be exposed to a hard vacuum in order to determine the degree of surface roughness incurred during transit. An attempt will also be made to perform short-time fatigue tests of aluminum specimens in a vacuum to simulate boost vibration. Tests will be performed to measure the effect of extremely low temperatures on impact strength and notch sensitivity.

I. Propulsion

1. *Introduction*

The spacecraft mid-course correction, attitude control during main retro operation, and incremental velocity corrections are accomplished by a liquid bipropellant vernier propulsion system. Main spacecraft deceleration during the terminal phase of flight is performed by a spherical solid propellant retro-rocket engine. Development of the vernier system and main retro-engine has been subcontracted to the Reaction Motors Division (RMD) and the Elkton Division, respectively, of Thiokol Chemical Corporation.

2. *Progress Summary*

During the report period, fabrication and testing of experimental propulsion system components and assemblies have been the principal subcontract activities. Design of all experimental configurations has been completed and design of the flight systems are in the final phases. In addition, major effort has been devoted to the fabrication and checkout of special test equipment. Three significant milestones have been reached: (1) the successful test firing of the first heavy-wall main retro-engine, (2) fabrication and checkout of the RMD high-altitude test facility, and (3) completion of contract negotiations with the two subcontractors.

Plans for the altitude test program are near completion. A comprehensive study of the capabilities of available altitude test facilities with respect to the specific program objectives has been the principal task. The program objectives include the evaluation of performance and heat-transfer and vibration effects with respect to both the main retro and the vernier propulsion systems.

Design integration of both the main retro and the vernier propulsion system with respect to the spacecraft is near completion. Only minor modifications are expected in the future, as the over-all system design becomes finalized. Of specific significance was the location and attachment of the vernier propulsion system components, including the line routing, and optimization of the main retro-spaceframe attachment interface.

3. *Main Retro-Engine*

The first main retro-engine was successfully fired on August 25, 1961. The thermocoupled engine for use in temperature gradient studies and the second engine for test firing have been cast. The design of the flight-type inert components is near completion. Thiokol has placed a CPFF contract with Kaiser-Fleetwings Division for the fabrication of the flight-weight case and has requested from qualified vendors for fabrication of the flight-type altitude nozzle. Proposals have been received and evaluated for fabrication of the horizontal test stand and altitude test facility.

a. Rocket engine testing. In the firing of the first main retro-engine, the major test objectives were the evaluation of: (1) engine ballistics, (2) inert component design, and (3) the pyrogen ignition system. The test was conducted using a heavy wall case, containing the flight type case insulation, a sea-level nozzle, and 1427 lb of propellant. The engine was mounted in a horizontal thrust stand and was conditions to 70°F. Prior to firing, the internal cavity was evacuated to a pressure corresponding to a simulated altitude of 82,000 ft. The recorded data were: (1) two channels each of pyrogen and chamber pressures, (2) two thrust channels, (3) eight thermocouple locations, and (4) nine strain gages located on the case exterior.

Figure 108 shows the retro-engine during operation. The test results (Fig 109) compared favorably with the predicted retro-engine ballistics. No evidence of combustion instability was detected.

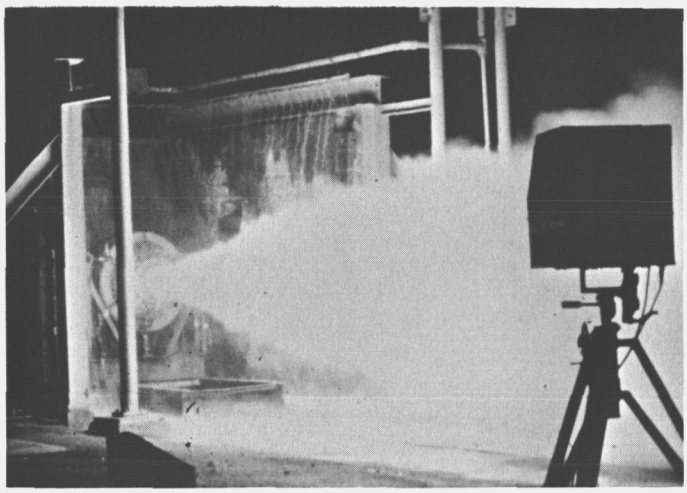

Figure 108. First firing of main retro-engine

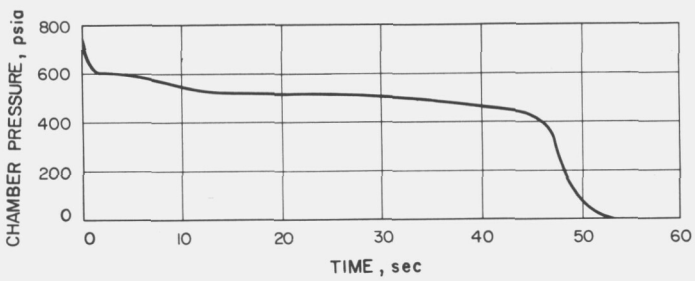

Figure 109. Main retro-engine performance

The pressure peak of 740 psia produced during pyrogen operation under the simulated vacuum conditions was higher than predicted. The ignition time interval of 51 milliseconds indicates that little difficulty should be experienced in meeting the ignition time requirements. Consequently, the size of the pyrogen grain may be reduced as a means of eliminating the pressure peak without compromising the ignition time. The engine operated for a burning time of 47.15 sec at an average thrust of 6353 lb. Table 25 compares the measured sea level test results and the sea level results corrected to vacuum conditions with the performance as predicted prior to testing.

Table 25. Retro-engine performance in Test No. 1

Parameter	Measured at sea level	Predicted *prior to test* (sea level)	Corrected to vacuum
Total impulse, lb-sec	318,547	326,000	409,728
Burning time, sec	47.15	48.4	47.15
Thrust (average), lb	6353	6700	8188
Thrust (maximum), lb	7174	8000	9246
Specific impulse, lb-sec/lb	223	230	287

Prior to final assembly and after X-ray inspection, an aft end propellant separation was visually detected. The separation extended around the entire circumference and measured approximately 1 in. deep. The separation was filled with an epoxy-polysulfide sealant to prevent burning on the exposed surfaces. It has been concluded that the separation was caused by thermal stresses induced during cure and post-cure cooling. The pressure-vs-time record did not indicate any increase in surface area due to the propellant separation.

b. Development of inert components.

Flight weight case. As a result of optimization studies of the main retro-to-spaceframe attachment methods, there has been a major redesign of the flight weight case attachment fittings. The new fitting is essentially a truss design, attaching to the more rigid areas at the equatorial plane and the nozzle attachment ring of the case. The major advantage is that bending loads will not be transmitted to the thin-wall portion of the case.

Kaiser Fleetwings has initiated detailed forging and tooling drawings for the flight weight case. The case material will be Ladish D6C, heat-treated to 220,000 psi yield strength. The two hemispheres will be forged, machined, heat-treated and girth-welded at the hemisphere. The attachment fittings will be final machined after assembly to the thin-wall case.

Case insulation. Based on results of the first test, the thickness of the case insulation has been reduced. The maximum increase in case temperature recorded during operation did not exceed 30°F. Visual examination of the case insulation after firing indicated only minor surface charring. Reduction of the insulation thickness will be fully evaluated on the third heavy-wall engine test.

Nozzle. The design of the flight-type altitude nozzle has been completed and submitted to several qualified vendors for competitive bidding. The first test using the sea level nozzle demonstrated the practicability of the submerged nozzle concept. No adverse effect was observed due to the absence of the conventional convergent entrance section. Erosion occurred at the throat of the graphite insert. The erosion was uniform and is not considered a significant problem during this phase of the development program.

Pyrogen ignition system. The pyrogen ignition system, shown in Figure 110, is essentially a small rocket engine. The pyrogen consists of (1) an initiator assembly containing the two squibs and the boron pellets, (2) an internal burning propellant grain, and (3) the reinforced fiberglas body containing the steel mounting adapter and the pyrogen nozzle assembly. Prior to testing the first engine, pyrogen ignition system tests were conducted under open air and vacuum conditions. Data from the test series confirmed the expected flame pattern, pressure and time characteristics. The length of the propellant charge and the initial exposed surface area will be reduced on subsequent pyrogen tests to reduce the operating pressure below that recorded during the first main retro firing.

Propellant development. The PBAA propellant formulation for use in the retro-engine has been modified. Minor adjustments of the formulation may be required to control burning rate variations.

The propellant modulus for the thermocouple engine was reduced as a means of preventing the propellant separation observed in the first test. A controlled post-cure cooling cycle was used after casting the engine.

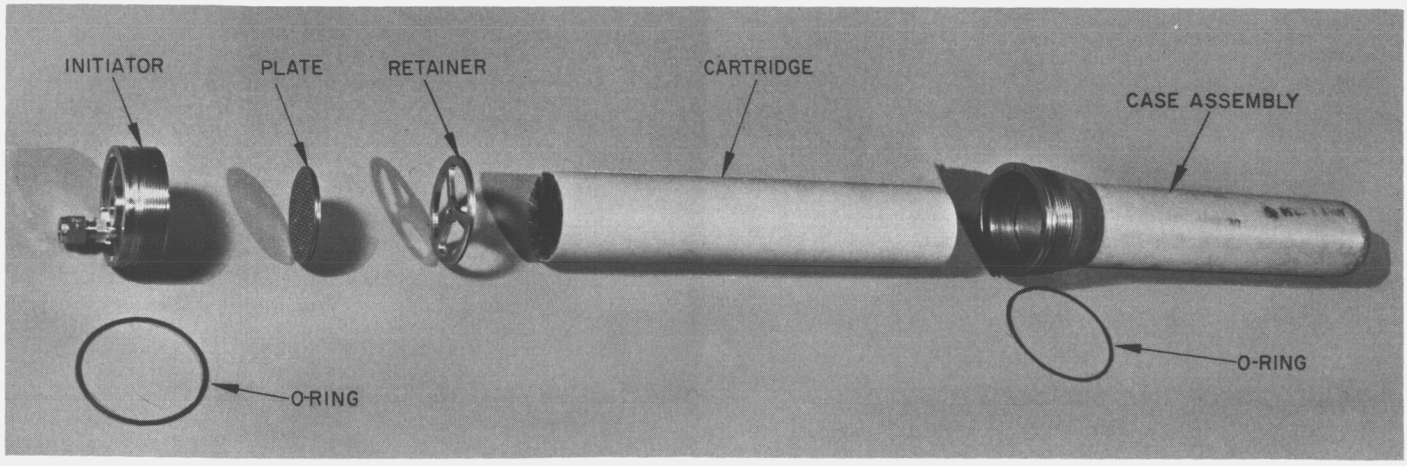

Figure 110. Pyrogen ignition system

However, the combination of the lower modulus and controlled cooling cycle did not prevent a similar separation from occurring in the thermocouple engine. The Elkton Division has designed an elastomeric stress relief boot to be used in the aft hemisphere, as shown in Figure 111. The first boot has been fabricated and will be evaluated in the second heavy-wall engine test.

Test facility status. Proposals for fabrication of the horizontal test stand and altitude test facility have been received by the Elkton Division. The basic altitude facility provides a vacuum capability comparable to a simulated altitude of 70,000 ft. The facility will accommodate both the horizontal and vertical test stands.

4. Vernier Propulsion System

The *Surveyor* vernier propulsion system consists of three thrust chambers, each capable of providing any thrust level between 30 and 104 lb on command, and the associated liquid propellant tankage and helium pressurization system. Monomethyl hydrazine, the fuel, is used to regeneratively cool the thrust chambers. The oxidizer is nitrogen tetroxide with 10% by weight nitric oxide added as a freezing point depressant. The system is capable of providing approximately 50,000 lb-sec impulse.

The major accomplishments of the report period were: (1) completion of propulsion system design integration with the spaceframe for early models; (2) initiation of thrust chamber development in the altitude facility; (3) design release, fabrication, and test initiation of system components; (4) initiation of ground support equipment negotiations; and (5) completion of the altitude test facility. The following paragraphs present details of the more significant items.

a. Propulsion system design integration. During the report period, the design of the propulsion system to spaceframe attachments was completed for initial test vehicles. These attachments include mounting provisions for the helium-supply tank, the six propellant tanks, and the three thrust chambers. Initial designs of thrust chamber and propellant tank mounting provisions were revised, as well as the mating spaceframe attachment points.

b. Thrust chamber development. Thrust chamber development (Fig 112) was started on 8 September in the

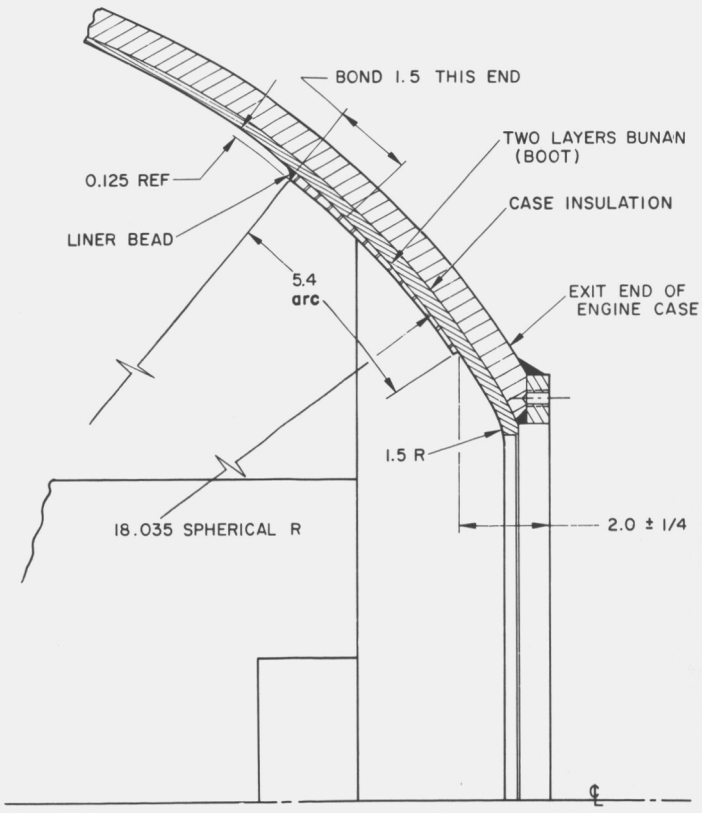

Figure 111. Stress relief boot

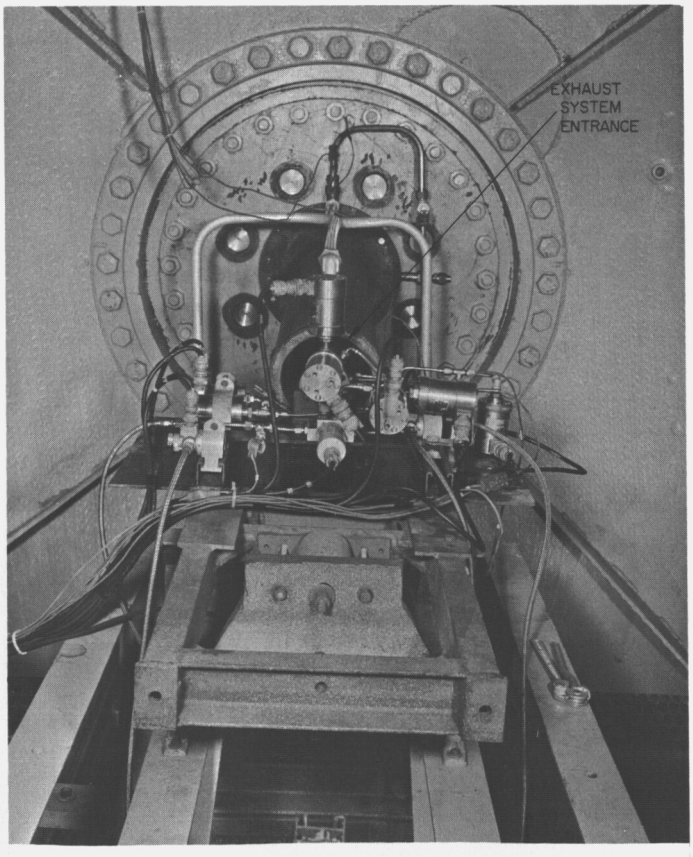

Figure 112. Altitude testing of vernier thrust chamber

altitude test facility (the facility is discussed later in this section).

Initial testing has been accomplished utilizing developmental thrust chamber hardware with a flight type, radiation-cooled nozzle extension (Fig 113) at simulated altitudes in excess of 100,000 ft. As a result of this testing, it has been concluded that the nozzle extension is structurally sound and provides a nozzle efficiency of approximately 99.3%. Testing of the flight-type four-hole injector has also been initiated.

c. Component development. Component designs have been released, fabrication of developmental and flight components has been initiated, and initial component testing is in progress. The following paragraphs present component-by-component status.

Helium storage tank. The design of the flight helium storage tank has been released, the vendor selected and fabrication initiated. The tank is spherical, approximately 14 in. in diameter, and is made of 7-4 titanium alloy.

Helium fill-release-dump valve. The design of the helium fill-release-dump valve has been released, the vendor selected, and vendor development testing initiated. Test units are expected to be delivered at the beginning of the next report period.

The helium fill-release-dump valve is attached directly to the helium storage tank and utilizes squibs to activate the release of helium to the propellant tankage and the overboard helium dump. The tank is to be filled through a check valve which is capped after filling.

Helium regulator. The design of the helium regulator assembly has been released and the vendor selected. During the initial development testing, it was determined that a two-stage regulator was required to hold the necessary accuracy of $\pm 1.5\%$ and that the original design which utilized O-ring seals was inadequate at low inlet temperatures ($-120°F$). The design now includes a two-stage regulator with bellows seals. The first tests of this design were satisfactory.

Separate testing of the relief valve has been carried out with over 80 cycles of pressure relieving on one valve. After the 80 cycles, no significant helium leakage could be detected.

Propellant tankage. Propellant tankage and bladder designs have been released, vendors selected, and fabrication initiated. The first development model with expulsion bladders (Fig 114) is currently in test, and the first flight tank forgings are expected to be completed early in the next report period.

Bladder materials have been tested for permeability, and initial bladder expulsion tests have been completed. Results of the sample bladder material tests indicate that a TFE-FEP Teflon laminate is most promising with a permeability rate of 0.066 gm of nitrogen tetroxide per $in.^2$-hr under conditions of 100°F and 37 psig helium pressure. Complete bladder permeability tests will be made early in the next report period.

Propellant expulsion testing has been carried out with efficiencies (amount of propellant expelled divided by

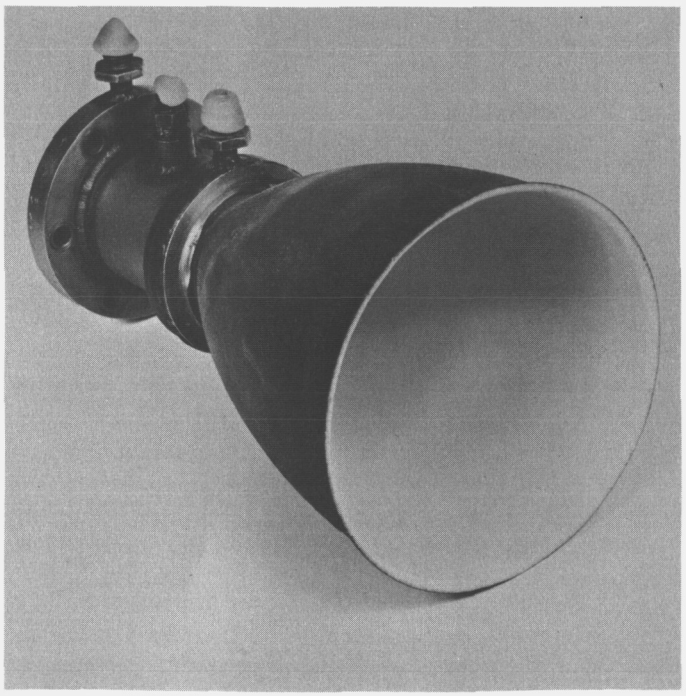

Figure 113. Test-type thrust chamber with flight-type nozzle extension

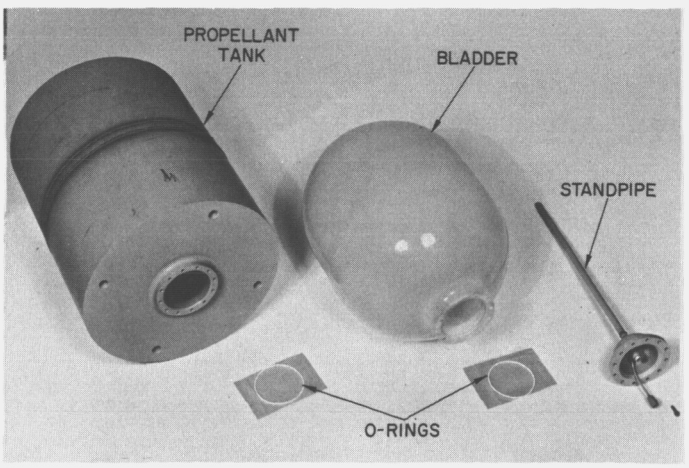

Figure 114. Developmental propellant tank

amount of propellant contained in the tank, excluding that in the probe) very near 100%. Twelve cycles have been accumulated on the first bladder at both ambient temperatures and 0°F.

Propellant throttle valve. Throttle valve designs have been released, fabrication initiated, and developmental unit testing begun. A cross section of the valve is shown in Figure 115. Initial testing has indicated a very nearly linear signal vs flow characteristic with low hysteresis.

Propellant on-off valve. The on-off valve design has been released, fabrication initiated, and hardware testing begun. A cross section of the unit is shown in Figure 116.

Initial testing has resulted in over 1100 cycles of operation with no significant signs of wear. Early seal leakage problems have been solved, and after 300 cycles no helium leakage was detected during an 8-min test. The valve without the solenoid pilot has demonstrated a 7-millisecond opening time with a 14-millisecond closing time, and with the solenoid pilot a 35-millisecond opening time and a 25-millisecond closing time. The requirement is 75 milliseconds from signal to 90% thrust, or to 10% thrust during shutdown. The data indicate adequate margin for injector filling and initiation of combustion.

d. Ground support equipment. Specifications were prepared to define the propellant and pressurant loading procedures, the preflight checkout procedures, and the equipment for these processes. These specifications have been coordinated and negotiations on the ground support equipment initiated.

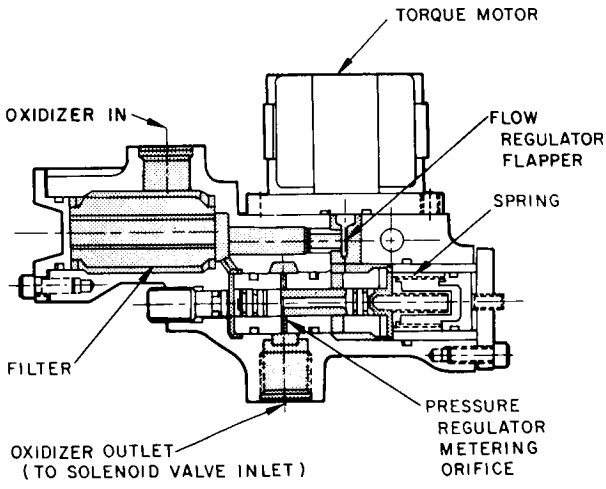

Figure 115. Propellant throttle valve

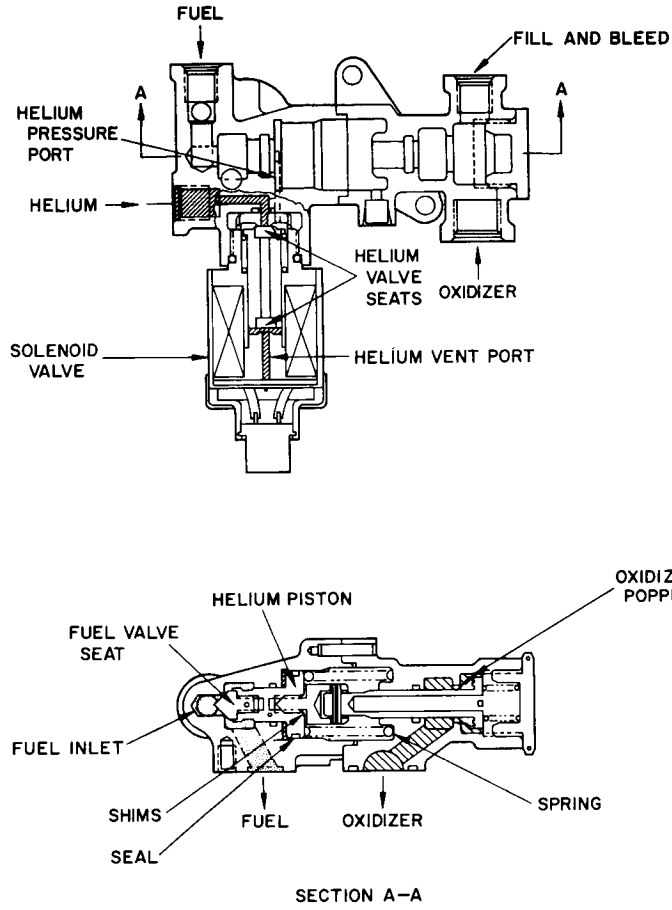

Figure 116. Propellant on-off valve

The propellants are to be loaded by an evacuate-fill procedure, which obviates venting and assures the required precision loading. Preflight checkouts will include: (1) leak checking; (2) functional regulator, check valve, relief valve, and propellant valve checks; and (3) qualitative throttle valve check.

e. Test facility status. Fabrication, checkout, and initiation of development testing in the RMD altitude test facility (Fig 117) was accomplished. This facility, which includes a test tank approximately 8 ft in diameter and 20 ft long, has demonstrated capability for firing the vernier propulsion system at simulated altitudes in excess of 100,000 ft.

The evacuation system includes a hydrogen peroxide steam generator which produces 6 lb/sec of decomposition products. Gaseous hydrogen and water are added to the decomposition products to increase the driving steam flow rate to approximately 24 lb/sec.

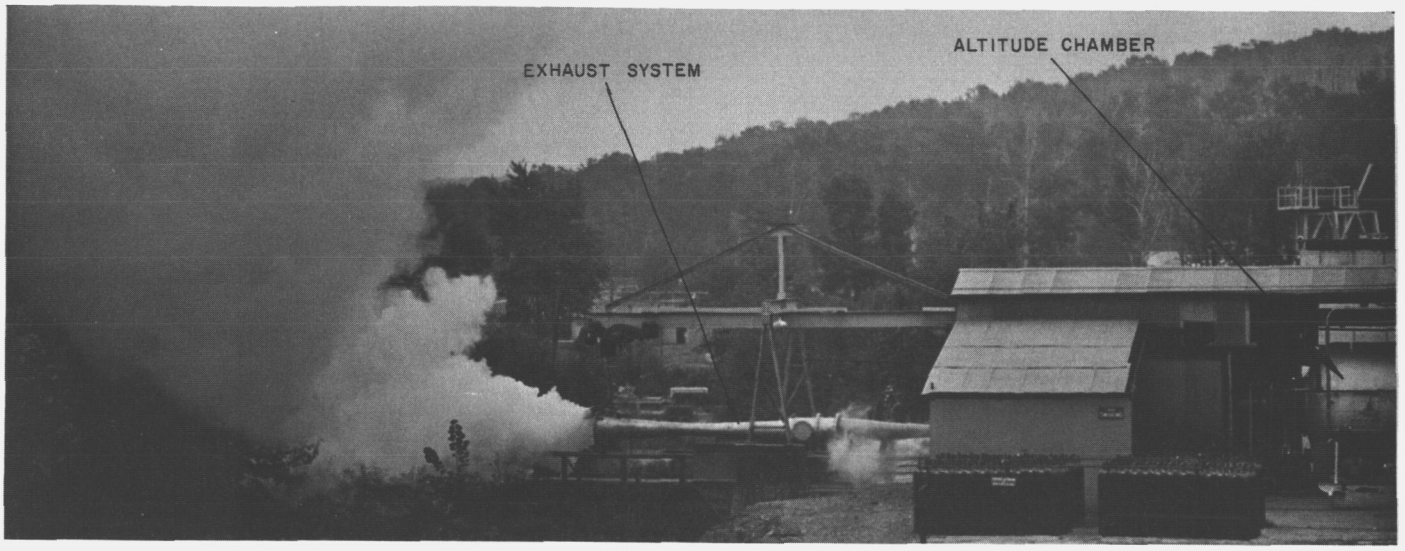

Figure 117. Altitude test facility

J. Spacecraft Vehicle and Mechanisms

1. Spacecraft Vehicle

a. Configuration and general arrangement. The spacecraft assembly can be stowed within the *Centaur* shroud having only a 4-ft extension (Fig 26). Included in the definition of spacecraft envelope requirements are the lateral deflection characteristics based on the assumption of rigid payload adapter structure. Based on the present lateral load conditions, the maximum deflection at the upper tip of the planar array antenna is less than 1.5 in. The total envelope allowance varies from 2 in. at the upper end of the spacecraft assembly to zero in. at the attachment plane to the payload adapter.

The selection of the List II scientific payload to be carried on the first three flight spacecraft will permit the completion of the general arrangement design. Figures 24 and 25 show the present configuration. A number of spacecraft subsystems or units have been relocated or changed in configuration; the major changes are described below.

(1) As a means of providing unobstructed thermal radiator area above Compartment B, the high-resolution telescope has been relocated and redesigned. Related to this change was the desire to provide improved telescope resolution capability and reduced mechanical complexity.

(2) Raising the spacecraft to provide some 9 in. clearance from the *Centaur* tank vent has permitted elimination of the requirement to fold the dipole feed on the altitude marking radar.

(3) The area of the solar panel has been increased from 8.4 to 9.2 ft^2 as a means of providing adequate power margin during lunar daytime operation.

(4) The optimization of the arrangement of electronic equipment in Compartments A and B is continuing. A number of important ground rules have been used in carrying on this effort:

(a) Since the wiring leads which pass through compartment walls constitute a major heat loss during the lunar night, the number of such leads is being minimized.

(b) Clear separation is desired between those equipment items which form a part of the bus and those which are part of the scientific payload.

(c) The dissipation of thermal energy as a result of normal functional operation ideally should be balanced between the two major equipment compartments.

The present design provides a balance among these three basic ground rules and succeeds in locating most of the bus modules in Compartment A and the majority of scientific payload modules in Compartment B. Figure 118 shows the design approach.

b. Wiring harness design. A full-scale mockup of the planar array/solar panel assembly has been fabricated and used in kinematics and cable design studies. The mockup includes provisions for extending the mast vertically and rotating the planar array about each of the four gimbal axes. A flexible planetary wound jacketed

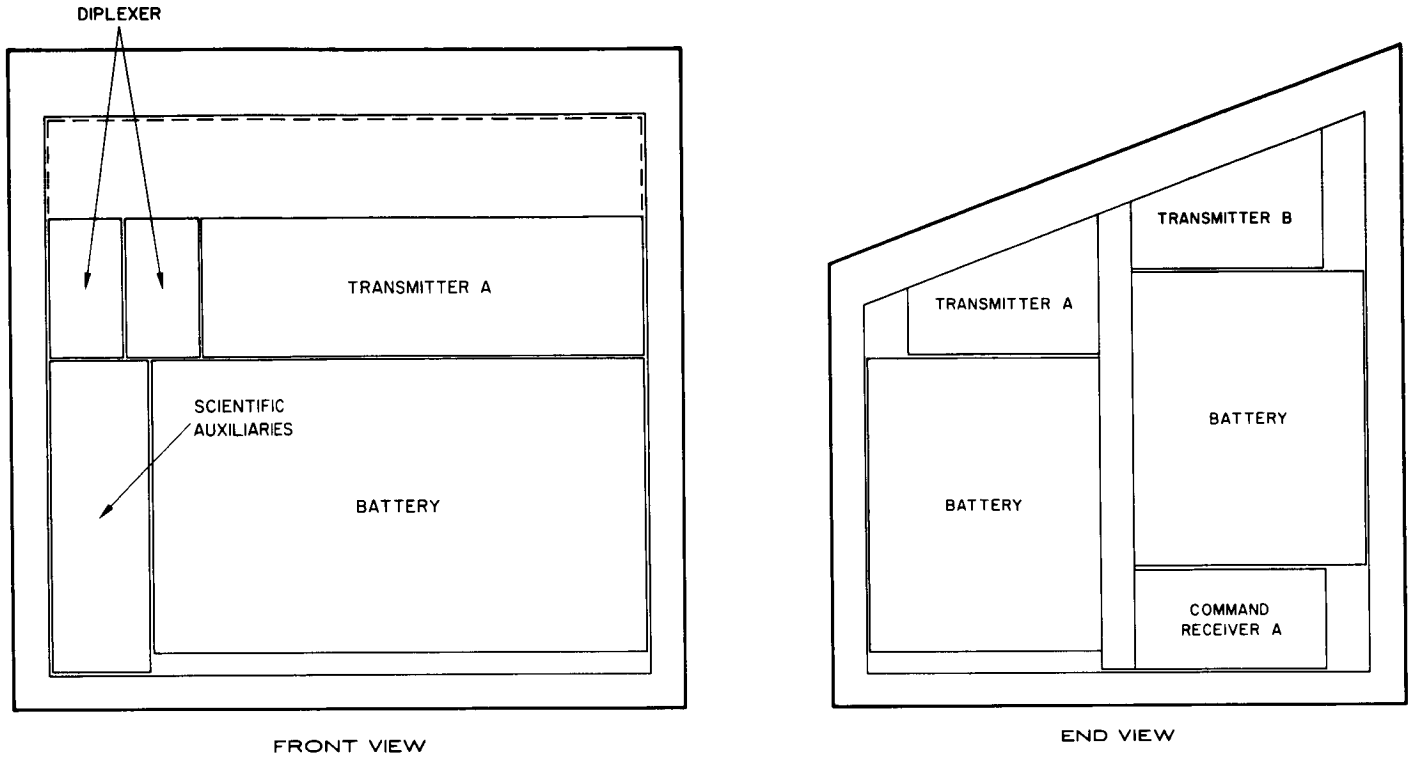

Compartment A

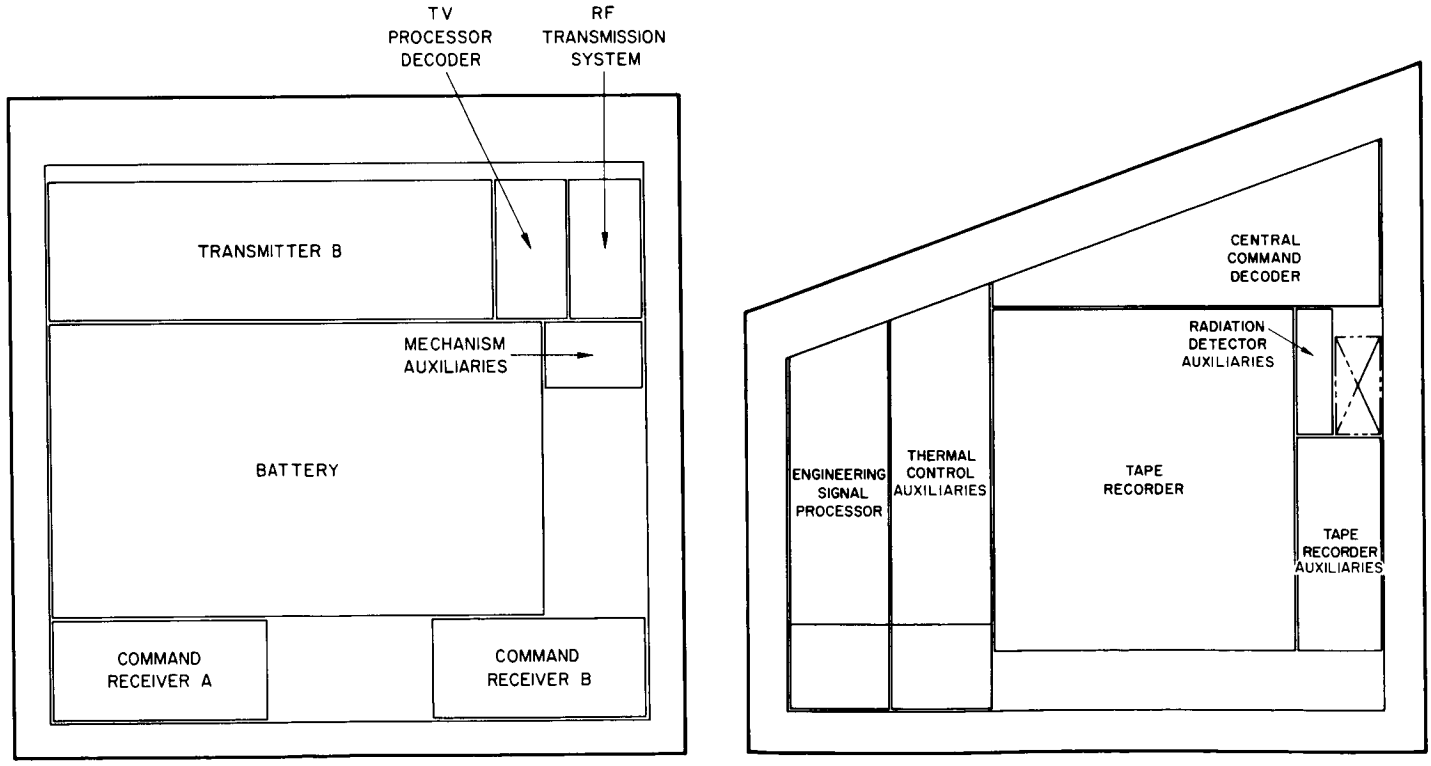

Compartment A **Compartment B**

Figure 118. Arrangement of Compartments A and B

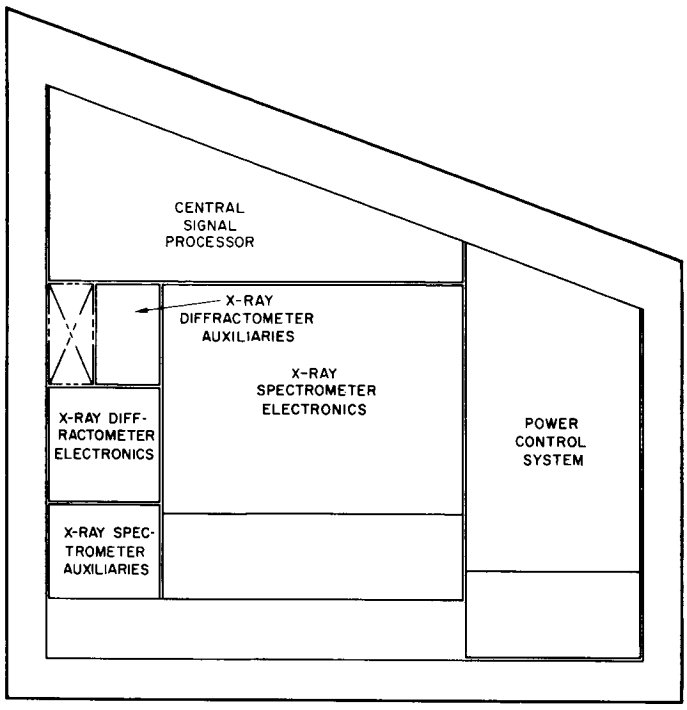

END VIEW

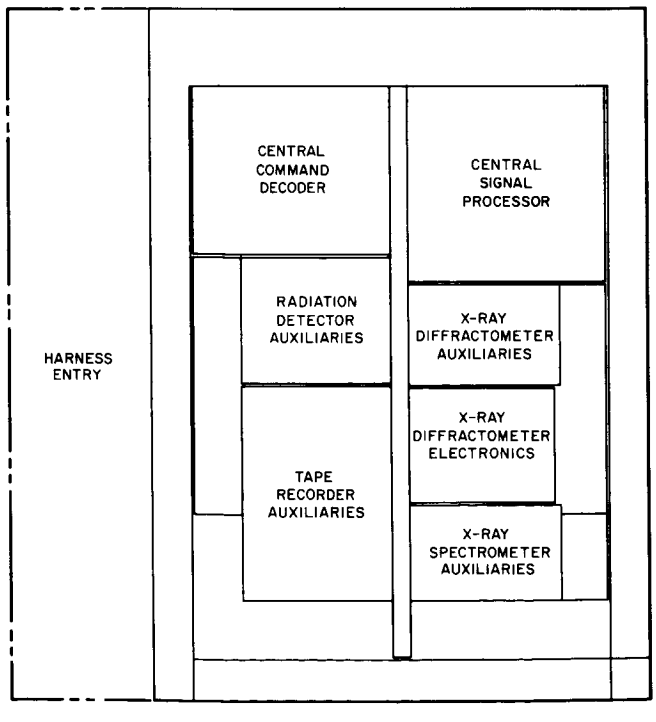

REAR VIEW

Compartment B

Figure 118. Arrangement of Compartments A and B (continued)

cable of 80 conductors was fabricated and routed along the mast to the various breakout points at which using mechanisms are located. From this study it is apparent that the conventional harness treatment results in large service loops, some difficulty in harness stowage prior to extension, and sizable drag forces during extension and rotation.

An alternate design is in the process of mockup. This design includes the use of several retractile cables stowed in tubular magazines bonded to the fixed portion of the support mast and using a Hughes rotary joint to carry cabling across the roll axis joint, which requires a full 360 deg of unrestricted motion (Fig 119).

As a part of the effort in establishing the requirements for harness design, tests were run to determine the current-carrying capability of electrical wiring under simulated lunar environmental conditions. The results of these tests indicate that even under these conditions the teflon insulated wiring used for this application can safely carry currents in excess of the values given in Specifications

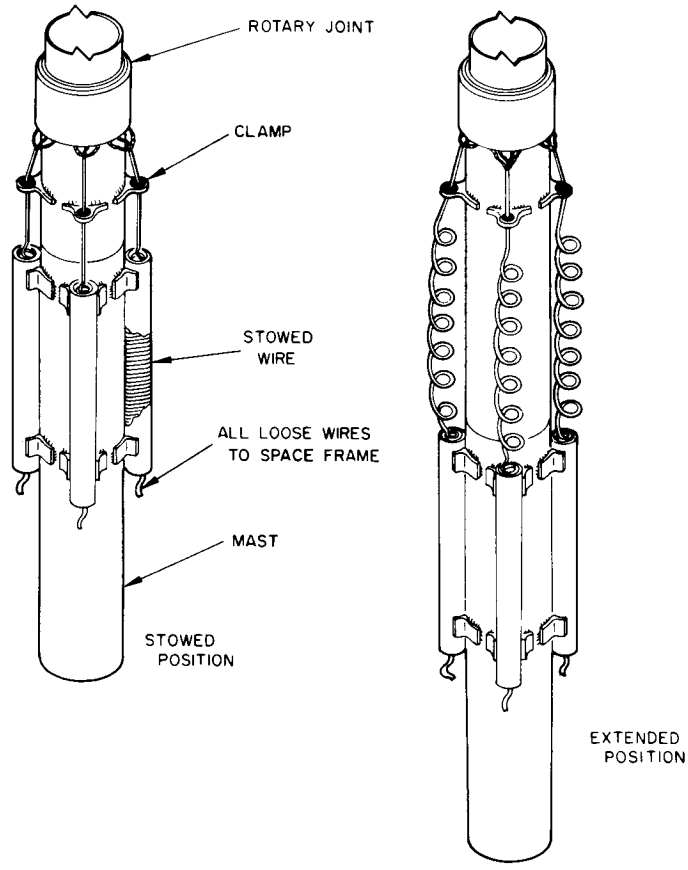

Figure 119. Wiring harness arrangement for antenna/solar panel mast

MIL-W-5088 and MIL-W-8160. It may be possible to take advantage of this capability to save weight and space.

c. Special test vehicles. The first of the vehicles to be used for evaluating the response of the *Surveyor* to the *Centaur* input excitation is designated S-1. During this report period, the fabrication of S-1 has been completed along with its associated payload adapter. Both S-1 and its adapter are presently being instrumented for vibration testing (Figs 120 and 121).

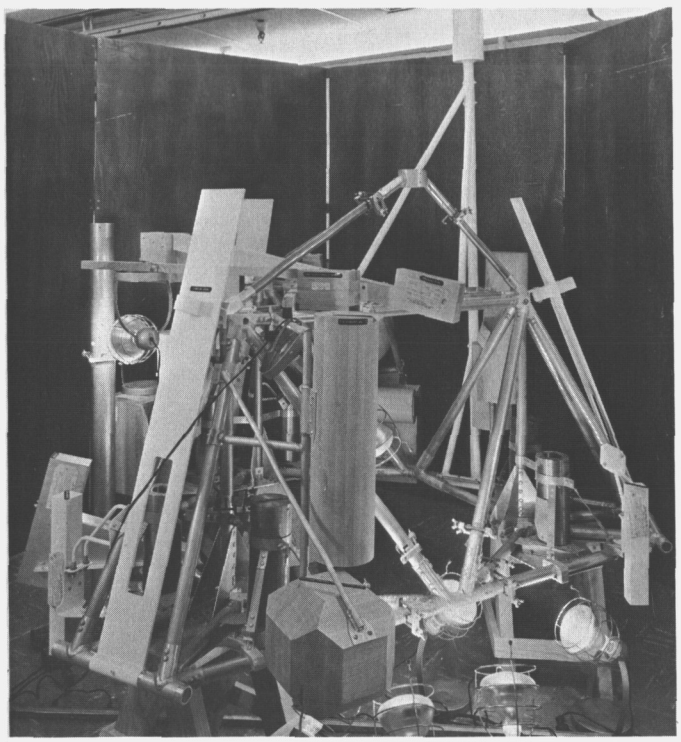

Figure 120. Vibration Test Vehicle S-1

A similar airframe (S-4) for use in vernier engine system installation and test is presently being fabricated for delivery to Reaction Motors Division, Thiokol Chemical Corporation. Two additional spaceframes for use by RMD, S-5 and S-6, have had their drawing releases completed and are scheduled to be delivered on December 1 and February 10. Three other test vehicles are well along in the design phase and will provide the hardware for the following purposes:

T-1 (landing gear drop test)

L-1 and L-2 (landing gear subsystem test)

S-2 (upgraded design based on the results of S-1 testing)

The last of the major test vehicles presently under design is the control system test vehicle, T-2. Its present configuration is shown in Figure 122.

d. Weight, balance, and alignment equipment. A multipurpose alignment device (Fig 123) has been designed

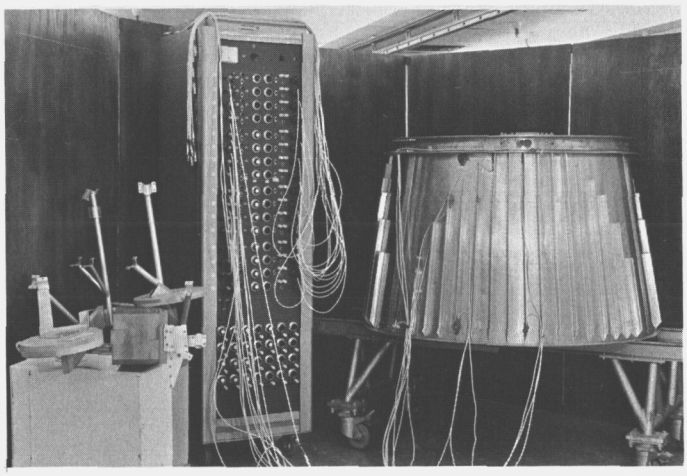

Figure 121. Payload adapter for tests of Vehicle S-1

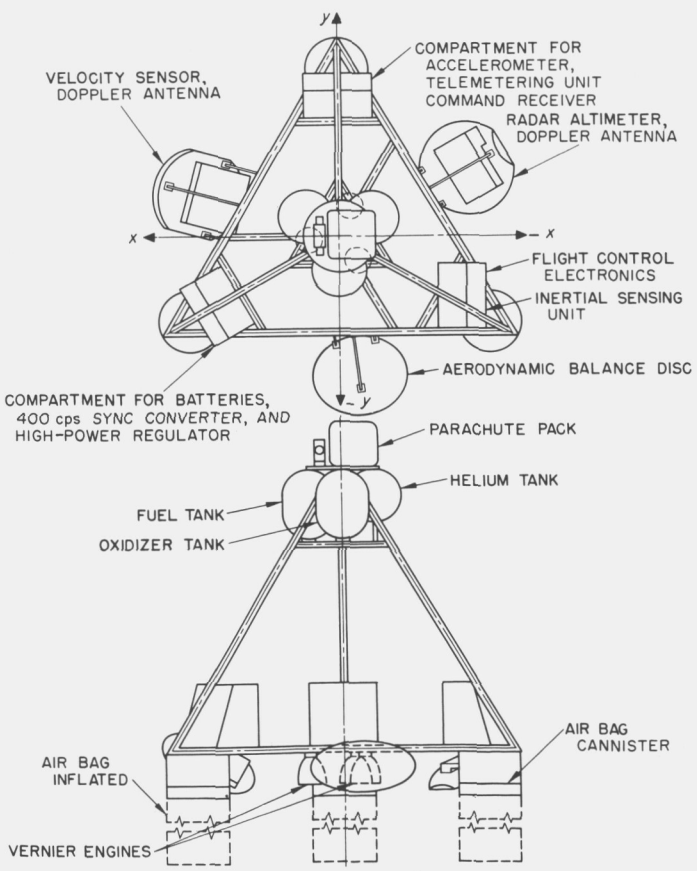

Figure 122. System Test Vehicle T-2

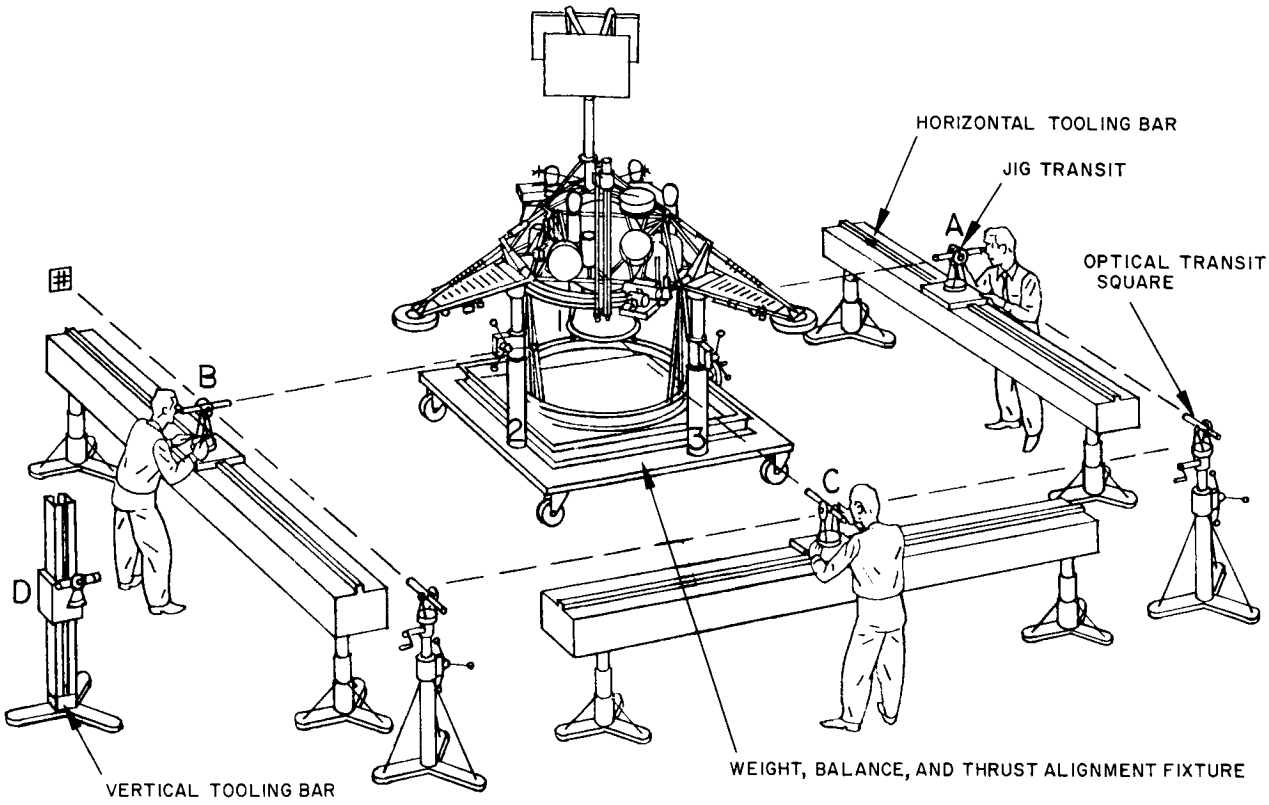

Figure 123. Weight, balance, and thrust alignment equipment

to locate the center of gravity of the spacecraft and to align the thrust axis of the main retro, the vernier engines, the cold gas jets, the flight control sensor package, and certain mechanisms. This device uses optical techniques and will permit alignment of the main retro thrust axis to the spacecraft center of gravity within 0.018 in. Alignment is established by using three tooling holes on the base of the spaceframe as references, each being adjacent to a mounting hole for the main retro. Spherical pins are used in the three holes and provide target points for the optical measuring equipment. The three pins will rest on a fixture which will permit each pin to be independently adjusted either vertically or laterally. The fixture has been designed to support the main retro-engine and to allow its positioning in both lateral and vertical planes.

2. Mechanisms

a. Extension booms–antenna and instrument. Telescoping, cold-gas-actuated extension booms will be used to extend the two omnidirectional antennas and to deploy the surface geophysical and lunar atmosphere experiments.

Detail drawings of the tube sections and vehicle attach housings have been completed and initial hardware has been fabricated for developmental testing (Figs 124 and 125). Dynamic testing of dry film lubricants under environmental conditions is being conducted in the laboratory. Preliminary tests indicated that properly applied molybdenum disulfide will be satisfactory in this application.

The possibility of obtaining a substantial weight reduction through the use of beryllium tubing has been explored. Limitations on wall thicknesses because of present fabrication techniques prohibit significant weight reductions at this time.

b. Antenna/solar panel positioner. The antenna/solar panel positioner, controlling the position of the high-gain

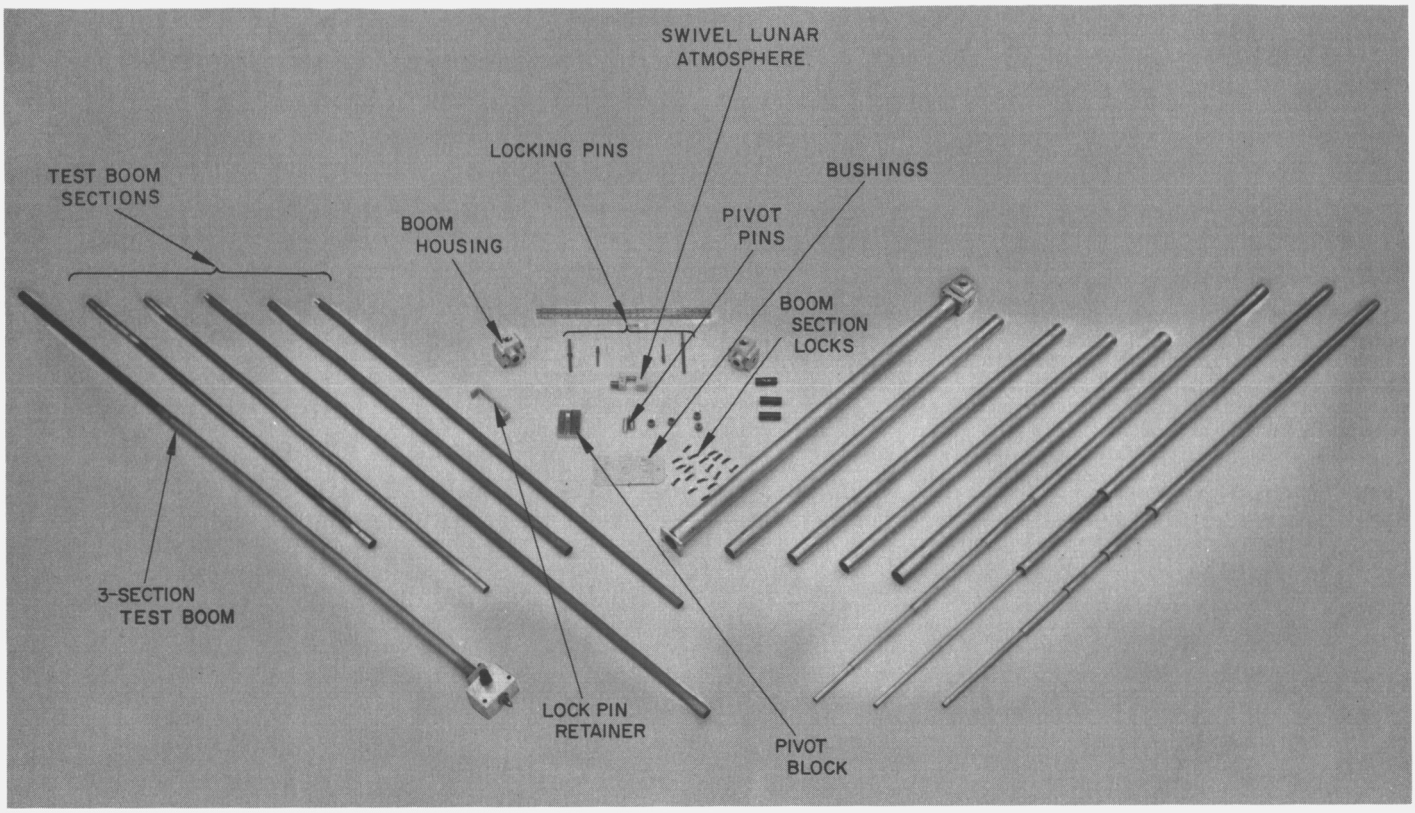

Figure 124. Instrument boom

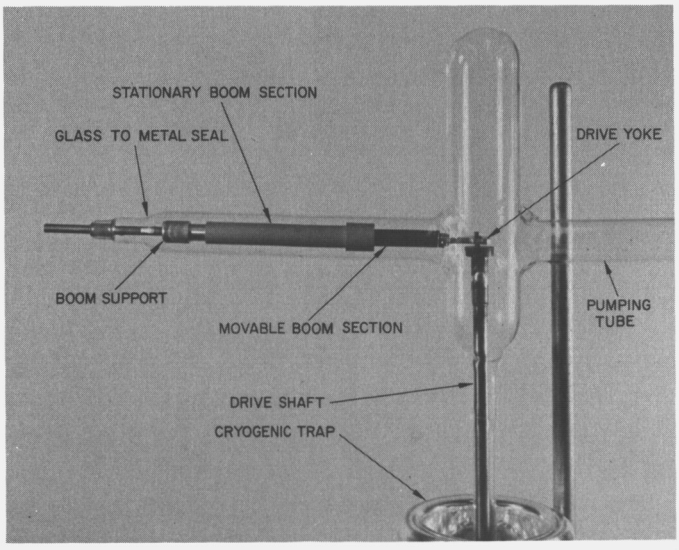

Figure 125. Vacuum test of boom section

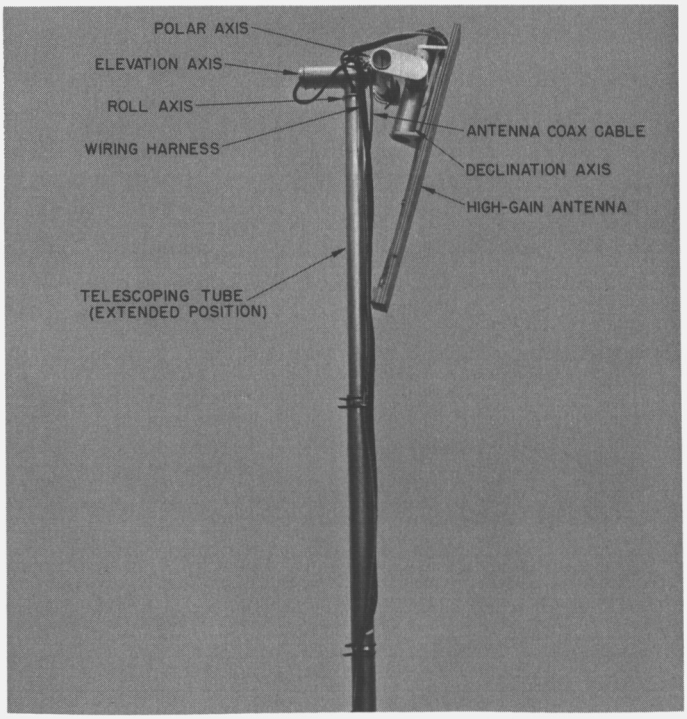

Figure 126. Antenna/solar panel positioner wiring harness test model

antenna and solar panel, has been redesigned to provide the necessary angular excursions required by the extended lunar landing capability.

A special test model of the elevating post and gimbal system has been fabricated and used to determine the

torque effects due to the stiffness of the antenna coaxial cable and the wiring harness (Fig 126). The drive mechanism torque and inertia test fixture has been reworked for compatibility with the new inertia loads imposed by the extended angular capability. A test fixture for the gas-operated elevating mechanism has been fabricated. A scale model tube and gimbal structure assembly is also being fabricated to explore the use of adhesive bonding, which would permit the use of very high-strength nonweldable alloys.

A modified, unsealed rotary solenoid has been successfully tested at −125°F and +250°F in conjunction with a reduction gear box and conical wobble bellows. The drive package is being further modified to include labyrinth type sealing and a direct shaft output drive for testing under full loads in a simulated lunar environment.

Gimbal relocking, to sustain touchdown shock loads, constitutes a major problem area. A full-size model of the antenna/solar panel positioner is being fabricated and will be used to test the strut and hinge line locking methods already designed.

c. TV mirror drives. The mirror assemblies, providing tilt and pan capabilities for the television cameras, are driven in elevation and azimuth by rotary solenoids. Detail drawings of the dust protection hood and mirror assembly have been released and a developmental model is being fabricated. This model will contain a pyrex mirror with a vacuum deposited aluminum front surface.

Environmental test results of the mirror assembly rotary solenoid drive have confirmed that certain design modifications are necessary. Two motors incorporating the required design modifications are on order and will be tested with the developmental mirror and hood assembly. A deposited-film ceramic base potentiometer for

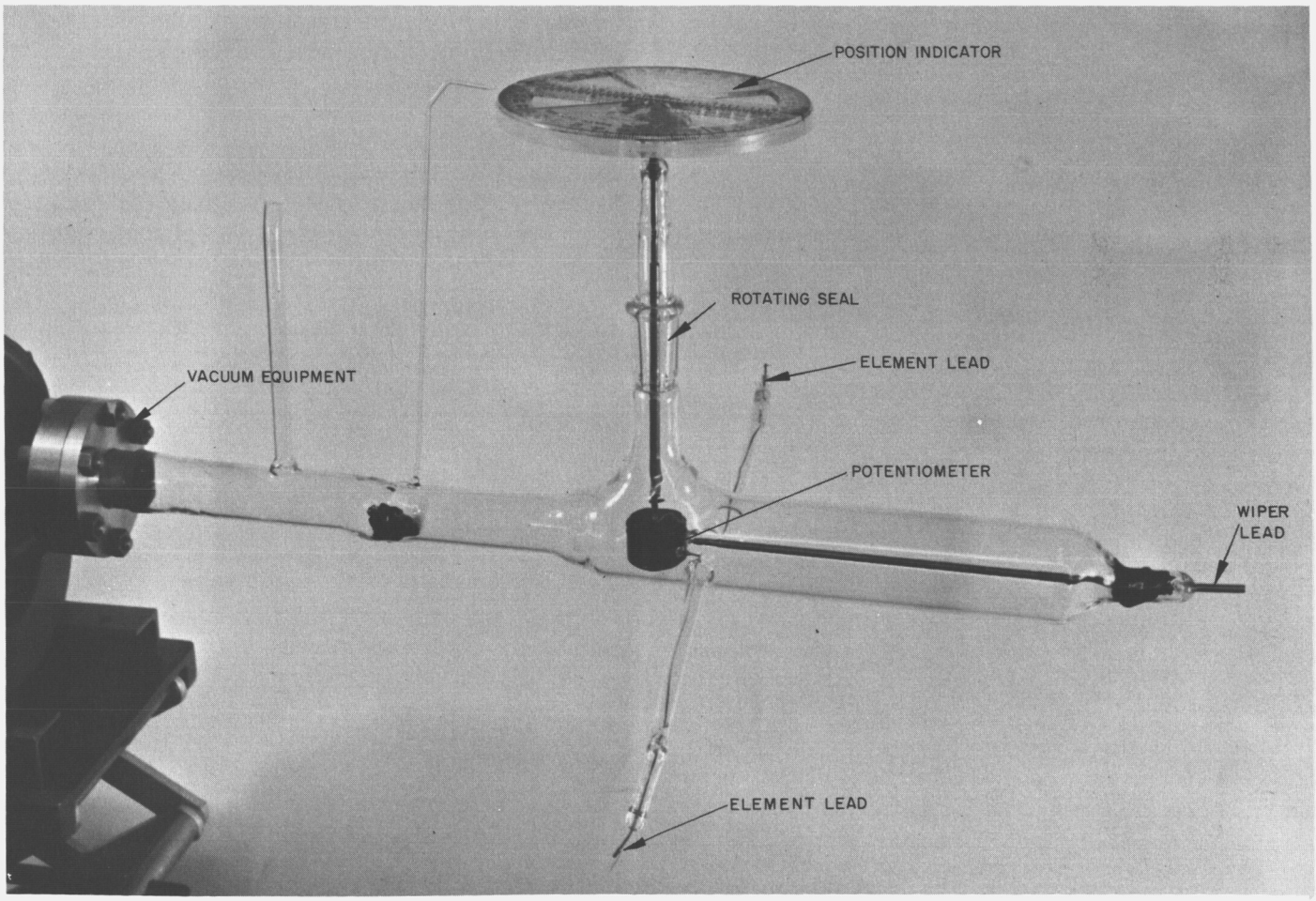

Figure 127. High-temperature vacuum test of potentiometer

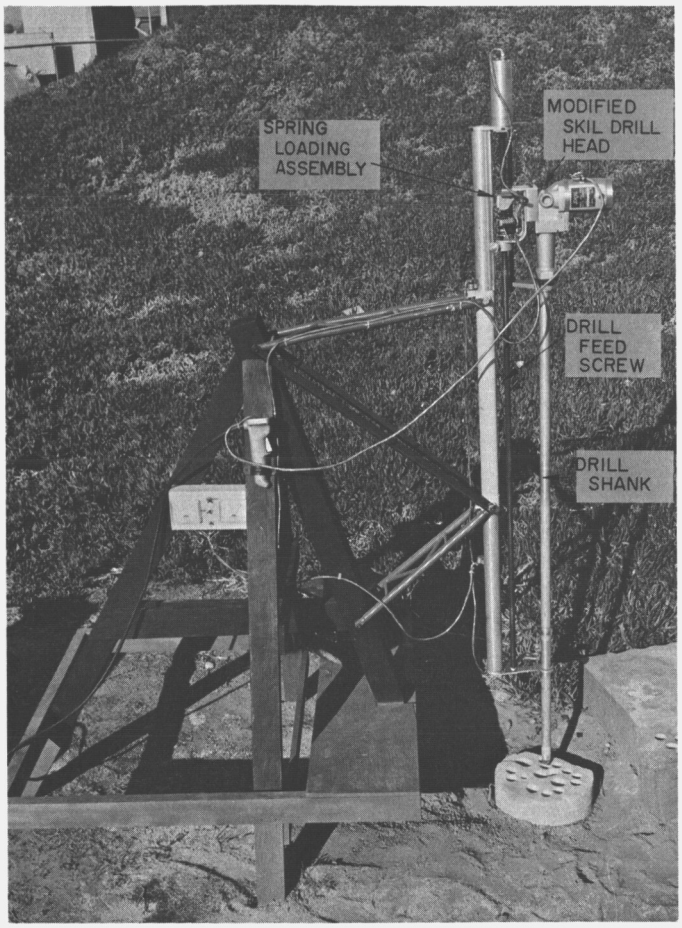

Figure 128. Developmental subsurface sampler

mirror position indication is presently undergoing high-temperature vacuum tests (Fig 127). Recent technological advances in beryllium fabrication techniques have led to the production of high optical quality beryllium mirrors of high strength and stability. A berryllium mirror having a reflective aluminum coating has been ordered for environmental evaluation.

d. Subsurface sampler. The subsurface sampler obtains samples from various depths down to 5 ft beneath the lunar surface and delivers the samples to the sample processing system. The subsurface sampler (Fig 128) consists of a drill head, drill shank, bit, dump mechanism, vertical drill drives, supporting structure, subsurface geophysical probe lowering drive, and jettison device.

The subsurface sampler drill head shown in Figure 129 was fabricated by modifying a Skill electric rock drill. Modifications consist in substituting a coil spring for the piston and air spring normally used in the unit. This resonant oscillating hammer type of mechanism has the highest efficiency of any rock drilling mechanism tested to date.

A full-scale breadboard model and several components of the subsurface sampler are undergoing operational tests in a 10^{-8} mm Hg vacuum. The tests are being performed to verify design features now being incorporated in the developmental model drawings. These tests are: (1) The use of a teflon-glass nut on a square thread screw for the drill feed and lift mechanisms instead of the ball

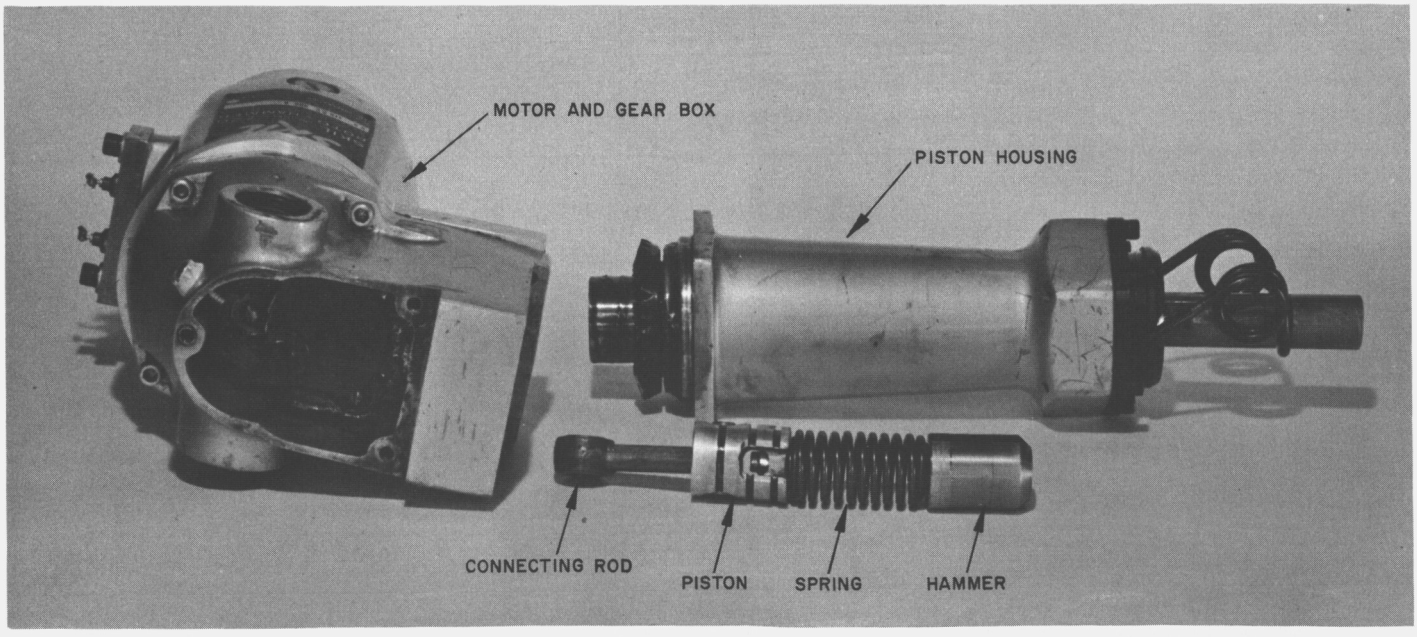

Figure 129. Developmental subsurface sampler drill head

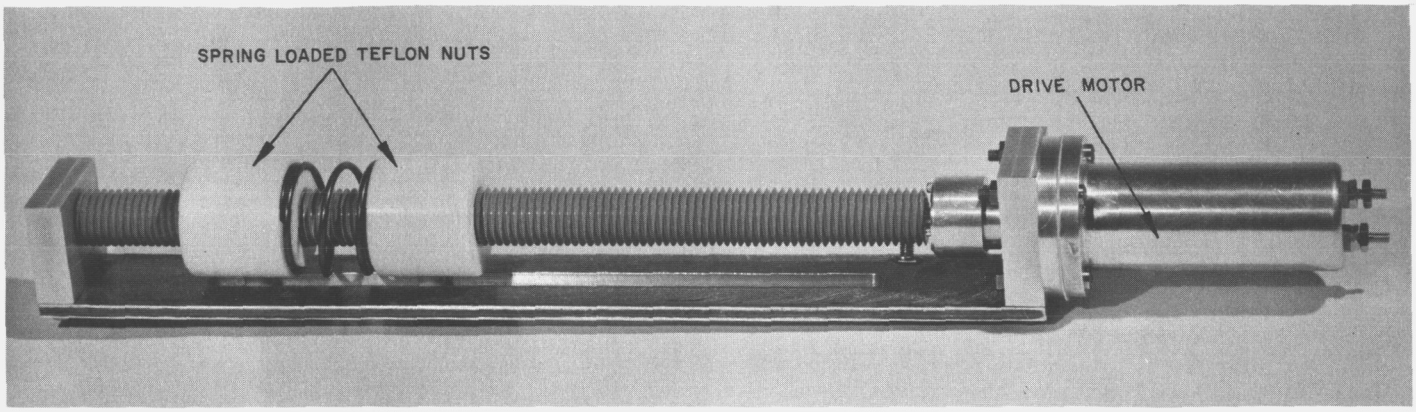

Figure 130. Test fixture for teflon nut and screw assembly

bearing screws originally considered, since this design is less apt to wear and jam with rock dust when operating in a high vacuum. (2) Investigation of the system for collecting and discharging drill samples. The entire sampling mechanism is operated at an angle of approximately 60 deg from vertical in the vacuum chamber so that a rough simulation of lunar gravity is achieved. (3) The operation of the drill head of a modified Skil rock drill in a vacuum. Tests to date indicate satisfactory results. (4) The use of labyrinth seals in order to maintain a pressure in the drill head calculated to be not less than 10^{-5} mm Hg when operating in the lunar environment. Thus, with the use of high-vacuum lubricants, bearing galling can be avoided.

In addition, the motor torque carriage with teflon bearing surfaces is being given a life test in a vacuum. The teflon nut and screw assembly (Fig 130) has been tested for 1280 in. of travel in a vacuum up to 3 times 10^{-7} mm Hg at design loads without showing appreciable wear.

e. Sample processing system. Samples of lunar soil received from the subsurface sampler or surface sampler are measured and delivered to the pulverizer or directly to the gas chromatograph by the measure and transfer device as shown in the block diagram (Fig 131). A single pulverizer reduces the sample to the specified particle size. A sample cup transport system screens the sample and delivers it to the X-ray spectrometer or X-ray diffractometer. The sample processor is shown in Figure 132.

The measure and transfer device consists of a hopper, measure piston, feed piston, linkage, and three stepper motors. Upon receipt in the hopper, the sample is screened through a 1/16 in. mesh screen. The vibration of the subsurface sampler is used to assist in screening to prevent large particles from jamming the sample processor. The excess particles are removed from the feed

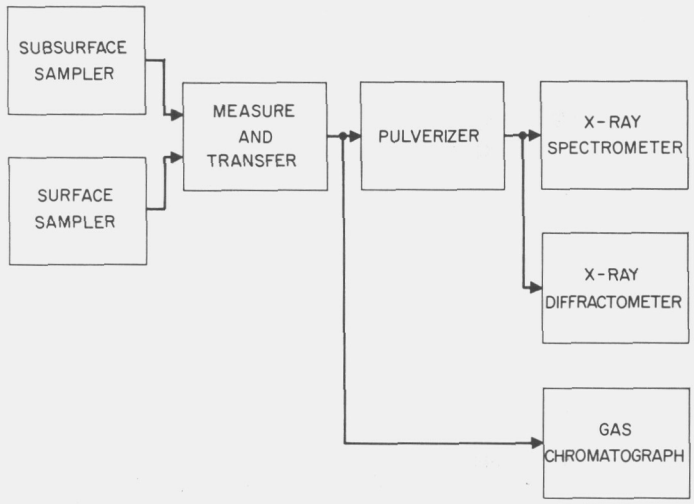

Figure 131. Lunar sample processor block diagram

chamber by operating the pulverizer feed piston so that a known amount of sample remains in the measure chamber. The measure-feed assembly is lifted to the gas chromatograph feed position. The measure piston is raised, placing 4 cc of sample ahead of the feed piston. The feed piston advances, dumping the sample into the gas chromatograph. Two more samples are delivered to the gas chromatograph by the operation of the measure piston as described above. The measure-feed assembly is then moved to the pulverizer feed position. The measure piston and feed pistons are again operated, delivering a sample to the pulverizer. The measure-feed assembly is then returned to its initial position.

The pulverizer consists of a high-speed particle accelerator rotor operating at 14,000 rpm. Particles are reduced in size by impact with each other. This type of pulverizer increases in efficiency in a vacuum where no atmosphere is present to inhibit high particle velocities.

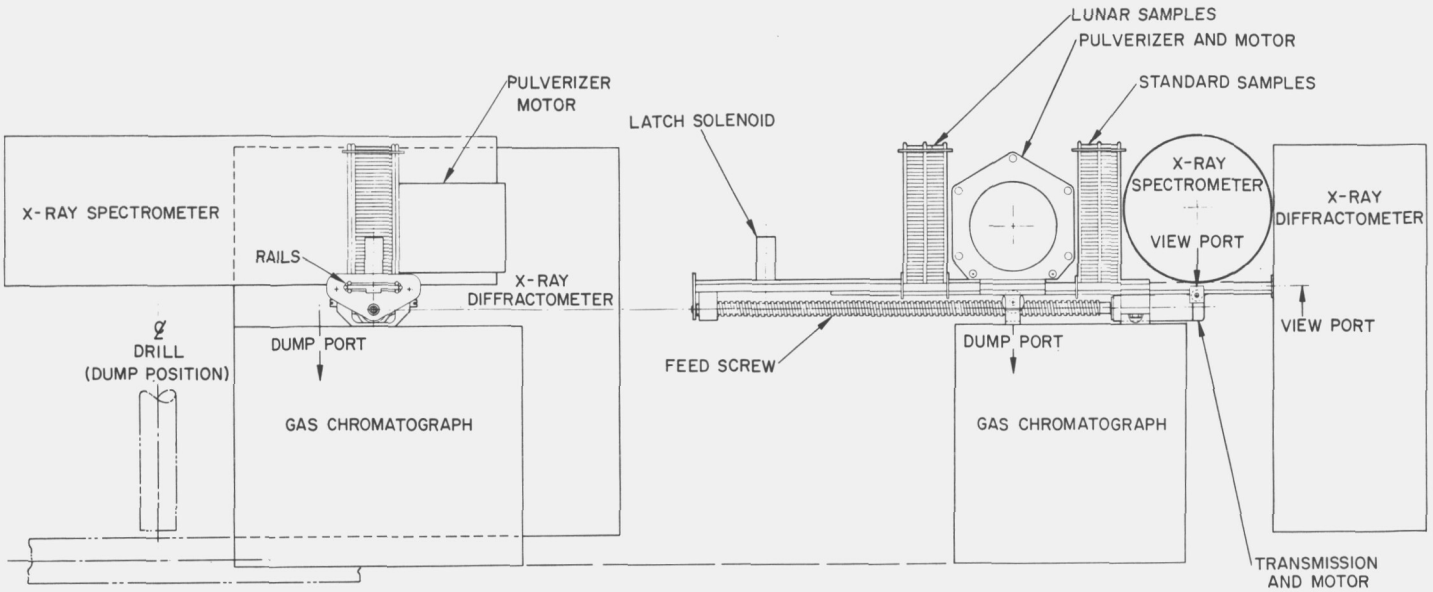

Figure 132. Lunar sample processor

A change in design from multiple pulverizer segments to a single driven motor mounted unit is in progress. Table 26 lists the advantages and disadvantages of the single and multiple designs.

Table 26. Comparison of single and multiple pulverizer sample processor design concepts

Single pulverizer design	*Multiple pulverizer design*
Less weight	More weight
12 lunar samplings	6 lunar samplings
Direct feed to gas chromatograph	Gas chromatograph receives pulverized samples
Sample feed to any instrument in any order	Fixed order of feed
5 to 10% biasing from preceding samplings	<2% biasing from preceding samplings
Simpler design	More complex
Pulverizer jettison for direct sample cup loading	No direct sample cup loading provision
Higher reliability	Lower reliability

The test pulverizer has been modified to incorporate a sliding conveyor mechanism using a split sample container, simulating the mechanics of the flight unit (Fig. 133). This system allows tests to be made of the basic functions of grinding, container filling, shear, compacting, and sample surface preparation in a vacuum. Present vacuum equipment is adequate for tests in 10^{-4} mm Hg. Figure 134 shows three samples of quartz rock which were pulverized, sized, compacted, and delivered in this vacuum by three different methods:

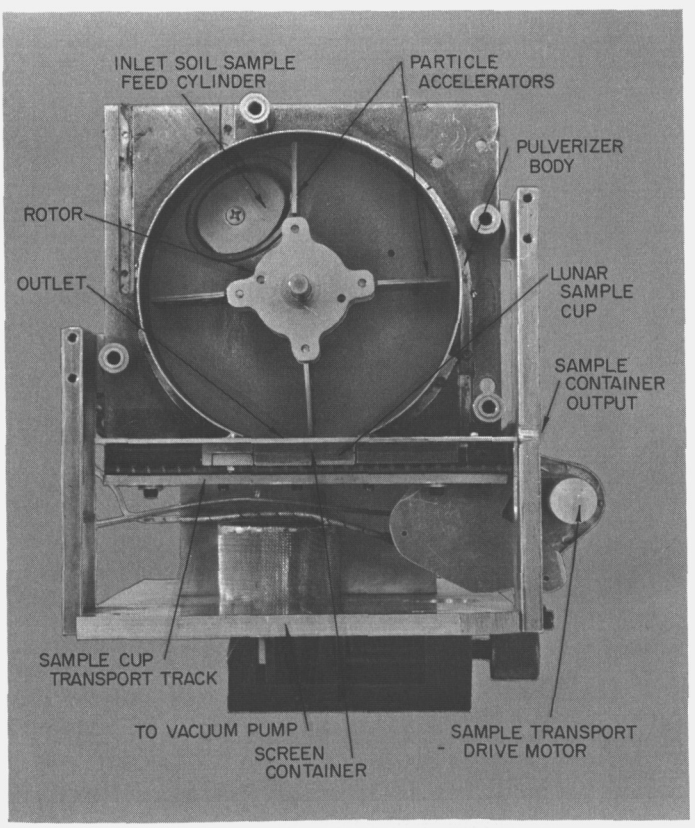

Figure 133. Pulverizer test unit (one side removed)

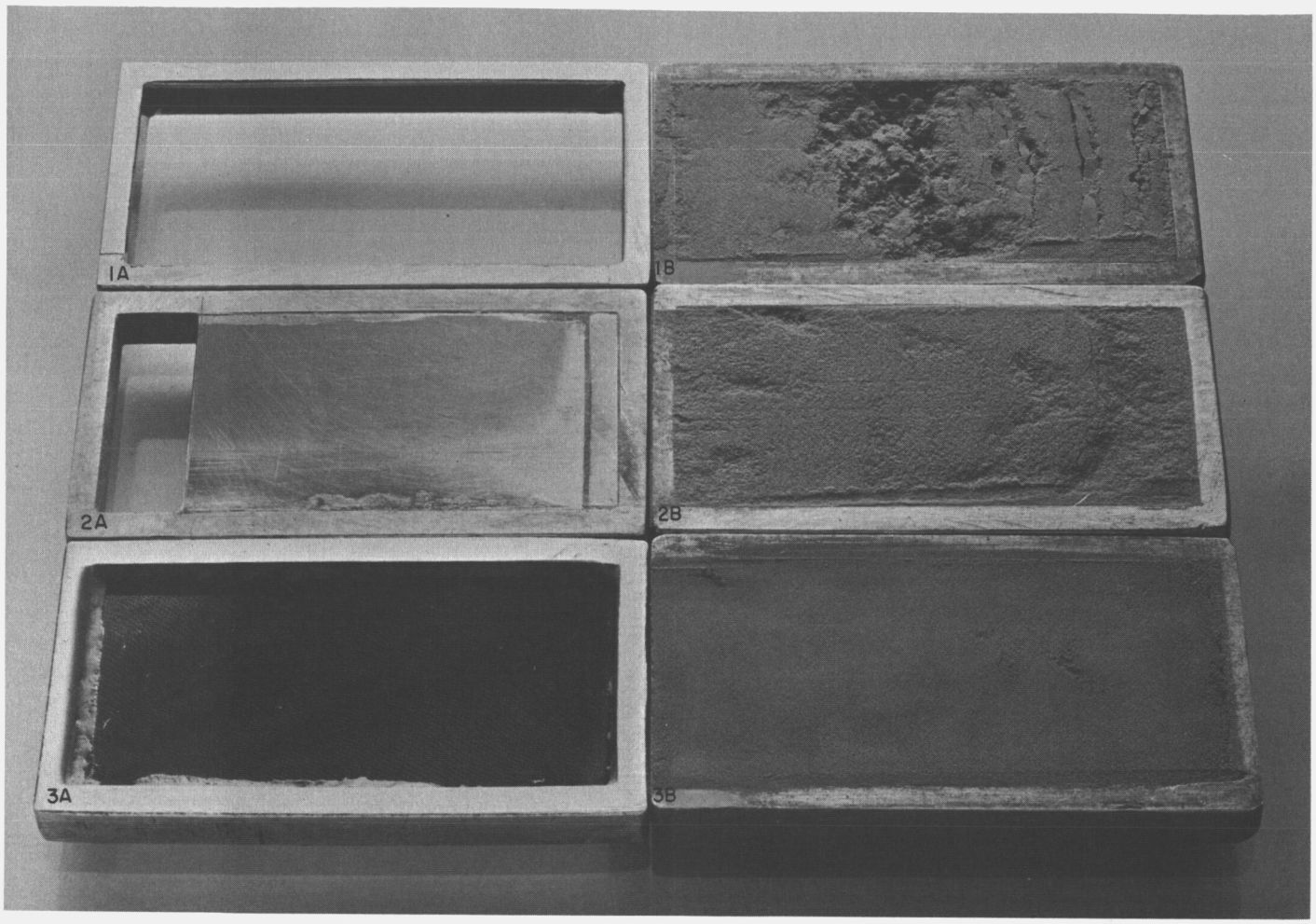

Figure 134. Samples prepared by three different methods

(1) Open sample cup; pulverize before filling; no screen (1A and 1B, Fig 134).

(2) Slot fill; pulverize before filling (2A and 2B, Fig 134)

(3) 200-mesh screen; simultaneous pulverizing and filling (3A and 3B, Fig 134).

The best results were obtained by the third method, which will be incorporated in the sample processing system.

Two magazines of cups are used. One magazine, placed ahead of the pulverizer, is loaded with a number of alternate lunar sample cups and 200-mesh screen containers. The other magazine is loaded with standard samples. A receiver cup and screen are positioned below the pulverizer. Upon receipt of the pulverized sample, a screw feed mechanism advances the lunar sample

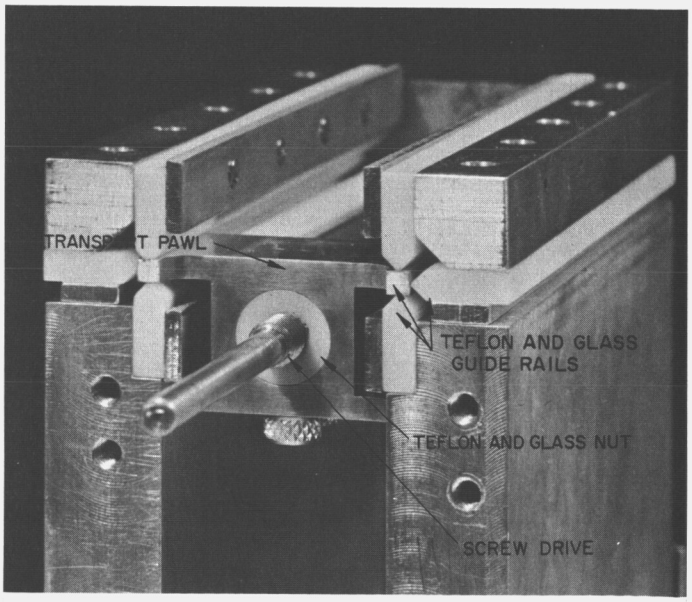

Figure 135. Experimental sample transport system

cup, removes the upper screen container, and by a shearing action levels and compacts the sample surface. A standard sample resting on the track is picked up and pushed by the lunar sample cup. The standard cup is positioned beneath either the X-ray spectrometer or X-ray diffractometer. After calibration, the lunar sample cup is positioned beneath the instrument. The feeder mechanism has the capability of obtaining additional standard samples. Expended samples are discarded into the X-ray diffractometer.

Tests are being conducted with a breadboard transport system to determine the forces required to move sample cups over a rock-dust-covered transport track in a 10^{-4} mm Hg vacuum (Fig 135).

K. Reliability and System Test

1. Reliability

a. Spacecraft reliability estimate: flight and landing phase. The reliabilities of the spacecraft system and its subsystems have been estimated for the flight and landing phase, in the first of a series of estimates to be made at appropriate points in the development program to provide a basis for tradeoff actions. The spacecraft reliability for the flight and landing phase is defined as the probability that the spacecraft, after successful injection, will not malfunction to preclude soft landing successfully on the prescribed portion of the Moon.

With the present design, it is estimated that there is 0.80 probability that a reliability greater than 0.67 will be achieved for the spacecraft over the flight and landing phase of the *Surveyor* mission. It is further estimated that there is 0.20 probability that a reliability greater than 0.85 will be achieved. The mean value of the estimated reliability is 0.78. The estimated reliability ranges for the spacecraft system and its subsystems or groups are listed in Table 27.

It can be seen that the minium reliability specified by the Jet Propulsion Laboratory (0.75) for the same mission phase lies within the estimated range. Despite this fact, it is judged important to improve the basic design with respect to its inherent reliability, since as engineering test data on equipment become available, unexpected reliability problems will be likely to arise. Further, certain design compromises, trading reliability for weight, volume, etc., may become necessary. Even barring these possibilities, it is desirable to be able to meet the reliability requirement with a greater probability than that currently estimated. It is anticipated that future estimates will gradually narrow the range of uncertainty in the design reliability value. As design improvements are incorporated in the spacecraft, both ends of the range should move to higher values.

Table 27. Reliability estimates for flight and landing phase

Equipment	Reliability Lower limit R_L[a] — upper limit, R_U[b]
Surveyor system	0.67-0.85[c]
Flight control group Altitude reference sensors, control equipment Roll vernier actuator, retro burnout sensor	0.88-0.97
Propulsion group Vernier engine system, retro-rocket	0.77-0.95
Electrical power group Solar panel, batteries	>0.999-≯0.999
Electronics group Power system control, command receiver-transponder circuitries, telemetering transmitters, central command decoder, essential signal processing circuitry, altitude marking radar, radar altimeter, doppler velocity sensing radar, Television No. 4 electronics	0.95-0.989
Vehicle group Harness and interconnections, retro-rocket separation mechanism, vehicle structure, landing gears	0.93-0.99
Mechanics group Drive mechanisms and structures of antennas and solar panel, vehicle anchoring devices, Television No. 4 optics	0.98-0.998
Thermal control group Compartment thermal control	0.98-0.998

[a]0.8 probability that reliability greater than R_L will be achieved.
[b]0.2 probability that reliability greater than R_U will be achieved.
[c]Mean value of estimated system reliability is 0.78.

b. Components and materials. A continuing components and materials study is being made to provide the optimum wire and insulation for the proper balance between electrical and thermal requirements in a lunar environment. The following tasks have been completed or are in progress.

A preliminary 1 in. diameter by 96 in. glass test chamber has been constructed and operated. This unit achieved vacuums of the order of 10^{-5} mm Hg. The ex-

terior of the chamber was wound with nichrome wire covered with asbestos which successfully supplied the required 261°F environment. Testing is underway on temperature rise versus current for candidate copper wire. Work has started on a new 6 in. diameter by 120 in. glass chamber, which should be ready about October 15. The new chamber can be used to test heavy gage wire, cables, and thermal tunnels and should greatly improve the accuracy of the data obtained.

Preliminary qualitative flexure tests have been made on various coaxial cable configurations at —300°F. Results indicate that cables with extruded teflon dielectrics, such as RG 87A, fail when flexed at —300°F. Cables with teflon tape dielectrics (such as RG 115), however, appear to flex satisfactorily at this temperature. Modifications are being made in the basic equipment to allow electrical measurements during flexing at —300°F.

Testing is scheduled to start on a wire-flex-life tester to obtain required information on the relative durability of various types of wires and terminations. In initial evaluations 22 and 26 AWG wire will be used to determine the smallest signal lead wire sizes consistent with reliable mechanical strength and lunar temperature.

c. Electric squibs. The reliability requirements of the retro-rocket separation mechanisms and electrically activated squibs have been analyzed. The retro-rocket is to be attached to the spaceframe at three places by ½ in. bolts and separation (explosive) nuts. On command, an electrical pulse detonates the squibs which separate nuts from bolts and drive the bolts out of the structure. Two squibs will be installed in each nut, so that detonation of either or both produces the desired separation. As further assurance of reliable action, each squib will have two bridge wires, either of which will detonate the squib when the firing current is applied.

The reliability requirement for satisfactory operation of the retro-rocket separation mechanisms is 0.990, with 80% confidence. Since three of the mechanisms must operate for separation to occur, each device must function with 99.7% reliability. The reliability test program requires that 537 of the separation mechanisms (including squibs) function without failure after exposure to typical flight environments. It is further required that 75 units be subjected to a 3-year storage life test, with 25 fired after each year of storage. The specification for the squibs is a demonstrated reliability of at least 99.9%, with 80% confidence.

d. Canopus sensor. The Canopus sensor is required to identify Canopus and discriminate against all other individual stars, groups of stars or planets. The reliability goal is 99.50% when operated under the specified conditions for a period of 66 hr. The reliability test program will demonstrate a confidence level of 0.20 far exceeding a reliability of 99.5% over a 66-hr interval and a confidence level of 0.80 far exceeding a reliability of 97.0% over this interval. A comprehensive reliability plan has been submitted by Santa Barbara Research Center.

e. Reliability assurance test program. The quantitative reliability objectives established for the basic bus are reflected in detail equipment specifications. These requirements provide two of the four parameters necessary to define the individual test plans. The remaining two parameters are the assumed risk of accepting equipment when its reliability is below the specified minimum and the risk of rejecting equipment when its reliability is at least as good as a specified value.

An estimate of spacecraft reliability must be made prior to shipment to AMR. One input will consist of sequential time-sample testing of each equipment type (Ref 5). Combinations and sequences of appropriate mission environments are also planned at stress/time levels to provide quantitative assurance at appropriate confidence levels that equipment is satisfactory. For example, each test plan includes hard vacuum (10^{-7} mm mercury) operation of the equipment for a period equal to three times its expected space life, but in no case more than 450 hr. Recent studies (Refs 6 and 7) indicate that the effects of the combined thermal/hard vacuum environments on the materials selected for *Surveyor* can be evaluated within the planned exposure time.

The test plans are summarized in Table 28, defining the item and sample size for reliability assurance testing, expected mission environmental and operating profile, duration of reliability test, and acceptance criteria. The use of the table is illustrated by observing the entries for the transmitter, part number 231800 (Table 28).

Two transmitters will be selected for reliability test; the expected mission operational requirement is 14 hours in transit and continuous thereafter. For greater reliability, it is planned to operate one transmitter until it fails and then to use the other.

Vibration testing will include simulation of Phase A, B, and C (Fig 136) with the equipment operating during Phase C. Equipment temperature will be cycled between 0 and 50°F during the vibration test, which will include the appropriate number of shocks, D-J (Fig 136). A hard vacuum soak of 450 hr during which the transmitter will be operating and the temperature cycled between 0 and 125°F is included in the test plan.

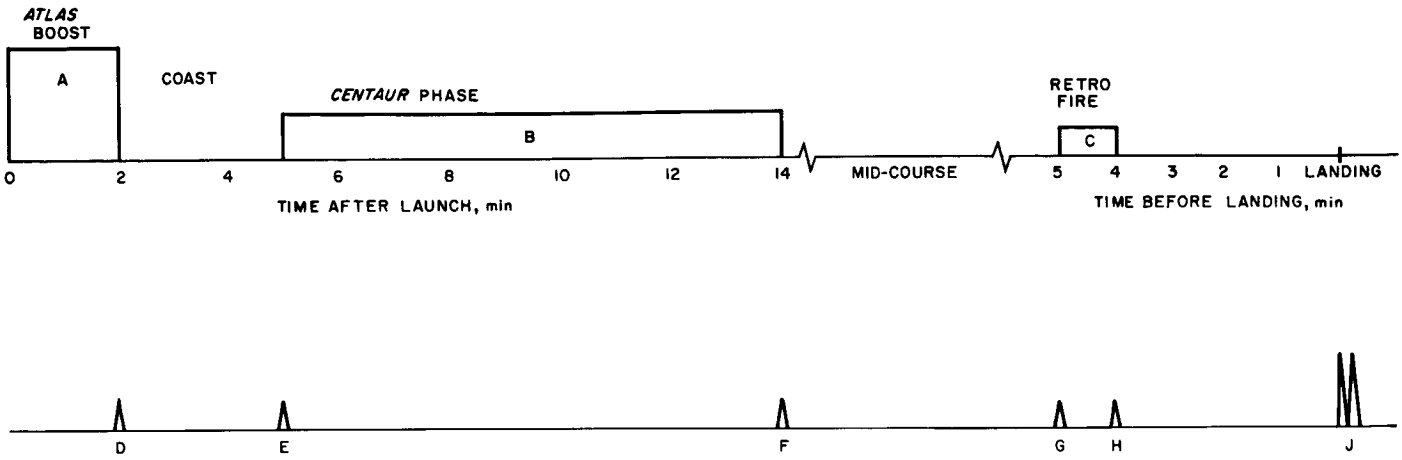

A. 6 *g* 36 rms NOISE 20 TO 2000 cps
1.3 *g* PEAK <50 cps SINUSOIDAL VIBRATION
2 *g* PEAK 50 TO 400 cps SINUSOIDAL VIBRATION
5 *g* PEAK 400 TO 2000 cps SINUSOIDAL VIBRATION

B. 2.4 *g* 36 rms NOISE 20 TO 2000 cps SINUSOIDAL VIBRATION

C. UNKNOWN AT THIS TIME

D, E, F, G AND H. EXPECTED TO BE LESS THAN LOADS EXPECTED UNDER VIBRATION

J. 30 *g* 5 ms ALONG THRUST AXIS AND 15 *g* 5 ms ALONG TRANSVERSE AXES

Figure 136. Vibration and shock environment

The operational test cycle will be based on 80 hr providing adequate assurance of transit reliability without increasing the test time prohibitively. However, since the transmitter is operated approximately 14 times during the transit phase, each cycle of 80 hr will include 14 on-off cycles with suitable cooling time between cycles. The reliability calculations will be based on a continuous function. The sequential plan will assure a risk of accepting equipment with a reliability of 0.97 no more than 20% of the time and a producer's risk of 20% at the desired value of reliability (0.996). This plan will require operating the two transmitters a maximum of 10,667 hr for a decision, and the test program is expected to last 10 months.

2. System Test

a. Flight control system test equipment. Design of the flight control group test equipment of the system test equipment assembly (STEA) is based on limiting part of the flight control group to qualitative testing. The most difficult flight control system parameter to test is the electromechanical and optical-electrical-mechanical alignments of the inertial reference unit, the Canopus sensor, and the primary Sun sensor with respect to each other and to the spacecraft.

To test the inertial reference unit, electromechanical alignment on a system basis requires an angular rotation of approximately 2 deg/sec of the 800-lb spacecraft in at least two axes. The time period of angular input must be accurately measured while observing the command signals to the gas jet system or vernier engine system. To test the Canopus sensor and Sun sensor system optical-electrical-mechanical alignment requires precision collimated light sources accurately positioned with respect to the spacecraft reference axes.

Investigation of the sources of system alignment error for these devices indicates that approximately 95% should be detected and corrected by proper subsystem tests. For example, the inertial reference unit electromechanical alignment to the flight control compartment can be tested using the compartment/spacecraft mounting surface as a reference for precise rate and position inputs and monitoring the flight control system electronics outputs. The optical sensor can be tested in a similar manner.

Therefore, it was decided that the flight control group system test philosophy would rely on the integrity of the flight control group subsystem tests. Figure 137 illustrates

Table 28. Reliability assurance test plan

EQUIPMENT INFORMATION			TEST ENVIRONMENT[a]							
Nomenclature	Part number	Number to be tested	Mission time or cycles			Vibration		Shock[b]	Hard vacuum	
			In-flight	Lunar					Time, hr	Temperature cycle, °F
				80 hr	1 mo	Phase[b]	Temperature cycle, °F			
Flight control accelerometer	236XXX	4	2 min	NA	NA	A, B	0-50	D-F	75	0-50
Inertial switch	236002	4	1 operation	NA	NA	A, B, C_o	0-50	D-F, G_o, H_o	198	0-50
Telemetering accelerometer	236001	2	66 hr	NA	NA	A, B, C_o	0-50	D_o-J_o	198	0-50
Roll control actuator	235000	3	6 min	NA	NA	A, B, C_o	0-25	D-F, G_o, H_o	198	0-25
Battery	237900	1 set, 2 ea	66 hr	80 hr	672 hr	A_o, B_o, C_o	0-50	D_o-J_o	450	0-125
Flight control electronics	235800	2	66 hr	NA	NA	A, B, C_o	0-50	D-F, G_o, H_o	198	0-50
Flip-flop and gating circuits	——	2 groups 50 ea	66 hr	80 hr	672 hr	A_o, B_o, C_o	0-50	D_o-J_o	450	0-125
Gas jet system	235600 235700	2	20 operations	NA	NA	A, B	—10-(—50)	D-F	198	—100-(—50)
Inertial gyro	236XXX	2 sets, 2 ea	66 hr	NA	NA	A_o, B_o, C_o	0-50	D_o-H_o	198	0-50
Mirror drive mechanism	2362XX	8	NA	630 cycles	Unknown	A, B, C	—50-0	D-J	450	—300-100
Antenna/solar panel positioner	2364XX	8	720 operations	90 operations	650 operations	A, B, C	—50-0	D-J	450	—300-150
Power control system "A"	233400	2	66 hr	80 hr	672 hr	A_o, B_o, C_o	0-50	D_o-J_o	450	0-125
Power switch	——	2 groups 50 ea	Unknown	Unknown	Unknown	A_o, B_o, C_o	0-50	D_o-J_o	450	0-125
Radar altimeter and doppler velocity sensor	232903 232904 232905 232906 232907	1	10 min	NA	NA	A, B, C_o	0-50 —100-(—50)	D-F, G_o, H_o	198	0-50 —100-50
Altitude marking radar	232600	1	8 min	NA	NA	A, B	10-50	D-F	198	10-50
Receiver and transponder	231400	3	66 hr	80 hr	672 hr	A_o, B_o, C_o	0-50	D_o-J_o	450	0-125
Solar panel	237700	1	66 hr	80 hr	336 hr	A, B, C	—200-160	D-J	450	—300-220
Canopus sensor	235300	2	66 hr	NA	NA	A, B	0-50	D-F	198	0-50
TV decoder and processer	233101 233000	1	18 min	14 hr	Unknown	A, B, C	—100-(—50)	D-J	450	—300-500
Transmitter and diplexer	231800 232500	2	14 hr	80 hr	672 hr	A, B, C_o	0-50	D-F, G_o-J_o	450	0-125

CONFIDENTIAL

Table 28. (continued)

TEST PLAN CRITERIA

Nomenclature	Single test cycle			Acceptance criteria				Test duration	
	Time	Operations	Discrete or continuous	Minimum acceptable reliability	Probability of acceptance	Desired reliability	Probability of acceptance	Total operating time	Expected length, mo
Flight control accelerometer	2 min	—	C	0.999	0.10	0.9999	0.80	164 hr	1
Inertial switch	—	1 pulse	D	0.999	0.20	0.9999	0.80	4130 cycles	1
Telemetering accelerometer	—	5 operations	D	0.999	0.20	0.9999	0.80	20,650 cycles	1
Roll control actuator	—	9000 operations	C	0.999	0.20	0.9999	0.80	36.9 mc	1
Battery	80 hr	—	C	0.94	0.10	0.998	0.90	7720 hr	10½
Flight control electronics	66 hr	—	C	0.98	0.20	0.998	0.80	13,530 hr	11
Flip-flop and gating circuits	80 hr	—	C	0.99944	0.10	0.99993	0.80	690,000 hr	10
Gas jet system	—	20 operations	D	0.999	0.20	0.9999	0.80	82,600 cycles	3
Inertial gyro	66 hr	—	C	0.90	0.20	0.99	0.80	2710 hr	3
Mirror drive mechanism	—	360 cycles	C	0.999	0.20	0.9999	0.80	2.5 mc	2
Antenna/solar panel positioner	—	1440 operations	D	0.999	0.20	0.9999	0.80	5.9 mc	2
Power control system "A"	80 hr	—	C	0.97	0.20	0.997	0.80	10,950 hr	9
Power switch	—	1000 cycles	D	0.9999	0.10	0.99999	0.80	49 mc	1
Radar altimeter and doppler velocity sensor	—	1 operation	D	0.993	0.20	0.9986	0.80	548 cycles	1
Altitude marking radar	—	1 operation	D	0.999	0.20	0.9999	0.80	4100 cycles	1½
Receiver and transponder	80 hr	—	C	0.97	0.10	0.999	0.90	15,440 hr.	9
Solar panel	402 hr	4[c]	C	0.95	0.20	0.995	0.80	85,200 hr	10
Canopus sensor	66 hr	—	C	0.97	0.20	0.995	0.80	8470 hr	9
TV decoder and processer	14 hr	7[c]	C	0.97	0.10	0.999	0.90	2602 hr	10
Transmitter and diplexer	80 hr	14[c] in flight, continuously on moon	C	0.97	0.20	0.996	0.80	10,667 hr	10

[a]See Figure 117.
[b]Subscript "o" indicates equipment operating.
[c]Number of on/off cycles during indicated times.

CONFIDENTIAL

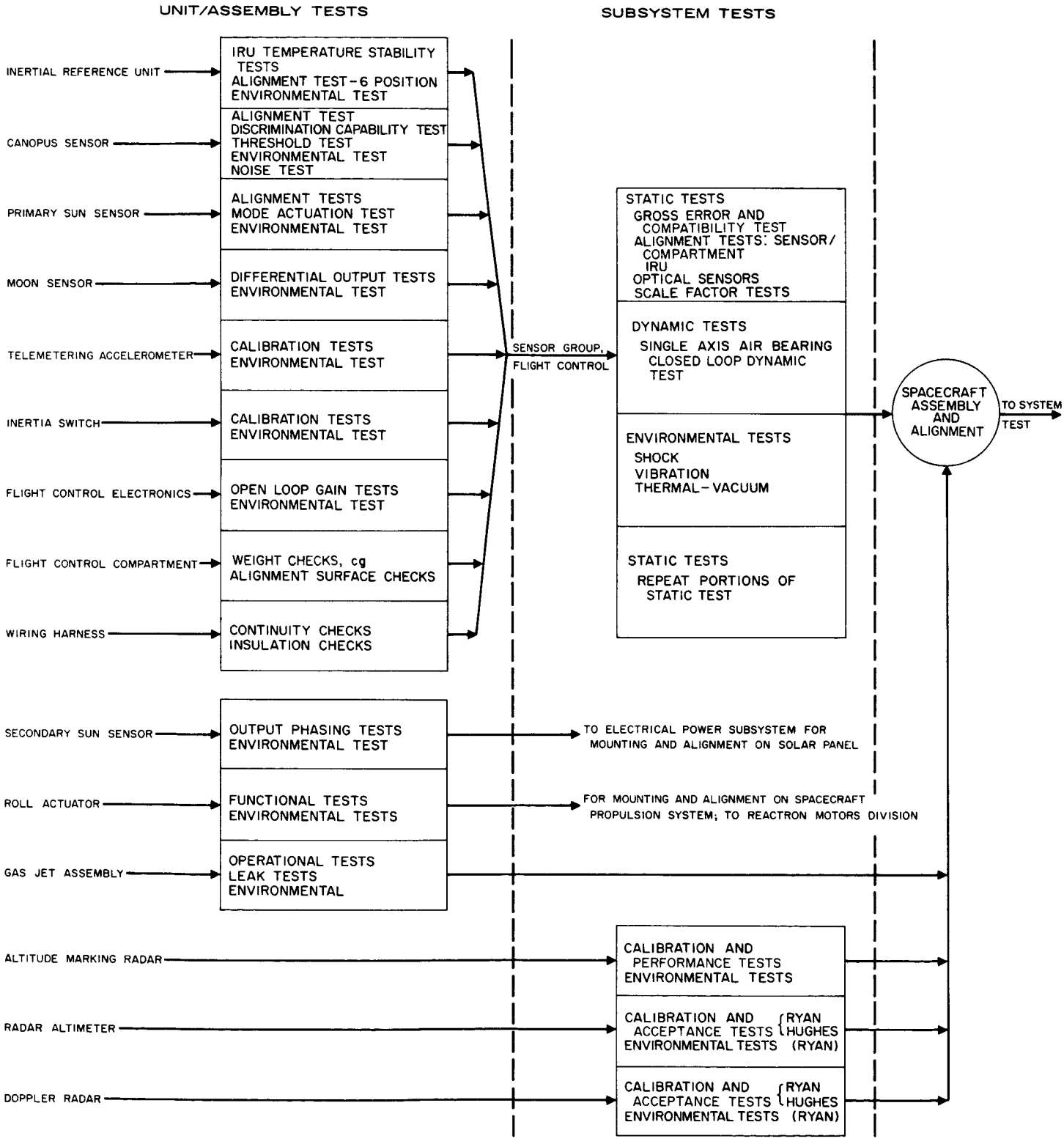

Figure 137. Flight control flight acceptance tests

the flow of the flight control system unit and subsystem tests.

The optical-electrical-mechanical alignments will be accurately checked at the subsystem test level and accurately transferred to the spacecraft coordinate system using optical alignment techniques. The spacecraft system tests will not involve high-order optical-mechanical alignment tests but will be oriented toward subsystem interaction and system open-loop gain and phasing tests.

The subsystem checkout of the flight control equipment during the spacecraft system tests will be divided into two groups: (1) the radars (Fig 138) and (2) the optical sensors, inertial reference unit, and flight control electronics (Fig 139). Both group tests can be performed simultaneously, keeping the total testing time to a minimum.

In the end-to-end system tests of the planned sequence, the radar and flight control groups will be integrated with the other spacecraft groups to form an integrated system (Fig 140). A test "T" connector will be connected into the spacecraft wiring harness at the system cable connectors to the flight control electronics unit, providing access to the flight control system telemetry signals, channel isolation points, and integrator caging leads. Access to the telemetry signals at the source will provide means of checking the calibration of the telemetry system from the signal source to the output of the command and data handling console with the associated integrated system interfaces. The test "T" will be removed on completion of the sequence tests in order to check connector pin connections while performing the final mission simulation tests.

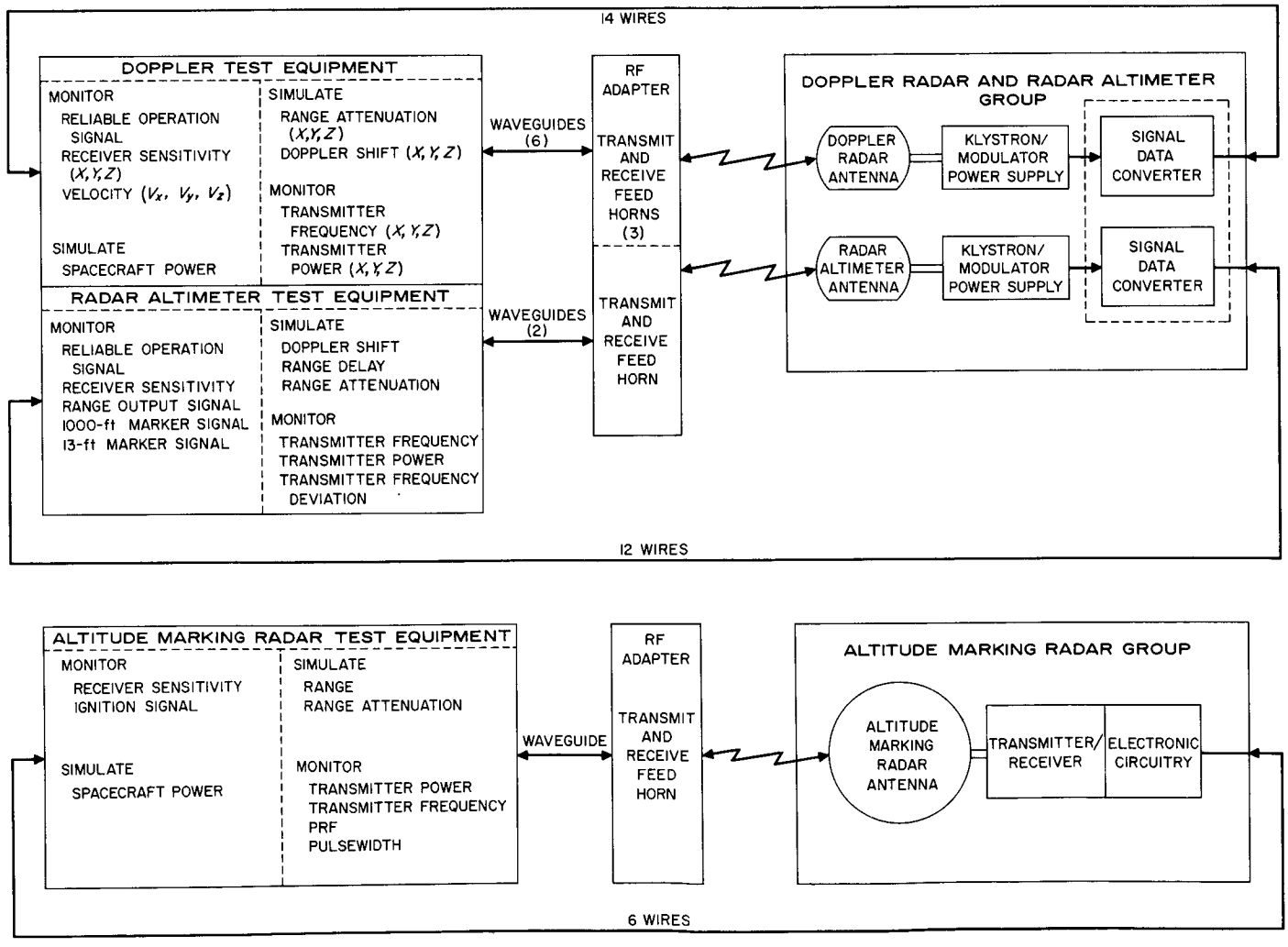

Figure 138. Radar group test sequence

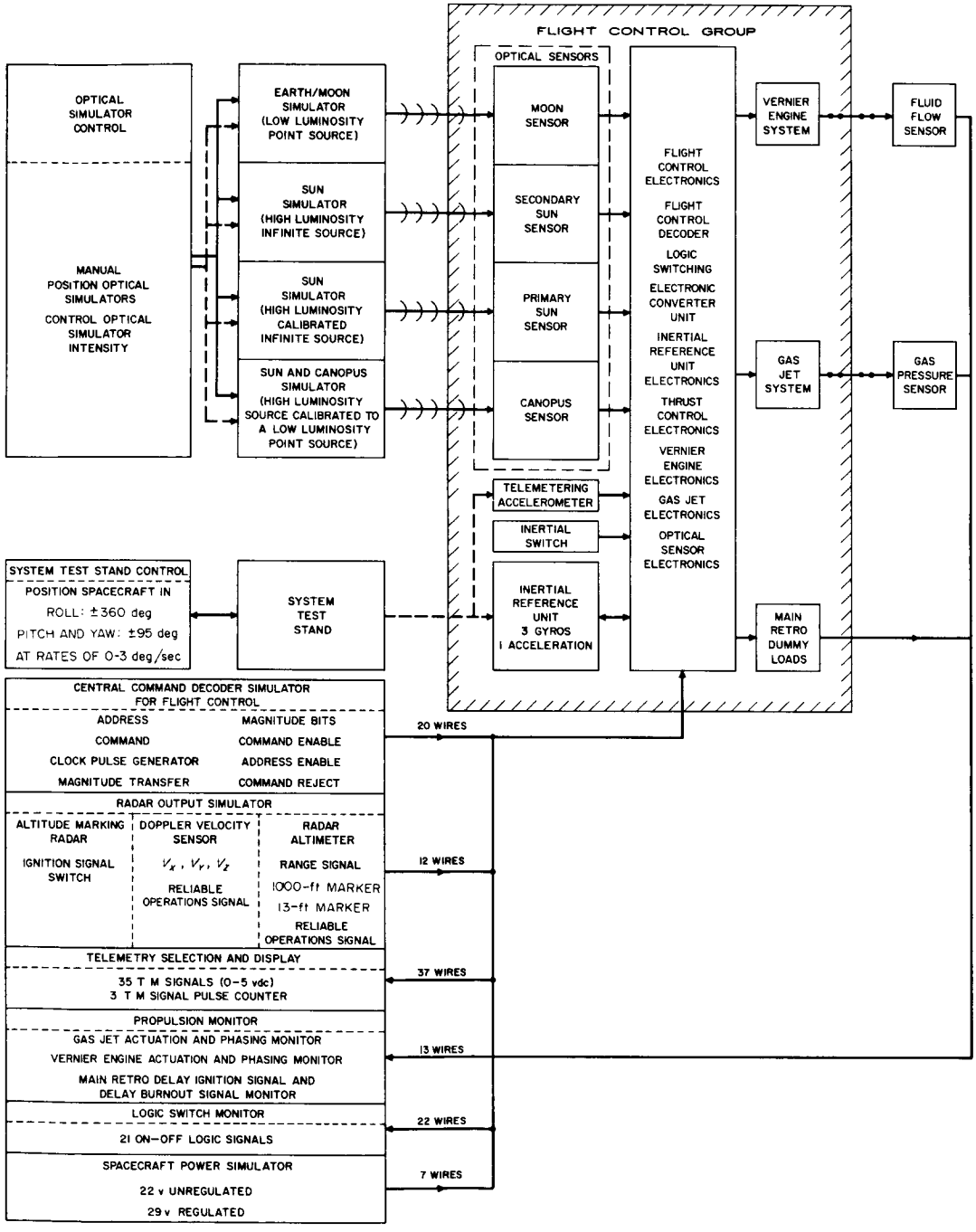

Figure 139. Flight control group test

The portion of the STEA directly related to flight control system testing will comprise seven standard JPL 85-2 racks, five containing equipment for radar group tests and two for flight control group tests. Portions of the equipment in all seven racks will be used in end-to-end system tests of the spacecraft.

Radar group functional tests. The radar portion of the flight control STEA will be capable of performing the checks listed in Table 29. The radar portion will also be capable of simulating range attenuation, range delay, doppler shift, and noise for performing end-to-end system tests and mission simulations.

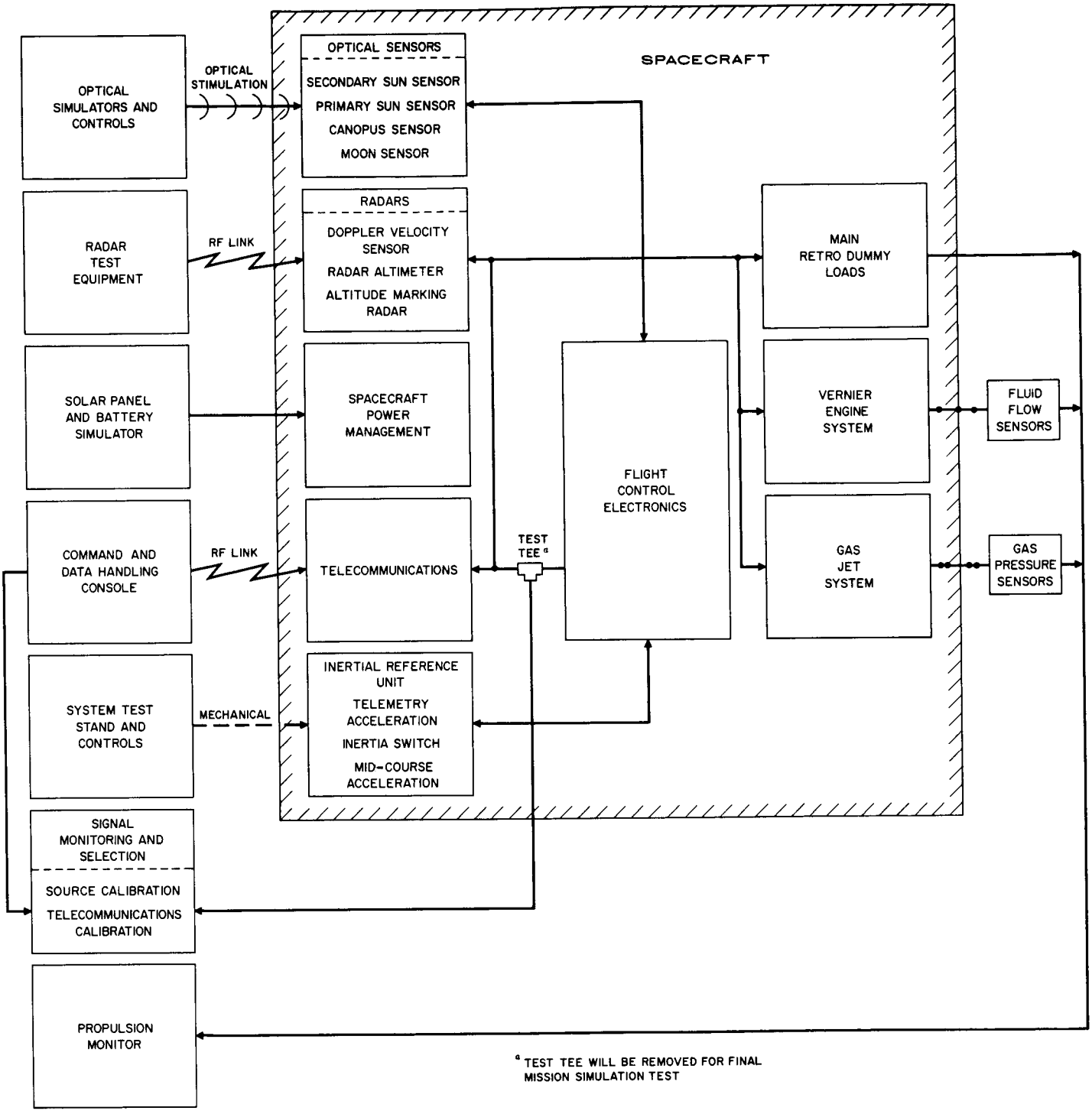

Figure 140. Flight control system test

Flight control group function tests. The flight control portion of the STEA will be capable of isolating a malfunction to the unit level. However, if a malfunction occurs in any unit of the flight control compartment, the present maintenance philosophy is to replace the complete compartment, owing to the critical interaction of the electrical-mechanical-optical alignments of the sensor group and the compartment. The functional parts of the

Table 29. Radar portion of STEA

Doppler velocity sensor checks
Transmitter power
Transmitter frequency
Receiver sensitivity
Tracking rate
Velocity output scale factor accuracy
Reliable operation signal
Radar altimeter checks
Transmitter power
Transmitter frequency
Transmitter frequency deviation and rate
Receiver sensitivity
Tracking rate
Range output scale factor accuracy
Scale change signal
Thrust termination signal
Reliable operation signal
Altitude marking radar checks
Transmitter power
Transmitter frequency
PRF
Transmitter pulse width
Receiver sensitivity
Tracking rate
Local oscillator frequency
IF center frequency and bandwidth
AGC operation
60- and 61-mile gate outputs
Retro-ignition signal accuracy

flight control group test equipment are described as follows:

(1) *Central command decoder simulator* – used to commmand the various modes of operation of the flight control group when performing group tests, simulating only that portion of the central command decoder required for flight control operation. The simulator will be designed to provide static address, command, address enable, command enable, and command reject signals by using toggle and pushbutton switches. The magnitude bits, clock pulses, and magnitude transfer signals are video signals which will be provided in the logic design of the simulator.

(2) *System test stand* – used to maneuver the spacecraft in attitude for qualitative tests of the flight control group. It will provide angular rates and positions of the inertial reference unit and telemetry accelerometer for gain and phasing tests. The complete spacecraft less retro-engine will be mounted on the stand. The test stand will be capable of rotating the spacecraft ± 360 deg about the roll axis and ± 95 deg about the pitch and yaw axis at rates of 0 to 3 deg/sec.

(3) *Radar output simulator* – capable of simulating the lunar radar outputs to the flight control group independent of the radars, to keep radar operating time to a minimum when performing group tests.

(4) *Signal selection and display equipment* – capable of:

(a) Selecting and quantitatively displaying hard wired telemetry signals from the flight control group.

(b) Selecting and quantitatively comparing RF relayed flight control telemetry signals received by the CDC with the same signals hard wired directly to the equipment from the spacecraft via the test "T" access cable.

(c) Displaying gas jet actuation and phasing and providing ignition signal load simulation and monitoring for the main retro-engine.

(d) Selecting and providing proper output combinations of flight control telemetry and actuation signals for real-time recording during various flight control modes of operation.

The equipment will contain analog readout devices for continuous or selected display signals and digital readouts for checking the calibration of the telemetry signals.

(5) *Optical simulators* – used to functionally test the flight control optical modes of operation (Fig 139) and consisting of:

(a) *Canopus simulator* – designed to optically simulate inputs to the Canopus sensor for checking gas jet phasing (roll), lock-on signal (false lock-on), Sun shutter signal, and dead band about null (gain). The equipment will be designed to accurately simulate Canopus in intensity and color and will be used in performing end-to-end system gain and phasing tests.

(b) *Sun simulators* – designed to optically simulate inputs to the secondary and primary Sun sensors for checking acquisition capability (gas jet phasing) of the secondary sensor and gas jet phasing, lock-on capability – acquisition field, dead band about null (gain), and false lock-on discrimination capability (intensity threshold) of the primary sensor. The equipment will be designed to accurately simulate the Sun in intensity and part of the color spectrum for performing end-to-end system gain and polarity tests.

(c) *Moon simulator* – designed to simulate inputs to the Moon detector for checking the differential output voltage from the detector with varying input intensity and angular position.

b. Television system testing. The general procedures have been outlined for system and subsystem testing of

the television system. Standard TV test patterns have been designed for engineering evaluation of the spacecraft television one-unit, subsystem, and system levels.

The standard engineering test pattern (Fig 141) has been designed to provide the best possible calibration of the television system, including the following features:

(1) Square framing for the pattern.
(2) Circular gray scales in the center portion of the test pattern, each of the two scales dividing the range from white to black into ten levels identical to the RETMA standard.
(3) Center reference bull's eye with 400-line resolution.
(4) Two horizontal and two vertical resolution wedges within the circular gray scales, with linear taper and 100 line indexes ranging from 300 to 700 lines.
(5) 200-line bull's eye at each corner, with wedges for evaluating resolution at these points without shifting the test pattern.
(6) High frequency response lines from 2 to 300 kc.
(7) Low frequency response lines from 800 to 2000 cps. (800 cps is considered the practical limit.)

A separate linearity mapping pattern has been designed consisting of 20 equally spaced vertical and horizontal lines. This pattern will allow quantitative measurements of images as small as 1/400 of the picture area with accuracies of $\pm 0.1\%$.

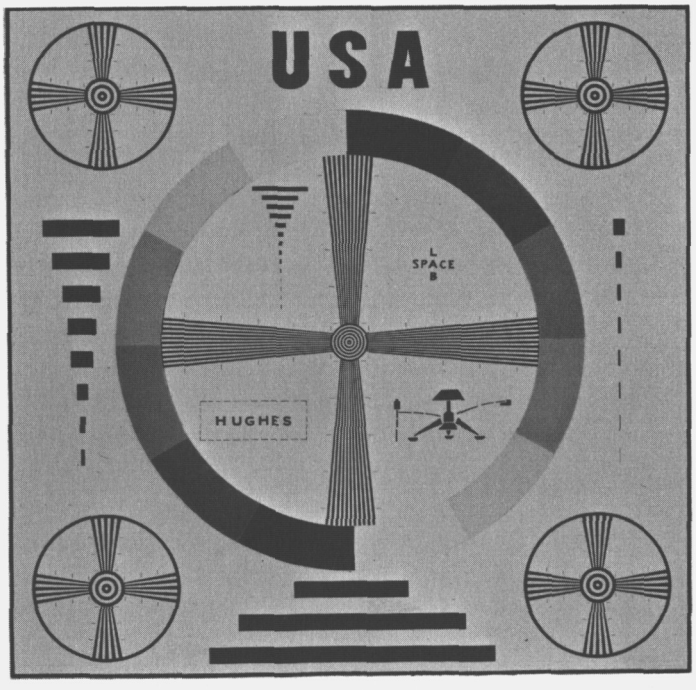

Figure 141 Television test pattern

Microscopic reading techniques will be developed to read the photographic images of the television picture. A method similar to the Kodak shadow-graph comparator may be suitable.

The technique to be used for gray scale calibration is presently being studied. The problem involves definitions of error sources affecting (1) exposure of the vidicon, (2) transfer of the vidicon image to an amplitude-modulated video signal, (3) calibration of monitor equipment to be used for reproducing the video signal as a TV picture, and (4) calibration of photographic techniques to be used for producing an enlarged photograph.

Preliminary conclusions of the study are to use 0 and 4 volt video levels as white and black references. Illumination sources will be standardized to this video voltage, and gray scales will be increments of voltage. A brightness meter and regulated brightness source will be used for comparative calibration, giving accuracies better than 5%.

An electronic gray scale (gray bar) generator is being designed to provide the steps in video voltage at sweep speeds compatible with *Surveyor*. This generator will produce linear or logarithmic gray scales that will simulate the output of the vidicon and will be used to calibrate the monitor scope in known increments of brightness.

A gray bar test pattern is being developed to allow exposure of the vidicon in a manner that will produce a video signal similar to the output of the gray bar generator. In this way, the cause for degradation in gray scale accuracy can quickly be isolated. All the tests involving visible light will use the brightness meter as a standard.

Horizontal resolution will be measured during systems tests by two methods: one using an electronic square wave generator capable of changing pulses in 100-line increments to determine the maximum horizontal resolution in the center 30% of the monitor scope and other recording devices and the other using the RETMA resolution wedge to expose the camera vidicon. This measurement will demonstrate the capability of the *Surveyor* television to produce horizontal line resolution in an enlarged photograph. The combination of the two methods will allow rapid determination of resolution degradation. Vertical resolution will be measured by using the shrinking raster technique as well as the RETMA resolution wedge.

Preliminary concepts have been outlined for system testing the television system. The following types of tests

are planned: (1) wide and narrow angle mapping coverage, (2) electrical interference, (3) photometric/stadiometric calibrations, (4) colorimetric/polarimetric calibrations, (5) video erasure, (6) picture characteristics affected by diffused reflections, (7) stereoscopic mapping capabilities, (8) punched tape command procedures, (9) evaluation of operator techniques and learning times, (10) strobe light illumination, (11) observation and response time for surface/subsurface sampling, (12) physical alignments.

The general layout for test equipment to be used is shown on Figure 142. The television cameras will be initially tested and calibrated at the system level using a "hard-line" connection to each camera. Required commands to a particular camera will be encoded by means of a STEA camera control panel. An STEA targets control panel will provide means for directing the target illumination and color throughout the system evaluation. The intensity of light radiating from the test targets will be controlled accurately to maintain gray scale calibration during the focus, stereoscopic, and depth of field tests.

Pan angle and tilt angle calibration boxes will be used to measure alignment accuracies. These boxes will also be used to map the wide and narrow angle coverage and determine the angular coverage of photographic mosiacs.

An f/stop light input box will provide uniform amounts of illumination to calibrate the vidicon response and iris servo. This box will be capable of providing an intensity sufficient to evaluate the camera protective circuit as a function of the Sun's angle being viewed.

The television monitor in the CDC will be the main source of data in system tests. An additional oscilloscope with land camera will record television information directly from the test access connections.

Data reduction type photographs will be produced directly from the magnetic tape, and these photographs will be used as standards for evaluating the television system. By maintaining close correlation between the data-type photograph and photographs from the monitor scope, a high confidence level will be developed in the ability of the STEA to calibrate the television system and detect degradations or failures.

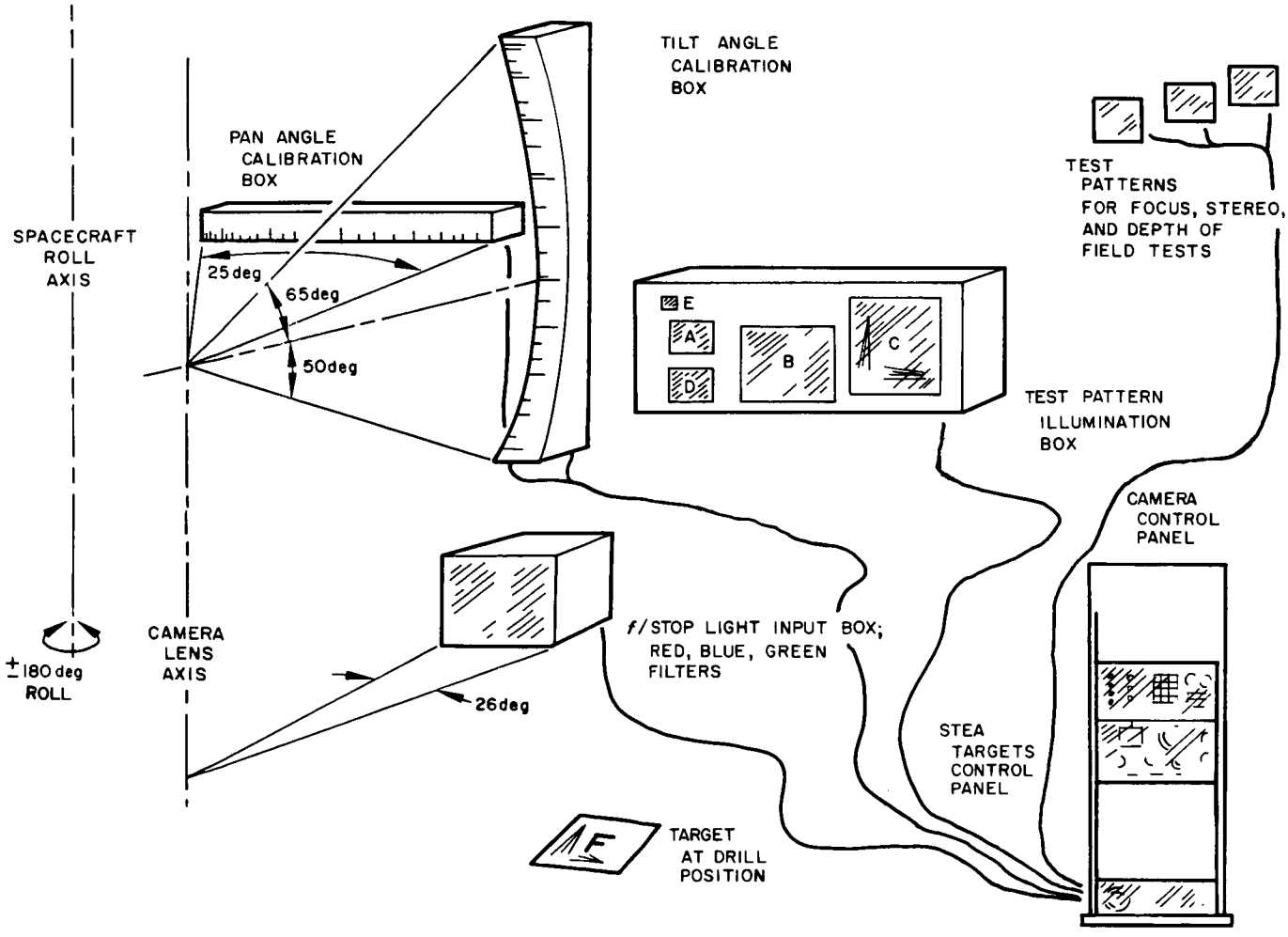

Figure 142. Test equipment for television system tests

L. Mission Operations

1. Launch Operations

During the report period, a preliminary spacecraft launch countdown bar chart was developed showing the functions to be accomplished and the times required for the period from installation of the *Surveyor* on the *Centaur* to launch. For purposes of this chart, the assumption was made that *Surveyor* final surface sterilization would be accomplished after mating with the *Centaur*. Utilizing the data obtained from the preliminary *Surveyor/Centaur* flight operations bar chart from General Dynamics, Astronautics Division, it appears that *Surveyor* on-stand operations including sterilization could be accomplished without any delay in the countdown. Hughes Aircraft Company is continuing to plan for a minimum of testing on the launch stand (as shown on the chart) and for all testing to be accomplished by RF link from the remote STEA location. The *Surveyor* launch countdown chart is shown in Figure 143.

A preliminary mission operations phasing chart for AMR operations has also been issued showing the planned test sequence and times involved in checking out the first three spacecraft at AMR (Fig 144). It should be noted that while time is allotted for a complete Joint Flight Acceptance Composite Test (JFACT) on the first spacecraft, schedule limitations do not permit, nor is it felt desirable to perform, a complete JFACT test on each subsequent spacecraft. Figures 143 and 144 are the result of Hughes spacecraft operational planning. Discussions with GDA are continuing so that an integrated operational plan can be developed.

2. Operational Procedures for Initial Spacecraft Acquisition

Analysis of the effect on acquisition of the spacecraft by the Deep Space Instrumentation Facility imposed by limitations associated with the choice of trajectory, the spacecraft capabilities, and the DSIF capabilities are described in Section C. The following discussion is concerned with the operational procedures for initial acquisition indicated by the results of this analysis.

As part of the prelaunch procedure, the spacecraft low-power transmitter is turned on and the transmitter and receiver are set into the transponder configuration. The transmitter frequency is monitored during preflight and at launch (and as long as possible thereafter) and the measured value sent to the Data, Operations and Control Facility. Computations at the DOC, based on this data

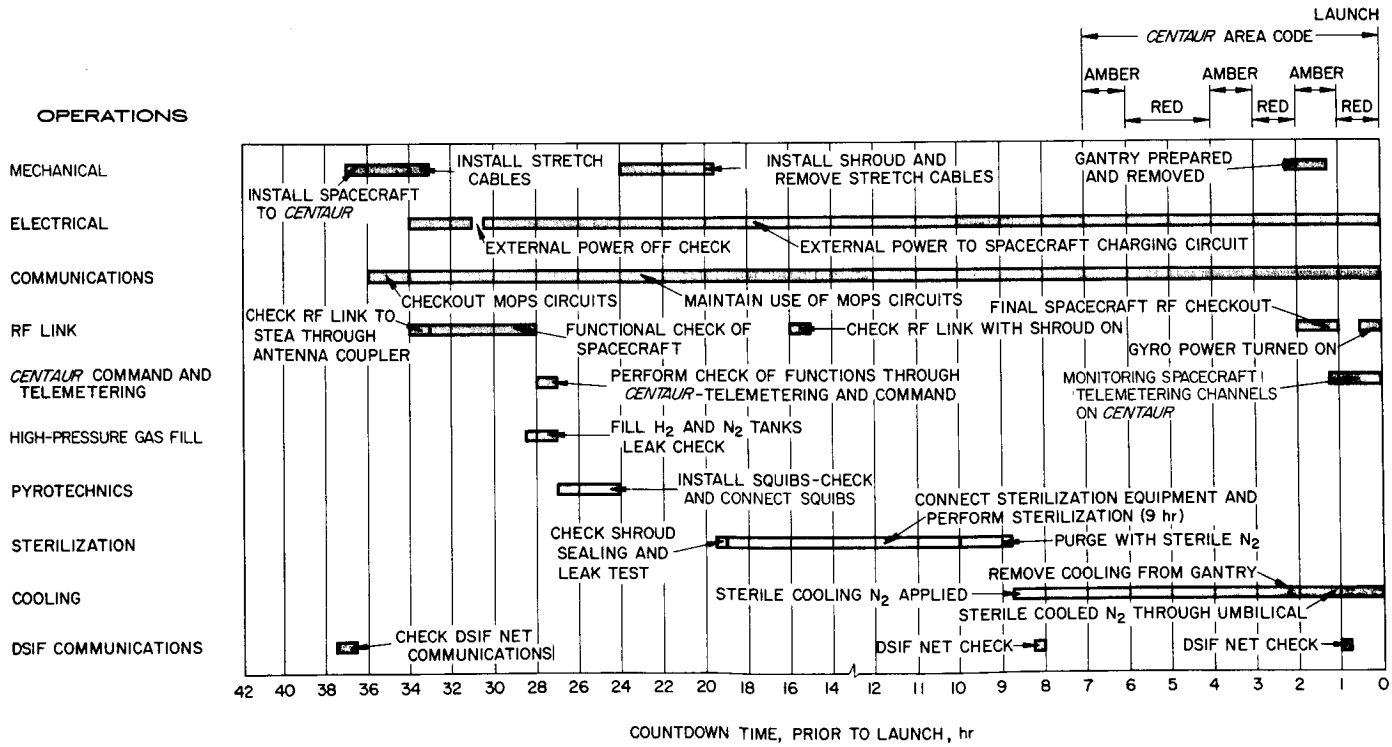

Figure 143. Spacecraft launch countdown

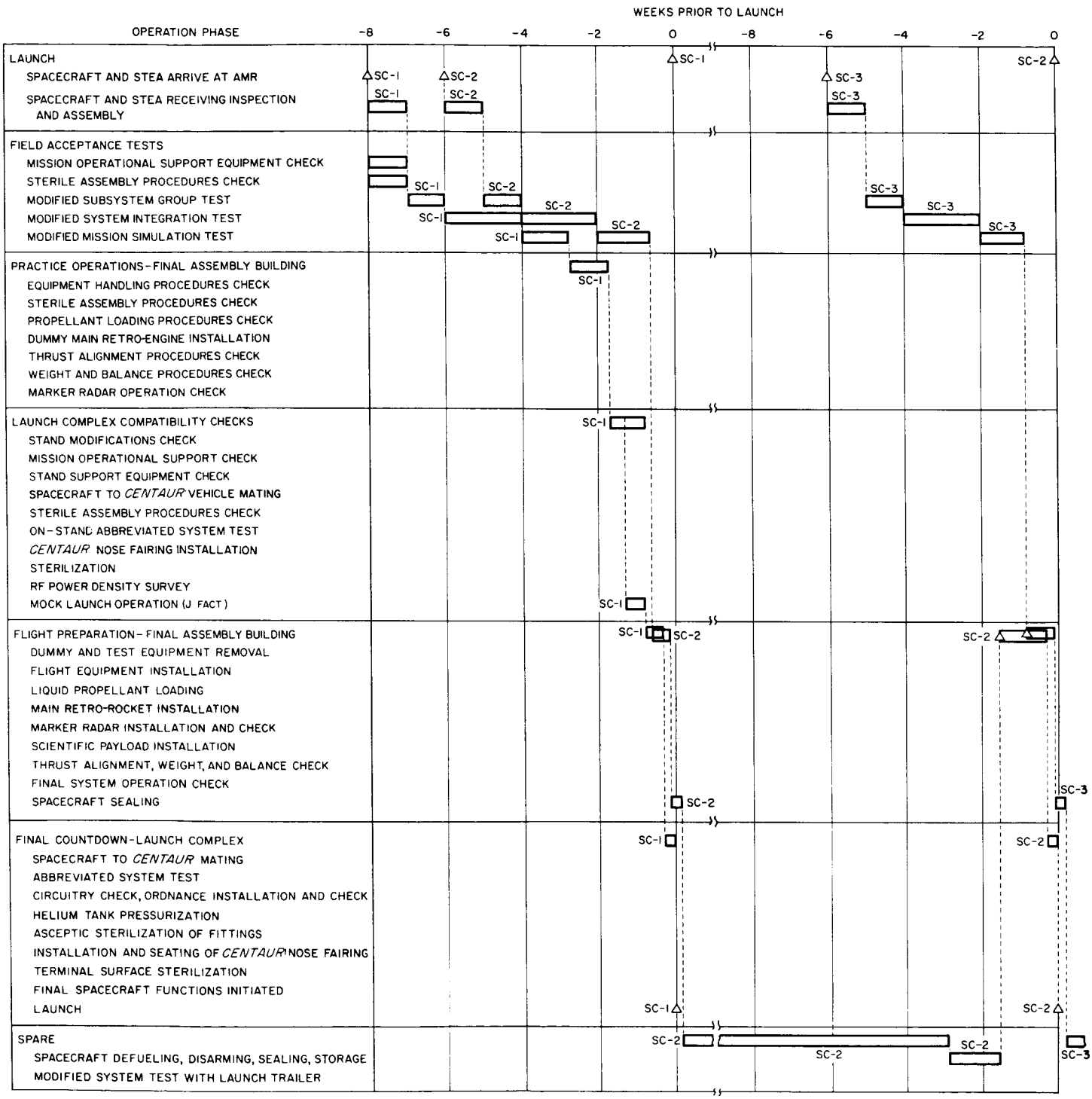

Figure 144. AMR operations phasing chart

and the known characteristics of the crystal which determines transmitter frequency are sent to the acquiring Deep Space Station. The uncertainty relative to spacecraft transmitter frequency at acquisition is thus reduced and the proper choice of crystals for the DSIF receiver can be made.

Since the spacecraft receiver local oscillator is driven by a separate crystal, prior to phase lock, it will also be necessary to monitor the receiver frequency in order to determine the appropriate DSIF transmitter crystals. This can be done by phase-locking the spacecraft receiver to a test transmitter at the launch site, measuring the new

spacecraft transmitter frequency, and applying the known transponder frequency ratio. (In phase-lock condition, both the receiver local oscillator and the spacecraft transmitter are driven by the crystal which, prior to phase lock, determines the receiver local oscillator frequency.) Determination of receiver frequency is further complicated by the frequency pulling of the crystal associated with the phase lock process. The method is still under study and it is possible that the measurement can be simplified.

Design redundancy, incorporating an alternate receiver and transmitter in the spacecraft, implies the need for selecting alternate equipment crystals having characteristics similar to those of the crystals in use at launch. Comparable measurements for these crystals will be included in the prelaunch checkout as late as possible in the countdown. However, since the probability of failure of the receiver/transmitter combination in use at lift-off prior to acquisition is very low, no effort will be made to monitor the frequencies of the alternate equipment crystals after the prelaunch check. The same basic reason precludes the use of on-board failure sensing and switching to automatically replace a faulty transmitter; the added circuitry required would result in a degradation of the over-all probability of successful acquisition.

The choice of the transponder connection at lift-off is also dictated by the need to maximize the over-all probability of successful acquisition. Initial operation of the transmitter in the AFC mode would require successful telemetry of spacecraft receiver AGC and AFC signals in order to have an indication that the DSIF transmitter is properly tuned. Switching to the transponder mode could then occur via ground command. Utilizing the transponder connection immediately, however, provides tuning information for the ground transmitter even if the spacecraft engineering data are not available. Tuning of the DSIF transmitter through the spacecraft receiver passband will result in automatic phase tracking by the latter, and hence a shift in spacecraft transmitter frequency which is detectable on the ground.

Between lift-off and separation a number of spacecraft events relevant to the acquisition process occur. The *Centaur* commands extension of the omnidirectional antenna, and the event is verified through the *Centaur* telemetry link. The power level of the spacecraft transmitter is also telemetered via *Centaur* link. A *Centaur* command turns on the spacecraft commutator containing the receiver AGC, the static phase error AFC, and the transmitter power signals, and the data are telemetered via the spacecraft link.

The DSIF station expected to be in view of the spacecraft at initial acquisition is supplied with prediction data, such as spacecraft transmitter frequency, time-tagged tracking angles, and expected doppler frequency shift. The data are based on the previously described frequency measurements, the known crystal characteristics, and the precalculated standard trajectories as modified by AMR down-range tracking data. The DSIF antenna is positioned according to the angular data and the DSIF receiver is centered at the predicted frequency of the spacecraft transmitter corrected for doppler. The receiver is then monitored at the 3.3 mc bandwidth point and the frequency manually adjusted to obtain phase lock on the carrier, presumably the strongest signal in the passband and fairly close to the predicted frequency. A comparison of calculated and measured signal strength provides a check that the spacecraft is in the main lobe of the antenna pattern. (If no signal is received, the antenna is programmed for a space search or, if means are available to do so, the beam is widened.)

When one-way RF lock has been achieved, the telemetry discriminators in the CDC are phase-locked to the telemetry subcarriers. A check of the telemetry channels then provides further assurance that RF lock has been achieved on the carrier rather than one of the side bands and that the spacecraft is in view of the main lobe. With the DSIF antenna in automatic tracking, the station transmitter is tuned to the predicted value of the spacecraft receiver corrected for doppler. The station transmitter is then slewed in frequency about the predicted value until the telemetered spacecraft receiver AGC and/or a frequency shift in the DSIF receiver indicates that the spacecraft receiver has phase-locked to the ground transmitter. If this process causes the station receiver to lose lock, the receiver is retuned until RF lock is re-obtained and the telemetry discriminators are relocked. The ground transmitter frequency is then varied to adjust the telemetered static phase error to zero.

A procedural problem still exists relative to the emergency procedures to use in the event that the spacecraft transmitter in use at lift-off does fail prior to acquisition. The situation then requires that a ground command to switch transmitters be sent to a vehicle whose space position and receiver frequency are not exactly known. The problem may be resolved by sending repeated commands at different frequencies utilizing a widened DSIF antenna pattern. Further study of the problem is under way.

3. Command and Data Handling Console

The command and data handling console is used in conjunction with the transmitting and receiving equip-

ment at each DSIF station to control spacecraft guidance and lunar experiments and to receive and record data from the spacecraft. For each of the 19 subsystems involved, detail specifications have been prepared, make or buy decisions have been made, and general arrangement of drawings completed. On the six subsystems to be made by Hughes, a final development plan has been completed, and development is well under way.

4. Telemetry Data Display Console

The configuration of the console display for telemetry data has been established. This display will be located on the left-hand panel of the CDC operator's console (Fig 145).

Three types of displays are included on the panel: on-off lamps, analog meters, and decimal readouts. To provide maximum flexibility, none of these displays will have permanent relationships to specific spacecraft parameters; that is, each display is multi-purpose. The meaning of each display will be altered to correspond with the data being received at a particular time and in response to a predetermined analysis of the operator's need to have the information displayed at that time.

At the bottom of the panel are five sets of three-decimal readouts. These displays receive information from the five binary coded decimal outputs of the pulse code modulation (PCM) decommutator and show information the operator needs to know very accurately. Such information as television camera azimuth and elevation would be displayed.

The next row of displays consists of 16 analog meters that derive information from the 16 analog outputs of the PCM decommutator. The data displayed would be that which the operator needs to know somewhat less accurately than the ultimate accuracy of the PCM telemetry system. An example of the data is spacecraft receiver AGC.

The next row of displays has 16 lamps which are turned on to indicate a "yes" condition. These lamps receive information from the binary outputs of the PCM decommutator. Since 50 binary bits are available from the decommutator, expansion capability is provided to allow for more displays. An example of data displayed is the retro engine ignition signal.

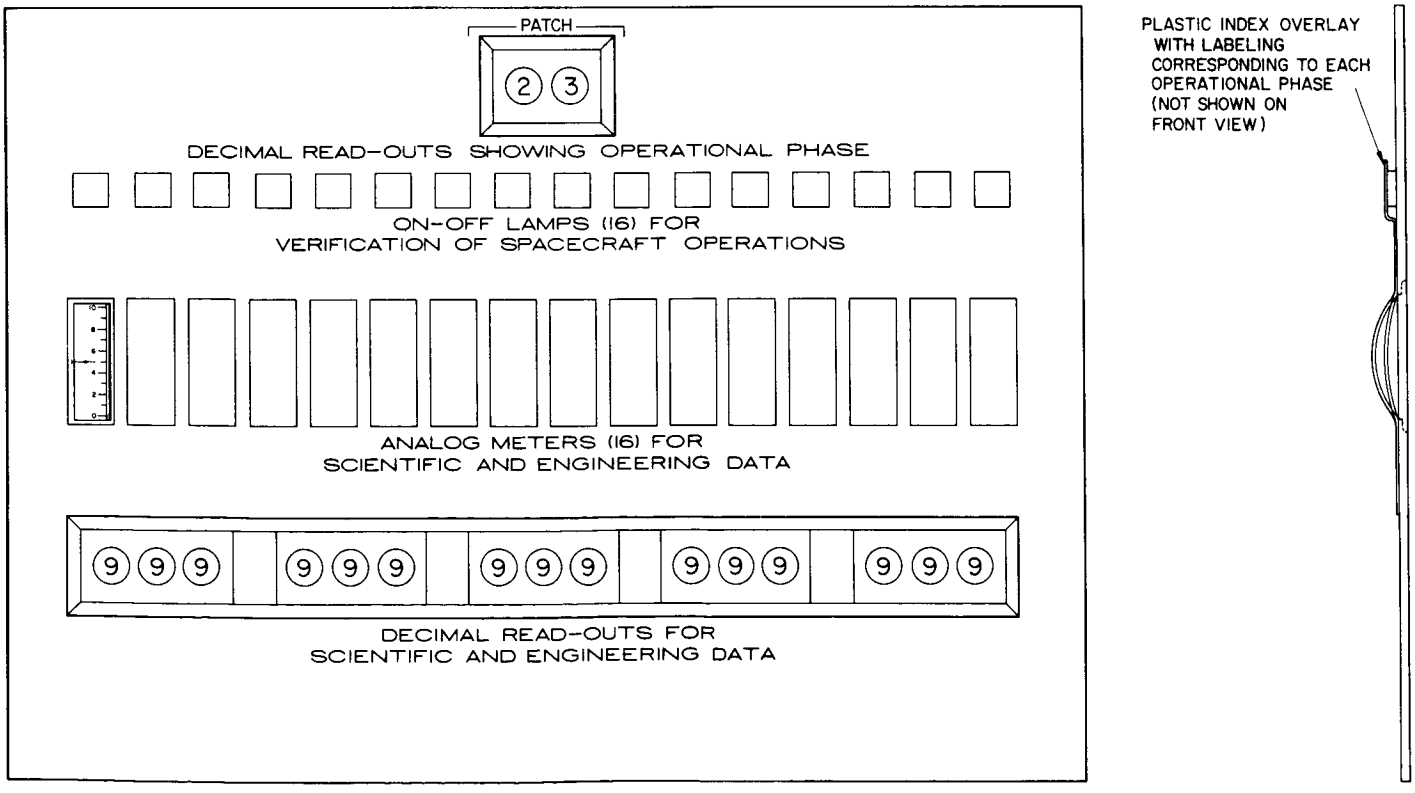

Figure 145. Telemetry display panel

Displays are identified by means of numbered cards mounted on the panel naming the function and giving meter scale factors. The card number corresponds to a number on the decommutator patch board which controls the distribution of the data. To assist the operator, each patch board will have an automatically connected remote identification, appearing as two numbers on the readout at the top of the panel.

5. Magnetic Tape Recording

The *Surveyor* spacecraft will transmit several subcarriers with frequencies exceeding 100 kc. By using predetection recording techniques in conjunction with the FR-700[a] tape recorders, a primary method of recording all the data can be provided. It is then necessary to provide a method of backing up the primary recorder. All low frequency composite FM/FM data can be recorded on the CEC 752 with no problem. However, the high frequency subcarriers will require separation and demodulation before recording. The resulting data from each of the subcarrier channels can be recorded on a separate track of the CEC 752. The number of tape tracks varies with the number of high frequency subcarriers in the composite signal.

The separation, demodulation, and direct or FM recording processes result in increased complexity of data handling at the DSS. In the case of launch and landing data played back from the spacecraft tape recorder, a total of seven tracks will be required on the CEC 752. It may not be possible to allocate all seven tracks of the CEC 752 to *Surveyor* data. The problem can be simplified if the launch and landing data is acquired only at Goldstone and recorded on the FR-600.

The next most complex data recording problem for the DSS is during acquisition of data from hardness and acoustic experiments and during playback of spacecraft recordings made during DSS down-times. During these times, a total of five tracks would be required on the CEC 752. Possibly an operational procedure can be arranged so that Goldstone will be the only station to acquire this data, in which case the FR-600 could be used.

The X-ray experiment data presents the least troublesome recording problem of the high-frequency subcarrier cases. In this case, only one high-frequency subcarrier is employed, so that a total of four tracks is required, only one more than the number of tracks needed for normal low-frequency recording.

A possibility presently being studied is to lower spacecraft subcarrier frequencies. The data handling complexity would thereby be diminished. However, as long as the spacecraft has the capability to send high-frequency data, it should be expected that this capability will be demanded.

There are two distinct disadvantages to recording the data on separate tracks of the CEC 752. If the original data is in analog form (for example the launch and landing data), accuracy will be sacrificed in the demodulation and remodulation process. Some of this accuracy can be regained by careful calibration of the subcarrier discriminator and the recorder modulators. If the data is PCM or pulse data – for example, X-ray data – no accuracy is lost in the demodulation process. However, high-speed PCM data could not be recorded by FM techniques but would be recorded direct with the attendant problem of bit dropouts. Since the method is only for back up, these disadvantages are not considered serious.

At first it was thought that utilizing the FR-700 simultaneously with the CEC 752 would increase tape costs exorbitantly. The study shows only a negligible increase, however. This unexpected fact results from the different tape speeds of the machines – 12½ in./sec for the FR-700 and 60 in./sec for the CEC 752 and FR-600.

The results of the study may be summarized as the following equipment requirements:

(1) Goldstone station
- One FR-700 tape recorder (three tracks)
- One FR-600 type tape recorder (three tracks)
- Two CEC 752 type tape recorders (three tracks each)

(2) Overseas stations (each)
- One FR-700 tape recorder (three tracks)
- Two CEC 752 type tape recorders (five tracks each)

This is the minimum requirement, and expanded *Surveyor* data requirements could increase the recording requirements. The data recording requirements are summarized in Table 30.

[a]In the interests of simplicity the manufacturers' model numbers, FR-700, FR-600, and CEC 752, are used in this report. FR-700 refers to a video tape recorder, FR-600 refers to an ordinary recorder having 250 kc capability, and CEC 752 refers to an ordinary recorder having 100 kc capability.

Table 30. Surveyor data recording

Data	Maximum data frequency, kc	Subcarrier frequency, kc	Recording times	Total recording times, min.	FR-600/ CEC 752 tape costs, dollars	FR-700 tape costs, dollars	CEC 752 tracks required
Spacecraft tape playback							
Launch data — acceleration	1	90,110, 130, 150	Once/launch	12	42.00	47.00	Seven total (1) Accelerometer No. 1 (FM record) (2) Accelerometer No. 2 (FM record) (3) Accelerometer No. 3 (FM record) (4) Accelerometer No. 4 (FM record) (5) Composite telemetering signal (direct record) (6) Commands and time (direct record) (7) Voice (direct record)
Terminal descent — acceleration	1	90,110, 130, 150	Once/landing	12	42.00	47.00	Same as above.
Engineering data and magnetometer data (digital)	5.4, 16.2	130, 150	24 min./ playback	1800	6375.00	7050.00	Five total (all direct record) (1) 16.2 kc (2) 5.4 kc (3) Composite telemetering signal (4) Commands and time (5) Voice
Hardness experiment	7	100, 150	1 min./ penetron drop	12	42.00	47.00	Five total (1) Experimental data No. 1 (FM record) (2) Experimental data No. 2 (FM record) (3) Composite telemetering signal (direct record) (4) Commands and time (direct record) (5) Voice (direct record)
Acoustic velocity experiment	5	100, 136	1 min./charge	12	42.00	47.00	Five total Same as above, for hardness experiment.
X-ray spectrometer	30	150	2 hr/sample	900	3187.00	3525.00	Four total (all direct record) (1) 30 kc (2) Composite telemetering signal (3) Commands and time (4) Voice
X-ray diffractometer	10 (pulses)	150	2 hr/sample	900	3187.00	3525.00	Four total (all direct record) (1) 10 kc pulses (2) Composite telemetering signal (3) Commands and time (4) Voice

PART THREE
PLANETARY—INTERPLANETARY PROGRAM

I. Program Status

A. Objectives

The primary long range objective of the NASA Planetary–Interplanetary Program is the development of automatic, unmanned, interplanetary spacecraft technology and the use of this technology in the form of space probes to gather fundamental scientific knowledge concerning the planetary and interplanetary environments, the planets themselves, and solar phenomena, both out of and within the plane of the ecliptic.

The secondary long-range objective of the program is the development of technology and the collection of scientific data which will contribute to the successful manned exploration of the planets and interplanetary space.

The primary objective of the program by 1970 is to have rather completely demonstrated and, to some reasonable extent, exploited (in terms of acquired scientific data) spacecraft capable of (1) being put into orbit around and (2) landing on the surface of Mars and Venus.

A secondary objective during this period will be the initial efforts toward extending the above capability toward the planets Mercury and Jupiter and space shots out of the plane of the ecliptic and in toward the Sun. The immediate objective of the program is the initial probing of Mars and Venus.

B. Missions

1. General

The Planetary–Interplanetary Program at present consists of three projects: *Mariner* R using the *Atlas–Agena* B vehicle, *Mariner* B using the *Atlas–Centaur* vehicle, and *Voyager*, using the *Saturn* vehicle. The missions planned for these projects are defined below and are obviously subject to change because of such influences as new scientific discoveries or unexpected developments in vehicle availabilities.

2. Mariner *R Project*

The intent of the *Mariner* R project is to perform flyby missions to Venus in 1962 using the *Atlas–Agena* B vehicle. These missions are a replacement for the *Mariner* A project which was cancelled during September 1961 due to unavailability of *Centaur* launch vehicles. The primary objective of the *Mariner* R project is to develop and launch two spacecraft to the near vicinity of the planet Venus in 1962, to receive communications from the spacecraft while in the vicinity of Venus, and to perform a radiometric temperature measurement of the planet. A secondary objective is to make interplanetary field and/or partial measurements on the way to Venus and in the vicinity of Venus. Missions are numbered P-37 and P-38.

3. Mariner *B Project*

The primary purpose of the *Mariner* B project is to permit scientific investigations of the planets Venus and Mars during their periods of availability in 1964 through 1967. Secondary purposes in order of priority are (1) to make interplanetary scientific investigations in the regions between Earth and Mars, (2) to develop experience in the design of a spacecraft that has considerable flexibility with regard to the specific missions it is basically capable of covering, (3) to provide experience and knowledge which will permit a quality and efficient design of the later *Voyager* spacecraft. To these ends, the spacecraft will be designed for a precision flyby mission and will incorporate the capability of either carrying or not carrying a small landing capsule. The *Mariner* B spacecraft will be injected by the *Centaur* launch vehicle and it is expected to launch two identical probes at each of the planet launching opportunities. Deep space probes, to be launched in between periods of Mars and Venus availability, are included in the *Mariner* B project.

4. Voyager *Project*

Voyager missions are envisioned to evolve to sophisticated orbiters and landing experiments beginning in 1966 or 1967 using *Saturn* vehicles. Planetary orbiters are a necessary part of the evolution and are a logical step in the development of spacecraft technology. Orbiters are probably required to permit sufficient observation of the planet to know how to proceed with the landing missions. Furthermore, orbiters may well constitute an important step in the actual landing experiments. The emphasis on planetary orbiters, therefore, will be to contribute to the successful accomplishment of the landing objective.

C. Program Activities

1. *Effect of* Centaur *Slippage*

A slippage in the schedule of the *Atlas–Centaur* vehicle, announced during September 1961, resulted in the cancellation of the *Mariner* A project and a reprogramming of the *Mariner* B project. To provide a mission to Venus in 1962, the *Mariner* R project was initiated, with a reduced weight spacecraft based on *Mariner* A and *Ranger* technology for use with the *Atlas–Agena* B vehicle. This new *Mariner* B design, to be used with the *Centaur* vehicle, is intended to be used at all Mars and Venus opportunities in the period 1964–1967.

2. *Status of* Mariner *A*

Cancelled as of this report.

3. *Status of* Mariner *R* (Agena)

Preliminary design was started on September 1, 1961 and completed in mid-October. Equipment will consist largely of modified *Ranger* and *Mariner* A hardware. Fabrication and rework are underway with start of spacecraft assembly scheduled for mid-January 1962. A Preliminary Project Development Plan has been prepared and is under review by MSFC and NASA Headquarters.

4. *Status of* Mariner *B* (Centaur)

Mission objectives and design criteria have been generated; preliminary design was initiated during October, with a scheduled completion date of April 1962. A Preliminary Project Development Plan is under preparation.

II. Mariner R

A. Guidance and Control

1. Central Computer and Sequencer

The central computer and sequencer (CC&S) for *Mariner* R is the subsystem that supplies timing, sequencing, and computational services for other subsystems on the spacecraft. The services are:

(1) Provide timing reference (38.4 kc) to the power supply.

(2) Provide cyclic commands every 16.7 hours to update antenna hinge-angle and for the scientific data-conditioning system.

(3) Provide launch sequence commands for solar panel extension, attitude control power turn-on, and Earth acquisition and telemetry rate changes.

(4) Propulsion sequence, to execute the mid-course maneuver.

(5) Provide encounter sequence commands (start- and stop-commands in the vicinity of the planet.)

In developing the *Mariner* R CC&S, components, circuit designs, and packaging approach planned for the *Mariner* A CC&S have been used and, in fact, several *Mariner* A module layouts were incorporated with only modest redesign, enabling fabrication of a majority of the system to commence at an early date. Final tests of a complete breadboard have been successfully accomplished (late October). Final assembly of the first flight system should commence in mid-November with flight acceptance testing anticipated to begin in mid-December.

2. Attitude Control

a. Coasting attitude control. The coasting attitude control system for *Mariner* R incorporates a minimum change from the previous *Mariner* A design. It retains the essential features of *Mariner* A. These are:

(1) Automatic acquisition of Sun and Earth; accomplished by a logic system incorporating Sun and Earth sensors.

(2) Roll override, to release lock from any undesirable object acquired by the Earth sensor.

(3) A hinge follow-up system, that stores the value of the high-gain antenna hinge angle, to be used as a reference angle for a roll search whenever Earth acquisition is lost. This angle storage is updated once every 16.7 hours.

(4) Gyros, for control system stabilization during any Sun or Earth acquisition process.

(5) Derived rate compensation (passive network), for stabilization during the cruise limit cycle operation, during which time the gyros are turned off.

The basic changes in *Mariner* R are:

(1) Sun sensors (RA-1B) are to be used for pitch and yaw attitude control.

(2) The short-range Earth sensor has been deleted. The *Mariner* A long-range Earth sensor will be used for roll control during the major portion of the flight, Earth acquisition being delayed until 167 hours after launch. During the period before acquisition, all communication is through the low-gain antenna.

(3) A hinge override command has been added to allow the antenna to be positioned, in steps, through the entire range of the hinge servo. This capability allows the hinge field of view of the Earth sensor to cover any Earth-probe-Sun angle, to permit Earth acquisition during non-standard situations.

To date, design parameters and tolerances for the mechanization of the pitch and yaw control systems (Fig 146) have been derived. The design of the roll control system (Fig 147) is partially complete. Its completion awaits derivation of parameters and tolerances for the derived rate stabilization system. A problem to be overcome is the interaction of the noise content of the Earth sensor and its time response. If the time response is made small enough to allow acquisition, the noise level is too high to allow acceptable performance during the cruise limit cycle operation. Some change in the derived rate stabilization system from the original *Mariner* A design may be necessary to permit acceptable performance during both the acquisition and cruise modes.

3. Autopilot

The autopilot maintains vehicle dynamic stability during the interval of mid-course propulsion. Stability is maintained by the use of movable jet vanes mounted in the exhaust of the mid-course propulsion motor. Deflection of the jet vanes aligns the direction of the motor thrust with the center-of-gravity of the spacecraft and thus maintains stability.

a. Analysis. The *Mariner* R autopilot is essentially the same as the *Mariner* A autopilot, with the exception that its gain is increased by a factor of 1.75 to improve its response to the start transient. The block diagrams of the *Mariner* R autopilot are shown in Figures 148 and 149.

The *Mariner* R (and *Mariner* A) autopilots differ from the *Ranger* autopilot in that it does not have an outer loop for correction of the pointing direction of the thrust

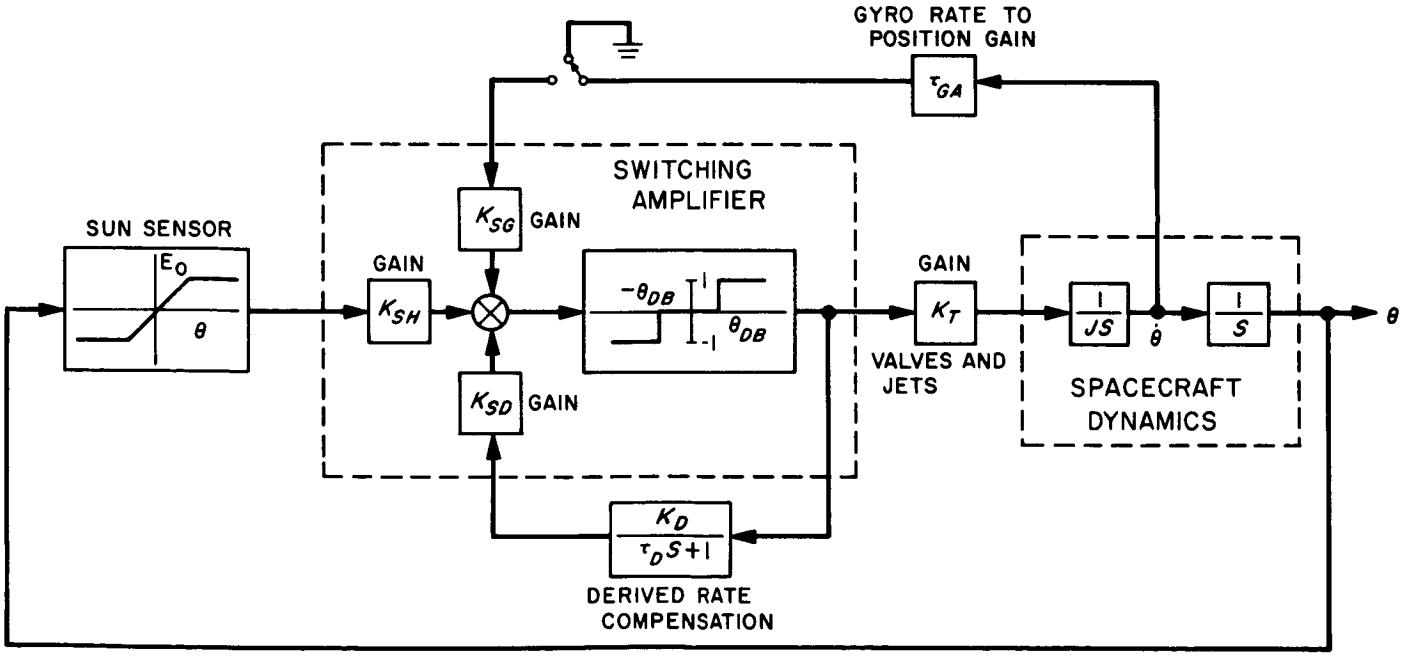

θ = PITCH OR YAW ANGLE ERROR
θ_{DB} = SWITCHING AMPLIFIER DEADBAND
J = PITCH OR YAW AXIS MOMENT OF INERTIA

Figure 146. Coasting attitude control pitch and yaw axis

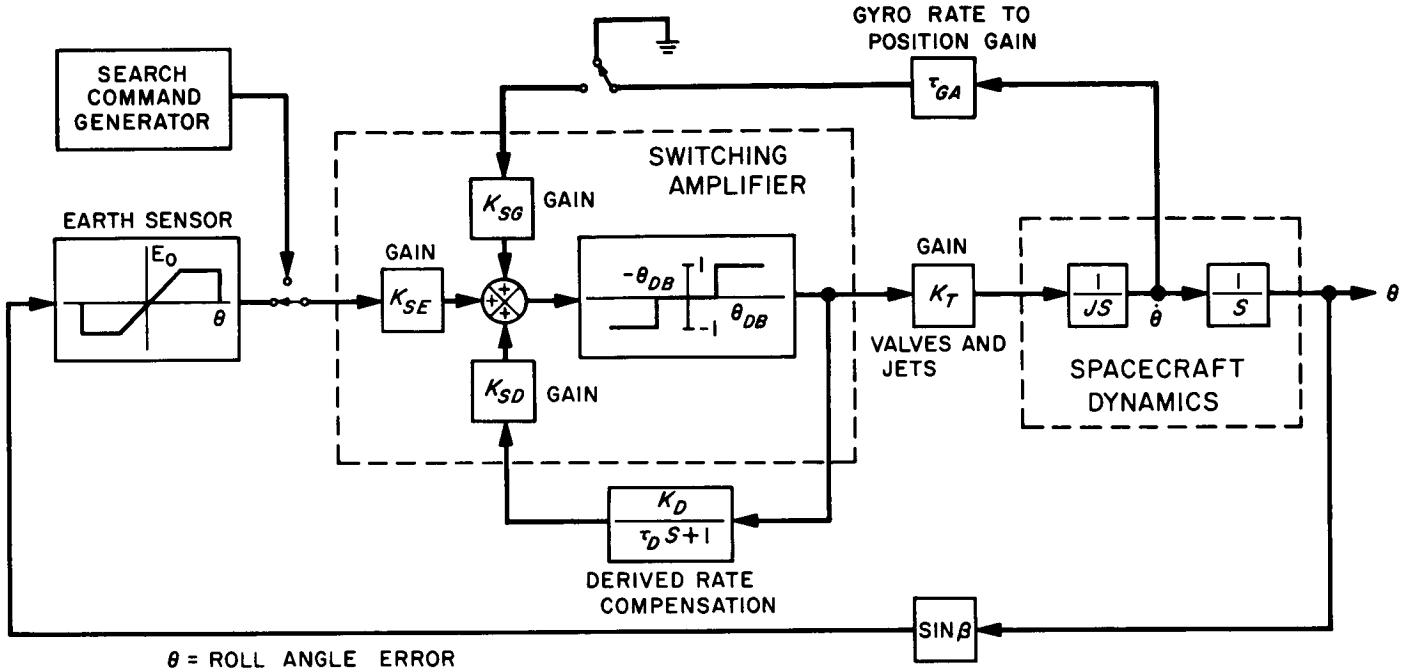

Figure 147. Coasting attitude control roll axis

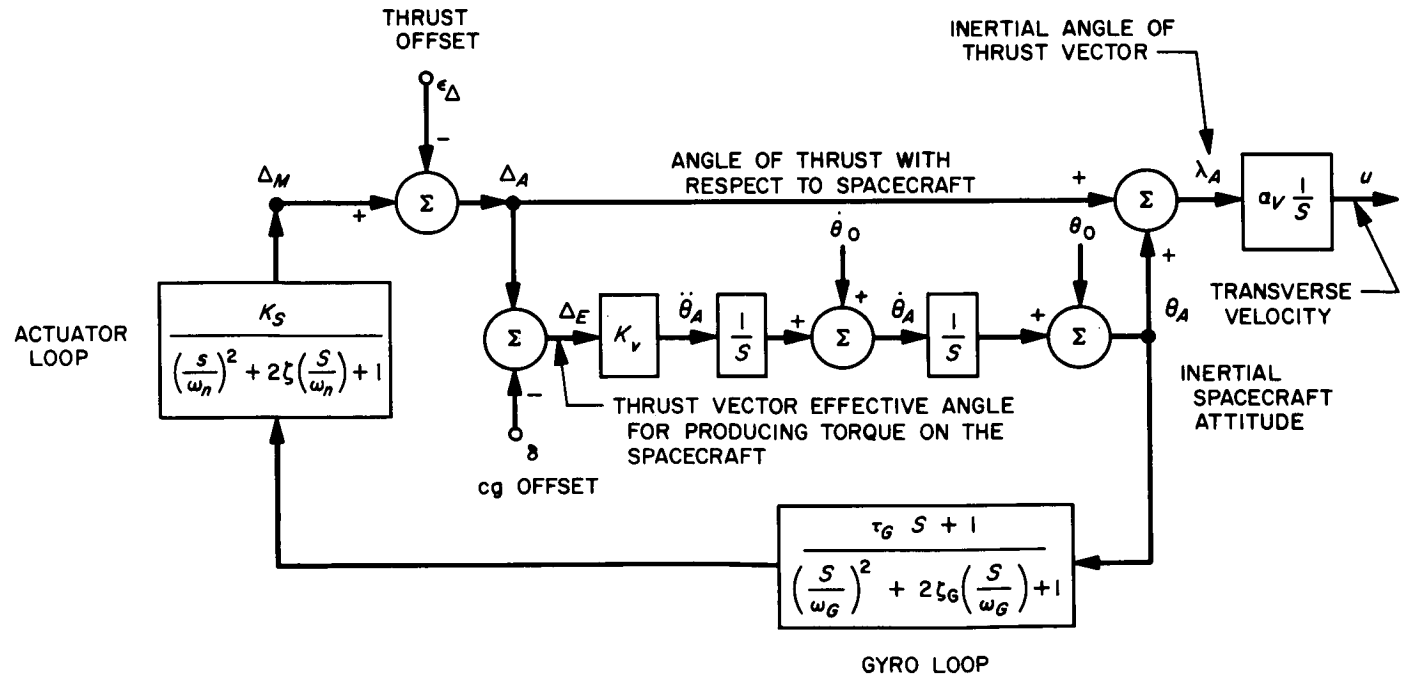

Figure 148. Single-axis pitch/yaw autopilot

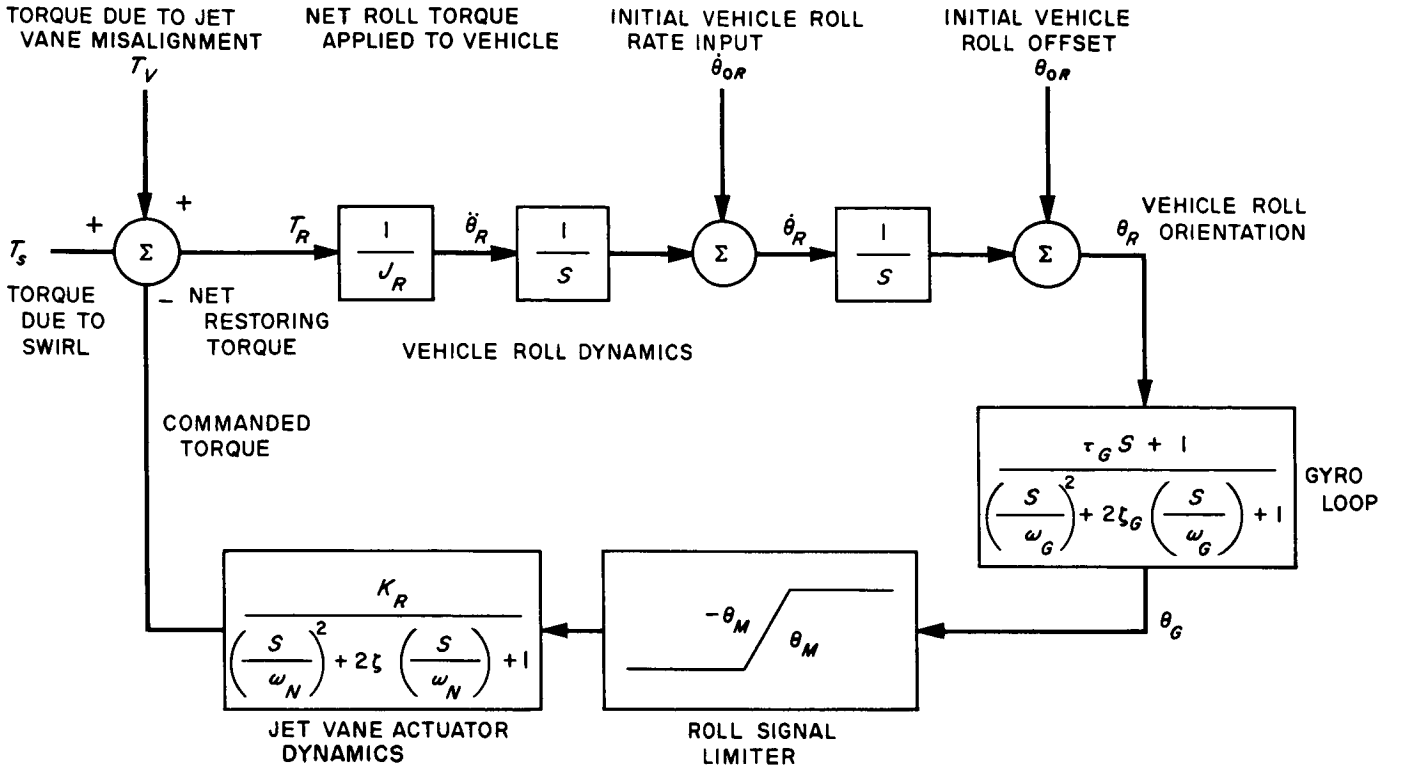

Figure 149. Single-axis roll autopilot

vector. The *Mariner* R autopilot thus controls only the spacecraft attitude; consequently, the pointing direction of the thrust vector can be in error by approximately the equivalent angular offset of the spacecraft center-of-gravity. This equivalent angle can be as large as 23 milliradians, but *Mariner* R mid-course guidance does not require greater accuracy.

An analog computer analysis of the basic autopilot has been completed. The gain margins have been determined, by instability, for gain increase and gyro loop saturation for gain decrease. The gain increase margin is 4.4 based on nominal parameters, and the gain decrease margin is 3.5 based on the combination of tolerances which produces the biggest transient in the gyro loop. With the worst combination of in-tolerance parameters for gyro loop saturation, no more than 50% of the gyro loop capability is used. With the worst combination of in-tolerance parameters for jet vane saturation, no more than 43% of the jet vane capability is used.

Studies are now in process to determine the effects on the autopilot of elastically coupled spacecraft masses, such as the solar panels and the mid-course propellant. Initial indications are that the relatively small mass of the propellant causes virtually no deleterious effect. The poles of the transfer function resulting from propellant sloshing are very close to the propellant zeros because the propellant mass is small; hence, the autopilot dynamics are not appreciably affected. The first bending mode of the solar panels produces a small decaying oscillation in the start transient that is not of major importance. Analysis of the second bending mode of the solar panels is not completed. This mode appears to be more of a problem because of its higher natural frequency. Other structural elements that have been examined are the superstructure and the high-gain antenna; these appendages will have negligible effect on vehicle stability.

b. Mechanization. Vehicle rate and position are sensed by body fixed integrating rate gyroscopes. The electrical outputs of the gyros control the positions of the respective jet vanes, as shown in the mechanization block diagram of Figure 150. The position of each of the four jet vanes is controlled by a position-servo consisting of an actuator amplifier, actuator torque motor, and an output coupled potentiometer for position feedback. The torque motor is a dc moving magnet device. The feedback pot is excited with dc.

The feedback and input signals are summed at the input to the dc amplifier. The amplifier has an RC network in a feedback path to provide lead compensation for servo stability.

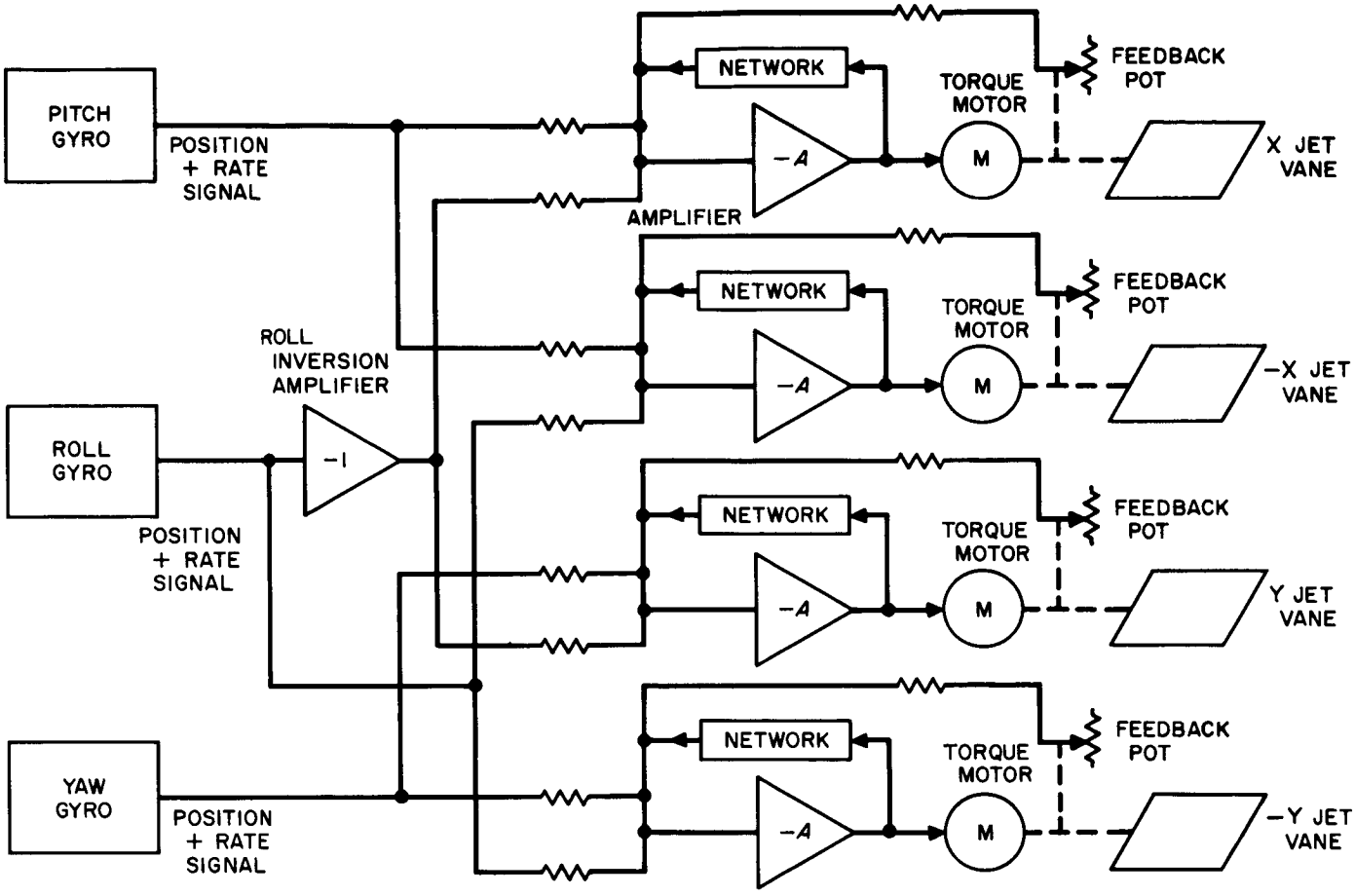

Figure 150. Autopilot system

Pitch and yaw corrections require equal deflection of the respective pitch and yaw jet vanes. A roll correction requires a differential deflection on the pitch jet vanes and also on the yaw jet vanes. A positive roll input must then produce equal and opposite voltages at the inputs of the X, Y and −X, −Y actuator amplifiers. This signal inversion is obtained in the roll inversion amplifier.

The schematic diagram of the actuator amplifier is shown in Figure 151. The amplifier uses shunt mixing of input and feedback signals. R1, R2 and R3 are the input resistors for the pitch and roll gyros, and actuator position signals. R4, 5, 6, 7 and C1 and C2 comprise the feedback network. The open loop gain of the amplifier is sufficiently high that its closed loop transfer function is determined by the feedback and is independent of amplifier component variations. The dc gain is 13.3 referred to the 75K input and is low enough to enable the dc operating point of each stage to be stabilized by feedback around the entire amplifier.

The emitter of the input transistor Q1 is clamped by CR2 which compensates for the base-emitter characteristic of Q1 and provides a low-emitter circuit resistance. The second stage is coupled to the first by the forward-biased zener diode, CR1. The resistor in series with the second stage collector limits the maximum possible dissipation of the transistor. This limiting is required when the amplifier output is saturated in the negative direction and there is no stabilization of the collector current of the second stage. The output stage consisting of Q4, Q5 and CR4 is designed for Class B operation. A negative output is produced by an increase of Q5 collector current. The load current flowing through CR4 reverse biases output transistor Q4. Transistor Q3 operates as a constant current source for the base current of Q4. When the Q5 collector current becomes less than the collector current of Q3 the output polarity becomes positive. As the negative load current diminishes, CR4 becomes reverse biased and isolates the Q5 collector from the output. Q5 then drives the base of Q4 which in turn is emitter coupled to the output.

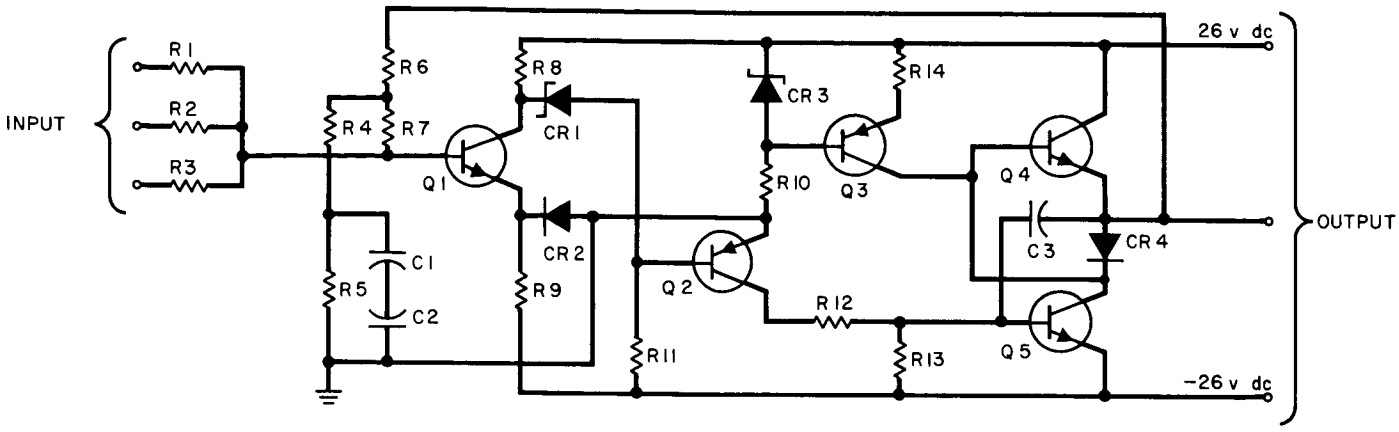

Figure 151. Actuator amplifier

The amplifier has a dc current gain of 6500 and a maximum phase lead of 50 degrees at 12.5 cps. The maximum power output is 2.7 watts with a 150-ohm load. The maximum dc offset is less than 0.5 volt referred to the 75K input.

4. Logic Functions

The *Mariner* R logic is similar to that used in *Mariner* A. Modifications have been made to accomplish Earth acquisition 7 days after launch, and to provide ground hinge override capability.

a. Automatic acquisition. The Sun is automatically acquired when the attitude control system is turned on. Automatic Earth acquisition takes place only when the Sun is acquired and the Earth acquisition inhibit signal is removed. The Earth acquisition inhibit order is in effect for the first 7 days after launch. It is also turned off during the mid-course maneuver and for a 2-hour period after the propulsion maneuver. To prevent the Earth sensor from seeing the Sun, the Earth sensor is turned off until after Sun acquisition and lock is made.

b. Hinge and roll override. During certain portions of flight, the possibility exists that the Earth sensor may acquire an object other than the Earth (the Moon) or be pulled off the Earth reference by a bright object (Venus) passing close to the center of the sensor field of view. The ground-commanded hinge and roll override sequences are used to permit one reference to be dropped and another to be acquired.

The hinge override incrementally adjusts the antenna reference angle. The roll override command energizes the gyros, and switches the Earth sensor out of the roll and hinge channels, initiates a roll-turn in search of the Earth, and returns the antenna servo to the reference mode so that the antenna moves to the reference angle set by the hinge override command. The normal acquisition sequence then continues until another object (presumably the Earth) is acquired and the system returns to the cruise mode.

c. Gyro control. Whenever the Sun is not acquired, or the Earth is not acquired and the Earth acquisition inhibit is not in effect, the gyros are automatically turned on. The gyros are also turned on from launch until the automatic acquisition is initiated, and during the premid-course period for the purpose of drift stabilization. The premid-course period starts 1 hour before the commanded turn sequence is initiated. Whenever acquisition of both the primary and secondary reference bodies (presumably the Sun and Earth) has been accomplished, the gyros are turned off after a 180-second delay period inserted to allow acquisition transients to decay.

5. Antenna Hinge Servo

The *Mariner* R antenna hinge servo is a combination of the RA-3 gear box, with the RA-1 gear ratio and modified *Mariner* A electronics. This combination of components, comprises a hinge servo which fits the *Ranger* structure, adapts easily to the *Mariner* R power system, and has good stability margins, as a result of the low slewing rate provided by *Ranger* RA-1 gearing.

The block diagram of the hinge servo is shown in Figure 152. As on *Mariner* A, there is an update servo to provide a reference angle for the antenna in case the Earth should pass out of the sensor field of View. This reference is updated to the current Sun-probe-Earth angle once each 16.7 hours, unless the Earth is not acquired; e.g., during the mid-course maneuver.

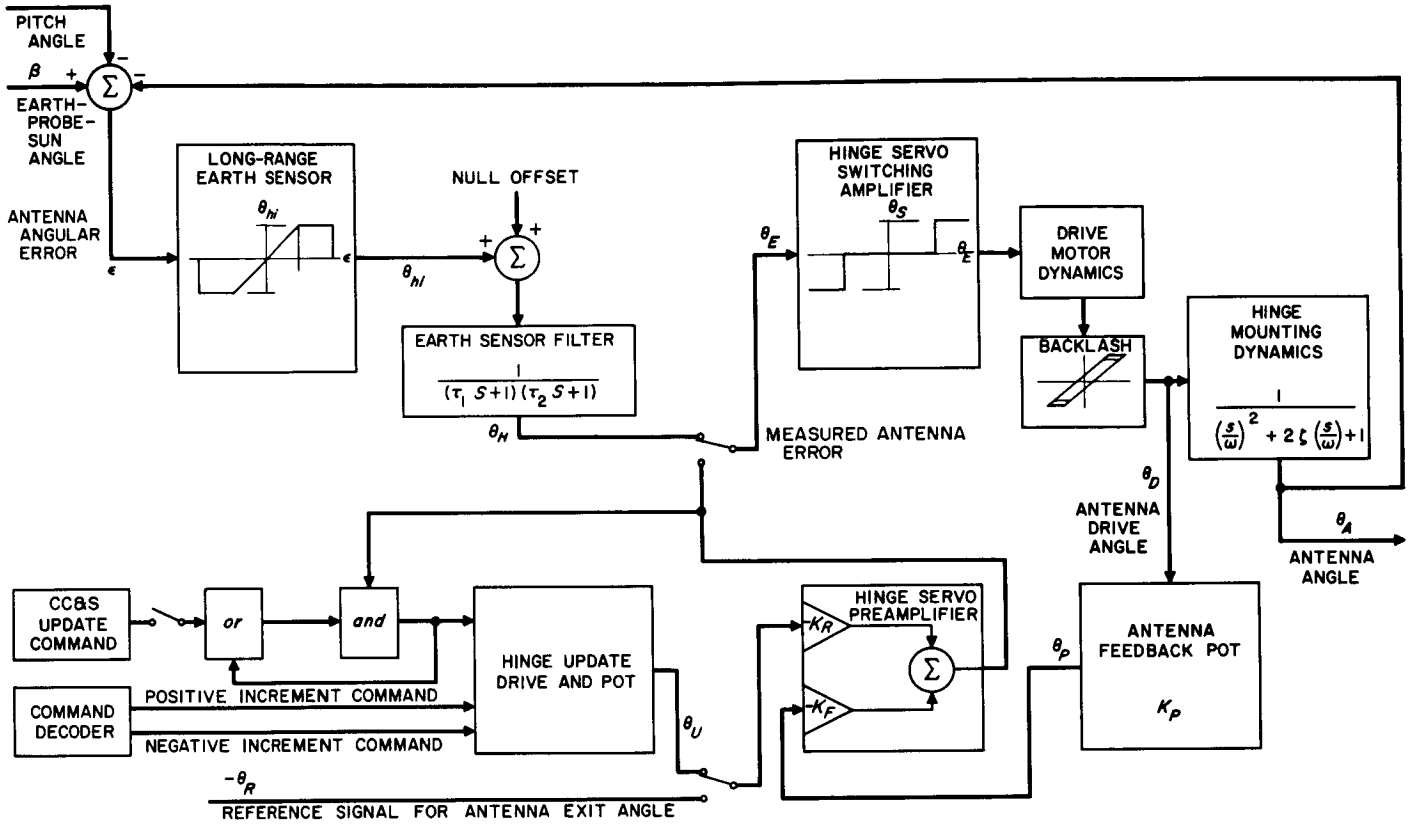

Figure 152. Antenna hinge servo

An additional feature called hinge override, which was not provided on *Mariner* A, is the capability for ground-commanded incremental changes in the update reference angle during flight. Two ground commands are provided: one for positive, and the other for negative increment. A change of several steps is accomplished by repetition of the appropriate command. The increment is slightly less than 3 degrees of antenna motion. By using hinge and roll override command, it is possible for most geometrical situations to break acquisition of an undesired object, such as the Moon or a planet, and to acquire the Earth. If, at a given time, the geometry is such that this cannot be done, within a few days the geometry will always change in such a way that Earth acquisition can then be accomplished.

An analog computer study of the hinge servo has been completed. Included in the simulation are all of the known deleterious effects, such as backlash, overshoot, and the noise-reducing second order binomial filter of the Earth sensor. Under the worst combination of tolerances, the antenna servo can slew from the saturation region into the linear region of the Earth sensor at the maximum slewing rate and yet stop quickly enough that it will not reverse direction. For this worst-tolerance situation, three-fourths of the dead zone of the switching amplifier is traversed. In the nominal case, less than half of the dead zone is traversed.

6. Control Gyro Module

As discussed in *SPS 37-11*, the Kearfott 2519-005 gyro was determined to have non-linear response characteristics resulting from excess jewel and pivot clearance. This effect was determined early enough in the Kearfott build schedule of *Mariner* R gyros to allow a design change. A jewel and pivot clearance of 25 to 50 microinches was determined to be an optimum value. Since previous jewel and pivot tolerances provided for a clearance of 300 to 500 microinches, the proposed change uncovered certain deficiencies in both manufacturing and measuring techniques. Initial units were kept reasonably close to delivery schedule by matching pivots and jewels using a special test fixture developed by Kearfott and existing stocks of jewels and pivots. JPL assisted by having a quantity of new pivots made to match jewels provided by Kearfott. This matching was accomplished by Lincoln Park Industries in Lincoln Park, Michigan. Although

clearances of 50 microinches have not been realized to date, the first five units produced by Kearfott are known to have jewel and pivot clearances of less than 100 microinches. This is borne out by response testing of the first three units at JPL which shows greatly improved response characteristics. Kearfott is continuing to improve their matching techniques as well as investigating new pivot and jewel configurations which are deisgned to allow closer control of clearance.

Assembly of a prototype module, using three JPL reworked Kearfott gyros has been completed. This assembly will be used for preliminary system evaluation and power inverter testing. A second unit using the first three new Kearfott gyros will be fabricated as a spare flight unit to be used for system testing until actual flight units are available. Negotiations are in process to have Nortronics fabricate and environmentally test the three flight units. Included in the fabrication will be the burn-in testing of all electrical components as a part of the overall high reliability program of the *Mariner* R attitude control system.

7. Antenna Electronics

The antenna electronics module contains all the components associated with the antenna servo loop except for the Earth sensor, the power supplies, and the feedback potentiometer in the actuator. The narrow beamwidth, high-gain antenna is the deep space telemetry link between the Earth and the spacecraft. The antenna is rotated with respect to the spacecraft about a hinge-axis which is perpendicular to the roll-axis and parallel to the pitch-axis.

The recent program change required extensive circuit modification to the module due to the removal of the planetary horizontal platform (PHP) control circuitry, the substitution of a *Ranger* RA-1 actuator to drive the antenna, the elimination of the short-range Earth sensor, and the addition of extra control modes for the update servo. The removal of the PHP electronics made available the necessary space for the additional circuitry.

The drive amplifier circuitry required extensive modification in order to utilize the *Ranger* RA-1 antenna actuator. The *Ranger* actuator consists of a high-speed 400-cps servomotor driving several stages of speed reducing gears. In order to achieve the required antenna rates, the motor must operate at maximum speed during the commanded period. The motor will not operate from either a square-wave or half-wave sine-wave source due to its unique design, which was required to minimize power consumption. The drive amplifier accepts either a dc or suppressed carrier analog input signal and supplies drive power to the actuator motor. The transfer characteristic of the amplifier is a fixed deadband, on-off switch. The drive amplifier (Fig 153) can be divided into two sections, the input chopper and the output switches.

The input circuit is a half-wave chopper which excepts either a dc signal from the Earth sensor or square-wave suppressed carrier signal from the command channel amplifier. The chopper output signal at the input to the gate of the semiconductor switches (Points A and B) a 2400-cycle zero-reference pulse train whose polarity depends on the input signal polarity and whose magnitude is proportional to the peak input signal.

The output of the chopper (Points A and B) is clamped in order to maintain a zero-referenced signal and to prevent transformer voltage backswing from false triggering the semiconductor switch. Signal current drawn at the firing point is approximately 100 microamperes. In order to obtain satisfactory system performance with the actuator's long coastdown characteristic, the deadzone of the drive amplifier was widened and the temperature stabilization was improved by adding a thermistor network (RT1, R2, R3) that inversely tracks the temperature characteristic of the input silicon controlled rectifiers (SCR) (Q1 and Q3). The output stage was redesigned in order to provide a full-wave sine-wave drive. If the input drive signal is missing, all SCR switches, Q1, Q2, Q3, Q4, are nonconducting. Q2 and Q4 cannot conduct as their cathodes and gates are at the same potential. If the CW drive signal is present, Q1 conducts for the positive half-cycle permitting in-phase current to flow in the control winding and phase shifted current to flow in reference winding. Also capacitor C1 is charged through R4 with the gate of Q2 positive with respect to its cathode. Q2 cannot fire as its cathode is back biased with respect to its anode for the positive half-cycle supply voltage. When the supply voltage goes negative, Q1 is biased off independent of the presence of a gate signal. Q2 is triggered on by the positive potential difference stored on C1. R6 prevents excessive gate current to flow. The circuit time constant is adjusted so C1 is discharged during the negative half-cycle. Supply polarity reversal turns off Q2 but will not turn on Q1 unless the CW drive signal is still present.

The antenna update servo (contained in the electronic module) is an electromechanical device which stores as a potentiometer ratio the desired reference angle of the antenna. In the basic mode, the update potentiometer periodically stores the current Sun-probe-Earth angle for use as a reference in case the Earth sensor loses its target. The update is inhibited if the Earth sensor is off target.

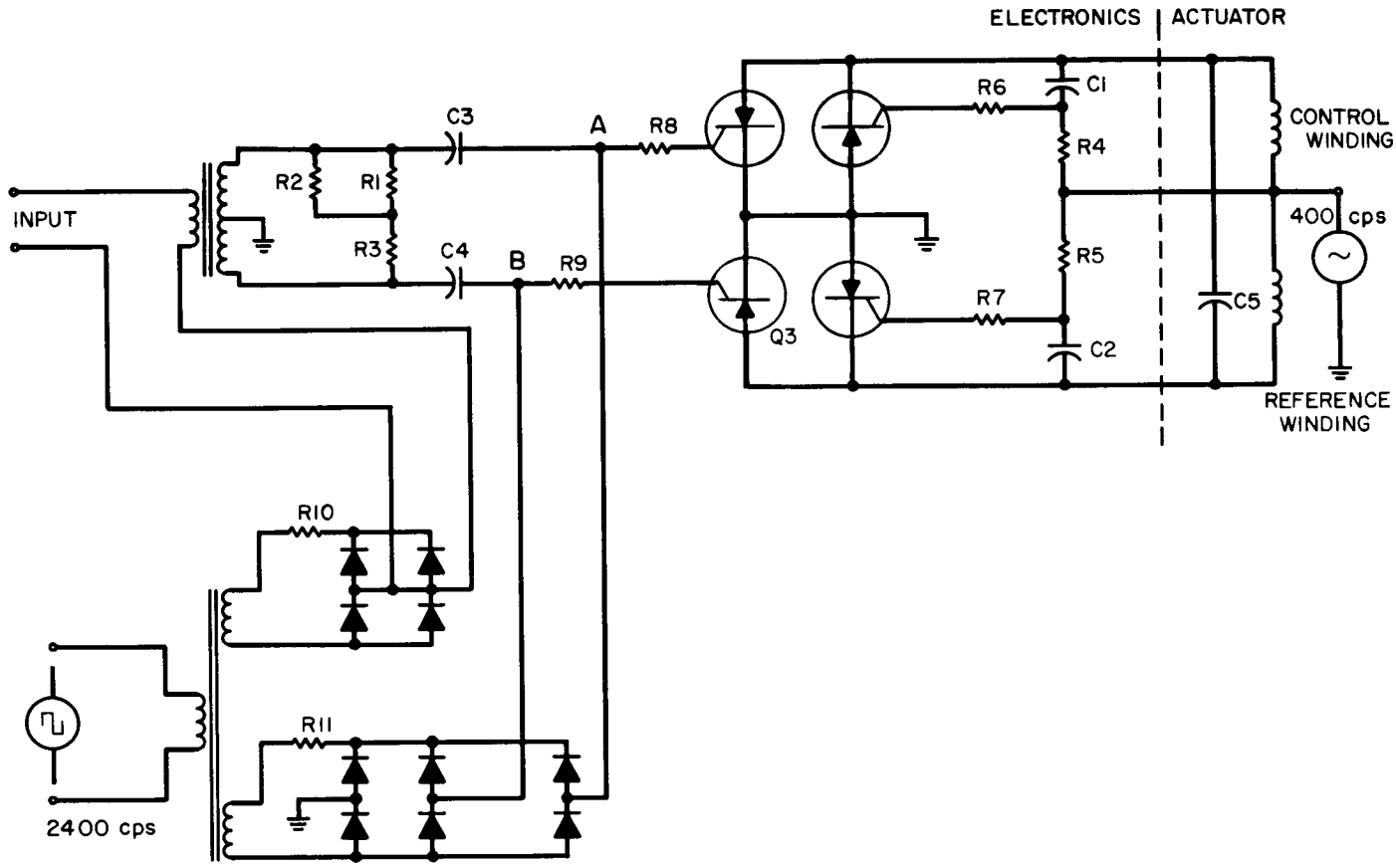

Figure 153. Antenna drive amplifier

The schematic diagram of the *Mariner* R update servo is shown in Figure 154. In the basic mode (R1, R2, R3, R4) the update command signal, transmitted by the CC&S switches Relay 1, activating the error signal chopper and the drive assembly clutch-brake. The error signal chopper (T1, D1, D2, D3, and R4) phase demodulates the input signal into a zero-referenced pulse train. The positive pulse train turns on one of the SCR switches (Q1 or Q2) when of sufficient amplitude, thereby determining the direction of the update potentiometer position signal. Capacitor C1 furnishes the proper phase shifted voltage for the opposite motor coil. The conducting SCR is turned off by the start of the negative half-cycle of the 400 cps-voltage. As the CC&S pulse may be shorter than the period required for updating, Relay 1 is held in by a circuit (R1, D5, and C2) which rectifies and filters the half-wave motor drive signal. Resistors R1, R2 and R3 stabilize the SCR switches in a high-temperature environment. Capacitors C3 and C4 serve as noise filters for the error chopper signal.

The clutch-brake is used to lock the storage pot shaft so that the angle will be maintained throughout the injection phase and to stabilize the system. The position error of this system has been consistently better than 10 minutes of arc, referred to the antenna position. The update servo was modified to add two modes of operation. Due to the elimination of the short range Earth sensor the initial setting of the update angle, the acquisition angle, is critical and new settings are required several times during one firing window. The adjustment must be made from the control center while the spacecraft is in position on the launcher and with only raw battery power and 400-cps sine-wave power available.

In the slew mode the update motor is actuated from the control center and the acquisition angle readout via the umbilical wires. The motor is driven by one solid-state switch (Q1 or Q2) controlled by dc pulses from the ground station. The brake is actuated by relay closure, which is driven by same signal as the motor switch via diode gates D4 and D6 or D5 and D7. The square-wave power must be off, otherwise the error signal demodulator would be turned on by the relay closure.

The other mode indexes the update potentiometer a fixed incremental angle ($3 + 2° - 0°$), in either direction,

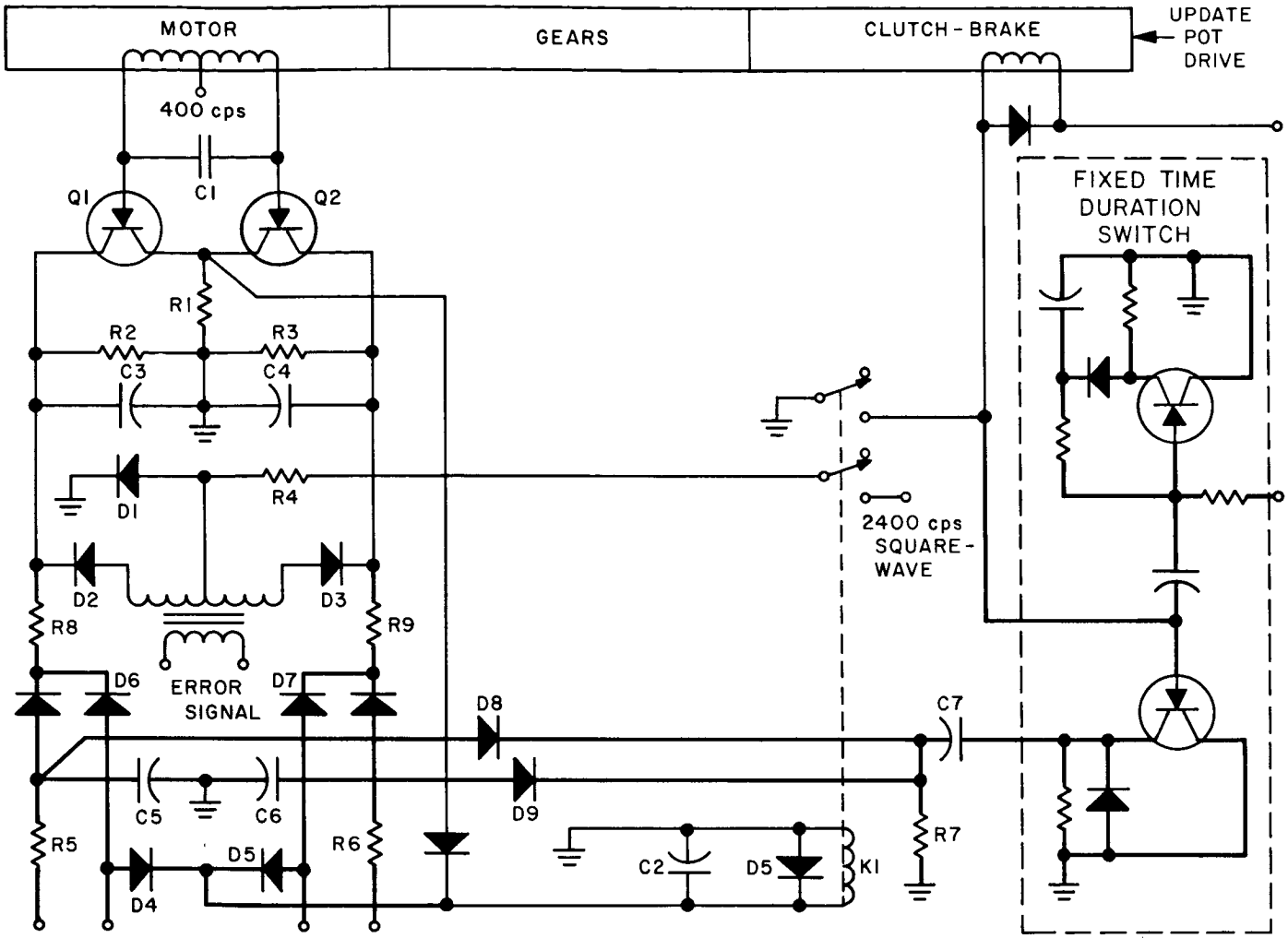

Figure 154. Antenna update servo

by ground command via the command decoder link. Indexing is achieved by operating the brake from a solid state fixed time duration switch shown inside the enclosed block in Figure 154. The motor switch (Q1 or Q2) is driven by a capacitor voltage storage system (C5 or C6) energized by the command decoder pulse. Resistors R5 (and R6) limit the current surge through the command decoder semiconductor switch. The storage system is required as the command decoder pulse is not of sufficient duration to obtain the required increment. One time switch serves for both directions of rotation as it is controlled by either command via diodes D8 and D9. Capacitor C7 and Resistor R7 form the trigger pulse to initiate the timing cycle. Resistor R8 is used in conjunction with R2 as a voltage divider to reduce the 28 volts dc command signals to a safe level to drive the SCR gate.

The *Mariner* R circuitry has met all performance requirements throughout an extensive series of bench and environmental tests. The basic *Mariner* A housing has been modified and new printed circuit boards have been designed. All components have been tested to the requirements of the Laboratory's high reliability parts program. A new tester for the module has been designed and is now in fabrication.

B. Engineering Mechanics

As a result of the program change to put the *Mariner* on an *Atlas–Agena* B for the 1962 Venus shot, the Engineering Mechanics Division has started the design process on an essentially new spacecraft. The dimensional

confines of the *Agena* nose fairing (shroud) combined with the extreme weight reduction from *Mariner* A dictated a smaller, lighter spacecraft. The basic building block for the *Mariner* R is a *Ranger* RA-3 type basic hexagonal structure, the use of which introduced only minor changes to the well-checked-out interface with the *Agena*. To this only slightly changed structure, the essential elements for the mission were added, all of the structural and mechanical elements being of new design. Many of the design and fabrication techniques used on *Mariner* A were applied to the new design. By keeping together the established working team and using all of the experience gained on *Mariner* A, the design of the configuration, the detail design of the spacecraft, and the fabrication of prototype and some flight hardware has progressed rapidly and with a minimum of troubles.

Many of the development activities aimed at solving *Mariner* A problems have been diverted toward solving *Mariner* R problems, with only minor changes in scope. Much of the temperature control and related materials development falls into this category. Other *Mariner* A development activities have been completed since the program change where the basic principle or the verification of a design approach would be applicable to either *Mariner* R or future programs. The modal vibration survey of the structure falls into this category, as do tests planned to verify the scheme for separating the launch vehicle.

1. Spacecraft Development

During the reporting period the *Mariner* R spacecraft has progressed through the preliminary design phase. The spacecraft utilizes a *Ranger* RA-3 basic structure modified to reduce weight and increase the cable access. A trough to support the ring harness cables and connectors has been located under the structure and provides clearance for the installation of the modified *Ranger* RA-3 mid-course propulsion system from the bottom.

The Sun sensors and attitude control jets are mounted at the same locations as *Ranger* RA-3. The *Mariner* A spherical attitude control bottles are mounted together between the battery box and high-gain antenna. The regulator is located between the bottles.

Three fixed thermal shields are provided. One is located under the bottom of the spacecraft in the cable trough-motor nozzle area; a second, consisting of layers of aluminized mylar film on fiber glass honeycomb is mounted immediately above the hex structure to shield the hex electronic boxes from the Sun; and the third shields the Earth sensor from the Sun. The cosmic dust experiment mounts on the top thermal shield, and the solar corpuscular detector is mounted in a primary hex box and protrudes from under the shield to see the Sun.

A superstructure mounts through the top thermal shield to the top of the primary hex. The structure consists of three truss sections bolted together, with equipment support frames between each. The *Ranger* RA-1 type omni-antenna mounts on the top and the *Mariner* A fluxgate magnetometer is mounted under it. The *Mariner* A ion chamber experiment and particle flux detector are mounted on the middle frame which also contains the top solar panel ties.

The radiometer and infrared radiometer are mounted above the top thermal shield and below the lower superstructure frame. These experiments will be articulated at planet encounter approximately 120 degrees about an axis parallel to the roll axis by a scan actuator mounted on the lower superstructure bulkhead. The radiometer package will be restricted from rotating during boost by a pyrotechnic latch.

The high-gain antenna mounts under the basic structure in the same manner as in the *Ranger* series. A 4-foot diameter *Mariner* A dish structure and a redesigned *Ranger* feed are used. There is not enough space between the *Agena* adapter and the spacecraft for the larger *Mariner* A long range Earth sensor to be mounted in the *Ranger* Earth sensor position. Because of these space restrictions, the sensor is mounted on the redesigned high-gain antenna yoke, and is enclosed at an angle with respect to the high-gain antenna radiation pattern. A mirror mounted on the yoke allows the sensor to see in the antenna pointing direction. The mirror is also used as a Sun shade.

Two solar panels employing the *Ranger* actuator and hinge points are provided. Each panel is rectangular and is latched during boost to the structure by three pyrotechnic latches: two at the top of the hex structure and one at the top of the panel. The omni-antennas (command) mount on the front and back of one of the panels.

2. Structures and Dynamics

a. Changes in spacecraft structure. As mentioned previously, the *Mariner* R spacecraft is basically a *Ranger* RA-3 primary hex structure, with minor modifications, to which has been added new solar panels and a superstructure. The primary modifications to the primary hex structure include the following:

All X-shaped back panel ties have been replaced with single diagonal tubular members. The new members,

which are similar to those used on *Mariner* A, are somewhat lighter than those used on *Ranger*.

All top and bottom shear panels have been replaced with single diagonal solid members. A requirement for cable access in the bottom panel area and the lighter weight of the single diagonals made the new structure very desirable.

The cantilevered cable trough located below and inboard of the primary electronics packages on *Ranger* has been changed to a hanging cable trough at approximately the same location. A requirement to install the mid-course propulsion system from beneath the spacecraft, rather than from above, made necessary this change. The cables now protrude through the aft surface of the electronic packages and must be disconnected prior to the opening of the chassis.

The superstructure is a three-tier tubular spaceframe type structure fabricated in a manner similar to that used on *Mariner* A. The absence on *Mariner* R of the planetary horizontal platform used on *Mariner* A made possible the use of a more symmetrical structure than that used on *Mariner* A.

The solar panels have been designed and are being fabricated by the Ryan Aeronautical Company using techniques developed during the *Mariner* A program. Although of more than 20% greater area than the *Ranger* panels, the total weight, including solar cells, glue, and wiring will be less than that of the *Ranger* series panels.

Each solar panel is supported through two hinges and actuator as in *Ranger*, and three links, two of which are at the top of the primary hex and one on the second tier of the superstructure. The major problem area in the design of the panel support system was the proximity of the panel to the temperature control louvers (a separation of only ⅛ inch exists in the static condition). The panel and supports have been designed, however, to maintain a positive separation in this area. Results of a computer analysis indicate that the first torsional frequency of the panel is sufficiently high, with one support at the top of panel, to keep deflections within the prescribed envelope.

b. Analyses and test programs. A computer analysis of the spacecraft structure is being performed with particular emphasis in the following areas. Load distribution analysis is being performed to the extent that margin of safety calculations may be made for critical members and members which are different from those used on the *Ranger* spacecraft. Dynamic analyses are being performed to the extent that adequate correlation may be made with modal survey and composite vibration tests.

The primary structural qualification tests which are planned for the *Mariner* R spacecraft include, (1) static and dynamic type approval tests of the solar panel structure, (2) developmental vibration tests of the superstructure, (3) modal survey tests of the spacecraft, both with the spacecraft supported on the adapter and with the spacecraft supported in the free-free mid-course maneuver configuration, and (4) composite vibration tests of the spacecraft supported on the adapter both with and without a shroud.

3. Packaging

a. Component packaging. Packaging of the *Mariner* R electronic equipment was basically a return to the *Ranger* configuration (Fig 155), since *Mariner* R largely utilizes *Mariner* A primary hex electronics, which were designed to use *Ranger* techniques. Thus, communications, attitude control, central computer and sequencer, data encoder, and the command electronics required only minor packaging changes in those few areas where new circuits were used.

The power subassemblies which were uniquely packaged in the secondary hex and on the intercostals for the *Mariner* A had to be adapted to the *Mariner* R vehicle. This was accomplished without any changes to the subassemblies by fabricating a new assembly chassis, which accepted the *Mariner* A subassemblies and yet was compatible with the *Mariner* R vehicle. Also, a new battery chassis was developed.

Several basic magnesium chassis which were fabricated for the *Mariner* A will be used for the *Mariner* R. Hinges were added to these chassis for more convenient service and checkout. For other vehicles, the assembly chassis have typically been gold plated for thermal control purposes; however, these chassis will not be gold plated, but rather will have polished aluminum shields located in those areas where low emissivity surfaces are required.

b. Description of the assemblies.

Electronic Assembly I. This assembly contains scientific equipment: plasma experiment, magnetometer electronics, scientific data conditioning, and scientific power switching. This assembly contains all newly designed equipment. To conserve weight as much as possible, the scientific equipment and electronics are integrated in a standard hex chassis.

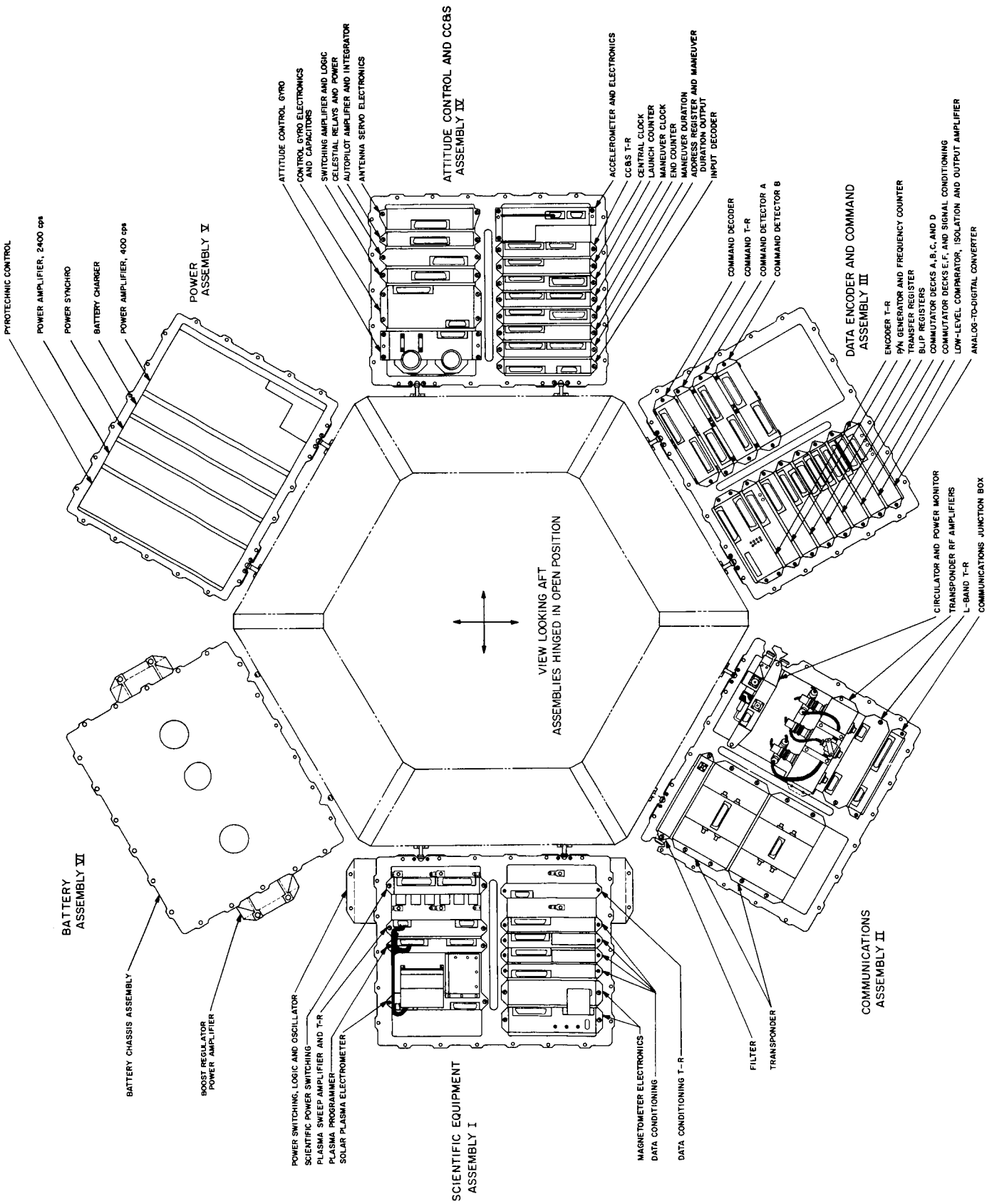

Figure 155. *Mariner R* packaging assembly

Electronic Assembly II. This assembly is basically the same as the *Mariner* A L-band communications. Only the junction box, T-R unit, and circulators were repackaged.

Electronic Assembly III. The command and data encoder subsystems are located in this assembly. These subsystems use the *Mariner* A equipment with some modification for new circuits.

Electronic Assembly IV. This assembly has the attitude control electronics located with the same arrangement as was in the *Mariner* A. The central computer and sequencer is also in this assembly and required only one new subassembly.

Electronic Assembly V. This assembly contains the power subsystems, except for the power switching and booster regulator amplifier. The *Mariner* A secondary hex subassemblies are used; however, a new assembly chassis was made to accommodate these subassemblies and yet fit the *Mariner* R hex bolting pattern. The pyrotechnic control subassembly was also packaged in this *Mariner* A secondary hex shape so that it could be located in this assembly.

Electronic Assembly VI. This assembly contains the battery. Although the assembly shape was designed to match the standard chassis, the original *Mariner* A cell configuration was retained.

Intercostal power subassemblies. For *Mariner* A, both the power switching and logic, and the power amplifier were located on the intercostals by using special chassis designed to fit the intercostal mounting. The same units without repackaging were retained for *Mariner* R by locating the power switching and logic assembly on the outside of Assembly I, and by locating the power amplifier assembly on the outside of the battery. These locations appear compatible with temperature control of the battery and Assembly I equipment.

Radiometer. The three dish *Mariner* A radiometer is being modified and repackaged as a one dish unit for *Mariner* R. Many of the original components are being used, but a new chassis-dish structure is under development.

4. Temperature Control

The temperature of the hex portion of the *Mariner* R spacecraft is to be controlled in much the same manner as that intended for the *Mariner* A. This is primarily dictated by the similarity of the mission and the availability of developed hardware. However, these constraints are not expected to compromise the temperature control of the *Mariner* R.

a. Primary hex. As in the *Mariner* A and *Ranger* spacecrafts, the assemblies dissipating electrical power are to be packaged near the radiating surfaces of the hex with conduction resistances held to a minimum. The upper and lower surfaces of the hex are to be insulated using multiple layers of light-weight radiation shields to reduce the heat losses from these surfaces as much as practical. The insulation of the upper surface also helps make the temperature of the hex independent from the intensity of the solar radiation which increases as the spacecraft approaches Venus and gets closer to the Sun.

The dissipation of power in the hex is not constant during the various modes of the mission. This variation in internal power occurs primarily in only two of the six hex boxes. These two boxes are fitted with louvers which will change the effective emittance of the box surfaces as the box face temperature changes. The power variations in the other hex boxes are small and will not require an active control. The louvers were developed for use on the *Mariner* A spacecraft for the purpose of compensating for variation in internal power and for uncertainties in the prediction of the steady state temperature of a passive control.

Unfortunately, spacecraft weight limitations preclude the use of louvers to compensate for uncertainties in temperature prediction for *Mariner* R. Although the schedule will be demanding, it is planned that these uncertainties will be reduced to a minimum as a result of space-simulator testing.

The temperature of the mid-course propulsion system will be slaved to the temperature of the surrounding hex boxes and thermal shields. Except in those cases where it is impractical or would result in excessive weight all interconnecting cables will be routed to the interior of the spacecraft hex and temperature controlled in much the same manner as the mid-course propulsion system.

Variations in the heat conducted to the hex from the spacecraft structure will occur due to changes in solar radiation; however, these effects will be held to a minimum. The heat conducted into and out of the hex will be reduced by using either gold plated surfaces (hex legs) or polished aluminum (superstructure). The structure will be painted in such a way to act as a heat sink to the hex when the solar radiation is less than 1½ times that of its intensity in the Earth orbit, and as a heat source with intensities greater than this value.

b. Long range Earth sensor. The long range Earth sensor (LRES) is shielded from the Sun and continuously

supplied with electrical power. Approximately ¾ of the power dissipated during the operation of the sensor will be supplied to heaters before the sensor is turned on at the beginning of the Earth acquisition. When acquisition is initiated, the heaters will be turned off and the sensor will be turned on resulting in a minimum of change in internal power. This power, dissipated as heat, will be conducted to those surfaces which have the least variation in view factor and from these surfaces be radiated to space. Since the LRES would present various surfaces to the Sun as a result of tracking the Earth and because the intensity of the solar radiation will vary by a factor of two, solar shields will be provided to reduce these effects as much as possible. This will make the temperature control of the LRES primarily dependent on the internal power that is dissipated as heat. The antenna assembly is insulated from the spacecraft by means of a fiberglass plug to reduce the conduction heat exchange between the antenna and the LRES.

c. Passive control items. The assemblies mounted on the superstructure will be predominately scientific instrument sensors and will be temperature controlled passively. The majority of the electronics and data conditioning of these sensors is located in one of the hex boxes. Except for the radiometer, these items will have a fixed orientation with respect to the incident solar radiation. Even in the case of the radiometer, its motions will be small and it is expected that it will also be controlled by appropriately chosen surface coatings. All of the items passively controlled in this manner have been so positioned on the spacecraft that some portion of their surface will be illuminated by sunlight to compensate for the unavoidable heat losses either to space or to other parts of the spacecraft.

The solar panels of the *Mariner* R spacecraft are constructed and thermally controlled in such a manner as those designed for *Mariner* A. The cells will be covered with a glass filter designed to reduce the solar absorptance at certain wavelengths. The energy that is absorbed and is not converted to electrical power is conducted through the solar panel and radiated to space. The resulting temperature of the solar cells is not as low as desired for the most efficient operation, but it is expected that it will be within tolerable limits.

5. Mechanisms

Radiometer integration and scan activator. The *Mariner* R spacecraft will be equipped with a radiometer for planet temperature measurement. The radiometer consists of a 19.25-inch diameter dish and supporting electronics. It will scan the planet about an axis parallel to the spacecraft roll axis. The radiometer has its lower mount on the top of the hex over support F and is attached at the top to the superstructure. The scan actuator mechanism is mounted at the top of the radiometer and is attached to the superstructure. Prior to planet encounter, the radiometer will go through a 1-deg/sec search scan of ±60 degrees about its axis. As soon as the planet is acquired in the radiometer view cone, the scan rate is reduced to 0.1 deg/sec and the scan amplitude is governed by signals from the radiometer so that it can scan from horizon to horizon.

The scan drive mechanism consists of two Size 8 synchronous motors to accommodate the two speed scan and reduction gearing. Both motors are equipped with gearheads which reduce the 12,000-rpm motor speed to 8.16 rpm. These motors and gearheads are the same as were used on the *Ranger* Lyman-alpha experiment. Since time is at a premium on the *Mariner* R program, it was felt that *Ranger* experience should be used where possible. There is little time to conduct a study program to select another motor which would operate on the allotted 2 watts of power and would be compatible with type spacecraft power available.

To accomplish the speed shift without the necessity of shifting gears, two motors were used. Each motor drives one side of a differential and the output is from the carrier. When one motor is operating, the other holds the opposite side of the differential fixed. The input from one motor into its side of the differential is 1.10 the speed of the other input and thus the speed shift from 1 deg/sec to 0.1 deg/sec is effected by switching from one motor to the other. Using this system, the output gearing is common to both motors.

The entire motor and gear assembly will be pressurized for vacuum protection. Tests are presently being organized to study the effects of losing pressure. The radiometer position during boost is set so that if the scan actuator fails to move it, there will still be a fair probability of seeing Venus.

6. Pyrotechnics

The pyrotechnic subsystem (SPS) presently being designed for *Mariner* R spacecraft will perform the functions of unlatching solar panels, unlatching the radiometer scan mechanism, opening pressurization, fuel, and oxidizer explosive valves on the mid-course motor and closing pressurization and fuel explosive valves on the mid-course motor (Fig 156).

The design of the pyrotechnic control subassembly will be basically that used on *Ranger* RA-3.

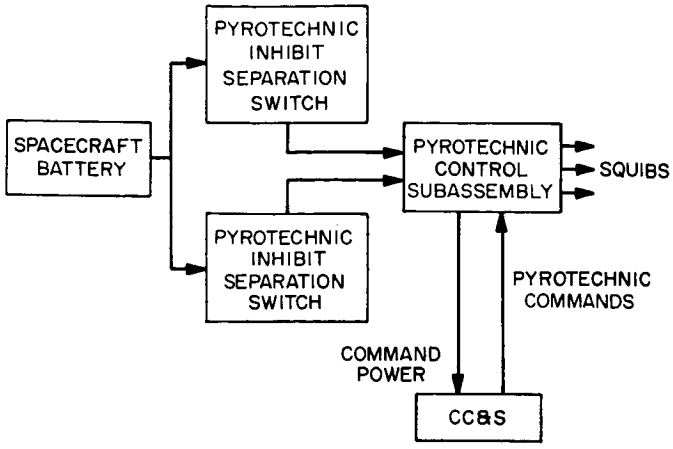

Figure 156. Pyrotechnic subsystems

Squibs will be identical to those used on *Ranger* RA-3, with the following exceptions:

(1) Powder cans on all squibs will be hermetically sealed.

(2) Mid-course motor explosive valve squibs will contain dual bridgewires.

Some of the techniques that will be used to achieve reliability in the pyrotechnic subsystem are:

(1) Redundancy, all squib actuated devices will be supplied with two independent electrical circuits.

(2) All components used in fabricating the pyrotechnic control subassembly will undergo rigid preassembly tests. The final subassembly will undergo type approval and flight acceptance tests.

(3) Type approval, reliability and flight acceptance tests will be performed on all squib lots.

(4) Command and power arming of spacecraft pyrotechnics will be accomplished only upon separation of the spacecraft and *Agena* through the use of dual, spring loaded plunger switches installed on the mating surfaces of the separation joint.

Explosive valves and pin pullers used in the pyrotechnic subsystem will be the same type as those used on *Ranger* RA-3 with the exception that the pin pullers will contain an integral electrical switch, the purpose of which will be to provide a telemetered indication of the actuation of the pin puller.

7. Ground Handling Equipment

The design of the *Mariner* R ground handling equipment (GHE) started during this reporting period. In general the equipment will be similar in appearance to the *Ranger* and *Mariner* A equipment.

a. Hoisting gear. This consists of the upper sling, spreader frame, lower sling and lifting bars. This assembly is used for all lifting of the spacecraft by overhead cranes.

b. Support and adapter. These two parts are used with either the shop dolly or the transport trailer for assembly and local transport of the spacecraft. The upper portion of this assembly also serves to position the high-gain antenna dish for installation and alignment. The lower part provides the mount for the *Agena* shroud. The height of the two part assembly is designed to protect the antenna feed from damage. Thus, the adapter and support are never separated during normal use.

c. Dolly. This is used with the support and adapter assembly for convenience during assembly of the spacecraft and operations within a shop.

d. System test stand. This item will be the same stand that was to be used for *Mariner* A. The systems test stand will be capable of holding the spacecraft in an upright position, then swinging it 90 degrees to a horizontal position with the hinge axis of the high-gain antenna vertical for operations of the antenna through its entire range of travel. The stand can then rotate the spacecraft 90 degrees about its own roll axis to place the hinge axis of the solar panels vertical for operation of their actuation system.

This stand will consist of two principal assemblies: a commercial welding positioner, and a fixture to adapt the spacecraft to the welding positioner.

e. Support for motor loading. A stand is required to hold the spacecraft in the vertical position approximately 5 feet from the floor to allow the high-gain antenna to swing down for installation of the mid-course motor. The stand will be installed in the explosive safe facility at AMR.

f. Packaging and shipping. Shipment by truck, both local and to AMR, will be used for the *Mariner* R. The spacecraft will be packaged complete except for the solar panels, mid-course propulsion system, top superstructure tier, and high-gain antenna. Packaging would consist of putting a plastic bag over the spacecraft and sealing it around the base. Purging with dry nitrogen will probably be required for overnight storage and transportation.

g. Handling. The basic structure of the *Mariner* R is similar to the *Ranger's* structure, but the *Mariner* R

requires different handling techniques than the *Ranger* because it will be shipped with the first and second tier of forward structure mounted. This precludes use of the metal dome used for shipping the *Ranger* spacecraft. *Mariner* R's shipping container will consist of a plastic bag and a light tubular support structure.

8. Materials

a. Hardware design and fabrication.

High-gain antenna feed. Design changes were made to the feed assembly and brazing tooling to insure highest reliability consistent with short fabrication schedules.

(1) Hardware changes were made to simplify brazing by substituting an all gold furnace braze process for a combination gold furnace braze and silver induction brazing.

(2) Pins and self-aligning joints were incorporated. Threaded attachments were eliminated to allow easier removal of brazing mandrel tooling.

(3) Complex machined fittings were changed to a combination of simple sheet metal components and stock size materials; e.g., dipoles.

(4) Tolerances of mating surfaces were made compatible with the gold brazing process.

b. Temperature control materials.

Stable white surfaces. A variety of white surface systems have been exposed to high-intensity ultraviolet radiation in the 2000 to 4000Å range at 10^{-5} mm Hg to find a stable white for use on *Mariner* R (*SPS 37-10*). These tests were conducted by the Material and Process Division of Hughes Aircraft Company in Culver City under JPL sponsorship.

Initial screening tests at the equivalent of approximately 200 hours Earth orbit solar intensity indicated moderate to high yellowing (i.e., increase in solar absorptance) for all paints and pigmented polymer films. Most of these exhibited sufficient change at this exposure to eliminate them from further consideration. Anodized high purity aluminum and aluminized teflon (FEP) film showed very little change.

Further tests at shorter and longer exposure period indicated radical changes in yellowing rate with exposure time for the various systems, as illustrated schematically in the curves in Figure 157. Some of the white paints tested demonstrated a decreasing rate of yellowing, such as illustrated by Curve A. (Note: The indicated trends are for moderate changes in solar absorptance; in Cases b and c, as $d_s \rightarrow 1.0$ the slope of the curve must also change, and may have an acceptable terminal d_s.) Anodized aluminum showed no measurable change at short exposure, but showed an increasing rate at longer exposures, indicating a trend as illustrated by Curve B.

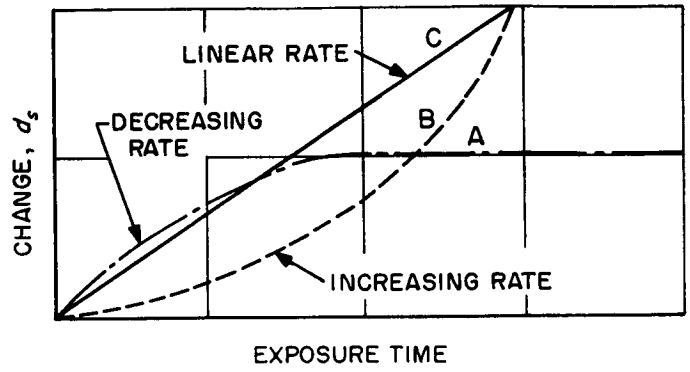

Figure 157. Yellowing curves for white surfaces

Longer exposure tests are being conducted to verify the trends for those materials which may have acceptable final solar absorptance values and to provide a reasonable prediction of the solar absorptance that can be anticipated at the termination of the *Mariner* mission.

On the basis of incomplete testing to date, the leading candidates for use on *Mariner* R are a zinc sulfide pigmented silicone paint and aluminized FEP teflon. If these continue to show promise with longer duration ultraviolet testing, both will probably be used on *Mariner* R. In order to meet deadlines, sufficient stock of aluminized teflon is being procured for possible use for the *Mariner* R solar shield.

Stable black surfaces. Surfaces possessing high-solar absorptances are being tested to measure degradation in: (1) high-vacuum at 175 to 225°F, and (2) at 70°F in high-vacuum under ultraviolet irradiation.

Coatings exposed only to high-vacuum consist of black pigmented paints that contain different vehicles. The test group is made up of several epoxy grades, a commercial polyurethane, a common modified alkyd, a modified silicone, and a pure silicone.

Since the test program started, the contractor, Hughes Aircraft, has tested an alkyd, polyurethane, and a modified silicone for 1 week in a high-vacuum at approximately 200°F. More extensive testing has been halted, because the equipment is being redesigned to accommodate an increased number of test specimens. However, added tests are being run at JPL to verify reported results and to investigate other variables.

What little data is available indicates that a week's exposure results in up to 7% weight loss. However, not enough testing has been performed to establish the superiority of one vehicle over another.

Exposure to ultraviolet irradiation has been completed for a black dyed anodized coating. Other surface treatments now scheduled for a 200-hour exposure are: black copper oxide, black nickel plate, hard black anodized coating plus an epoxy and a polyurethane black pigmented paint.

After exposure for 72 hours and 198 hours at approximately 10 solar intensities, little change was noted in the visible reflectance of black, dyed anodized coating. Although the test is only of a single species of dyed, sealed anodized coating, the results show that the dyed black does not bleach as much as has been rumored.

Measurement of optical properties. It has become apparent from continued comparison of JPL spectral reflectivity measurements with those of UCLA that the resulting JPL reflectance curves have differed consistently by a significant number of percentage points of reflectance (up to 12%, in fact) for both specular and diffuse reflectance materials. During the past report period, the deficiencies in the P-E 4000 equipment have been investigated and new methods of deposition of magnesium oxide smoke for reflectance standards and on the integrating sphere surfaces have been tried and adopted. Spectral reflectance curves currently obtained from this equipment compare very closely with those of UCLA for specular and diffuse reflectance.

Deficiencies in the P-E Model 13 equipment have not been fully analyzed yet. A measured temperature difference of 15°C exists between the top and bottom of the heated cavity and a wavelength dependent behavior of the relative intensities of the two beams as measured at the thermocouple detector have been demonstrated as areas for investigation.

A drawing of a modified total emissivity unit (*SPS 37-10*, Vol II) has been completed preliminary to construction of the unit for experimental use. It is hoped that such a unit will permit reasonably accurate direct determination of very low emittances.

Nylon. The use of nylon grommeting strip for cable protection is prevalent on the *Ranger* and *Mariner* spacecraft. There is some question about its ability to withstand the space environment. Where possible, a silicone, fluorosilicone, fluorocarbon, or other more stable material should be used.

The particular nylon in question is highly plasticized to achieve flexibility. Upon exposure to the heat sterilization environment (125°C for 24 hours), the plasticizer diffuses to the surface and evaporates. The resulting part is much less flexible and darker but does retain a hard, low coefficient of friction surface.

Where deposition of the plasticizer and/or degradation products on colder surfaces would not interfere, the nylon will probably be acceptable. However, a more stable material is desirable.

Teflon. The following work was done in connection with the plasma boom hinge for *Mariner* A. While this hardware will not be used on *Mariner* R, it is felt that the information obtained has broad application.

Both teflon and fluorosint (filled teflon) were evaluated for use on the *Mariner* A plasma boom hinge. Because of the low temperature creep (cold flow) tendencies of teflon, the filled teflon (fluorosint) was also considered because it has greater creep resistance without appreciably sacrificing its low coefficient of friction.

Both materials performed satisfactorily under type approval testing. However, when more than the maximum 0.0005 interference was encountered, the fluorosint bushing tore. It did not have the integrity of the teflon. It was, therefore, recommended that teflon (or similar homogenous fluorocarbon) be used.

The use of a fluorocarbon as a bushing is attractive from several viewpoints. First, teflon has a low coefficient of friction (0.04). Second, it is one of the most stable polymers for spacecraft application. When the section thickness is kept to a minimum, it can bear reasonable loads without appreciable creep (cold flow).

Fused tin electroplates. In the spacecraft, there are several applications of fused tin electroplate being used in radio frequency devices. Because of the wide temperature environment to which these parts are subjected, a potential problem of *tin pest* arises. Tin pest is actually an allotropic transformation of tin, taking place at low temperature, causing the coating to flake off. It is obvious that such a phenomenon could cause failure of a device.

A study was undertaken to determine if it were possible to make simple modifications to commercial tin electroplates which would suppress any transformations at temperatures encountered during spacecraft operation.

From a study of the literature, it was found that small additions of bismuth, antimony, or lead are effective in

suppressing the reaction. A program was started to modify the popular stannate tin electroplating bath by adding a small amount of bismuth to the solution as well as bismuth to the plating anode. In plating samples with this technique, bismuth contents up to 0.3% were obtained. Sample electroplates, after being subjected to −40°F for four 24-hour periods, were found to be satisfactory.

Subsequent electroplating tests to determine repeatability of the process were performed. These tests showed that the bismuth percentage in the tin plate was erratic and uncontrollable. Preliminary modifications to produce more controllable deposits have, so far, been unsuccessful.

Until a satisfactory solution to this potential problem can be worked out, the use of tin electroplates must proceed with caution. An accurate knowledge of the thermal environment of devices so coated is mandatory.

III. *Mariner* B

The studies described, along with those described in previous *Space Programs Summaries*, summarize all of the work accomplished prior to the start of preliminary design of *Mariner* B.

A. Guidance and Control

1. Secondary Power

The *Mariner* B feasibility study (*SPS 37-8*) discussed the relative merits of thermionic and photovoltaic conversion of solar energy as the prime source of electrical power. Further studies have indicated that solar thermionic systems with the required efficiency and reliability will not be available in time for this spacecraft, and thus all work on this program is now directed toward the development of a photovoltaic system.

The preliminary design of solar panels for both Mars and Venus missions is in progress. Based on an expected primary requirement of 400 watts, it is expected that approximately 130 ft^2 of panel will be required for the Mars and 60 ft^2 for the Venus missions.

a. Mars solar panels. For the Mars vehicle, it is anticipated that the solar array will consist of four identical fold-out panels with a combined area of 82 ft^2 and a body-fixed array of six identical truncated triangular panels of 48 ft^2. The body-fixed array will not be as effective as the fold-out panels for the following reasons: (1) the fixed panels will operate at a higher temperature and, thus, lower efficiency than the fold-out panels; and (2) the triangular configuration of fixed panels will make it difficult to use the area as completely as the fold-out panel.

Because the fixed and fold-out panels operate at substantially different temperatures, the design of the two types of panels must be such that mismatch losses are minimized at Mars where power is at a premium. Matching at Earth is not as critical since the output of the fold-out panels will be more than adequate to meet the vehicle power demands. To minimize these mismatch losses it is extremely important that the temperatures of the fixed and fold-out panels be predictable. For this reason the possibility is being investigated of insulating the back of a fixed panel so that it will reject heat from its front surface only. The effect of such a design on matching would be twofold: (1) the temperature of the fixed array would be independent of the vehicle temperature control system; hence, both the temperature of the

array and its output characteristics would be much more predictable, and (2) the fixed panel would operate a uniform temperature, thereby eliminating the mismatch problems due to severe temperature gradients in the panel. In addition to simplifying matching problems, the insulated panel would shield the electronic equipment from the Sun and possibly simplify the design of the temperature control system.

Figure 158 presents the results of preliminary calculations of solar cell operating temperature as a function of both solar intensity and solar-panel back-surface emissivity ε_B. These calculations have neglected the effect of the heat rejected from the electronics equipment packages on the solar panel. It was further assumed that the temperature drop through the panel was small and could also be neglected. At Mars aphelion, the temperature of the fixed panels ($\varepsilon_B = 0$) will be about 18°C. The temperature of the fold-out panels ($\varepsilon_B = 0.9$) in the same environment will be −32°C. At Earth perihelion, the temperatures of the fixed and fold-out panels will be about 105 and 40°C, respectively.

b. Venus solar panels. To meet the Venus mission area requirements, four identical fold-out panels which are somewhat smaller than those required for the Mars mission are being considered. The fixed area that was used for the Mars mission cannot be utilized for the Venus mission because at Venus the temperature of an insulated-body ($\varepsilon_B = 0$) fixed solar panel would approach 180°C. The temperature of the fold-out-type panel would be about 98°C. Because solar cell efficiency decreases with increased temperature, this temperature difference means that 1 ft² of fold-out panel supplies the same power output as approximately 2 ft² of fixed panel.

c. Photovoltaic solar concentrators.

Development. In an effort to reduce *Mariner* B solar panel cost and possibly weight, the use of photovoltaic solar energy concentrators is being evaluated. In August, 1961, JPL awarded a research contract to the Boeing Company for the development of a concentrator structure concept. The design objective of this program is to develop a concentrator structure which possesses high electrical–optical efficiency, minimum weight consistent with the required structural properties, and reliable electrical connections.

Boeing has completed two electrical–optical models, designated EOM-1 and EOM-2, and has delivered them to JPL. Forty-five Hoffman *blue* solar cells, rated at a minimum of 10% efficient at air mass zero and 25°C, are used on each EOM in conjunction with OCLI No. 207-SCC450-2 cover glasses. The cells are connected 15

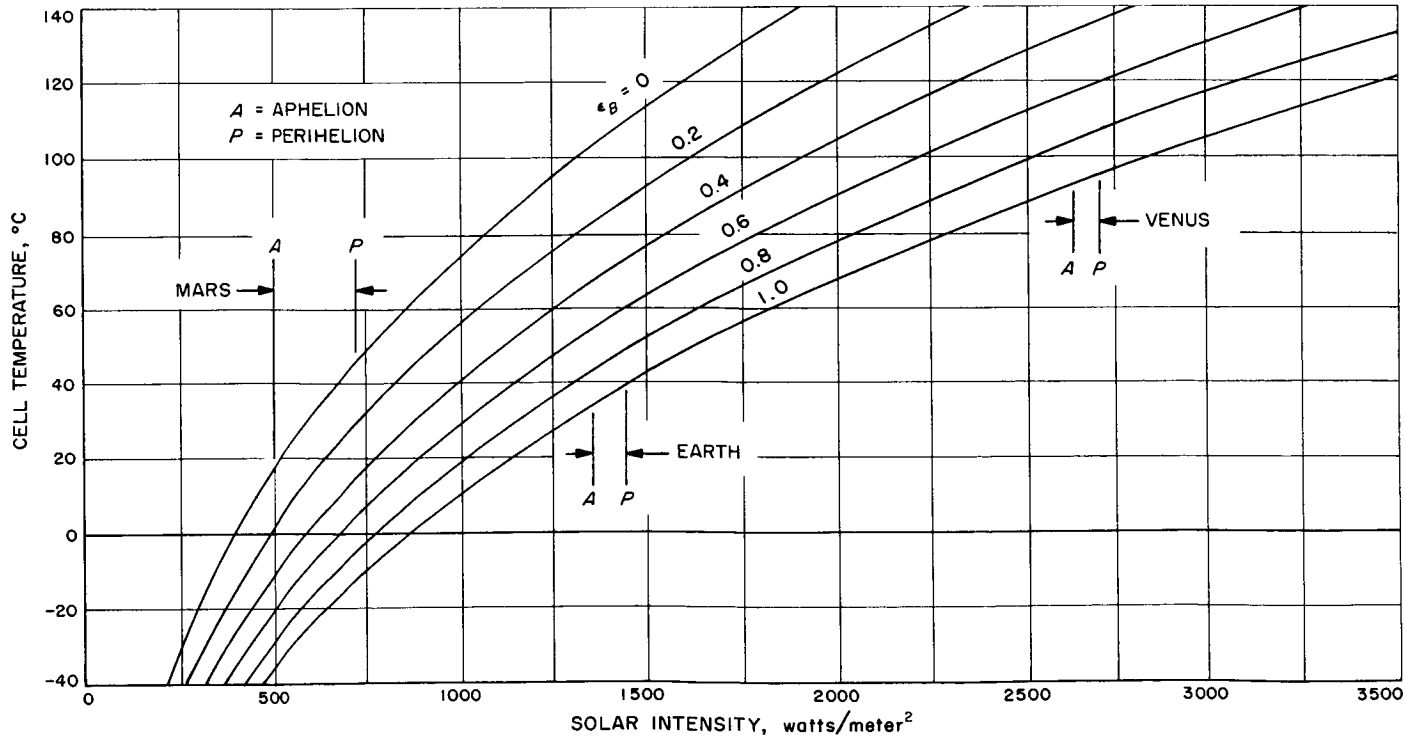

Figure 158. Mars solar panels

in series and 3 in parallel. The EOM-1 uses 5 cell shingles while the EOM-2 uses 15 cell shingles. The EOM-1 was tested by JPL personnel at Table Mountain in October. Its output was measured both with the reflectors exposed and covered at constant temperature. The ratio of the power output with reflectors exposed to that with reflectors covered was 1.87. Disregarding temperature effects, the tests show that (based on equal panel areas) this concentrating system will produce 93% of the power of a non-concentrating system having a space utilization factor of 0.90. A unit area of this concentrator would have half the number of cells of the non-concentrating system.

Additional tests are being planned to determine the reflecting characteristics of various surfaces under ground and space environmental conditions. A preliminary design of the *Mariner* B will be conducted utilizing this concept to determine over-all characteristics.

Temperature intensity tests. As was mentioned in *SPS 37-11*, a special vacuum chamber, 6½ inches in diameter and 7¼ inches deep, has been built for the testing of photovoltaic cells. This chamber contains a mounting panel for solar cells which may be temperature controlled by pumping liquid through it at the desired temperature. Temperatures in the range of −38 to 100°C have been obtained with this heat transfer scheme. Improvements are being made on the heat transfer system in order to obtain lower temperatures and greater stability at the low temperatures. The vacuum chamber is mounted on a clock-driven Sun tracker which has three long (21 in.) mirrors attached to it. These mirrors, with adjustable reflecting angles, may be used to obtain light intensities up to about 350 mw/cm². By using no mirrors and directing the face of the chamber away from the Sun, light intensities down to 35 mw/cm² will be obtained.

The main purpose of this special chamber is to observe the performance of solar cells at various light intensities and temperatures within the ranges stated above. Tests have been run on a 40-cell panel of Hoffman red cells. The following is a summary of the data obtained from these tests:

(1) For the temperature range from −10 to 95°C and with a light intensity of 328 mw/cm², the change in maximum power output is

$$\frac{P_{max}}{T} = -0.01 \text{ watt/°C}$$

or, referenced to the maximum power output at 30°C

$$\frac{P_{max}}{T} = -0.435\%/°C$$

Below −10°C the power output versus temperature curve begins to flatten out until it has zero slope at −40°C.

(2) For a single cell and with a light intensity of 328 mw/cm², the variation in open-circuit voltage with temperature in the range 0 to 100°C is

$$\frac{V_{oc}}{T} = -2.3 \text{ mv/°C}$$

(3) For a light intensity of 328 mw/cm² and a temperature range of 0 to 100°C, the change in short-circuit current of a single cell with temperature is

$$\frac{I_{sc}}{T} = 0.075 \text{ ma/°C}$$

(4) For constant light intensities of 300 ±20 mw/cm² and a temperature range of −10 to 90°C, the maximum power current from the 40-cell panel remains constant.

At the present time, 40-cell panels of Heliotek blue cells and Hoffman semi-conductor blue cells are on order, to be delivered in October and November, respectively. Tests will be run on these blue cells at light intensities from 35 to 350 mw/cm² and at temperatures from about −40 to 100°C. These temperature and intensity ranges are representative of what is expected at Mars and Venus. The data which will be taken from these tests are:

(1) Maximum power versus temperature at different intensities.

(2) Short-circuit current versus temperature at different intensities.

(3) Open-circuit voltage versus temperature at different intensities.

(4) Cell conversion efficiency versus intensity at different temperatures.

2. Sun Simulator

For several months it has appeared increasingly desirable to have a small simulator for alignment and testing of Sun sensors. *Ranger* Sun sensor deliveries have been behind schedule because of poor weather and remoteness of the coelostat installation at Chilao.

A feasibility study has shown that a Sun simulator using a xenon-arc energy source would be practical for Sun sensor testing. The study was based on the use of a 900-watt xenon source. Arc stability, energy distribution and intensity measurements were also made during operation of the lamp to determine its characteristics. The results of the study indicate that a 900-watt simulator

can provide a 2.25-inch diameter collimated energy bundle with an equivalent solar constant when testing the Sun sensor. An equivalent solar constant will energize the detector to the same output signal level as will sunlight extrapolated to zero atmosphere (0.140 watts/cm^2). To do this the xenon lamp will need to radiate only 0.058 watts/cm^2 since its spectrum contains more energy in the near infrared region to which silicon detectors are sensitive. This energy level will allow initial adjustment of the sensors and other test results will be compared to data taken at the Chilao facility. The validity of all tests will be determined by the correlation of tests performed using the simulator and tests performed at Chilao.

The optical design employs a standard refractive condensing system that reimages the arc at an aperture which controls the apparent diameter of the Sun. A lens focused on the aperture provides the collimated energy bundle. A spherical mirror is used to reimage the arc back on itself to gain intensity and to improve the uniformity of energy across the collimated bundle. By changing the aperture size, the simulator can provide different apparent Sun diameters as seen from Mars, Earth or Venus.

The simulator is visualized as a portable assembly making it also useful for energizing Sun sensors while they are being environmentally tested. It will be designed to operate in conjunction with a small temperature chamber.

Larger xenon sources, which are available up to 10,000 watts, could be utilized for construction of a simulator to provide an equivalent solar constant in a larger diameter bundle. The increased brightness would also allow filtering to more nearly simulate the Sun's spectrum.

3. Image Dissector

The primary objective of this program is to develop an electronic scanable photosensitive detector with the following characteristics:

(1) A package size suitable for space applications.

(2) Mechanical and electrical design suitable for space environment.

(3) Both electrostatic focusing and scanning for simplicity and low power requirements.

Figure 159 shows the image dissector configuration and its protective housing. When an optical image is focused on the photocathode, electrons are emitted from each element of the photocathode in a ratio directly proportional to the image intensity at that point. The electrostatic focus system accelerates the emitted electrons and forms an electron image at the aperture plate identical with the optical image at the photocathode. Only the electrons passing through the aperture in the aperture plate are detected and multiplied by the electron multiplier section. By suitable choice of an aperture shape, any desired portion of the total image can thus be detected. By applying voltages to the deflection plates, the electron image can be moved across the aperture in any desired fashion, thus scanning and dissecting the total image.

The design objectives of the image dissector are as follows:

(1) Electron image resolution (referred to the photocathode) 0.002 inch (10 line pairs per mm).

(2) Minimum deflection of $\pm$0.25 inch.

(3) Linearity of deflection position versus deflection voltage, 1%.

(4) Spectral response (S-11 type) with peak sensitivity of 0.060 amp/watt.

(5) Electron multiplier gain of 10^6.

(6) Variation of sensitivity over photocathode surface not to exceed 2 to 1.

Assembly of the first prototype image dissector was completed during October. Initial performance tests are now being conducted.

B. Engineering Mechanics

1. Structures and Dynamics

The spacecraft configuration is affected by many structural and non-structural considerations. The basic design now being considered for the *Mariner* B spacecraft consists primarily of five rings and six longerons, which form a hexagonal cylinder when cover plates are added. These cover plates also are used as a part of the electronic packaging assemblies. The fixed portion of the solar power array will then be supported at the base of the cylinder and at the outer edge by truss members attached to the top of the cylinder. The folded solar panels will be also hinged at these outer truss points.

The structure has been idealized by a system of 45 concentrated mass points and 197 truss members. Anal-

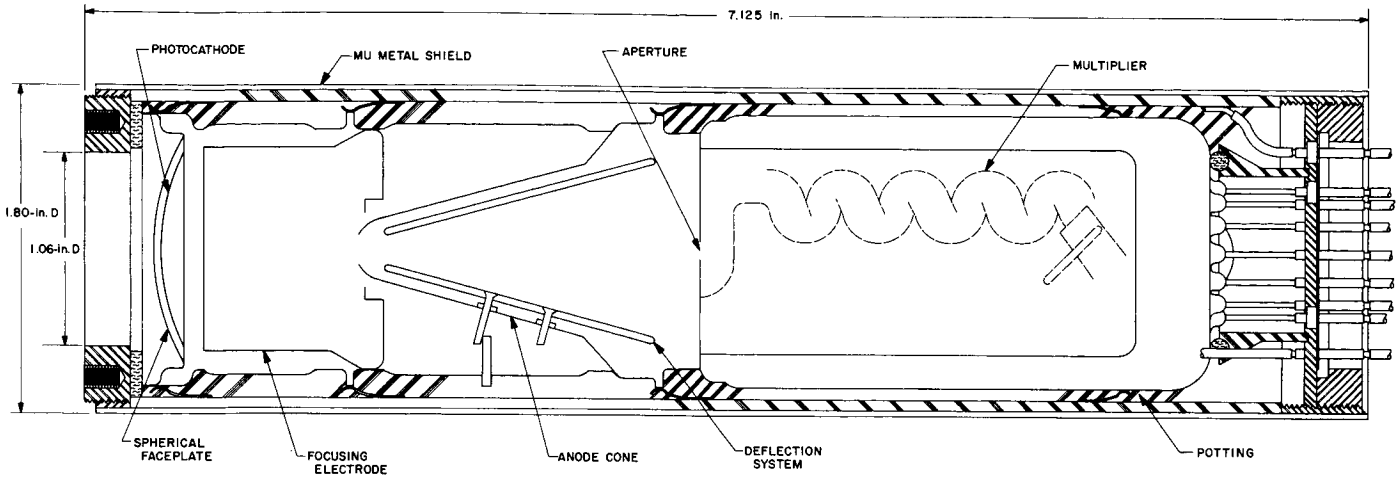

Figure 159. Image dissector

yses of several trial designs have been made, utilizing a previously developed computer program. This program generates stiffness, mass, and load matrices from coordinate, member stiffness, mass, and load input data. Static deflections and stresses are computed and dynamic solutions are obtained using a modified Stodolas procedure. Dynamic deflections and stresses are then computed for the first six modes based on assumed normalizing factors.

This analysis is limited, due to lack of consideration of: (1) the absence of inertial effects of individual masses, (2) beam action, and (3) limitations on the number of mass points which can be considered. Some consideration of mass inertias has been made by using dummy members to distribute mass points, but the program size limits this. The beam problems were considered in a separate analysis.

A preliminary structural test model is now being designed. It is believed that such a model will be helpful in the verification of the analytical procedures and in the evaluation of possible coupling problems between the bending and the truss solutions. It is believed that the concept of this design is sound, but it is expected that several local structural problems may show up. The test results will also be used to refine the later analysis procedures. Testing of this model is scheduled to start by January 1, in time to affect the preliminary design of the structure.

It is envisioned that the solar array for the Mars flight will consist of a 48 ft^2 fixed panel and four 20.5 ft^2 fold-out panels. Shorter fold-out panels with no fixed panels are planned for the Venus flight. Some preliminary studies have been made considering a *Mariner* A type of panel structure for the fold-outs. The fixed array may require a different type of panel structure.

The present solar panel design criteria are that the frequency of the extended panels should exceed 4 cps cantilevered from a rigid support and that the panels should be capable of withstanding the structural type-approval vibration input without excessive deflection in the boost configuration. The methods of panel support may differ significantly from those of previous programs, since it may be possible that two folded panels can provide a self-supporting system.

Unitized reflectors have been suggested as an alternative to the standard solar cell arrangement, especially for the fold-out panels on the Mars mission. Such panels appear to be entirely feasible from a purely structural viewpoint. The relative weight of a reflector panel compared to that of an equivalent standard panel depends entirely on the required area increase. The area increase affects unit weight as well as total weight, since the required stiffness increases with panel length while it decreases with reduced cell weight. Preliminary calculations indicate that a reflector panel with a 10 to 15% area increase will have about the same weight as an equivalent standard panel.

2. Packaging

A study was made of several configurations for packaging of the *Mariner* B spacecraft equipment. The basic design parameters used in the study were: (1) good conductive paths between subassemblies and the thermal control surface would be maintained, (2) the primary mode of temperature control would be passive and

the heat flow would be inward and upward to conserve heat and keep the capsule and mid-course motor warm, (3) existing *Ranger* type subassemblies could be utilized but the over-all design would not necessarily be restricted to using this shape for all assemblies, (4) electrical cable access, routing, and junction points would be provided for, and (5) equipment assemblies would serve to stiffen the basic spacecraft structure.

The resulting assembly cross-section was defined as using approximately a 6 by 6 subassembly with a 1¼ by 6 area for interconnections. The minimum bolt-down dimension across the width of the assembly that looked practical evolved to 8.700 inches. When this dimension was checked with the proposed structure, it appeared that with the addition of a few inches to the width of the bay, a pattern of three assemblies could be defined that would allow either horizontal or vertical mounting. This would provide the greatest flexibility for arranging and dividing assemblies to maintain the functional integration desired by the various operating divisions. The resulting assembly chassis length was 26.1 inches which would allow a slight increase in volume over the present *Ranger* assembly. The interspaced chassis mounting allows about a 2.9-inch increment in chassis length.

It presently appears that the system cabling could be installed on the internal side of the basic hex structure. A vertical separation of the signal and power cable could be obtained and separate connectors would be used for these functions. The connection to the system cabling from each assembly would be through the bottom mounting plate by either a pig-tailed connector requiring approximately ¼ inch of travel or by a plug-in approach if tolerances can be resolved.

An artist's conception of what the spacecraft would look like (Fig 160) using existing subassemblies, was made as a visual aid in early packaging discussions.

The present configuration utilizes five bays of three assemblies in each bay with a capability of an additional assembly in each bay for scientific experiments. The sixth bay contains the planetary horizontal platform, boom, and associated equipment.

A test chassis was defined (Fig 161). A set of test chassis was fabricated in aluminum and magnesium and is now undergoing vibration testing to determine resonant frequencies and amplification factors. Although the testing to date has only been cursory, it appears that additional stiffening of the assembly chassis will have to be incorporated in order to assure adequate performance of contained equipment under dynamic conditions.

3. Gasdynamics

SPS 37-11 referred to the Rand Corporation Study RM-2817 for JPL, assigning probable bounds to Martian atmosphere properties.

Tables 31, 32, and 33 give the JPL interpretation of this study. Quantities in Table 33 result from the basic Rand data in Tables 31 and 32 being arbitrarily combined in such order as to obtain maximum spread between extreme values in Table 33.

Within these tolerances a vast array of atmosphere profiles could be defined. Figure 162 shows possible temperature distributions vs altitude, where, for lack of more detailed knowledge, idealized ground-convection constant-lapse-rate is used in a troposphere and isothermal gravity-pressure equilibrium assumed for a stratosphere. Profiles A and C outline the possible bounds of temperature. Profiles B, D, and E are other possible profiles within the expected range. Figure 163 shows density profiles corresponding to the previous temperature plots.

In order to establish a required body m/C_DA (ballistic coefficient) for a prescribed Vot (parachute fall time, times impact velocity) after a deployment at a prescribed Mach number, *SPS 37-11* used the low ballistic coefficient envelope of a band of m/C_DA versus Vot curves corresponding to these various possible atmospheres. The envelope consists of the curves from Atmospheres A and D for deployment altitudes up to 66,000 feet, and the curve of Atmosphere B from 66,000 feet up to 120,000 feet. Thus, a given assumed atmosphere could be critical (require lowest m/C_DA) over only part of the altitude range.

4. Temperature Control

The thermal environment of payload to be provided for the *Mariner* B spacecraft will be controlled by the heat exchange between the external vehicle surfaces and their space environment, and the local heat flow pattern in the immediate area of the component.

a. Internal heat exchange. A payload isothermal environment of a spacecraft which is to simulate ground test conditions, must rely on internal heat exchange and the total payload mass as a large thermal reservoir.

The proposed design of a slender toroidal payload configuration with a continuous cavity will implement these principles by:

(1) Peripheral heat flow along a solid interior base plate on which all electronic subassemblies will be mounted.

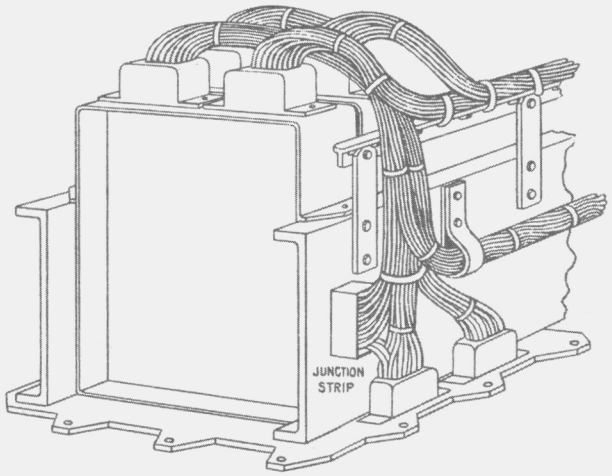

ASSEMBLY SYSTEM CONNECTORS

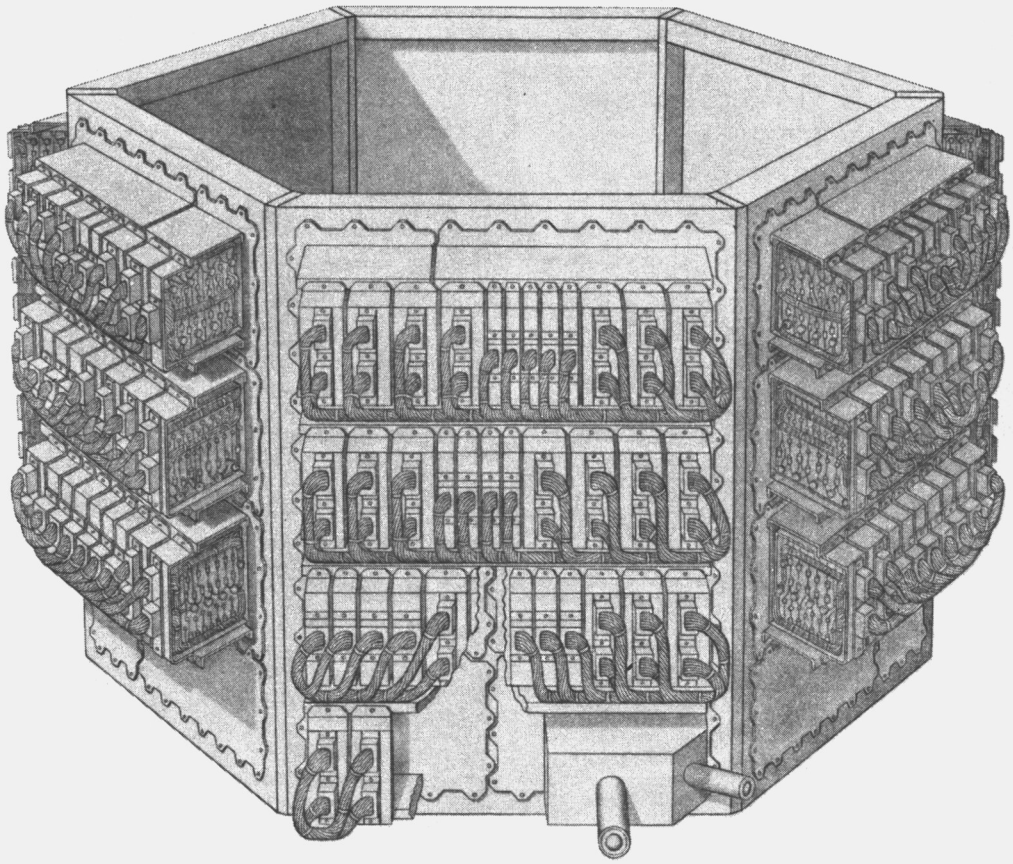

Figure 160. Electronic packaging

(2) Creation of a large central space which will provide temperature stabilization for the mid-course motor.

(3) Radiative heat exchange across the central cavity.

(4) Short heat flow paths from the large heat sources to radiators at the end surfaces.

(5) Selective location of components according to their heat dissipation.

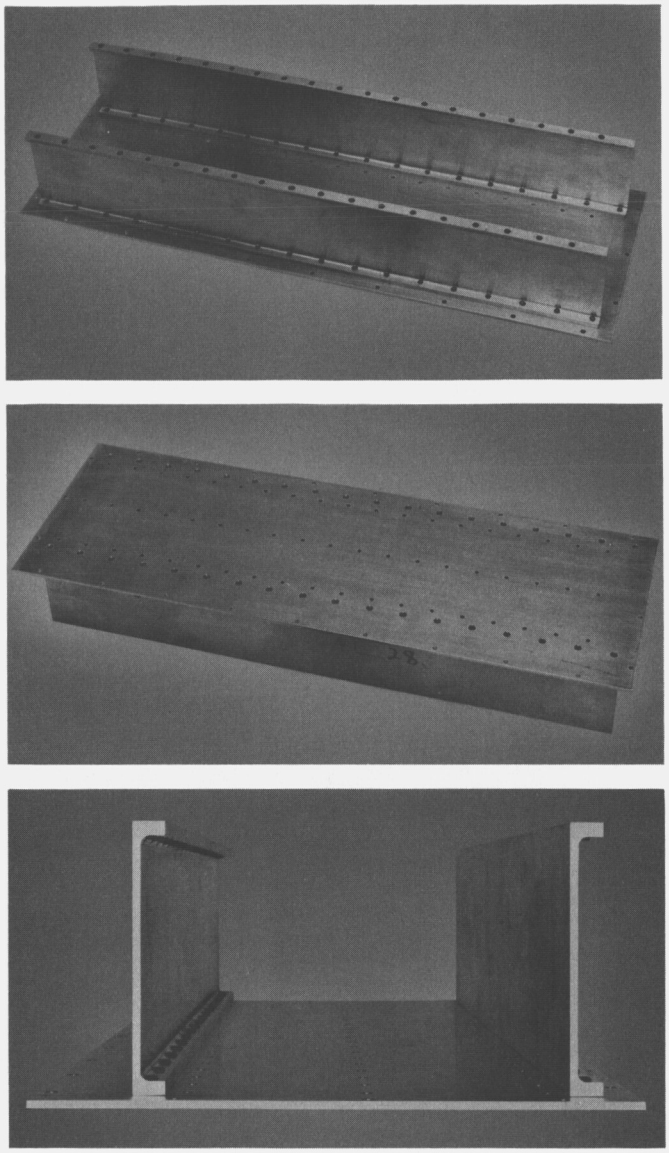

Figure 161. Test chassis

Table 31. Mars atmosphere[a], independently determined parameters

Symbol	Parameter	Unit	Low	Nominal	High
g_o	Acceleration of surface gravity	ft/sec^2 cm/sec^2	12 360	12 375	13 390
M_m	Surface Mass pressure	slug/ft^2 gm/cm^2	9.5 150	16 250	22 350
T	Stratosphere temperature	°R °K	230 130	320 180	410 230
T_o	Surface temperature	°R °K	380 210	410 230	470 260
C_p	Specific heat at constant pressure	BTU/slug °R cal/gm°K	7.4 0.23	7.7 0.24	8.1 0.25

[a] Tentative.

Table 32. Mars atmosphere, Parameters dependent[a] on selected composition of atmosphere

Symbol	Parameter	Unit	Low ← (g) → High High ← (M_m) → Low		
C_{cv}	Concentration of constituents by volume	%			
	CO_2		0.7	1.9	7.2
	A		0.6		6.0
	O_2[b]		0		–
	N_2		98.7		86.8
C_{cm}	Concentration of constituents by mass	%			
	CO_2		1.1	3	11
	A		0.8		8.7
	O_2		0		(2.7)
	N_2		98.1		80.3
M	Average molecular weight by volume		28.2	28.4	29.9
γ	Ratio of specific heats		1.42	1.41	1.41
			High ← (g, M_m) → Low		
P	Surface pressure	lb/ft^2 mb	284 136	196 94	113 54

[a] Data are consistent within columns.
[b] Conjectural oxygen not considered in average molecular weight.

(6) Local radiative heat exchange inside the payload volume.

Adjacent to a heat source in the interior of the payload a solid metal heat conduction path will be provided to transport heat efficiently. Thus, the mounting of all electronic parts has to be designed with considerable care and joint thermal resistance kept to a minimum.

After spreading the heat over somewhat larger areas in the structure, a vapor convection system might be employed; however, difficulties due to the pressurization of the payload and of handling make this method less desirable. A second method of internal radiation on a local level becomes significant as soon as the heat distribution reaches approximately one third the size of a base plate area. A combination of solid heat conduction and internal radiative exchange will result in a payload environment with not more than 30°F internal temperature gradient and at a level approximately 100°F above the mean radiator temperature.

Table 33. Mars atmosphere, derived[a] parameters

Symbol	Parameter	Unit	Low←g, P_o, M, M_m→High High←T,→Low		
ρ_o	Surface density	slug × 10^{-4}/ft^3 gm × 10^{-4}/cm^3	1.4 0.75	2.7 1.4	4.3 2.2
H	Scale height	ft × 10^3/km	59 18	41 12.5	29 9
β	Reciprocal of H	1 × 10^{-5}/ft 1 × 10^{-2}/km	1.7 5.6	2.4 8.0	3.4 11.0
Γ	Dry adiabatic	°R × 10^{-3}/ft °K/km	−1.96 −3.43	−2.04 −3.75	−2.13 −4.10
a_o	Speed of sound at surface	ft/sec m/sec	1064 325	1013 309	985 300
a_{ii}	Speed of sound in stratosphere	ft/sec m/sec	1013 309	903 275	765 233
Γ/T_o	Lapse rate/Surface temperature	1 × 10^{-6}/ft 1 × 10^{-2}/km	−4.17 −1.32	−4.98 −1.63	−5.61 −1.95

[a] Data are consistent within columns.

More precise temperature control with smaller tolerances may be obtained by a supplementary active control system. This would be formed by louvers on a part of the radiator area, which would reduce excess temperature excursions of sensitive equipment. An active control

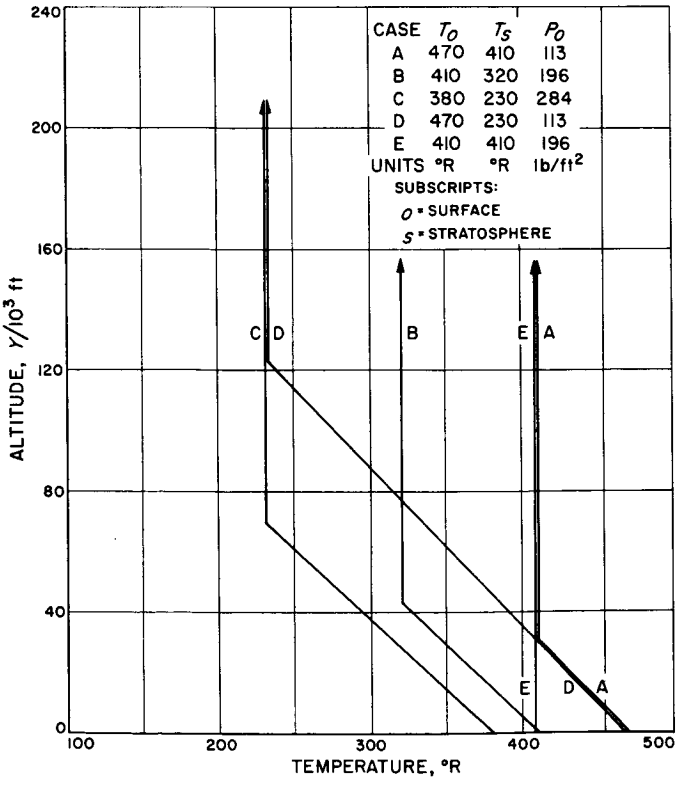

Figure 162. Temperature of Mars atmosphere

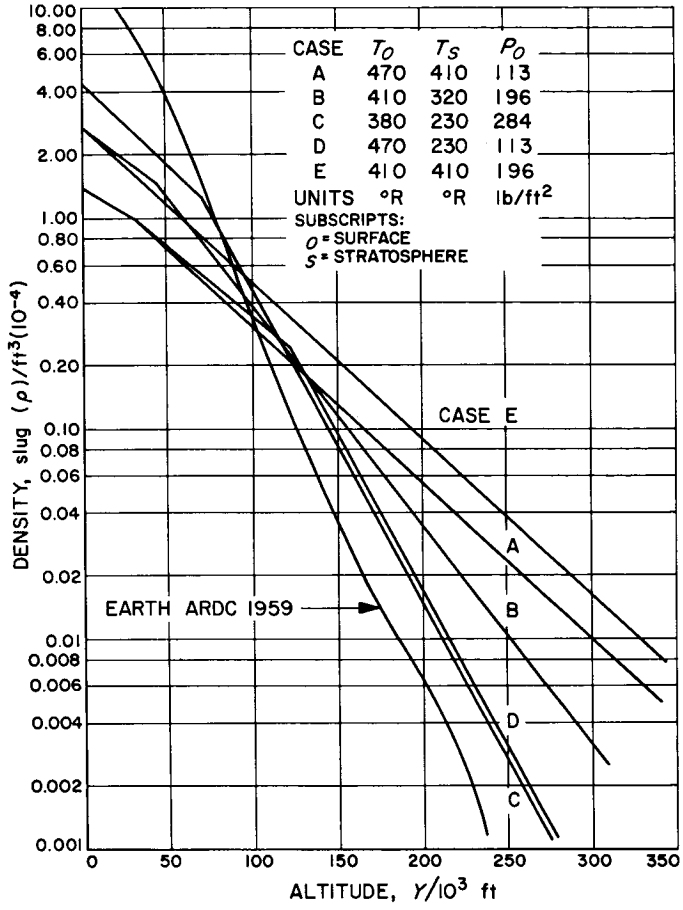

Figure 163. Density of Mars atmosphere

scheme is necessary if gradual changes of the spacecraft equilibrium temperature due to deterioration of radiator surfaces after long duration space exposure, can not be tolerated. The amount of louver covered area required to compensate for changes in the long wavelength emissivity of the radiating surface is a function of the nominal value of the radiator emissivity and the span of emissivity variation available from shutter actuation (Fig 164). For higher original values of ε_{nom}, the required louver area grows at a faster rate which, in effect, reduces the average emissivity of the vehicle radiator surfaces at the start, and thus, does not lend itself to the use of extreme ε values.

The variation of internal energy dissipation is estimated to be within ±10% of the nominal power level of the payload as a whole. For the planned payload configuration of toroidal shape, $H/D = 1/4$, such duty cycle power variations would change equilibrium temperatures by ±15°F. However, local areas of high intensity heat flow may be subject to larger variations. Decisions on the need for active control devices for cases of duty cycle

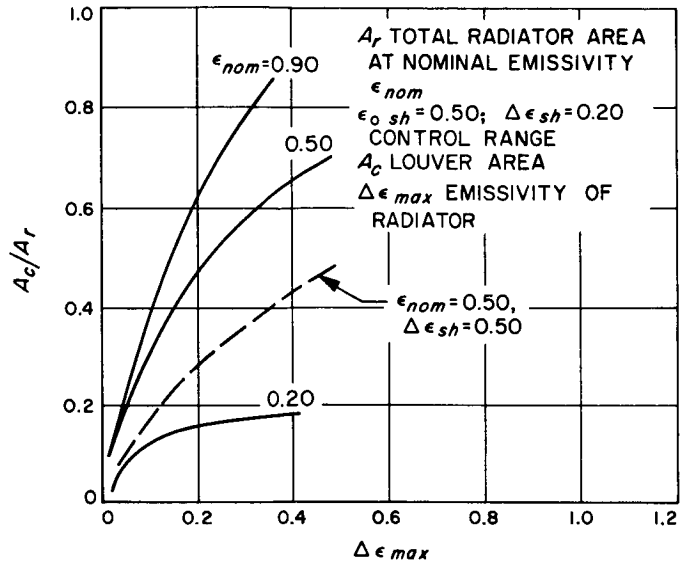

Figure 164. Lower area required versus emissivity of radiator

extremes, thermal disturbances arising from vehicle attitude changes, initial uncertainty of optical properties of space vehicle surfaces, and many others will have to await a closer definition of vehicle subsystems and an established design of payload structure and packaging.

b. Structure interactions. The thermal control system ultimately adapted for the *Mariner* B spacecraft will be affected by the design of the vehicle powerplant.

Utilization of the solar panel near the main payload chassis will depend on the temperature distribution, and radiation view factors. It would seem highly desirable to restrict the area covered by solar cells to the outside of the maximum diameter or periphery of the hexagonal boxes, since this central area might be useful for heat rejection. An alternate approach would require thorough thermal insulation between the solar panel and the payload.

IV. *Voyager*

Specific efforts directed to accomplishment of the *Voyager* Project were initiated at the start of FY 62. A brief synopsis of these efforts is as follows:

The Systems Division is participating with the technical divisions in the generation of mission objectives and the preparation of preliminary systems design specifications for interplanetary spacecraft to be used as planetary orbiters and landers and out-of-the-plane-of-the-ecliptic probes using the *Saturn* vehicle as the booster.

The Space Science Division is conducting *Voyager* scientific feasibility studies, establishing the feasibility of meteorological, biological, and certain adaptations of geological experiments for the *Voyager* as well as refining our knowledge of the Mars and Venus environments as they affect experiments and spacecraft for these flights.

The Guidance and Control Division is continuing its studies of guidance and control requirements, methods, and techniques for advanced planetary missions, both those currently planned and those that become necessary or desirable as a result of discoveries on early planetary exploration missions that require further exploratory operations. The methods to be used include study of possible mission requirements to deduce the general requirements for guidance and control subsystem performance, evolution of subsystem configurations to accomplish the required tasks, and parametric and error analyses of typical missions and operating situations to determine the ranges of parameters and tolerances required.

The Engineering Mechanics Division is performing *Voyager* spacecraft studies, including analytical investigations of configuration, thermal control, entry and landing dynamics, post landing and roving techniques, booster compatibility, multiple mission or universal design concepts and compromises, and structural design problems.

PART FOUR
ADVANCED DEVELOPMENT

I. Lunar

The Lunar Advanced Development Program consists of those projects and efforts which will extend the state-of-the-art and will provide knowledge applicable to a specific problem or a technical field of interest, thus leading to the development of hardware necessary in the planned and orderly Lunar Exploration Program. It also establishes a mechanism to ensure that advances in the state-of-the-art are exploited.

A. Friction and Lubrication in a Space Environment

With respect to design problems in the broad area of moving parts for spacecraft, two points are clear. (1) The current state-of-the-art of bearing and material development to cope with frictional problems in space environments is in its infancy. Existing literature provides little to help the designer in his efforts. Existing research and development programs are inadequate to supply direction. (2) The scope of design and development effort directed to interplanetary space vehicles involves a large variety of frictional problems that require individual attention. Time prohibits testing each one separately. A unified approach is required to establish the most efficient research and development effort.

Accordingly, as a first phase effort, the Marlin-Rockwell Corporation of Jamestown, New York has been retained to survey the field of frictional problems connected with space vehicles. One of their men is currently in residence at JPL obtaining information to be included in a report to be issued in a few months. In addition, another Marlin-Rockwell engineer is surveying others with knowledge in this problem area. These inputs will also be included in the report.

B. Development of Stable White Surfaces

A contract has been awarded to the Armour Research Foundation of Illinois Institute of Technology to develop a brush or spray type white coating ($\alpha/\varepsilon < 0.40$) which can be utilized on spacecraft temperature control surfaces which will be exposed continuously to the vacuum

and ultraviolet (solar) radiation of space for periods of up to 2 years. All known white paints will yellow seriously (solar adsorptance increases) under such conditions.

The first planning meeting was held at Armour recently. It was agreed initial research efforts will emphasize determination of yellowing characteristics of candidate pigments and binders separately. Types of coating systems being considered include the inorganic phosphate and silicate types, taking advantage of Armour's recent experience with high temperature strain gage cements. The Lockheed Laboratories in Palo Alto have published some promising results with similar coatings. Investigations into organic binders will be initially confined to fluorinated polymers. Limited work will also be initiated on multilayer coatings, some of which may combine an organically bound undercoat protected by an inorganic overlayer.

C. Thermal Control Device Evaluation

Two thermal control devices were investigated to determine the weight versus power regulation relationships. The analyses of the Space Technology Laboratory Maltese Cross (Ref 8) and the JPL louver systems (*SPS 37-9*) were made under the constraints of shading from solar radiation, and simplifying assumptions related in the respective descriptions.

Maltese Cross. This device consists of a four-bladed shield which masks one-half of the swept area. The rotational position is thermally controlled so as to expose a temperature dependent ratio of two different surface treatments. The STL 5-inch diameter device, weighing 13 grams, was used in the calculation.

To simplify the analysis, heat losses through the blades were neglected, the blades were assumed fabricated of an insulation material and with a low emissivity, ε. The results are plotted in Figures 165 and 166 as the weight per watt difference in heat rejection at the limits of the temperature range of the bimetallic actuators versus the lower actuating temperature, T_{lower}, for $\Delta T = 25$ and 100°R.

Louver system. The louver mechanism can be likened to venetian blinds that rotate in response to thermal variations. At the lower temperature limit, the louvers are shut and act as a radiation shield. At the upper temperature limit, the louvers are opened 90 degrees, to present the minimum obstruction to radiation.

The simplifying assumptions were that there were no heat losses due to the actuating structure and there was no conduction to the louvers. The latter assumption means that the louver is constructed of an insulating material. The analysis requires that values of emissivity of the louvers and the base surface be arbitrarily chosen. The results are plotted in Figure 167 as the variation in power rejected per unit area versus the lower actuating temperature for $\Delta T = 25$ and 100°R.

It is extremely hard to compare these two systems at the present state of evaluation. The assumptions made

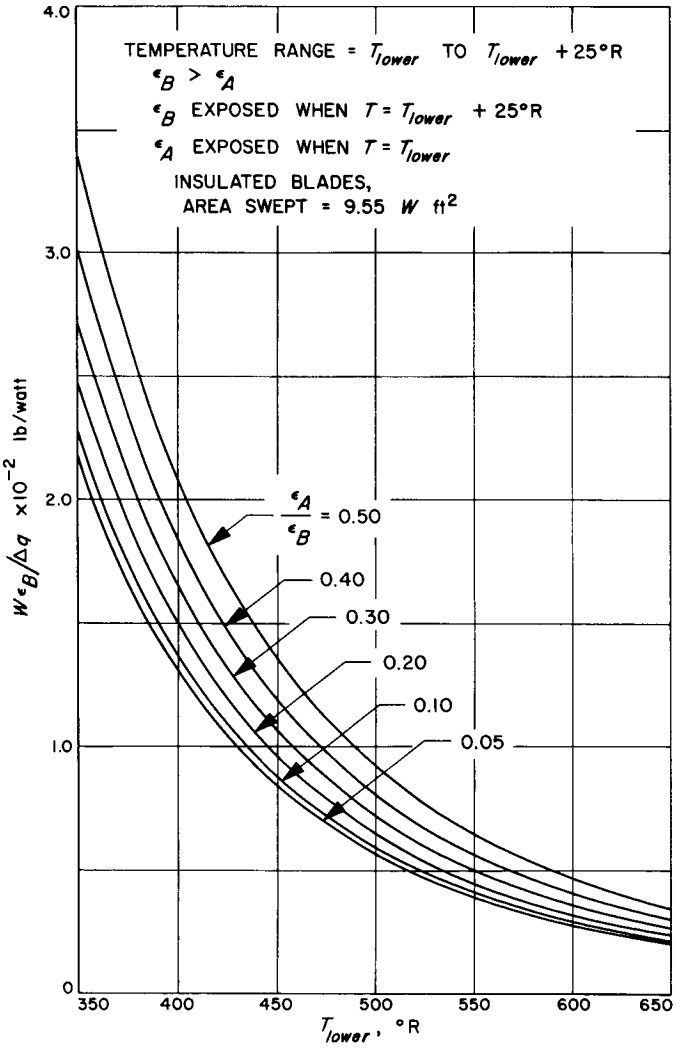

Figure 165. Pound/watt variation required $\Delta T = 25$°R

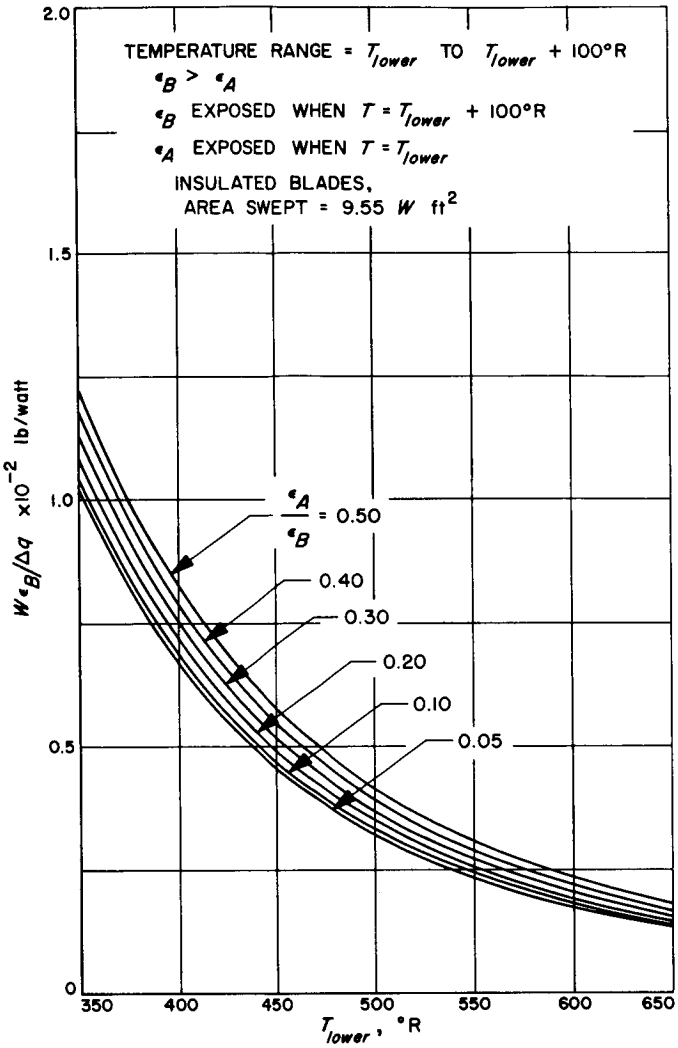

Figure 166. Pound/watt variation required $\Delta T = 100°R$

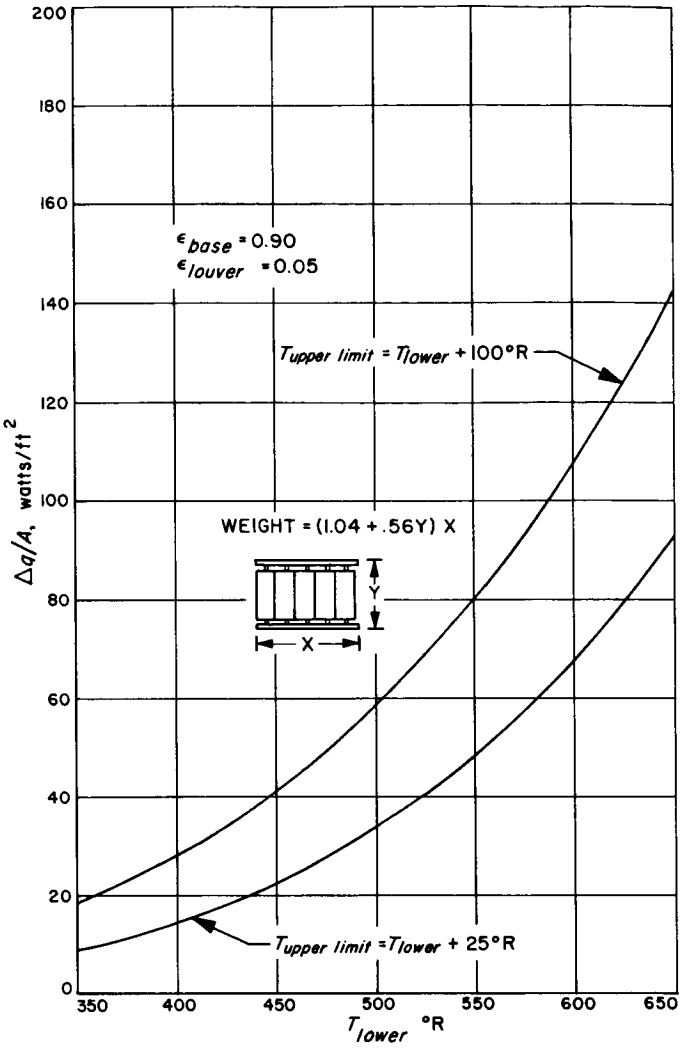

Figure 167. Power radiation differential versus lower temperature limit

were different in that the mechanisms of control are different; the STL device changes the surface properties exposed while the louvers change the effective area exposed. The analysis was made with arbitrary emissivities for the louver mechanism and no size was assumed.

Solar radiation enhances the effectiveness of the STL device since another variable is introduced: the absorptivity α. Surface coatings with high α/ϵ and low α/ϵ can be chosen for the cold temperature and hot temperature exposed surfaces, respectively. The louvers are complexly affected by sunlight because the amount absorbed is related to the angle of the louvers. In addition, presently, at the cold temperatures, the blinds are shut, excluding sunlight. Further study is required.

D. Determining Relative Humidity in Sterilizing Gas Mixtures Containing Ethylene Oxide

The important role (Ref 9) that moisture plays in the bacteriacidal activity of ethylene oxide makes it imperative that a rapid, reliable method for determining moisture be available if there is to be effective moisture control.

The solubility of ethylene oxide in water renders the wet and dry-bulb thermometer readings meaningless and pyschrometric chart inapplicable. Hygrometers based on mechanical means involving dimensional changes in

human hair or other water absorbing materials are slow acting and almost certain to be adversely affected in their response by the ethylene oxide. Hygrometers based on some measure of electrical resistance are also likely to be unreliable in the presence of ethylene oxide. The classical method for determining moisture, or relative humidity, in gases by the dew point technique can be used within certain limitations on sterilizing gas mixtures of the composition used at this Laboratory.

The sterilizing binary mixture available as a liquid in steel cylinders and used at JPL, has a volume composition in the gaseous state of 27.3% ethylene oxide and 72.7% Freon 12 (dichlorodifluoromethane).

At one atmosphere pressure the partial pressure of ethylene oxide in the mixture is 208 mm Hg; consequently the dew point temperature can not be less than −17°C, otherwise an ethylene oxide mist will be formed. In other words, the % relative humidity of the sterilizing gas mixture at a temperature of 20°C can not be less than 6% because of interference from ethylene oxide. This is not a serious limitation because the optimum relative humidity is about 30%.

Having decided that the dew point technique is applicable to moisture determinations in the sterilizing mixture being used, the Alnor dew pointer which uses the principle of adiabatic cooling of a rapidly expanded gas to obtain the dew point temperature was tried and found to give rapid, reliable dew point temperatures. The Alnor dew pointer is manufactured by Alnor Instrument Co., Chicago, Illinois.

The Alnor unit is quite rugged and simple to operate. The gas, whose moisture content it is desired to determine, is subjected to a series of compressions in an illuminated chamber. When the chamber is rapidly exhausted to atmospheric pressure, the expanding gas undergoes adiabatic cooling, and the compression which just produces a mist is referred to as the *end point* and the resulting temperature is the dew point temperature.

A fundamental equation expressing the relationship between temperature during adiabatic expansion and pressure is:

$$\text{Final temperature} = \text{Initial temperature}\left(\frac{\text{Final pressure}}{\text{Initial pressure}}\right)^{(K-1)/K}$$

and $K = C_p/C_v$. The temperature is expressed in °K, while the remaining terms, being ratios, can be expressed in any self consistent units.

In the Alnor dew pointer, the initial temperature is read on a thermometer in the illuminated compression chamber, and the ratio of pressures is read directly on a gage.

The equation for adiabatic expansion can be rewritten in a form better suited to the Alnor unit. The dew point temperature t_{ap} in °F reached when a mist just forms is given by the following:

$$t_{dp} = (t_i + 460)\,(PR)^{Q} - 460$$

where

$$Q = \frac{K-1}{K}$$

The Alnor instrument comes with a calculator for conveniently handling the above equation.

When working with gas mixtures, the Q value must be determined for the mixture from specific heats of each gas component. The Q value for a gas mixture, Q_m, is calculated as follows:

$$Q_m = \frac{K_m - 1}{K_m}.$$

where

$$K_m = \frac{C_{pm}}{C_{rm}}$$

and

$$C_{pm} = \frac{vol\ \%X}{100} C_{px} + \frac{vol\ \%Y}{100} C_{py} + etc$$

$$C_{vm} = \frac{vol\ \%X}{100} C_{vx} + \frac{vol\ \%Y}{100} C_{vy} + etc$$

C_{px} is specific heat at constant pressure, and C_{vx} is specific heat at constant volume both for gas X. Since the volume % is known for the various gases, the specific heats must be expressed in cal/mole, °C.

C_p and C_v for oxygen and nitrogen are essentially the same, making the Q value also the same. Air can therefore be treated as if it were a single component gas.

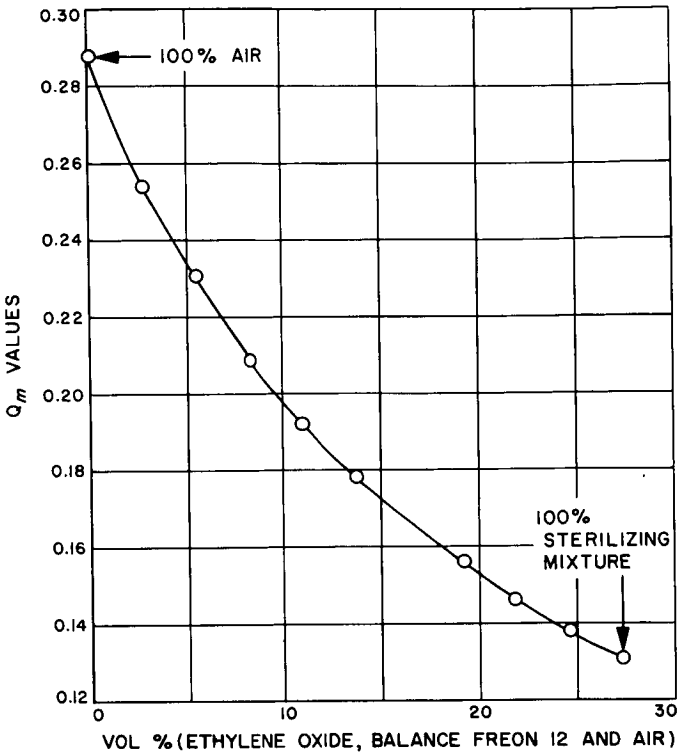

Figure 168. Q_m values calculated for gas mixtures consisting of ethylene oxide, Freon 12 and air

Figure 168 is a plot of calculated Q_m values of gas mixtures consisting of ethylene oxide, Freon 12, and air.

Table 34 shows the relative humidity results obtained in a series of prepared mixtures containing known quantities of water, and indicates the kind of precision to be expected.

Table 34. Comparison of calculated relative humidities with the dew point technique

Run	Volume, %			Relative humidity, %		
	C_2H_4O	CCl_2F_2	N_2	Alnor unit	Calculated from H_2O added	Difference
1	0.0	0.0	100.0	32	30.6	1
2	6.8	18.2	75.0	38	41.1	3
3	8.6	22.8	68.6	32	31.9	0
4	13.8	36.6	49.6	28	26.4	2
5	20.5	54.6	24.9	14	12.0	2
6	25.5	74.5	0.0	24	23.4	1
7	25.5	74.5	0.0	36	35.9	0
8	25.5	74.5	0.0	48	48.0	0

II. Planetary–Interplanetary

The Planetary–Interplanetary Advanced Development effort during FY 62 includes the following long-term studies, analyses, and developments leading to feasibility demonstrations of advances in state-of-the-art techniques intended for application to future planetary–interplanetary projects beyond the first flight missions now scheduled.

The Systems Division is conducting systems analysis studies related to trajectory and guidance problems associated with the return of a vehicle from a planet to the Earth, studies of trajectory and guidance analysis problems for missions to planets other than Venus and Mars, studies in planetary entry and descent from planetary orbits, and studies of extended trajectories to the planets. In addition, studies are being conducted to determine the values and effects of errors in the fundamental solar system constants.

The Space Science Division is developing an exobiology microscope, a soil sample gathering microscope vidicon system capable of performing visible analysis on soil samples which have been graded according to particulate size and density, and a companion microscope spectrophotometer to provide a spectral scan in the range 2000 to 5000 Å of a sample located on the stage of a microscope. Additional efforts are directed to developing sample handling systems for the above equipment. Also underway are developments of microwave receivers to provide research tools for the scientific study of lunar and planetary surfaces, atmospheres, and ionospheres; development of instrumentation utilizing solid state radiation techniques for making measurements of fluxes and energy spectra of charged particles in space; study on both a theoretical and an experimental basis of the merits of the interferometer type of infrared spectrometer; and a study of wet chemical analysis techniques applicable to biochemical analysis and life detection.

The Telecommunications Division is pursuing the development of a planet-based capsule communication system; the study, design, fabrication, and testing of erectable large spacecraft antennas; the investigation of the application of all magnetic logic circuitry to spacecraft time-multiplexing and programming subsystems; the development of a high-capacity data storage system; the evaluation of various methods of range acquisition; and the analysis and development of various circuit techniques applicable to long range communications.

The Guidance and Control Division is conducting advanced development efforts in the area of logical designs for guidance computers, developing experimental models of 9-foot concentrators and a 500-watt thermionic converter in order to provide techniques which may prove feasible as spacecraft power sources, and survey-

ing and developing advanced attitude control system mechanization methods and the various design techniques unique in their implementation.

The Engineering Mechanics Division is performing advanced development of the use of crushable structures for entry capsules, the thermal stress plastic analysis of radiator structures, the development of inflatable instrumentation booms for spacecraft application, the study of atmosphere entry and temperature control aspects of various spacecraft configurations, and the development of techniques applicable to the environmental survival of equipment.

The Engineering Facilities Division is developing instrumentation components, equipment, and systems to support the advanced development efforts of the other divisions.

In the field of chemical propulsion, the Propulsion Division is conducting an industry-wide survey of high energy solid propellant development activities in order to select a few propellants for more thorough investigation for use in spacecraft propulsion. Efforts are also being expended in the evaluation of throat and nozzle materials.

In the field of electric propulsion, the Propulsion Division is keeping abreast of preliminary descriptions of the SNAP-VIII Reactor System, its power conversion system and its thrust units, and is evaluating the constraints they place on the spacecraft and/or the spacecraft should place on these units. Supporting the electric propulsion are the following efforts being undertaken by other divisions: trajectory and guidance analysis, systems studies and preliminary analysis of spacecraft designs, communication analysis, analytical design of guidance and control subsystems; and studies and analyses in the areas of structural dynamics, structural configuration, shielding, and temperature control for electric propulsion spacecraft.

A. Space Sciences

1. Jovian Environment

In planning a space probe to investigate the planet Jupiter, it is necessary to bring together all that is known about the planet. Only then can one most effectively decide what scientific experiments should be included in the payload.

The following is a summary of quantitative knowledge concerning the atmosphere and environment of Jupiter. This summary represents the conclusions following a review of the papers presented on Jupiter in the professional literature, and is subject to revision as more is learned about the planet.

Atmospheric depth. The pressure of the Jovian atmosphere increases very rapidly in depth. The atmosphere should solidify between about 80 and 700 km below the cloud level, depending on the form of the temperature gradient. The probable depth is between 100 and 230 km below the clouds.

Sidereal period of the solid surface. This period lies in the range $9^h\,55^m\,29.45^s \pm 0.10^s$ and the best determination so far is $9^h\,55^m\,29.35^s$ using data from decameter radio bursts over a period of 9 years. The constant location of the radio sources implies that they are anchored to the solid surface.

Magnitude. The magnitude of Jupiter at zero phase and unit distance from the Sun and the Earth is -9.25 and is variable by 0.45 of a magnitude over a century of observation.

Colors. The photometric color magnitudes of Jupiter with respect to the Sun are given for V (Jupiter) $-$ V (Sun) set equal to zero: $U = +0.54$, $B = +0.20$, $V = +0.00$, $R = -0.05$, and $I = +0.27$. Each value has an error of about ± 0.04 of a magnitude.

Albedo. The geometric albedo is given to 5% accuracy: $p(U) = 0.27$, $p(B) = 0.37$, $p(V) = 0.45$, $p(R) = 0.47$, and $p(I) = 0.35$. The bond albedo is $A = pq$ where p is the geometric albedo and q is taken to be near 1.65. A in the visual region (5440Å) is 0.73 to 12% accuracy.

Mean molecular weight $\bar{\mu}$ of upper atmosphere. The mean molecular weight of the upper atmosphere is likely to lie in the range of $2 < \bar{\mu} < 5$.

Composition. The composition of the planet is: hydrogen, 5 km-atm ± 1 km-atm; ammonia, 7 m-atm ± 2 m-atm; methane, 150 m-atm ± 50 m-atm; and helium, perhaps 3 times as much as hydrogen.

Variation of height of cloud level over disk. The cloud layer on Jupiter probably rises by about 10 to 12 km from the center of the disk to latitude 60° and descends polewards of 60°. The presence of a tenuous fog may suppress this effect. The temperature difference between the morning and evening levels ($\pm 60°$ from the central meridian) is 4 to 5°, the morning level being the cooler. In the presence of a tenuous fog these temperatures are those of the mean level of penetration of light.

The polar regions appear to be free of clouds since light scattered is polarized as expected for a pure gas.

Temperatures. The mean radiation temperature with an albedo 0.73 is about 90°K, and the corresponding maximum for the mid-solar point is about 125°K. These refer to vicinity of the cloud level. These values are approximate and assume that the infrared albedo near 20μ is zero. A non-zero value would act to increase these temperatures.

The radiometric temperature of Jupiter is 140°K and two measurements give deviations of ±10°K. This is the *grey body* temperature as determined from flux in the infrared.

Limb darkening. The limb darkening is approximated by:

$$I(\mu) = I(1.0)\,[1 - b\,(1 - \mu) + c\,(1 - \mu)^2]$$

where $\mu = \cos\theta$.

$$\text{Let } X = \frac{2I(\mu = 0.5)}{I(\mu = 1.0)} = 2 - b + \tfrac{1}{2}c$$

then X is about 0.8 in the red and 1.2 in the blue.

Polarization. The polar regions may be covered by a fairly thick atmosphere in which Rayleigh scattering takes place, whereas the clouds at the equator leave only a thin atmosphere above them. A tenuous fog may exist above the cloud layer.

Microwave radiation. Radio emission up to about 5 cm wavelength is primarily thermal in character. Thereafter, a nonthermal component is increasingly manifest, giving black body temperatures of about 70,000°K at 68 cm. This radiation is not black body in character but rather is emitted with a constant flux in the non-thermal region of the spectrum.

This radiation is also polarized and comes from an area 2 or 3 times the disk size of Jupiter. The polarization increases in the radial direction. This emission zone is similar to the Earth's Van Allen belt, but either the number of particles/cm^3 or the magnetic field is much greater in magnitude. The radiation seems most likely to come from either synchrotron or cyclotron emission. Synchrotron emission can exist with fields on the order of 10 gauss but the electron particle density must be on the order of 10^5 electrons/cm^3. Cyclotron radiation can accommodate a much smaller particle density but a magnetic field of at least 1200 gauss is necessary.

Decameter radiation. This occurs in short pulses of effective dynamic bandwidth about 0.5 mc and lasts from 0.2 to 2 seconds in duration. Millisecond pulses also occur. Bursts of pulses last from a few seconds to several minutes. They are right circularly or elliptically polarized. The most active frequencies are 18 to 19 mc. Little emission has been observed above 27 mc. The average power (for a strong pulse) is about 100 kw/cps and the total radiated energy (for a strong pulse) is about 10^{11} joules. Frequency drifts are observed on the order of a few mc/min for a storm. The sources exhibit strong directional characteristics which may not be due to the ionosphere of Jupiter. The sources of the radiation appear to be anchored to the solid surface of the planet.

Definition of terms. The photometric color magnitudes are magnitudes obtained through broad-band pass filters of effective wavelengths:

Color magnitude	*Effective wavelength*
U (ultraviolet)	0.353μ
B (blue)	0.448μ
V (visual)	0.554μ
R (red)	0.690μ
I (infrared)	0.820μ

The geometric albedo is the ratio of flux that is scattered by the planet at zero phase angle to that incident. The flux may have an effective wavelength defined by U, B, etc.

1 km-atm is an atmospheric thickness corresponding to a gas at standard conditions 1 km in depth.

$I(\mu)$ is the intensity from that part of the surface of the planet whose zenith is inclined at an angle $\theta = \cos^{-1}\mu$ to the line of sight to the observer.

b and c are coefficients in the expansion of $I(\mu)$ in powers of $(1 - \mu)$.

B. Secondary Power

1. Solar Concentrator

As was initially reported in *SPS 37-8*, JPL is acting as technical monitor of a NASA contract with Electro-Optical Systems, Inc. (EOS), on a research and development program directed to the investigation of techniques

for fabricating light-weight, efficient solar concentrators for space applications. Investigations have led to the fabrication of a number of mirrors which were evaluated both by JPL and EOS. The construction of a water-flow calorimeter which is used in the evaluation program at JPL was described in *SPS 37-9*. The results of efficiency measurements performed on the first 5-foot-diameter, nickel-electroformed solar concentrator delivered to JPL were reported in *SPS 37-10*. This concentrator was environmentally tested at JPL and the results reported in *SPS 37-11*. Two additional 5-foot-diameter mirrors are scheduled for delivery to JPL on or before November 1, 1961. One concentrator will be electroformed nickel and the other electroformed copper. The nickel mirror has been fabricated and is under test at EOS. Both concentrators will incorporate electroformed torus support structures around the periphery.

Copper electroforms of a hardness suitable for the task have been repetitively produced in small-scale test tanks at the Laboratory. The large 6-foot tank is being modified to duplicate conditions in the test tank. Copper electroforms, approaching the structural qualities of nickel, have been produced. The copper concentrator to be delivered by the end of the present contract is not expected to be representative of the best possible, since some plating problems have not been solved.

To circumvent the problem of uneven electrodeposition, the master or cathode is rotated through a contoured anode array. By balancing and optimizing the bath conditions, skins with a total variation of less than 0.001 inch have been obtained. This variation represents 10% of the total skin thickness, and a study is underway to determine whether structurally this can be tolerated. Small-scale tests have shown that by using these rotational techniques, thickness variations of less than 0.0002 inch for a 0.010-inch-thick plate can be obtained.

The main problems associated with this program were those resulting from the production of stress-free electroforms suitable for use as space-borne, high-efficiency solar concentrators. These problems are well known and solutions have been obtained.

One of the problems encountered has been the fabrication of masters of suitable geometry and adaptable to electroforming. So far the masters used were surplus mirrors used in searchlights. Some effort has been expended in a study of master fabrication. A 24-inch fiberglass-reinforced epoxy shell with a polyester surface layer has been fabricated. The techniques, equipment, and materials used are compatible with those that would be used in fabrication of a larger master (9½-ft diameter).

Reflectivity measuring devices are being calibrated and the production of small electroformed replicas is in process. This effort will serve as a basis for checking reflective coatings of various combinations of materials.

Test equipment for performing the modified Hartman spot test, photographic image evaluation, and calorimetric tests on the 60-inch mirrors have been completed. Tracking accuracies of less than ½ minute-of-arc have been achieved on the EOS tracking platform. Instrument and equipment calibration has also been completed, and final performance tests will be completed prior to delivery of the two mirrors.

C. Engineering Mechanics

1. Thermally Switched Fins as a Possible Temperature Control Device

A possible technique for controlling the temperature of a localized hot spot in a spacecraft is the extension of the available radiating area by the incorporation of a fin. If the heat flux into a component or unit is variable, the usefulness of the fin could be extended by the addition of a thermal switch resulting in an active control device. If such a device were to be used, passive control would be utilized to maintain the temperature of a component at the required operating temperature when the heat load is minimal by treating the enclosing surfaces in the vicinity of the hot spot. On the other hand, the fin would be designed for a maximum heat load. The switch would then route any excess heat above the minimum into the fin. Provided that the switch is responsive to small temperature changes, the temperature of a component could be maintained accurately. In considering any such device, the weight as a function of the degree of control is of prime importance.

In analyzing this device, it was assumed that the conductive resistance and also the weight of the switch is negligible. Assuming that no active device is involved, the relationship between the excursion in heat flux and a corresponding excursion in temperature is

$$\Delta q = \varepsilon\sigma A\left[(T_0 + \Delta T)^4 - T_0^4\right] = q_0\left[\left(1 + \frac{\Delta T}{T_0}\right)^4 - 1\right] \qquad (1)$$

where Δq is the variation in heat flux, ΔT is the corresponding excursion in temperature, q_0 is the minimum heat rate, and T_0 (absolute) is the resulting temperature at the minimum heat rate. Thus, the purpose of this device is the limitation or elimination of ΔT as a variation in Δq occurs.

Assuming that the temperature of the unit is to remain within the tolerance $T_0 + \Delta T_c$, then the heat to be dissipated from the fin is

$$\Delta q_c = \Delta q - q_0\left[\left(1 + \frac{\Delta T_c}{T_0}\right)^4 - 1\right] \tag{2}$$

where Δq_c is the excess heat to be dissipated by the fin in order to maintain the temperature of the unit within the permissible temperature excursion ΔT_c. Now, the heat that can be dissipated from a fin is

$$\Delta q_c = \eta L \varepsilon \sigma T^4 \tag{3}$$

where η is the fin efficiency and T is the fin root temperature. When Δq exceeds $q_0\,[(1 + \Delta T_c/T_0)^4 - 1]$, then the fin is activated and the fin root temperature becomes

$$T = T_0 + \Delta T_c \tag{4}$$

Since weight is the primary consideration, the optimum fin weight required to dissipate Δq_c is computed from

$$W_{opt} = \rho l_{opt} L_{opt} \tag{5}$$

where L_{opt} is the optimum fin length and l_{opt} is the optimum fin thickness. The optimization of the fin can be carried out by rewriting Equation 3 as $\eta L = \Delta q_c/\varepsilon\sigma T^4$ and by iteration determining the optimum fin efficiency from the curves in Reference 10. The fin efficiency is plotted as a function of the dimensionless parameter R where R is the ratio of the fin emittance to the fin conductance. Now, it can be shown that the fin weight is proportional to $1/\eta^3 R$. So, by selecting η and from the graph obtaining R, $1/\eta^3 R$ by iteration can be minimized. Using the optimum fin efficiency thus obtained, the optimum fin length can be computed from Equation 3 and using the optimum R and optimum fin length corresponding to the optimum η the fin thickness can be computed from R.

This procedure was carried out for a unit operating at 300°K when the heat is minimal. Figure 169 is a plot of the weight of fin required to dissipate a unit of excess heat as a function of the ratio of the variation in the heat rate to the minimum heat rate for various controlled temperature excursions. A coated aluminum fin having a surface emissivity of 0.9 was considered.

2. An Application of the Heat Pump in a Spacecraft

To ensure the reliable operation of a spacecraft it is necessary to provide a controlled temperature environment for its many subsystems. Usually, a favorable environment is produced by controlling the rate at which heat is exchanged between a subsystem and its external environment by controlling the thermal properties of the enclosing surface since the mechanism of exchange is generally radiation. However, when the rate at which heat enters or is generated within a subsystem exceeds the rate at which it can be dissipated from the enclosing surfaces, it is necessary to employ a somewhat more

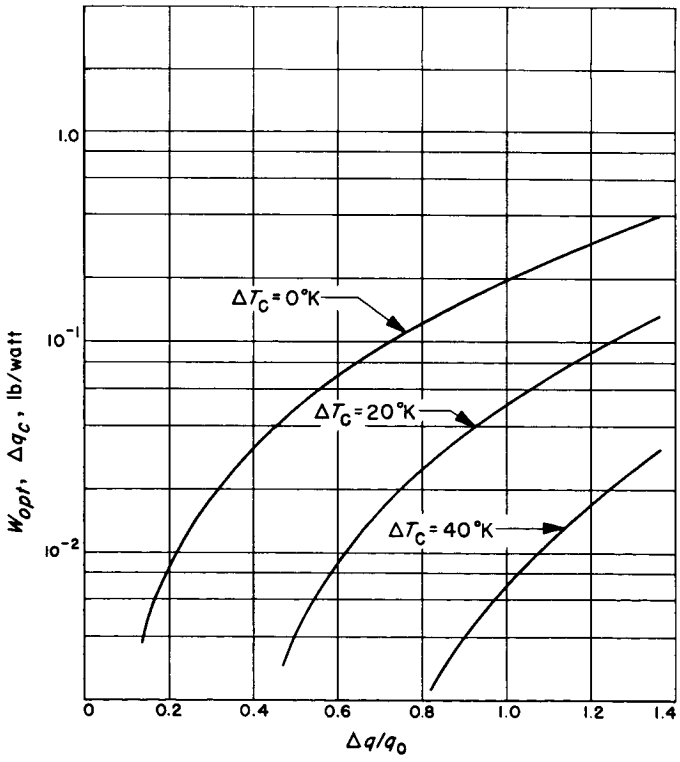

Figure 169. Weight of fin required to dissipate 1 watt for various excursions in temperature

sophisticated cooling technique. When the excess heat is large, it has been proposed that a radiator, coupled to the subsystem by a fluid loop, be used. However, analyses of radiators indicate that the weight would be large. As an alternative, it has been further proposed that a heat pump be added to increase the radiating temperature of the radiator and, thus, decrease the required radiator area needed for the disposal of the heat, resulting in a decrease in total weight. Advocates of this cooling scheme presuppose that the weight is dominated by the weight of the radiator concluding, therefore, that the heat pump weight would not appreciably influence the total weight. To determine, if, indeed, a weight savings could be realized, a cursory investigation was undertaken.

For a cooling system employing only a radiator, the weight is given by

$$W = \frac{Q}{\varepsilon\sigma T_R^4}\omega_R' \qquad (1)$$

where ω_R' is the specific weight of the radiator in terms of lb/ft^2, Q is the excess heat rate, and T_R is the temperature of the radiator. The temperature of the radiator and the temperature of the cooled subsystem are assumed to be the same.

For a system employing a heat pump, the total weight is the summation of the weight of the radiator required to dissipate the heat at an elevated temperature, the weight of the heat pump, and the weight of the power source for the heat pump. The total heat to be dissipated from the radiator is now the sum of the excess heat and the power supplied to the heat pump. The total weight of such a system is given by

$$W = Q\left[\frac{\omega_R'}{\varepsilon\sigma T_R^4}\left(\frac{\xi\eta}{\xi\eta+1}\right) + \frac{\omega_S}{\xi\eta} + \omega_P\right] \qquad (2)$$

where η is the Carnot coefficient of performance, ξ is that percentage of the Carnot coefficient of performance which is actually obtained, and ω_P and ω_S are, respectively, the specific weights of the heat pump and power supply in terms of lb/watt.

To determine if a weight savings is theoretically feasible, it is assumed that the heat pump operates at 100% of Carnot coefficient of performance ($\xi = 1.0$). Because no definitive data is available regarding the specific weight of the heat pump, its weight was ignored. Figure 170 is a plot of Equations 1 and 2 for various values of the Carnot coefficient of performance. Here, it was assumed that the specific weight of the radiator is 1.0 lb/ft^2 and that the specific weight of the power supply is either 0.10 lb/watt (shown by the dashed curve), or 0.001 lb/watt (shown by the solid curves). The straight line is for a system not incorporating a heat pump. From these curves, it is obvious that a weight savings can, at least, be theoretically realized, since the specific weight of the heat pump would have to be extremely large to nullify the difference between the curves over the entire range in which a savings occurs. From a cursory look at various refrigerants, a Carnot coefficient of performance as low as 0.5 is rather hypothetical due to the large pressure changes that the refrigerant would have to experience; therefore, this curve is dropped in Figure 171. However, it appears quite feasible to obtain Carnot coefficients of performance of 1.0 and greater.

Realizing that a system which operates at 100% of Carnot coefficient of performance is seldom obtained, Figure 171 was plotted for actual coefficient of performance of 25% ($\xi = 0.25$) of theoretical, which is probably a bit pessimistic for a reasonably sized heat pump. Here,

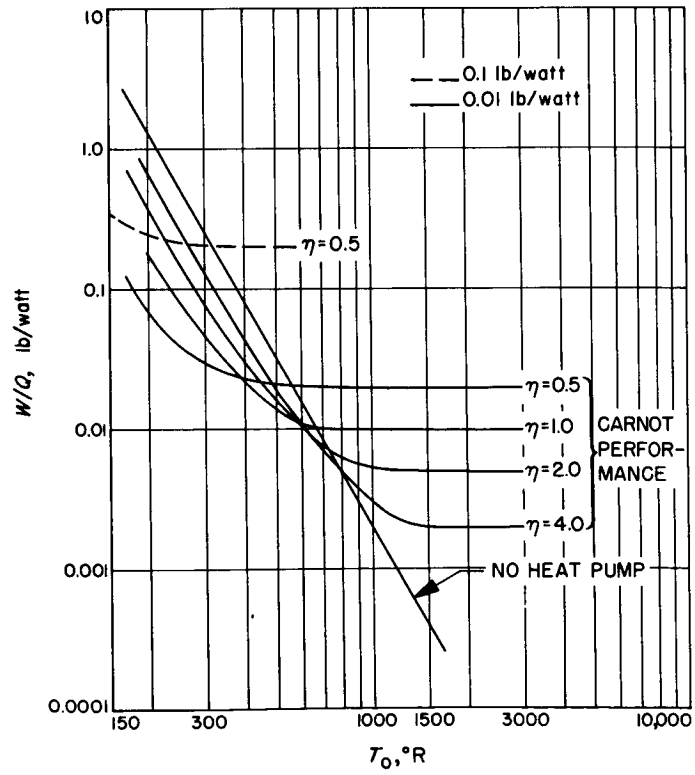

Figure 170. Comparison of weight of ideal heat pump for different coefficients of performance

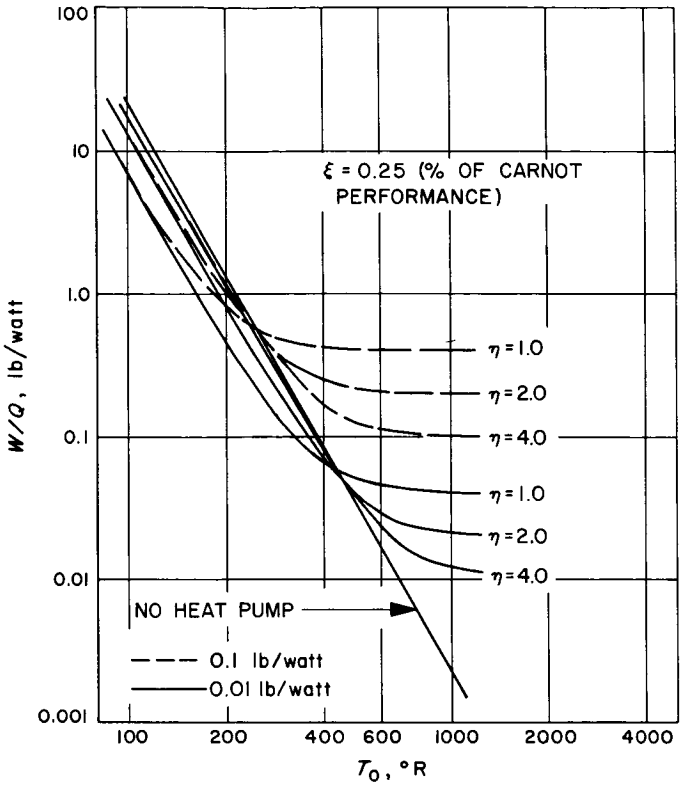

Figure 171. Comparison of weight of heat pump operating at 25% Carnot coefficient of performance

it can be seen that for large Carnot coefficients of performance, the weight saving is marginal.

Evidently, the curves for the heat pump system fall into three regions. In the first, the curves are horizontal and the weight of the system is dominated by the weight of the power supply. In the second, the slope of the curves are nearly equal to that of the radiator alone and weight is dominated by the weight of the radiator. Finally, there is the transition region which is probably dependent upon the specific weight of the heat pump.

The additional radiator weight needed to dissipate the power supplied to the heat pump is not predominant in influencing the cross-over point; rather, the weight of the power supply for the heat pump is the overriding influence.

3. *Peltier Cooling*

The preliminary investigation of Peltier cooling reported in *SPS 37-11* has been continued. This study covers the benefits to be obtained by staging or cascading thermocouples and the gain expected by optimizing the thermocouples for maximum heat absorption.

The results obtained with staged thermocouples are shown in Figure 172, where T_c is the cold junction temperature and T_h is the hot junction temperature, from which it is immediately obvious that this technique is only beneficial at the low temperature end of the range of T_c, and even there, that the gain is relatively small; at the high temperature values of T_c, the weight penalty is considerably greater for the staged thermocouples than for a single thermocouple working through the larger temperature differential. This is due to the fact that the thermocouples in any given stage must handle not only the heat absorbed by the previous stage, but also the total power input to that stage, leading to a compounding of the inefficiencies and a larger heat rejection fin system.

The maximum heat absorption which can be obtained for a given thermocouple when the couple is optimized on this as a criterion does not appear to have been inves-

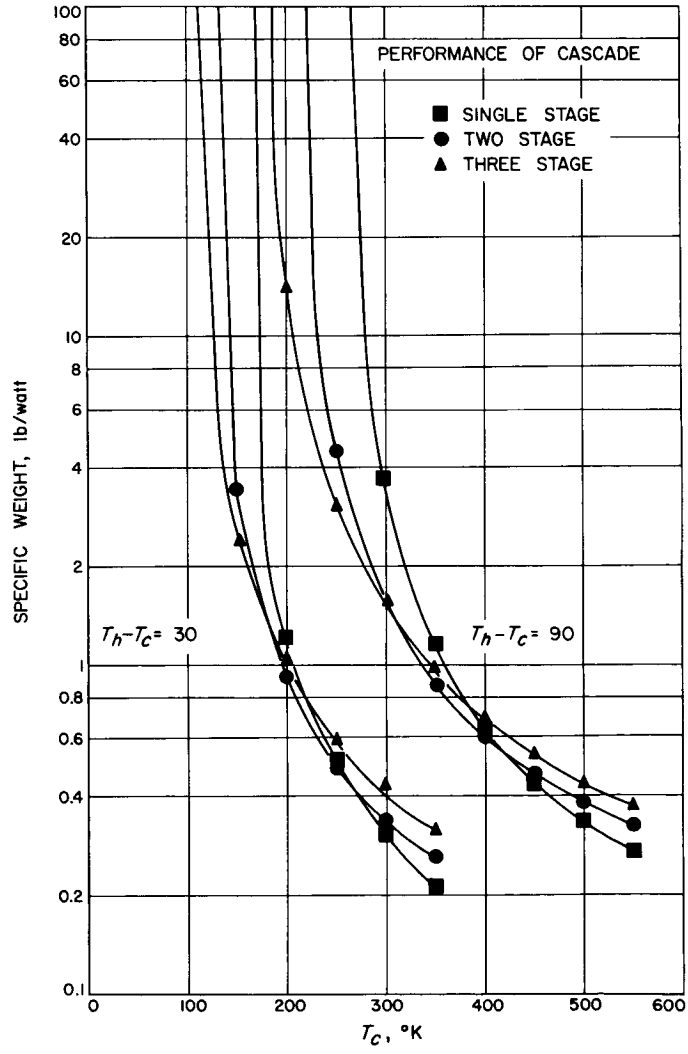

Figure 172. Performance of cascade

tigated thoroughly, possibly due to the fact that the optimum configuration is itself temperature dependent. The gain to be expected, however, is sufficient to warrant consideration for space applications. The maximum heat that can be absorbed by a given thermocouple $(Q_0)_{max}$ is given by a modification of the Equations in Reference 11,

$$(Q_0)_{max} = \frac{S_n}{L}\left(k_p + \frac{k_n}{m}\right)\left[\frac{Z_{eff}}{2}T_c^2 - (T_h - T_c)\right] \quad (1)$$

where: S = cross-sectional area of a semiconductor element, cm²; L = length of p-type and n-type elements, cm; k = specific thermal conductivity of a semiconductor element, watts/cm − °K; subscripts p and n refer to p-type and n-type semiconductors; m = ratio of cross-sectional areas of p-type and n-type elements; and Z_{eff} is the effective figure of merit, $(°K)^{-1}$ given by

$$Z_{eff} = \frac{(\alpha_p - \alpha_n)^2}{(mk_p + k_n)\left(\frac{\rho_n}{m} + \rho_n\right)}$$

If now $(Q_0)_{max}$ is maximized by differentiation with respect to m and setting the result equal to zero, one can show that the value for m which will give the optimized heat absorption per thermocouple, m_M, is given by

$$m_M = \frac{S_p}{S_n} = \frac{2k_n\rho_p\rho_n(T_h - T_c) + \rho_p(\alpha_p - \alpha_n)\sqrt{2k_n\rho_n}\,(T_c)\sqrt{T_h - T_c}}{(\alpha_p - \alpha_n)^2\rho_n T_c^2 - 2k_n\rho_n^2(T_h - T_c)}$$

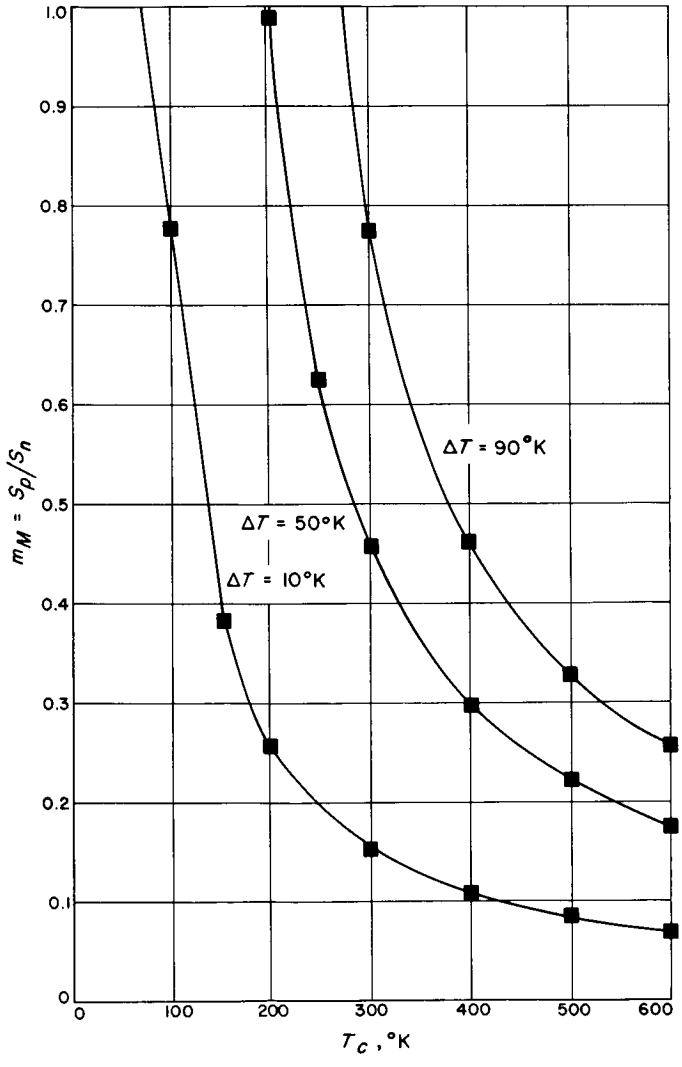

Figure 173. Variation of optimum thermocouple geometry with cold junction temperature

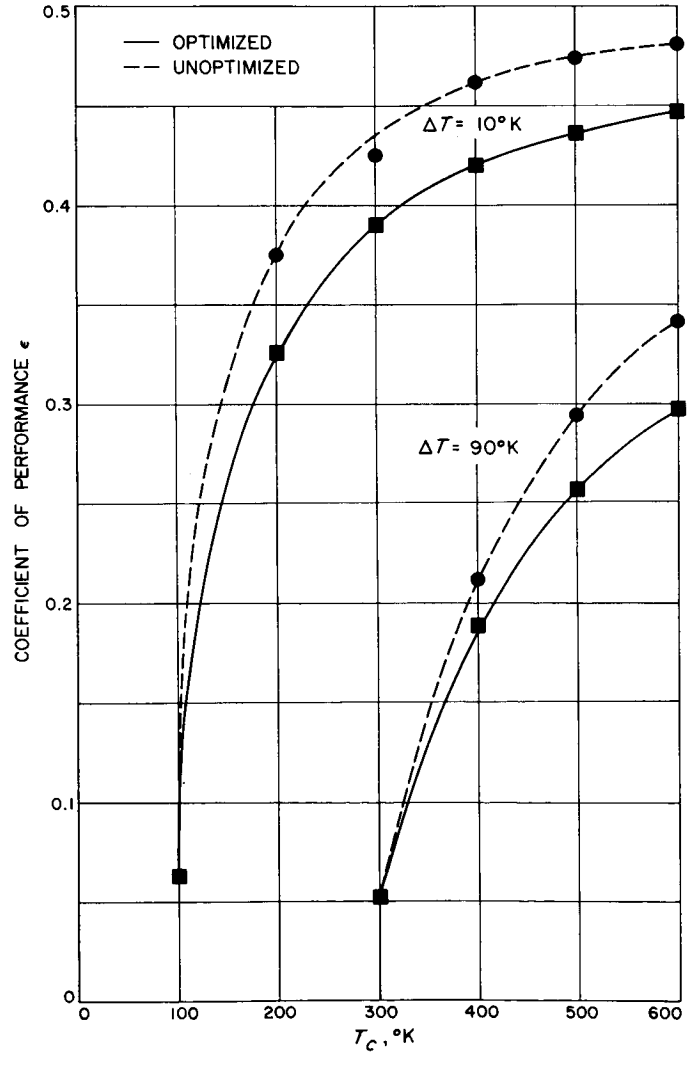

Figure 174. Variation of coefficient of performance with cold junction

where: ρ = electrical resistivity of a semiconductor element ohm/cm; α = Seebeck coefficient of a semiconductor element, μv/°K. This function is shown in Figure 173 for three values of $T_h - T_c = \Delta T$, and it will be seen that the optimum geometry of the thermocouple is extremely sensitive both to the temperature differential across the thermocouple and to the cold junction temperature.

The effect of this optimum geometry is shown in Figures 174 and 175 both for $(Q_0)_{max}$ and the coefficient of performance ξ, compared with the results obtained by using a thermocouple with legs of equal cross-sectional areas. The effect of optimum geometry is slight at lowest working temperatures for both values of temperature differential, which is to be expected since the value of m_M is approaching unity under these circumstances. At higher temperatures, the effect of optimum geometry is to give an increase in the heat absorbed per thermocouple on the order of 100% with small temperature differentials (10°K), and on the order of 50% with large temperature differentials (90°K). The coefficient of performance of the optimized couple working on the maximum heat pumping criterion is lower than that for the unoptimized couple, but this reduction is much smaller than the gain in heat pumping capacity; it is negligible at low temperatures and of the order of 8% where the temperature differential is 10°K and of the order of 25% where the temperature differential is 90°K for cold junction temperatures of 600°K.

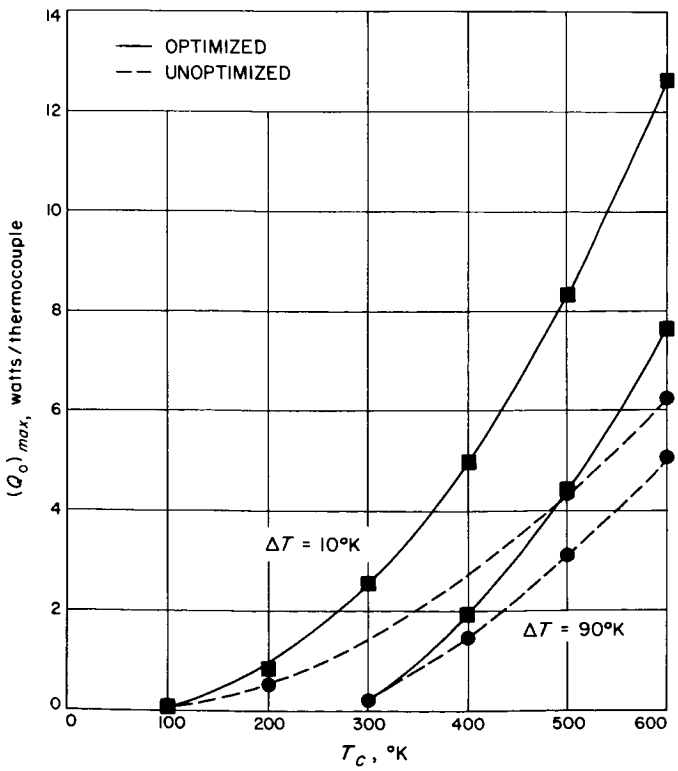

Figure 175. Variation of heat absorbed per thermocouple with cold junction temperature

D. Propulsion

1. Amine Nitrate Monopropellants

Analytical and experimental investigations of Cavea-B, a promising high-energy liquid monopropellant, have continued during this report period. Cavea-B is the designation of a monopropellant consisting of a nitric acid solution of the salt 1,2,4-trimethyl-1, 4-diazabicyclo (2,2,2) octane dinitrate. At acid-to-salt ratios of 1.50 to 1.80 this propellant exhibits high performance, favorable physical properties, and acceptable stability. These characteristics make utilization of this propellant attractive for certain low-velocity-increment space applications (Ref 12). Previous JPL investigations concerning this project have been reported in the classified volumes of *Research Summaries 36-2* through *-7*, and *Space Programs Summaries 37-9* through *-11*.

Recent experimental investigations have been concerned with rocket engine firings directed toward obtaining data defining the interrelationship among the fundamental rocket motor parameters: chamber pressure, combustion volume, and injector pressure drop. Conditions where good theoretical performance can be obtained while utilizing conventional engine hardware have been partially defined. For chamber pressures of 300 psia or less, the ability of the propellant to undergo sustained monopropellant combustion has been found to be markedly influenced by the degree of atomization of the propellant and also by the combustion chamber gas–side wall temperature. For 100-pound thrust operation in uncooled steel chambers it has been necessary to provide some form of combustion chamber insulation in order to obtain sustained monopropellant operation with a reasonable chamber volume ($L^* = 100$ to 200 inches). Insufficient insulation and/or insufficient atomization result in an unstable reaction zone which is evidenced by low-frequency chamber pressure oscillations as well as poor performance.

Space Programs Summary 37-10 contained the description and the results of a performance survey of an injector composed of multiple like-on-like doublet elements. Pre-

liminary results obtained with an alternate injector design composed of four atomizing spray nozzles were presented in *SPS 37-11*. The performance evaluation of the spray injector was completed during this report period and results to date for both injector types are presented in Figure 176. It is evident that, with proper insulation and atomization to afford stable combustion, essentially 98% of theoretical, equilibrium flow combustion efficiency can be obtained with either injector type under conditions of 300 psia chamber pressure, characteristic chamber lengths (L^*) of approximately 100 inches and at injector pressure drops ranging from 140 to 350 psid. Rapid performance degradation occurred in both cases at L^* below 100 inches.

In obtaining satisfactory performance of Cavea-B two distinct combustion aspects must be investigated. First, sustained combustion must be obtained, i.e., no severe reaction zone fluctuations or no incipient flooding conditions. Secondly, once sustained combustion is obtained, it is then possible to concentrate upon the optimization of conditions in order to obtain a high percentage of theoretical combustion efficiency. The ability to obtain sustained combustion is dependent upon both atomization and insulation as previously mentioned. Concurrently, with the injector performance survey shown in Figure 176, it was possible to investigate the conditions leading to unstable and/or non-sustaining combustion by varying three items: (1) chamber characteristic length, (2) chamber wall insulation properties, and (3) injector

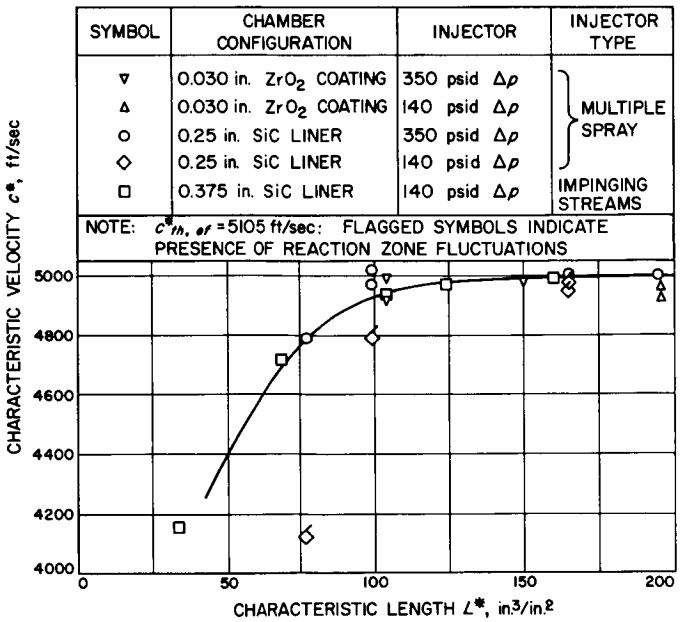

Figure 176. Experimental performance of Cavea-B monopropellant

atomization. For the specific test conditions utilized, sustained combustion was obtained with a 0.030-inch zirconium oxide coated chamber of 104-inch (L^*) when used with the multiple spray injector with a high (350 psid) injector pressure drop. Reduction of the chamber volume to an L^* of 55 inches, with other conditions remaining constant, resulted in non-sustaining monopropellant combustion. A similar type combustion chamber with an L^* of 196 inches was required in order to obtain sustained combustion with a low pressure drop (140 psid) multiple spray injector. This sustained combustion was accompanied with the reaction zone fluctuation condition, however. Thus the thin ZrO_2 coating does not appear to furnish sufficient reaction zone insulation to provide sustained combustion over a wide range of conditions.

Improved results were obtained when ¼ to ⅜-inch-thick chamber liners of silicon carbide, a high temperature ceramic, were utilized. Smooth, sustained combustion was evident with a high Δp multiple spray injector configuration in chambers with L^* values of from 77 to 165 inches, although an appreciable performance loss occurred at the lower chamber volumes. The low Δp multiple spray injector, when tested with the refractory-lined chamber having L^* values of 77 to 165 inches, produced sustained combustion, but the combustion was not stable and varying degrees of reaction zone fluctuation occurred. For example, at an L^* of 77 inches, the combustion produced chamber pressure fluctuations of 60 psi peak-to-peak random noise interspersed with 100 psi peak-to-peak sinusoidal at 90 cps.

As reported in *SPS 37-10*, Vol II, the doublet type injector produced stable combustion in similar ceramic-lined chambers at L^* values as low as 34 inches with an injector pressure drop of 140 psid. This injector is composed of twelve doublet pairs which apparently give better chamber cross-sectional mass distribution and perhaps better atomization than the multiple spray injector since the flow rate per element is only 0.037 lb/sec as compared to a flow rate per element of 0.11 lb/sec for the 4-spray configuration. Since the spray-injection technique is desirable, especially for scaling purposes and economy of manufacture, a modified configuration is now being fabricated to provide atomization through eight individual spray nozzles instead of four. Evaluation of this design should provide sufficient information to make a recommendation on which injection technique is more satisfactory with this propellant.

2. Center of Gravity Analysis

An evaluation of the change in the center of gravity (c.g.) of the complete ALPS propulsion system as a func-

tion of burning time has been conducted. The work was done using the results of the propellant c.g. study presented in *SPS 37-11*. Because the mass and c.g. location of the spacecraft are unknown, the analysis is limited to the propulsion system. The spacecraft will modify the results obtained in this study.

The original ALPS system configuration (Fig 177a) has an estimated dry mass of 349 pounds, burnout mass of 397 pounds, and a loaded mass of 5497 pounds, using the propellant combination nitrogen tetroxide and hydrazine at a mixture ratio (oxidizer to fuel) of 1.2. The main propellants are contained side-by-side in the single large tank with the nitrogen tetroxide on the right, the hydrazine on the left. Hydrazine required for the pressurization of the main tank is carried in the small spherical tank located above and to the left of the thrust chamber. During the analysis several modifications of the basic system were considered. Two major types of modifications are discussed here. The first modification (Fig 177b) was to move the pressurant tank to the right side of the thrust chamber. In this case the angle δ between the thrust axis (coincident with the centerline of the main tank) and a line connecting the c.g. of the system and the center of the top face of the thrust chamber (effective gimbal point) remains almost constant during operation. In the second modification (Fig 177c) the pressurant tank was again moved to the right of the thrust chamber and the main propellant tank was shifted laterally to the left of the thrust axis about two inches. In this arrangement the angle δ is equal to zero during a major portion of the firing time, i.e., the c.g. of the system falls on the thrust axis.

The results of this work are shown in Figure 178 plotted as the angle δ versus the burning time. The angle is equal in magnitude to the gimbal angle but opposite in sign. The nominal burning time of the system is 250 seconds. With a 2% reserve for holdup and trapped propellants the total possible burning time (until exhaustion of the main propellants) is 255 seconds. At exhaustion of the main propellants some of the pressurant remains in the small tank. This reserve is required to compensate for variations in the ambient temperature of the system and for a decay in the tank pressure during the times the system is not operating. These variations were not considered in the computations. Therefore, a separate calculation of the angle was made for complete exhaustion of the pressurant and plotted at 291 seconds which would be the nominal burning time of the pressurant under ideal conditions. The difference in the angle for this point compared to the angle at 255 seconds demonstrates the latitude in the burnout c.g. location. Because of the large mass of propellant compared to the mass of the pressurant, perturbations in the flowrate of the pressurant has little effect on the angle during the first 200 seconds of operation.

As can be seen in Figure 178 that the angle of the c.g. in the original ALPS system configuration varies from

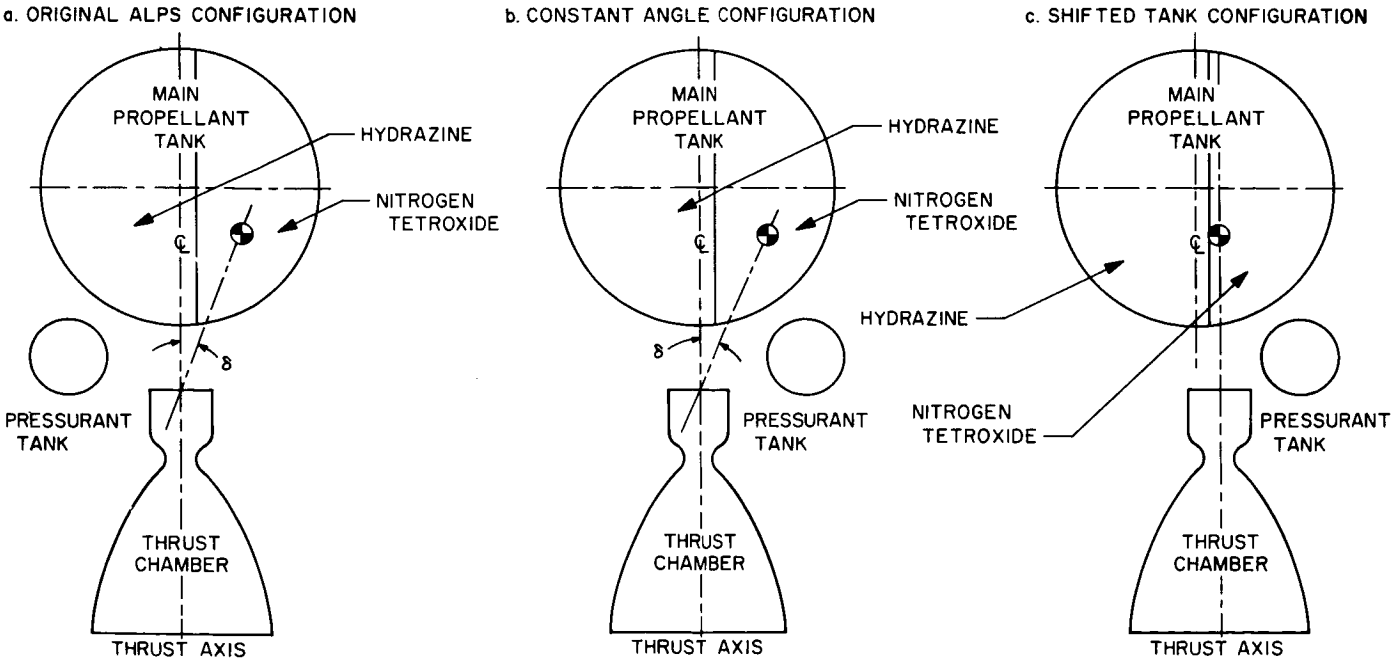

Figure 177. ALPS configurations

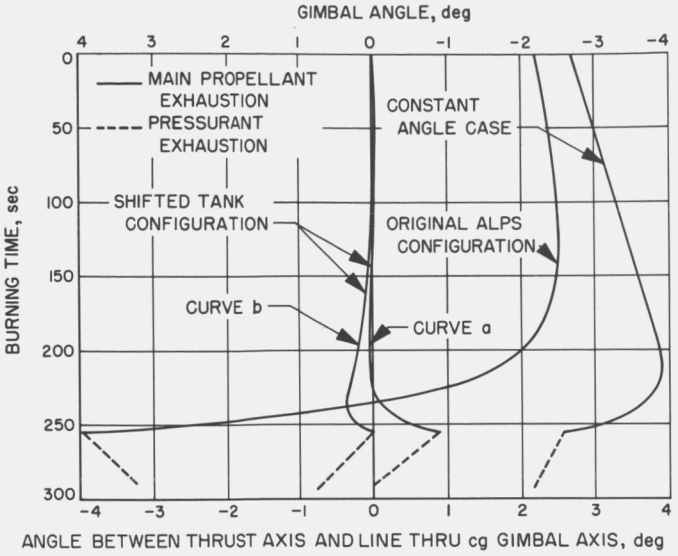

Figure 178. Variation of the angle to the center-of-gravity of the ALPS system

2.5 to −4.0 degrees, i.e., the thrust chamber operation to to swivel from −2.5 to 4.0 degrees during operation to eliminate turning moments. The effect of the lateral change in the c.g. of the thrust chamber, if it were to be gimballed, was not included in the computations, but it has been determined that correcting for chamber gimballing would reduce the angle by about 0.05 degree during the first 200 seconds and by about 0.6 degree at burnout. The angle to the c.g. in the *constant angle* case varies between 2 and 4 degrees. It was assumed that the chamber was fixed at a −3-degree gimbal angle for the calculations. Two possibilities for the shifted propellant tank are shown, zero angle at burnout of the main propellants (Curve b) and zero angle at exhaustion of the pressurant (Curve a). In these two cases the maximum angle to the c.g. is less than 1 degree.

From this data it would seem that the shifted tank configuration (Fig 177c) would be the best arrangement for minimum c.g. excursions. The addition of a spacecraft mass directly in line with the thrust axis would probably reduce the thrust chamber gimbal angle to less than 0.25 degree for elimination of turning moments.

3. *Monopropellant Combustion Devices*

A 200-pound thrust monopropellant hydrazine engine has been designed and fabricated to investigate the validity of the formulas used in scaling up this design from proven designs of lower thrust levels. The engine also has possible application for use in mid-course propulsion systems on future planetary spacecraft. The engine contains a quantity of catalyst to accelerate the hydrazine decomposition. A quantity of oxidizer (nitrogen tetroxide) is injected into the engine on start for initiation of the hydrazine decomposition. A hypergolic reaction ensues for approximately 1 second followed by continuous catalytic monopropellant decomposition of the hydrazine. A heavyweight version of the engine is shown in Figure 179 prior to test. Hydrazine is supplied to the engine through four spray nozzles. The oxidizer is injected into the engine through a single spray nozzle located at the center of the injector.

To date, a total of nine tests have been made with the engine. Successful starts followed by continuous monopropellant decomposition have been obtained in all tests. Start and shutoff transients as well as steady-state running of the engine have been very smooth. Chamber pressure variations during steady-state firing have been approximately ±0.25 psi. A total of 300 seconds of testing have been accumulated on the engine during the nine tests, with an average characteristic velocity of 4220 ft/sec being realized. Future tests will be aimed at increasing the characteristic velocity. This will be accomplished by

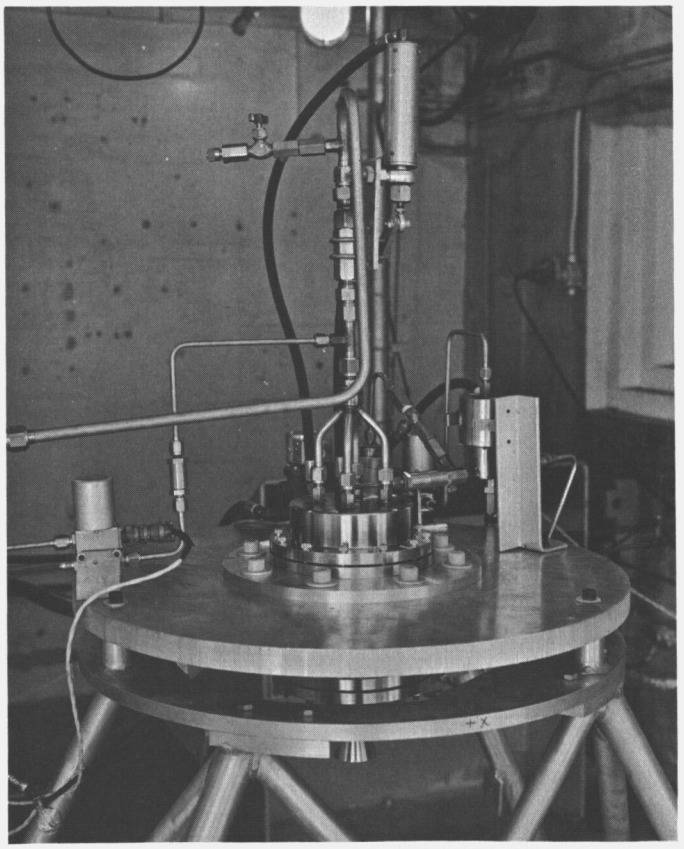

Figure 179. Test setup for monopropellant hydrazine engine

reducing the chamber length of the engine, thereby decreasing the amount of ammonia dissociation in the gas products and giving higher values of characteristic velocity.

4. Energy Conversion

The energy conversion system of an electric-powered spacecraft is defined as the equipment required to deliver electric power to the thrust motor from heat developed by a nuclear energy source. The nuclear source heats liquid metal. It is this heat energy in the liquid metal which is converted to electric energy of the required voltage (6000 volts dc for a cesium motor).

Possible methods of conversion are thermionic, thermodynamic, thermoelectric, and magnetohydrodynamic (MHD). Work is proceeding on thermionic, thermoelectric and MHD both at JPL and at other facilities, but it is anticipated that the thermodynamic system offers the earliest realization for flight application.

The various components of a thermodynamic conversion system are boiler, turbine, condenser, radiator, generator, and power conditioning. These components are being considered as separate elements which fit together into an operating system which must function without deviation or failure for periods of 10,000 to 20,000 hours after startup in orbit. Features of the vapor generation and heat rejection circuitry are shown in Figures 180 and 181.

Anticipated motor input power requirements for a Jupiter capture mission have been stated as 1.0 megawatt electrical. Considering internal pumping requirements, efficiencies, and internal power usages, the shaft power from the turbine will probably be 1.2 Mw.

The design parameters will largely determine the configuration of the energy conversion system and the selection of the working fluids. These parameters are turbine inlet temperature, turbine inlet pressure, radiator temperature, weight, size, reliability, power level. For the purpose of utilizing state-of-the-art materials 2300°R turbine inlet temperature and 150 psia pressure were selected. Previously published articles have shown that the radiator temperature should not in general exceed 75% of turbine inlet temperature, say 1725°R. The goal for specific weight is 8 to 10 lb/kwe. For 1.0 Mwe this

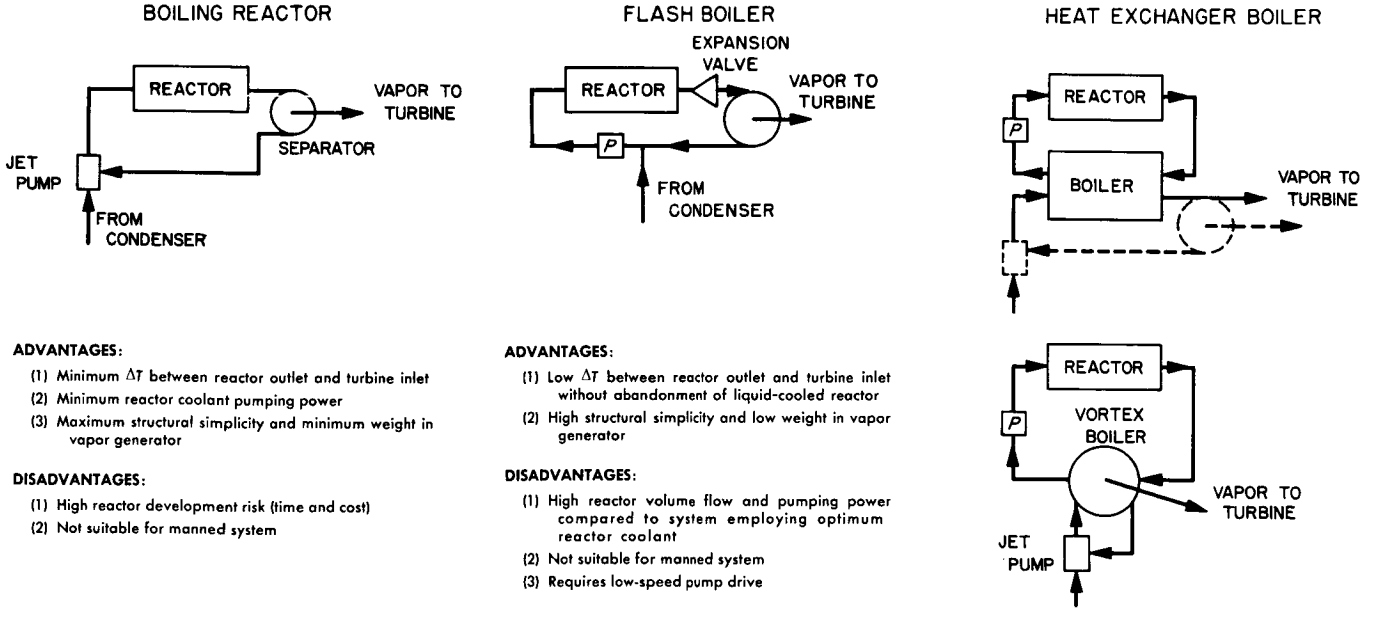

Figure 180. Vapor generator circuits

would be 8000 to 10,000 pounds of shielded power plant. Size is of importance from a launching standpoint. The dimensions considered have been 44 to 48 inches in diameter and 108 to 120 inches long. Reliability rates high on the scale of importance and should overrule all other requirements because to accomplish 10,000 to 20,000 hours of unattended operation is an extremely difficult goal.

Properties of five alkali metals were reviewed as potentially suitable working fluids. Table 35 shows a comparison of the properties of these fluids and pertinent remarks about each.

Sodium and potassium have been studied as a working fluid by other NASA centers and private contractors. Rubidium has been proposed as a working fluid for lower power level conversion systems but no extensive design effort has been expended.

Because of the apparent advantages of cesium as a working fluid it was selected for use in a research turbine. Cesium must also be carried aboard a spacecraft in large quantities when cesium ion motors are used. For this reason, the cesium price disadvantage ($300/lb) is not as important as it might be otherwise. Even if it were important the advantages of reduced overall weight of the turbine system, pumps, and tankage would compensate for the relative cost differential. Estimates of the value of each pound of weight saved vary from 5000 to $10,000.

A study of this type and size of turbines indicate that the Parsons or reaction turbine has been used in central station electric plants for many years. However, the DeLaval or impulse turbine has an equally long history, but is usually used for special applications where particular requirements are more important than the high-cycle efficiency attainable with the reaction type. In particular, the auxiliary power unit (APU) turbines for missile and aircraft have most often been the impulse type. The constant pressure across the blading avoids the tip loss of reaction turbines. Likewise, the high pressure drop per impulse stage reduces the wheels to one or two per turbine.

Reaction turbines for electric propulsion are being studied by contractors reporting to other NASA centers. To avoid duplication of effort, a design of an impulse research turbine was prepared. Because the design of the turbogenerator indicated that either the turbine or the generator must be overhung from the bearings, it appeared desirable to place the heavier generator between the bearings and overhang the turbine. This design provides for study of characteristics at two inlet pressures corresponding to two different stages. Change of inlet pressure will be accomplished by replacing wheels and nozzles (but still using same housing, shaft and bearings).

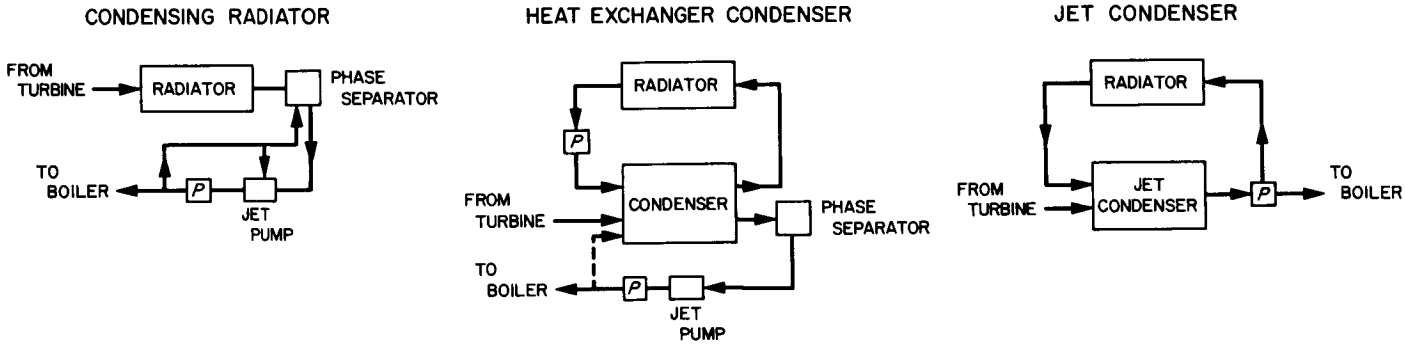

ADVANTAGES:

(1) Maximum simplicity
(2) Minimum radiator area
(3) Minimum pumping power
(4) Minimum system weight

DISADVANTAGES:

(1) Lack of design control over zero-g operation
(2) Inability to perform realistic development tests
(3) Inflexibility with respect to variation of radiator configuration

ADVANTAGES:

(1) Good design control of heat rejection system
(2) Permits use of optimum turbine and radiator fluids
(3) Allows turbine governing by use of condenser coolant bypass
(4) Permits radiator subdivision independent of turbogenerator subdivision

DISADVANTAGES:

(1) Increased complexity
(2) Increased weight
(3) Increased pumping power
(4) Increased meteorite vulnerability of liquid-filled tubes

ADVANTAGES:

(1) Good design control—high condenser structural simplicity and low weight
(2) Minimization of condenser heat transfer ΔT
(3) Allows turbine governing by use of condenser jet bypass

DISADVANTAGES:

(1) Requires low-speed pump drive to avoid cavitation in high flow pump
(2) Eliminates possibility of optimum fluids in both turbine and radiator

Figure 181. Waste heat rejection circuits

Table 35. Working fluids

Function	Phase	Desired properties	Na	K	Rb	Cs	NaK	Li	Remarks
Reactor coolant	Liquid	High volumetric heat capacity, Btu/ft³ °F	15.0	8.0	8.3	6.9	8.8	30.0	**Reactor Coolant** Lithium provides the smallest and lightest reactor, and requires the smallest pumping power. When contained in a columbium loop the corrosion and embrittlement are not serious problems. Sodium is the second best. The most important criteria are high volumetric heat capacity and low density.
		Low density, lb/ft³	50	40	92	115	42	30	
		High thermal conductivity, Btu/hr-ft °F	34	20	18	11	15	20	
		Low viscosity, lb/ft-hr	0.4	0.35	0.32	0.34	0.37	0.35	
		Low vapor pressure, psia	55	105	155	160	100	1.0	
		Low neutron capture cross section, barns	0.53	2.0	0.7	31.0	1.8	71.0	
Turbine working fluid	Vapor	Low specific volume at turbine discharge, ft³/lb	0.11	0.04	0.026	0.019			**Turbine Vapor Working Fluid** Cesium provides a turbine with few stages at relative high speed. This in turn reduces generator weight. Because of the large T in the turbine nozzle, cesium allows wheel and blade temperatures in a lower range than potassium or sodium at comparable turbine inlet temperature levels. At inlet temperature of 2000°F and above, the use of cesium as a working fluid allows high wheel speeds and the highest efficiencies.
		Low kinematic viscosity, stokes	5.0	0.34	0.45	0.38			
		Low heat of vaporization, Btu/lb	1800	900	380	260			
		High sonic velocity, ft/sec	2400	1930	1300	1030			
Boiler and condenser vapor	Vapor	Vapor pressure not too low at condensing temperature, psia	3–2	10–8	18–15	22–16			**Heat Transfer Equipment** Working fluid boilers and condensers are smaller in size and lower in weight when cesium is used. The highest exit vapor pressure of cesium provides suitable pump inlet pressurization to avoid cavitation.
Radiator and condenser coolant	Liquid	Low freezing temperature, °F	208	147	102	83	14	357	**Radiator and Condenser Coolant** Lithium provides minimum pumping power and radiator weight, but it has poor compatibility with stainless steel. Sodium is an excellent fluid also. However, the low freezing temperature of NaK and cesium are advantageous. If a spray condenser is used an over-all comparison must be made of turbogenerator and radiator weight including fluid inventory.

Other studies of a 1.2 Mwe turboelectric power plant have assumed a single turbine mounted with a single generator. A study of specific weight of turbine and generator indicates that the turbines have a minimum specific weight in the region of 250 to 300 kw each, and the generators minimize specific weight at 500 to 600 kw each. Therefore, a design was prepared showing two turbogenerator sets of 600 kilowatts mounted with counter-rotating shafts. Each turbogenerator has a generator mounted between two bearings with an overhung turbine on each end. Each turbine exhausts directly in a condenser. This compact arrangement measures 44 inches in diameter by 108 inches long (Fig 182).

It seemed desirable to investigate refractory metals for the entire turbine to reduce corrosion or contamination of the working fluid at the high temperatures involved. Based on price and availability, molybdenum 0.5% titanium alloy was selected for all parts of the turbine except the shaft. To provide a tough, strong and compatible shaft, Haynes-25 alloy was used.

Figure 183 shows a cross section of the turbine with partial spherical bearings lubricated by cesium vapor. The construction is arranged so that journal bearings can replace the spherical type, and so that liquid cesium can also be used as a lubricant. With such a research tool, the all-important lubrication problem can be explored along with the turbine working fluid problems.

The design incorporates several advanced features that must be proved during the construction and operation of the turbine. One is the use of Conoseal clamps instead of bolted flanges. The other is the use of electron-beam welding to join the various pieces of the case together. Still another is the use of the Elox process to fabricate the turbine wheel from a single disc so that the blades are integral with the hub. This same process is used to fabricate the nozzle section.

The Conoseal type of clamp flange incorporates a metal gasket which is deformed when the clamp is tightened.

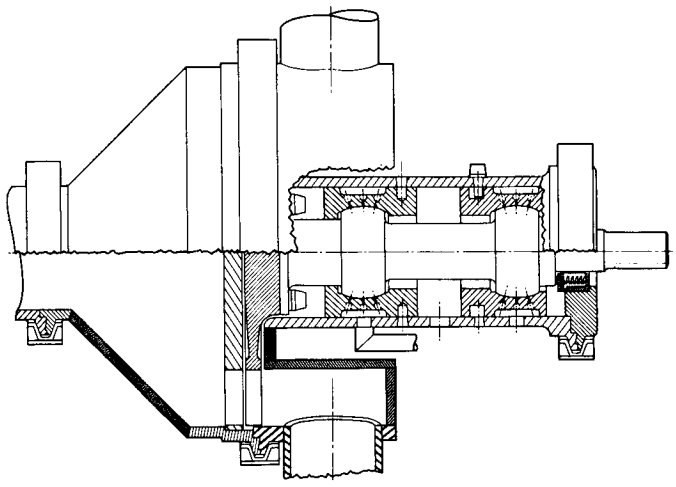

Figure 182. Test turbine assembly, 1-megawatt impulse turbine

When the clamp is loosened for inspection of the turbine wheel, the gasket is removed and replaced with a new one. In order to avoid looseness due to differential expansion, the Conoseal clamp is fabricated from the same material as the turbine case.

The electron-beam welding process has been thoroughly checked out by visits to the builders of the equipment and by observations at customer installations. Not only can refractory metals be joined to themselves, but welds can be made between dissimilar metals which have nearly the same melting temperatures. The process consists of focusing a stream of electrons with a suitably high voltage and intensity upon the metal which is retained on fixtures inside a vacuum chamber. The fixtures are motorized and controlled from an external console. The beam is adjusted for the work and penetration desired. Observation of the work during welding is through a glass window in the vacuum chamber.

The Elox process is otherwise described as an electrical disintegration procedure. The tool which has the shape of the desired turbine blade is pushed into the edge of the disc. The metal directly ahead of the tool is removed by the electrical arc. This process is useful on refractory metals or on other metals that are difficult to machine to intricate shapes.

The turbine, when fabricated, will be set up at the laboratory for exhaustive testing. The building selected for testing of the turbine was originally used for liquid rocket testing and, therefore, has all necessary protective equipment built in, such as an isolated room with thick concrete walls and armor plate partitions. Observations can be made from the control room by mirrors and by a closed circuit television camera and monitor. The turbine will be mounted to drive directly a centrifugal air compressor which will act as a dynamometer. A strain gage load cell mounted on an arm extending from the compressor will read the torque. Other instrumentation will record speed, temperature, pressures and stress in the turbine and working fluid loop.

The working fluid loop will consist of a boiler, an electromagnetic pump and a condenser. The boiler will be an electrically-heated pot-type and the condenser will be either air- or water-cooled. The loop will be fabricated of a metal which is compatible with the turbine construc-

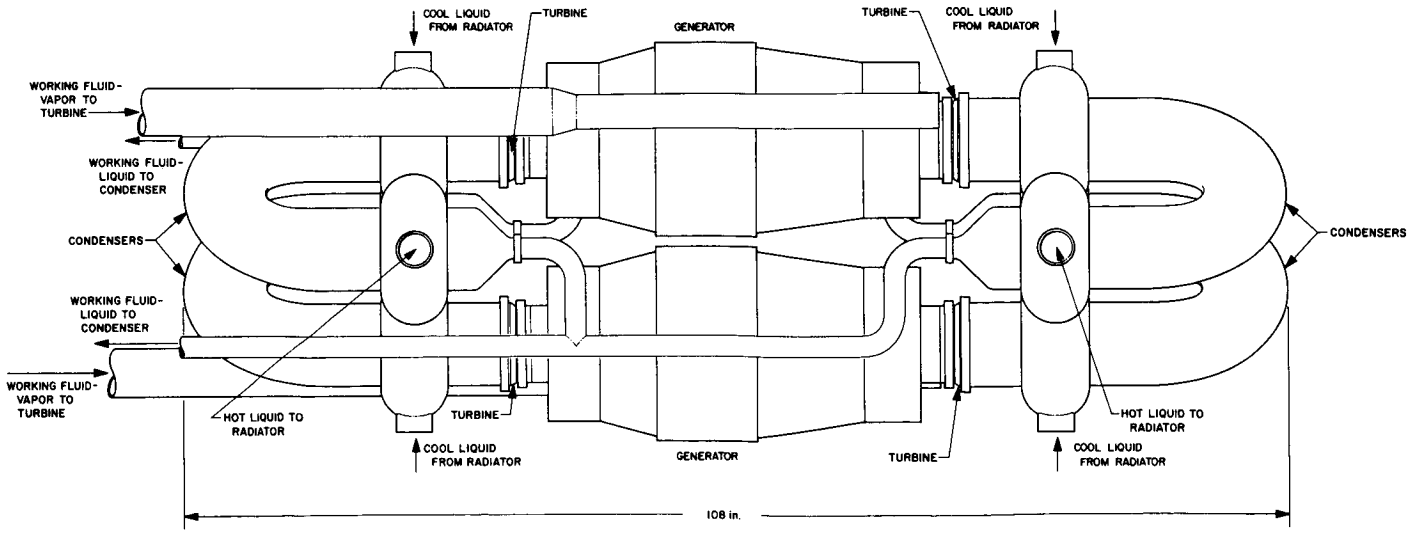

Figure 183. Turboelectric powerplant for a 1.2-megawatt conversion system

tion, possibly Haynes 25 or Moly 0.5% Ti. The electromagnetic pump will act like a feedwater pump, circulating the liquid from the condenser into the boiler. The loop will be installed adjacent to the turbine in the testing area but separated from it by a steel plate.

The desired tests to be carried out with the turbine can be considered in three categories. First, the characteristics of a cesium impulse turbine will be explored to determine optimum speed, pressures, temperatures and efficiencies. Second, the bearing development tests will provide information about vapor bearings at high-speeds and temperature. Alternatively, liquid bearings will replace vapor bearings to determine suitability and reliability. Third, operation of the liquid metal loop will determine liquid cesium compatibility with the refractory metals.

During a test, temperature pressures and other suitable parameters will be recorded on the central recording system through the twenty-two pairs of lines available. Readout will be both digital and analog to provide for quick look and permanent records.

References

1. Latvala, E. K., "*Spreading of Rocket Exhaust Jets at High Altitudes,*" Arnold Engineering Development Center, Tullahoma, Tenn. TR 59-11, June 1959.

2. Schaff, S. A., and Chambre, P. L., "Flow of Rarefied Gases," Sec H., Vol 3, *Fundamentals of Gas Dynamics, High Speed Aerodynamics and Jet Propulsion,* Princeton University, Princeton, N. J., 1958.

3. Altshuler, S., Moe, M. M., and Molmud, P., "*The Electromagnetics of the Rocket Exhaust,*" Space Technology Laboratories, Inc., Redondo Beach, Calif., Report TR-0165-00397, Chapter 5, June 1958.

4. Barton, M. V., "*The Dynamic Response of a Finite, Rigid Mass Concentrically Carried by a Viscoelastic Disk,*" Space Technology Laboratories, Inc., Redondo Beach, Calif. TR-60-0000-19331, September 1960.

5. Epstein, B. and Sabel, M., "Sequential Life Tests in the Exponential Case," *The Annals of Mathematical Statistics,* Vol 26, No. 1, March 1955.

6. Brueschke, E. E., "*Electronic Component Application Consideration for Space Vehicles,*" Hughes Aircraft Co., Components and Materials Laboratory, Culver City, Calif., Hughes Aircraft Special Research Study No. 424, May 15, 1961.

7. Lehr, S. N., Tronolone, B. J., and Horton, P. V., "*Equipment Design Consideration for Space Environment,*" Space Technology Laboratories, Inc., Redondo Beach, Calif. TR-60-0000-09224, September 1960.

8. Acker, R. M., Lipkis, R. P., and Vehrencamp, J. E., "*Temperature Control System for the Atlas Able-4 Lunar Satellite,*" Space Technology Laboratories, Inc., Redondo Beach, Calif.

9. Phillips, Charles R., "*Sterilizing Properties of Ethylene Oxide,*" (paper read at symposium on "Recent Developments in the Sterilization of Surgical Materials.") Pharmaceutical Press, 17 Bloomsbury Square, London, W.C.I., April 1961.

10. Plamondon, J. A., "*Thermal Efficiency of Coated Fins,*" Jet Propulsion Laboratory, California Institute of Technology, Pasadena, Calif., April 24, 1961.

11. Stelzriede, M. E., "Optimization of Off-Optimum Operation of Peltier Refrigerators for Space Applications," *Proceedings of the Institute of Environmental Sciences,* National Meeting, pp 253–266, 1961.

12. Lee, D. H., Breshears, R. R., Allen, D., and Wrobel, J. R., "*Applications for Monopropellants in Space Vehicles,*" Jet Propulsion Laboratory, California Institute of Technology, Pasadena, Calif., TR 32-174, October 5, 1961. (Confidential)